V. 120, NO. 5
SEPTEMBER 2023

ACI STRUCTURAL JOURNAL

A JOURNAL OF THE AMERICAN CONCRETE INSTITUTE

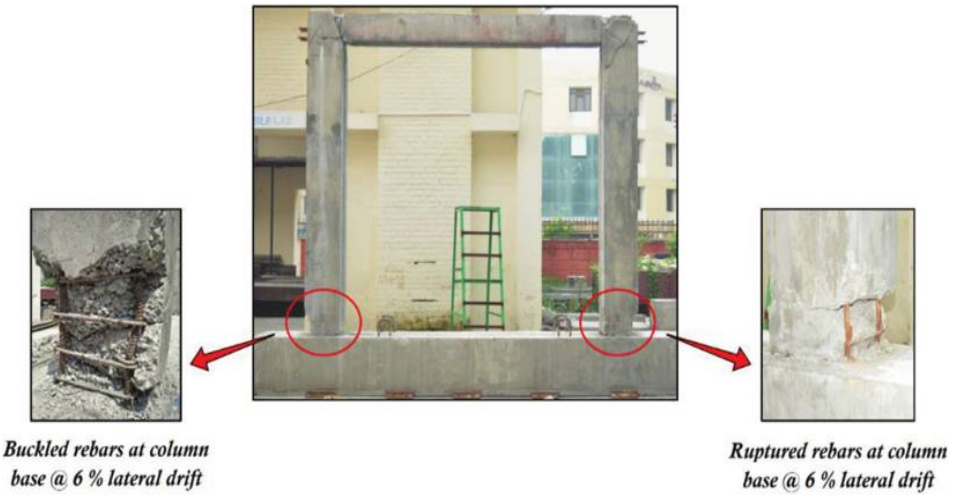

Buckled rebars at column base @ 6 % lateral drift

Ruptured rebars at column base @ 6 % lateral drift

American Concrete Institute

CONTENTS

ACI Structural Journal

September 2023, V. 120, No. 5

A JOURNAL OF THE AMERICAN CONCRETE INSTITUTE
AN INTERNATIONAL TECHNICAL SOCIETY

Contents continued on next page

Discussion is welcomed for all materials published in this issue and will appear ten months from this journal's date if the discussion is received within four months of the paper's print publication. Discussion of material received after specified dates will be considered individually for publication or private response. ACI Standards published in ACI Journals for public comment have discussion due dates printed with the Standard.

The *ACI Structural Journal* (ISSN 0889-3241) is published bimonthly by the American Concrete Institute. Publication office: 38800 Country Club Drive, Farmington Hills, MI 48331. Periodicals postage paid at Farmington, MI, and at additional mailing offices. Subscription rates: $192 per year, payable in advance. POSTMASTER: Send address changes to: *ACI Structural Journal*, 38800 Country Club Drive, Farmington Hills, MI 48331.

Canadian GST: R 1226213149.

Direct correspondence to 38800 Country Club Drive, Farmington Hills, MI 48331. Telephone: +1.248.848.3700. Facsimile (FAX): +1.248.848.3701. **Website: http://www.concrete.org.**

MEETINGS

SEPTEMBER

17-20—17th International Congress on Polymers in Concrete (ICPIC 2023), Warsaw, Poland, https://icpic23.org

17-20—4th Fiber Reinforced Concrete International ACI-fib-RILEM Joint Workshop: from Design to Structural Applications, Tempe, AZ, www.rilem.net/agenda/4th-fiber-reinforced-concreteinternational-aci-fib-rilem-joint-workshop-from-design-tostructural-applications-1537

18-22—16th International Congress on the Chemistry of Cement 2023 (ICCC 2023), Bangkok, Thailand, www.iccc2023.org

25-29—2nd Conference of the European Association on Quality Control of Bridges and Structures – EUROSTRUCT 2023, Vienna, Austria, https://eurostruct.org/eurostruct-2023

26-29—Greenbuild 2023: Building Transformation, Washington, DC, https://greenbuild.informaconnect.com/2023

27-30—ASCC 2023 Annual Conference, Grand Rapids, MI, https://ascconline.site-ym.com/event/ac2023

28-30—2023 Concrete NZ Conference, Hamilton, New Zealand, https://confer.eventsair.com/concretenz-conference-2023

OCTOBER

6-9—2023 APA Annual Convention, Delray Beach, FL, www.archprecast.org/annual-convention

9-11—Dni Betonu 2023, Wisła, Poland, www.dnibetonu.com/en

12-14—National Academy of Construction Annual Meeting, Boston, MA, www.naocon.org/annual-meetings

12-14—NPCA 58th Annual Convention, Oklahoma City, OK, https://precast.org/convention/

18-19—BUILDEX Alberta, Calgary, AB, Canada, www.buildexalberta.com

25-27—2023 Decarbonization Conference for the Built Environment, Washington, DC, www.ashrae.org/conferences/topical-conferences/2023-decarbonization-conference-for-the-built-environment

ACI CONCRETE CONVENTION: FUTURE DATES

2023—Oct. 29-Nov. 2, Westin Boston Seaport District & Boston Convention and Exhibition Center, Boston, MA
2024—March 24-28, Hyatt Regency New Orleans, New Orleans, LA
2024—November 3-7, Philadelphia Marriott Downtown, Philadelphia, PA
2025—Mar. 30-Apr. 3, Sheraton Centre Toronto Hotel, Toronto, ON, Canada

For additional information, contact:
Event Services, ACI
38800 Country Club Drive
Farmington Hills, MI 48331
Telephone: +1.248.848.3795
email: conventions@concrete.org

ON COVER: 120-S79, p. 29, Fig. 11—Damaged model frame after preliminary test.

Contributions to *ACI Structural Journal*

The *ACI Structural Journal* is an open forum on concrete technology and papers related to this field are always welcome. All material submitted for possible publication must meet the requirements of the "American Concrete Institute Publication Policy" and "Author Guidelines and Submission Procedures." Prospective authors should request a copy of the Policy and Guidelines from ACI or visit ACI's website at **www.concrete.org** prior to submitting contributions.

Papers reporting research must include a statement indicating the significance of the research.

The Institute reserves the right to return, without review, contributions not meeting the requirements of the Publication Policy.

All materials conforming to the Policy requirements will be reviewed for editorial quality and technical content, and every effort will be made to put all acceptable papers into the information channel. However, potentially good papers may be returned to authors when it is not possible to publish them in a reasonable time.

Discussion

All technical material appearing in the *ACI Structural Journal* may be discussed. If the deadline indicated on the contents page is observed, discussion can appear in the designated issue. Discussion should be complete and ready for publication, including finished, reproducible illustrations. Discussion must be confined to the scope of the paper and meet the ACI Publication Policy.

Follow the style of the current issue. Be brief—1800 words of double spaced, typewritten copy, including illustrations and tables, is maximum. Count illustrations and tables as 300 words each and submit them on individual sheets. As an approximation, 1 page of text is about 300 words. Submit one original typescript on 8-1/2 x 11 plain white paper, use 1 in. margins, and include two good quality copies of the entire discussion. References should be complete. Do not repeat references cited in original paper; cite them by original number. Closures responding to a single discussion should not exceed 1800-word equivalents in length, and to multiple discussions, approximately one half of the combined lengths of all discussions. Closures are published together with the discussions.

Discuss the paper, not some new or outside work on the same subject. Use references wherever possible instead of repeating available information.

Discussion offered for publication should offer some benefit to the general reader. Discussion which does not meet this requirement will be returned or referred to the author for private reply.

Send manuscripts to:
http://mc.manuscriptcentral.com/aci

Send discussions to:
Journals.Manuscripts@concrete.org

ACI STRUCTURAL JOURNAL TECHNICAL PAPER

Title No. 120-S78

Ultra-High-Toughness Concrete Retrofitted Boundary Column Shear Walls: Tests and Capacity Prediction

by Hongmei Zhang, Giorgio Monti, Yuanfeng Duan, Zhiyuan Chen, and Chen Gu

The rapid growth of the construction industry in Asia and the consequent updating of design specifications put forward higher performance requirements for structural components, which results in a large number of existing shear walls that are not compliant with the current seismic standards. A prospective retrofitting method, which is based on replacing the existing boundary concrete or attaching external boundary columns to nonconforming shear walls, is experimentally studied. Four shear-wall specimens were designed according to the current Chinese design code: one using plain concrete boundary columns and three using ultra-high-toughness boundary columns (UHTBCs), adopting three different strengthening strategies relevant to the boundary size and the connection form. Cyclic performance, damage patterns due to UHTBCs, and connection form are discussed based on the experimental results, from which it was ascertained that shear walls with UHTBCs show improved seismic performance, compatible with the requirements of the current seismic design code, even for the reduced-boundary UHTBCs and non-connection specimens. The predictive equation for the sectional moment capacity of shear walls with UHTBCs was discussed as a practical tool for retrofitting applications. This study highlights the most important features of a rapid retrofitting measure to improve the resilience of existing nonconforming shear-wall structures, while also proving to be an effective measure for newly constructed structures.

Keywords: boundary columns; cyclic loading test; retrofitting; seismic performance; shear wall; ultra-high-toughness.

INTRODUCTION

Background

Reinforced concrete (RC) shear walls are widely used in mid- and high-rise structures as seismic-resistant elements. Under the combined action of flexure, shear, and torsion, the damage tends to concentrate in the outer boundary zones of RC shear walls (Mutō 1969; Zhang et al. 2014). Cracked concrete weakens its compression capacity, which in turn expedites concrete crushing, leading to the failure of the shear walls (Fischer and Li 2002a; Zhang et al. 2014). This shear and flexure interaction combined with local damage makes retrofitting of such shear walls a challenging endeavor.

To improve the flexural and shear performance of existing and newly constructed shear walls, different retrofit strategies have been conceived—for example, the insertion of RC boundary columns (Al-Gemeel and Zhuge 2019), attaching a steel profile (Chrysanidis and Tegos 2020), or even enlarging the boundary elements. Attaching a steel profile to an existing concrete structure involves serious problems of effective collaboration and bond durability (Zhou et al. 2010). Inserting additional jacketed concrete columns increases the initial dimensions (Woods et al. 2016); besides, it presents the problem of transferring the bending action from the existing to the new elements (Woods et al. 2016).

Fiber-reinforced concrete (FRC) exhibited excellent strength, toughness, and damage tolerance (Li et al. 2001; Boshoff et al. 2009) due to crack prevention and strain-hardening effects. Fischer and Li (2002a) emphasized that the most important impact of high-performance FRC composites on the structural response is to maintain the integrity of and provide lateral stability to steel reinforcements, thereby ensuring adequate cyclic inelastic deformation and energy dissipation. Experiments involving columns (Mirmiran and Shahawy 1997; Fischer and Li 2002a, 2003), beams (Li and Xu 2009; Prota et al. 2004), and beam-column joints (Parra-Montesinos 2005; Prota et al. 2004) have proved that structural elements with FRC exhibit improved seismic resistance. The bridging effect helps the structural elements maintain the lateral bearing capacity (Naaman and Najm 1991) and alleviate damage evolution (Fischer and Li 2002b). Thanks to the high tensile-strength-to-weight ratio and durability, FRC is ideal for repairing and retrofitting infrastructures and historical buildings (Mustafaraj et al. 2020). Other authors (Xu et al. 2012; Li et al. 2009) proposed ultra-high-toughness cementitious composites (UHTCCs) containing high-strength short fibers, which showed excellent performance in bending elements and proved to be a viable alternative to plain concrete, thanks to their strain-hardening behavior and simple applicability to existing structural elements.

Applying FRC composites to improve the flexural capacity of shear walls has recently attracted research interest (Parra-Montesinos 2005; Parra-Montesinos et al. 2006; Dazio et al. 2008; Olsen and Billington 2011; Li et al. 2014), where the positive effects on the seismic performance were demonstrated. FRC composites are also considered to apply in shear-wall retrofitting (Kesner and Billington 2005; Liang et al. 2013; Dang et al. 2014; Lu et al. 2018; Zhang et al. 2020).

RESEARCH SIGNIFICANCE

In most of the existing shear walls constructed before 2001, due to material deterioration and old specification-based

ACI Structural Journal, V. 120, No. 5, September 2023.

MS No. S-2021-064.R5, doi: 10.14359/51738829, received July 15, 2022, and reviewed under Institute publication policies.

Table 1—Specimen parameters

Specimens	Section, mm	Cast-in-place concrete	Boundary columns width, material	Axial compressive force	Boundary columns longitudinal reinforcement	Longitudinal reinforcement in core wall	Boundary columns stirrups	Transverse reinforcement
SW-1	2000 x 1000 x 125	C40	200 mm, plain concrete	600 kN	HRB400_D10	2 x 5ϕ6	ϕ6@80	ϕ6@125
UCSW-2			200 mm, UHTCC					
UCSW-3			150 mm, UHTCC		HRB400_D10	2 x 6ϕ6		
UCSW-4								

designs, the bending capacity may not conform to current specifications. Besides, the application of strengthening measures is often impeded by limited available space. In this study, an alternative seismic strengthening method using ultra-high-toughness boundary columns (UHTBCs) on noncompliant shear walls with weak moment capacity is presented. With this scope, four shear walls—one of plain concrete representing the current seismic design code (as a reference specimen), two UHTBC shear walls with equal and reduced boundary elements, respectively (as strengthened specimens by inserting additional elements or replacing the boundary concrete), and one UHTBC shear wall without shear connections (representing a case of rapid retrofitting)—were cyclically tested to validate the corresponding strengthening strategies.

This study provides in-depth considerations on this rapid strengthening measure that proved to be effective in retrofitting slender shear walls, through the effective use of a high-performance material, with the significant advantage that the overall wall configuration is only slightly affected. Furthermore, it also improves the bending capacity without damaging the inner portions. The UHTBCs can be prefabricated and assembled on site, and even replaced at a later stage if needed. The developed predictive equation of the moment capacity also provides a reference for design.

EXPERIMENTAL TESTS

Specimen design

The experimental shear-wall specimens were designed referring to an existing high-rise building built in the 1990s in Shanghai in a second-category seismic site. In this area, the earthquake intensity level is Grade 7, which corresponds to a design peak ground acceleration (PGA) = 0.35*g* (*g* is gravity acceleration) having an exceedance probability of 10% in 50 years. A half-scale shear wall (SW-1) was designed and constructed with plain concrete as a reference wall, representing the shear wall satisfying the current seismic design code (GB 50011-2010 [2010]). Three half-scale shear-wall specimens (UCSW-2, UCSW-3, and UCSW-4) were designed with the same geometry and reinforcement as the reference shear wall but strengthened with UHTBCs. For all specimens, the 1:2 scale factor applies to all geometry quantities, while the materials are designed to be the same as in the original structure. Therefore, the load-bearing capacity is 1:4 of the original structure. Detailed descriptions of the specimens are presented in Table 1. The boundary column lengths of SW-1 and UCSW-2 were 200 mm, and those of UCSW-3 and UCSW-4 were 150 mm. The experiments were conducted in the State Key Laboratory of Disaster Reduction in Civil Engineering at Tongji University, Shanghai, China.

The specimen configurations and details are shown in Fig. 1. The boundary columns of Specimens UCSW-2 to UCSW-4 were cast with UHTCC. The RC core wall, top beam, and foundation were cast with plain concrete. Except for the boundary column type, UCSW-2 was identical to SW-1, which was tested to determine the effect of the UHTBCs on the seismic performance. UCSW-3 was designed with reduced boundary column widths and longitudinal bars to investigate the possibility of reduced boundary columns. For Specimens UCSW-2 and UCSW-3, there were key slots and shear reinforcing bars for connection to the inner core wall. Half-grouted sleeve connections were used to connect the longitudinal bars of the UHTBC elements and the RC foundation (JG/T 398-2012 [2012]). No connection was set for Specimen UCSW-4, which was designed to explore the possibility of no-connection retrofitting for ancient and protected buildings.

Material properties

The UHTCC used in the boundary columns of the tested shear walls was composed of: PO 52.5 cement, fly ash, silica fume, and fine sand; water-reducing additive; water; and high-strength polyvinyl alcohol (PVA) fibers (fiber content: 2%). The literature demonstrates that, as multiple cracking phenomena occur, UHTCC exhibits tensile strain-hardening behavior and attains a maximum strain capacity larger than 0.03, even with typical fiber volume fractions of 2% or less (Xu and Cai 2010; Li et al. 2009). The main properties of the high-strength PVA fibers include: length = 12 mm; diameter = 39 μm; tensile strength f_{tc} = 1620 MPa; tensile modulus of elasticity E_f = 42.8 GPa; ultimate strain = 0.07; and density = 1.3 g/cm^3.

Figure 2 shows the specimens and test views of dog-bone-shaped UHTCC specimens for tensile strength and cubic specimens of both plain concrete and UHTCC for compressive strength. Figures 3(a) and (b) show the stress-strain curves of the tested material specimens. The main properties, including the elastic modulus and compressive strength of the plain concrete and UHTCC, are presented in Table 2. Longitudinal reinforcement to the boundary columns was formed from HRB400, and the main material properties of

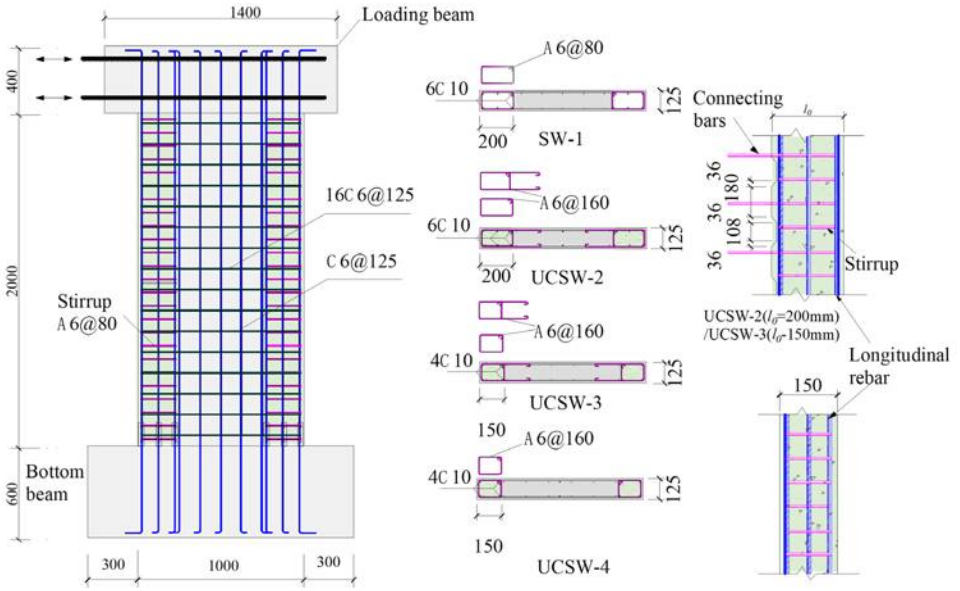

Fig. 1—Configuration details of tested shear walls.

Fig. 2—Dog-bone tensile and cubic compressive tests: (a) dog-bone-shaped specimen and tensile test; (b) UHTCC specimen; and (c) plain concrete specimen.

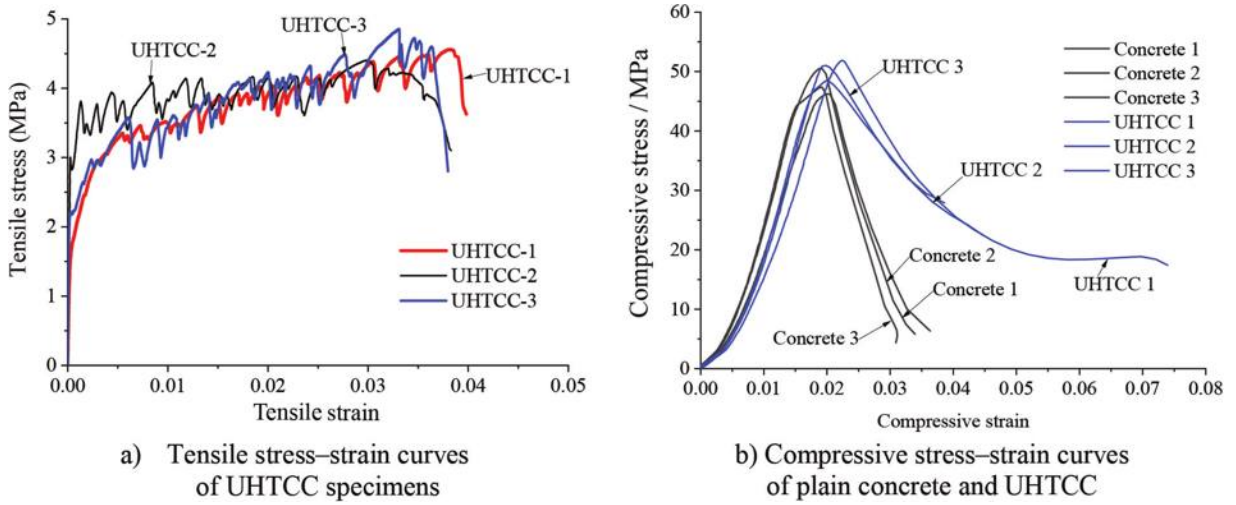

Fig. 3—Tensile and compressive properties of plain concrete and UHTCC.

the reinforcing bars are presented in Table 3. The Young's modulus is between 205 and 210 GPa.

The dog-bone-shaped specimens are 250 mm in length, 60 mm in width, and 13 mm in thickness, with an efficient testing length and width of 80 mm and 30 mm, respectively.

As Fig. 3(a) shows, the three dog-bone-shaped specimens show higher toughness. The tensile ultimate strain is over 0.03, which is significantly higher than that of plain concrete, typically assumed as zero. The compressive stress-strain curve was tested on cubic specimens of 150 mm sides, while the elastic modulus is obtained on 150 x 150 x 300 mm prismatic specimens. This study confirms the typically ascertained literature finding that fibers have a positive effect on the tensile strength, thanks to the beneficial crack prevention effect. It is also shown that larger fiber fractions may affect the compressive strength (Xu and Cai 2010), whereas the compressive toughness improves, thanks to the fiber bridging effect shown in Fig. 3(b).

As shown in Fig. 4, steel sleeves were employed to connect the UHTBC elements and the bottom beam. This method was confirmed to be reliable in a previous study (Dazio et al. 2008) and used to connect the retrofitted boundary columns. The tube is made of Q235 steel, which is plain carbon structural steel with a yield strength of approximately 235 MPa, and is filled with super-high-strength (≥60 MPa) non-shrink cement-based grouting material, with a grip strength of ≥4 MPa, to connect longitudinal C10 steel bars used in the boundary columns. Tensile tests of the three steel bar connection specimens were conducted before using them in the boundary elements, as shown in Fig. 4. The three specimens showed ductile behavior by steel bar necking outside the steel sleeve until breaking. This indicated that the half-grouted sleeve connection effectively transferred tensile force between the upper and lower steel bars.

The shear-wall specimens were manufactured based on the material test results. Pictures of the specimen manufacturing process are shown in Fig. 5, including the main ingredients, the mixed cement, boundary column casting, and the testing view of the specimens.

Test setup and loading program

The test setup was composed of a horizontal loading system, a vertical loading system, and a measurement system. The lateral load was applied by a horizontal servo-actuator (with a load capacity of 630 kN). The lateral load was applied to one end of the top beam by the actuator through four steel screw rods with two steel plates attached to the loading side. The vertical load was applied to the top beam by three hydraulic jacks. Rollers were used at the top of the jacks to reduce the friction of the reaction frame, as shown in Fig. 5(c). The lateral and vertical forces acting on the specimens were balanced by the reaction force of the bottom beam anchored to the foundation.

The loading scheme was designed according to the specifications of the Chinese standard JGJ/T 101-2015 (2015). Before the lateral load was applied, 40 to 60% of the designed vertical load was applied and removed three times to eliminate possible imperfections in the specimens. Subsequently,

Table 2—Properties of concrete from tests

Material	Cubic compressive strength f_{cu}, MPa	Cylinder compressive strength f_c, MPa	Elastic modulus E_c, MPa	Tensile strength f_t, MPa
Plain concrete	48.0	39.4	34,213	—
UHTCC	50.5	49.1	34,626	4.5

Table 3—Properties of HRB400 steel reinforcing bars from tests

Reinforcing bar	Yield strength, MPa	Yield strain	Ultimate strength, MPa	Ultimate strain	Elastic modulus, GPa
HRB400_D6	501	0.00235	539	0.0242	213
HRB400_D6	466	0.00224	598	0.1165	210

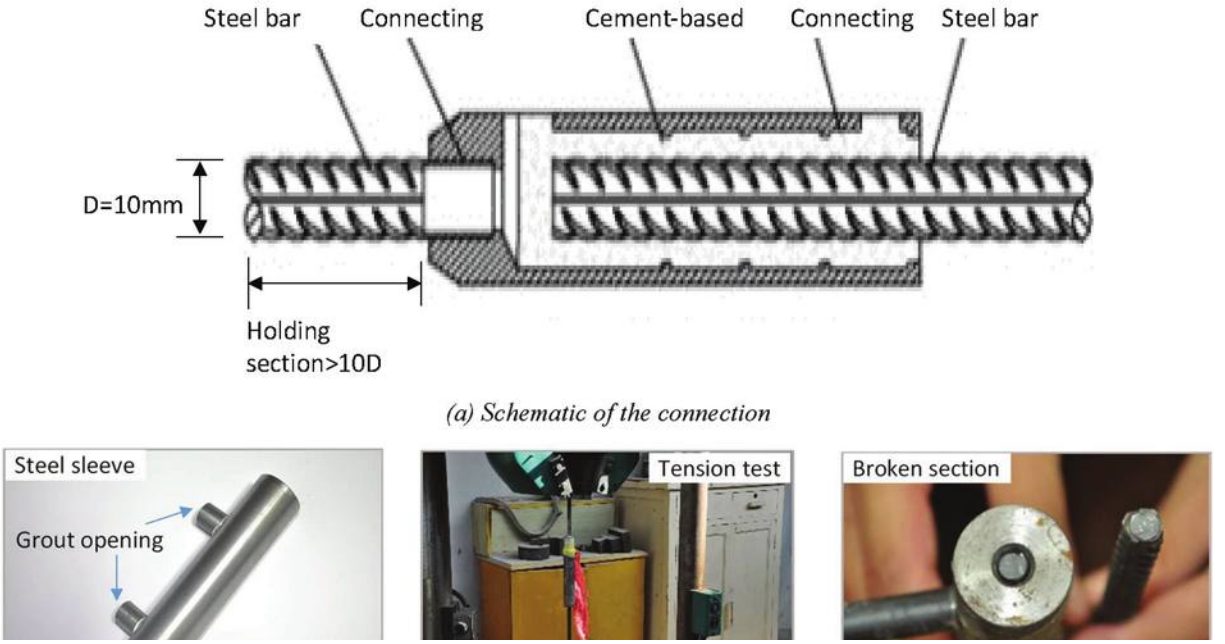

Fig. 4—Half-grouted steel sleeve connection.

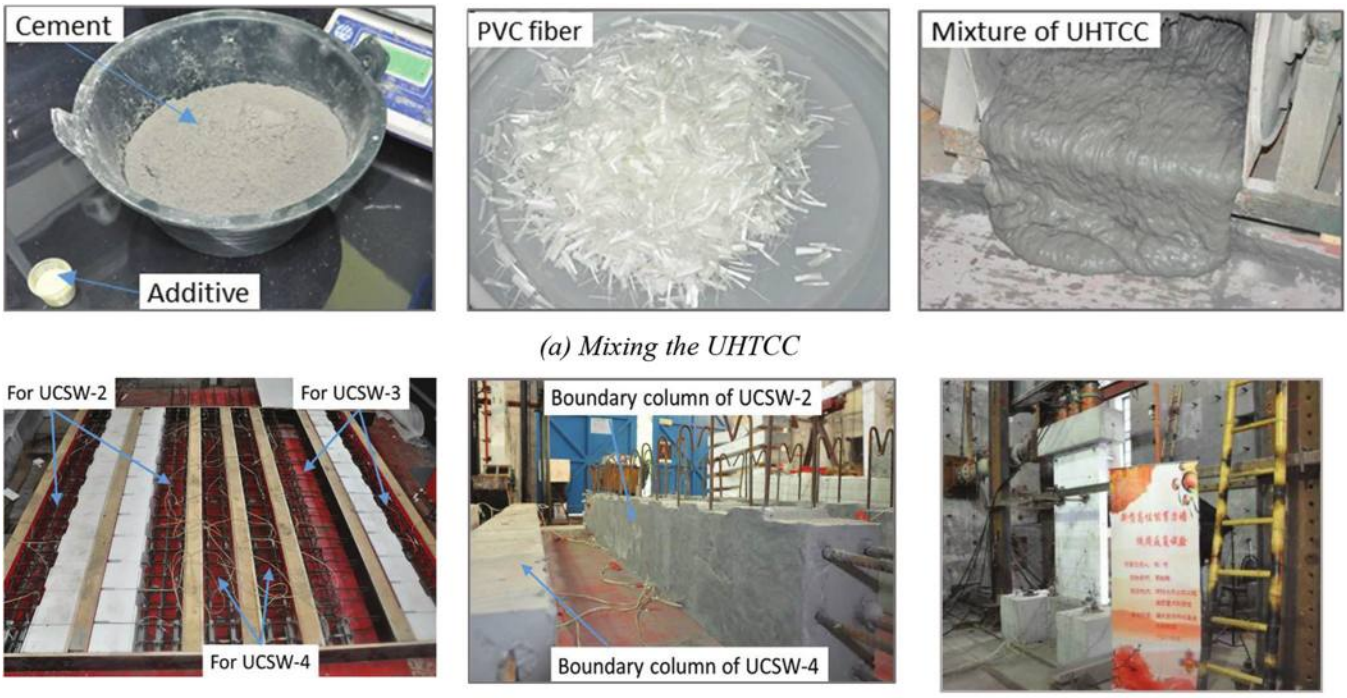

Fig. 5—Construction sequence of boundary columns and testing view.

the designed vertical load was applied and kept constant, and then the lateral load was applied according to a cyclic loading scheme. The loading sequence is designed as single cycles with a 1 mm displacement increment before the specimen yielded, followed by triplets of cycles with a 2 mm increment. Such a loading sequence allows for identifying the response envelope with good accuracy, and, at the same time, ascertaining both the global pinching effect and the local degradation effects of repeated cycles. The loading was terminated either when significant concrete crushing occurred at the corner or when the reinforcing bar buckled.

Linear variable differential transformers (LVDTs) were used to record the deformation of the shear walls, and strain gauges were attached to the reinforcing bars to monitor the strain development during the loading procedure. Forces were measured through load cells. All data were recorded by an automatic data acquisition system.

TEST RESULTS

Failure process and modes

The different patterns of concrete cracking and crushing at failure are shown in Fig. 6. Failure was defined as an 85% decrease in the lateral-force peak value. As shown in Fig. 6, UCSW-2 exhibited much richer cracks than SW-1, and most of them were horizontal orientation. Concrete crushing was observed at the corner of the plain core wall, which was finer and denser than that in SW-1. Fewer cracks were observed in UCSW-3 than in UCSW-2. The concrete-crushing areas of these two specimens were significantly smaller than those of SW-1. In contrast to UCSW-3, the cracks were horizontal for UCSW-4; additionally, the concrete at the corner of the core wall was seriously damaged at failure.

Bearing and deformation behavior

The hysteresis curves (obtained through load cells applied on the actuator and through LVDTs for the displacements) and crack development are shown in Fig. 7. In this case, the yield point was the cross point determined by the peak value and the secant line when the lateral load increased to 75% of the peak force; the failure was defined either at the 85% decrease of the lateral-force peak value or when the edge steel bars broke, whichever was less. The lateral loads and the corresponding lateral displacements at the yield, peak, and ultimate states are presented in Table 4. The lateral bearing forces at different drift ratios (1/500, 1/200, 1/100, and 1/50) are presented in Fig. 7.

As shown in Fig. 7 and Table 4, UCSW-2 showed a larger capacity at failure than SW-1. With the contribution of the UHTBCs, the hysteresis loops were enlarged, exhibiting constant growth. During the cyclic loading procedure, the lateral force and deformation are theoretically symmetric on the pull and push sides. However, the actual response turns out to be not perfectly symmetrical because, after the first semi-cycle, the specimen is already damaged when pushed toward the opposite direction. Thus, this slightly different behavior was regularized by averaging the values obtained on the two opposite semi-cycles. The lateral force and the corresponding lateral displacement of UCSW-2 were larger than those of SW-1 by 14% and 8% at failure, respectively. The lateral force of UCSW-2 was higher than that of SW-1, particularly in the "serious damage" to "no collapse" states. The strength results at different drift ratios also indicate that UCSW-2 maintained a good resistance capacity even when the lateral drift ratio was 1/50. Owing to the contribution of the UHTBCs, the shear wall exhibited an enhanced lateral bearing capacity and ductility.

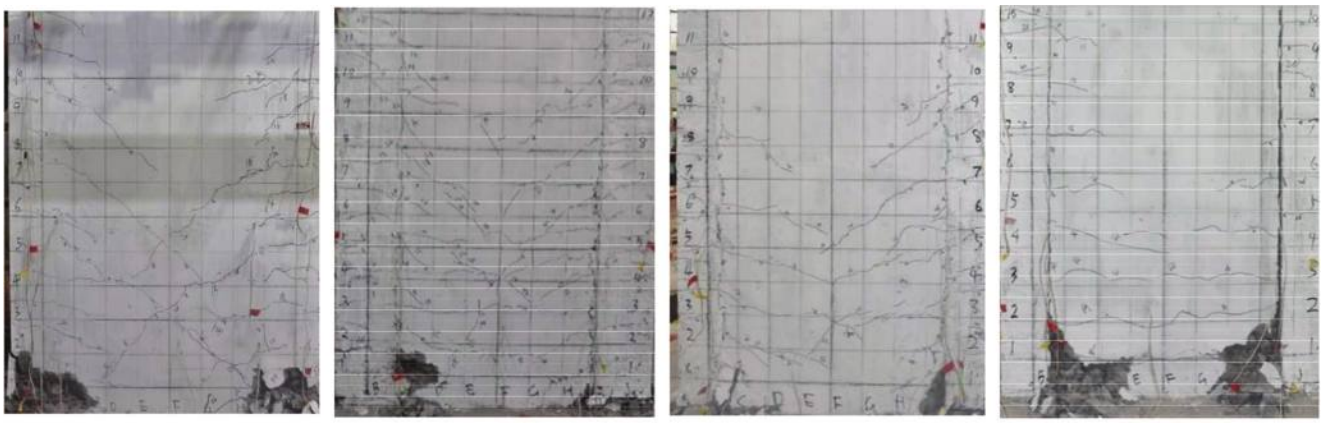

a) SW-1 (loading to 44 mm) b) UCSW-2 (loading to 50 mm) c) UCSW-3 (loading to 50 mm) d) UCSW-4 (loading to 56 mm)

Fig. 6—Failure modes and crack patterns of specimens.

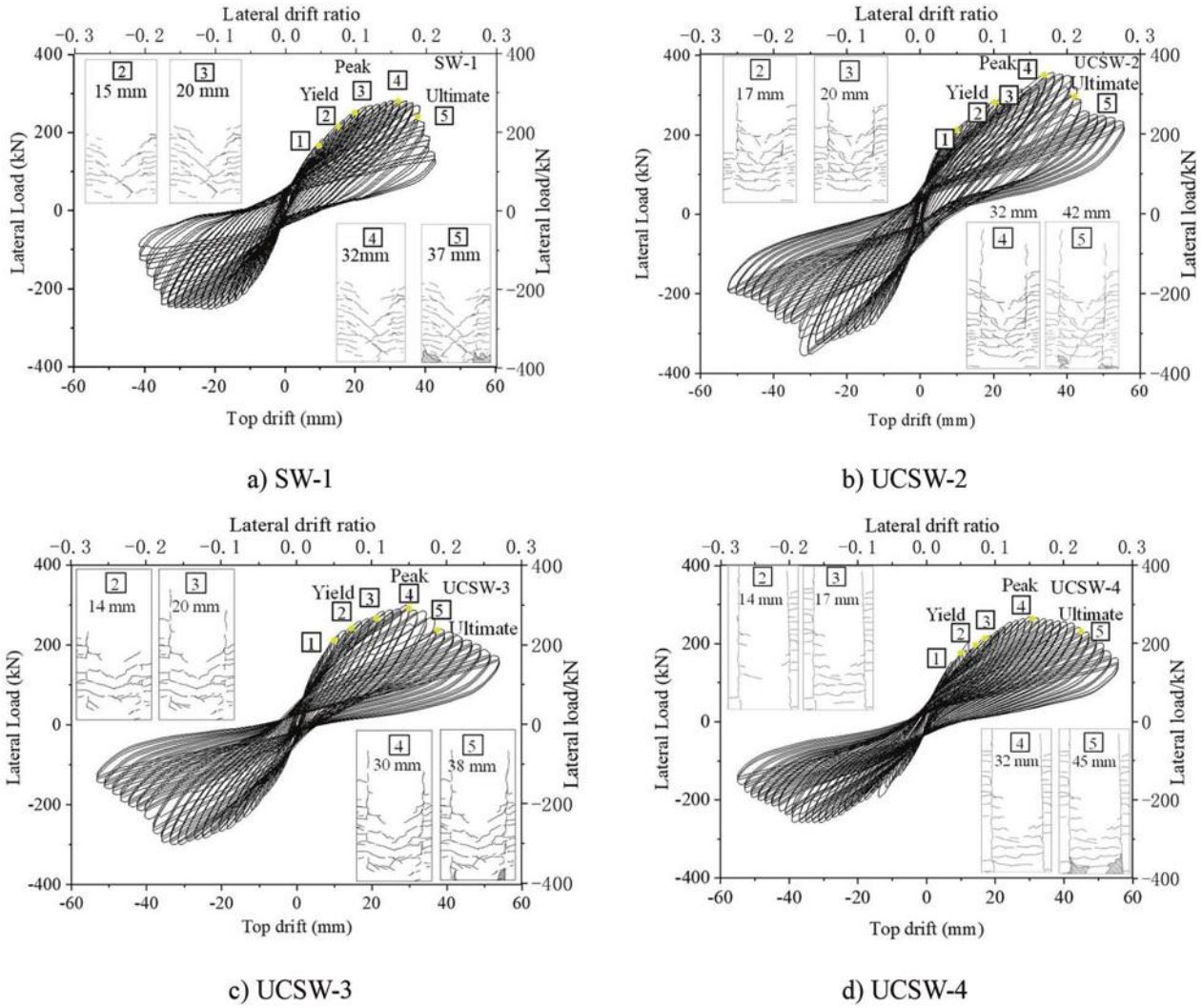

Fig. 7—Hysteresis curves and evolving crack pattern.

UCSW-3 exhibited higher initial stiffness, larger peak lateral bearing force, and higher stiffness than SW-1, although the confined length was smaller than that for SW-1. Additionally, the number of longitudinal steel bars in the confined boundary columns was reduced. The hysteresis loops of UCSW-3 were still well rounded and developed more gradually compared with SW-1 and close to UCSW-2. The lateral force of UCSW-3 in the peak state was increased by 12% compared with SW-1. As shown in Fig. 7, the lateral bearing force was almost identical to that of UCSW-2 before the

Table 4—Critical points of lateral force and deformation characteristics

Specimen	Loading direction	Yield		Peak		Ultimate	
		Δ_y, mm	F_y, kN	Δ_m, mm	F_m, kN	Δ_u, mm	F_u, kN
SW-1	Push	17	240	32	285	38	270
	Pull	13	225	33	252	36	246
	Average	15	232	32	269	37	258
UCSW-2	Push	19	283	36	328	45	279
	Pull	14	282	28	328	38	279
	Average	17	282	32	328	42	279
UCSW-3	Push	13	241	30	298	37	254
	Pull	15	255	30	303	38	257
	Average	14	248	30	301	38	256
UCSW-4	Push	15	222	33	267	46	227
	Pull	19	226	31	260	43	221
	Average	17	224	32	264	45	224

specimen was seriously damaged, and it decreased marginally faster than that of UCSW-2 near the "no collapse" stage. This indicates that the seismic performance of UCSW-3 satisfied the requirements of the current seismic design code.

Moreover, the specimen with a weak connection (UCSW-4) exhibited high toughness and collapse-resistance capacity in the experiment. Although the lateral force of UCSW-4 was smaller than those of UCSW-2 and UCSW-3 before the drift ratio reached 1/100, it was not smaller than that of SW-1. The lateral bearing force of UCSW-4 at a drift ratio of 1/50 was 34.3% and 5.6% larger than those of SW-1 and UCSW-3, respectively. The results indicate that the seismic performance was significantly improved through the connection-strengthening strategy involving UHTBCs, particularly in the large-deformation stage.

The hysteresis curves of Specimens UCSW-2, -3, and -4 show a pinching effect caused by slippage occurring at the interface between the boundary columns and core wall. As demonstrated by other authors (for example, Park [2006] and Sørensen et al. [2017a,b]), shear keys can be prevented from slipping by adopting concrete key slots and shear reinforcing bars, which, however, show different damage modes while differently affecting the shearing capacity. In this study, Specimens UCSW-2 and -3 have shear key slots and shearing reinforcing bars, as shown in Fig. 8(a). The shear reinforcing bars are placed at 160 mm spacing. Specimen UCSW-4 is constructed directly by precast and on-site cast concrete, as shown in Fig. 8(b). In principle, under shear force, the concrete shear strength at the interface is firstly overcome, then the concrete key slots and shear reinforcing bars continue to bear the shear force. In the tests, the interfaces of Specimens UCSW-2 and UCSW-3 slightly cracked along the key, indicating that key slots and shear reinforcing bars play an important role in the ultimate state and that they are activated after concrete cracks. The pinching effect is more significant for UCSW-4 because there are no connecting bars to resist shear. After the shear strength is overcome and the concrete cracks, the aggregate interlock contribution is weak and, without the reinforcing bars' dowel action, shear cannot be transferred between the boundary columns and core wall, which eventually end up carrying the horizontal force independently. To obtain an improved energy dissipation effect, connecting shear keys are essential (Park 2006).

Crack development

The toughness of FRC composites is essentially due to the cracking prevention by the bridging effect of the fibers. For this reason, the crack growth during the experiment was investigated. Figure 9 shows the crack distribution profile of each specimen at the yield, peak, and ultimate states and at drift ratios of 1/200 (~10 mm) and 1/100 (~20 mm), around which is approximately "medium damage" and "serious damage." The fractal index D (Mandelbrot 1982), as in Eq. (1), was used to evaluate the crack distribution as follows

$$D = -\lim_{r \to 0} \frac{\ln N(r)}{\ln r} \tag{1}$$

where r represents the size of a square grid cell; and N represents the number of grids with cracks inside. The vertical cracks appearing at the interface between the boundary column and the core wall are caused by a weak interface connection, which did not significantly impact the final failure and can be improved in actual use; thus, they were disregarded. In addition to the fractal index, the crushing ratio, defined as the crushing area divided by the total shear-wall surface area, was extracted from the images for each specimen and was used to evaluate the concrete-crushing performance at ultimate (Table 5).

Figure 9 reveals smaller horizontal cracks in the UCSW-2 specimen than in SW-1. The fractal indexes of the three UHTBC shear walls were significantly larger than that of SW-1, and the fractal-index growth rate of SW-1 was significantly higher than those of the UHTBC shear walls before the lateral drift ratio reached approximately 1/133. Subsequently, the fractal-index growth rate was lower than those of the UHTBC shear walls. The crushing areas of UCSW-2 and UCSW-3 were significantly reduced compared with

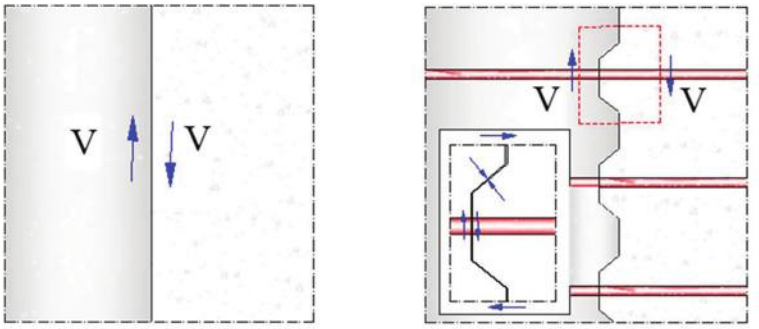

Fig. 8—Schematic of key slots and shear reinforcing bars adopted to improve interface connection between boundary columns and inner core wall, as opposed to simple friction connection.

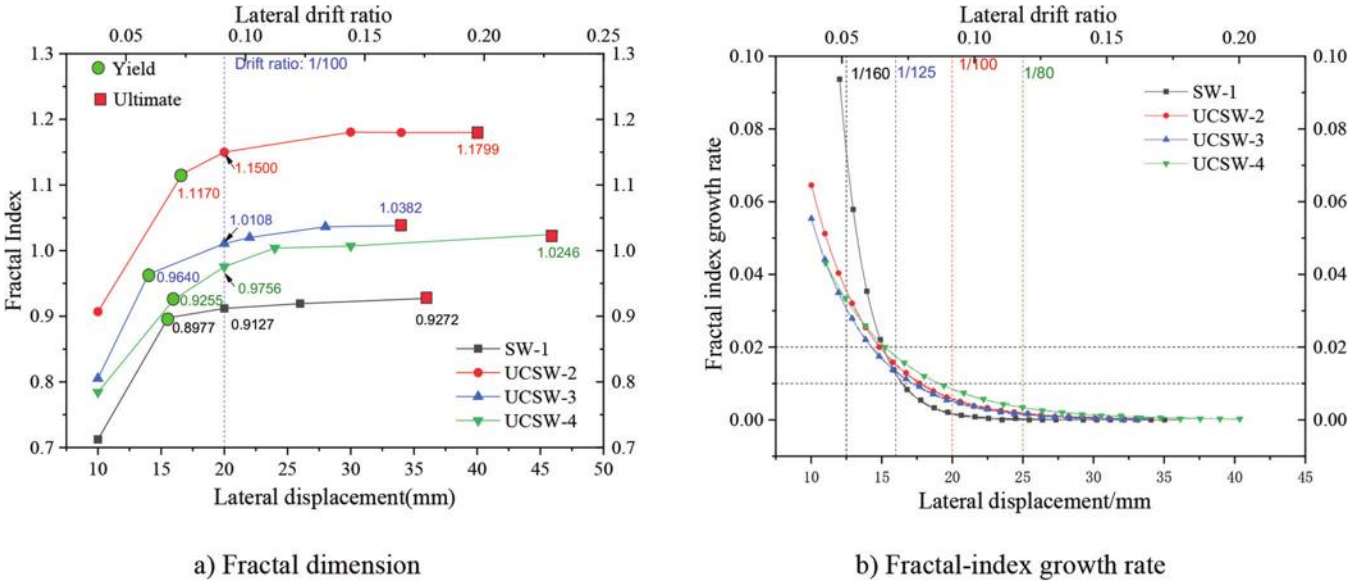

a) Fractal dimension

b) Fractal-index growth rate

Fig. 9—Fractal-index development.

that of SW-1. The small boundary column length specimen (UCSW-3) exhibited a reduced fractal index and growth rate compared with UCSW-2 but significantly higher values than SW-1. The development rate of the fractal index following the early crack formation of UCSW-3 was higher than that of SW-1, indicating that most of the cracks in SW-1 formed earlier than those in UCSW-3. For UCSW-4, the fractal index was larger than that of SW-1, and the growth rate was significantly higher than those of UCSW-3 and SW-1 after the lateral drift ratio exceeded 1/133. Subsequently, the fractal-index growth rate remained higher than those of the other specimens. The displacement of SW-1 was smaller than those of the other UHTBC specimens when the fractal-index growth rate decreased to 0.01, whereas that of UCSW-4 was significantly larger.

As shown in Fig. 9, the high toughness of the UHTBCs mitigated the damage concentration and prevented rapid crack development and local concrete crushing, which resulted in the constant production of new local fine cracks. The reduction in concrete damage can also be explained by the mitigation of the high toughness of the UHTBC elements. Despite the smaller edge-confined length and fewer steel bars, the UHTBC shear wall (UCSW-3) exhibited better cracking and a higher damage-prevention capacity than the plain concrete shear wall (SW-1). The weak-connection specimen (UCSW-4) exhibited a remarkable bending behavior and a high crack growth rate in the large-deformation stage. Thanks to the high-toughness columns, early crushing of the weak core wall was prevented. Prior to the failure of the corner of the core wall, the UHTBC elements functioned efficiently.

Table 5—Crushing zone in final stage

Specimen	Crushing area, m^2	Crushing percentage, %
SW-1	0.0532	2.67
UCSW-2	0.0146	0.73
UCSW-3	0.0113	0.56
UCSW-4	0.0609	3.05

Secant stiffness degradation

The secant stiffness in the lateral direction was adopted as the characteristic parameter to evaluate the shear-wall stiffness, which was defined by Eq. (2) as

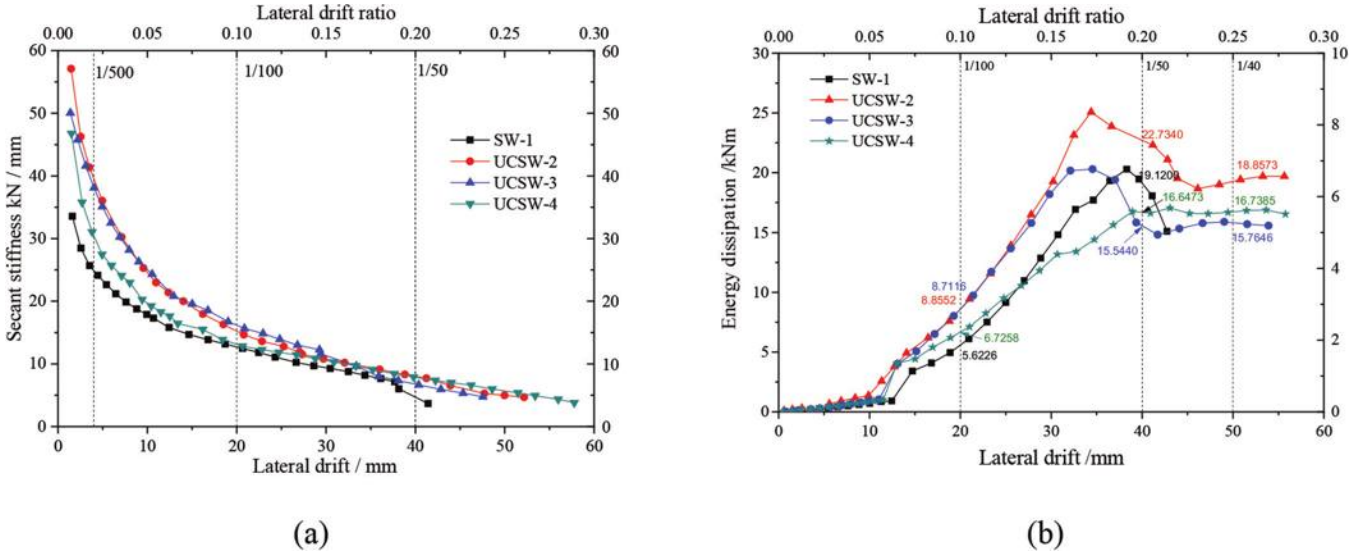

Fig. 10—(a) Secant stiffness; and (b) energy dissipation for single loops.

$$K_i = \frac{|F_i| + |-F_i|}{|\delta_i| + |-\delta_i|} \quad (2)$$

where F_i represents the forward peak lateral force of the i-th circle; δ_i represents the corresponding displacement; and $-F_i$ and $-\delta_i$ represent the corresponding reverse values. The variation in the lateral secant stiffness during the loading sequence is presented in Fig. 10(a). As the lateral load increased, the secant stiffness of each specimen decreased; the reduction was initially rapid and subsequently slowed down. The rapid degradation is attributed to the rapid crack development, as indicated by Fig. 11 and 12.

The lateral secant stiffness values of the UHTBC shear walls were significantly higher than that of the plain concrete shear wall throughout the loading sequence. The secant stiffness of UCSW-2 was significantly higher than that of SW-1 (by 51%, 14%, and 95% at drift ratios of 1/500, 1/100, and 1/50, respectively). This indicates that the fiber-reinforced boundary column specimen had a significantly higher lateral stiffness than SW-1 owing to the resistance to the crack development. For UCSW-3, the foregoing increases relative to SW-1 were 53, 27, and 50%; the lateral secant stiffness values were also significantly higher than those of the plain concrete shear wall. UCSW-4 exhibited a satisfactory remaining lateral stiffness, particularly after the drift ratio reached 1/50. The initial lateral secant stiffness of UCSW-4 was higher than that of SW-1 and marginally higher than that of UCSW-3 after the drift ratio reached 1/50. This indicates that a higher lateral secant stiffness remained to resist collapse in the case of the UHTBC shear wall with a weak connection between the UHTBC elements and the core wall.

Energy dissipation

The dissipation capacity of the FRC composites improves owing to fibers debonding and pullout from the matrix (Parra-Montesinos 2005). In this study, the improvement of FRC composites on dissipated energy is also observed for the increasing lateral displacement.

The energy-dissipation results indicated that the UHTBC elements increased the energy dissipation capacity, particularly in the large-deformation stage. The energy dissipations of UCSW-2 and SW-1 at a drift ratio of 1/100 were 5.62 and 8.85 kN·m, respectively, and those at a drift ratio of 1/50 were 19.12 and 22.73 kN·m, respectively, as shown in Fig. 10(b), which were 57% and 19% higher than those of SW-1 at drift ratios of 1/100 and 1/50.

The reduced boundary column length specimen (UCSW-3, confined length reduced by 25%) exhibited a higher energy dissipation capacity than the plain concrete shear wall. The energy dissipation of UCSW-3 was 55% larger than that of SW-1 at the drift ratio of 1/100.

The bending-mode specimen (UCSW-4, with a weak connection) exhibited better deformation and energy dissipation capacity in the large-deformation stage than the plain concrete shear wall. The hysteresis loop of the energy dissipation of the UCSW-4 specimen expanded gradually, even when the experiment was terminated.

When the lateral drift ratio was less than 1/100, the three UHTBC-strengthened shear walls exhibited higher energy dissipation capacity than the plain concrete boundary column specimens, which can be attributed to the fraction and cracking energy dissipated by the fibers. Furthermore, even with reduced boundary column length and longitudinal bars, UCSW-3 exhibited enhanced energy dissipation compared with the full-length plain concrete specimen, even close to the "no collapse" limit state. When the connection between the boundary column and the core wall was weakened, although the energy-dissipation value was less than the well-connected specimen (UCSW-3), it kept increasing throughout the loading procedure.

SECTIONAL BEARING CAPACITY CALCULATION

The strain development in the lower section (strain gauges above the foundation of 200 mm) is presented in Fig. 11. The horizontal and vertical axes indicate the section length of the shear wall and the strain values measured by the strain gauges, respectively. The lateral displacements of 2, 8, 16, and 32 mm, corresponding to drift ratios of 1/1000, 1/250, 1/125, and 1/62.5, respectively, were compared. The strain gauge on the one side of UCSW-4 failed to get data.

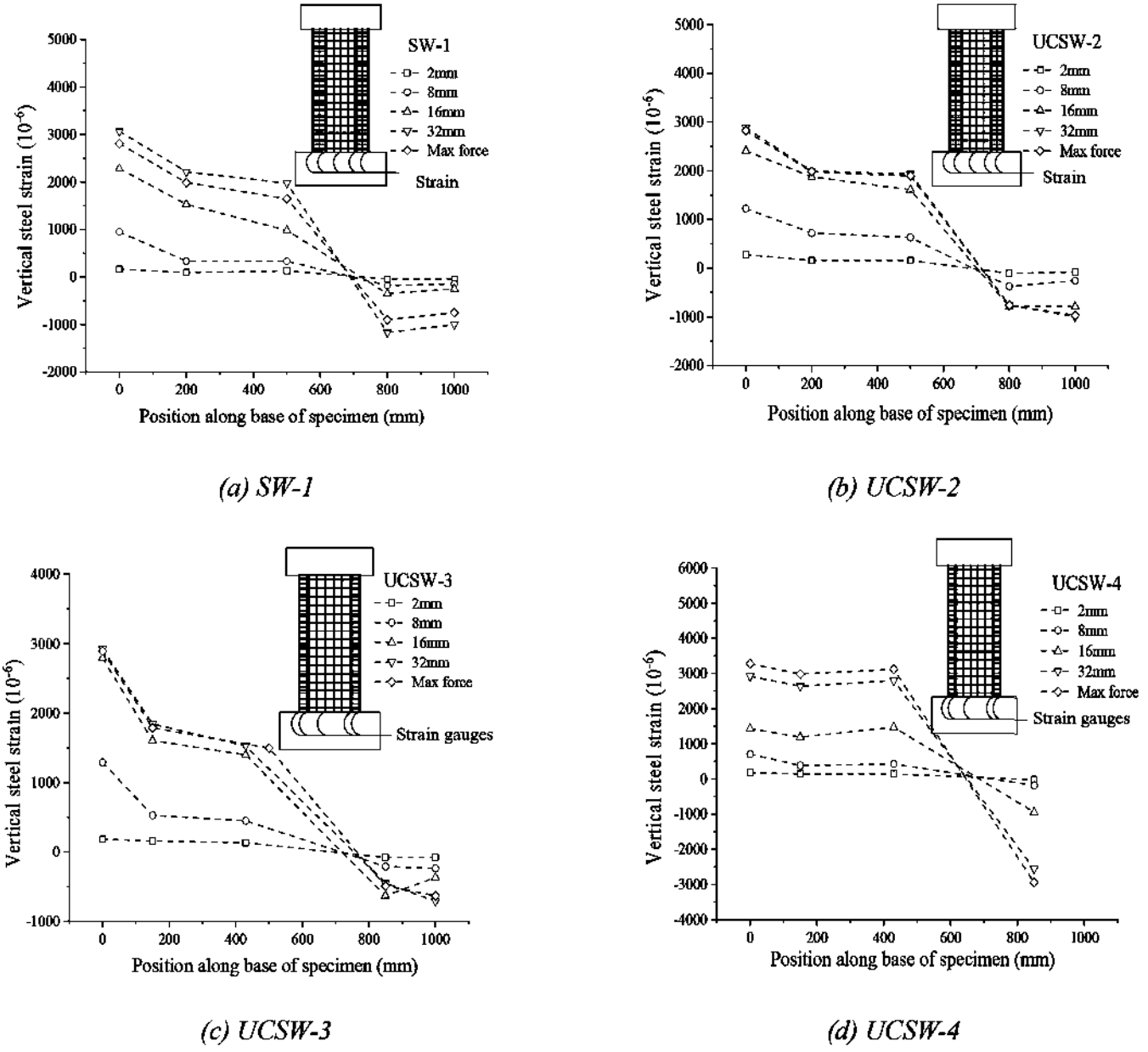

Fig. 11—Section strain distribution along shear-wall length.

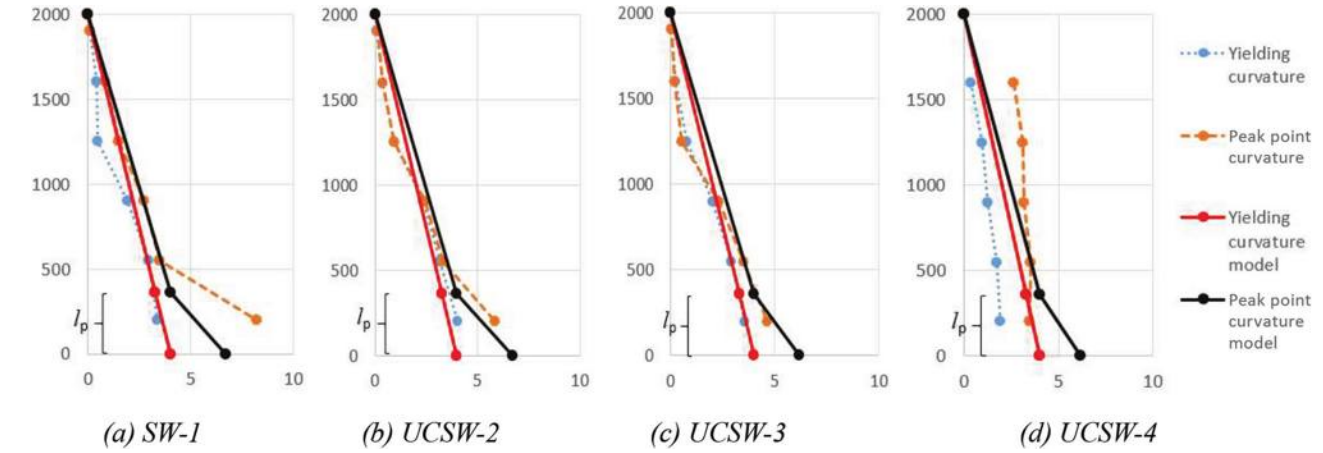

Fig. 12—Curvature and plastic hinge length, compared with model.

As indicated by the vertical strain behavior in Fig. 11, at the peak point state, strain within the confined column on the compression side reached the ultimate compressive stress, and the longitudinal steel bars yielded. Similar to SW-1, the outside longitudinal steel bar on the tension side reached the ultimate strength, and the longitudinal bars in the compressive area yielded at the peak point state for the other shear-wall specimens. The inner vertical strains of the tension-side longitudinal bars for UCSW-2 and UCSW-3 were marginally smaller than those of SW-1 at a lateral displacement of 32 mm (drift ratio of 1/62.5). The strains of UCSW-4 were larger than those of the other specimens owing to the complete bending moment behavior.

Curvature and plastic hinge

Regardless of the bending-shear coupling effect, the flexural displacement can be obtained by integrating the sectional curvature along the height of the wall. Bohl and Adebar (2011) proposed a plastic hinge model accounting for the shear aspect ratio. This model assumes a linear curvature distribution before the shear-wall base yields. In the post-yield stage, the plastic strain is assumed as uniformly distributed within the plastic hinge length. When the shear wall yields, the curvature is maximum at the wall base and zero at its top. In this case, the top yield flexural displacement (Δ_y) is

$$\Delta_y = \frac{1}{3}\varphi_y H^2 \tag{3}$$

where φ_y is the yield sectional curvature.

When the lateral force reaches the maximum value, the plastic hinge length is

$$l_p = 1.25(0.2h + 0.044H) \tag{4}$$

where H is the wall height; and h is the section depth.

The curvatures at yield and at the peak lateral force are shown in Fig. 12, as compared to those calculated according to the model (Bohl and Adebar 2011) and those obtained from the test results. The experimental yield and peak point curvatures are obtained from strain gauges applied on the outer steel bars along the wall height. The corresponding lateral displacements are approximately 14 to 17 mm and 32 mm (the lateral top drift is 1/62.5), respectively. The yield curvature is calculated when the outer strain reaches the yield value (0.002), while the peak point curvature is found when compressive concrete attains its strength according to the model. The peak point curvature depends on the boundary length, so the values obtained for UCSW-3 and -4 are slightly lower than SW-1 and UCSW-2. The plastic hinge length is obtained by Eq. (4) as 360 mm for all four specimens, as shown in Fig. 12.

In all four specimens, the yield curvature distribution is in good accordance with the model results for SW-1, UCSW-2, and UCSW-3, which indicates that the model is reasonable for shear walls with reliable shear keys. However, for specimen UCSW-4, the yield curvature is lower than the model results. The weak interface connection between the boundary column and inner core wall induced independent deformation of the two parts, so that the yield curvature is less than the cast-together shear walls. Moreover, the curvature distribution of UVSW-4 follows the typical bending deformation mode. At peak point, the shear walls' base curvature with UHTBCs is lower than or equal to the model value, while that of the plain concrete shear wall is significantly larger than the calculated value. The plastic hinge length is concentrated at the lower quarter of the wall height for SW-1, while the plastic zone is not so easily detectable for shear walls with UHTBCs. Thus, both curvature distribution and plastic hinge length prove the beneficial effect provided by the high toughness of the boundary columns on the bearing capacity, along with a significant reduction in damage.

Lateral bearing capacity estimation

The lateral bearing capacity stems from the series system arrangement of the two resisting mechanisms: shear and bending.

According to ACI 318-19 (ACI Committee 318 2019), the shear capacity is calculated as

$$V_n = \left(\alpha_c \lambda \sqrt{f_c'} + \rho_t f_y\right) A_{cv} \tag{5}$$

where $\alpha_c = 2$ for elements with an aspect ratio of 2.0; A_{cv} is the section area; $\lambda = 1$ for the concrete used in this study; $f_c' = 0.65 f_{cu} = 25.6$ MPa is the concrete compressive strength (0.65 is the reduction coefficient for this case); ρ_t is the transverse steel geometric ratio (in this study, $\rho_t = 0.0036$); and $f_y = 501$ MPa is the steel yield strength.

In the Chinese code (GB 50010-2010), the shear capacity is calculated as

$$V = \frac{1}{\lambda_0 - 0.5}\left(0.5 f_t b_w h_0 + 0.13 N \frac{A_w}{A}\right) + f_{yh}\frac{A_{sh}}{s} h_0 \tag{6}$$

where $\lambda_0 = 2$ is the aspect ratio; $f_t = 4.5$ MPa is the concrete tensile strength; b_w and h_0 are the shear-wall section width and length; $N = 600$ kN is the axial force; A_w and A are the shear web and entire section area, respectively; and $A_{sh} = 56$ mm^2, $s = 125$ mm, and $f_{yh} = 501$ MPa are the transverse reinforcement area, its vertical spacing, and its yield strength, respectively.

According to the aforementioned codes, the average shear capacity of the four specimens tested in this study is estimated as 895 kN and 445 kN, respectively. It is worth noticing that these two values are significantly different, thus proving the large discrepancies in the shear capacity equations of different codes (De Domenico et al. 2023). Nonetheless, because the shear capacity computed with both equations is higher than the bending capacity exhibited in the tests, which is at most 400 kN, this check confirms that the shear walls were correctly designed to prevent shear failure.

As far as the flexural capacity is concerned, both the Chinese code (GB 50010-2010) and ACI 318-19 are based on the cross-section equilibrium and stress-strain relationship at nominal strength. In both, it is assumed that: 1) the section strain is linearly distributed; 2) the longitudinal reinforcing bars in the tension boundary column have yielded;

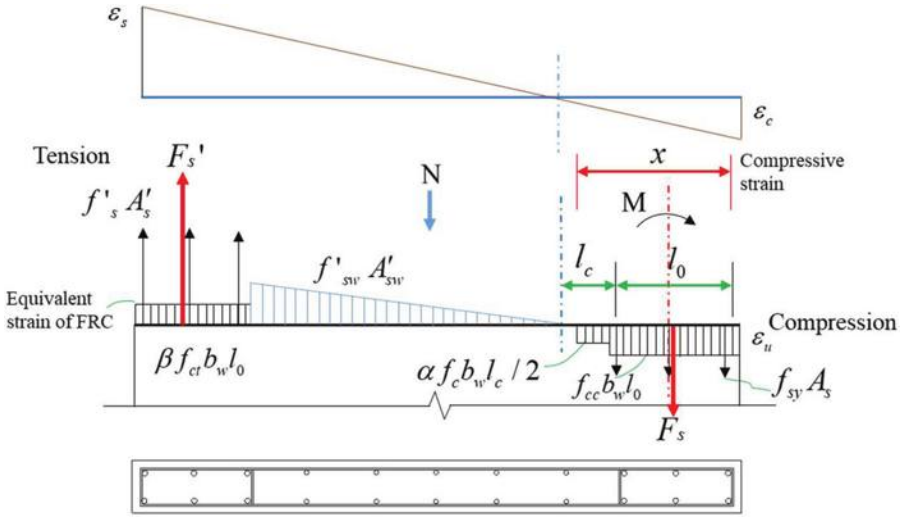

Fig. 13—Equilibrium diagram of RC shear-wall section at ultimate limit state.

3) the compressive concrete reaches its ultimate strain; and 4) concrete tensile stress is neglected. According to the strain-distribution diagram and the damage pattern, the tension area covers an average of 70% of the section length, and the outside steel bars on the tension side reach the ultimate strength at the peak lateral bearing capacity. The steel bar beside the outer longitudinal bars on the tension side yielded at the peak lateral bearing stage. Accordingly, the strain and stress distribution of the modified model are shown in Fig. 13. The steel bars' strain distribution still meets the plane sections assumption. To find the influence of FRC in the boundary regions, two models are proposed by considering the tensile strength of the UHTCC material due to the strain-hardening effect, as shown in Fig. 6(a), where f_{sy} and f_{sw} are the yield strength of the steel bars in the boundary columns and the yield strength of the distributed steel bars in the core wall, respectively; A_s' and A_s are the corresponding areas of the steel bars; l_0 and l_c are the boundary element length and the length of the compression zone of the core wall, respectively; b_w is the thickness of the shear wall; f_{cc}, f_c, and f_{ct} are the compressive and tensile strengths of the UHTCC and plain concrete, respectively; and F_s' and F_s are the resultant forces of the longitudinal bars within the boundary columns at the tension and compression region, respectively.

For equilibrium, the conditions $\Sigma F = 0$ and $\Sigma M = 0$ must be satisfied, and the vertical force equilibrium can be stated as

$$N = \alpha\beta_1 f_{cc} b_w l_0 + 0.5\beta_2 f_c b_w l_c + F_s - F_s' - f_{sw}' A_{sw}' \quad (7)$$

where α is the ratio of the peak stress to the concrete strength, equal to 1.0 for concrete strength lower than 50 MPa; β_1 and β_2 are the stress block shape factors of compressive concrete, equal to 0.8 for concrete strength lower than 50 MPa, according to GB 50011-2010; the first term $\alpha\beta_1 f_{cc} b_w l_0$ represents the compression resultant of the assumed uniformly distributed concrete stress in the boundary column; and the second term $0.5\beta_2 f_c b_w l_c$ represents the compression resultant of the linearly distributed concrete stress along the inner core wall, from the neutral axis to the interface with the boundary column. According to GB 50011-2010, $f_{cc} = 0.88\alpha_1\alpha_2 f_{cu}$, $\alpha_1 = 0.76$, and $\alpha_2 = 1.0$ are the ratios of uniaxial/cubic strength and the reduction factor to account for brittleness. The other terms F_s, F_s', and $f_{sw}'A_{sw}'$ are the resultants of the steel bars in the compression and tension boundary columns and in the inner core wall, respectively. Given a section configuration, knowing the strength of concrete and steel bars, l_c, can be obtained from Eq. (3) (assuming the compression zone is larger than l_0).

Because all tested specimens exhibited flexural-controlled failure and the calculated shear capacity is larger than the tested lateral force, the maximum section moment determines the lateral bearing capacity. For the rectangular-section shear walls, performing the moment equilibrium at the centroid of the confined compression zone, the ultimate moment stems from the two equilibrium equations

$$N = F_s + F_c = \alpha\beta_1 f_{cc} b_w l_0 + 0.5\beta_2 f_c b_w l_c + \Sigma f_{sy} A_s - \Sigma f_{sy}' A_s' - f_{sw}' A_{sw}' \quad (8)$$

$$M = M_s + M_c + M_N = f_s' A_s' (h_{w0} - l_0) + \Sigma f_{sy} A_s l_s + \Sigma f_{sw}' A_{sw}' l_{sw}' + \frac{1}{2}\beta_2 f_c b_w l_c \left(\frac{l_c}{3} + \frac{l_0}{2}\right) + \frac{1}{2} N (h_{w0} - l_0) \quad (9)$$

Because the post-cracking effect of FRC shows a significant impact on the seismic performance, two models are discussed and compared with the currently used model. As stipulated in the codes, the post-cracking tensile strength of concrete is not considered in the sectional bearing capacity (ACI 318-19; GB 50011-2010), and the fiber-reinforcement effect is not considered in Model 1. In Model 2, the boundary columns' steel bars are assumed to reach the ultimate strength according to the actual steel bar strain. In Model 3, the post-cracking FRC tensile strength is also accounted for based on the assumption of Model 2. The descriptions of the models are listed in Table 6.

In Model 2, the section moment is

Table 6—Lateral bearing capacity prediction model description

Specimens	Model 1*	Model 2	Model 3
SW-1	The steel bars in boundary areas yield, and the concrete in compression-confined areas reached ultimate strength.	The steel bars in boundary areas reached the ultimate strength, and the tensile strain of inner steel bars on the tension side is linearly distributed.	The steel bars in boundary areas reached the ultimate strength, the tensile strain of inner steel bars on the tension side is linearly distributed, and the tension contribution of the FRC is equivalent to γf_{ct}.
UCSW-2			
UCSW-3			
UCSW-4			

*Post-cracking tensile strength is not considered.

Table 7—Calculated flexural resistance and lateral bearing force

	Model 1		Model 2		Model 3		Tested specimens	
					γ = 0.5/0.75		Maximum lateral force	Equivalent maximum moment
Specimens	*M*, kN·m	Error %	*M*, kN·m	Error %	*M*, kN·m	Error %	*F*, kN	*M*, kN·m
SW-1	464,425	–13.54	545,255	1.51	—	—	268.57	537.14
UCSW-2	447,647	–31.76	541,471	–17.46	585,922/608,147	–10.68/–7.29	328.00	656.00
UCSW-3	446,848	–25.53	524,494	–12.58	559,955/577,686	–6.67/–3.72	300.00	600.00
UCSW-4	446,848	–23.22	524,494	–9.88	559,955/577,686	–3.79/–0.74	291.00	582.00

$$M = f_{su}'A_s'(h_{w0} - l_0) + \Sigma f_s A_s l_s + \Sigma f_{sw}'A_{sw}'l_{sw}' + \frac{1}{2}\beta_2 f_c b_w l_c\left(\frac{l_c}{3} + \frac{l_0}{2}\right) + \frac{1}{2}N(h_{w0} - l_0) \quad (10)$$

In Model 3, the equilibrium of vertical force gives

$$N = \alpha\beta_1 f_{cc} b_w l_0 + 0.5\beta_2 f_c b_w l_c + \Sigma f_{sy} A_s - \Sigma f_{su}'A_s' - f_{sw}'A_{sw}' - \gamma f_{ct} b_w l_0 \quad (11)$$

The section moment is then

$$M = f_{su}'A_s'\left(h_{w0} - \frac{l_0}{2}\right) + \sum f_s A_s l_s + \sum f_{sw}'A_{sw}'l_{sw}' + \gamma f_{ct} b_w l_0(h_{w0} - l_0) + \frac{1}{2}\beta_2 f_c b_w l_c\left(\frac{l_c}{3} + \frac{l_0}{2}\right) + \frac{1}{2}N(h_{w0} - l_0) \quad (12)$$

where f_s and f_{su}' are the yield and ultimate strengths of longitudinal steel bars in the boundary area on the tension and compression sides; A_s' and A_s are the area of the boundary-area steel bars on the tension and compression side, respectively; l_s' is the distance from the rotation center; γ is the reduction factor of the tensile strength of FRC in the confined boundary zone; and $\Sigma f_{sw}'A_{sw}'l_{sw}'$ represents the moment caused by distribution bars, which can be calculated according to the plane sections assumption.

Table 7 shows the calculated maximum section moment through Models 1 to 3. The sectional bearing moment and the corresponding lateral bearing force are also listed for comparison. In Model 3, the reduction factor γ of the tensile strength of FRC in the confined boundary region is set as 0.5 and 0.75, separately.

As Table 7 shows, the maximum lateral bearing capacity obtained from Model 1 is acceptable for plain concrete shear walls, but the error is 23 to 32% for the FRC-RC shear walls. When considering the ultimate strength of the outer-edge steel bars, the error is lower yet still 10 to 17%. In Model 3, considering the concrete tensile strength, for the two kinds of confined column shear walls, the error is significantly reduced. As the literature suggested (Zhang et al. 2022), the reduction factor of the fiber-reinforced concrete of post-cracking tensile strength is approximately 0.5 and the error is between 3.8 and 10%. When the reduction factor is 0.75, the error is between 0.7 and 7.3%.

As the calculation comparison based on different failure patterns indicates, the tensile strength of plain concrete shows a minor contribution to the bearing capacity, which meets with the current assumption. When the boundary column concrete is replaced by the UHTCC, the strength of steel bars in the boundary area and the post-cracking tensile strength of UHTCC contribute significantly to the lateral bearing capacity. With the fiber confinement, the edge longitudinal steel bars are more stable against buckling. Consequently, the boundary column steel bars are more likely to reach the ultimate strength.

DISCUSSION

Strengthening effect of UHTBC

The experimental results indicated that replacing plain concrete in the boundary columns with the UHTCC can significantly improve the seismic performance of shear walls.

The UHTBC used in this study demonstrates its effectiveness for strengthening the boundary elements of shear walls by mitigating the local cracks, reducing their configuration, and preventing rapid crack development and local concrete crushing. The shear walls with UHTBC elements exhibited improved lateral resistances and deformation capacities. The peak lateral force and the corresponding lateral displacement of UCSW-2 were 22% and 19% larger, respectively, than those of SW-1. The UHTBC specimens maintained a good resistance capacity even when the lateral bearing force dropped to 70% of the peak value. The secant stiffness of UCSW-2 was significantly higher than that of SW-1 (by 51%, 13%, and 95% at drift ratios of 1/500, 1/100, and 1/50, respectively). The UHTBC elements increased the energy dissipation capacity, particularly in the large-deformation stage. The energy dissipations of the single hysteresis loops

for UCSW-2 were 57% and 19% higher than those of SW-1 at drift ratios of 1/100 and 1/50, respectively. In these cases, it provides an alternate strengthening method for shear walls not conforming to the seismic design code, leading to better seismic performance than that of walls designed according to the current design code.

Possibility of reducing boundary column size and longitudinal bars

Comparing UCSW-3 with SW-1 reveals that the shear wall with a reduced boundary column configuration still exhibited better seismic performance than the shear wall designed according to the current standards. The lateral force and displacement of UCSW-3 in the peak state were increased by 12% and 13%, respectively, and the strength degradation of post-peak lateral force was significantly smaller. These characteristics contribute to the possibility of strengthening the existing shear walls with limited space.

Feasibility of no-connection UHTBC boundary elements

As the experimental results of UCSW-4 show, the shear wall strengthened with the UHTBC boundary elements satisfied the seismic demand of the current seismic design code GB 50011-2010. The non-connection UHTBC specimen (UCSW-4) had better deformation and energy dissipation capacity in the large-deformation stage than the plain concrete shear wall. The lateral force and displacement in the peak state were increased by 8.4% and 20%, and the lateral force at a drift ratio of 1/50 was increased by 34%, respectively. The strength degradation was significantly slower than that for the other specimens. The hysteresis loop of the energy dissipation for UCSW-4 expanded gradually, even close to specimen failure. The test results indicate the feasibility of shear-wall retrofitting without connecting with the existing structure, through the construction of an additional boundary element. That provides evidence for the feasibility of the proposed method being applied in the rapid replacement of the damaged boundary columns or retrofitting protected structures. Additionally, the non-connection boundary element shear wall exhibits a flexural failure pattern of the three separate parts.

Section design model

In contrast to the code-specified model, the models considering the ultimate strength of the edge steel bars on the tension side and the post-cracking tensile strength of the fiber-reinforced concrete provide more reasonable prediction results. The error of the predicted lateral bearing capacity to the test results is within 7% using the post-cracking tensile strength reduction factor $\gamma = 0.75$. Moreover, the steel bars at the boundary area of the tension side were more likely to reach the ultimate strength and contribute to the shear-wall lateral bearing capacity, thanks to the fiber-reinforced concrete protection.

Moreover, the energy dissipated by fiber pullout and debonding only takes place with increasing deformation amplitude. Thus, the contribution from UHTCC is especially significant during the strong shaking portion of the action in near-fault earthquakes.

CONCLUSIONS

The seismic performance of nonconforming slender shear walls strengthened by ultra-high-toughness boundary columns (UHTBCs) was experimentally validated in this study, and the main conclusions are as follows.

1. The shear walls strengthened by UHTBCs possess improved bearing and deformation capacity. Compared to the plain concrete shear wall designed according to the current code, the secant stiffness of the UHTBC-strengthened shear walls was higher by 51%, 13%, and 95% at drift ratios of 1/500, 1/100, and 1/50, respectively,

2. The shear walls with reduced-boundary UHTBCs conform with the bearing capacity of the specimen designed to the current specifications. The lateral force and displacement of the reduced-boundary shear wall with UHTBCs at the peak state were higher by 12% and 13%, respectively, compared to the standard specimen.

3. The slender shear wall strengthened by reduced no-connection UHTBCs exhibited a less disruptive interaction with the existing shear wall, thus preventing its shear failure and at the same time maintaining an appreciable bearing capacity even until the "collapse prevention" state. The peak lateral force and displacement were increased by 8% and 20%, and the lateral force at a drift ratio of 1/50 was increased by 34%, respectively, compared to the specimen designed to the current code.

4. The feasible prediction equation for the lateral bearing capacity of the UHTBC-strengthened shear walls is obtained by accounting for the tensile strength through a reduction factor of 0.75 and the ultimate strength of the boundary steel bars.

This technique can be used both in noninvasive and no-damage retrofitting measures to improve the seismic performance of shear walls, particularly in severe earthquake-prone areas, even using reduced-boundary UHTBCs, which ensure ample application feasibility for existing shear-wall structures.

AUTHOR BIOS

Hongmei Zhang *is a Professor at Zhejiang University, Hangzhou, Zhejiang, China. Before that, she was an Associate Professor at Tongji University, Shanghai, China. From 2014 to 2015, she was a Visiting Professor at the University of Illinois at Urbana-Champaign, Urbana, IL. She received her PhD in civil engineering from Tongji University in 2007. Her research interests include disaster reduction and seismic design of reinforced concrete structures.*

Giorgio Monti *is a Full Professor at Sapienza University of Rome, Rome, Italy, and a Visiting Professor at Zhejiang University. He graduated in civil engineering from Sapienza University of Rome in 1986; received his Master of Science from the University of California, Berkeley, Berkeley, CA, in 1993; and received his PhD in structural engineering from Sapienza University of Rome in 1994.*

Yuanfeng Duan *is a Full Professor at Zhejiang University. From 2014 to 2015, he was a Visiting Professor at the University of Illinois at Urbana-Champaign. He received his PhD in civil engineering from The Hong Kong Polytechnic University, Kowloon, Hong Kong, in 2004. His research interests include disaster reduction for structures.*

Zhiyuan Chen *is a Graduate of Zhejiang University. He received his BS in civil engineering from the Zhejiang University of Technology, Hangzhou, Zhejiang, China, in 2019.*

Chen Gu *is a Graduate of Zhejiang University. He received his BS in civil engineering from Henan Polytechnic University, Jiaozuo, Henan, China, in 2020.*

ACKNOWLEDGMENTS

This project was financially supported by the National Natural Science Foundation of China (Grant No. 52078459 and U1709216), the National Key R&D Program of China (2019YFE0112600), and the National Natural Science Foundation of Zhejiang Province (Grant No. LZ22E080005). The experimental data that support the findings of this study are available from the corresponding author upon reasonable request.

REFERENCES

ACI Committee 318, 2019, "Building Code Requirements for Structural Concrete (ACI 318-19) and Commentary (ACI 318R-19) (Reapproved 2022)," American Concrete Institute, Farmington Hills, MI, 624 pp.

Al-Gemeel, A. N., and Zhuge, Y., 2019, "Using Textile Reinforced Engineered Cementitious Composite for Concrete Columns Confinement," *Composite Structures*, V. 210, Feb., pp. 695-706. doi: 10.1016/j.compstruct.2018.11.093

Bohl, A., and Adebar, P., 2011, "Plastic Hinge Lengths in High-Rise Concrete Shear Walls," *ACI Structural Journal*, V. 108, No. 2, Mar.-Apr., pp. 148-157.

Boshoff, W. P.; Mechtcherine, V.; and van Zijl, G. P. A. G., 2009, "Characterizing the Time-Dependent Behaviour on the Single Fibre Level of SHCC: Part 1: Mechanism of Fibre Pull-Out Creep," *Cement and Concrete Research*, V. 39, No. 9, Sept., pp. 779-786. doi: 10.1016/j.cemconres.2009.06.007

Chrysanidis, T., and Tegos, I., 2020, "Axial and Transverse Strengthening of R/C Circular Columns: Conventional and New Type of Steel and Hybrid Jackets Using High-Strength Mortar," *Journal of Building Engineering*, V. 30, July, Article No. 101236. doi: 10.1016/j.jobe.2020.101236

Dang, Z.; Liang, X. W.; Deng, M. K.; Li, F.; and Yu, J., 2014, "Experimental and Theoretical Studies on Seismic Behavior of Fiber Reinforced Concrete Shear Walls," *Journal of Building Structures*, V. 35, No. 6, pp. 12-22.

Dazio, A.; Buzzini, D.; and Trüb, M., 2008, "Nonlinear Cyclic Behaviour of Hybrid Fibre Concrete Structural Walls," *Engineering Structures*, V. 30, No. 11, Nov., pp. 3141-3150. doi: 10.1016/j.engstruct.2008.03.018

De Domenico, D.; Quaranta, G.; Zeng, Q.; and Monti, G., 2023, "Shear Capacity of RC Elements with Transverse Reinforcement through a Variable-Angle Truss Model with Machine-Learning-Calibrated Coefficients," *Artificial Intelligence and Machine Learning Techniques for Civil Engineering*, V. Plevris, A. Ahmad, and N. D. Lagaros, eds., IGI Global, Hershey, PA.

Fischer, G., and Li, V. C., 2002a, "Effect of Matrix Ductility on Deformation Behavior of Steel-Reinforced ECC Flexural Members under Reversed Cyclic Loading Conditions," *ACI Structural Journal*, V. 99, No. 6, Nov.-Dec., pp. 781-790.

Fischer, G., and Li, V. C., 2002b, "Influence of Matrix Ductility on Tension-Stiffening Behavior of Steel Reinforced Engineered Cementitious Composites (ECC)," *ACI Structural Journal*, V. 99, No. 1, Jan.-Feb., pp. 104-111.

Fischer, G., and Li, V. C., 2003, "Deformation Behavior of Fiber-Reinforced Polymer Reinforced Engineered Cementitious Composite (ECC) Flexural Members under Reversed Cyclic Loading Conditions," *ACI Structural Journal*, V. 100, No. 1, Jan.-Feb., pp. 25-35.

GB 50011-2010, 2010, "Code for Seismic Design of Buildings," Ministry of Housing and Urban-Rural Development of the People's Republic of China, Beijing, China.

JGJ/T 101-2015, 2015, "Specification for Seismic Test of Buildings," Ministry of Housing and Urban-Rural Development of the People's Republic of China, Beijing, China.

JG/T 398-2012, 2012, "The Grouting Coupler for Rebars Splicing," Ministry of Housing and Urban-Rural Development of the People's Republic of China, Beijing, China.

Kesner, K., and Billington, S. L., 2005, "Investigation of Infill Panels Made from Engineered Cementitious Composites for Seismic Strengthening and Retrofit," *Journal of Structural Engineering*, ASCE, V. 131, No. 11, Nov., pp. 1712-1720. doi: 10.1061/(ASCE)0733-9445(2005)131:11(1712)

Li, H.; Xu, S.; and Leung, C. K. Y., 2009, "Tensile and Flexural Properties of Ultra High Toughness Cementitious Composite," *Journal of Wuhan University of Technology-Materials Science Edition*, V. 24, No. 4, Aug., pp. 677-683. doi: 10.1007/s11595-009-4677-5

Li, M.; Luu, H. C.; Wu, C.; Mo, Y. L.; and Hsu, T. T. C., 2014, "Seismic Performance of Reinforced Engineered Cementitious Composite Shear Walls," *Earthquakes and Structures*, V. 7, No. 5, pp. 691-704. doi: 10.12989/eas.2014.7.5.691

Li, Q. H., and Xu, S. L., 2009, "Experimental Investigation and Analysis on Flexural Performance of Functionally Graded Composite Beam Crack-Controlled by Ultrahigh Toughness Cementitious Composites," *Science in China Series E: Technological Sciences*, V. 52, No. 6, June, pp. 1648-1664. doi: 10.1007/s11431-009-0161-x

Li, V. C.; Wang, S.; and Wu, C., 2001, "Tensile Strain-Hardening Behavior of Polyvinyl Alcohol Engineered Cementitious Composite (PVA-ECC)," *ACI Materials Journal*, V. 98, No. 6, Nov.-Dec., pp. 483-492.

Liang, X.-W.; Zheng, Y.; Deng, M.-K.; Kou, J.-L.; and Che, J.-L., 2013, "An Investigation of Deformation Behavior of the Shear Wall with Fiber-Reinforced Concrete in Plastic Hinge Region," *Engineering Mechanics*, V. 30, No. 3, Mar., pp. 256-262.

Lu, X.; Zhang, Y.; Zhang, H.; Zhang, H.; and Xiao, R., 2018, "Experimental Study on Seismic Performance of Steel Fiber Reinforced High Strength Concrete Composite Shear Walls with Different Steel Fiber Volume Fractions," *Engineering Structures*, V. 171, Sept., pp. 247-259. doi: 10.1016/j.engstruct.2018.05.068

Mandelbrot, B. B., 1982, *The Fractal Geometry of Nature*, W. H. Freeman and Company, New York City, NY.

Mirmiran, A., and Shahawy, M., 1997, "Behavior of Concrete Columns Confined by Fiber Composites," *Journal of Structural Engineering*, ASCE, V. 123, No. 5, May, pp. 583-590. doi: 10.1061/(ASCE)0733-9445(1997)123:5(583)

Mustafaraj, E.; Yardim, Y.; Corradi, M.; and Borri, A., 2020, "Polypropylene as a Retrofitting Material for Shear Walls," *Materials*, V. 13, No. 11, June, Article No. 2503. doi: 10.3390/ma13112503

Mutō, K., 1969, *Newly-Devised Reinforced Concrete Shear Walls for High-Rise Building Structures*, Muto Institute of Structural Mechanics, Tokyo, Japan, 38 pp.

Naaman, A. E., and Najm, H., 1991, "Bond-Slip Mechanisms of Steel Fibers in Concrete," *ACI Materials Journal*, V. 88, No. 2, Mar.-Apr., pp. 135-145.

Olsen, E. C., and Billington, S. L., 2011, "Cyclic Response of Precast High-Performance Fiber-Reinforced Concrete Infill Panels," *ACI Structural Journal*, V. 108, No. 1, Jan.-Feb., pp. 51-60.

Park, K.-G., 2006, "Design and Analysis on the Connections of RC Precast Large Panel," *Journal of Korean Association for Spatial Structures*, V. 6, No. 2, Serial No. 20, pp. 85-92.

Parra-Montesinos, G. J., 2005, "High-Performance Fiber-Reinforced Cement Composites: An Alternative for Seismic Design of Structures," *ACI Structural Journal*, V. 102, No. 5, Sept.-Oct., pp. 668-675.

Parra-Montesinos, G. J.; Canbolat, B. A.; and Jeyaraman, G. R., 2006, "Relaxation of Confinement Reinforcement Requirements in Structural Walls through the Use of Fiber Reinforced Cement Composites," *Proceedings of the 8th U.S. National Conference on Earthquake Engineering*, San Francisco, CA, pp. 4045-4054.

Prota, A.; Nanni, A.; Manfredi, G.; and Cosenza, E., 2004, "Selective Upgrade of Underdesigned Reinforced Concrete Beam-Column Joints Using Carbon Fiber-Reinforced Polymers," *ACI Structural Journal*, V. 101, No. 5, Sept.-Oct., pp. 699-707.

Sørensen, J. H.; Hoang, L. C.; Olesen, J. F.; and Fischer, G., 2017a, "Tensile Capacity of Loop Connections Grouted with Concrete or Mortar," *Magazine of Concrete Research*, V. 69, No. 17, Sept., pp. 892-904. doi: 10.1680/jmacr.16.00466

Sørensen, J. H.; Hoang, L. C.; Olesen, J. F.; and Fischer, G., 2017b, "Test and Analysis of a New Ductile Shear Connection Design for RC Shear Walls," *Structural Concrete*, V. 18, No. 1, Feb., pp. 189-204. doi: 10.1002/suco.201600056

Woods, J. E.; Lau, D. T.; and Cruz-Noguez, C. A., 2016, "In-Plane Seismic Strengthening of Nonductile Reinforced Concrete Shear Walls Using Externally Bonded CFRP Sheets," *Journal of Composites for Construction*, ASCE, V. 20, No. 6, Dec., p. 04016052. doi: 10.1061/(ASCE)CC.1943-5614.0000705

Xu, S.-L., and Cai, X.-R., 2010, "Experimental Study and Theoretical Models on Compressive Properties of Ultrahigh Toughness Cementitious Composites," *Journal of Materials in Civil Engineering*, ASCE, V. 22, No. 10, Oct., pp. 1067-1077. doi: 10.1061/(ASCE)MT.1943-5533.0000109

Xu, S. L.; Wang, N.; and Zhang, X. F., 2012, "Flexural Behavior of Plain Concrete Beams Strengthened with Ultra High Toughness Cementitious Composites Layer," *Materials and Structures*, V. 45, No. 6, June, pp. 851-859. doi: 10.1617/s11527-011-9803-0

Zhang, H.; Zhang, Y.; Lu, X.; Duan, Y.; and Zhang, H., 2020, "Influence of Axial Load Ratio on the Seismic Behavior of Steel Fiber–Reinforced Concrete Composite Shear Walls," *Journal of Structural*

Engineering, ASCE, V. 146, No. 1, Jan., p. 04019171. doi: 10.1061/(ASCE)ST.1943-541X.0002444

Zhang, H. M.; Lu, X. L.; Duan, Y. F.; and Zhu, Y., 2014, "Experimental Study on Failure Mechanism of RC Walls with Different Boundary Elements under Vertical and Lateral Loads," *Advances in Structural Engineering*, V. 17, No. 3, Mar., pp. 361-379. doi: 10.1260/1369-4332.17.3.361

Zhang, Y.; Zhang, H.; and Lu, X., 2022, "Seismic Performance Evaluation and Experimental Validation of Steel-Fiber-Reinforced High-Strength-Concrete Composite Shear Walls," *Structures*, V. 35, Jan., pp. 765-779. doi: 10.1016/j.istruc.2021.11.038

Zhou, Y.; Lu, X.; and Dong, Y., 2010, "Seismic Behavior of Composite Shear Walls with Multi-Embedded Steel Sections. Part I: Experiment," *The Structural Design of Tall and Special Buildings*, V. 19, No. 6, pp. 618-636. doi: 10.1002/tal.598

ACI STRUCTURAL JOURNAL TECHNICAL PAPER

Title No. 120-S79

Hysteretic Model of Coupler Box Assembly for Seismic Retrofitting of Severely Damaged Reinforced Concrete Buildings

by Naveen Kumar Kothapalli, R. Siva Chidambaram, and Pankaj Agarwal

Cyclic tests are conducted on interlinked reinforcing bar coupler-box assemblies, adopted to retrofit buckled reinforcing bars at the plastic hinge locations of columns in multi-storied reinforced concrete building frames. The efficacy of the proposed retrofitting technique is evaluated by comparing the hysteresis behavior, computed parameters of performance index, and failure mechanism of the reconstructed frame with the original frame. An energy-based strength deterioration hysteresis model is developed on the basis of cyclic test results for analytically computing the post-yield behavior of retrofitted reinforced concrete (RC) frame with the proposed coupler-box assembly. The experimental test results manifest that the coupler-box assembly can be a promising futuristic approach for seismic retrofitting of severely damaged reinforced concrete buildings, where buckling of longitudinal reinforcing bars at the plastic hinge location of columns is inevitable, and the process of restoration is challenging under existing gravity loads. The suggested retrofitting mechanism restrains the section from any movement against rotation and helps in shifting the yield location of reinforcing bars. The main advantage of adopting the coupler-box is that there is no observed slip of reinforcing bar from the sleeve, and the entire retrofitted section remains intact even after a lateral storey drift of 6%, which is larger than the collapse prevention drift level of 4% as per Federal Emergency Management Agency guidelines.

Keywords: coupler-box assembly; deterioration strength hysteresis model; energy dissipation; hysteresis behavior; reinforcing bar coupler sleeve; seismic retrofitting.

INTRODUCTION

Buckling/yielding of longitudinal reinforcing bars at the plastic hinge locations of multi-storied building frames under severe earthquake excitations is one of the most common failure modes. As a result, the column member shortens and loses its capability to carry even its prescribed gravity load, which sometimes leads to the progressive collapse of buildings. Seismic retrofitting of buckled reinforcement at the hinge location of columns in such multi-story buildings proves to be challenging as there is no mechanism to realign the buckled bars under high compressive loads. Under these circumstances, removal of the buckled portion of reinforcing bar is inevitable, and new reinforcement is introduced either by welding, splicing, or through mechanical couplers. The conventional method of lap splicing at hinge locations is neither recommended nor practical as it requires large demolition of intact concrete in an existing structural member on either side of the cut reinforcement. Moreover, splicing reinforcing bars at hinge locations is incompetent in resisting large bending moments, which may lead to bond-slip failure. Welding can be an alternative technique for connecting broken reinforcing bars with new bars. However, it also requires removing a large amount of intact concrete on both sides of the damaged section to expose the required weld length and an all-around clear space for functioning. The length of lap weld for connecting reinforcing bars as per strength, and codal requirements, IS 9417:2018 (2018), is approximately 600 mm (23.62 in.), which is higher than the concrete removal area required for insertion of the proposed coupler sleeve, 500 mm (19.69 in.)—that is, two times the proposed coupler sleeve length. Further, welding causes metallurgical changes with the recrystallization of microstructures in particles and is not preferred in the potential hinge region of primary structural members. The study on mechanical properties of welded deformed reinforcing steel bars conducted by Ahmed (2015) shows that the strength and elongation of welded reinforcing bars decrease up to 40% and 60%, respectively.

The use of reinforcing bar couplers or coupling sleeves in joining the ends of reinforcing bar segments is a prevalent practice in the modernized construction of buildings or bridges, which safeguards the reinforcing materials at their lap-splice regions. The invention of grouted splice sleeves dates back to the late 1960s by Yee (1970, 1986, 2009). Several studies in the past on coupler/coupling sleeves are based on their shape, diameter, length, material characteristic, bonding properties of the grout material, anchorage capacity, and so on. Hybrid couplers with a combination of mechanical and grouting techniques were tested by Hope (1987). Threaded end reinforcing bars into grout-filled coupler sleeves were suggested by Lancelot (1995). Mechanical couplers in the form of tubular members with and without internal threading, along with a distinctive number of external bolts, were proposed by Holdsworth (1997, 2006). Annular-shaped seals at the ends of steel sleeves for locking reinforcing bar elements along with grout matter were recommended by Mochizuki and Nihei (1998). High-strength concrete grout in addition to large-headed reinforcing bars through pipe couplers was suggested

ACI Structural Journal, V. 120, No. 5, September 2023.

MS No. S-2021-120.R7, doi: 10.14359/51738831, received March 4, 2023, and reviewed under Institute publication policies.

by Dahl (2001). Taper-threaded reinforcing bar ends were associated with threaded collars and linked with a central circular sleeve in the research study by Allen et al. (2007).

The various failure modes in sleeve connections under direct tensile load were evaluated and analysed by Hua et al. (2008). The cyclic behavior of beam-column joint subassemblies with spiral threaded couplers at the joint's interface was investigated by Ingham and Bai (2009). Rowell and Hager (2010) studied the dynamic performance of various sleeves under higher strain rates, where the threaded reinforcing bar coupler system performs best with 99% ultimate dynamic tensile strength. Damaged columns were retrofitted by Huaco and Jirsa (2012), where the buckled reinforcing bars were replaced and reconnected through mechanical sleeves with high-strength bolts torqued to a prescribed level. The cyclic test on reinforcing bars connected through the mechanical sleeves shows that the rupture of reinforcing bar is at its last bolt in shorter sleeves and is distant away from the sleeve in longer ones. Column bridge bents with couplers attached to their longitudinal reinforcing bars at staggered heights in the plastic hinge zone were tested by Phillippi and Hegemier (2013), where lower compressive stress is experienced in the couplers outside the plastic hinge zone. The effect of sleeve diameter and development length on the bonding performance of connectors was studied by Alias et al. (2014), where the connectors with an optimum development length of 200 mm (7.87 in.) along with smaller internal and external diameters provided a better bonding performance. Research on the use of coupler sleeves to join precast elements like columns has been conducted in the past. The lateral load behavior of precast columns joined by corrugated steel sleeves was studied by Popa et al. (2015). A sleeve-connected column had a similar hysteretic response with energy dissipation capacity as a cast-in-place column. A design methodology to increase the plastic rotation capacity and ductility of precast columns by shifting their plastic hinge locations above the grouted sleeves, using transition splicing and high-strength steel dowels in the connection footings, was proposed by Haber et al. (2017). Grouted splice sleeve connectors were adopted to connect precast columns with their footings at various locations by Ameli et al. (2016). A column with a grouted sleeve in the plastic hinge region performs better than a specimen with the sleeve located inside its footing. A novel methodology for precast erection of columns with one-touch couplers guided into corresponding column reinforcing bars through mild steel plates was proposed by Nzabonimpa and Hong (2018). Inelastic behavior in reinforced concrete (RC) members connected through compact threaded and slender threaded sleeves was studied by Bompa and Elghazouli (2019). It was noticed that a slender coupler alters the plastic hinge behavior by localising curvatures and reducing the rotational capacity, whereas the compact couplers perform identical to specimens with continuous reinforcement. Bridge columns with interlocking spirals and fractured longitudinal reinforcing bars were repaired by mechanical splicing of reinforcing bars in the plastic hinge locations and external jacketing by Yang et al. (2015), which is efficient in restoring the lateral and torsional strength of the column. Severely damaged precast RC bridge columns were repaired by Parks et al. (2016) using grouted splice sleeves and composite shells, which relocate the column's plastic hinge.

The use of mechanical coupling devices for integrating reinforcing bar segments in modern and retrofitting solutions has been extensively reviewed. Hybrid couplers with external bolting and grouting are comparatively effective. Dimensions like development length and thickness of the coupler sleeve also decide the failure pattern in structural members. In practice, the commonly used standard couplers are threaded, where the ends of reinforcing bars are mechanically threaded and connected. Threaded couplers are generally shorter in length (approximately 2 to 2.5 times the diameter of connected reinforcing bar) and are used in new constructions in a staggered pattern. Their performance in bonding reinforcing bar segments is adequate under axial loads, but is uncertain under flexural loads. In the process of retrofitting damaged structures, the existing reinforcing bars yield at a common section. Further, threading of the embedded reinforcing bars is not practically feasible as it requires complete processing of reinforcing bar ends, such as enlargement of diameter and threading. Therefore, threaded couplers are suitable for new constructions and are unfit or ineffective in retrofitting projects, particularly in the plastic hinge region of severely damaged structures.

The use of reinforcing bar coupling devices in an existing structural component, as seen in Fig. 1—that is, specifically at the flexure-dominated plastic hinge regions—becomes a complicated task as threading the existing reinforcing bars is impractical. The present study focuses on a unique coupler-box assembly which not only connects the rupture ends of reinforcing bars at the severely damaged hinge locations of columns, but also significantly enhances the performance of a standalone coupling sleeve. A coupler-box confinement technique is proposed in the present study, where standalone couplers are integrated through flat steel bars to make a box section that helps resist high moment shear along with torsional forces and confines the frame section to withstand larger plastic deformations. The proposed coupling sleeves used in box formation are internally grooved, externally bolted, and grouted using high-strength epoxy mortar grout to avoid any bond-slip failure. Experimental verification on the efficiency of coupler-box association is conducted by testing a full-scale RC portal frame. Comparative performance of standalone coupler and coupler-box assemblage is evaluated by performing a cyclic test on RC columns. The obtained cyclic test results of portal frame pave the way for development of energy-based hysteresis models, which can be used in the numerical modeling of retrofitted structures with coupler-box assemblies and can possibly be a vital contribution to the field of structural and retrofitting engineering.

RESEARCH SIGNIFICANCE

Retrofitting or restoring damaged RC frame structures with buckled/yielded reinforcement proves complex under existing load conditions. The proposed research work provides a feasible solution to overcome this issue, where the recommended coupler sleeve slides freely over the existing

Fig. 1—Buckling failure of longitudinal reinforcement noticed during earthquake loading.

reinforcing bar without any cross-sectional modification and is further interlinked with flat steel bars to form a box-shaped assembly. The adaptability of the proposed technique is verified by experimental testing, and energy-based hysteresis models are proposed for analytical modeling, which is believed to be a significant contribution to the field of retrofitting.

UNIAXIAL TENSILE BEHAVIOR OF PROPOSED STANDALONE COUPLER SLEEVE

The proposed coupler/sleeve is particularly preferred in the field of retrofitting buckled longitudinal reinforcing bars in damaged columns of RC buildings subjected to severe earthquake excitations. Under these circumstances, removing the buckled portion of reinforcing bars is inevitable for retrofitting the frame sections. The present study focuses on a probable solution to connect two separated ends of reinforcing bars at the plastic hinge location of existing columns, and their efficiency is evaluated under extreme forces or deformations that may arise in case of impending earthquakes. The proposed coupler sleeve grips the connected reinforcing bar elements with external bolts and high-strength epoxy grout, as shown in Fig. 2. The filler grout used to seal void spaces between reinforcing bar and sleeve is a dual-component epoxy-based mortar with a mixture proportion of 3:1 (epoxy resin:amine hardener). The mixed resin maintains a viscosity of 23 Pa-s (0.0033 lbf-s/in.^{2}), bond strength of 16.4 MPa (2.38 ksi), compressive strength of 102 MPa (14.79 ksi), and tensile strength of 45 MPa (6.53 ksi). The coagulated resin mixture is injected against gravity through one of the bottom bolt-holes of the coupler sleeve. To allow the free flow of resin and disseminate it around the reinforcing bar surface, the inner bore is provided with 5 mm (0.19 in.) additional gap than the reinforcing bar diameter, which provides an annular gap of 2.5 mm (0.09 in.) around the reinforcing bar surface. Further, this gap allows the free insertion of the sleeve onto the reinforcing bar segment. The reinforcing bars at connected plastic hinge locations are assumed to be ineffective, and to maintain an equivalent shear area in the hinge location of structural member, the thickness of sleeve or wall thickness is considered to be half the diameter of reinforcing bar. The bond strength required for each coupled reinforcing bar segment is the primary design criteria to determine the length of sleeves and the diameter of external bolts. The bonding strength over each coupled reinforcing bar is a cumulative effect of epoxy grout and external bolt, and the computed strength should be greater than the yield strength of connected reinforcing bars. A factor of 1.25 is applied in Eq. (3), which considers the strain-hardening effect in connected reinforcing bars—that is, the UTS/YS ratio. The total number of bolts required to fix the coupler system is calculated based on the shear strength of each bolt, and the combined strength for clamping each reinforcing bar segment should be greater than the ultimate tensile strength of the reinforcing bar. The additional sleeve bolts are provided for the interlinking purpose and their orientation is kept perpendicular to one another. This establishes a connection with adjoining sleeves which are positioned at right angles to each other. The estimated geometrical dimensions for a proposed coupler sleeve are calculated based on the reinforcing bar diameter (Ø) using the following simplified empirical equations.

The inner bore diameter of coupling sleeve ($Ø_{inner}$) is

$$Ø_{inner} = Ø + 5 \text{ mm} \tag{1}$$

Thickness of the sleeve or wall thickness (t) is

$$t_{(\text{mm})} = Ø_{(\text{mm})}/2 \tag{2}$$

Length of the coupler sleeve (L) is

$$L_{(\text{in. cm})} = 1.25 \times Ø_{(\text{in. mm})} \tag{3}$$

The diameter of the external bolt ($Ø_{bolt}$) is computed as $Ø_{bolt} = Ø/2$ with a standard center-to-center spacing of 20 mm (0.79 in.), and an estimated number of six bolts are clamped over each reinforcing bar segment—that is, half-length of the coupler sleeve.

In the present study, a coupler sleeve with a reinforcing bar of 20 mm (0.79 in.) diameter is considered to retrofit the plastic hinge locations of damaged columns in a building frame. It is specifically designed using a hollow circular mild steel pipe of 45 mm (1.77 in.) external diameter with inner walls grooved at a rate of 10 grooves per in. length. Twelve numbers of 10 mm (0.39 in.) diameter high-strength 12.9 graded Allen bolts are used to clasp the reinforcing bar elements against the sleeve walls, and four numbers of 8 mm (0.32 in.) diameter bolts are used to interconnect them laterally. The grooved surface/lining at the inner walls provides additional frictional resistance between the reinforcing bar and coupler sleeve. Photographs of the proposed coupler

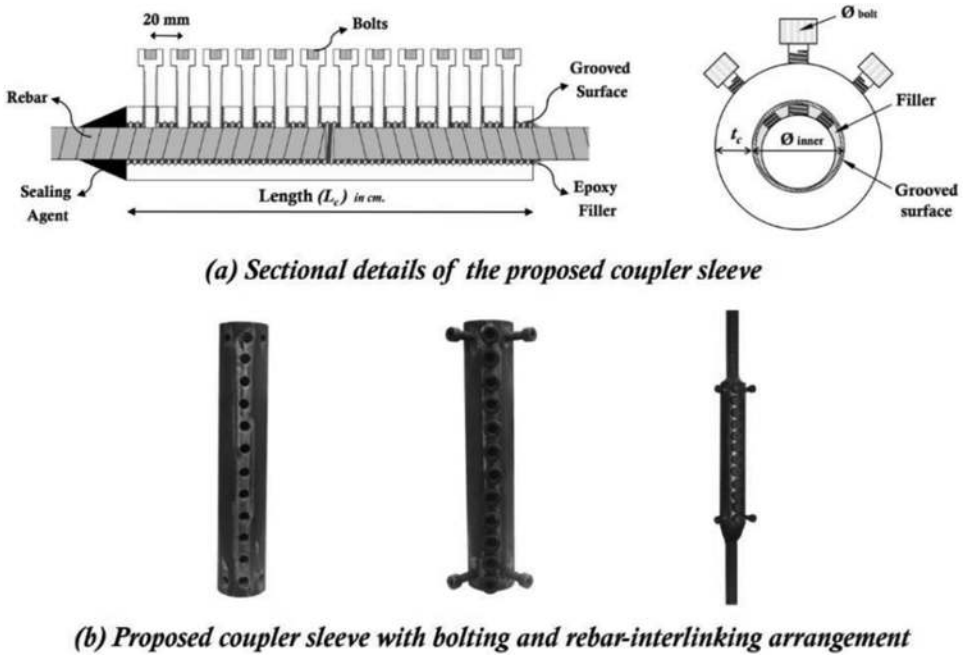

Fig. 2—Typical details of proposed coupler sleeve.

sleeve, along with its bolting and reinforcing bar interconnection, are shown in Fig. 2.

Uniaxial direct tension testing on reinforcing bars with and without coupler connection is carried out to examine the performance of proposed coupler sleeve, as shown in Fig. 3(a). There is no failure noticed in the coupled region of specimen, and yielding of the reinforcing bar gets shifted with a rupture pattern similar to that of the intact reinforcing bar. The failure in coupler-connected reinforcing bars occurs at a comparatively low axial deformation than the original reinforcing bar. However, the computed stress-strain parameters of coupled reinforcing bars qualify the minimum codal specifications of high-strength reinforcing bars for concrete reinforcement, as per IS 1786:2008 (2008). The post-yield behavior in coupler-connected reinforcing bar is influenced by the number of external bolts and the strength of epoxy-grout material. The cumulative effect of external bolting, skin frictional resistance from the internal grooved surface, and epoxy-based grout provides additional gripping to the connected reinforcing bars, which constrains them to fail with slightly high initial stiffness and relatively low axial deformation.

A slip test on the coupler sleeve connection is performed by loading the specimen with stress variation from $0.60f_y$ to 20 MPa (2.9 ksi), and a linearly variable differential transformer (LVDT) is used to estimate the possible amount of slip. Figure 3(b) shows the cyclic plot of coupled reinforcing bar specimen subjected to slip test, where a minimum slip of 0.10 mm (0.0039 in.) is noticed. The proposed coupler sleeve connection is subjected to 100 cyclic loading stress cycles with stress variations from 0.05 to $0.95f_y$ to examine its efficiency under recurrent loading. The coupled connection effectively resists the applied loading cycles without failure, and the load is statically increased until failure post-completion of 100 cycles, where no loss in tensile strength capacity of the specimen is noticed. Figure 3(c) shows the cyclic behavioral plot of coupled reinforcing bar specimen based on the applied machine stroke. Low-cycle fatigue test of 10,000 cycles with stress variations from +173 to –173 MPa (+25.1 to –25.1 ksi) and a high-cycle fatigue test of 2 million stress cycles with variations from 270 to 330 MPa (39.2 to 47.9 ksi) are performed on the proposed coupler sleeve connection. Post completion of 10,000 cycles, no failure is noticed in the sleeve connection, and the load is statically increased until failure, as shown in Fig. 3(d). Similarly, after the completion of 2 million cycles, the sleeve connection remains intact and is monotonically loaded until failure, as shown in Fig. 3(e). In the high-cycle fatigue test, the axial stress reduces post the ultimate strength of the reinforcing bar—that is, post 685 MPa (99.3 ksi), which is by the probable slip in connected reinforcing bar. However, the coupled reinforcing bar achieves the minimum required reinforcing bar elongation percentage as per the codal requirements in IS 1786:2008 (2008). The accomplished tests on coupler-connected reinforcing bars comply with the requirements of codal specifications for the use of reinforcement couplers as mechanical splices to bars in concrete, IS 16172:2014 (2014), which authenticates the efficiency and competency of the proposed coupler sleeve.

COMPARATIVE HYSTERESIS PERFORMANCE OF STANDALONE COUPLER WITH COUPLER BOX ASSEMBLY

The design basis for interlocking coupler sleeves is to apprehend the bond-slip or flexural failure of reinforcing bar from the sleeve, which may develop at regions of high moment and rotation—that is, the plastic hinge locations. Symmetric design of the box assembly is ensured as the direction of earthquake loading is reversible. The advantage of interlinking is that it allows the collective participation of all the coupler sleeves, similar to trusses. The truss ideology designed is as per the equilibrium (plasticity) truss

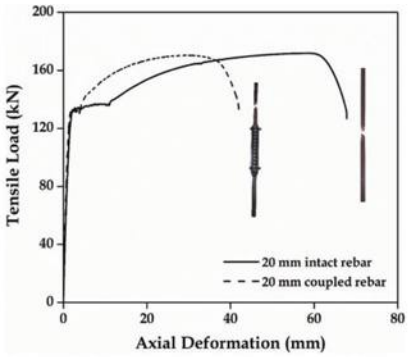

(a) Uni-axial tension behaviour in coupler-connected and intact rebars.

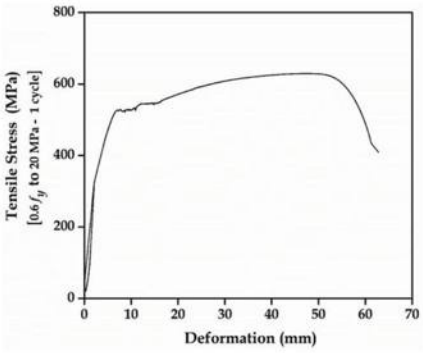

(b) Slip test on the coupled rebar

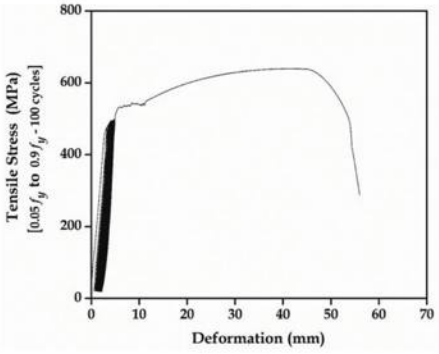

(c) Cyclic tensile test on the coupled rebar

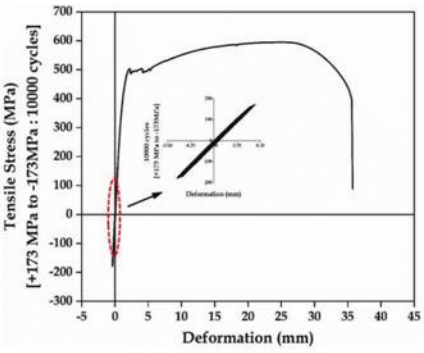

(d) Low-cycle fatigue test on coupled rebar

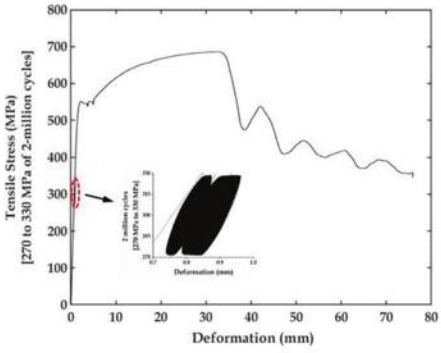

(e) High-cycle fatigue test on coupled rebar

Fig. 3—Performance requirements of proposed coupler sleeve as per standard code of practice (IS 16172:2014).

model by Hsu and Mo (2010). The strut-and-tie model is adopted in designing column regions with the concept of stress flows. Interaction relationship for shear-torsion-bending is derived. The interconnecting flat steel bars undergo tension and compression based on the direction of loading, and the diagonal connection assists in the additional confinement of concrete enclosed between sleeves, which is expected to withstand higher axial loads without failure. The process of interlinking further prevents the local buckling of surrounding sections of reinforcing bars. The procedure for interlinking coupler sleeves is carried out using mild steel rectangular-shaped flat bars of 25 mm (0.98 in.) width and 5 mm (0.19 in.) thickness, while the dimensions are determined using equivalent cross-sectional area of shear reinforcement in the plastic hinge region. The 8 mm (0.32 in.) diameter inclined bolt holes of the sleeve are used for interlinking, as shown in Fig. 4(a). The interlinking process in the case of more than four reinforcing bars is shown in Fig. 4(a). In such a case, the length of flat steel bars varies and remains subjective with the distance between adjacent sleeves. Further, the flat bar thickness reduces as per the computed shear area at the plastic hinge. In columns of rectangular cross section, where the number of reinforcing bars are greater than four, the intercepting coupler sleeves of intermediate reinforcing bars are positioned with their interlinking bolt-holes oriented towards the column face and the maximum number of interlinking flat bars that converge at an intermediate coupler in any column configuration is four.

To compare the structural efficiency of coupler-box assembly (interlinked coupler sleeve) over standalone coupler (stirrup bound coupler, Fig. 4(b)), reverse cyclic tests are conducted on two-full scale RC columns of length 3.3 m (10.83 ft) and cross-sectional size 400 x 400 mm (15.75 x 15.75 in.), as shown in Fig. 5. The coupler connections are

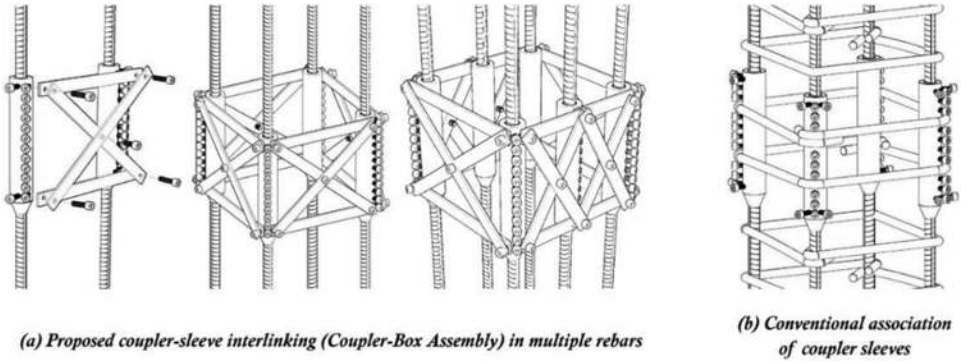

Fig. 4—Pictorial representation of recommended and existing coupler sleeve applications.

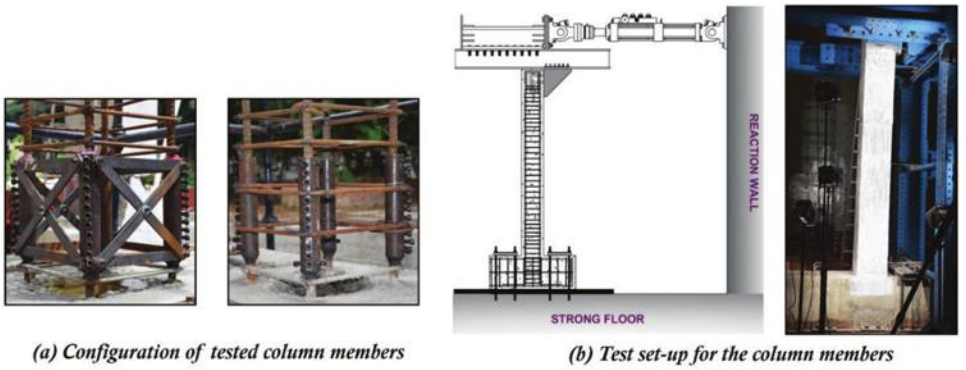

Fig. 5—Details and experimental test setup for RC columns.

maintained above the foundation level with the bars originally connected prior to casting. Four numbers of 20 mm (0.79 in.) diameter reinforcing bars with a yield strength of 500 MPa (72.52 ksi) are provided as longitudinal reinforcement with two-legged, 10 mm (0.39 in.) diameter reinforcing bars (500 MPa [72.52 ksi]) as shear reinforcement. Column casting is executed using ordinary portland cement (OPC) of Grade 43 (C), locally available river sand as fine aggregate (FA), and well-crushed granite stone of 20 mm (0.79 in.) maximum size as coarse aggregate (CA). A conventional mixture ratio of Grade M20 concrete—that is, 1.00 (C):1.50 (FA):3.00 (CA) with a water-cement ratio (w/c) of 0.50—is adopted for column casting. Reinforcement detailing in the column specimens is kept identical to that of the columns of selected RC portal frame. The column specimens are tested under a consistent vertical dead load of 30 kN (6.74 kip)—that is, the self-weight of the loading beam in the frame test setup. The column study aims to examine the efficiency of coupler sleeves under the worst possible mode of failure that occurs near the plastic hinge region of columns. Tension failure of the column due to flexure is one such significant failure mode, where the reinforcing bars may possibly slip out from their respective sleeve connections. The proposed sleeve connections are strong in shear and compression, as the effective cross section doubles near the connection. Thus, the columns are projected to fail in tension, where the axial load must be in the range of zero to balanced load condition—that is, approximately 20% of pure axial load capacity. The axial load is kept minimum, so that tension failure prevails under any test conditions. Further, the secondary moments at higher drifts are not preferred to be developed in the system, as there is no mechanism to quantify them. The columns are tested under cyclic incremental lateral drifts until failure, with the testing and loading protocols remaining similar to the model frame. Thus the reinforcement detailing and the test setup for columns can be inferred from the subsequent section of frame testing.

The load-deflection behavior of tested columns in the form of hysteresis loops and envelope plots are shown in Fig. 6. Cyclic test results of the columns are detailed in Table 1. There is a significant increase in the hysteretic performance of standalone couplers by interlinking them into a box-shaped confinement system. Performance of both the columns is identical up to their yield point—that is, the hysteretic backbone curves follow a similar path until the yield point, after which a minor difference in lateral load is noticed towards the negative half-cycle of the coupler-stirrup column, and a significant variation in the post-yield behavior of coupler-box column is noticed towards positive half-cycle. The column with box arrangement sustains a stable post-yield behavior up to a lateral drift ratio of 6.25%, which is around two times more than the column with standalone coupler. The integral confinement action of reinforcing bars provided by the coupler-box assembly favours a balanced and symmetric hysteretic loop behavior in the box assemblage column. The reinforcing bars of conventional coupler-stirrup column undergo stress reversals independently, unlike the coupler-box column where the interlinking flat steel bars develop a truss mechanism inside the plastic hinge region and distribute the stresses over the interlinked group

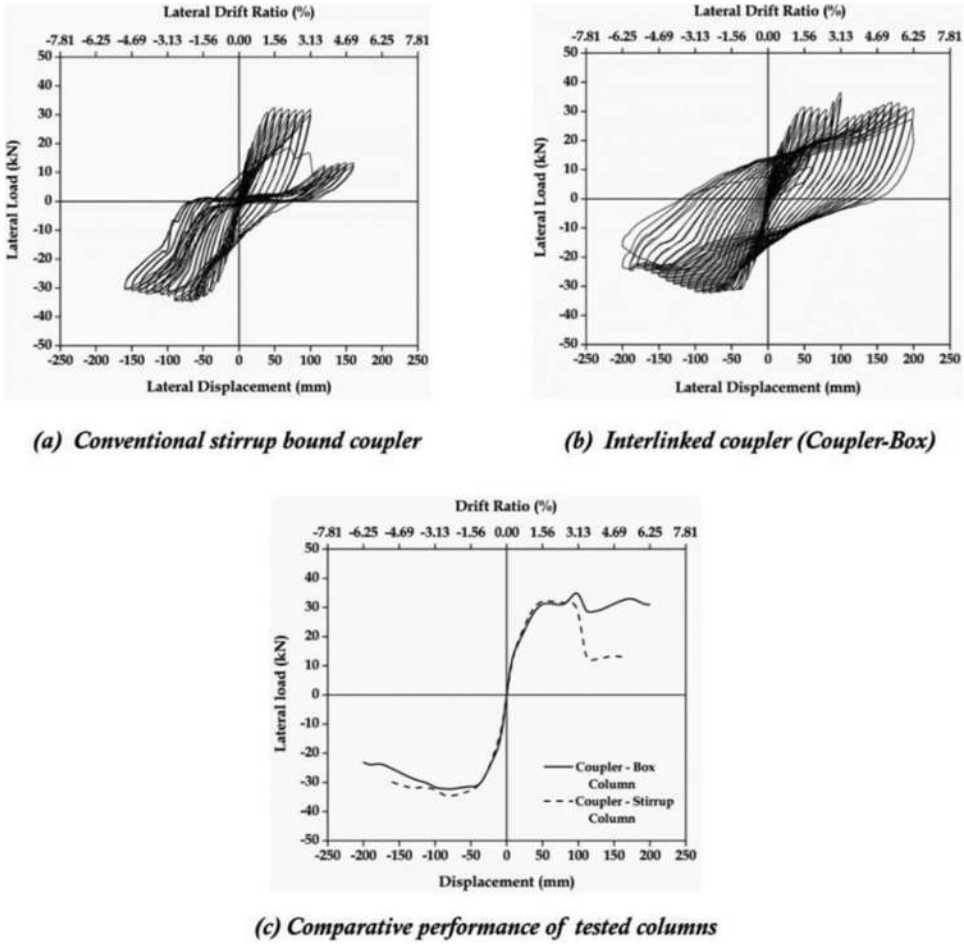

Fig. 6—Comparative performance of interlinked coupler-box technique.

Table 1—Cyclic test results of tested RC specimens

Specimen ID	Compressive strength on testing day, MPa (ksi)	Yield stage				Maximum stage				Ultimate stage				Ductility factor (μ)	Energy dissipation, kN-mm (kip-in.)
		Positive		Negative		Positive		Negative		Positive		Negative			
		P_y, kN (kip)	Δ_y, mm (in.)	P_y, kN (kip)	Δ_y, mm (in.)	P_m, kN (kip)	Δ_m, mm (in.)	P_m, kN (kip)	Δ_m, mm (in.)	P_u, kN (kip)	Δ_u, mm (in.)	P_u kN, (kip)	Δ_u, mm (in.)	Δ_u/Δ_y	
Coupler-stirrup column	25.52 (3.70)	20.5 (4.6)	19.5 (0.77)	20.9 (4.7)	19 (0.75)	32.5 (7.3)	49.6 (1.95)	34.8 (7.8)	79.8 (3.14)	26 (5.8)	102.3 (4.03)	29.8 (6.7)	159.9 (6.29)	6.83	43,089.15 (381.36)
Coupler-box column	25.14 (3.65)	17.4 (3.9)	15.5 (0.61)	19.9 (4.5)	15 (0.59)	36.5 (8.2)	99.8 (3.93)	32.4 (7.2)	79.3 (3.12)	30.9 (6.9)	199.3 (7.85)	25.9 (5.8)	154.9 (6.09)	11.59	145,824.05 (1290.60)
Control frame	26.28 (3.81)	60.1 (13.5)	18.5 (0.73)	60.6 (13.6)	18 (0.71)	91.2 (20.5)	59.49 (2.34)	90.8 (20.4)	69.4 (2.73)	72.9 (16.4)	166.9 (6.57)	72.7 (16.3)	166.2 (6.54)	9.12	312,629.33 (2766.89)
Restored frame	31.71 (4.59)	66.9 (15)	20.5 (0.81)	62.4 (14)	19.7 (0.78)	108.6 (24.4)	59.52 (2.34)	99.4 (22.4)	59.2 (2.33)	86.4 (19.4)	141.8 (5.58)	79.5 (17.9)	132.7 (5.22)	6.83	267,472.44 (2367.24)

of reinforcing bars. This leads to a conventional failure or rupture in reinforcing bars of the coupler-stirrup column with an asymmetric behavior. The irregular behavior in Fig. 6(a) is due to the rupture of reinforcing bars at the right edge of the column face—that is, for classification, rupture occurs in reinforcing bars that experience tensile stresses under the negative half-cycle, which causes a sudden reduction in lateral strength post 3.2% lateral drift. This aspect is not noticed during the negative half-cycle of testing. Moreover, the pinching effect in the hysteretic loops is noticed in the coupler-stirrup column, which is absent in the coupler-box column.

Interlinking the proposed coupler sleeves essentially unites the strength of the standalone coupler under flexure, which minimizes the chance of flexural yielding and the restored section is subjected to shear force where the strength of the coupler sleeve is resistive. Thus, the entire box assembly functions as a rigid link section which shrinks the plastic hinge length and compels the adjacent reinforcing bar segments to yield away from the coupled region. Energy dissipation capacity of the box assembly column is

enhanced by 3.3 times, and the ductility factor is improved by 1.7 times compared to the standalone coupler column. The failure mode remains identical in both columns, where the yielding of longitudinal reinforcing bars occurs at the column-foundation interface at 3% lateral drift. Subsequently, with the increase in lateral drift, a sudden brittle failure is observed in the coupler-stirrup column, whereas a ductile and balanced behavior, even at a drift of 6% (which is higher than the prescribed codal provision of 4% by FEMA 356 [2000]) is observed in coupler-box column, as shown in Fig. 7.

HYSTERETIC PERFORMANCE EVALUATION OF RC PORTAL FRAME RETROFITTED WITH COUPLER-BOX ASSEMBLY

The primary model frame opted for this study is an RC portal frame of height 3.35 m (10.99 ft), which is cast and tested under the combined effect of vertical and lateral loads in a large-scale structural test facility at the Department of Earthquake Engineering, Indian Institute of Technology (IIT) Roorkee. Columns of cross-sectional size 400 x 400 mm (15.75 x 15.75 in.) are connected by a 3.0 m (118.11 in.) length beam of size 300 x 300 mm (11.81 x 11.81 in.). The frame assembly is supported by a 5.0 m (196.85 in.) length foundation beam of sectional size 550 x 600 mm (21.65 x 23.62 in.). A minimum longitudinal reinforcement of 0.8%—that is, four numbers of 20 mm (0.79 in.) diameter thermomechanical treatment (TMT) processed reinforcing bars with an average yield strength of 500 MPa (72.52 ksi)—are used for reinforcing the beam and column sections. Two-legged stirrups of 10 mm (0.39 in.) diameter reinforcing bar with 500 MPa (72.52 ksi) yield strength are used to reinforce the sections for shear. Stirrup detailing of the frame is provided as per the codal specifications for ductile detailing of reinforced concrete structures subjected to seismic forces, IS 13920:2016 (2016). Section details, along with the reinforcement detailing of the portal frame, are shown in Fig. 8. The mixture ratio adopted for frame casting in the preliminary study is 1.00 (C):1.50 (FA):3.00 (CA) with a *w*/*c* of 0.50.

The RC portal frame is tested under displacement-controlled reverse cyclic load as per interim test protocols for determining seismic performance characteristics of structural and nonstructural components (FEMA 461 2007). A constant loading frequency of 0.01 Hz is adopted with an initial loading rate of 0.2 mm/sec (0.0079 in./sec), which is increased at a rate of 0.2 mm/sec (0.0079 in./sec) until 20 mm (0.79 in.) lateral displacement. After the 20 mm (0.79 in.) displacement cycle, the loading rate is increased at a pace of 0.4 mm/sec (0.016 in./sec) until the end of the test sequence. The test is executed using three servo-controlled hydraulic actuators (one horizontal: 500 kN [112.4 kip]; ±250 mm [9.84 in.] and two vertical: 250 kN [56.2 kip]; ±250 mm [9.84 in.]), as shown in Fig. 9. All the three actuators are integrally connected to the loading beam, which is bracketed to the model frame through tie-rods. The vertical actuators with swivel-end assemblies at both edges are fixed atop steel stands and placed in line with the columns of the model frame. The loading beam enforces vertical load through two rollers placed at a meter's distance (3.28 ft) from joints and is kept consistent throughout the test sequence (refer to Fig. 9). The deformation/deflection profile of beam under uniformly distributed infill wall load is simulated by applying two-point loading on top of the beam. The axial load is preferred to be low to make the columns fail in flexure/tension and to minimize the secondary moments (P-Δ) at large lateral displacements, as there is no mechanism to monitor them in the test setup. The horizontal actuator associated with the top face of the loading beam exercises lateral displacements in an incremental sinusoidal wave pattern and the lateral force response obtained from it is used in plotting hysteresis curves. The test is carried out until comprehensive damage to the model frame is achieved. Hence, the number of load cycles are high and the frame can withstand a higher lateral drift of 6%.

The hysteresis behavior of the conventional portal frame (hereby referred to as the CON frame) is plotted, as shown in Fig. 10. A stable behavior with gradual post-peak performance is observed up to a lateral drift of 6%. Eventually, buckling of longitudinal reinforcing bars occurs at the plastic hinge location of columns—that is, at the column base along with shear cracks at upper beam-column joints at a higher lateral drift of 6%. The damaged CON frame model after its preliminary test is shown in Fig. 11.

The damaged model frame after the preliminary test is repaired at its hinge locations using the proposed retrofitting methodology of coupler-box assembly. The sequence for restoring a damaged column base is shown in Fig. 12. The fundamental procedure consists of six main steps, namely: (a) supporting the damaged frame by redistributing the vertical dead loads through jacks and chipping of crushed concrete at hinge regions to expose the buckled reinforcing bars (the amount of concrete that is demolished is two times the length of the sleeve, with the provision of one length of sleeve on either side of the cut reinforcement; this decision remains subjective with the available length of concrete removal); (b) rectification of reinforcing bars along with the insertion of coupling sleeves on repositioned reinforcing bars; (c) proper positioning and fixing of sleeves with high-strength external bolts at a proportion of six bolts (half the total number of bolts) on each connected reinforcing bar segment; (d) interlinking the coupling sleeves in lateral and diagonal directions, respectively, using flat steel bars to generate a box-shaped assembly; (e) injection of high-strength epoxy mortar grout to fill the void spaces between reinforcing bar and coupler sleeve and eventually reinstating the transverse reinforcement near adjacent frame sections; and (f) laying freshly prepared concrete (mixture ratio: 1.00 (C):1.40 (FA):2.20 (CA)) using letter-box shuttering. A resin-based concrete bonding agent is applied to the existing old concrete's surface to create a better bond with the new concrete.

The retrofitted (RET) frame is tested under identical loading conditions as of the CON frame, and the hysteresis plot is shown in Fig. 13. The test results of model frames are detailed in Table 1. The comprehensive performance of the RET frame is monitored using extensive instrumentation during the cyclic test. LVDTs are used to monitor the

(a) Stirrup-bound coupler column with failure @ 3 % lateral drift

(b) Interlinked coupler-box column with failure @ 6 % lateral drift

Fig. 7—Failure patterns noticed in RC columns.

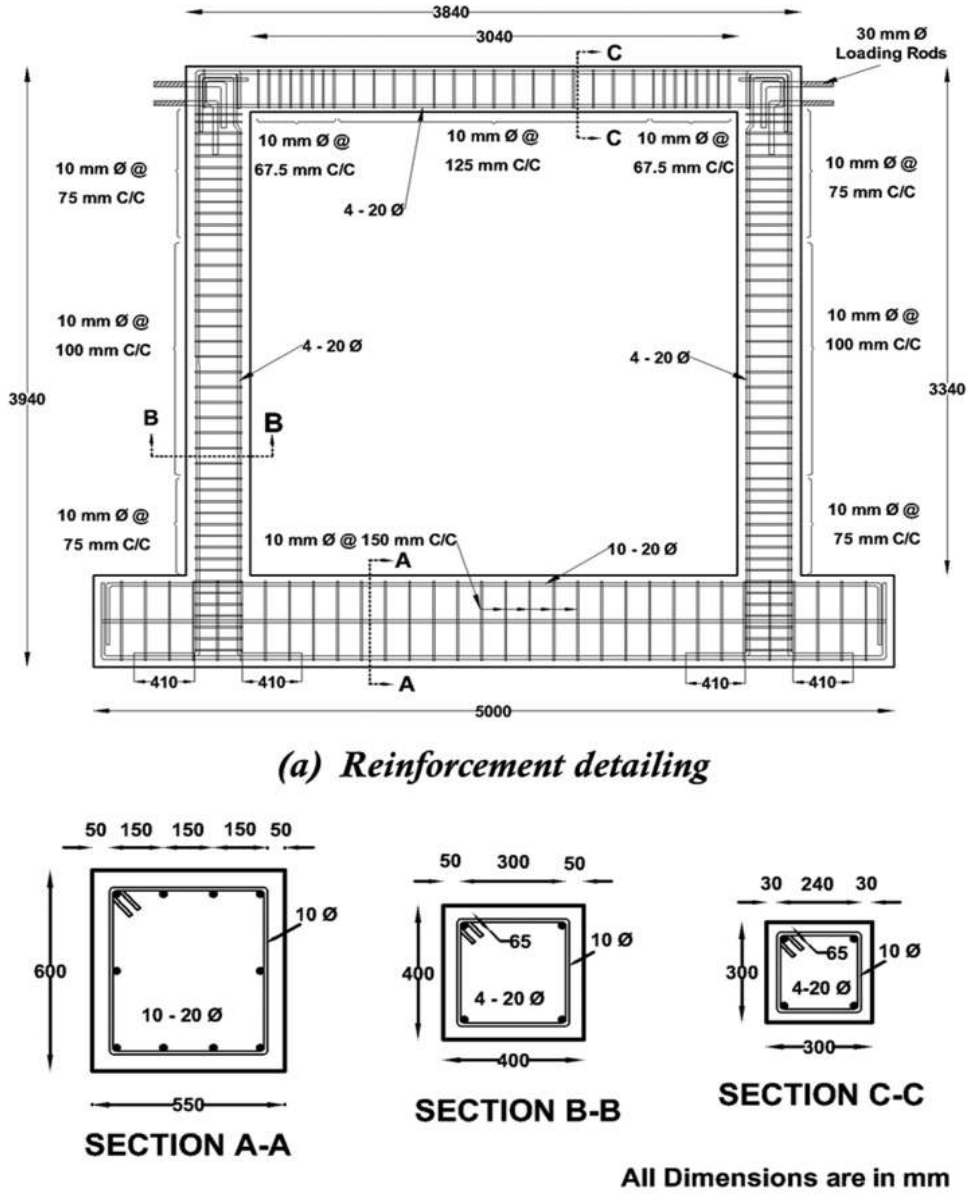

Fig. 8—Reinforcement detailing in tested RC model frames.

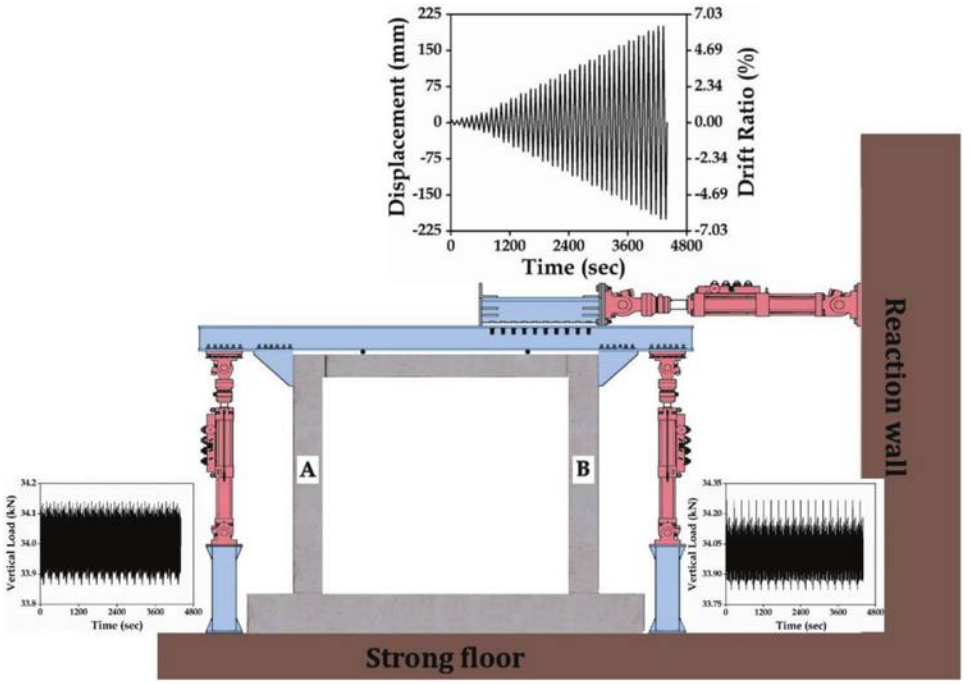

Fig. 9—Schematic diagram showing test setup for RC frames.

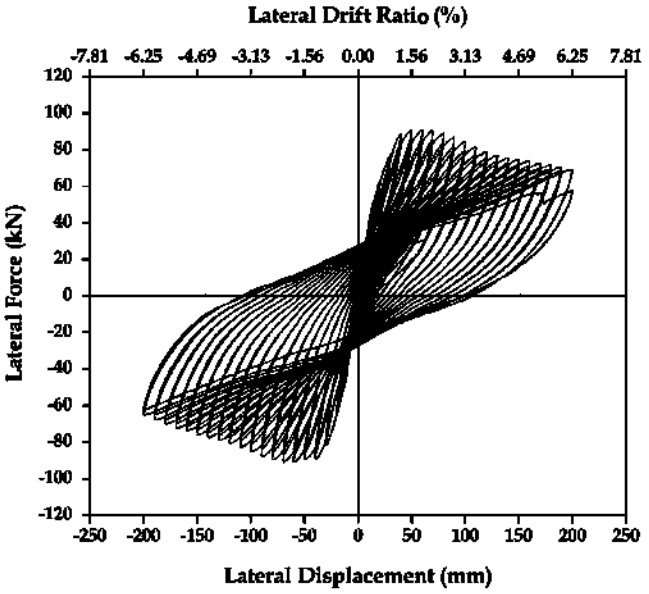

Fig. 10—Hysteresis curves of CON model frame.

lateral displacement of frames at various heights—that is, (i) just above the foundation level at 150 mm (5.91 in.); (ii) mid-level of the column at 1525 mm (60.04 in.); and (iii) upper section of the column below bracket attachment at 2750 mm (108.27 in.). Strain variations in reinforcing bars above and below the box assemblies of RET frame are acquired by a 32-channel data acquisition (DAQ) system through 10 mm (0.39 in.) strain gauges fixed at these locations. Further, a noncontact full-field deformation measurement technique known as digital image correlation (DIC) is used to inspect the column surface of RET frame for variation in superficial principal strains and lateral displacements. This technique adopts a three-dimensional (3-D) DIC system, which analyzes high-definition speckled images captured using the Vic-Snap software. Complementary metal oxide semiconductor (CMOS) camera sensors of 8.9 megapixels are equipped with 10 mm (0.39 in.) lens, and a calibration plank of 40 mm (1.57 in.) size is used along the column height, which is pre-speckled with a 0.20 in. (5.08 mm) sized roller. Test images are captured at a rate of two frames per second, and post-processing is performed using the Vic-3D software, where the selected subset size is 45 pixels, step size is 11, and the strain computation filter size is 29 pixels.

The comparative performance of CON and RET frame models in the form of an envelope curve of hysteresis loops is shown in Fig. 14. The initial strength and stiffness of RET frame are similar to that of the CON frame, which signifies the efficiency of the adopted retrofitting technique. A considerable increase in the post-yield behavior of the RET frame in comparison to the CON frame is observed. The enhancement in gradual post-peak behavior of the RET frame is noticed until a lateral drift ratio of 5%, which is higher than the collapse limiting drift of 4% as prescribed by FEMA 356. This manifests the fact that the coupler-box assembly sustains higher strains without any slip of longitudinal reinforcing bars from their respective sleeves. An average increment of 20% in lateral strength is noticed, which emphasizes that the coupler-box confinement resists the high amount of shear and moment developed at the plastic hinge region. The box assembly induces rigidity to the frame section which shifts the formation of failure hinges away from the coupled region—that is, near the foundation at column-foundation junction.

The linear deflection profiles of column members in the CON and RET frame models are determined using the recorded data of LVDT and DIC. The peak displacement readings obtained from the three equidistant LVDTs are plotted against their corresponding peak loads, as shown in

Fig. 11—Damaged model frame after preliminary test.

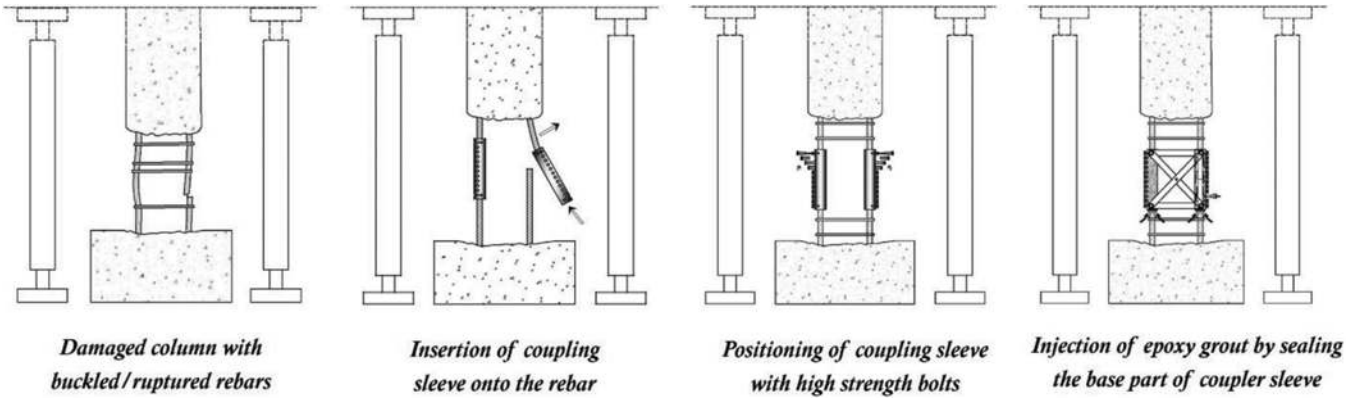

Fig. 12—Schematic diagram depicting procedure for reestablishing damaged column.

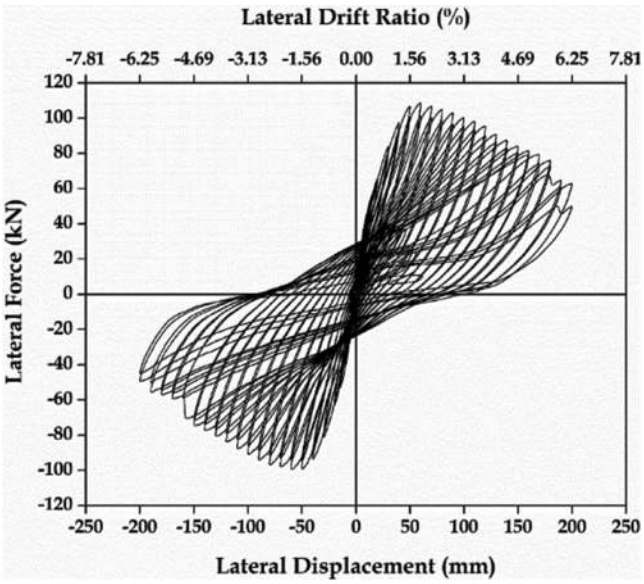

Fig. 13—Hysteresis curves of RET model frame.

Fig. 14. The plotted displacement contours distinctly indicate that the RET frame retained its initial stiffness along with an enhanced lateral load capacity. A similar trend of variation in deflections is observed in both the model frames, with a meagre variation in RET frame post 5% lateral drift.

The damage patterns observed in the RET frame with superficial crack propagations inferred from DIC output images are shown in Fig. 15. Selective output images in their left and right sway directions are presented at the lateral displacement cycles of 10, 100, and 200 mm (0.39, 3.94, and 7.87 in.)—that is, at initial, midway, and end of the test sequence, respectively. The variation in principal strains along the column length helps in recognizing the regions of high-strain concentrations—that is, the possible location of cracks/damage. It is clearly manifested that the percentage of principal strain variation is comparatively low at the coupler-confined region of column, which indicates the absence of concrete cracking. This emphasizes the suitability of the employed retrofitting technique in confining core concrete and providing better stiffness retention to the coupler-confined column sections. In the eventual part of the test run, flexural cracks are noticed at the base part of columns—that is, away from the coupler-box section, which enlarges with a gain in lateral drift ratio. Diagonally inclined shear cracks and spalling of cover concrete at beam-column joint locations of the frame are noticed at a higher lateral drift of 6%.

Strain variations at possible locations of longitudinal reinforcing bars placed above and below the box assemblies in the columns of the RET frame are plotted against their corresponding lateral drifts, as shown in Fig. 16. Strain values in gauges below the box section show larger variation than the gauges above it, which indicates the yield/rotation of reinforcing bars below the assembly. The average

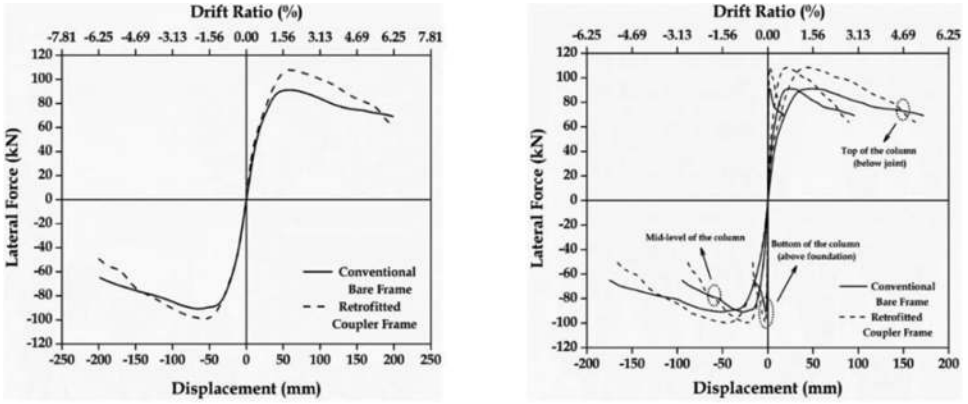

(a) Hysteresis envelope of frame models

(b) Deflection profiles of columns in tested frames

Fig. 14—Comparative performance in tested RC model frames.

strain variation value in reinforcing bars below the assembly is 0.015, whereas it is only 0.005 above it, which is much lower than the yield strain of the adopted reinforcing bar.

The cumulative amount of energy dissipated by the CON and RET frame models is plotted against corresponding lateral drifts, as shown in Fig. 17. The energy-dispersion capacities of both the model frames are identical up to a lateral drift of 5%, after which a meager drop in the capacity of the RET frame is noticed in comparison with the CON frame. The CON frame model undergoes a flexural mode of failure and dissipates higher energy until the yielding of reinforcing bars, which occurs at 6% drift. The coupler-box assembly of RET frame increases the local rigidity of column section and consecutively transfers the lateral force to an adjacent frame section near to column-foundation junction, where the longitudinal reinforcing bars undergo a repeated reversal of stresses until failure. This leads to the formation of a plastic hinge at column base, which reduces the relative amount of energy dissipated post 5% drift. The equivalent viscous damping (EVD) coefficient/ratio ξ_{hyst} of frame models is computed based on the elastic strain energy approach, and the percentage of variations is plotted against the corresponding drift, as shown in Fig. 17. The calculated value of the EVD ratio is directly proportional to the amount of energy dissipated and thus, a similar trend of deviation as that of the dispersion capacity is noticed, where a variation in the damping ratio of RET frame occurs post 5% drift.

The degradations in strength and stiffness of model frames post their elastic state are computed and plotted against corresponding lateral drifts, as shown in Fig. 18. The variation in stiffness degradation pattern is similar in both model frames, with a marginally reduced rate in the RET frame. The variation in strength degradation parameter of frame models shows a deviation in the RET frame post 5% drift by virtue of its declination in lateral strength capacity. Thus, it is affirmed that the RET frame regains strength and stiffness up to its original level by adopting the recommended retrofitting technique.

$$D = \frac{\delta_m - \delta_y}{\delta_f - \delta_y} + \beta \frac{\int_{E=E_1}^{E=E_m} dE}{F_y \delta_f} \quad (4)$$

The damage tolerance capacities of tested frames are computed using the modified damage index (DI) proposed by Park and Ang (1985) (Eq. (4)), and the computed values are plotted against corresponding lateral drifts, as shown in Fig. 19. A similar trend of variation in DI values of frame models is noticed with the RET frame reaching its collapse stage at a lateral drift of 3.73% and the CON frame attaining it at 4% drift.

STRENGTH DEGRADATION MODELS BASED ON HYSTERETIC ENERGY DISSIPATION

The peak-oriented cyclic deterioration modes of basic and post-capping strength for the CON and RET frame specimens are developed based on model equations proposed by Ibarra and Krawinkler (2005). The backbone curve for the hysteretic model is defined by initial stiffness (K_e), hardening stiffness (K_s), post-capping stiffness (K_c), and residual strength (F_r), as described in Fig. 20 (Ibarra and Krawinkler 2005), where α_s represents the strain-hardening coefficient; α_c denotes the post-capping stiffness coefficient; and λ is the coefficient of residual strength. Strength-degradation modes of the tested portal frames are stimulated when the lateral load value exceeds yield strength, and the degradation rate is computed based on hysteretic energy dissipated during cyclic loading (Rahnama and Krawinkler 1993). The deterioration parameter β_i is defined as

$$\beta_i = \left(\frac{E_i}{E_t - \sum_{j=1}^{i} E_j} \right)^C \quad (5)$$

where E_i represents the hysteretic energy dissipated in the i-th cycle; $\sum E_j$ indicates the summation of energy dissipated in all previous cycles until i; and E_t is the energy dissipation capacity expressed as a function of twice the elastic strain energy at yielding—that is, $F_y\delta_y$

$$E_t = \gamma F_y \delta_y \quad (6)$$

Here, the factor γ is calibrated from the experimental test results and is different for each deterioration parameter. The

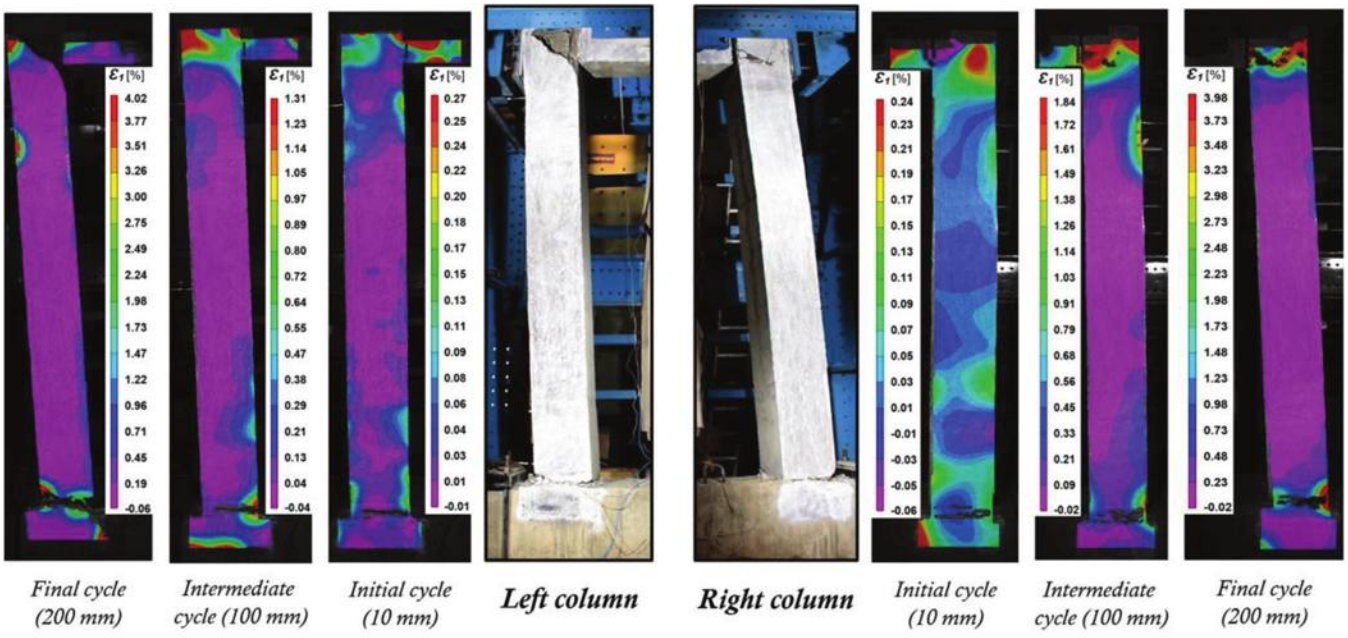

Fig. 15—Variation of superficial principal strains in RET frame monitored using DIC.

exponent factor C defines the rate of degradation in evaluated hysteresis parameters—that is, strength and stiffness, with values ranging between 1.0 and 2.0. The quantified value of β_i must be within the range of $0 < \beta_i \leq 1$, and the hysteretic energy is assumed to be exhausted for conflicting values.

Basic and post-capping strength degradation modes

The basic strength degradation mode of a peak-oriented hysteretic model is defined by translating the strain-hardening branch of the backbone curve towards origin by an amount equal to its reduced yield strength. This strength deterioration mode also includes the degradation of strain-hardening slope computed using parameter $\beta_{s,i}$ and rotated towards the horizontal axis using corresponding equations. This degradation mode is well-explained in Fig. 21, where the mode initiates post the yield point (1). The reduced yield strength in the negative direction F_i^- (4, 10) is computed using Eq. (8) when the curve traverses the horizontal axis (3, 9). In succession, the strain-hardening slope of the curve $K_{s,i}^-$ is modified using Eq. (10), corresponding to which the coordinates (5, 11) are computed. The reduced yield strength in the positive direction F_i^+ (7, 13) after every negative inelastic excursion

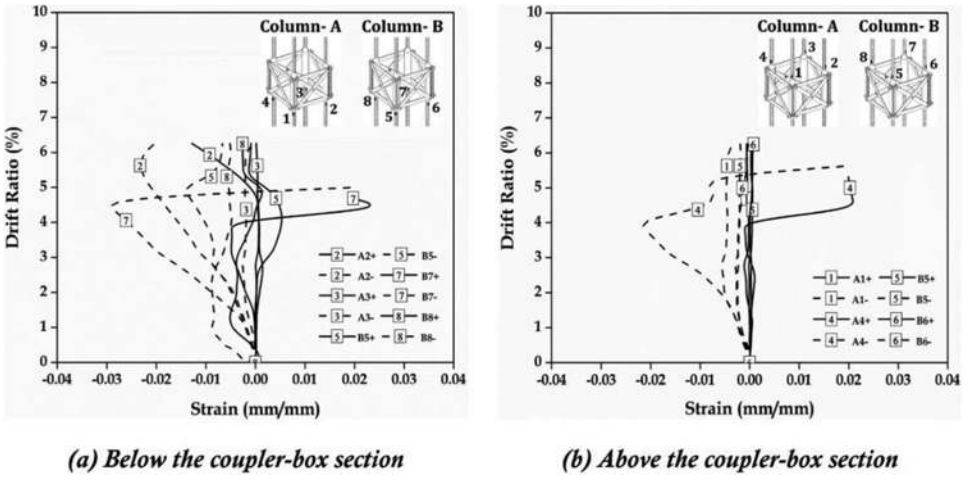

Fig. 16—Strain variations in longitudinal reinforcing bars of RET frame.

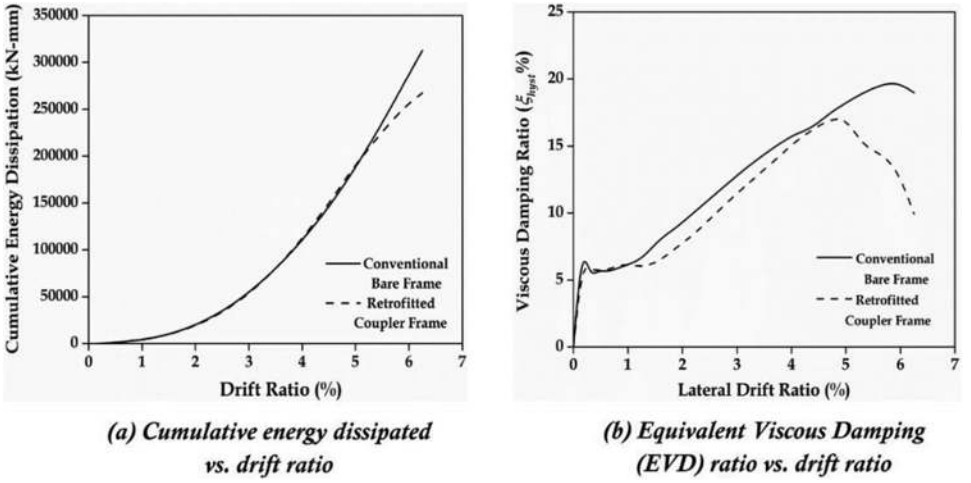

Fig. 17—Energy-based parametric comparison in tested frames.

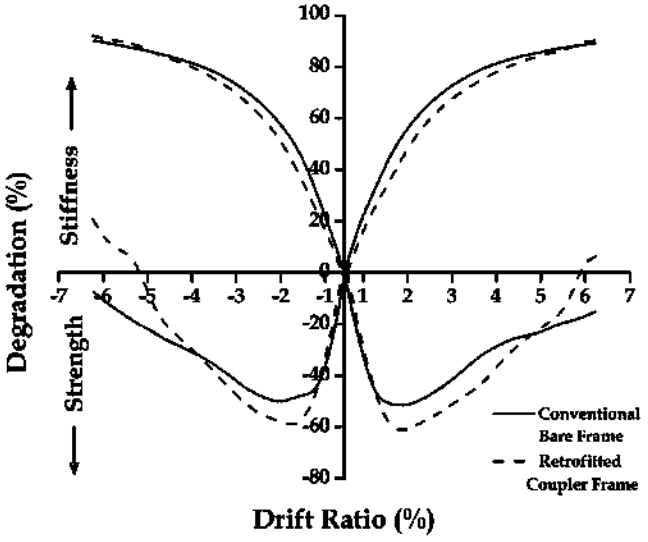

Fig. 18—Comparative plots of strength and stiffness degradations in tested model frames.

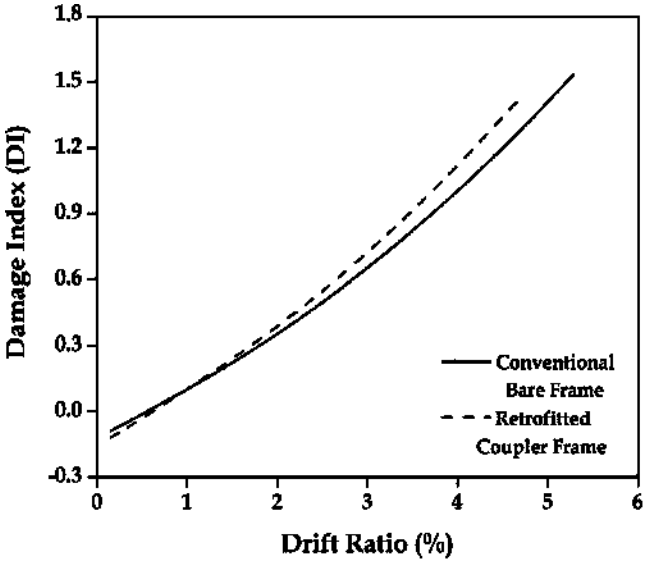

Fig. 19—Damage index versus drift ratio plots of model frames.

(6, 12) is computed using Eq. (7), and the strain-hardening slope $K_{s,i}^{+}$ is altered using Eq. (9) to attain corresponding coordinates (8, 14). The downward branch of degradation curves maintains a slope equal to the initial elastic curve through which the abscissa of points (3, 9, 6, and 12) on the horizontal axis are computed. This computation of the

degradation model of the curve is plotted until the exhaustion of hysteretic energy—that is, until $\beta_{s,i} > 1$

$$F_i^+ = (1 - \beta_{s,i}) F_{i-1}^+ \quad (7)$$

$$F_i^- = (1 - \beta_{s,i}) F_{i-1}^- \quad (8)$$

where $F_i^{+/-}$ is the deteriorated yield strength after expedition/cycle i; and $F_{i-1}^{+/-}$ is the deteriorated yield strength before expedition/cycle i

$$K_{s,i}^+ = (1 - \beta_{s,i}) K_{s,i-1}^+ \quad (9)$$

$$K_{s,i}^- = (1 - \beta_{s,i}) K_{s,i-1}^- \quad (10)$$

where $K_i^{+/-}$ is the deteriorated slope of strain-hardening curve after expedition i; $K_{i-1}^{+/-}$ is the deteriorated slope of strain hardening curve before expedition i; and $\beta_{s,i}$ is determined using the relevant γ_s factor in the aforementioned equations.

The post-capping strength degradation mode of the peak-oriented hysteretic model translates the post-cap stiffness branch of the backbone curve towards origin by an amount equal to its reduced reference strength F_{ref}, which is estimated as the intersection ordinate of the vertical force axis with the projection of the post-cap branch, as shown in Fig. 21. The reduced reference strengths in both positive and negative and directions, $F_{ref,1}^+$ and $F_{ref,1}^-$, are computed using Eq. (11) and (12) when the curve crosses the horizontal axis (3, 8, 6, and 10), respectively. The slope of post-capping branch is kept unaltered and the abscissa of points on the horizontal axis is obtained by the intersection of downward branch of the degradation curve, whose slope is identical to the initial elastic curve. Computation of the degradation mode is carried until hysteretic energy exhaustion—that is, until the value of $\beta_{c,i}$ exceeds unity

$$F_{ref,i}^+ = (1 - \beta_{c,i}) F_{ref,i-1}^+ \quad (11)$$

$$F_{ref,i}^- = (1 - \beta_{c,i}) F_{ref,i-1}^- \quad (12)$$

where $F_{ref,i}^{+/-}$ is the deteriorated reference strength after expedition i; $F_{ref,i-1}^{+/-}$ is the deteriorated reference strength before expedition i; and $\beta_{c,i}$ is computed using the relevant γ_c factor in the aforementioned equations.

The computed parametric values, along with the cyclic degradation modes of basic and post-capping strength for tested RC portal frames, are presented in Fig. 22, where the value of degradation parameter γ is calibrated based on the experimentally obtained hysteresis behavior of the individual frame. The value of γ is high for the CON frame specimen owing to its larger cumulative energy dissipation capacity. The model ductility (δ_c/δ_y) is relatively high by 7% for the CON frame, whereas the peak strength of the model backbone is comparatively high by 7% for the RET frame. The post-capping stiffness coefficient (α_c) for the CON frame model is half the value of the RET frame, which signifies the gradual post-peak behavior. However, the strain-hardening

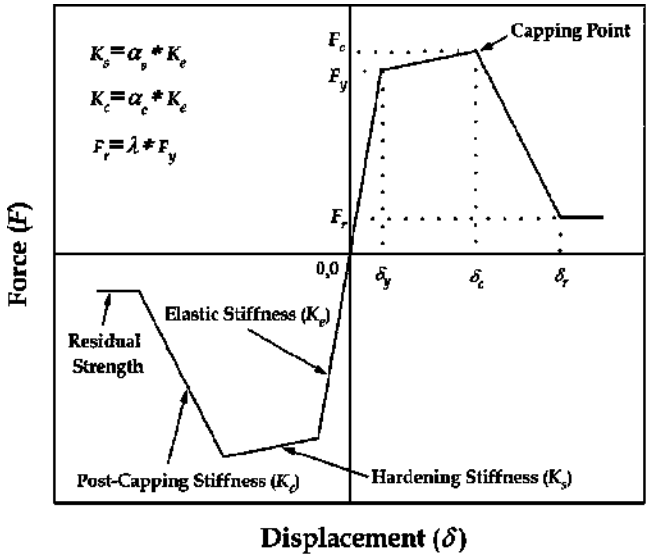

Fig. 20—Backbone curve for hysteretic models (Ibarra and Krawinkler 2005).

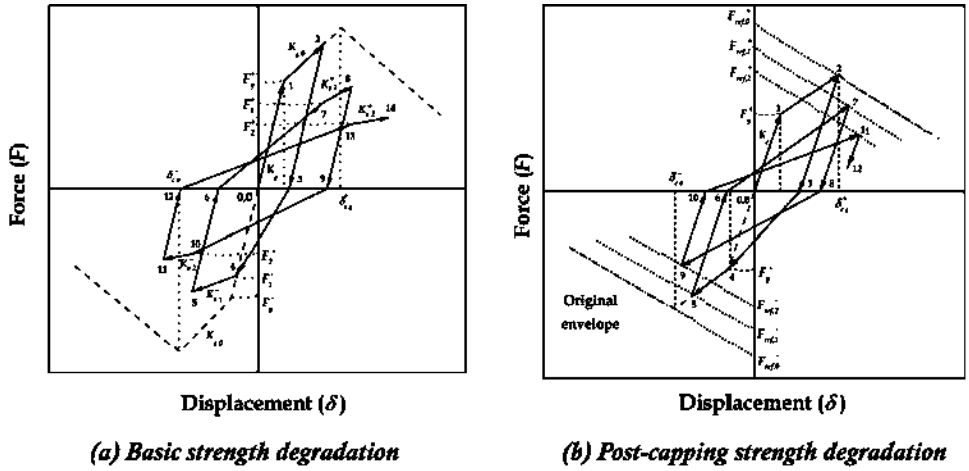

Fig. 21—Peak-oriented models with computed deterioration modes (Ibarra and Krawinkler 2005).

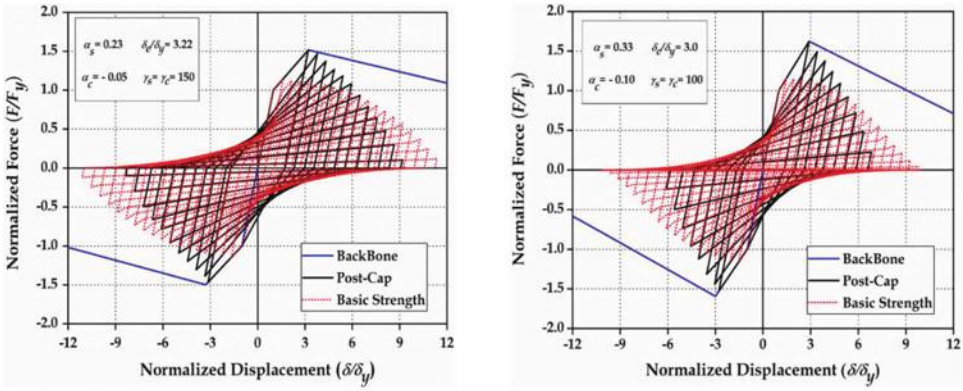

Fig. 22—Cyclic degradation effect on hysteretic response: peak-oriented models.

coefficient (α_s) is high for the RET frame, which is indicated by a sharp rise in the slope of curve post its yield point. The basic strength cyclic degradation mode in CON and RET frame specimens reaches its collapse stage—that is, $\beta_i > 1$—at normalized displacement ratios of 11 and 10, respectively. The post-capping cyclic degradation mode depreciates the peak point of model curve based on its modified reference strength, and the declination rate is comparably high in the RET frame due to its higher descent in the post-capping branch. These cyclic deterioration modes are computed based on experimentally dissipated hysteretic energy, and the CON frame model shows better variation than the RET frame.

CONCLUSIONS

Most of the past earthquake damage survey reports worldwide show that the buckling of reinforcing bars at the hinge location of frame members is a common failure mode during earthquake loading. The current research focuses on seismic retrofitting such as severely damaged frame sections in reinforced concrete (RC) buildings using the coupler-box confinement technique, which is validated by an experimental investigation. The efficiency of the proposed retrofitting scheme is evaluated by conducting reverse cyclic tests on RC columns and frames with four numbers of longitudinal reinforcing bars. The test results are further used in developing hysteresis models for RC frames retrofitted with the recommended technique. The following conclusions are drawn from the study:

1. The uniaxial tensile test on proposed coupler sleeve reveals that its post-yield behavior depends on the diameter of the connected reinforcing bar, and its performance is enhanced by increasing its bond strength through: (a) external bolts; (b) high-strength epoxy filler material; and (c) a grooved surface. The proposed coupler sleeve accomplishes the performance requirements of IS 16172:2014 through static, slip, cyclic tensile, low-cycle, and high-cycle fatigue tests.

2. The quasi-static cyclic test results of RC columns with standalone coupler and confined coupler-box assembly clearly manifest the significance of interlinking, which improves the column's load-deformation capacity by two times. Further, the provided box assembly confines the core concrete, integrates the reinforcing bar action against lateral forces, and alters the critical flexure failure of reinforcing bar slip from the sleeve connection.

3. A comparative hysteresis performance of the retrofitted frame shows that it regains the initial strength and stiffness of the preliminary damaged frame with a better post-yield behavior even at a lateral frame drift of 5.6%. This is more than the collapse prevention drift level of 4% as per FEMA 356 guidelines. Concurrently, an average increase of 20% in lateral strength is observed in the retrofitted frame, which emphasizes the efficiency of coupler-box assembly in sustaining high moments and shear developed at the plastic hinge regions. The induced rigidity of coupler-box assembly shrinks the plastic hinge length and allows its formation below the box assemblage—that is, near the column-foundation junction, under larger flexural moments.

4. The propagation of cracks and failure pattern in the retrofitted frame, as inferred from the digital image correlation (DIC) technique, illustrates that the superficial principal strain at the coupled region of columns shows a lower range of values than the cracking strain of concrete, which indicates the absence of concrete cracks. Simultaneously, the average strain variation values recorded by gauges fixed on reinforcing bars above the box assembly are relatively lower than those below. This authenticates the failure location in retrofitted frame—that is, yielding in reinforcing bars below the column at the foundation connection.

5. The comparative evaluation of performance parameters computed using the hysteresis behavior of frames, such as energy dissipation, viscous damping, strength, and stiffness degradations, clearly interprets the retrofitted frame's behavior in its elastic and inelastic range, which is relatively at par with the original bare frame. The computed damage index (DI) values show a similar variation, with the frames reaching their collapse stage at a nearly equal lateral drift ratio.

6. Strength-degradation hysteresis models for tested frames are determined based on experimentally obtained backbone curves and energies dissipated in their respective cycles. The deterioration models based on basic and post-capping strength modes can reasonably capture the cyclic performance of retrofitted frame with coupler-box assemblies, and can further be used to evaluate existing structures.

AUTHOR BIOS

ACI member **Naveen Kumar Kothapalli** *is a Research Scholar in the Department of Earthquake Engineering, Indian Institute of Technology (IIT) Roorkee, Uttarakhand, India. He received his BTech from Acharya Nagarjuna University, Guntur, Andhra Pradesh, India, in 2012, and his MTech from IIT Roorkee in 2015. His research interests include repair, retrofitting, and rehabilitation of reinforced concrete structures.*

R. Siva Chidambaram *is a Scientist at Central Building Research Institute, CSIR-CBRI Roorkee, India. He received his BE and ME from Anna University, Chennai, Tamil Nadu, India, in 2007 and 2010, respectively, and his PhD from IIT Roorkee in 2016. His research interests include shear strengthening of beam-column joints with high-performance materials in precast and reinforced concrete structures.*

Pankaj Agarwal *is a Professor in the Department of Earthquake Engineering at IIT Roorkee, where he received his ME and PhD in 1994 and 2000, respectively. He received his BTech from G.B. Pant University of Agriculture & Technology, Pantnagar, Uttarakhand, India, in 1989. His research interests include earthquake-resistant design of structures, repair, and retrofitting of masonry and reinforced concrete buildings.*

REFERENCES

Ahmed, G. H., 2015, "Mechanical Properties of Welded Deformed Reinforcing Steel Bars," *ARO-The Scientific Journal of Koya University*, V. 3, No. 1, pp. 28-39. doi: 10.14500/aro.10059

Alias, A.; Sapawi, F.; Kusbiantoro, A.; Zubir, M. A.; and Rahman, A. A., 2014, "Performance of Grouted Splice Sleeve Connector Under Tensile Load," *Journal of Mechanical Engineering Science*, V. 7, pp. 1096-1102.

Allen, P. B.; Colarusso, L. J.; Russwurm, D.; and Judson, W. M., 2007, "Reinforcing Bar Splice with Threaded Collars," U.S. Patent 20070175167A1, filed Jan. 10, 2007, published Aug. 2, 2007.

Ameli, M. J.; Brown, D. N.; Parks, J. E.; and Pantelides, C. P., 2016, "Seismic Column-To-Footing Connections Using Grouted Splice Sleeves," *ACI Structural Journal*, V. 113, No. 5, Sept.-Oct., pp. 1021-1030. doi: 10.14359/51688755

Bompa, D. V., and Elghazouli, A. Y., 2019, "Inelastic Cyclic Behaviour of RC Members Incorporating Threaded Reinforcement Couplers," *Engineering Structures*, V. 180, pp. 468-483. doi: 10.1016/j.engstruct.2018.11.053

Dahl, K. L., 2001, "High Strength Grouted Pipe Coupler," U.S. Patent 6,192,647, filed Apr. 15, 1999, published Feb. 27, 2001.

FEMA 356, 2000, "Prestandard and Commentary for the Seismic Rehabilitation of Buildings," Federal Emergency Management Agency, Washington, DC.

FEMA 461, 2007, "Interim Testing Protocols for Determining the Seismic Performance Characteristics of Structural and Non-structural Components," Federal Emergency Management Agency, Washington, DC.

Haber, Z. B.; Mackie, K. R.; and Al-Jelawy, H. M., 2017, "Testing and Analysis of Precast Columns with Grouted Sleeve Connections and Shifted Plastic Hinging," *Journal of Bridge Engineering*, ASCE, V. 22, No. 10, p. 04017078. doi: 10.1061/(ASCE)BE.1943-5592.0001105

Holdsworth, S., 2006, "Tubular Coupler for Concrete Reinforcing Bars," U.S. Patent 5909980A, filed Sept. 8, 1997, published June 8, 1999.

Holdsworth, S. E., 1997, "Tubular Coupler for Concrete Reinforcing Bars," U.S. Patent 5,664,902, filed June 16, 1996, published Sept. 9, 1997.

Hope, P. F., 1987, Reinforcing Bar Coupling System, U.S. Patent 4,666,326.

Hsu, T. T., and Mo, Y. L., 2010, *Unified Theory of Concrete Structures*, John Wiley & Sons Inc., New York.

Hua, L. J.; Rahman, A. B. A.; Mirasa, A. K.; and Hamid, Z. A., 2008, "Performance of Cs-Sleeve Under Direct Tensile Load: Part I: Failure Modes," *Malaysian Journal of Civil Engineering*, V. 20, No. 1. doi: 10.11113/mjce.v20.15759

Huaco, G., and Jirsa, J., 2012, "Performance of Damaged Column Retrofitted with Innovative Materials and Devices," *15th World Conference on Earthquake Engineering, 15WCEE*, 10 pp.

Ibarra, L. F., and Krawinkler, H., 2005, "Global Collapse of Frame Structures Under Seismic Excitations," Pacific Earthquake Engineering Research Center, Berkeley, CA, pp. 29-51.

IS 1786:2008, 2008, "High Strength Deformed Steel Bars and Wires for Concrete Reinforcement – Specification (Fourth Revision)," Bureau of Indian Standards, New Delhi, India.

IS 9417:2018, 2018, "Welding of High Strength Steel Bars for Reinforced Concrete Construction – Recommendations," Bureau of Indian Standards, New Delhi, India.

IS 13920:2016, 2016, "Ductile Design and Detailing of Reinforced Concrete Structures Subjected to Seismic Forces - Code of Practice (First Revision)," Bureau of Indian Standards, New Delhi, India.

IS 16172:2014, 2014, "Reinforcement Couplers for Mechanical Splices of Bars in Concrete – Specification," Bureau of Indian Standards, New Delhi, India.

Ingham, J. M., and Bai, A. S. H., 2009, "Seismic Performance of Mechanically Coupled Reinforcing Bars," *Magazine of Concrete Research*, V. 61, No. 7, pp. 529-537. doi: 10.1680/macr.2008.00098

Lancelot, H. B. III, 1995, "Combination Mechanical/Grout Sleeve Coupling for Concrete Reinforcement Bars," U.S. Patent 5,383,740, filed Aug. 2, 1993, published Jan. 24, 1995.

Mochizuki, H., and Nihei, T., 1998, "Mortar Grout Splice Sleeve for Reinforcing Bars," U.S. Patent 5,732,525, filed Nov. 15, 1996, published Mar. 31, 1998.

Nzabonimpa, J. D., and Hong, W. K., 2018, "Novel Precast Erection Method of Interlocking Mechanical Joints Using Couplers," *Journal of Construction Engineering and Management*, ASCE, V. 144, No. 6, p. 04018036. doi: 10.1061/(ASCE)CO.1943-7862.0001482

Park, Y. J., and Ang, A. H. S., 1985, "Mechanistic Seismic Damage Model for Reinforced Concrete," *Journal of Structural Engineering*, ASCE, V. 111, No. 4, pp. 722-739. doi: 10.1061/(ASCE)0733-9445(1985)111:4(722)

Parks, J. E.; Brown, D. N.; Ameli, M. J.; and Pantelides, C. P., 2016, "Seismic Repair of Severely Damaged Precast Reinforced Concrete Bridge Columns Connected with Grouted Splice Sleeves," *ACI Structural Journal*, V. 113, No. 3, May-June, pp. 615-626. doi: 10.14359/51688756

Phillippi, D. J., and Hegemier, G. A., 2013, "Use of Mechanical Couplers in Concrete Columns," *AEI 2013: Building Solutions for Architectural Engineering,* pp. 715-724.

Popa, V.; Papurcu, A.; Cotofana, D.; and Pascu, R., 2015, "Experimental Testing on Emulative Connections for Precast Columns Using Grouted Corrugated Steel Sleeves," *Bulletin of Earthquake Engineering*, V. 13, No. 8, pp. 2429-2447. doi: 10.1007/s10518-014-9715-9

Rahnama, M., and Krawinkler, H., 1993, "Effects of Soft Soil and Hysteresis Model on Seismic Demands," Report No. 108, John A. Blume Earthquake Engineering Center, Standford, CA.

Rowell, S. P., and Hager, K. P., 2010, "Investigation of the Dynamic Performance of Large Reinforcement Bar Mechanical Couplers," *Structures Congress*, pp. 2059-2075.

Yang, Y.; Sneed, L. H.; Morgan, A.; Saiidi, M. S.; and Belarbi, A., 2015, "Repair of RC Bridge Columns with Interlocking Spirals and Fractured Longitudinal Bars – An Experimental Study," *Construction and Building Materials*, V. 78, pp. 405-420. doi: 10.1016/j.conbuildmat.2015.01.010

Yee, A. A., 1970, "Splice Sleeve for Reinforcing Bars," U.S. Patent 3,540,763, filed June 17, 1968, published Nov. 17, 1970.

Yee, A. A., 1986, "Splice Sleeve for Reinforcing Bars with Cylindrical Shell," U.S. Patent 4,627,212, filed Aug. 9, 1985, published Dec. 9. 1986.

Yee, A. A., 2009, "Rebar Splice Sleeve and Method of Splicing," U.S. Patent Application 12/081,539.

JOIN AN ACI Chapter!

The American Concrete Institute has Chapters and Student Chapters located throughout the world. Participation in a local chapter can be extremely rewarding in terms of gaining greater technical knowledge and networking with leaders in the concrete community.

Because chapters are distinct and independent legal entities, membership includes both ACI members and non-ACI members and is made up of a diverse blend of architects, engineers, consultants, contractors, educators, material suppliers, equipment suppliers, owners, and students—basically anyone interested in concrete. Many active ACI members initially became involved in ACI through their local chapter. In addition to technical programs and publications, many chapters sponsor ACI Certification programs, ACI educational seminars, project award recognition programs, and social events with the goal of advancing concrete knowledge.

Check out the Chapters Special Section from the November 2020 *Concrete International*: www.concrete.org/publications/concreteinternational.aspx

---

Student Chapters

Join or form an ACI Student Chapter to maximize your influence, knowledge sharing, and camaraderie! ACI has 240+ student chapters located throughout the world, each providing opportunities for students to:

- Connect with their peers and participate in concrete-related activities such as: student competitions, ACI Conventions, ACI Certification Programs, ACI Educational Seminars, local chapter meetings, social events, and community service projects;
- Network with members of local chapters, many of whom have been in the industry for decades and can help to develop professional relationships and offer career advice;
- Win recognition for their universities through the University Award; and
- Learn about the many scholarships and fellowships offered by the ACI Foundation and by ACI's local chapters.

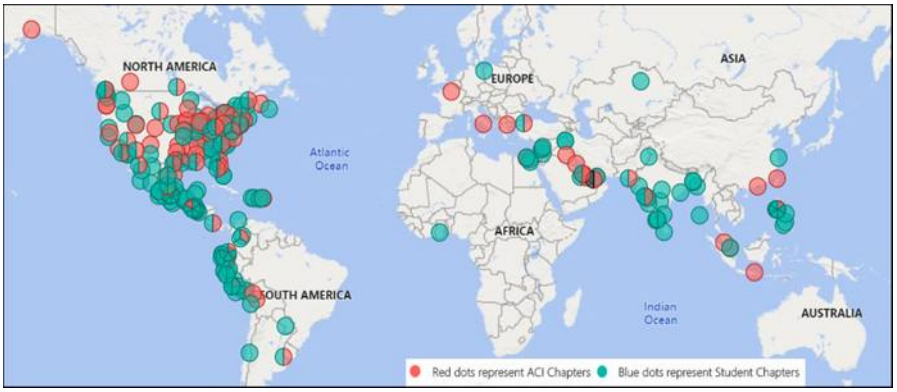

American Concrete Institute

www.concrete.org/chapters

ACI STRUCTURAL JOURNAL TECHNICAL PAPER

Title No. 120-S80

Seismic Performance of Five-Spiral Concrete Columns with Large-Diameter Longitudinal Reinforcement

by Yu-Chen Ou and Brandon Li

Large-diameter longitudinal reinforcement (D43 [No. 14]) and multi-spiral reinforcement were examined for use in the construction of concrete columns to reduce labor demand. Two full-scale columns were tested to investigate their seismic performance. The test column was reinforced with large-diameter longitudinal reinforcement (D43 [No. 14]) and the control column with normal-diameter longitudinal reinforcement (D36 [No. 11]). Both columns were laterally confined by five-spiral reinforcement. Test results showed that the seismic performance of the test column was similar to the control column. Both columns showed ductile behavior with good energy dissipation. Based on the test observations, a buckling model was developed to predict the buckling behavior of longitudinal bars laterally supported by five-spiral reinforcement. Based on the proposed model, it was found that for the same amount and within the practical spacing range of five-spiral reinforcement, the calculated buckling slenderness ratio and hence the compressive stress-strain behavior of D43 (No. 14) bars is similar to that of D36 (No. 11) bars.

Keywords: buckling; columns; cyclic test; five-spiral reinforcement; large-diameter bars; multi-spiral reinforcement; reinforced concrete; seismic.

INTRODUCTION

Due to the shortage of workers, the construction industry in Taiwan has been developing methods to decrease labor demand. In this research, two ways to reduce labor demand are employed for the construction of reinforced concrete columns, including multi-spiral transverse reinforcement and large-diameter longitudinal reinforcement.

Multi-spiral reinforcement is developed to allow non-circular columns to use and take advantage of spiral reinforcement. Several forms of multi-spiral reinforcement have been developed and studied, including two-spiral reinforcement for oblong columns,[1-6] five-spiral reinforcement for square columns,[7-9] six-spiral reinforcement for rectangular columns,[10] seven-spiral reinforcement for oblong columns,[11-13] and 11-spiral reinforcement for rectangular columns.[12] It has been demonstrated that multi-spiral reinforcement can be fabricated by a machine and assembled rapidly on a construction site, significantly reducing labor demand.[7] Moreover, multi-spiral reinforcement shows a better confinement effect than rectilinear tie reinforcement. Even with a smaller amount of transverse reinforcement, columns with multi-spiral reinforcement show better seismic performance than columns with rectilinear transverse reinforcement. In this research, five-spiral reinforcement is used. Figure 1 shows the five-spiral column tested in this research. It can be seen that five-spiral reinforcement consists of one central large spiral and four small spirals at the corners of the column cross section. The reinforced concrete design code of Taiwan[14] is the only design code globally that includes the five-spiral reinforcement. The code requires that the maximum distance between the inner faces of small and large spirals in the overlapping region shall not be less than 0.3 times the inner diameter of the small spiral and 60 mm (2.36 in.) to ensure proper interlocking between small and large spirals. Moreover, the volumetric ratio of each spiral of five-spiral reinforcement in the plastic hinge region shall satisfy the requirements for conventional spiral reinforcement.[7,14]

The large-diameter longitudinal reinforcement used in this research has a diameter of 43 mm (1.69 in.) (D43 [No. 14]). Large-diameter longitudinal reinforcement can reduce the number of mechanical splices and hence decrease labor demand associated with splicing operations. Previous studies have investigated the bond behavior of large-diameter bars. Ichinose et al.[15] studied the bar size effect on the bond strength of bars with a diameter up to 52 mm (2.05 in.). Research results showed bond strength tended to decrease with increasing bar diameter. However, this size effect decreased with increasing confinement to the bars provided by concrete or transverse reinforcement. Steuck et al.[16] investigated the bond behavior of bars grouted in corrugated steel ducts for a bar diameter up to 57 mm (2.24 in.). Research results showed that the bar size effect on bond strength was insignificant. Note that good confinement was provided for bars tested in Steuck's study. The bond failure was governed by shearing along the bar-grout interface, which reduced the size effect according to Ichinose's study. The bond tests by Ichinose et al. and Steuck et al. were carried out using monotonic loading. Murcia-Delso et al.[17] studied the bond behavior of bars with a diameter up to 57 mm (2.24 in.) using cyclic loading. The bars were embedded and well confined in a large circular concrete member reinforced with a dense transverse reinforcement. This simulated the confined situation for a column longitudinal bar embedded into an enlarged pile shaft. A development length equation was proposed for large-diameter bars based on the test results and analytical study.

ACI Structural Journal, V. 120, No. 5, September 2023.

MS No. S-2021-347.R2, doi: 10.14359/51738834, received April 5, 2022, and reviewed under Institute publication policies.

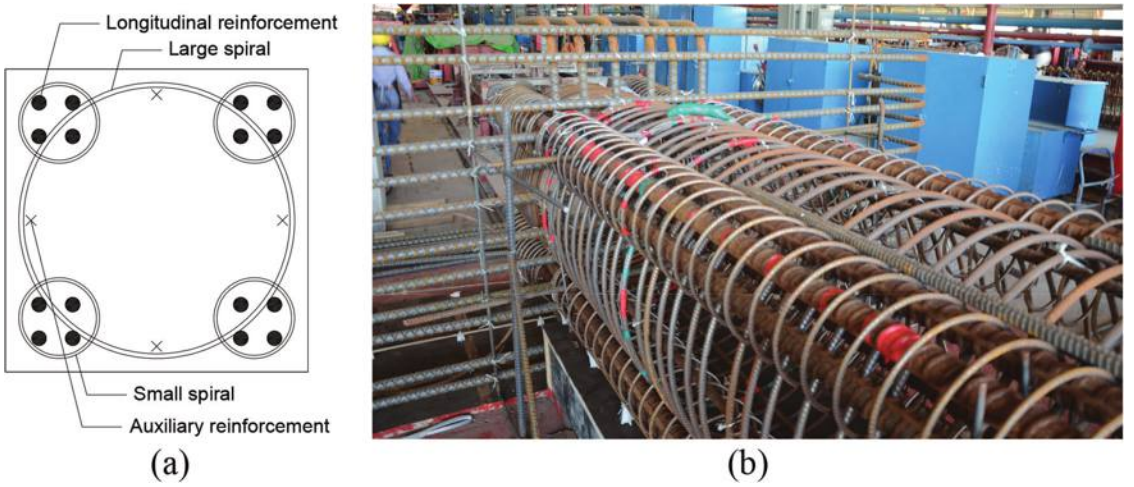

Fig. 1—Column with five-spiral transverse reinforcement and large-diameter longitudinal reinforcement tested in this research: (a) column cross-sectional view; and (b) fabrication of reinforcement cage.

Table 1—Specimen design parameters

Specimen	f_c', MPa	f_{ca}', MPa	Axial load ratio, $P/f_{ca}'A_g$	Transverse reinforcement				Longitudinal reinforcement			
				f_{yt}, MPa	f_{yta}, MPa	Size @ spacing, mm	ρ_s, %	f_y, MPa	f_{ya}, MPa	Quantity-size	ρ_g, %
C36	35	41.2	0.0425	420	538.8	Large: D14 @ 75	1.18	420	465.7	24-D36	2.98
				420	494.9	Small: D9 @ 75					
C43	35	40.5	0.0432	420	538.8	Large: D14 @ 75	1.18	420	461.5	16-D43	2.87
				420	494.9	Small: D9 @ 75					

Note: 1 MPa = 145.04 psi; 1 mm = 0.0394 in.

Murcia-Delso et al.[18] tested two full-scale columns supported by enlarged shafts using lateral cyclic loading. One column used longitudinal reinforcement with a diameter of 36 mm (1.42 in.), which is typically the maximum bar diameter used for construction, and the other one with a diameter of 43 mm (1.69 in.). Test results showed the embedded lengths designed for both columns were adequate. Moreover, both columns showed seismic performance with good energy dissipation and ductility capacities. However, because the two columns were designed with different column heights and different ratios of longitudinal and transverse reinforcement, it is difficult to conclude the performance difference between columns with normal-diameter (36 mm [1.42 in.]) and large-diameter (43 mm [1.69 in.]) longitudinal bars.

The objective of this research is to investigate the difference in seismic performance of multi-spiral columns with normal-diameter (36 mm [1.42 in.]) and large-diameter (43 mm [1.69 in.]) diameter longitudinal bars. Two full-scale column specimens were designed with the same height and same amount of transverse reinforcement, and a similar longitudinal reinforcement ratio. A new bar buckling model was developed for bars laterally supported by multi-spiral reinforcement and used to investigate the difference in buckling behavior of normal-diameter (36 mm [1.42 in.]) and large-diameter (43 mm [1.69 in.]) longitudinal bars.

RESEARCH SIGNIFICANCE

Very few test data exist for concrete columns reinforced with large-diameter steel bars (bar diameter ≥ 43 mm [1.69 in.]) as longitudinal reinforcement. This research provides valuable cyclic test data on a full-scale five-spiral column with D43 (No. 14) longitudinal bars. A control column with D36 (No. 11) longitudinal bars is also provided for comparison. Furthermore, a new buckling model is provided for longitudinal bars laterally supported by five-spiral reinforcement.

EXPERIMENTAL PROGRAM

Specimen design and test setup

Two full-scale rectangular columns with cross-sectional dimensions of 900 x 900 mm (35.43 x 35.43 in.) and a height of 5020 mm (197.64 in.) were designed and tested in this research. The column was from the column of a prototype elevated expressway located in Taiwan. One column (C36) was designed with D36 (No. 11) reinforcing bars for longitudinal reinforcement and served as a control specimen, representing a conventional column. The other column (C43) was designed with D43 (No. 14) bars for longitudinal reinforcement and served as a test specimen to investigate the seismic performance of columns with large-diameter longitudinal reinforcement. The design details of both columns are listed in Table 1 and shown in Fig. 1. Both columns had the same specified material properties. Column C36 was designed to have a nominal flexural strength of 3923 kN-m (2893.46 kip-ft), close to the nominal flexural strength of

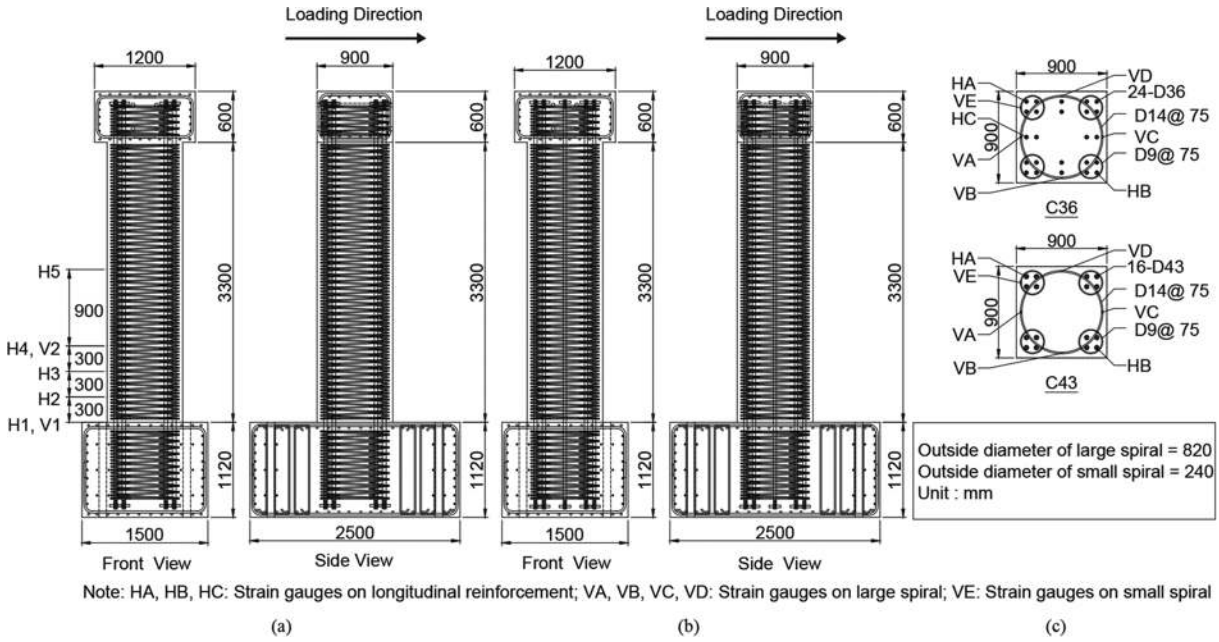

Fig. 2—Dimensions and reinforcement details for: (a) column C36; (b) column C43; and (c) column cross section. (Note: 1 mm = 0.0394 in.)

column C43—that is, 3827 kN-m (2822.65 kip-ft). As shown in Fig. 2, 24 longitudinal bars were used for column C36. The number was significantly reduced to 16 for column C43. The reinforcement ratio ρ_g for columns C36 and C43 was 2.98% and 2.87%, respectively.

Both columns were designed with the same type of five-spiral transverse reinforcement consisting of a large spiral with an outer diameter of 820 mm (32.28 in.) and four small spirals with an outer diameter of 240 mm (9.45 in.). The maximum distance between the inner faces of small and large spirals in the overlapping region was 97 mm (3.81 in.), larger than the smaller value of 0.3 times the inner diameter of the small spiral (0.3 × 240 = 72 mm [2.83 in.]) and 60 mm (2.36 in.) as required by the reinforced concrete design code of Taiwan.[14] D9 and D14 steel bars were used for small and large spirals, respectively. The vertical center-to-center spacing of small and large spirals was 75 mm (2.95 in.). The volumetric ratio of transverse reinforcement was 1.181%, which was calculated based on the confinement requirement for the plastic hinge region of a column.[7,14,19] The columns were designed to fail in flexure. The shears corresponding to the nominal flexural capacities of columns C36 and C43 were 1189 and 1160 kN (267.3 and 260.78 kip), respectively—much lower than the nominal shear capacity[9] of 2315 kN (520.43 kip) of both columns.

The columns were tested with an axial load (Table 1) applied vertically to the top of the column first. The axial load was maintained constant throughout the testing. Then, displacement-controlled cyclic loading was applied laterally to the top of the column with the bottom of the column fixed to the strong floor. The columns were tested in a single-curvature fashion, as shown in Fig. 3. The lateral cyclic loading contained drift ratios of 0.25, 0.375, 0.5, 0.75, 1.0, 1.5, 2.0, 3.0, 4.0, 5.0, 6.0, 7.0, 8.0, and 9.0%. The drift ratio is defined as the relative horizontal displacement between the column base and the point of lateral load divided by the height of the loading point from the column base (3600 mm [141.73 in.]). Loading to each drift ratio was repeated three times. The test setup was used to simulate the loading condition of a column subjected to axial gravity and lateral seismic loading. During testing, crack development was monitored by visual inspection. Strains of reinforcement were recorded by strain gauges installed on reinforcement during specimen fabrication. Deformation of the column was tracked using an optical motion tracking system.

Damage process and hysteresis behavior

During testing, flexural cracks first appeared at the 0.25% drift ratio for both columns. As the drift ratio increased, more flexural cracks occurred. Moreover, the cracks gradually propagated towards the neutral axis of the column cross section. During drift ratios of 0.5 to 0.75%, flexural cracks started to turn diagonally into flexural-shear cracks for both columns. At the 1.5% drift ratio, most of the flexural cracks had been developed for both columns. Figures 4(a) and 5(a) showed one of the column faces perpendicular to the loading direction at the 1.5% drift ratio for C36 and C43, respectively. At the 3% drift ratio, spalling concrete at the column toe appeared, as shown in Fig. 4(b) and 5(b) for C36 and C43, respectively. As the drift ratio increased, the extent of concrete spalling increased. Until the 5% drift ratio, the damage progress of C36 was similar to that of C43 except for the crack spacing. The average spacing of cracks on the column faces perpendicular to the loading direction of C43 was approximately 1.25 times that of C36. This is because the maximum spacing of longitudinal bars in C43 was 500 mm (19.69 in.), two times larger than in C36. The cracking spacing has been shown to increase with increasing spacing of longitudinal bars.[20] However, the difference in the crack spacing appeared not to have a significant effect on the seismic performance of the column.

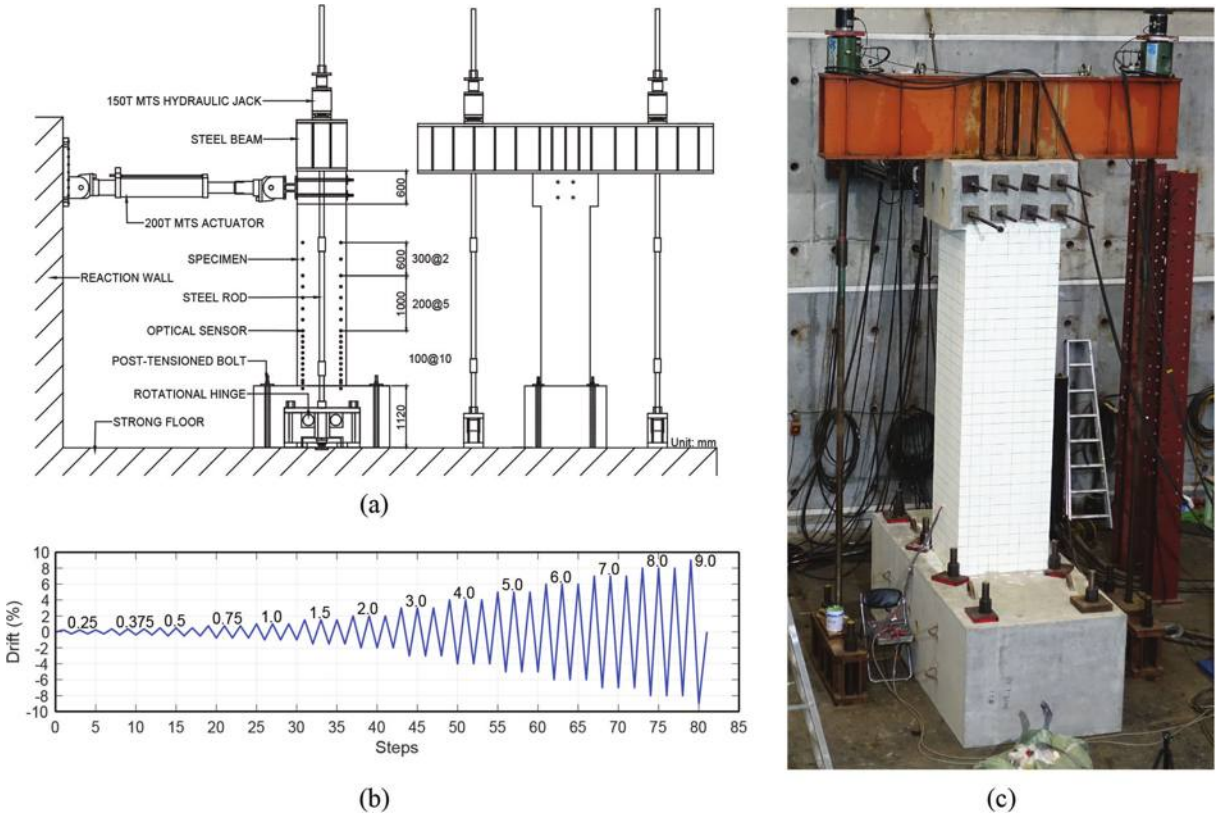

Fig. 3—(a) Test setup; (b) loading protocol; and (c) photo of test setup. (Note: 1 mm = 0.0394 in.)

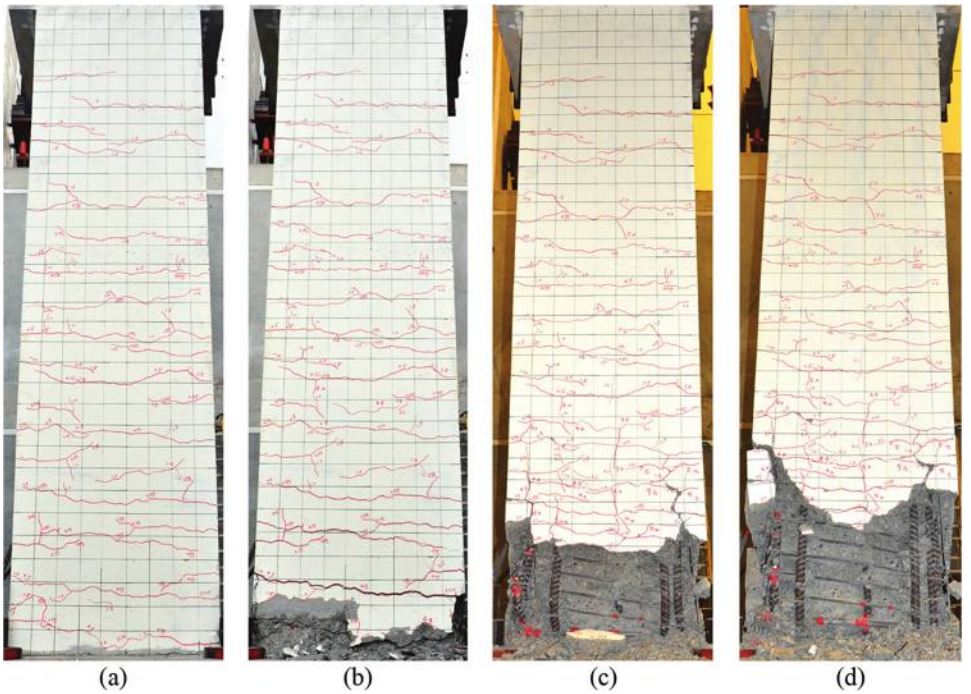

Fig. 4—C36 damage pattern at: (a) 1.5% drift ratio; (b) 3% drift ratio; (c) buckling of longitudinal bars (7% drift ratio); and (d) fracture of longitudinal bars (8% drift ratio).

At the 7% drift ratio, for C36, buckling of longitudinal bars occurred during the third cycle of loading, as shown in Fig. 4(c). The maximum lateral strength of the column dropped to 83% of the peak strength during the 7% drift loading. At the 8% drift ratio, fracture of longitudinal bars occurred, as shown in Fig. 4(d). The maximum lateral strength dropped to 47% of the peak strength during the 8% drift loading. The testing was terminated at the 9% drift ratio when the lateral strength dropped to 38% of the peak strength.

For C43, buckling of longitudinal reinforcement also occurred at the 7% drift but during the second cycle, slightly

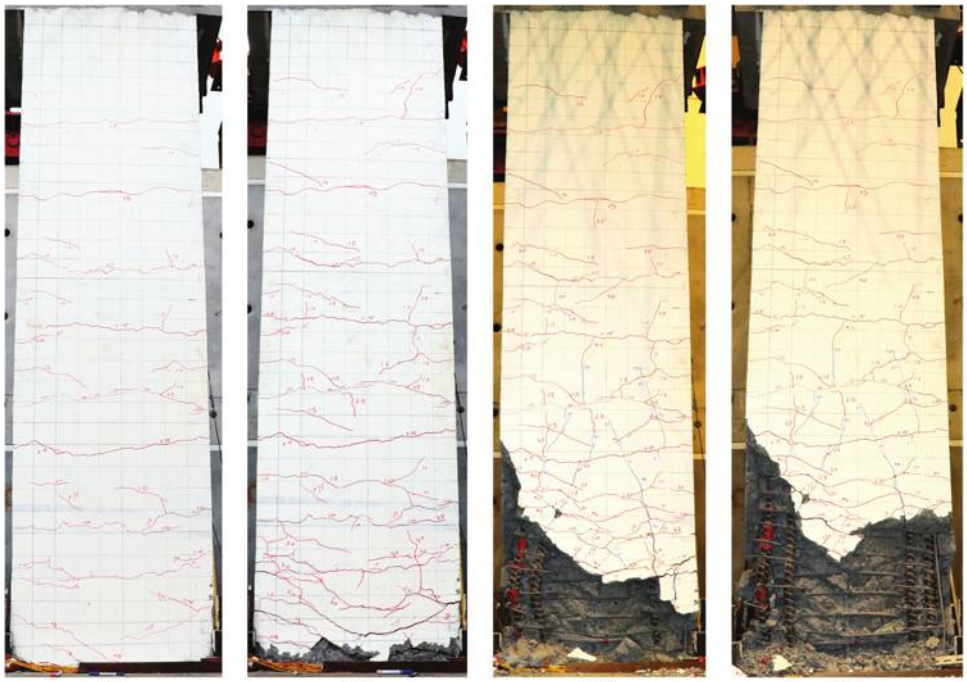

Fig. 5—C43 damage pattern at: (a) 1.5% drift ratio; (b) 3% drift ratio; (c) buckling of longitudinal bars (7% drift ratio); and (d) fracture of longitudinal bars (8% drift ratio).

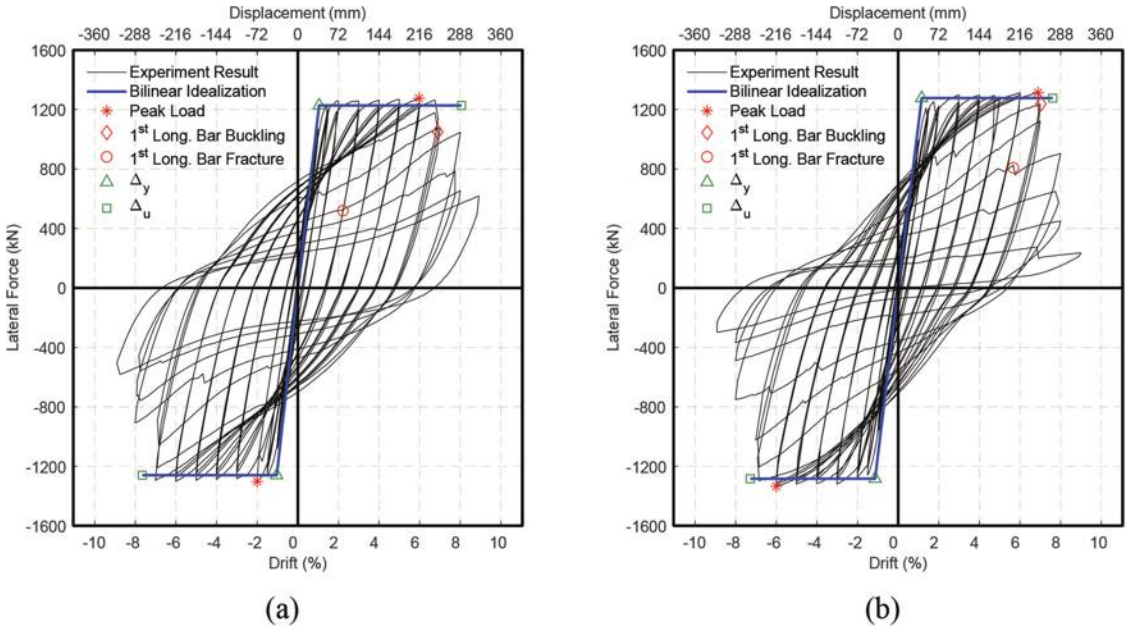

Fig. 6—Force and displacement diagram for: (a) C36; and (b) C43. (Note: 1 kN = 0.22481 kip; 1 mm = 0.0394 in.)

earlier than C36. The maximum lateral strength decreased to 84% of the peak strength during the 7% drift loading. Figure 5(c) shows the damage condition of the column at the 7% drift ratio. At this drift ratio, fracture of five-spiral reinforcement was observed. This was not found in C36. Fracture of longitudinal bars also occurred at the 8% drift ratio, causing the lateral strength to drop to 34% of the peak strength during the 8% drift loading. The testing was stopped at the 9% drift ratio when the lateral strength dropped to 23% of the peak strength.

The relationship between the lateral force and drift ratio (hysteretic behavior) of C36 and that of C43 are shown in Fig. 6. Note that the axial loading system tilted as the column deformed laterally during testing, causing an additional moment at the column base. This additional moment was removed from the force presented in Fig. 6. Both columns showed ductile behavior with drift capacities significantly higher than 3%, a seismic performance target used in the literature for columns.[21] The difference in behavior between the two columns was not significant until the 7% drift ratio, at which the longitudinal bars started to buckle. After the

Table 2—Displacement and moment capacities

Specimen	V_y, kN	Δ_y, mm	Δ_u, mm	μ	M_{test}, kN-m	M_n, kN-m	M_{test}/M_n
C36	1243.09	37.58	282.99	7.53	4533	3907	1.16
C43	1279.56	41.31	267.11	6.47	4618	3832	1.21

Note: 1 kN = 0.22481 kip; 1 m = 3.28 ft; 1 mm = 0.0394 in.

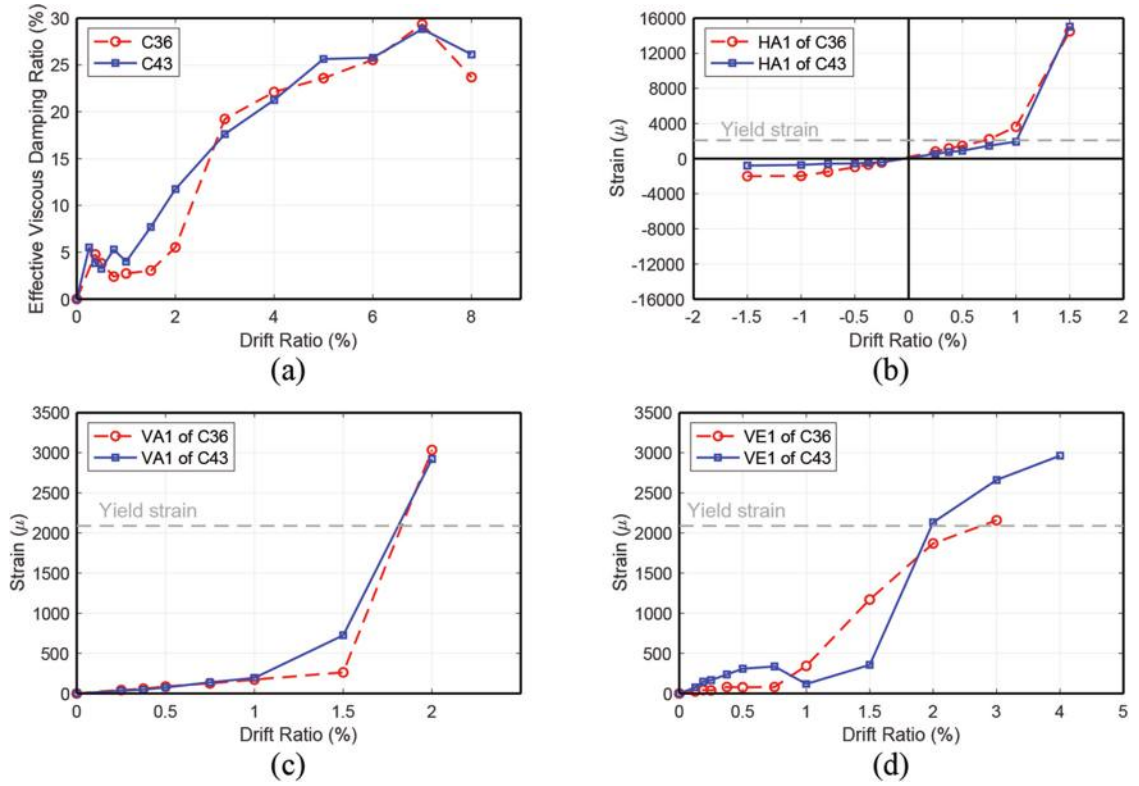

Fig. 7—(a) Equivalent viscous damping ratio; (b) strain of longitudinal reinforcement; (c) strain of large spirals; and (d) strain of small spirals.

7% drift ratio, the lateral strength of C43 degraded faster than that of C36. The number of longitudinal bar fractures for C36 was the same as that for C43. However, because the area of one longitudinal bar of C43 was larger than that of C36, the strength degradation for C43 related to each bar fracture was higher than C36.

The envelope of the hysteretic behavior was idealized by a bilinear relationship based on FEMA 365.[22] The first segment of the bilinear relationship intersected the envelope response at 60% idealized yield force V_y, which is the force at the idealized yield point. The second segment ended at the ultimate drift ratio Δ_u, defined as the drift ratio when the envelope response drops to a point with a lateral force equal to 80% of the peak lateral strength. The intersection of the two linear segments, which defines the idealized yield point, was selected so that the area below the envelope response and below the idealized bilinear relationship were similar. The displacement ductility μ of each column is defined as the ratio of Δ_u to the displacement of the idealized yield point Δ_y. The V_y, Δ_y, Δ_u, and μ of the bilinear relationship for the two columns are listed in Table 2. C36 had a slightly larger displacement capacity (Δ_u and μ) than C43. The maximum column moment measured from testing M_{test}, the nominal moment strength M_n calculated based on measured material properties,[19] and M_{test}/M_n are also listed in Table 2. C43 exhibited a slightly higher overstrength (M_{test}/M_n) than C36. In general, the performance difference between the two columns was not significant.

Energy dissipation and reinforcement strain

The hysteretic energy dissipation in terms of the equivalent viscous damping ratio for both columns is shown in Fig. 7(a). C43 exhibited an energy dissipation capacity similar to C36. The use of D43 (No. 14) longitudinal bars did not significantly alter the energy dissipation capacity of the column. Fig. 7(b), (c), and (d) show the strain responses of the longitudinal reinforcement, the large spiral, and the small spiral, respectively, from the plastic hinge region of the columns. The locations of the strain gauges used in these plots can be found in Fig. 2. The longitudinal reinforcement of C43 generally showed a smaller strain response than C36 for the same drift ratio. The longitudinal reinforcement of C43 yielded at the 1% drift ratio, later than C36, which occurred at the 0.75% drift ratio. However, at the 1.5% drift ratio, the longitudinal reinforcement of both columns showed similar strain responses. The strain gauges of both columns failed later at this drift ratio. The strain responses of the large and small spirals of C43 were similar to those of C36. The

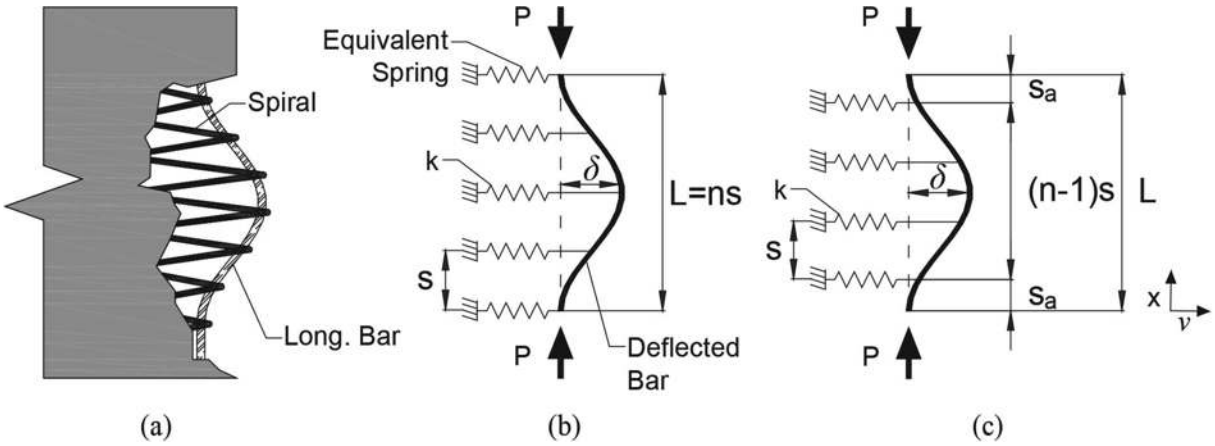

Fig. 8—Relationship between buckling length and spacing of transverse reinforcement in: (a) buckled bar restrained by spiral; (b) Dhakal and Maekawa's model; and (c) proposed model.

large and small spirals yielded early at drift ratios from 2 to 3% for both columns. The spirals were effectively mobilized to confine the core concrete. The large spirals yielded earlier than the small spirals. This is because the volumetric ratio of the large spiral was smaller than the small spiral. This is typically the case for five-spiral reinforcement.

PROPOSED BUCKLING MODEL FOR LONGITUDINAL BARS

As observed from testing and shown in Fig. 6, buckling of longitudinal bars occurred during the 7% drift ratio. The buckled bars started to fracture when stretched again in tension during the following drift ratio (8%), causing the strength of the column to degrade significantly. This observation demonstrates that buckling of longitudinal bars has an important effect on the ultimate drift ratio and displacement ductility of the columns. To investigate the buckling behavior of D36 (No. 11) and D43 (No. 14) longitudinal bars constrained by five-spiral reinforcement, a buckling model to determine the buckling length was developed in this research and presented as follows.

Proposed buckling model

The proposed buckling model was developed based on Dhakal and Maekawa's model[23] with modifications to remove the limitation that the buckling length has to be integral multiples of transverse reinforcement spacing and consider the unique constraint behavior of five-spiral reinforcement.

Dhakal and Maekawa's model

Figure 8(b) shows Dhakal and Maekawa's buckling model, consisting of a laterally displaced bar supported by equivalent springs. The deflected bar represents a longitudinal bar buckled in compression, and the equivalent springs represent transverse reinforcement. The buckling length L is assumed to be an integral multiple of transverse reinforcement spacing s—that is, $L = n \times s$, where n is an integer. Based on Dhakal and Maekawa's model, the total potential energy of the model consists of the energy stored in the buckled bar, the energy stored in the equivalent springs, and a decrease in the potential energy due to work done by the applied compression P to the buckled bar. This is described by Eq. (1), in which the function for the deflected shape of the buckled bar v is assumed to be Eq. (2)

$$U = U_{buckled\ bar} + U_{spring} - U_P = \frac{1}{2}\int_0^L EI(v'')^2\,dx + \frac{1}{2}k\left(\frac{\delta}{2}\right)^2\sum_{i=1}^{n-1}\left(1-\cos\frac{2\pi i}{n}\right)^2 - \frac{1}{2}P\int_0^L (v')^2\,dx \quad (1)$$

$$v = \frac{\delta}{2}\left(1-\cos\frac{2\pi x}{L}\right) \quad (2)$$

where U is total energy of the buckling system; $U_{buckled\ bar}$ is energy stored in the buckled bar; U_{spring} is energy stored in the equivalent springs; U_p is potential energy due to work done by the applied compression to the buckled bar; E is effective modulus of elasticity of longitudinal steel bars, taken as 2.5% initial modulus of elasticity of longitudinal steel bars to consider the effect of inelastic behavior[24]; I is moment inertia of the buckled bar; v is shape function of buckling deflection; k is equivalent spring stiffness of a spiral and will be discussed in the section "Stiffness of equivalent spring for five-spiral reinforcement"; δ is maximum deflection of the buckled bar; n is number of buckling spacings; P is applied axial compressional force; and L is buckling length. As stated previously, the longitudinal bars of both columns yielded early at the 0.75 to 1% drift ratios, much earlier than the buckling of the reinforcement at the 7% drift ratio. This supports the use of the effective modulus of elasticity for longitudinal bars.

According to the principle of stationary total potential energy, the stable equilibrium of the model is achieved when the total potential energy of the system is minimum.[25] Therefore, by taking the partial derivative of the total potential energy with respect to the maximum deflection of the buckled bar δ and setting the derivative to be zero, the equation for buckling load P can be established.

$$\frac{\partial U}{\partial \delta} = 0 \Rightarrow P = \frac{4EI\pi^2}{L^3} + \frac{kL}{2\pi^2}\sum_{i=1}^{n-1}\left(1-\cos\frac{2\pi i}{n}\right)^2 \quad (3)$$

As can be observed from Eq. (3), P varies with L. The L that produces the minimum P is the governing buckling length. Knowing $L = n \times s$, by taking the partial derivative of P with respect to n and setting the derivative to be zero, Eq. (4) is obtained.[24]

$$\frac{\partial P}{\partial n} = 0 \Rightarrow k = \frac{EI\pi^4}{s^3} \frac{16}{n^3 \sum_{i=1}^{n-1} \left(1 - \cos\frac{2\pi i}{n}\right)\left[\left(1 - \cos\frac{2\pi i}{n}\right) - \frac{4\pi i}{n}\sin\frac{2\pi i}{n}\right]} \tag{4}$$

As stated previously, n should be an integer. For each value of n, Eq. (4) can be used to determine the stiffness of the equivalent spring k required for this buckling length $L = n \times s$. The stiffness of the equivalent spring provided in a column is compared with the required k for various values of n. If the provided k is between the required k for $L = (n - 1) \times s$ and that for $L = n \times s$, the provided k is sufficient to restrain a buckling length of $n \times s$ but not enough to restrain a buckling length of $(n - 1) \times s$. Because n is an integer, the L is conservatively assumed to be $n \times s$ in Dhakal and Maekawa's model. However, the actual buckling length is between $(n - 1) \times s$ and $n \times s$. To consider this, in the proposed model, the locations of the equivalent springs are rearranged, as shown in Fig. 8(c). The L is set equal to $(n - 1) \times s + 2s_a$ and has a value range of $(n - 1) \times s < L \leq n \times s$. This makes the buckling length to be more precise.

Proposed model

Before using the proposed model, Dhakal and Maekawa's model is used first to determine the value of n. Then, by resetting $L = (n - 1) \times s + 2s_a$ with s_a unknown, the total potential energy of the proposed model is

$$\begin{aligned} U &= U_{buckled\ bar} + U_{spring} - U_P \\ &= \frac{1}{2}\int_0^L EI(v'')^2 dx + \frac{1}{2}k\left(\frac{\delta}{2}\right)^2 \sum_{i=1}^{n+1}\left(1 - \cos\frac{2\pi(s_a + (i-1)s)}{L}\right)^2 - \frac{1}{2}P\int_0^L (v')^2 dx \end{aligned} \tag{5}$$

where s_a is additional buckling length beyond $(n - 1) \times s$.

The shape function v is the same as Eq. (2). Following the same derivation as that for Dhakal and Maekawa's model, Eq. (6) and (7) can be obtained

$$\frac{\partial U}{\partial \delta} = 0 \Rightarrow P = \frac{4EI\pi^2}{L^2} + \frac{kL}{2\pi^2}\sum_{i=1}^{n+1}\left(1 - \cos\frac{2\pi(s_a + (i-1)s)}{L}\right)^2 \tag{6}$$

$$\frac{\partial P}{\partial L} = 0 \Rightarrow$$

$$k = \frac{16EI\pi^4}{L^2 \sum_{i=1}^{n+1}\left(\begin{array}{l} L\left(\cos\frac{2\pi(s_a + (i-1)s)}{L} - 1\right) + 4\pi(s_a + (i-1)s) \times \\ \sin\left(\frac{2\pi(s_a + (i-1)s)}{L}\right)\cos\left(\frac{2\pi(s_a + (i-1)s)}{L} - 1\right) \end{array}\right)} \tag{7}$$

With the k and n already known, s_a can be solved; and the buckling length L can be obtained as $(n - 1) \times s + 2s_a$.

Stiffness of equivalent spring for five-spiral reinforcement

As shown in Fig. 9(a), the cross section of C36 is used to illustrate that in a five-spiral column, longitudinal bars can be either constrained by a large spiral, a small spiral, or an overlapping region. According to Dhakal and Su,[26] longitudinal bars that buckle first in a spiral/circular hoop are those in the first layer from the extreme compression fiber, and those overlap with the first layer of bars on a projected straight line along the buckling direction. Based on this concept, the longitudinal bars of the five-spiral column shown in Fig. 9(a) are projected on a line along the loading direction (buckling direction). It can be seen that the two bars (shown in blue color) in each of the two small spirals in the compression side and the one bar (shown in red color) in the large spiral are prone to buckle. Bars in overlapping regions are assumed not to buckle because they are further away from the extreme compression fiber and are subjected

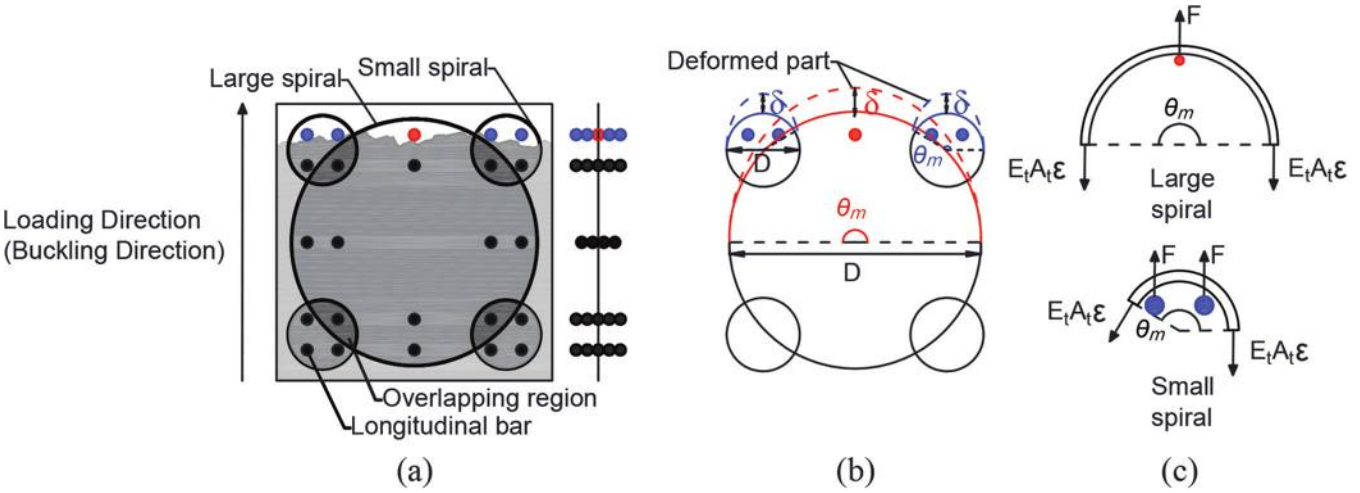

Fig. 9—(a) Locations of buckled bars; (b) deformed parts of small and large spirals; and (c) equilibrium to determine pushing force from buckled bar. (Note: Full-color PDF can be found at www.concrete.org.)

Table 3—Buckling parameters of specimens

Specimens	k, MPa-mm	S, mm	n	s_a, mm	L, mm	L_{test}, mm	L/d_b
C36	284.15	75	7	18.85	487.70	487.5	13.547
C43			8	28.80	582.59	562.5	13.549

Note: 1 MPa-mm = 5.7101 psi-in.; 1 mm = 0.0394 in.

to strong confinement from a large and a small spiral. Moreover, because the overlapping region is subjected to strong confinement and is typically designed with longitudinal bars to enhance the capability of the region to interlock the large and small spirals, the overlapping region is assumed to act as a stiff column and hence provides a strong anchorage for the small spiral anchored to the region. As a result, buckling of the two longitudinal bars in each small spiral is assumed not to affect the large spiral. Due to different constraints from the large or small spiral and different numbers of buckled bars within the large or small spiral, the stiffness of equivalent springs for the large spiral and that for the small spiral need to be calculated and compared. The bar within a spiral with a smaller stiffness buckles first.

When the bar in the large or small spiral buckles, the large or small spiral is pushed to deform outwardly, as shown in Fig. 9(b). Due to the constraint by concrete, only a portion of the spiral is deformed. The deformed part of the large spiral is assumed to be one-half of the large spiral and has a central angle θ_m of 180 degrees. This assumption is the same as that used by Dhakal and Su.[26] The effect of the small spiral is ignored. The deformed part of the small spiral is assumed to be one-half of the small spiral, excluding the overlapping region, as shown in Fig. 9(b). The portion of the small spiral within the overlapping region is assumed not to deform due to the strong confinement effect. The central angle of the deformed part is smaller than 180 degrees. With these assumptions, the tensile strain developed in the large or small spiral due to the push from the buckled bar can be calculated as

$$\varepsilon = \frac{\theta_m (D+\delta) - \theta_m D}{2\pi D} = \frac{\theta_m \delta}{2\pi D} \tag{8}$$

where ε is strain of a spiral due to bar buckling; θ_m is angle corresponding to the deformed part of a spiral; and D is diameter of a spiral. For the large spiral of C36 and C43, θ_m = 180 degrees and D = 820 mm (32.28 in.). For the small spiral of C36 and C43, θ_m = 143 degrees and D = 240 mm (9.45 in.).

From the free-body diagram shown in Fig. 9(c), the pushing force from the buckled bar F can be determined by equilibrium with ε from Eq. (8)

$$n_b F = E_t A_t \varepsilon \left(\cos(\pi - \theta_m) + 1\right) = E_t A_t \left(\cos(\pi - \theta_m) + 1\right) \frac{\theta_m \delta}{2\pi D} \tag{9}$$

where n_b is number of buckled bars; E_t is post-yield modulus of elasticity of spiral steel, taken as 1.5% the initial modulus of elasticity of spiral steel[27]; and A_t is cross-sectional area of a spiral. For the large spiral of C36 and C43, n_b = 1 and 0, respectively. For the small spiral of C36 and C43, n_b = 2. As stated previously, the spirals of the columns tested yielded at the 2 to 3% drift ratios, earlier than the buckling of the longitudinal bars, which occurred at the 7% drift ratio. This supports the use of the post-yield modulus of elasticity for spirals.

The stiffness of the equivalent spring k for the large or small spiral can be obtained by the following equation with F from Eq. (9)

$$k = \frac{F}{\delta} = \frac{E_t A_t \left(\cos(\pi - \theta_m) + 1\right)\left(\frac{\theta_m}{2\pi}\right)}{D n_b} \tag{10}$$

where k is equivalent spring stiffness of a spiral. For the large spiral of C36, k = 563.34 MPa-mm (3216.75 psi-in.) based on Eq. (10). The large spiral of C43 has no longitudinal bars for buckling consideration (n_b = 0). For the small spiral of C36 and C43, k = 284.15 MPa-mm (1622.54 psi-in.) based on Eq. (10). Therefore, the governing value of k for both C36 and C43 is 284.15 MPa-mm (1622.54 psi-in.). And, for both columns, buckling of longitudinal bars in small spirals is the governing buckling behavior.

Comparison with test observation

Table 3 lists the values of important parameters for the analytical buckling behavior of the D36 (No. 11) and D43 (No. 14) bars of C36 and C43, respectively. As stated previously, the governing value of k is from the small spiral. This means buckling of longitudinal bars within the small spiral governs the buckling behavior. This is consistent with the experimental observation, as shown in Fig. 4 and 5 for C36 and C43, respectively. The longitudinal bars within the large spiral of C36 did not show significant buckling until the end of testing. Note that for C43, no longitudinal bars were designed within the large spiral close to the extreme compression fiber of the section (Fig. 2). Experimental observation also showed that longitudinal bars within the overlapping regions did not expose and were still well confined by surrounding concrete and spirals until the end of testing. This is consistent with the assumption used in the proposed buckling model that the overlapping regions provide a strong anchorage for small spirals to restrain buckling of longitudinal reinforcement.

The calculated buckling lengths are 477.70 and 582.59 mm (18.81 and 22.94 in.) for C36 and C43, respectively, close to measured buckling lengths—that is, 487.5 and 562.5 mm (19.19 and 22.14 in.), respectively—from the experiment. Because the test data are still limited, more tests are needed to further validate the applicability of the proposed model to the buckling behavior of longitudinal bars laterally supported by five-spiral reinforcement. According to Dhakal and

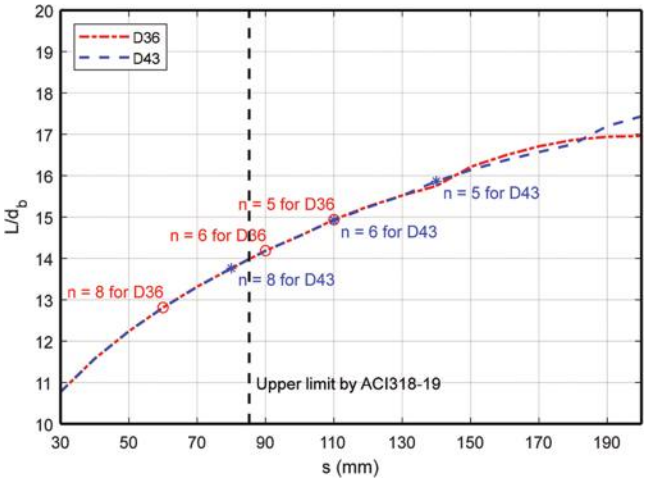

Fig. 10—Relationships between buckling slenderness ratio and center-to-center spacing of spiral. (Note: 1 mm = 0.0394 in.)

Maekawa,[28] the compressive stress-strain behavior of longitudinal bars in compression mainly depends on the buckling slenderness ratio, defined as the buckling length divided by the diameter of the longitudinal bar L/d_b. As shown in Table 3, the calculated L/d_b for D43 (No. 14) bars in C43 is similar to that for D36 (No. 11) bars in C36. This is consistent with the experimental observation that both columns showed buckling of longitudinal bars at the same drift ratio (7%). Note that the lateral strength of C43 degraded faster after buckling than that of C36. This is mainly because for C43, the cross-sectional area of longitudinal bars within the small spiral was higher than that for C36.

With the proposed buckling model and the same equivalent spring stiffness as used for C36 and C43, the relationship between L/d_b and the center-to-center spacing of the spiral s for D36 (No. 11) bars and that for D43 (No. 14) bars were calculated and shown in Fig. 10. The value of s ranges from 30 to 200 mm (1.18 to 7.87 in.). According to ACI 318-19,[19] the clear spacing of spirals should not be greater than 76.2 mm (3 in.), which corresponds to s = 85.2 mm (3.35 in.) for the case of the small spiral used in C36 and C43. From Fig. 10, it can be seen that with the same amount and spacing of five-spiral reinforcement, the buckling slenderness ratios of D36 and D43 (No. 11 and No. 14) bars are very similar for the values of s within the upper limit by ACI 318-19. The difference becomes notable only when the value of s is larger than approximately 190 mm (7.48 in.), far beyond the upper limit set by ACI 318-19 for spirals. This means D43 (No. 14) bars have a similar compressive stress-strain behavior to D36 (No. 11) bars for the practical range of s of five-spiral reinforcement.

CONCLUSIONS

Two full-scale five-spiral columns were tested to investigate the difference in seismic performance between a column with normal-diameter longitudinal bars (D36 [No. 11]) bars with a bar diameter of 36 mm (1.42 in.) (column C36) and that with large-diameter longitudinal bars (D43 [No. 14]) bars with a bar diameter of 43 mm (1.69 in.) (column C43). Moreover, a buckling model was developed for longitudinal bars laterally supported by five-spiral reinforcement. Conclusions are summarized as follows.

1. Both columns showed similar damage progress, force-displacement behavior, and energy dissipation until the 7% drift ratio. Buckling of longitudinal reinforcement of both columns started at the same drift ratio (7%). D43 (No. 14) bars buckled slightly earlier than D36 (No. 11) bars. Because the total cross-sectional area of D43 (No. 14) bars of column C43 in the buckling critical region (within the small spiral) was higher than that of column C36, column C43 showed a faster strength degradation after buckling than column C36. As a result, column C36 showed a slightly larger displacement capacity than column C43. Both columns exhibited flexural-dominated behavior with good displacement capacities and energy dissipation. The performance difference between the two columns was, in general, not significant.

2. The average spacing of flexural cracks of C43 was approximately 1.25 times that of C36. This is because the maximum spacing of longitudinal bars of C43 was two times larger than C36. However, the difference in the crack spacing appeared not to have a significant effect on the seismic performance of the column.

3. Based on the proposed buckling model, the buckling of longitudinal bars within the small spiral governs both columns' buckling behavior. This is consistent with the experimental observation. The calculated buckling length for D36 (No. 11) and that for D43 (No. 14) bars are close to the measured buckling lengths from the experiment. The calculated buckling slenderness ratio of D36 (No. 11) bars is similar to that of D43 (No. 14) bars, which means both bars are expected to have a similar buckling behavior. This is consistent with the experimental observation that buckling of longitudinal reinforcement started at the same drift ratio (7%). For the same amount and within the practical spacing range of five-spiral reinforcement, the calculated buckling slenderness ratio of D43 (No. 14) bars is similar to that of D36 (No. 11) bars.

AUTHOR BIOS

Yu-Chen Ou *is a Distinguished Professor of Civil Engineering at National Taiwan University, Taipei, Taiwan. He received his PhD from the State University of New York at Buffalo, Buffalo, NY. His research interests include reinforced concrete structures and earthquake engineering. He is the President of the ACI Taiwan Chapter.*

Brandon Li *received his BS and MS from the Department of Civil Engineering, National Taiwan University. His research interests include reinforced concrete structures and buckling behavior of longitudinal bars.*

ACKNOWLEDGMENTS

The authors would like to thank the financial support from the Ministry of Science and Technology of Taiwan under Contract No. 109-2923-M-002-006-MY3 and from Ruentex Engineering & Construction Co.

NOTATION

A_g	=	gross area of concrete cross section
A_t	=	area of an individual transverse reinforcement
D	=	outside diameter of longitudinal bar
d_b	=	diameter of longitudinal bar
E	=	Young's modulus of longitudinal bar
E_t	=	Young's modulus of transverse reinforcement
f_c'	=	specified compressive strength of concrete

f_{ca}' = actual compressive strength of concrete
f_y = specified yield strength of longitudinal reinforcement
f_{ya} = actual yield strength of longitudinal reinforcement
f_{yt} = specified yield strength of transverse reinforcement
f_{yta} = actual yield strength of transverse reinforcement
I = moment inertia of longitudinal bar
i = order of spring
k = equivalent stiffness of transverse reinforcement
k_{LS} = equivalent stiffness of large spiral reinforcement
k_{MSR} = equivalent stiffness of multi-spiral reinforcement
k_{SS} = equivalent stiffness of small spiral reinforcement
k_c = equivalent stiffness of circular/spiral reinforcement
L = buckling length calculated from proposed model
L_{test} = buckling length obtained from experiment
M_n = nominal moment strength
M_{test} = maximum moment strength obtained from experiment
n = number of buckling spacing
n_b = number of buckling participant longitudinal bars
P = applied axial compressional force
s = spacing of transverse reinforcement
s_a = additional buckling length beyond $(n - 1) \times s$
U = total energy of buckling system
$U_{buckled\ bar}$ = energy stored in buckled bar
U_p = potential energy due to work done by applied compression to buckled bar
U_{spring} = energy stored in equivalent springs
V_y = idealized yield strength
v = shape function of buckling deformation
Δ_u = ultimate displacement
Δ_y = yield displacement
δ = maximum deflection of buckled bar
μ = member ductility
ρ_g = ratio of longitudinal reinforcement area to gross area
ρ_s = volumetric ratio of transverse reinforcement

REFERENCES

1. Tanaka, H., and Park, R., "Seismic Design and Behavior of Reinforced Concrete Columns with Interlocking Spirals," *ACI Structural Journal*, V. 90, No. 2, Mar.-Apr. 1993, pp. 192-203.

2. McLean, D. I., and Buckingham, G. C., "Seismic Performance of Bridge Columns with Interlocking Spiral Reinforcement," Report No. WA-RD 357.1, Washington State Transportation Center, Seattle, WA, 1994.

3. Otaki, T., and Kuroiwa, T., "Test of Bridge Columns with Interlocking Spiral Reinforcement and Conventional Rectangular Hoop with Ties," *Reports of the Technological Research Institute*, Construction Co. Ltd, Tokyo, Japan, No. 25, 1999, pp. 33-38.

4. Shito, K.; Igase, Y.; Mizugami, Y.; Ohasi, G.; Miyagi, T.; and Kuroiwa, T., "Seismic Performance of Bridge Columns with Interlocking Spiral/Hoop Reinforcements," First *fib* Congress, Osaka, Japan, 2002.

5. Kawashima, K., "Enhancement of Flexural Ductility of Reinforced Concrete Bridge Columns," *First International Conference on Urban Earthquake Engineering*, Tokyo Institute of Technology, Tokyo, Japan, 2004, pp. 85-95.

6. Correal, J. F.; Saiidi, M. S.; Sanders, D.; and El-Azazy, S., "Shake Table Studies of Bridge Columns with Double Interlocking Spirals," *ACI Structural Journal*, V. 104, No. 4, July-Aug. 2007, pp. 393-401.

7. Yin, S. Y. L.; Wu, T. L.; Liu, T. C.; Sheikh, S. A.; and Wang, R., "Interlocking Spiral Confinement for Rectangular Columns," *Concrete International*, V. 33, No. 12, Dec. 2011, pp. 38-45.

8. Yin, S. Y. L.; Wang, J. C.; and Wang, P. H., "Development of Multi-Spiral Confinements in Rectangular Columns for Construction Automation," *Zhongguo Gongcheng Xuekan*, V. 35, No. 3, 2012, pp. 309-320. doi: 10.1080/02533839.2012.655528

9. Ou, Y. C.; Li, J. Y.; and Roh, H., "Shear Strength of Reinforced Concrete Columns with Five-Spiral Reinforcement," *Engineering Structures*, V. 233, 2021, p. 111929. doi: 10.1016/j.engstruct.2021.111929

10. Wu, T.-L.; Ou, Y.-C.; Yen-Liang Yin, S.; Wang, J.-C.; Wang, P.-H.; and Ngo, S.-H, "Behavior of Oblong and Rectangular Bridge Columns with Conventional Tie and Multi-Spiral Transverse Reinforcement under Combined Axial and Flexural Loading," *Zhongguo Gongcheng Xuekan*, V. 36, No. 8, 2013, pp. 980-993. doi: 10.1080/02533839.2012.747047

11. Ou, Y. C.; Ngo, S. H.; Yin, S. Y.; Wang, J. C.; and Wang, P. H., "Shear Behavior of Oblong Bridge Columns with Innovative Seven-Spiral Transverse Reinforcement," *ACI Structural Journal*, V. 111, No. 6, Nov.-Dec. 2014, pp. 1339-1349. doi: 10.14359/51686873

12. Ou, Y. C.; Ngo, S. H.; Roh, H.; Yin, S. Y.; Wang, J. C.; and Wang, P. H., "Seismic Performance of Concrete Columns with Innovative Seven- and Eleven-Spiral Reinforcement," *ACI Structural Journal*, V. 112, No. 5, Sept.-Oct. 2015, pp. 579-592. doi: 10.14359/51687706

13. Ou, Y. C., and Ngo, S. H., "Discrete Shear Strength of Two- and Seven-Circular-Hoop and Spiral Transverse Reinforcement," *ACI Structural Journal*, V. 113, No. 2, Mar.-Apr. 2016, pp. 227-238. doi: 10.14359/51688058

14. CPAMI, "Design Specifications for Reinforced Concrete Structures," Construction and Planning Agency, Ministry of the Interior, R.O.C., 2019.

15. Ichinose, T.; Kanayama, Y.; Inoue, Y.; and Bolander, J. E., Jr., "Size Effect on Bond Strength of Deformed Bars," *Construction and Building Materials*, V. 18, No. 7, 2004, pp. 549-558. doi: 10.1016/j.conbuildmat.2004.03.014

16. Steuck, K. P.; Eberhard, M. O.; and Stanton, J. F., "Anchorage of Large-Diameter Reinforcing Bars in Ducts," *ACI Structural Journal*, V. 106, No. 4, July-Aug. 2009, pp. 506-513. doi: 10.14359/56616

17. Murcia-Delso, J.; Stavridis, A.; and Shing, P. B., "Tension Development Length of Large-Diameter Bars for Severe Cyclic Loading," *ACI Structural Journal*, V. 112, No. 6, Nov.-Dec. 2015, pp. 659-669. doi: 10.14359/51687937

18. Murcia-Delso, J.; Liu, Y.; and Shing, P. B., "Required Development Length of Column Reinforcement Extended into Enlarged Pile Shafts," *Seventh National Seismic Conference on Bridges & Highways*, Oakland, CA, May 2013.

19. ACI Committee 318, "Building Code Requirements for Structural Concrete (ACI 318-19) and Commentary (ACI 318R-19) (Reapproved 2022)," American Concrete Institute, Farmington Hills, MI, 2019, 624 pp.

20. Frosch, R. J., "Another Look at Cracking and Crack Control in Reinforced Concrete," *ACI Structural Journal*, V. 96, No. 3, May-June 1999, pp. 437-442.

21. Elwood, K. J.; Maffei, J.; Riederer, K. A.; and Telleen, K., "Improving Column Confinement Part 1: Assessment of Design Provisions," *Concrete International*, V. 31, No. 11, Nov. 2009, pp. 32-39.

22. FEMA 356, "Prestandard and Commentary for the Seismic Rehabilitation of Buildings in Rehabilitation Requirements," Federal Emergency Management Agency, Washington, DC, 2000.

23. Dhakal, R. P., and Maekawa, K., "Reinforcement Stability and Fracture of Concrete Cover in Reinforced Concrete Members," *Journal of Structural Engineering*, ASCE, V. 128, No. 10, 2002, pp. 1253-1262. doi: 10.1061/(ASCE)0733-9445(2002)128:10(1253)

24. Su, J.; Wang, J.; Bai, Z.; Wang, W.; and Zhao, D., "Influence of Reinforcement Buckling on the Seismic Performance of Reinforced Concrete Columns," *Engineering Structures*, V. 103, 2015, pp. 174-188. doi: 10.1016/j.engstruct.2015.09.007

25. Chen, W. F., and Lui, E. M., *Structural Stability Theory and Implementation,* Elsevier Science Publishing Co., Inc., New York, 1987.

26. Dhakal, R. P., and Su, J., "Design of Transverse Reinforcement to Avoid Premature Buckling of Main Bars," *Earthquake Engineering & Structural Dynamics*, V. 47, No. 1, 2018, pp. 147-168. doi: 10.1002/eqe.2944

27. Bae, S.; Mieses, A. M.; and Bayrak, O., "Inelastic Buckling of Reinforcing Bars," *Journal of Structural Engineering*, ASCE, V. 131, No. 2, 2005, pp. 314-321. doi: 10.1061/(ASCE)0733-9445(2005)131:2(314)

28. Dhakal, R. P., and Maekawa, K., "Modeling for Postyield Buckling of Reinforcement," *Journal of Structural Engineering*, ASCE, V. 128, No. 9, 2002, pp. 1139-1147. doi: 10.1061/(ASCE)0733-9445(2002)128:9(1139)

We're Building the Future

Mission: We make strategic investments in ideas, research, and people to create the future of the concrete industry

Through its councils and programs, the ACI Foundation helps to keep the concrete industry at the forefront of advances in material composition, design, and construction. Our focus:

Our Concrete Innovation Council identifies technologies and innovation that are aligned with ACI and industry strategies and helps facilitate their use when appropriate

Our Concrete Research Council advances the knowledge and sustainable aspects of concrete materials, construction, and structures by soliciting, selecting, financing, and publishing research

Our Scholarship Council supports our future concrete innovators and leaders by administering fellowships and scholarships to help bridge the financial gap for students

Our Veterans Rebate for ACI Certification program helps honorably discharged veterans and increases skills in the industry's workforce. ACICertification.org/veteranrebate

aci Foundation
Building the Future

ACI STRUCTURAL JOURNAL TECHNICAL PAPER

Title No. 120-S81

Rehabilitation of Exterior Beam-Column Joint by Geopolymer Mortar under Quasi-Static Loading

by Arshad Hussain Choudhury and Aminul Islam Laskar

Most of the studies conducted on the rehabilitation of reinforced concrete (RC) beam-column joints are on pre-1970 structures. Recently, it was reported that seismically designed beam-column joints might also suffer damage under lateral loading. On the other hand, there is an increasing interest among researchers to study the effectiveness of geopolymer as an alternative repair material. To date, no study has been conducted to examine the performance of geopolymer for the rehabilitation of seismically detailed beam-column joints following the removal and replacement method under cyclic loading. In the present investigation, two groups of exterior beam-column joints with different flexural strength ratios were rehabilitated with geopolymer mortar. For comparison, another set of beam-column joints (one from each group) were rehabilitated with cement mortar following the same rehabilitation technique and testing. Test results indicated that geopolymer rehabilitated specimens exhibited 20 to 21% higher initial stiffness, 19 to 22% higher displacement ductility, 24 to 37% higher cumulative energy dissipation, 14 to 17% higher initial equivalent viscous damping ratio, 21 to 26% higher ultimate equivalent viscous damping ratio at failure, and 10 to 14% lower damage index compared to specimens rehabilitated with cement mortar. However, irrespective of repair material, removal and replacement technique was only able to partially restore the cyclic performance of rehabilitated specimens.

Keywords: beam-column joint; cyclic loading; geopolymer; removal and replacement method; seismically detailed.

INTRODUCTION

An abundant number of literatures are available on the repair and strengthening of beam-column joints damaged under earthquake loading. Most of the studies are limited to substandard pre-1970 structures with inadequate detailing.[1] With the advent of the seismic code of practice, beam-column joints are being constructed with special confining hoop reinforcement and adequate anchorage. Such seismically detailed beam-column joints exhibit better strength, ductility, and higher energy dissipation capacity.[2] Recently, some studies revealed that reinforced concrete (RC) structures designed as per seismic code of practice exhibited damage in the joint region when maximum force acting on the joint exceeded the code expectation level.[3-5] Only a limited number of studies are available on the rehabilitation of seismically designed and detailed structures.[3,6,7] The failure of such structures opened new research avenues in the field of rehabilitation of ductile beam-column joints.

Rehabilitation of damaged structures provides an economically viable alternative to demolition and reconstruction. The aim of seismic rehabilitation of beam-column joints is to establish a strength hierarchy between members framing into the joint, thereby preventing brittle joint failure in the column and promoting ductile beam failure (strong-column, weak-beam).[8] Several techniques such as concrete jacketing, steel jacketing, haunch solution, fiber-reinforced polymer (FRP) wrapping, removal and replacement technique, and so on are available to rehabilitate damaged beam-column joint. Concrete jacketing has been found successful in restoring the cyclic performance of damaged beam-column joints.[1] However, concrete jacketing is a time-intensive process that increases the structural weight and size of the members. Construction time decreases due to the use of prefabricated steel plates and steel haunch retrofit systems. Both techniques change the brittle joint shear of control specimens to ductile beam failure of rehabilitated specimens.[9-11] Along with increased weight and size of repaired joint, corrosion is a major concern. Moreover, drilling through slabs poses a practical implementation problem for haunch retrofit systems. FRP has shown exemplary performance in the rehabilitation of damaged beam-column joints.[1] Nevertheless, high cost, debonding due to incompatibility between the epoxy and concrete substrate, decreased performance in high temperatures, and wet environments are some of the demerits associated with FRP.

FEMA 308[12] suggests that the removal and replacement technique should be carried out for rehabilitation of highly damaged specimens subjected to severe earthquakes. In this technique, damaged concrete is removed and replaced with high-strength, low-shrinkage repair material.[1,13-16] Lee et al.[13] adopted a removal and replacement method to repair extensively damaged exterior beam-column joints under severe earthquake loading. Concrete of the damaged joint was removed followed by subsequent replacement with higher strength concrete (compressive strength 48 MPa [6.96 ksi]). Experimental results showed that the removal and replacement method was able to restore structural integrity of the rehabilitated specimens up to control specimens. Karayannis et al.[14] removed the fragmented joint concrete of exterior beam-column subassemblies. Voids were filled with high-strength (83 MPa [12.04 ksi]), rapid-hardening, and low-shrinkage cement paste. When tested under cyclic loading, a significant increase in ultimate load, stiffness,

ACI Structural Journal, V. 120, No. 5, September 2023.

MS No. S-2021-494.R2, doi: 10.14359/51738835, received December 2, 2022, and reviewed under Institute publication policies.

and energy dissipation was observed in repaired specimens. Tsonos[15] repaired two exterior beam-column joints by complete removal of joint core concrete, followed by replacement with non-shrink, higher-compressive-strength (70 MPa [10.15 ksi]) mortar. Results indicated the rehabilitation scheme was successful in enhancing cyclic performance of the rehabilitated test specimens. Marthong et al.[16] removed concrete entirely from the affected joint panel of a beam-column subassembly damaged under severe loading. Damaged concrete was replaced by commercially available micro-concrete (compressive strength 50 MPa [7.25 ksi]). Repaired specimens exhibited higher load-carrying capacity, displacement ductility, energy dissipation, and lower stiffness degradation. It is worthwhile to mention that all exterior beam-column joints repaired and strengthened by the removal and replacement technique were substandard in nature and were lacking ductile detailing provisions, according to seismic code of practice.

In late 1970, Davidovits[17] developed a cementless inorganic binder known as geopolymer. Geopolymer is formed when aluminosilicate-sourced materials react with alkaline activator, resulting in an amorphous alkali aluminosilicate with a three-dimensional polymeric chain of sialate (–Si–O–Al–O–). Use of industrial by-products such as ground-granulated blast-furnace slag (GGBS) and fly ash as source material contributed to lower CO_2 emissions and energy consumption during the production stage, making geopolymer an eco-friendly green material. Numerous research has been conducted on geopolymer since its development. Geopolymer has better mechanical properties including high early strength, low shrinkage, acid resistance, durability, and thermal stability when compared to ordinary portland cement (OPC).[18] This makes geopolymer a potential alternative repair material to cement-based materials. Vasconcelos et al.[19] worked out a cheap metakaolin-based repair material to retrofit concrete slab and beam. The metakaolin geopolymer mortar displayed high mechanical resistance and relevant adhesion to concrete substrate. Duan et al.[20] proposed a geopolymeric material having low setting time, high compressive strength, high bond strength, and better water resistance capacity to repair marine structures and concrete roads. Phoo-Ngernkham et al.[21] observed that compared to commercial repair binders, fly ash (FA)-based geopolymer mortar exhibited a denser interface transition zone with higher bond, shear, and bending strength when used as repair binder. Most geopolymer-based repair was associated with structures subjected to monotonic loading.

It may be summarized from the literature review that beam-column subassemblies rehabilitated so far by the removal and replacement technique were substandard in nature and lacked ductile detailing provisions, according to the seismic code of practice. Seismically detailed beam-column joints suffered joint damage under lateral loading in some cases. No study was undertaken to explore the effectiveness of the removal and replacement technique in the rehabilitation of seismically detailed beam-column joints. Further, performance of geopolymer mortar as repair material under cyclic loading for seismically detailed beam-column joint is yet to be investigated.

The present study was undertaken to investigate the effectiveness of the removal and replacement method in rehabilitation of seismically detailed beam-column joints using geopolymer. Results were compared with another set of the same specimens repaired with cement mortar adopting same repair technique.

RESEARCH SIGNIFICANCE

Though the removal and replacement method of rehabilitation has performed satisfactorily for substandard beam-column joints, the performance of this method is unknown for seismically designed and detailed beam-column joints. In the last decade, geopolymer has shown immense potential as an alternate repair material for structures subjected to monotonic loading, but repair studies concerning structures under cyclic loading are scarce. The findings of this paper will provide insight into the performance of the removal and replacement technique for rehabilitation of seismically detailed beam-column joints subjected to cyclic loading using geopolymer.

MATERIALS AND METHODS

Materials for beam-column subassembly

Grade M20 concrete[22] was prepared by mixing Grade 43 OPC, crushed coarse aggregate 10 mm (0.39 in.) down, locally available river sand, and potable water. Grade Fe 550 reinforcement of was used in the longitudinal direction and Grade Fe 250 reinforcing bar was provided in the transverse direction. Upon laboratory testing as per IS:1608-2005,[23] the yield stress of Grades Fe 550 and Fe 250 was found to be 590 MPa (85.55 ksi) and 300 MPa (43.5 ksi). All the ingredients of concrete were machine mixed in a 50 L (13.2 gal.) pan-type concrete mixer.

REPAIR MATERIALS

Geopolymer mortar (GM)

GGBS, in combination with Class F FA, was used as a binder in the geopolymer mixture. The proportion of GGBS to FA was fixed at 80:20 for all trial mixtures. A higher proportion of GGBS was used as it is the primary binding agent and can contribute to strength grain in ambient temperature.[24] FA was used as an additive to regulate setting time. The chemical composition and physical properties of GGBS and Class F FA are shown in Table 1. A sodium hydroxide (NaOH) pellet (specific gravity 2.13 and purity of 97%) was used as an alkali activator.

For selecting a suitable geopolymer mixture to carry out rehabilitation, three sets of trial mixtures (T1, T2, and T3)

Table 1—Chemical composition of GGBS and FA

Chemical composition	GGBS, % by mass	FA, % by mass
Silicon dioxide (SiO_2)	35	66.39
Aluminium oxide (Al_2O_3)	20	22.63
Ferric oxide (Fe_2O_3)	2	5.30
Calcium oxide (CaO)	34	0.67
Sulfur oxide (SO_3)	0.8	0.41
Magnesium oxide (MgO)	8	0.16

Table 2—Properties of geopolymer trial mixtures

Trial mixture	Molarity	Compressive strength, MPa			Initial setting time, min	Final setting time, min
		3 days	7 days	28 days		
T1	8M	28	35	43	24	60
T2	10M	30	40	46	20	50
T3	12M	33	42	48	15	42

Note: 1 MPa = 0.145 ksi.

with various molarities—8M, 10M, and 12M—of activator solution were prepared. The binder (GGBS + FA) to sand proportion was maintained at 1:3. For rapid strength gain and high compressive strength, the ratio of alkali to binder was kept constant at 0.65.[25] The codal provisions of IS 1727-1957[26] were followed to prepare trial mixtures in standard 50 cm (7.75 in.) mortar cubes and to evaluate setting times. Test results of trial mixtures are provided in Table 2. According to Duan et al.[20] and Yun and Choi,[27] desired properties for suitable repair materials are early strength, rapid setting (low initial and final setting time), and high compressive strength. Among all the trial mixtures, T3 displayed the earliest strength gain, least initial and final setting time, and highest compressive strength. Therefore, T3 was selected as the most suitable repair material to carry out the rehabilitation work.

Cement mortar (CM)

Grade 43 OPC was used to prepare mortar mixture for repair work.[28] Cement to sand ratio was maintained at 1:3 for mortar preparation, and water-cement ratio (w/c) was fixed at 0.35. For higher workability, a high-range water-reducing admixture (HRWRA) at the rate of 1.5% by weight of cement was used in the mixture. All these ingredients were mixed to prepare 50 cm (7.75 in.) mortar cubes to determine the compressive strength. Cubes were demolded after 24 hours and cured under water. Compressive strength was determined as per IS:1727-1967[26] and was found to be 25 MPa (3.63 ksi), 34 MPa (4.93 ksi), and 52 MPa (7.54 ksi) at the third, seventh, and 28th days, respectively.

Test specimens

In the present study, one-third scaled-down beam-column joint specimens were used. ACI 374.1-05[29] allows scaling down of specimens up to one-third of full-size specimens, as the scaled-down specimens are large enough to represent load transfer mechanism along with all the real material complexities and behavior of full-scaled specimens. The size of columns and beam components were kept uniform at 150 x 120 mm (4.72 x 5.91 in.) for all specimens. Beam-column joints were designed on the assumption that the point of contraflexure occurs at the beam midspan and column midheight.[30] Column length measured from one contraflexure point to another was 1400 mm (55.12 in.). The length of the beam measured from inner face of column to the point of contraflexure in beam was 690 mm (27.17 in.). Beam-column subassemblies were designed following the strong-column, weak-beam concept.[31] Based on the flexural strength ratio, test specimens were grouped into two categories: Group 1 (flexural strength ratios = 1.2); and Group 2 (flexural strength ratios = 1.4). The flexural strength ratio of a joint is defined as the ratio of summation of nominal design strength of all the columns to the summation of nominal design strength of all the beams framing into the joint.[32] Such flexural strength ratios were achieved by varying beam and column reinforcement. The structural design of beam and column components of specimens was done as per provisions laid down in IS 456-2000.[33] The joint panel of the specimens was designed and detailed as per codal provisions of IS 13920-2016.[32] Special confinement reinforcement in the form of rectangular hoop reinforcement was provided in and around the joint region by taking into the provision of codal requirement of IS:13920-2016.[32] The cross-sectional area of the bar (A_{sh}) of rectangular hoop reinforcement as per IS:13920-2016[32] is calculated by the following equation

$$A_{sh} = \text{maximum of} \left[0.18 s_v h \frac{f_{ck}}{f_y} \left[\frac{A_g}{A_k} - 1 \right] \text{ or } \left[0.05 s_v h \frac{f_{ck}}{f_y} \right] \right] \quad (1)$$

where s_v is center-to-center spacing of stirrup; h is longer length of rectangular stirrup measured up to outer face; A_g is gross cross-sectional area of column; A_k is area of concrete confined in the core; f_{ck} is characteristic compressive strength of concrete; and f_y is 0.02% proof strength of transverse steel reinforcement bars.

Adequate anchorage length was provided following IS:13920-2016[32] to prevent pullout failure of beam reinforcement. In all specimens, both top and bottom bars of beams were bent at 90 degrees heading towards joint core. As per IS:13920-2016,[32] the total anchorage length was determined by Eq. (2)

$$\text{Anchorage length} = (L_d + 10\text{Ø} - \text{allowance for 90-degree bend}) \quad (2)$$

where Ø is bar diameter; and L_d is development length given by Eq. (3) as per IS:456-2000

$$L_d = \frac{\text{Ø}\sigma_s}{4\tau_{bd}} \quad (3)$$

where Ø is bar diameter; σ_s is stress in longitudinal reinforcing bars; and τ_{bd} is design bond stress.

Dimensions and reinforcement details of test specimens are provided in Fig. 1.

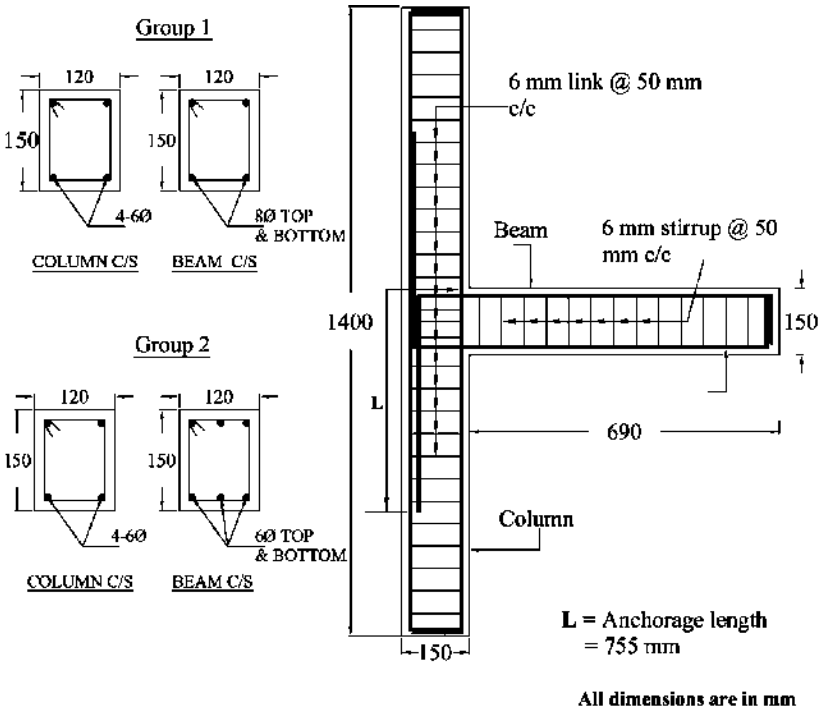

Fig. 1—Reinforcement details and dimensions of test specimens under study. (Note: 1 mm = 0.0394 in.)

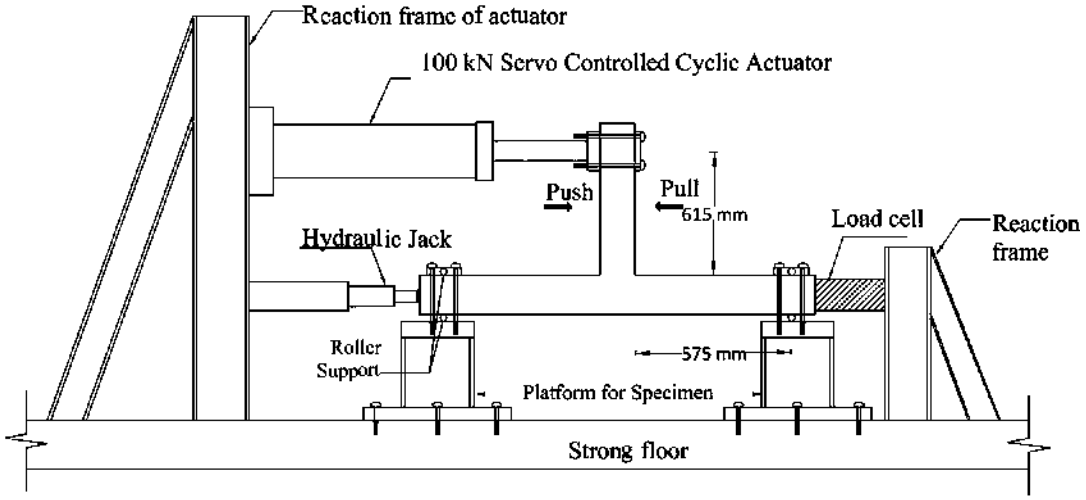

Fig. 2—Schematic representation of cyclic test setup. (Note: 1 kN = 0.2248 kip; 1 mm = 0.0394 in.)

Test setup and experimental procedure

The experimental setup to test beam-column joints under cyclic loading is shown in Fig. 2. Quasi-static cyclic loading was applied to beam-column joints by means of a servo-controlled hydraulic actuator having a maximum capacity of ±100 kN (22.48 kip) and peak displacement of ±90 mm (3.54 in.). The ends of the columns were mounted horizontally on a roller steel support to simulate hinged-boundary condition, and the beam was placed in the vertical plane, as shown in Fig. 2. The beam was hinged connected to the actuator through swivel base assembly. A uniform axial load of 10% gross capacity of the column was applied to the column with a hydraulic jack to replicate gravity loading condition.[34]

In this study, the loading protocol was selected following codal provision mentioned in ACI 374.1-05.[29] The experiment started by applying a displacement of magnitude 1 mm (0.039 in.) to the beam-end. Displacement progressed with an increment of 1 mm (0.039 in.) having 0.25 Hz frequency until failure of the joint. The failure was marked by a drop in peak load by 25% as per ACI 374.1-05.[29] Each displacement level is comprised of three cycles of push and pull loading. Typical loading history is presented in Fig. 3. Similar loading protocol was also adopted by Mukherjee and Joshi,[35] Chidambaram and Agarwal,[36] and Kheni et al.,[37] among others. The displacement applied by the actuator was gauged with linear variable differential transformers (LVDTs) fitted in the actuator, and the corresponding load was recorded by a coaxially mounted load cell. A data acquisition system collected all test data and stored it in the computer connected to the actuator.

Rehabilitation procedure

The control specimens of Groups 1 and 2 were tested under cyclic loading as per loading protocol, discussed in the previous section. Once control specimens were tested, fractured concrete from the joint region was removed with an air hammer to expose the joint reinforcements. A similar procedure for concrete removal was followed by Ghobarah and Said[38] during the rehabilitation of beam-column joints with glass fiber-reinforced polymer (GFRP). Attention was paid to the removal of any concrete fragments from the reinforcement. For exposed surface preparation, a chisel and hammer were used to make the interface rough up following the provisions of ACI 318-08 to ensure proper shear transfer between old, hardened concrete and new repair materials. Subsequently, compressed air was used to remove any debris, dust, or loose materials. Cleaned specimens were then placed on wooden formwork that was constructed for rehabilitation, as shown in Fig. 4(a). Geopolymer mixture T3 was used to fill the voids left from the removal of damaged joint concrete. The placed geopolymer mixture was thoroughly compacted to filled up all cavities. The wooden formwork was removed the next day, and specimens were ambient cured from 28 days. Rehabilitated specimens were termed as 1GM and 2GM. 1GM means Group 1 specimen rehabilitated with GM. Similarly, 2GM implied specimen of Group 2 rehabilitated with GM. The finished specimen is shown in Fig. 4(b).

To evaluate the performance of geopolymer with respect to OPC under cyclic loading, the study was further extended to include cement-based repaired beam-column joints. For this purpose, another two specimens (one from each group) were tested under cyclic loading. The damaged specimens were rehabilitated with CM (compressive strength 52 MPa [7.54 ksi][26]) following the same rehabilitated technique as discussed in the preceding paragraph. Rehabilitated specimens were named 1CM and 2CM, where numeric 1 or 2 implied group number and CM implied cement mortar. After repair, specimens 1CM and 2CM were wrapped with a wet jute bag to cure for 28 days.

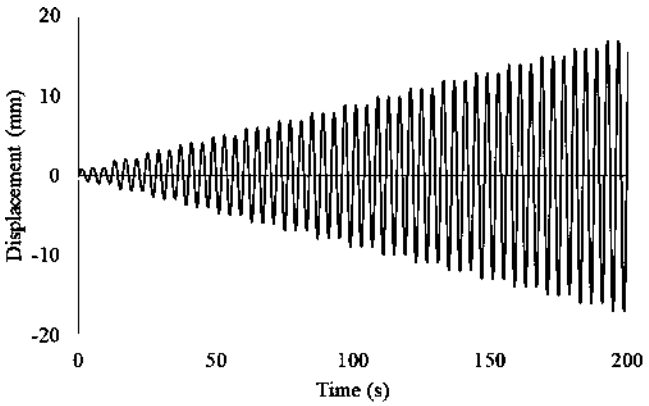

Fig. 3—Loading history applied to all test specimens. (Note: 1 mm = 0.0394 in.)

RESULTS AND DISCUSSION

Crack formation and failure mode

The typical failure crack patterns of control specimens 1C and 2C are shown in Fig. 5. In specimen 1C with flexural strength ratio 1.2, the first crack was observed at the 2 mm (0.079 in.) displacement level. With an increase in flexural strength ratio to 1.4 (specimen 2C), formation of the first crack was delayed to a displacement of 3 mm (0.118 in.). However, the first visible crack started to appear in the corner of beam-column connection and expanded towards the entire depth of the beam with progressive loading in both specimens. This ultimately led to the formation of flexural crack in the beam. With repeated opening and closing of flexural crack due to load reversal, minor diagonal cracks started to appear in the joint core. The appearance of diagonal crack in the joint would mean that transverse steel crossing diagonal crack began to yield.[39-41] With further increase in displacement, the flexural crack in the beam widened and resulted in failure of control specimens by formation of plastic hinge in the beam. Such failure is in accordance with "strong-column, weak-beam" design philosophy. No concrete bulging was observed at any stage of loading in the joint region of control specimens.

The crack patterns of specimens 1GM, 2GM, 1CM, and 2CM are shown in Fig. 6. Irrespective of repair material and flexural strength ratio, the first visible crack in all rehabilitated specimens was observed in the corner of the beam at

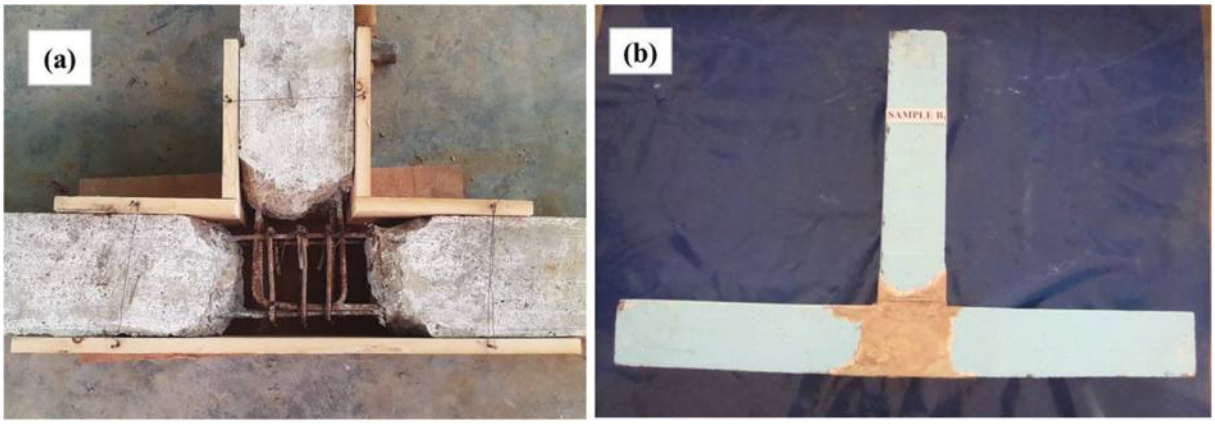

Fig. 4—(a) Typical specimen after removal of damage concrete from joint region; and (b) typical beam-column joint after rehabilitated by GM.

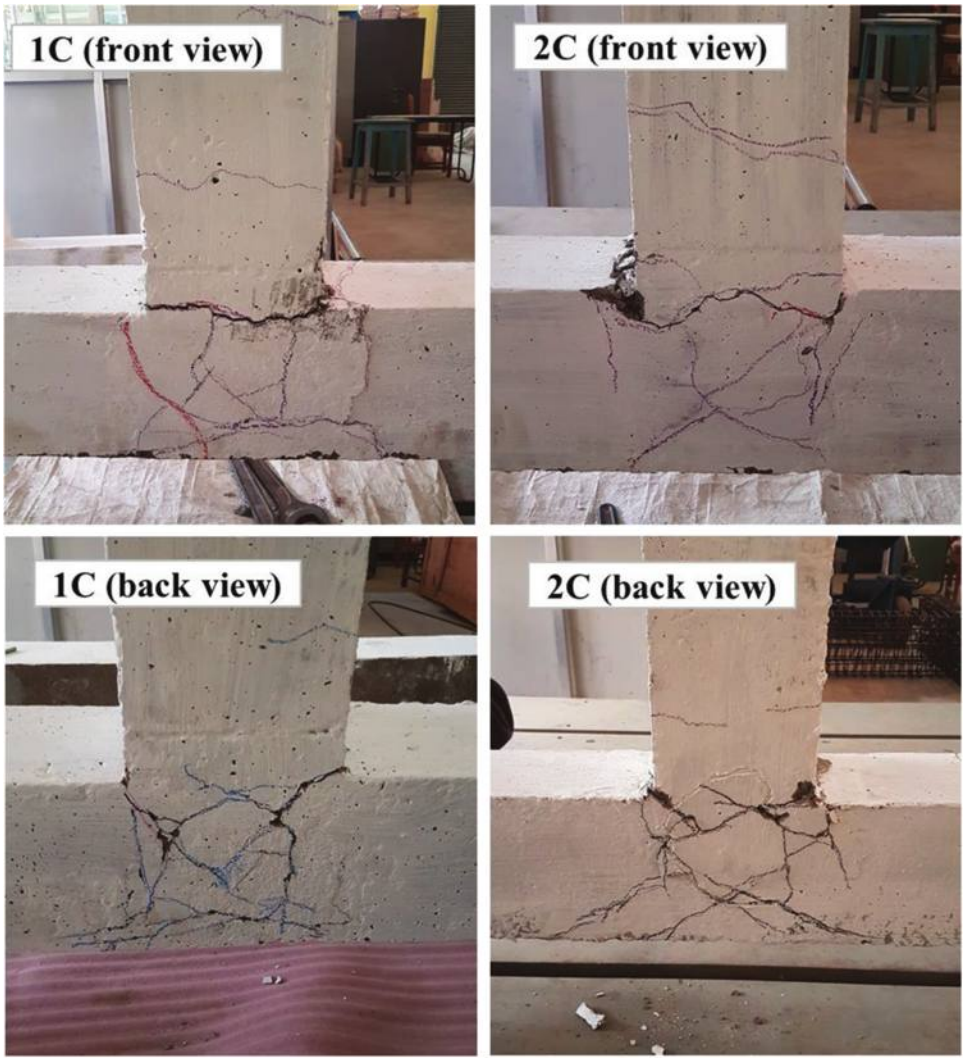

Fig. 5—Typical crack pattern of control specimens at failure.

a displacement of 1 mm (0.039 in.). With initiation of crack in the beam corner, the crack started to penetrate across the entire depth of the beam with increasing displacement. After the flexural cracking of beam, major diagonal cracks in the joint panels of all four rehabilitated specimens began to appear. Diagonal cracks in the joint regions of 1GM and 1CM and 2GM and 2CM were higher in number than that of respective control specimens. Moreover, bulging of the repair material leading to spalling was observed in rehabilitated specimens. The effect of the cold joint between the old concrete of beam-column subassembly and new repair material was also observed. The cold joint is the plane of low bond strength.[42] Therefore, when the magnitude of tensile stress becomes high, repair materials from damaged areas tend to get separated from old concrete substrate of beam-column subassembly. This led to debonding at the interface of old concrete and repair material resulting in cracking formation at cold joints at the column. Such cracks in the column are undesirable as per strong-column, weak-beam design philosophy. However, it may be seen that effect of cold joints is less prominent in case of 1GM and 2GM specimens than that of 1CM and 2CM, respectively. This was due to better bond between geopolymer and old concrete substrate. Such improvement was resultant of the reaction between the surface product of concrete substrate and alkali activator.[43,44] Higher bond strength of GM resisted degradation of bond between GM and old concrete due to tensile stress, which decreased intensity of crack formation at the cold joint in 1GM and 2GM.

When control specimens were tested under cyclic loading, joint hoop reinforcement would yield and develop residual deformation.[45] In the removal and replacement technique, only the damaged concrete was removed and replaced with suitable repair material. Pre-yielded hoop reinforcement remained inside rehabilitated specimens after repair. Therefore, when rehabilitated specimens were subjected to cyclic loading, yielded hoop reinforcements having residual deformation were reloaded. Reloading exaggerated the force-deformation characteristics of such hoops, and hence, small amount of stress caused large amounts of strain in the joint hoops.[45] GM and CM, being brittle in nature, were not able to sustain such large strain, thus resulting in the formation of many major cracks in the joint core. Furthermore, splitting cracks at the outer face of column were observed in the case of all such specimens. This was due to the inability of pre-yielded hoop reinforcement to confine the joint core

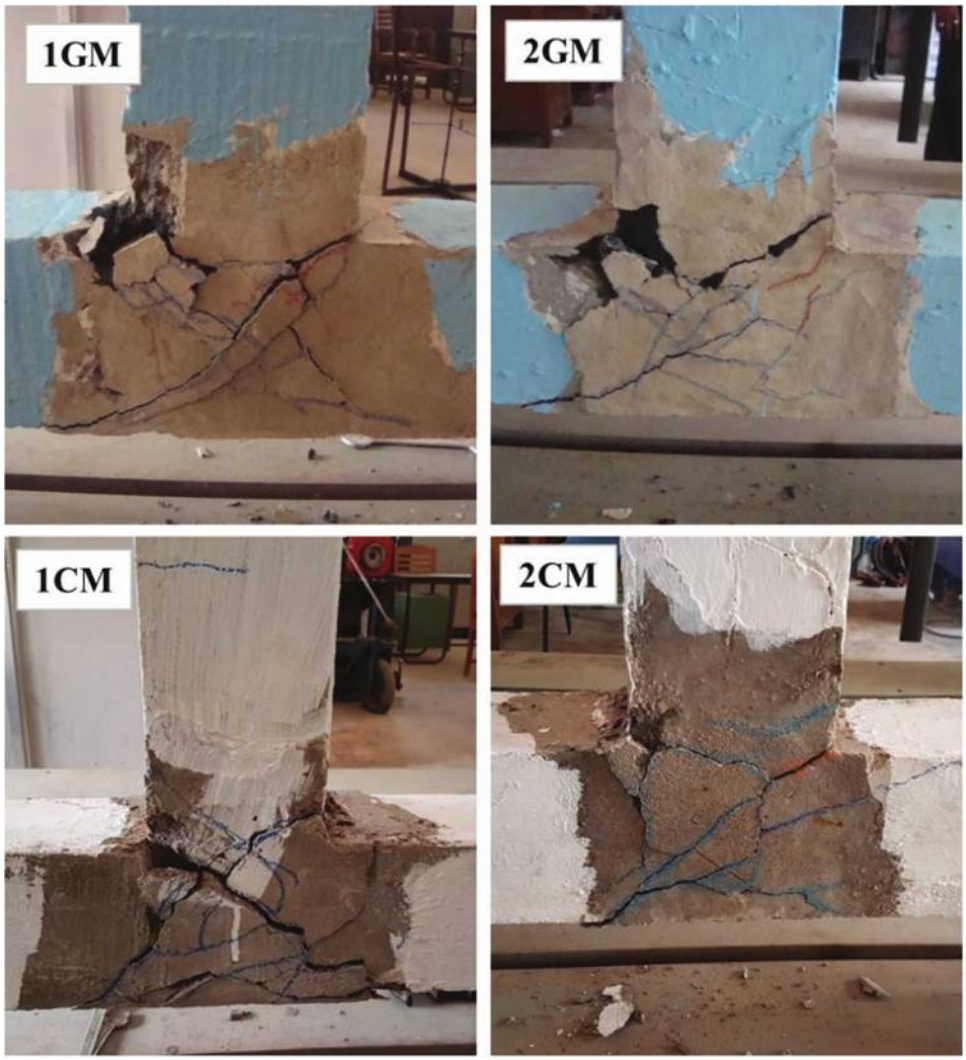

Fig. 6—Typical crack pattern of rehabilitated specimens at failure.

effectively, resulting in column reinforcement buckling. All these factors contributed to the failure of rehabilitated specimens by beam failure accompanied by brittle joint failure.

Hysteresis response and envelope curve

The typical hysteresis response of Group 1 specimen is plotted in Fig. 7, and load-displacement envelope curves all specimens are plotted in Fig. 8. Peak loads of test specimens were tabulated in Table 3. An increase of 14 and 12% was observed in 1GM and 2GM from their respective controls. A similar increase in peak load of 17 and 18% was also observed in 1CM and 2CM, respectively. The increase in peak load of rehabilitated specimens was due to higher compressive strength of repair materials. 1CM and 2CM exhibited an even higher peak load than 1GM and 2GM due to higher compressive strength of CM (52 MPa [7.54 ksi]) compared to GM (48 MPa [6.96 ksi]), respectively.

However, it may be observed from Fig. 8 that rehabilitated specimens exhibited brittle behavior with respect to control. This was due to a sudden decrease in the load-carrying capacity of rehabilitated specimens after attaining peak load. This can be attributed to the brittle nature of the repair materials (GM and CM), debonding failure at the cold joint interface, and loss of confinement due to the presence of yielded hoop reinforcement in rehabilitated specimens. Initiation of load at the beam-end led to the formation of cracks at cold joint interfaces, resulting in a decrease in lateral confinement of the joint core.[46] With progressive loading, such cracks became a secondary source for new joint crack generation. Due to the higher compressive strength of GM and CM, repair materials resisted crack formation momentarily, thereby increasing the maximum peak load of such specimens. However, after attaining peak load when the magnitude of shear stress was generated in the joint significantly increased, GM and CM failed to resist further crack development due to its brittle nature. Moreover, yielded hoops could not confine the joint core effectively.[39] Loss in confinement at the joint core leads to easier crack development. All these factors combinedly caused significant cracking of joint core resulting in rapid loss of load-carrying capacity, as observed in Fig. 8.

Joint stresses

The design shear capacity of the exterior beam-column joint as per IS 13920:2016[32] is as follows

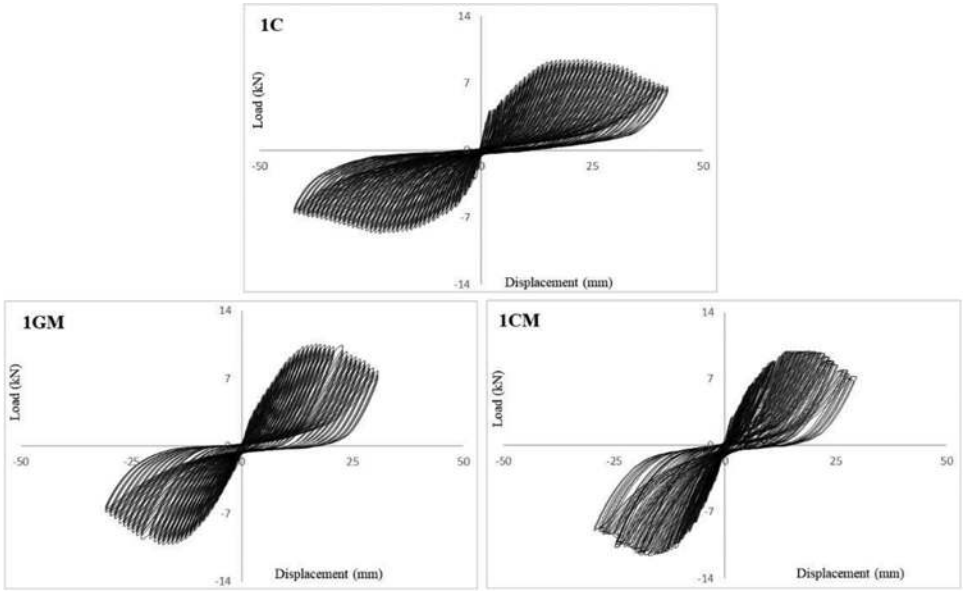

Fig. 7—Typical hysteresis curve of Group 1 test specimens. (Note: 1 kN = 0.2248 kip; 1 mm = 0.0394 in.)

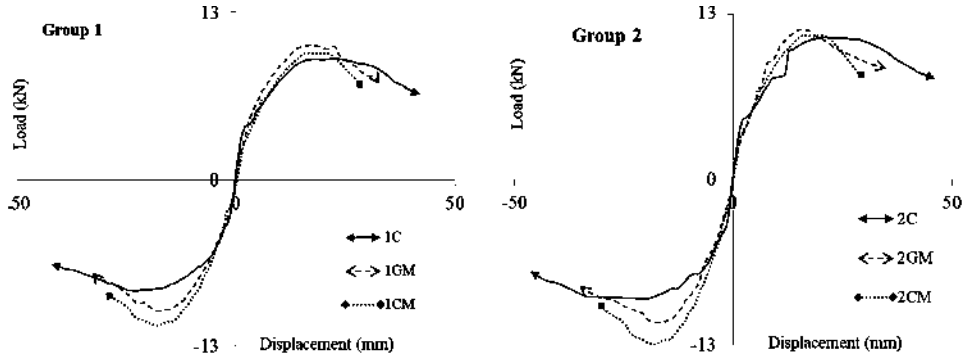

Fig. 8—Load-displacement curve of test specimens. (Note: 1 kN = 0.2248 kip; 1 mm = 0.0394 in.)

Table 3—Peak load and joint shear stress of specimens

Specimens	Peak load, kN	τ_{IS}, MPa	τ_{jh}, MPa	τ_{jh}/τ_{IS}
1C	9.10	5.37	2.31	0.43
1GM	10.40	8.31	2.64	0.32
1CM	10.66	8.65	2.70	0.31
2C	10.27	5.37	2.60	0.49
2GM	11.51	8.31	2.92	0.35
2CM	12.16	8.65	3.08	0.36

Note: 1 kN = 0.2248 kip; 1 MPa = 0.145 ksi.

$$\tau_{IS} = 1.2\sqrt{f_{ck}} \quad (4)$$

where f_{ck} is the characteristic strength of concrete.

For the exterior beam-column joint, horizontal shear force attained in the joint during loading is taken as follows (Murty et al.[47])

$$\tau_{jh} = \frac{P}{A^{h}_{core}}\left(\frac{L_b}{d_b} - \frac{L_b + 0.5D_c}{L_c}\right) \quad (5)$$

where P is the peak load of the test specimens; A^{h}_{core} is horizontal cross-sectional area of the joint resisting horizontal shear force; L_b and d_b are length and effective depth of beam, respectively; L_c is column length; and D_c is the overall column depth. The value of τ_{jh} is presented in Table 3. The value of designed shear stress τ_{IS} is dependent on compressive strength of joint concrete. As in rehabilitated specimens, joint core was strengthened with higher compressive strength repair materials (f_{ck} = 48 MPa [6.96 ksi] for GM and f_{ck} = 52 MPa [7.54 ksi] for CM) compared to control specimens (f_{ck} = 20 MPa [2.9 ksi]); the value of τ_{IS} for rehabilitated specimens increased significantly. On the other hand, due to the same geometrical dimensions of all specimens, τ_{jh} is dependent primarily on P. The τ_{jh} of rehabilitated specimens also increased with an increase in peak load owing to the use of high-strength GM and CM. A large increase in τ_{IS} compared to τ_{jh} decreased the value of τ_{jh}/τ_{IS} so that it is less than 1. Apparently, the ratio of τ_{jh}/τ_{IS} for all rehabilitated specimens indicates that specimens have adequate shear strength capacity and enabled adjoining beam to reach its ultimate capacity. However, rehabilitated specimens failed due to beam failure accompanied by joint failure, as observed from Fig. 6. This may be because Eq. (5) does not reflect the effect of cold joints formed due to rehabilitation and the presence of yielded hoop reinforcement in the joint.

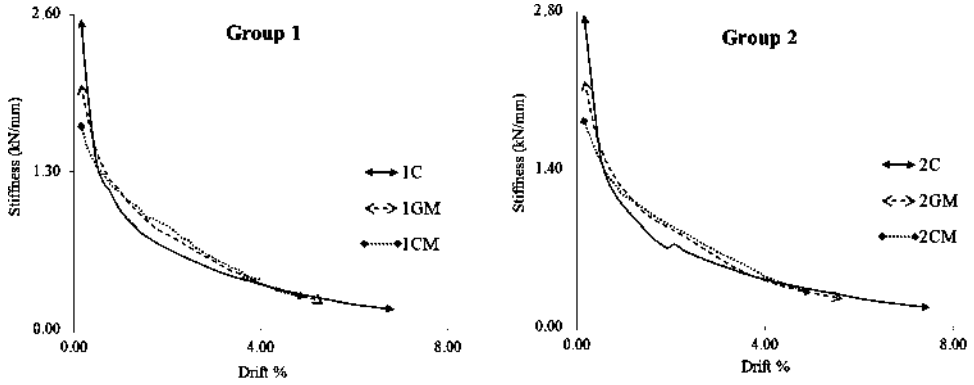

Fig. 9—Stiffness degradation curve of all specimens. (Note: 1 kN/mm = 5.71 kip/in.)

Stiffness degradation

Stiffness degradation is used to quantify the loss of lateral stiffness in reinforced concrete structures subjected to reversed cyclic loading.[45] In this investigation, secant stiffness is used to represent stiffness of test specimens. Stiffness at an *i*-th displacement is calculated by the following expression

$$K_i = \frac{|F_{+i} - F_{-i}|}{|\delta_{+i} - \delta_{-i}|} \quad (6)$$

where F_{+i} and F_{-i} are maximum positive and negative load at corresponding displacement δ_{+i} and δ_{-I}; respectively.

The stiffness calculated from Eq. (6) is plotted against drift angle to obtain stiffness degradation curve, as shown in Fig. 9. Control specimens 1C and 2C displayed initial stiffness of 2.561 and 2.722 kN/mm (14.62 and 15.83 kip/in.), respectively. GM and CM were only able to restore 79 to 80% and 65 to 67% of initial stiffness in rehabilitated specimens in comparison to control. This was due to the presence of the cold joint interface between new repair mortars and old concrete. When load was applied on rehabilitated specimens, the cold joint being a weak interface between concrete and the repair material, a small amount of force opened the interface. This led to earlier crack formation at lower displacement levels, as observed in the previous section where crack was first observed in rehabilitated specimens at 1 mm (0.039 in.), irrespective of repair materials. On the other hand, initial crack at 1C and 2C were observed at 2 and 3 mm (0.079 and 0.118 mm) displacement levels, respectively. Thus, earlier crack at lower displacement lowered initial stiffness of all rehabilitated specimens. Higher initial stiffness of 1GM and 2GM than 1CM and 2CM was due to higher bond strength of geopolymer with concrete substrate compared to OPC.[44] As a result, a higher amount of force is required to form first crack in 1GM and 2GM thereby leading to 20 to 21% increase in initial stiffness compared to 1CM and 2CM, respectively.

Figure 9 reveals that 1GM, 2GM, 1CM, and 2CM exhibited lower initial stiffness, yet they displayed lower stiffness degradation at lower drift level compared to controls. This can be attributed to higher compressive strength of repair materials which increases the strength of diagonal strut, as performance of diagonal strut depends on compressive strength of joint core material. Hence, 1GM, 2GM, 1CM,

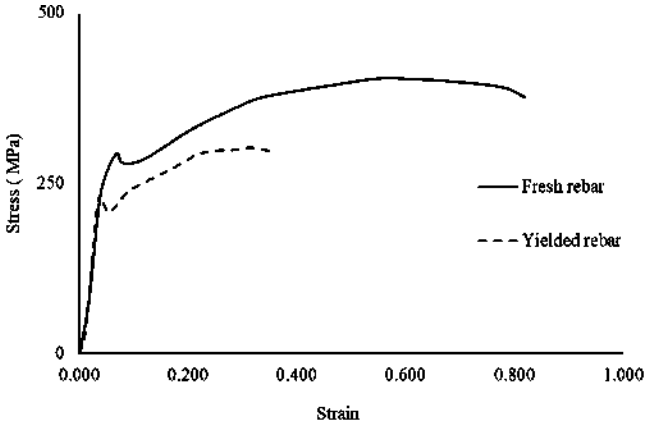

Fig. 10—Typical stress-strain graph of hoop reinforcement. (Note: 1 MPa = 0.145 ksi.)

and 2CM were able to resist diagonal tensile cracks formation at lower drift levels. Nevertheless, with increasing drift, cracks at the cold joint interface expanded and caused development of new cracks in the joint. On the other hand, yielded hoop reinforcement also contributed to formation of crack in the joint. When yielded hoops were reloaded under reversed cyclic loading, yielded hoops yield at lower stress level and sustain lower ultimate strain. This is evident from the stress-versus-strain graph of fresh hoops (tested before cyclic loading) and yielded hoops (taken out from control specimens after cyclic loading), as shown in Fig. 10. Similar stress-strain curve of fresh and yielded reinforcing bar was also reported by Mukherjee and Jain.[48] Yielding of yielded hoops at a lower stress level produced loss of confinement and deterioration of bond at lower beam-tip load compared to control specimens. As a result, confinement of joint hoops deteriorates significantly and becomes ineffective against volumetric expansion of joint core. Such expansion of joint core cannot be resisted by the brittle nature of GM and CM, resulting in a large number of cracks in the joint. These factors contributed to higher crack development in joint, thereby initiating higher stiffness degradation of 1GM, 1CM, 2GM, and 2CM at higher drift.

Pinching width ratio (PWR)

The pinching width ratio (PWR) is a dimensionless parameter developed by Mostofinejad and Akhlaghi[49] to measure pinching associated with hysteresis loops under cyclic

loading. The higher the value of PWR, the lower will be the pinching and vice-versa. Pinching of the hysteresis loops is largely influenced by stiffness degradation, characterized by crack formation. It is defined as follows

$$\text{PWR} = P_a/P_i \quad (7)$$

where P_a is actual pinching of a hysteretic loop at a particular loading cycle; and P_i is the pinching width of the idealized hysteresis loops at same displacement. These parameters are illustrated in Fig. 11. P_a is the least distance between the positive and negative loading path of actual hysteresis loop of that loading cycle at approximately zero displacement level. P_i is the distance between two sides of parallelogram at approximately zero displacement. K_1 and K_2 are initial uncracked stiffness of positive and negative loading cycle. Using all the parameters, PWR was determined for all specimens against displacement (Fig. 12). Lower stiffness degradation of rehabilitated specimens at initial displacement levels contributed to higher PWR, indicating lower pinching of the hysteresis curve then control specimens initially. However, with increasing displacement, rehabilitated specimens experienced higher degradation of PWR value than control specimens such that towards the ends, it was observed that the PWR of 1GM and 1CM, and 2GM and 2CM, was lower than 1C and 2C, respectively. Higher stiffness degradation of rehabilitated specimens caused rapid decrease in PWR at a higher drift level.

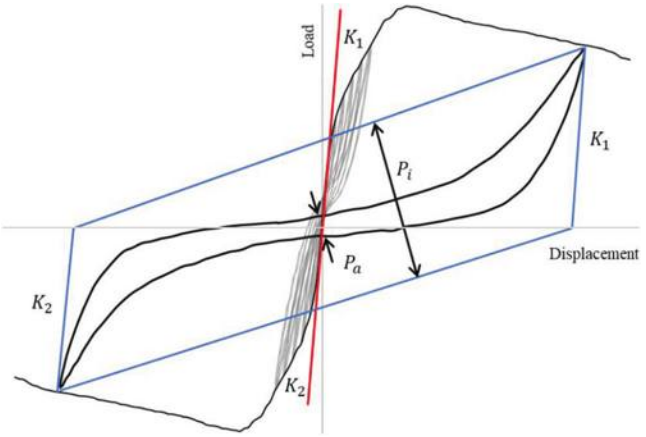

Fig. 11—Illustration of parameters used to measure PWR.

Displacement ductility

Ductility of the specimens was quantified by displacement ductility, which is defined as the ratio of ultimate displacement (δ_u) to yield displacement (δ_y). Ultimate displacement (δ_u) represents post-peak deformation corresponding to 75% peak load.[31] Yield displacement (δ_y) is taken as displacement corresponding to secant stiffness at 0.75 times of the design load of the equivalent elasto-plastic curve.[50] Displacement ductility of all the test specimens is tabulated in Table 4. Geopolymer mortar and cement mortar were able to restore 74 to 78% and 61 to 67% ductility for rehabilitated specimens with respect to control specimens. Geopolymer repaired specimens exhibited 19 to 22% better ductility compared to CM repaired specimens. The increased ductility of 1GM and 2GM was predominantly due to the increase in ultimate displacement (Table 4). Higher bond strength of GM with concrete substrate decreased crack formation intensity at cold joint interface. Better bonding ability of GM with embedded steel reinforcement prevented reinforcement slippage and decreased intensity of concrete wedge separation from the outer face of column. Higher tensile strength of geopolymer reduced diagonal tensile crack formation in GM repaired specimens. As a result, the crack resistance ability of specimens 1GM and 2GM significantly increased, enabling specimens to sustain loading to higher displacement level compared to CM-repaired specimens.

From Table 4, the ultimate displacement of the rehabilitated specimens was smaller compared to control specimens. This was mainly due to presence cold joint and yielded hoops in rehabilitated specimens. With progressive loading, cracks in the cold joint interface eventually penetrated the entire depth of columns and beam, reaching the level of longitudinal reinforcement crossing cold joint interfaces. At that instant, the total shear force acting at the cold joint interfaces is resisted entirely by longitudinal reinforcements at that interface,[42,46] causing early yielding of longitudinal reinforcements in the case of repaired specimens. Such early yielding of reinforcement reduced post-yield performance of such specimens. Also, cracks at the cold joint interface led to the development of new cracks in the joint with

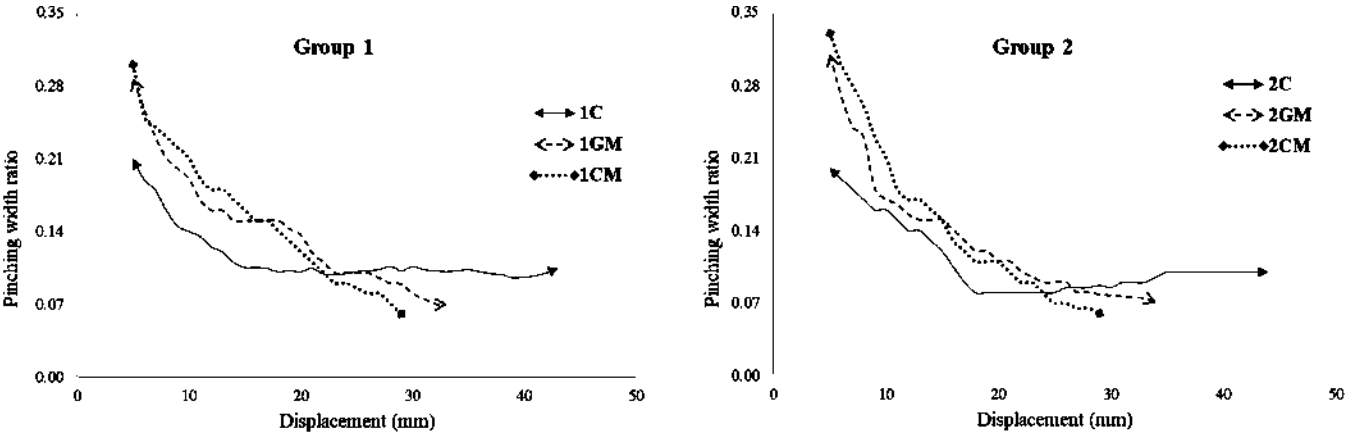

Fig. 12—PWR of specimens under study. (Note: 1 mm = 0.0394 in.)

increased loading. Due to their brittle characteristics, CM and GM could not arrest new crack formation. Moreover, as mentioned earlier when rehabilitated specimens were tested under cyclic loading, hoop reinforcements yielded at lower stress levels, resulting in bond degradation and confinement loss of joint core at lower loads. These contributed to easier crack formation in the repaired joint, subsequently causing larger cracks in the joint core. These factors initiated early failure as rehabilitated specimens could not sustain load up to higher displacement levels, resulting in partial enhancement of ductility.

Cumulative energy dissipation

Energy dissipation is a measure to evaluate the capacity of a structure to endure an earthquake through dissipation of energy from ground motion in the post-elastic deformation phase.[34] The area of load-deformation hysteresis loops gives an estimate of energy dissipation capacity of specimens under cyclic loading. A plot of cumulative energy dissipation of specimens against displacement is shown in Fig. 13. It may be seen that GM restored 74 to 80% of total cumulative energy dissipation in rehabilitated specimens with respect to control specimens. On the other hand, 1CM and 2CM dissipated 60% and 58% of total cumulative energy dissipation of specimens 1C and 2C, respectively. Higher ductility enabled 1GM and 2GM to maintain load-carrying capacity to higher deformation in the post-elastic range of loading. This resulted in a larger inelastic zone of deformation (Table 4).

Table 4—Displacement ductility of test specimens

Specimens	Yield displacement (δ_y), mm	Ultimate displacement (δ_u), mm	Ductility (δ_u/δ_y)
1C	7.85	41.50	5.29
1GM	7.94	32.94	4.15
1CM	8.12	28.37	3.49
2C	4.42	43.89	9.93
2GM	4.74	34.84	7.35
2CM	4.82	29.13	6.04

Note: 1 mm = 0.0394 in.

The maximum amount of energy is dissipated in the inelastic range of deformation.[35] Therefore, a larger inelastic zone resulted in 24 to 37% higher energy dissipation by 1GM and 2GM compared to 1CM and 2CM, respectively.

Full enhancement of cumulative energy dissipation in rehabilitated specimens was hindered due to the presence of cold joints and yielded hoops in the joint. Due to the low initial stiffness and higher stiffness degradation of rehabilitated specimens at higher drift level, energy dissipated though viscous damping decreased. Also, early yielding of longitudinal reinforcement due to the formation of cracks at the cold joint interface[42] and yielding of pre-yielded hoops at lower stress level (Fig. 10) reduced the performance of rehabilitated specimens in the post-yield range of loading thereby causing failure at lower displacement. This resulted in a smaller inelastic zone in rehabilitated specimens compared to controls (Table 4), which reduced the energy dissipation capacity through hysteretic damping. Therefore, reduced energy dissipation by viscous and hysteretic damping combinedly reduced the total energy dissipation capacity of rehabilitated specimens.

Equivalent viscous damping ratio

The equivalent viscous damping ratio represents the ability of a structure to dampen peak excitation that arises due to inelastic deformation during earthquake loading. Cumulative energy dissipation gives an idea about combined energy dissipated by the structure up to a loading cycle, whereas the equivalent viscous damping ratio is associated with energy dissipated by the structure during a particular loading cycle. It is determined as follows[51]

$$\xi_{equ_i} = \frac{E_i}{2\pi F_{m_i} D_{m_i}} \tag{8}$$

where $\xi_{equ}i$ is equivalent viscous damping ratio; E_i is the energy dissipation; F_{m_i} is the peak load; and D_{m_i} is corresponding displacement at the i-th loading cycle, respectively. The equivalent viscous damping ratio for the test specimens is plotted against displacement in Fig. 14. Due to the higher compressive strength of GM and CM, initial crack

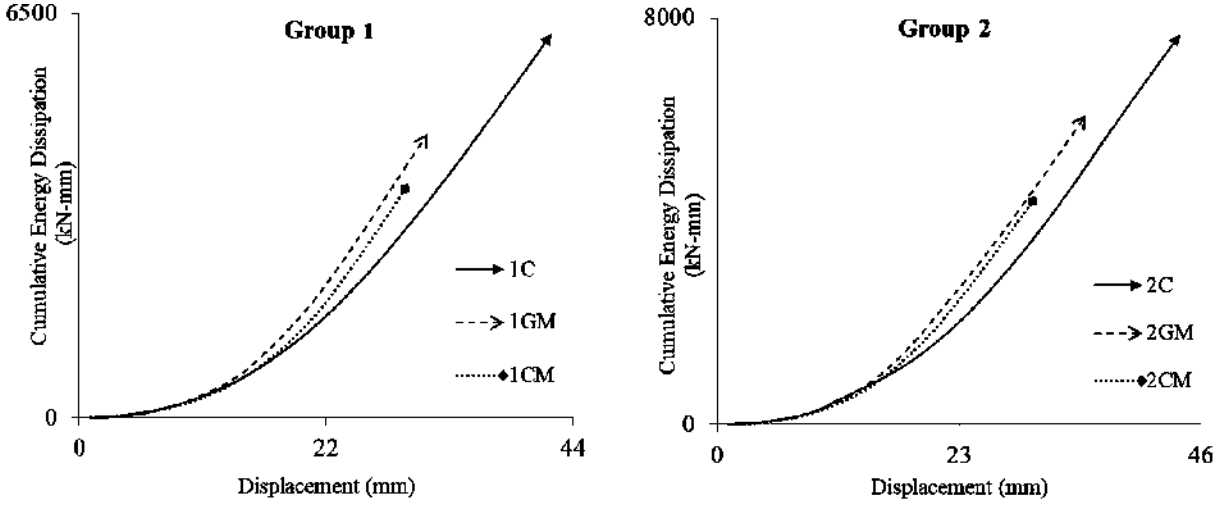

Fig. 13—Comparison of cumulative energy dissipation. (Note: 1 kNm = 0.0088 kip-in.; 1 mm = 0.0394 in.)

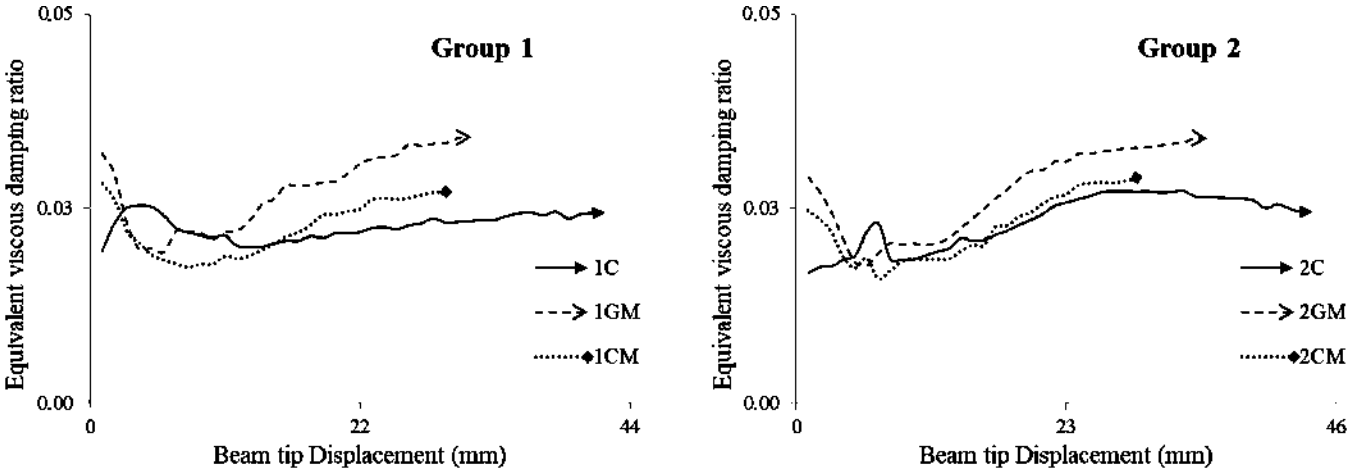

Fig. 14—Equivalent viscous damping ratio of specimens. (Note: 1 mm = 0.0394 in.)

formation in rehabilitated specimens released higher energy. This contributed to an increase in ξ_{equ} by 64 to 73% and 44 to 48% in GM and CM rehabilitated specimens at initial displacement compared to control specimens, respectively. Also, the higher initial stiffness of GM rehabilitated specimens contributed to higher energy dissipation leading to 14 to 17% higher initial ξ_{equ} than CM rehabilitated specimens. Nevertheless, with increasing displacement, a dip in ξ_{equ} was observed in rehabilitated specimens. This was due to crack propagation in cold joint interfaces during the subsequent loading cycle, which lowered energy dissipation per cycle. When cracks started to penetrate the joint core, the higher compressive strength of GM and CM resisted crack formation, leading to higher energy dissipation per loading cycle until failure. Release in higher energy per loading cycle increased ξ_{equ} value such that 1CM and 2CM, and 1GM and 2GM, displayed 13 to 16% and 36 to 42% higher ξ_{equ} than control specimens, respectively. Higher energy dissipation at failure contributed to 21 to 26% higher ξ_{equ} in GM rehabilitated specimens compared to CM rehabilitated specimens.

Damage index

Park and Ang's[52] damage index model is used in the current investigation to quantify damage suffered by the specimens in the inelastic phase of deformation under cyclic loading. The following formula proposed by Park and Ang[52] was used to determine the damage index in the present investigation

$$D = \frac{\delta_M}{\delta_u} + \frac{\beta}{Q_y \delta_u} \int dE \tag{9}$$

where δ_M is the maximum deformation at the *i*-th displacement; δ_u is the maximum displacement sustained by a beam-column joint under monotonic loading; β is a non-dimensional coefficient related with strength degradation of beam-column joint; in the current study, the value of β is taken as 0.15;[53] Q_y is the yield force calculated from load-deformation envelope; and dE is the cumulative energy dissipation considered up to the *i*-th displacement. Because monotonic loading was not applied on the tested specimens, ultimate displacement δ_u was approximately estimated from the load-deformation envelope.[53] Here, δ_u was taken as the post-peak displacement when load comes down to 75% of peak load. Damage indexes for all the beam-column joints were calculated from Eq. (9) and plotted against displacement in Fig. 15. 1GM and 2GM suffered 10 to 14% lower damage than 1CM and 2CM. This is also evident from Fig. 15, showing damage index values of the test specimens at 25 mm (1 in.) displacement level. The damage index of the beam-column joint depends on cumulative energy dissipation and ultimate deformation.[52] The higher the amount of deformation that a beam-column joint could sustain and the higher the energy dissipation, the lower will be the damage index and vice-versa. 1GM and 2GM exhibited higher ultimate deformation (Table 4) and higher energy dissipation than 1CM and 2CM (Fig. 13); hence, 1GM and 2GM sustained lower damage than 1CM and 2CM, respectively. On the contrary, control specimens showed the highest ultimate deformation and the highest energy dissipation in Group 1 and Group 2 specimens, respectively. This resulted in least damage suffered by such specimens under cyclic loading as shown in Fig. 15.

CONCLUSIONS

The present work was undertaken to study the effectiveness of removal and replacement techniques in the rehabilitation of seismically detailed beam-column joints. For this purpose, two groups of beam-column specimens with different flexural strength ratios were selected. High-strength geopolymer mortar (GM) was used as a repair material to rehabilitate two beam-column joints of each group. The test results were compared with another set of specimens from the same group, rehabilitated by cement mortar (CM) adopting the same technique. Based on the test results, the following general conclusions may be drawn:

1. Control specimens failed due to beam failure only, whereas both GM- and CM-rehabilitated specimens failed due to beam failure accompanied by joint failure. The effect of cold joints and splitting cracks at the outer face of the column was less prominent in GM-rehabilitated specimens than CM-rehabilitated specimens.

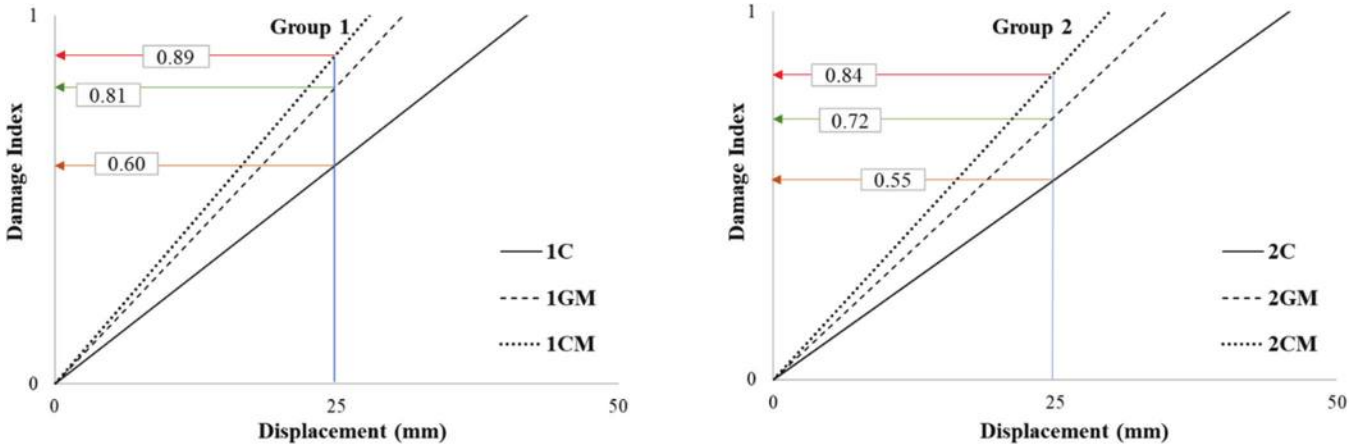

Fig. 15—Damage index of test specimens. (Note: 1 mm = 0.0394 in.)

2. GM- and CM-repaired specimens exhibited 12 to 14% and 17 to 18% higher peak load than their respective controls.

3. GM and CM could restore 79 to 80% and 65 to 67% of the initial stiffness of rehabilitated specimens. Specimens rehabilitated with GM and CM displayed lower stiffness degradation during initial drift levels compared to control specimens, while GM and CM displayed higher stiffness degradation compared to control specimens at higher drift.

4. Rehabilitated specimens initially exhibited higher pinching width ratio (PWR) than control specimens, but at failure, the PWR of rehabilitated specimens was lower than control.

5. GM was able to restore ductility and cumulative energy dissipation in rehabilitated specimens up to 74 to 78% and 72 to 74%, respectively, while CM restored 61 to 67% of control specimens' ductility and 58 to 64% of control specimens' cumulative energy dissipation.

6. The equivalent viscous damping ratio of GM- and CM-rehabilitated specimens were 64 to 73% and 44 to 48% higher than control specimens, respectively, during initial loading. The ultimate equivalent viscous damping ratio at failure was 36 to 42% higher for GM-rehabilitated specimens and 13 to 16% higher for CM-rehabilitated specimens

7. Control specimens sustained the least damage, and CM-rehabilitated specimens sustained the highest damage in terms of damage index in each group.

8. GM-rehabilitated specimens exhibited 20 to 21% higher initial stiffness, 19 to 22% higher displacement ductility, 24 to 37% higher cumulative energy dissipation, 14 to 17% higher initial equivalent viscous damping ratio, 21 to 26% higher ultimate equivalent viscous damping ratio at failure, and 10 to 14% lower damage index compared to CM-rehabilitated specimens.

The removal and replacement technique was only able to enhance peak load, PWR at initial displacement, and the equivalent viscous damping ratio of rehabilitated specimens up to the level of control specimens. Other parameters such as initial stiffness, PWR at failure, cumulative energy dissipation, displacement ductility, and damage index were only restored partially. Furthermore, rehabilitated specimens failed due to beam failure accompanied by joint failure. Thus, the removal and replacement technique was not able to fulfill the objective of seismic rehabilitation for seismically detailed beam-column joints. Irrespective of repair material, the removal and replacement technique could partially restore the cyclic performance of rehabilitated specimens. Nevertheless, GM exhibited better performance as a repair material than CM for rehabilitation of seismically detailed beam-column joints using the removal and replacement technique under cyclic loading.

AUTHOR BIOS

Arshad Hussain Choudhury *is an Assistant Professor in the Department of Civil Engineering, Chaitanya Bharathi Institute of Technology (CBIT), Hyderabad, India. He received his BE (civil) from Assam Engineering College, India, and his MTech and PhD from the National Institute of Technology (NIT) Silchar, Silchar, India.*

Aminul Islam Laskar *is a Professor in the Department of Civil Engineering, NIT Silchar. He received his BE (civil) from NIT Silchar; his MTech from the Indian Institute of Technology (IIT) New Delhi, New Delhi, India; and his PhD from IIT Guwahati, Guwahati, India.*

REFERENCES

1. Engindeniz, M.; Kahn, L. F.; and Zureick, A.-H., "Repair and Strengthening of Reinforced Concrete Beam-Column Joints: State of the Art," *ACI Structural Journal*, V. 102, No. 2, Mar.-Apr. 2005, pp. 187-197.

2. Shafaei, J.; Hosseini, A.; Marefat, M. S.; Ingham, J. M.; and Zare, H., "Experimental Evaluation of Seismically and Non-Seismically Detailed External RC Beam-Column Joints," *Journal of Earthquake Engineering*, V. 21, No. 5, 2017, pp. 776-807. doi: 10.1080/13632469.2016.1185052

3. Shafaei, J.; Hosseini, A.; Marefat, M. S.; and Ingham, J. M., "Rehabilitation of Earthquake Damaged External RC Beam-Column Joints by Joint Enlargement Using Prestressed Steel Angles," *Earthquake Engineering & Structural Dynamics*, V. 46, No. 2, 2016, pp. 291-316. doi: 10.1002/eqe.2794

4. Alavi, B., and Krawinkler, H., "Behavior of Moment-Resisting Frame Structures Subjected to Near-Fault Ground Motions," *Earthquake Engineering & Structural Dynamics*, V. 33, No. 6, 2004, pp. 687-706. doi: 10.1002/eqe.369

5. Alavi, B., and Krawinkler, H., "Effects of Near-Fault Ground Motions on Frame Structures," Report No. 138, John A. Blume Earthquake Engineering Center, Stanford, CA, 2001, 311 pp.

6. Vatani-Oskouei, A., "Repairing of Seismically Damaged RC Exterior Beam—Column Connection Using CFRP," *Journal of Reinforced Plastics and Composites*, V. 29, No. 21, 2010, pp. 3257-3274. doi: 10.1177/0731684410371407

7. Zamani Beydokhti, E., and Shariatmadar, H. "Strengthening and Rehabilitation of Exterior RC Beam–Column Joints Using Carbon-FRP Jacketing," *Materials and Structures/Materiaux et Constructions*, V. 49, No. 12, 2016, pp. 5067-5083.

8. Pantelides, C. P.; Okahashi, Y.; and Reaveley, L. D., "Seismic Rehabilitation of Reinforced Concrete Frame Interior Beam-Column Joints with FRP Composites," *Journal of Composites for Construction*, ASCE, V. 12, No. 4, 2008, pp. 435-445. doi: 10.1061/(ASCE)1090-0268(2008)12:4(435)

9. Arzeytoon, A.; Hosseini, A.; and Goudarzi, A., "Seismic Rehabilitation of Exterior RC Beam-Column Joints Using Steel Plates, Angles, and Posttensioning Rods," *Journal of Performance of Constructed Facilities*, ASCE, V. 30, No. 1, 2016, p. 04014200. doi: 10.1061/(ASCE)CF.1943-5509.0000721

10. Marchisella, A.; Muciaccia, G.; Sharma, A.; and Eligehausen, R., "Experimental Investigation of 3D RC Exterior Joint Retrofitted With Fully-Fastened-Haunch-Retrofit-Solution," *Engineering Structures*, V. 239, 2021, p. 112206. doi: 10.1016/j.engstruct.2021.112206

11. Sharma, A.; Reddy, G. R.; Eligehausen, R.; Genesio, G.; and Pampanin, S., "Seismic Response of Reinforced Concrete Frames with Haunch Retrofit Solution," *ACI Structural Journal*, V. 111, No. 3, May-June 2014, pp. 673-684. doi: 10.14359/51686625

12. FEMA 308. "Repair of Earthquake Damaged Concrete and Masonry Wall Buildings," Federal Emergency Management Agency, Washington, DC, 1998, 80 pp.

13. Lee, D. L. N.; Wight, J. K.; and Hanson, R. D., "Repair of Damaged Reinforced Concrete Frame Structures," *Proceedings of the Sixth World Conference on Earthquake Engineering*, New Delhi, India, 1977. pp. 2486-2491.

14. Karayannis, C. G.; Chalioris, C. E.; and Sideris, K. K., "Effectiveness of RC Beam-Column Connection Repair Using Epoxy Resin Injections," *Journal of Earthquake Engineering*, V. 2, No. 2, 1998, pp. 217-240. doi: 10.1080/13632469809350320

15. Tsonos, A. G., "Seismic Rehabilitation of Reinforced Concrete Joints by the Removal and Replacement Technique," *International Journal of European Earthquake Engineering and Engineering Seismology*, V. 3, 2001, pp. 29-43.

16. Marthong, C.; Dutta, A.; and Deb, S. K., "Seismic Rehabilitation of RC Exterior Beam-Column Connections Using Epoxy Resin Injection," *Journal of Earthquake Engineering*, V. 17, No. 3, 2013, pp. 378-398. doi: 10.1080/13632469.2012.738284

17. Davidovits, J., "Geopolymers - Inorganic Polymeric New Materials," *Journal of Thermal Analysis*, V. 37, No. 8, 1991, pp. 1633-1656. doi: 10.1007/BF01912193

18. Zhang, P.; Zheng, Y.; Wang, K.; and Zhang, J., "A Review on Properties of Fresh and Hardened Geopolymer Mortar," *Composites. Part B, Engineering*, V. 152, 2018, pp. 79-95. doi: 10.1016/j.compositesb.2018.06.031

19. Vasconcelos, E.; Fernandes, S.; Barroso De Aguiar, J. L.; and Pacheco-Torgal, F., "Concrete Retrofitting Using Metakaolin Geopolymer Mortars and CFRP," *Construction and Building Materials*, V. 25, No. 8, 2011, pp. 3213-3221. doi: 10.1016/j.conbuildmat.2011.03.006

20. Duan, P.; Yan, C.; and Luo, W., "A Novel Waterproof, Fast Setting and High Early Strength Repair Material Derived from Metakaolin Geopolymer," *Construction and Building Materials*, V. 124, 2016, pp. 69-73. doi: 10.1016/j.conbuildmat.2016.07.058

21. Phoo-Ngernkham, T.; Sata, V.; Hanjitsuwan, S.; Ridtirud, C.; Hatanaka, S.; and Chindaprasirt, P., "High Calcium Fly Ash Geopolymer Mortar Containing Portland Cement for Use as Repair Material," *Construction and Building Materials*, V. 98, 2015, pp. 482-488. doi: 10.1016/j.conbuildmat.2015.08.139

22. IS 516:1959, "Methods of Tests for Strength of Concrete," Bureau of Indian Standards, New Delhi, India, 1959.

23. IS 1608:3005, "Metallic Materials - Tensile Testing at Ambient Temperature," Bureau of Indian Standards, New Delhi, India, 2005.

24. Laskar, S. M., and Talukdar, S., "Preparation and Tests for Workability, Compressive and Bond Strength of Ultra-Fine Slag Based Geopolymer as Concrete Repairing Agent," *Construction and Building Materials*, V. 154, 2017, pp. 176-190. doi: 10.1016/j.conbuildmat.2017.07.187

25. Singhi, B.; Laskar, A. I.; and Ahmed, M. A., "Investigation on Soil–Geopolymer with Slag, Fly Ash and Their Blending," *Arabian Journal for Science and Engineering*, V. 41, No. 2, 2016, pp. 393-400. doi: 10.1007/s13369-015-1677-y

26. IS 1727:1967, "Methods of Test for Pozzolanic Materials," Bureau of Indian Standards, New Delhi, India, 1967.

27. Yun, K.-K., and Choi, P., "Causes and Controls of Cracking at Bridge Deck Overlay with Very-Early Strength Latex-Modified Concrete," *Construction and Building Materials*, V. 56, 2014, pp. 53-62. doi: 10.1016/j.conbuildmat.2014.01.055

28. IS 8112:2013, "Ordinary Portland Cement, 43 Grade - Specification," Bureau of Indian Standards, New Delhi, India, 2013.

29. ACI Committee 374, "Acceptance Criteria for Moment Frames Based on Structural Testing (ACI 374.1-05) and Commentary (Reapproved 2019)," American Concrete Institute, Farmington Hills, MI, 2005, 9 pp.

30. Ghobarah, A., and El-Amoury, T., "Seismic Rehabilitation of Beam – Column Joint Using GFRP Sheets," *Engineering Structures*, V. 24, No. 11, 2002, pp. 1397-1407. doi: 10.1016/S0141-0296(02)00081-0

31. Park, R., and Paulay, T., *Reinforced Concrete Structures*, John Wiley & Sons, Inc., New York, 1975.

32. IS 13920:2016, "Ductile Design and Detailing of Reinforced Concrete Structures Subjected to Seismic Forces - Code of Practice," Bureau of Indian Standards, New Delhi, India, 2016.

33. IS 456:2000, "Plain and Reinforced Concrete - Code of Practice," Bureau of Indian Standards, New Delhi, India, 2000.

34. Choudhury, A. H., and Laskar, A. I., "Rehabilitation of Substandard Beam-Column Joint Using Geopolymer," *Engineering Structures*, V. 238, 2021, p. 112241. doi: 10.1016/j.engstruct.2021.112241

35. Mukherjee, A., and Joshi, M., "FRPC Reinforced Concrete Beam-Column Joints Under Cyclic Excitation," *Composite Structures*, V. 70, No. 2, 2005, pp. 185-199. doi: 10.1016/j.compstruct.2004.08.022

36. Chidambaram, R. S., and Agarwal, P., "Seismic Behavior of Hybrid Fiber Reinforced Cementitious Composite Beam–Column Joints," *Materials & Design*, V. 86, 2015, pp. 771-781. doi: 10.1016/j.matdes.2015.07.164

37. Kheni, D.; Scott, R. H.; Deb, S. K.; and Dutta, A., "Ductility Enhancement in Beam-Column Connections Using Hybrid Fiber-Reinforced Concrete," *ACI Structural Journal*, V. 112, No. 2, Mar.-Apr. 2015, pp. 167-178. doi: 10.14359/51687405

38. Ghobarah, A., and Said, A., "Seismic Rehabilitation of Beam-Column Joints Using FRP Laminates," *Journal of Earthquake Engineering*, V. 5, No. 1, 2001, pp. 113-129. doi: 10.1080/13632460109350388

39. Pantazopoulou, S., and Bonacci, J., "Considerations of Questions of Beam-Column Joints," *ACI Structural Journal*, V. 89, No. 1, Jan.-Feb. 1992, pp. 27-36.

40. Hwang, S. J.; Lee, H. J.; and Liao, T. F., "Role of Hoops on Shear Strength of Reinforced Concrete Beam-Column Joints," *ACI Structural Journal*, V. 102, No. 3, May-June 2005, pp. 445-453.

41. Lee, J.-Y.; Kim, J.-Y.; and Oh, G.-J., "Strength Deterioration of Reinforced Concrete Beam–Column Joints Subjected to Cyclic Loading," *Engineering Structures*, V. 31, No. 9, 2009, pp. 2070-2085. doi: 10.1016/j.engstruct.2009.03.009

42. Roy, B., and Laskar, A. I., "Cyclic Behavior of In-Situ Exterior Beam-Column Subassemblies with Cold Joint in Column," *Engineering Structures*, V. 132, 2017, pp. 822-833. doi: 10.1016/j.engstruct.2016.12.001

43. Hu, S.; Wang, H.; Zhang, G.; and Ding, Q., "Bonding and Abrasion Resistance of Geopolymeric Repair Material Made with Steel Slag," *Cement and Concrete Composites*, V. 30, No. 3, 2008, pp. 239-244. doi: 10.1016/j.cemconcomp.2007.04.004

44. Wang, Y.-S.; Peng, K.-D.; Alrefaei, Y.; and Dai, J.-G., "The Bond Between Geopolymer Repair Mortars and OPC Concrete Substrate: Strength and Microscopic Interactions," *Cement and Concrete Composites*, V. 119, 2021, p. 103991. doi: 10.1016/j.cemconcomp.2021.103991

45. Choudhury, A. H., and Laskar, A. I., "Effect of Hoop Reinforcement Yielding on the Cyclic Behavior of Beam-Column Joint," *Journal of Earthquake Engineering*, V. 26, 2020, pp. 1-18.

46. Roy, B., and Laskar, A. I., "Beam–Column Subassemblies with Construction Joint in Columns Above and Below the Beam," *Magazine of Concrete Research*, V. 70, No. 2, 2018, pp. 71-83. doi: 10.1680/jmacr.17.00155

47. Murty, C. V. R.; Rai, D. C.; and Bajpai, K. K., "Effectiveness of Reinforcement Details in Exterior Reinforced Concrete Beam-Column Joints for Earthquake Resistance," *ACI Structural Journal*, V. 100, No. 2, Mar.-Apr. 2003, pp. 149-156.

48. Mukherjee, A., and Jain, K. K., "Performance of the FRPC Rehabilitated RC Beam-Column Joints Subjected to Cyclic Loading BT - Advances in Structural Engineering," Springer, New Delhi, India, 2015, pp. 2025-2042.

49. Mostofinejad, D., and Akhlaghi, A., "Experimental Investigation of the Efficacy of EBROG Method in Seismic Rehabilitation of Deficient Reinforced Concrete Beam–Column Joints Using CFRP Sheets," *Journal of Composites for Construction*, ASCE, V. 21, No. 4, 2017, p. 04016116. doi: 10.1061/(ASCE)CC.1943-5614.0000781

50. Park, R., "State of the Art Report-Ductility Evaluation from Laboratory and Analytical Testing," *Proceedings of the 9th World Conference on Earthquake Engineering*, V. 3, Science Council of Japan, Tokyo, Japan, 1988, pp. 605-616.

51. Blandon, C. A., and Priestley, M. J. N., "Equivalent Viscous Damping Equations for Direct Displacement Based Design," *Journal of Earthquake Engineering*, V. 9, No. Sup2, 2005, pp. 257-278.

52. Park, Y. J., and Ang, A. H. S., "Mechanistic Seismic Damage Model for Reinforced Concrete," *Journal of Structural Engineering*, ASCE, V. 111, No. 4, 1985, pp. 722-739. doi: 10.1061/(ASCE)0733-9445(1985)111:4(722)

53. Karayannis, C. G.; Chalioris, C. E.; and Sirkelis, G. M., "Local Retrofit of Exterior RC Beam–Column Joints Using Thin RC Jackets—An Experimental Study," *Earthquake Engineering & Structural Dynamics*, V. 37, No. 5, 2008, pp. 727-746. doi: 10.1002/eqe.783

ACI STRUCTURAL JOURNAL TECHNICAL PAPER

Title No. 120-S82

Strength and Behavior of Glass Fiber-Reinforced Polymer-Reinforced Concrete Box Girders without Web Reinforcement under Pure Torsion

by Ibrahim T. Mostafa, Salaheldin Mousa, Hamdy M. Mohamed, and Brahim Benmokrane

The torsional behavior of solid reinforced concrete (RC) members reinforced with fiber-reinforced polymer (FRP) bars has been the subject of several experimental studies. No experimental research, however, seems to have focused on RC box girders reinforced with FRP bars under a pure torsional moment. This paper reports the results of an experimental investigation on the torsional strength and behavior of full-scale RC box girders reinforced with longitudinal glass FRP (GFRP) bars. All specimens measured 380 mm (15 in.) in height, 380 mm (15 in.) in width, 100 mm (4 in.) wall thickness, and 4000 mm (157.48 in.) in length. They were tested under pure torsional loading over a clear span of 2000 mm (78.74 in.). The test specimens consisted of four RC box girders with longitudinal GFRP bars and one RC box girder with longitudinal steel bars as a reference. All the specimens were constructed without web reinforcement to study the contribution of the longitudinal reinforcement to torsional strength. The test variables included the longitudinal reinforcement ratio (ranging between 1.10 and 2.74%) and the type of longitudinal reinforcement (GFRP or steel). The test results indicate that increasing the GFRP longitudinal reinforcement ratio increased the torsional strength after the initiation of the first diagonal crack, especially for specimens with a high reinforcement ratio. In addition, theoretical torsional moment-twist curves were developed and gave predictions consistent with the experimental test results. Lastly, the ultimate torsional strength of the GFRP-RC box girders without web reinforcement was estimated with the CSA S806-12 (R2017) design equation with a modification related to the GFRP tensile strain limit.

Keywords: cracking pattern and modes of failure; design codes; glass fiber-reinforced polymer (GFRP) bars; reinforced concrete (RC) box girders; reinforcement ratio; theoretical modeling; torsional crack width and toughness; torsional loading; torsional moment-twist response; torsional strength.

INTRODUCTION

Reinforced concrete (RC) box girders can be found in many civil engineering applications. The most notable are cable-supported bridges, pedestrian bridges, curved bridges, and modern elevated structures for light rail transport (Rahal and Collins 1995). There are economic and structural benefits to using box girders, such as low self-weight of structures and higher torsional stiffness (Jeng et al. 2013). Torsion in bridges could occur as a consequence of the geometric complexities of horizontally curved bridges and/or the large eccentricity of gravity loads. Such structures are usually exposed to aggressive and/or harsh marine environments, leading to corrosion of the steel reinforcement. This type of corrosion in concrete structures is a prime cause of structural deterioration, particularly in North America, resulting in costly repairs, rehabilitation, and a considerable reduction in the service life span. Fiber-reinforced polymer (FRP) reinforcing bars, on the other hand, can be used as an alternative to steel reinforcement to combat corrosion, thereby lowering maintenance costs and extending service life. There are numerous advantages to using FRP bars instead of steel bars, such as higher tensile strength, weight one-quarter to one-fifth lighter than steel, noncorroding nature, and longer service life than steel (ACI 440.1R-15 [ACI Committee 440 2015]). The last two decades have seen a rapid increase in the use of FRP reinforcing bars in many applications, such as bridges, piles, parking garages, marine structures, water tanks, and tunnels (El-Salakawy et al. 2004; Eladawy et al. 2019; Mohamed and Benmokrane 2014; Mousa et al. 2018; Mohamed et al. 2020).

Due to the scarcity of experimental studies on torsion members reinforced with FRP bars, the FRP-RC design guidelines (ACI 440.1R-15; JSCE 1997) do not include any provisions pertaining to torsion. In addition, the torsion provisions in FRP-RC design codes (CSA S806-12 [2017]; CSA S6 [2019]; AASHTO 2018) are mainly modifications of steel-RC codes. These modifications include the mechanical properties of FRP reinforcement (modulus of elasticity and stirrup bending strength). The design of torsion in FRP-RC codes (CSA S806-12; CSA S6:19; AASHTO 2018) is based on a thin-walled tube space-truss analogy. Once RC members have cracked under torsion, the torsional strength is mainly provided by closed stirrups and longitudinal bars. CSA S806-12 provides an equation to estimate the torsional strength based on the contribution of the GFRP longitudinal reinforcement; this equation is a function of the total area and tensile strength of the GFRP longitudinal bars. The experimental program of the current study was intended to evaluate the accuracy of the CSA S806-12 design equation.

Valuable research work has been carried out in the last decade to investigate the torsional behavior of the FRP-RC members with a solid cross section (Deifalla et al. 2014; Hadhood et al. 2020; Mohamed and Benmokrane 2015; Shehab et al. 2009; Zhou et al. 2017). These studies

ACI Structural Journal, V. 120, No. 5, September 2023.

MS No. S-2022-137.R3, doi: 10.14359/51738836, received November 28, 2022, and reviewed under Institute publication policies.

considered a wide range of parameters such as reinforcement type (glass or carbon), concrete type (normal-strength or fiber-reinforced concrete), stirrup configurations (ties or spirals), transverse reinforcement ratio, and cross-section configurations (rectangular or L-shaped). Mohamed and Benmokrane (2016) conducted an experimental investigation to study the torsional behavior of full-scale rectangular members reinforced with carbon FRP (CFRP), glass FRP (GFRP), and steel reinforcement with and without transverse torsional reinforcement. The results revealed that the torsional failure was controlled by concrete splitting for the specimens only reinforced with CFRP, GFRP, or steel longitudinal bars. The torsional behavior and strength of all specimens without transverse reinforcement were similar. Hadhood et al. (2020) demonstrated the torsional strength of large-scale rectangular members reinforced with GFRP bars and spirals. They concluded that the ultimate torsional strength of the specimen with no web reinforcement coincided with the cracking torsional strength. In addition, the failure of this specimen was controlled by concrete splitting. In contrast, Khagehhosseini et al. (2013) conducted an experimental and numerical investigation to evaluate the effect of the longitudinal reinforcement ratio on the torsional capacity of RC members reinforced with steel reinforcement and without transverse torsional reinforcement. Their test results showed that increasing the longitudinal reinforcement ratio resulted in a consistent increase in the post-cracking strength and torsional rigidity.

So far, the torsional strength and behavior of GFRP-RC box girders have not been investigated. In addition, experimental results have yet to demonstrate the influence of the longitudinal reinforcement ratio on the torsional behavior of GFRP-RC box girders. This study discusses the experimental results from five full-scale concrete box girders reinforced internally with longitudinal GFRP and steel bars without web reinforcement to study the contribution of the longitudinal reinforcement to the torsional strength of the specimens.

RESEARCH SIGNIFICANCE

Valuable experimental work has been conducted to investigate the torsional behavior of solid concrete sections reinforced with FRP. The torsional behavior and strength of FRP-RC box girders, however, have not been addressed. The effect of different test parameters on the cracking patterns, modes of failure, cracking and ultimate strengths, measured crack widths, and strain behavior of the box girders was investigated. Furthermore, the torsional moment-twist curves were predicted theoretically. This study also examined the accuracy of the available theories and design provisions for the cracking torsional strength of GFRP-RC box girders. In addition, the ultimate torsional strength of the GFRP-RC box girders without web reinforcement was estimated with the CSA S806-12 design equation with a modification related to the GFRP tensile strain. The results reported in this paper represent a significant contribution to the relevant literature and provide end users, engineers, and code committees with much-needed data and recommendations to advance the use of GFRP reinforcement in RC box girders and to extend the design and code provisions related to GFRP reinforcement for concrete structures.

EXPERIMENTAL PROGRAM

Materials

Reinforcement—The GFRP bars employed in this study were manufactured and developed by a manufacturer in Thetford Mines, QC, Canada (Pultrall Inc. 2019). The GFRP bars had a sand-coated surface, as shown in Fig. 1(a), to improve the bond performance and force transfer between the bars and the surrounding concrete. The GFRP bars and stirrups were made of continuous boron-free glass longitudinal fibers impregnated in a vinyl-ester resin with fiber contents of 83.10% and 79.50%, respectively, in accordance with CSA S807 (2019). Number 5 Grade III (nominal diameter of 15.90 mm) GFRP bars (CSA S807:19) were used as longitudinal reinforcement in this study. Number 3 Grade II (nominal diameter of 9.50 mm) GFRP stirrups (CSA S807:19) were used at 1 m from both sides of the box girder as stiffeners. The stress-strain relationship of the GFRP bars was linear elastic in tension up to failure. The ultimate tensile strength f_{fu} and modulus of elasticity E_f of the GFRP bars and straight portions of the GFRP stirrups were determined according to ASTM D7205/D7205M (2021), as reported by the manufacturer. In addition, the ultimate tensile strength of the GFRP stirrups at the bent portions $f_{fu,bent}$ was determined according to ASTM D7914/D7914M (2021). The steel control specimen was reinforced in the longitudinal direction with deformed M15 (nominal diameter of 16 mm) steel bars and at 1 m from both sides with M10 (nominal diameter of 9.50 mm) stirrups. Table 1 gives the mechanical properties of the GFRP and steel reinforcement.

Concrete—The specimens were cast from the same concrete batch with normal-strength, normalweight concrete provided by a local ready mixed supplier; all specimens were cast at the University of Sherbrooke, Sherbrooke, QC, Canada. Fifteen concrete cylinders measuring 100 x 200 mm (4 x 8 in.) were cast and cured under the same conditions as the test specimens. Twelve were tested in compression according to ASTM C39/C39M (2021), including six after 28 days and six cylinders on the day of specimen testing. The remaining three cylinders were tested in tension according to ASTM C496/C496M (2017) by performing split cylinder tests. Table 2 provides the average compressive (f_c') and tensile (f_t') strength of the concrete on the testing day of the specimens.

Specimen fabrication

Before the concrete was cast, the cages were placed in the forms; spacers were used to keep the concrete cover equal on all sides during casting. All specimens were cast at the same time from the same concrete batch. Two electrical needle vibrators were used to ensure adequate concrete quality and prevent segregation. The cages were expected to rise during the casting process for two reasons: the expanded polystyrene rigid insulation panel representing the void, and the weight of the GFRP bars. Consequently, two threaded rods were attached to the top of the cages and to a wooden plate that was fastened to the formwork with two steel angles, as

Fig. 1—(a) Sand-coated No. 5 GFRP bars; (b) casting; (c) storage; and (d) curing.

Table 1—Mechanical properties of GFRP and steel reinforcement

Bar size	Bar type	Diameter, mm	Nominal area, mm^2	Immersion area, mm^2	Elastic tensile modulus, GPa	Tensile strength, MPa	Tensile strain, %
No. 3	GFRP stirrups	9.50	71	88	58.20	f_{fu} = 1225 $f_{fu,bent}$ = 671	2.10
No. 5	GFRP bars	15.90	198	230	62.50	f_{fu} = 1500	2.40
M10	Steel stirrups	9.50	71	—	200	f_y = 460	0.23
M15	Steel bars	16	200	—	200	f_y = 460	0.23

Note: 1 mm = 0.0394; 1 mm^2 = 0.00155 in.^{2}; 1 MPa = 0.145 ksi.

Table 2—Test matrix and specimen details

Specimen ID	f_c', MPa	f_t', MPa	Bar type	Longitudinal reinforcement	
				No. of bars Uniform distribution	Reinforcement ratio ρ_L, %
BSW-12	39.84	3.33	Steel	12 M15	1.66
BGW-8	39.84	3.33	GFRP	8 No. 5	1.10
BGW-12	39.84	3.33	GFRP	12 No. 5	1.66
BGW-16	39.84	3.33	GFRP	16 No. 5	2.20
BGW-20	39.84	3.33	GFRP	20 No. 5	2.74

Note: $\rho_L = A_L/A_c$, where A_L is total area of longitudinal reinforcement and A_c is area of outer perimeter of concrete cross section. 1 MPa = 0.145 ksi.

shown in Fig. 1(b). Once the concrete was cast, the specimens were covered with wet burlap and plastic sheets to prevent moisture loss and were cured for 7 days. All specimens were stored in the laboratory until the day of testing. Figure 1 shows the casting, curing, and storage process of the test specimens.

Specimen design

The experimental program of this study was designed to provide experimental data on the torsional behavior of RC box girders reinforced with longitudinal GFRP bars but without transverse reinforcement. A total of five large-scale RC box girders—including four reinforced with longitudinal GFRP bars and one reinforced with longitudinal steel bars as a control specimen—were tested under pure torsional loading. The test matrix was designed to study the effect of longitudinal reinforcement on the torsional behavior of RC box girders reinforced with GFRP bars. The test parameters included the type of longitudinal reinforcement (GFRP versus steel) and the longitudinal reinforcement ratio. The

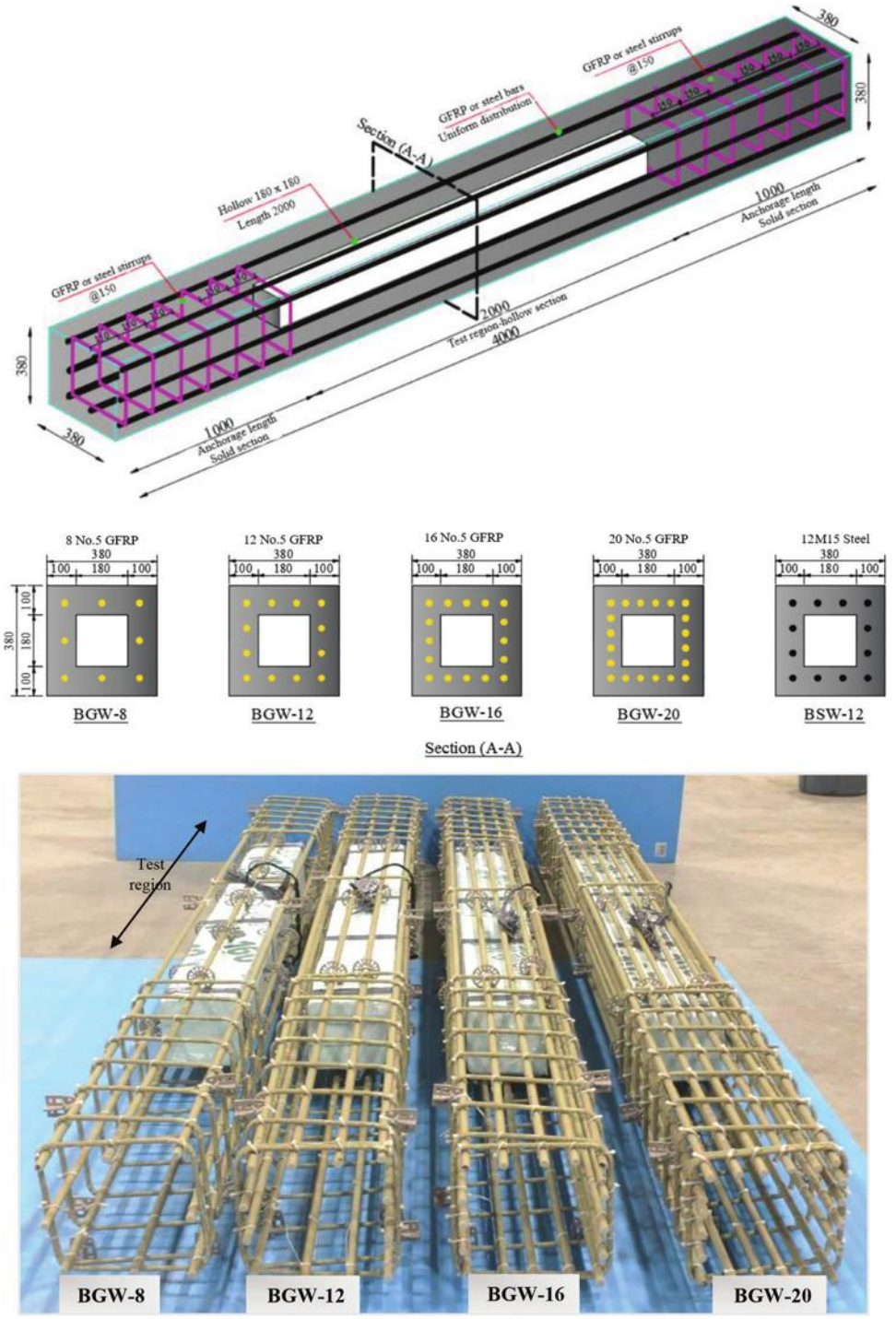

Fig. 2—Reinforcement details and dimensions of RC box girders. (Note: Dimensions in mm; 1 mm = 0.0394 in.)

specimens were 4000 mm (157.48 in.) long, 380 mm (15 in.) wide, and 380 mm (15 in.) deep, with a wall thickness of 100 mm (4 in.). The cross-sectional dimensions were chosen to be similar to those used by Mitchell and Collins (1974) (beams PT5 and PT6). The test region was kept constant at 2000 mm (78.74 in.) to ensure that each specimen developed at least one complete helical crack. All girders had a 1000 mm (40 in.) solid section overhang past the supports as an anchorage length on each side to prevent any premature failure before torsional failure. Moreover, the solid section was reinforced with transverse reinforcement spaced at 150 mm (6 in.). The test region was made hollow with a 180 mm (7 in.) square void that consisted of thick sheets of expanded polystyrene rigid insulation panel. Three 60 mm (2.36 in.) thick layers of expanded polystyrene rigid insulation panel were combined to create the square void measuring 180 mm wide (7 in.) by 2000 mm (78.74 in.) long. The concrete cover was kept clear at 40 mm (1.57 in.) in all specimens. Figure 2 shows the dimensions and reinforcement details of the test specimens. The GFRP-RC box girders were reinforced longitudinally with eight, 12, 16, and 20 No. 5 (15.9 mm) GFRP bars. The GFRP bars were uniformly distributed around the perimeter of the cross section, with reinforcement ratios of 1.10%, 1.66%, 2.20%,

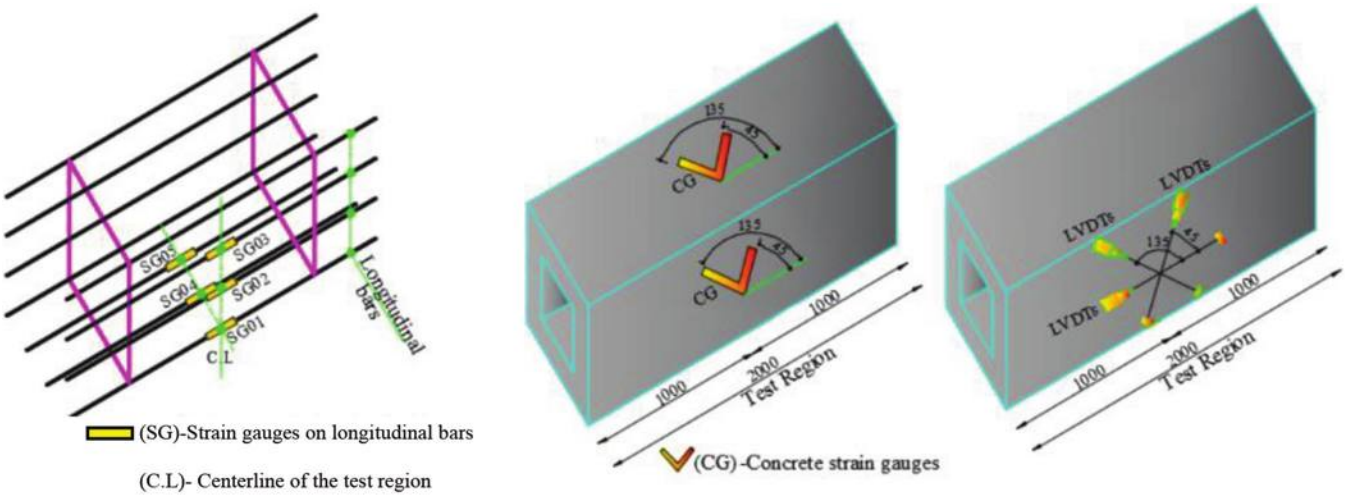

(a) Distribution of bar strain gauges

(b) Measurement of concrete surface strains

Fig. 3—Instrumentation details of test specimens. (Note: Dimensions in mm; 1 mm = 0.0394 in.)

and 2.74%, respectively. The longitudinal reinforcement ratio (ρ) was calculated by dividing the total nominal area of longitudinal reinforcement by the total cross-sectional area of the girder. The control steel-reinforced specimen was reinforced longitudinally with 12 M15 (16 mm) deformed steel bars with a reinforcement ratio of 1.66%. The specimens were designated with this pattern: the letter B refers to the girder specimen, the letters G and S stand for GFRP or steel as longitudinal reinforcement, and the letter W indicates specimens without transverse reinforcement. The number stands for the total number of longitudinal bars in each specimen. Table 2 provides the test matrix and details of the test specimens.

Instrumentation and test setup

Electrical-resistance strain gauges with a gauge length of 6 mm (0.24 in.) and a gauge factor of 2.09% were used to measure the strain in the longitudinal reinforcing bars. Five strain gauges were mounted on longitudinal bars in the middle section of the test region, as shown in Fig. 3(a). To measure the concrete strains, four strain gauges with a gauge length of 60 mm (2.36 in.) and a gauge factor of 2.06% were attached to the concrete front and top surfaces at 45 and 135 degrees measured from the longitudinal axis. Furthermore, three linear variable differential transformers (LVDTs) were used to measure the concrete surface strain as well as specimen longitudinal elongation. The three LVDTs were mounted on the concrete front surface in a rosette format to measure average concrete strains in three directions at the midspan of the test region, as shown in Fig. 3(b). Two LVDTs were placed at 45 and 135 degrees measured from the longitudinal axis of the girder; the other one was placed along the longitudinal axis of the girder. To measure the relative rotation of the cross section, four potentiometers were placed at two different locations within the test region. In addition, one potentiometer was placed under the applied vertical load. Two potentiometers were placed at the fixed end to make sure that no vertical movement was induced during specimen testing. Once the first crack appeared, a crack comparator (an optical measurement device consisting of a microscope and measuring scale) was used to measure the initial crack width, which ranged from 0.10 to 0.15 mm. Subsequently, two high-accuracy LVDTs were installed to measure the crack width electronically with load increase. The instrumentations for measuring the load, twist, concrete surface strain, longitudinal bar strains, and the crack width of the girder were recorded on a data acquisition system connected to a computer. The loading procedures of the actuator prescribed a displacement-control rate of 0.5 mm/min. A torsion test setup was designed and fabricated at the University of Sherbrooke's structural laboratory for testing the RC box girders under pure torsional loading. It was similar to that used by Koutchoukali and Belarbi (2001). The torsional moment was applied to the RC box girder with a servo-controlled, 1000 kN (224.8 kip) hydraulic actuator attached to a rigid steel arm fastened to the girder. The load had a 715 mm (28.15 in.) lever arm from the centroidal axis of the girder, giving the test rig a 715 kN·m (527.40 kip·ft) torque capacity. All specimens were supported on a fixed hinge 2000 mm (78.74 in.) apart. The hinge support was designed to allow rotation about the longitudinal axis of the girder. The fixed support was a rigid steel beam resting on the girder and attached to the laboratory's rigid floor with two steel bars. The girders were allowed to slide and elongate freely to avert any longitudinal strain and subsequent compression after cracking. This was achieved by resting the girder on rollers at the fixed end. Figure 4 shows the details of the test setup.

TEST RESULTS AND DISCUSSION

Cracking pattern and modes of failure

Crack formation and propagation in each girder and the corresponding loads were marked and recorded during testing. When the applied principal tensile stresses reached the concrete tensile strength, the first crack initiated in all specimens at the middle of the front face of the test region. The cracking torsional strength of girders BGW-8, BGW-12, BGW-16, BGW-20, and BSW-12 was 36.1, 36.6, 36.9, 36.2, and 36.9 kN·m (26.64, 27.01, 27.23, 26.72, and 27.23 kip·ft), respectively. As the applied torsional loading increased,

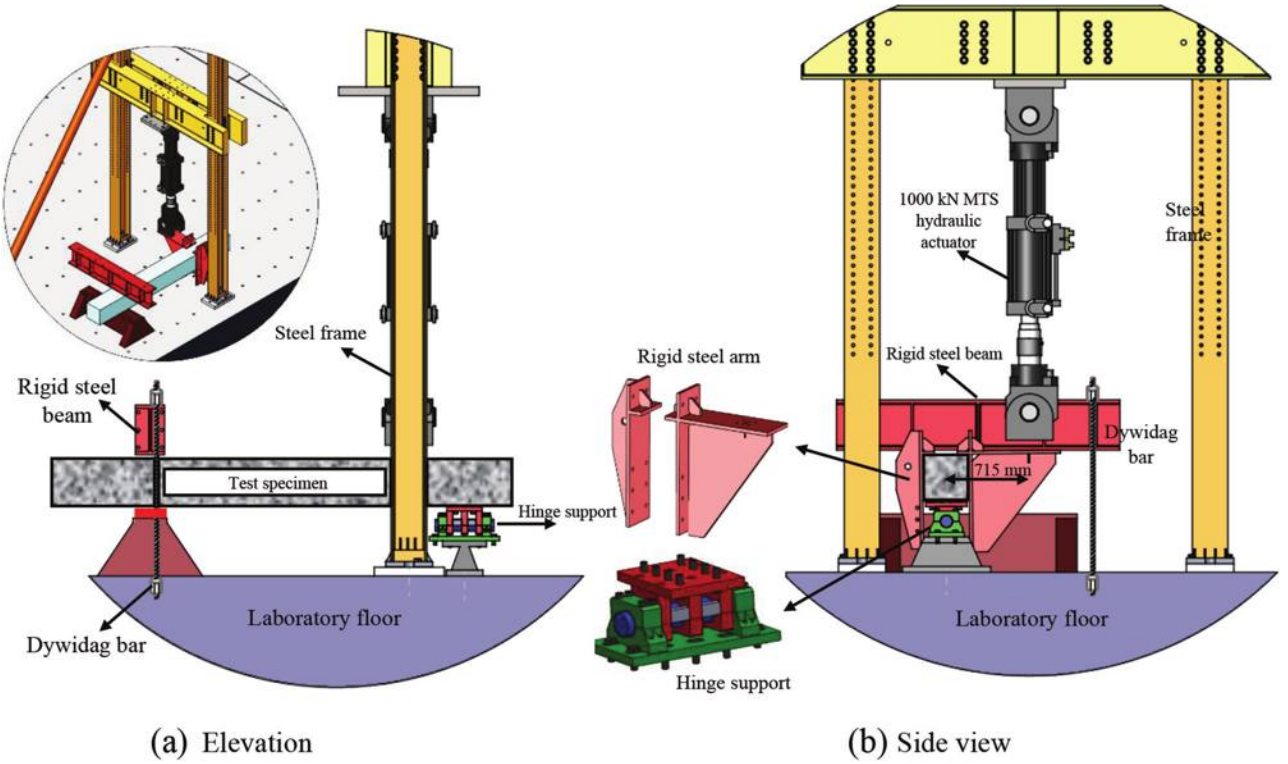

Fig. 4—Test setup schematic.

more cracks appeared on each side and then linked with the crack on the front face, forming a spiral shape along the periphery of the specimen. The cracking pattern was affected by the longitudinal reinforcement ratio. Increasing the longitudinal reinforcement ratio increased the number of cracks and decreased crack inclination in the longitudinal direction. The cracking patterns of specimens BGW-12 and BSW-12 were almost similar in terms of the failure plane angle and the number of cracks. The failure plane angle of specimens BGW-8, BGW-12, BGW-16, BGW-20, and BSW-12 was approximately 55, 49, 40, 37, and 47 degrees, respectively, with respect to the longitudinal direction. Generally, the principal stress distribution in RC members subjected to pure torsional loading consists of diagonal compression and tension. Therefore, all cracks appeared diagonally, similar to what was observed in past studies on GFRP-RC members under torsion (Mohamed et al. 2015). The cracks observed on the face of the specimens with a high longitudinal reinforcement ratio (BGW-16 and BGW-20) were diagonal. Unlike in the case of girders reinforced with a relatively lower longitudinal reinforcement ratio (BGW-8, BGW-12, and BSW-12), the cracks started diagonally, followed by more longitudinal cracks that propagated from the diagonal cracks. These longitudinal cracks were due to dowel action in the longitudinal bars, which were distributed uniformly throughout the box girder. The dramatic increase in the dowel action in these bars produced vertical tensile stress in the concrete around the bars. In general, all specimens failed by concrete splitting due to a lack of transverse torsional reinforcement. A major diagonal spiral crack developed within the formed crushed surface at the midheight of the front face. A similar mode of failure was observed in previous studies on FRP-RC beams with solid rectangular cross sections and no transverse reinforcement (Mohamed and Benmokrane 2016; Hadhood et al. 2020). The mode of failure observed in these studies was concrete splitting, with a failure plane angle that ranged between 27 and 30 degrees in the longitudinal direction. Figure 5 shows the observed cracking patterns and modes of failure of the test specimens.

Torsional moment-twist response

This section presents the torsional moment-twist curves for the tested specimens in two groups to show the effect of test parameters on the torsional behavior of the GFRP-RC box girders, as depicted in Fig. 6. From initial loading until the formation of the first diagonal concrete crack, all specimens displayed almost identical linear torsional moment-twist responses, regardless of their reinforcement ratio and type, representing the uncracked condition governed by the properties of the concrete section, as shown in Fig. 6(a) and (b). The uncracked torsional stiffness of all the specimens ranged between 11,650 and 14,470 kN·m^2 (28,193 and 35,017 kip·ft^2). As the load increased, torsional cracking eventually occurred within the torsion test region. At this stage, all the specimens exhibited a very low twisting angle (ranging from 0.0026 to 0.0031 rad/m [0.00079 to 0.00095 rad/ft]), which reflects the concrete's gross section stiffness. After cracking, the GFRP-RC box girders reinforced with a relatively lower longitudinal reinforcement ratio (1.10 and 1.66%) experienced a significant loss of strength and stiffness. In contrast, the specimens reinforced with a higher longitudinal reinforcement ratio (2.20 and 2.74%) exhibited an increase in torsional strength after cracking. Table 3 presents the cracking torsional strength and the corresponding twist and stiffness, the post-cracking

BGW-8

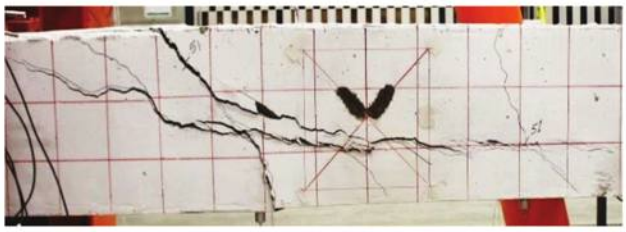

BGW-12

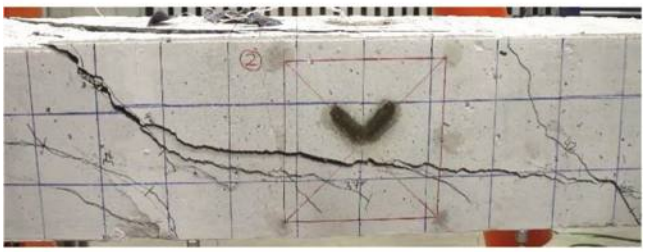

BSW-12

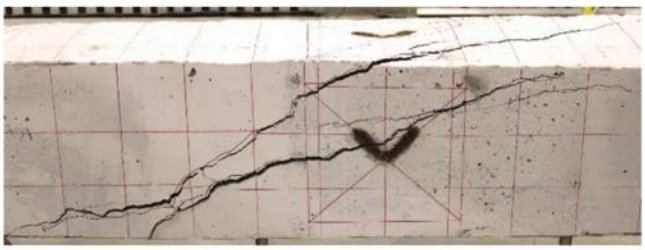

BGW-16

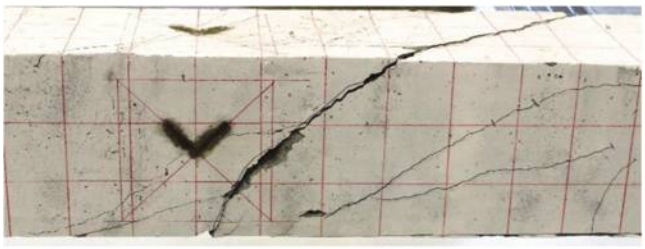

BGW-20

Fig. 5—Cracking patterns at failure of test specimens.

torsional strength and the corresponding twist and stiffness, and the failure mode.

Effect of longitudinal reinforcement ratio on torque-twist response

Figure 6(a) shows the effect of the longitudinal reinforcement ratio on the torsional moment-twist behavior. Specimens BGW-8 and BGW-12, with relatively lower reinforcement ratios (1.10 and 1.66%), exhibited a sudden drop in the torsional moment with the appearance of the first diagonal crack, as shown in Fig. 6(a). The reduction in torsional strength was 36.5% and 32.9% of the cracking torsional strength for specimens BGW-8 and BGW-16, respectively. This reduction could be attributed to the absence of the transverse reinforcement and the fact that such a low longitudinal reinforcement ratio did not provide enough confinement to the concrete hollow core to allow the redistribution of the internal forces developed in the specimens. Subsequently, the specimens (BGW-8 and BGW-12) showed a slight increase in torsional strength after their strength reduction by almost 9% and 12%, respectively. After that, increasing the angle of twist resulted in a drop in stiffness and strength. Consequently, it can be concluded that increasing the GFRP longitudinal reinforcement ratio of the RC box girders from 1.10% (BGW-8) to 1.66% (BGW-12) had an insignificant impact on the post-cracking torsional stiffness strength. Moreover, the ultimate capacity of these specimens was controlled by concrete splitting and coincided with the corresponding cracking torque. This finding is in good agreement with the test results of Mohamed and Benmokrane (2016) and Hadhood et al. (2020). The ultimate torsional capacity of the specimens with GFRP longitudinal reinforcement ratios of 1.33 and 0.75% but no web reinforcement coincided with the cracking strength. Figure 6(a) indicates that, for the specimens with relatively higher GFRP longitudinal reinforcement ratios (BGW-16 and BGW-20), a significant increase in the torsional strength was observed after the first diagonal crack appeared. BGW-16 and BGW-20 had enhanced strength of approximately 8% and 14%, respectively, after the initiation of the first diagonal crack. This is in good agreement with the experimental studies reported by Hsu (1968) for specimens with only longitudinal reinforcement. The test results revealed that increasing the longitudinal reinforcement ratio increased the torsional strength up to 15%. Subsequently, BGW-16 and BGW20 exhibited gradual reductions in their strength of 26% and 14%, respectively, with increased angles of twist. After that, a torque-twist plateau formed, and degradation in stiffness and strength resulted from increasing the angle of twist.

Increasing the reinforcement ratio by approximately 100% and 150% (from 1.10 to 2.20% and from 1.10 to 2.74%) increased the torsional strength by 10% and 14.2%, respectively. In addition, increasing the reinforcement ratio by 33% and 67% (from 1.66 to 2.20% and from 1.66 to 2.74%) enhanced the torsional strength by 8.5% and 12.8%, respectively. The increase in the torsional strength was more noticeable in the specimens with relatively higher reinforcement ratios. The torsional strengths of all GFRP-RC box girders were compared versus the longitudinal reinforcement ratio at 0.01 rad/m (0.003 rad/ft) (approximately four times the angle of rotation at cracking) to evaluate their post-cracking torsional strength, as shown in Fig. 7. This figure indicates that increasing the longitudinal reinforcement ratio had a significant effect on the post-cracking torsional strength of the GFRP-RC box girders.

Table 3—Experimental test results

Specimen ID	T_{cr}, kN·m	φ_{cr}, rad/m	$K_{un(exp)}$, kN·m^2	T_u, kN·m	φ_u, rad/m	$K_{cr(exp)}$, kN·m^2	Toughness, kN	Failure mode
BSW-12	36.88	0.0026	14,185	39.30	0.0030	6050	1.04	Concrete splitting
BGW-8	36.10	0.0031	11,650	36.10	—	—	0.43	Concrete splitting
BGW-12	36.55	0.0029	12,600	36.55	—	—	0.93	Concrete splitting
BGW-16	36.90	0.0030	12,725	39.65	0.0039	3055	1.21	Concrete splitting
BGW-20	36.18	0.0025	14,470	41.20	0.0037	4190	1.82	Concrete splitting

Note: T_{cr} is torsional moment corresponding to first diagonal crack; T_u is maximum torsional moment; $K_{un(exp)}$ is uncracked torsional stiffness (T_{cr}/φ_{cr}); and $K_{cr(exp)}$ is cracked torsional stiffness ($[T_u - T_{cr}]/[\varphi_u - \varphi_{cr}]$). 1 kN·m = 0.7376 kip·ft; 1 kN·m^2 = 2.42 kip·ft^2; 1 kN = 0.225 kip; 1 rad/m = 0.305 rad/ft.

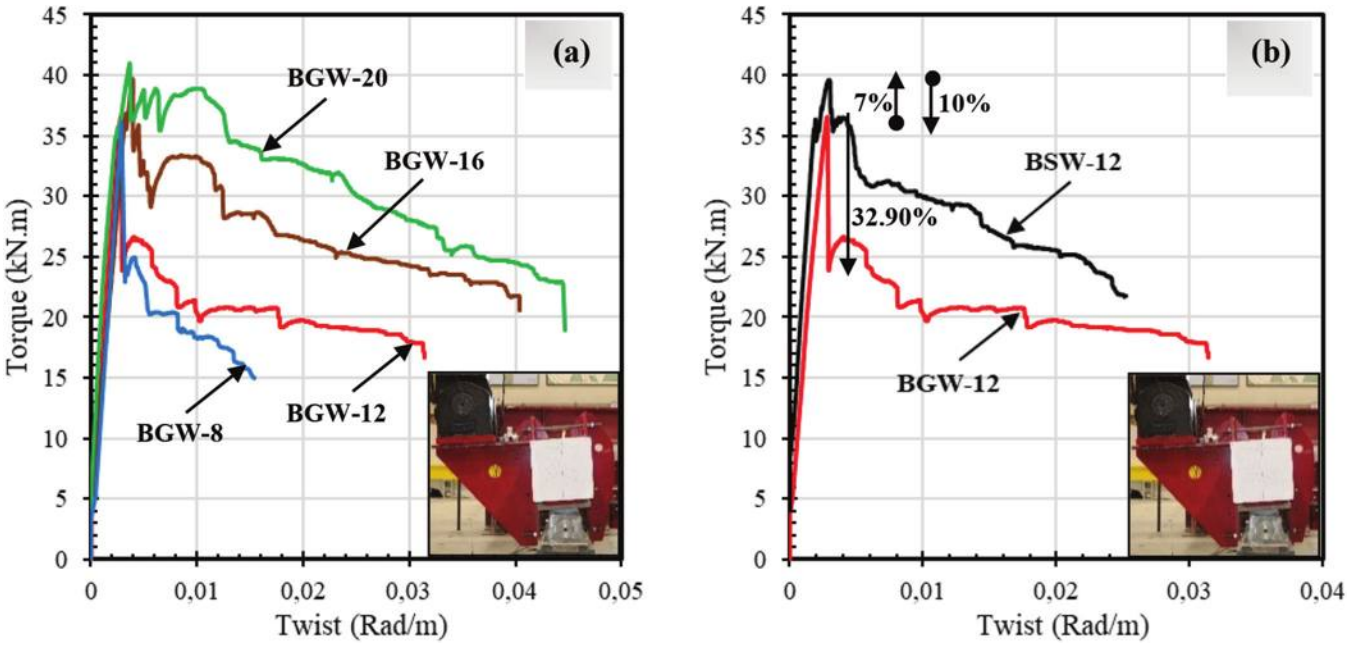

Fig. 6—Effect of test parameters on torsional moment-twist behavior. (Note: 1 kN·m = 0.7376 kip·ft; 1 rad/m = 0.305 rad/ft.)

Effect of type of longitudinal reinforcement on torque-twist response

Figure 6(b) shows the effect of longitudinal reinforcement type on the torsional moment-twist behavior. Specimen BGW-12 and its counterpart steel-reinforced specimen (BSW-12) were designed to have the same longitudinal reinforcement ratio (1.66%). The figure indicates that the cracking strength and the pre-cracking torsional stiffness were almost the same for both specimens. Table 3 indicates that the torsional cracking strength of BGW-12 and BSW-12 was 36.55 and 36.88 kN·m (26.97 and 27.22 kip·ft), respectively. After cracking occurred, the specimens' torsional performance was highly dependent on the axial stiffness of the longitudinal reinforcing bars, which is a function of the area A and modulus of elasticity E of the longitudinal reinforcement. Figure 6(b) indicates that the steel-reinforced specimen (BSW-12) experienced less of a drop in torsional strength than its counterpart GFRP-reinforced specimen (BGW-12) after the first diagonal crack appeared. In contrast, BSW-12 achieved a slight increase in torsional strength of 7% after the first crack, followed by a reduction of 10% in ultimate torsional strength. The reduction in the torsional strength of the GFRP-RC box girder (BGW-12) was almost 3.29 times that of its steel counterpart (BSW-12). This value is similar to the ratio of the modulus of elasticity of the steel (200 GPa [29,000 ksi]) to that of the GFRP bars (62.5 GPa [9063 ksi]). Afterward, the two specimens showed degradation in stiffness and strength as the angle of twist increased.

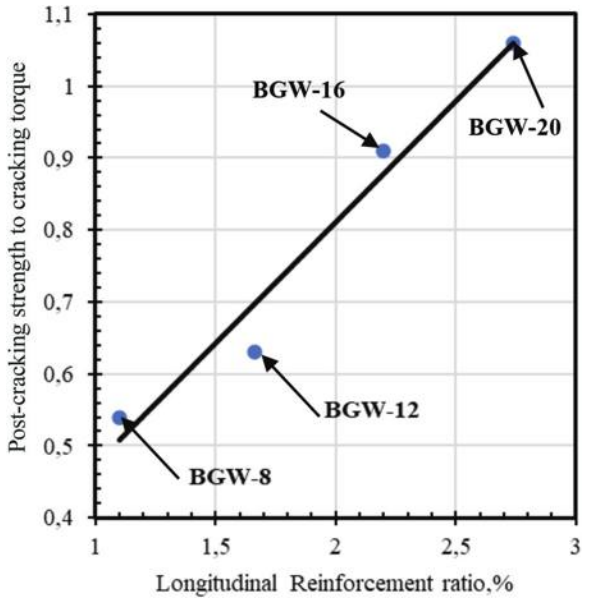

Fig. 7—Ratio of post-cracking to cracking strength versus reinforcement ratio.

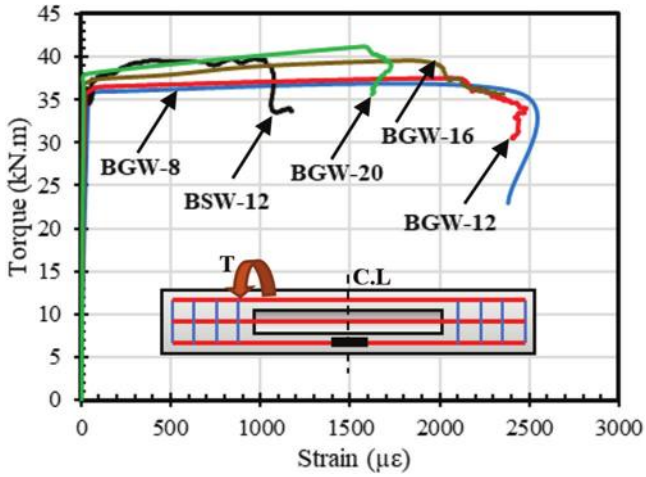

Fig. 8—Torsional moment-longitudinal strain behavior. (Note: 1 kN·m = 0.7376 kip·ft.)

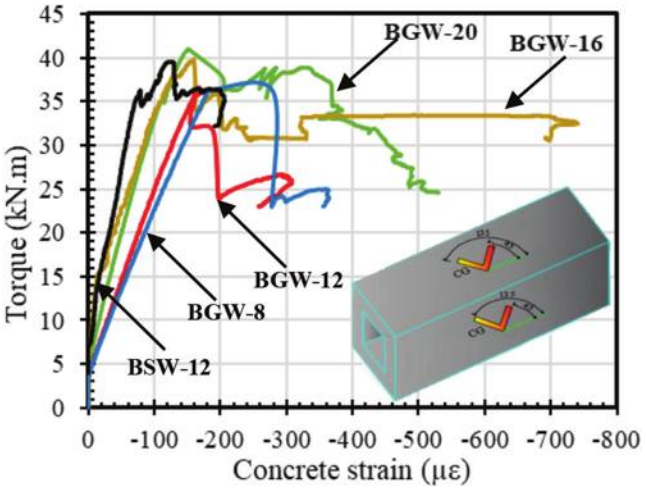

Fig. 9—Torsional moment-concrete strain behavior. (Note: 1 kN·m = 0.7376 kip·ft.)

Torsional moment-longitudinal strain behavior

Figure 8 plots the measured applied torsional moment on the specimens versus the strain behavior relationships for the internal GFRP and steel longitudinal bars. All the RC box girders had negligible strain readings and similar behavior from the initial loading up to the first diagonal crack, regardless of the reinforcement ratio and type. After cracking occurred, a redistribution of the internal forces from the concrete section to the longitudinal reinforcement resulted in a significant increase in the longitudinal reinforcement strains. The specimens reinforced with longitudinal GFRP bars exhibited higher bar strain after concrete cracking than the steel-reinforced specimen at the same torque level. This could be attributed to the variation in the modulus of elasticity of the two materials. In contrast, increasing the longitudinal reinforcement ratio from 1.10 to 1.66, 2.20, and 2.74% decreased the measured strain value at all load levels. The maximum recorded strains in the GFRP bars were 2400, 2160, 1840, and 1580 με, representing 10%, 9%, 7.7%, and 6.6% of the ultimate tensile GFRP bar strain for specimens BGW-8, BGW-12, BGW-16, and BGW-20, respectively. Generally, these low strain values emphasize that the torsional failure was not controlled by the rupture of GFRP longitudinal bars. Furthermore, the test results indicate that no slippage or anchorage problems occurred throughout testing. In contrast, the maximum recorded strain value of BSW-12 was 1060 με, which is less than the yield strain of the steel reinforcement.

Torsional moment-diagonal compressive concrete strain

Figure 9 gives the measured diagonal compressive strains versus the applied torsional moment for the GFRP- and steel-reinforced specimens. The figure indicates that the diagonal compressive strain decreased by increasing the GFRP longitudinal reinforcement ratio. In addition, all specimens exhibited a minimal value of diagonal compressive concrete strain up to failure. The recorded diagonal compressive strain corresponding to the maximum torsional moment was –280, –175, –160, –150, and –135 με for BGW-8, BGW-12, BGW-16, BGW-20, and BSW-12, respectively. These readings are significantly lower than the concrete crushing strain of 3000 με specified in ACI 318-19 (ACI Committee 318 2019) and 3500 με specified in CSA S806-12 (2017) and CSA A23.3 (2019), indicating that the specimens failed by concrete splitting. Generally, the diagonal concrete strain dropped by approximately 46% with a 150% increase in the longitudinal reinforcement ratio (from 1.10% in BGW-8 to 2.74% in BGW-20). In contrast, BSW-12 showed lower strain values compared to all GFRP-RC box girders at the same torque level. This can be attributed to the effect of the axial stiffness of the longitudinal reinforcement on the induced strain deformation of the tested specimens.

Torsional crack width

The crack widths for all specimens were measured with two LVDTs and recorded on a data acquisition system throughout the testing. Figure 10 shows the measured crack width versus the applied torsional moment for all specimens. Each curve started with the cracking torsional moment and terminated with specimen failure. The experimental investigation and numerical analysis conducted by Park et al. (2001) revealed that the maximum crack width was controlled by the relative amounts of torsional reinforcement in the longitudinal direction. As shown in Fig. 10, increasing the longitudinal reinforcement ratio decreased the crack widths at specimen failure. In addition, specimen BGW-12 exhibited wider crack widths than BSW-12, which was reinforced with steel. The maximum recorded crack width at the end of the test was 3.70, 2.90, 2.10, 1.50, and 1.80 mm (0.15, 0.11, 0.083, 0.059, and 0.071 in.) for BGW-8, BGW-12, BGW-16, BGW-20, and BSW-12, respectively.

Torsional toughness

Toughness refers to the material's capacity to absorb energy and deform plastically without fracturing. The torsional toughness of the examined specimens can be estimated as the area under torsional moment-twist curves, as illustrated in Fig. 6, because the cross-sectional dimensions of all the specimens were constant. Table 3 shows the torsional toughness of all the test specimens. As can be seen, increasing

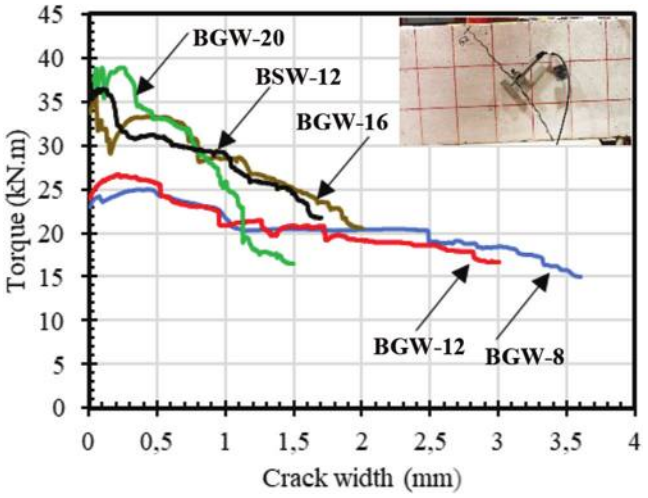

Fig. 10—Torsional moment-crack width. (Note: 1 kN·m = 0.7376 kip·ft; 1 mm = 0.0394 in.)

the longitudinal reinforcement ratio from 1.10% in BGW-8 to 2.74% in BGW-20 increased the torsional toughness by approximately 325%. The steel-reinforced specimen exhibited torsional toughness approximately 12% higher than its counterpart with GFRP reinforcement. It can be concluded that the torsional toughness significantly increased as the longitudinal reinforcement ratio increased.

THEORETICAL INVESTIGATION

Theoretical prediction of torsional moment-twist curve

In RC members subjected to the pure torsional moment, the torque is generally resisted by longitudinal reinforcement, transverse reinforcement, and concrete diagonal struts. Therefore, the torsional moment-twist curve comprises three distinct zones (Bernardo and Lopes 2008). The first zone is characterized by the linear-elastic behavior of materials and represents the torsional behavior until the first diagonal crack occurs. The cracking strength in this zone can be predicted theoretically with the skew-bending theory, Bredt's thin-tube theory, and the theory of elasticity. The slope of the curve in the first zone represents uncracked torsional stiffness, which can be predicted with Saint-Venant stiffness. The second zone corresponds to the torsional behavior in a cracked state with linear-elastic behavior of the materials, and the slope of the curve represents the post-cracking torsional stiffness. The space-truss analogy with an inclination angle of diagonal concrete struts of 45 degrees can theoretically predict the torsional behavior in the second zone. The third zone represents the nonlinear behavior of the materials with a softening effect because at least one of the reinforcement types (longitudinal or transverse) reaches the ultimate strength or because of the nonlinearity of the diagonal concrete struts. In contrast, based on the experimental test results from this study, the ultimate torque for the specimens reinforced with relatively lower GFRP longitudinal reinforcement ratios (1.10 and 1.66%) coincided with the cracking torque. Therefore, the torsional moment-twist curve for these specimens terminated in the first zone. In contrast, the specimens reinforced with relatively higher GFRP longitudinal reinforcement ratios (2.20 and 2.74%) achieved torsional strength higher than the cracking strength. Consequently, the torsional moment-twist curve for these specimens can be predicted theoretically until the second zone. The following sections discuss the prediction of the torsional moment-twist curve theoretically for the first and second zones.

Uncracked torsional behavior (first zone)

Pre-cracking torsional stiffness—Saint-Venant's theory can be used to calculate the torsional stiffness of RC members before cracking with reasonable accuracy (Hsu 1973). The torsional stiffness can be calculated as

$$K_{un(Theo)} = \frac{T}{\varphi} \tag{1}$$

where T is the applied torque to the girder; φ is the twist per unit length; and $K_{un(Theo)}$ is the theoretical pre-cracking torsional stiffness ($K_{un(Theo)} = RGC$); R is the reduction factor ($R \approx 0.60$); G is the shear modulus of concrete and is equal to $E_c/(2(1 + \upsilon))$; E_c is the modulus of elasticity of the concrete; υ is the Poisson's ratio; and C is the Saint-Venant torsional constant.

The reduction factor (R) considers the stiffness loss observed in the laboratory tests, which was almost 20 to 40% of the $K_{un(Theo)}$ value. It was already reported by Leonhardt and Schelling (1974) and adopted by Bernardo and Lopes (2008). The torsional reinforcement can be neglected in calculations of the $K_{un(Theo)}$ (Bernardo and Lopes 2008; Hsu 1973). For rectangular hollow sections, the Saint-Venant torsional constant (C) is calculated as

$$C = \frac{4A^2h}{u} \tag{2}$$

where A is the area enclosed by the centerline of the wall of the hollow section; h is the wall thickness of the hollow section; and u is the perimeter of the centerline of the wall of the hollow section.

Cracking torsional strength—The cracking torsional strength (T_{cr}) can be theoretically predicted with three different theories (the skew-bending theory, Bredt's thin-tube theory, and the theory of elasticity), in addition to three codes (CSA A23.3:19, CSA S6:19, and AASHTO 2018), which are briefly described as follows.

Skew-bending theory—Hsu (1968) derived an equation for the nominal torsional strength of solid concrete members based on the bending mechanism of torsional failure. This theory contends that the failure of a torsional member is reached when the tensile stress induced by a 45-degree bending component of torque on the wider face reaches a reduced modulus of rupture of concrete. The torsional cracking strength is given by

$$T_{cr} = 6y(x^2 + 10)\sqrt[3]{f_c'}\left(\frac{4h}{x}\right) \text{ for } h \le \frac{x}{4} \tag{3}$$

where x and y are the shorter and longer dimensions of the cross section (in.), respectively; and f_c' is the concrete

compressive strength (psi). If $h > (x/4)$, h should be considered as $h = (x/4)$.

Bredt's thin-tube theory—Hsu and Mo (1985) proposed a formula for the torsional cracking of tubular sections based on Bredt's thin-tube theory. This theory relates to the shear stresses due to torsion in a thin-walled tube. The shear stress is set equal to the tensile strength of concrete in a biaxial tension-compression state. The torsional cracking strength is expressed as

$$T_{cr} = 2A_c t\left(2.5\sqrt{f_c'}\right) \quad (4)$$

where A_c is the area enclosed by the outer perimeter of the hollow section (in.^{2}); and t is the wall thickness of the hollow section (in.).

Theory of elasticity—Saint-Venant's theory has also been extended to calculate the torsional cracking strength. The torsional failure of a solid concrete section occurs when the maximum principal tensile strength σ_{max} is equal to the tensile strength of concrete f_t'. When $\sigma_{max} = \tau_{max}$, the elastic cracking torque can be considered as

$$T_{cr} = 2Ahf_t' \quad (5)$$

Canadian design code CSA A23.3:19—CSA A23.3:19 presents the cracking torsional strength in accordance with the thin-walled tube, hollow space-truss analogy of the RC cross section as follows

$$T_{cr} = 0.38\phi_c\sqrt{f_c'}\left(\frac{A_c^2}{P_c}\right) \quad (6)$$

where P_c is the outer perimeter of the concrete cross section (mm); and ϕ_c is the resistance factor for concrete and is equal to 0.65. For hollow sections, A_c is replaced by $1.5A_g$ if the wall thickness is less than $0.75(A_c/P_c)$; A_g is the gross area of the section. Note that f_c' is in MPa.

Canadian Highway Bridge Design Code CSA S6:19—The Canadian Highway Bridge Design Code (CSA S6:19) uses the same basic equation as CSA A23.3:19 with a different concrete tensile strength ($0.33\sqrt{f_c'}$). This equation is identical to the cracking torsional strength equation adopted in ACI 318-19, where the cracking torsional strength is given as

$$T_{cr} = 0.33\phi_c\sqrt{f_c'}\left(\frac{A_c^2}{P_c}\right) \quad (7)$$

AASHTO LRFD Bridge Design Guide Specifications (AASHTO 2018)—According to the "AASHTO LRFD Bridge Design Guide Specifications for GFRP-Reinforced Concrete" (2018), the cracking torsional strength T_{cr} is given as

$$T_{cr} = 0.126\sqrt{f_c'}2A_o b_e \quad (8)$$

where A_o is the area enclosed by the shear flow path, including any area of holes (in.^{2}) (for hollow sections, this can be taken as the area limited by the centerlines of the exterior webs and flanges that form the closed section); and b_e is the minimum thickness of the exterior webs or flanges comprising the closed box section (in.) and does not exceed A_c/P_c. Note that f_c' is in ksi.

Cracked torsional behavior (second zone)

Post-cracking torsional stiffness—Hsu (1973) proposed an equation to predict the torsional stiffness after cracking by considering a concrete thin tube with a constant wall thickness. He demonstrated the validity of this theory through laboratory tests in which the torsional behavior after cracking was unaffected by the concrete core of the cross section. The post-cracking torsional stiffness equation was derived based on the equilibrium and compatibility equations of the space-truss analogy proposed by Rausch (1953). The post-cracking torsional stiffness is given as

$$K_{cr(Theo)} = \frac{E_s x_1^2 y_1^2 A_c}{(x_1 + y_1)^2\left(\frac{2nA_c}{(x_1 + y_1)h} + \frac{1}{\rho_l}\right)} \quad (9)$$

where E_s is the modulus of elasticity of the reinforcement; x_1 and y_1 are the shorter and longer dimensions of the area limited by the centerline of the reinforcement, respectively; $n = E_s/E_c$; and ρ_l is the longitudinal reinforcement ratio.

Ultimate torsional strength—CSA S806-12 provides an equation to calculate the ultimate torsional strength of RC members based on the contribution of the GFRP longitudinal reinforcement only. This equation is based on a thin-tube space-truss analogy. Because the shear flow due to torsion is constant at all points around the tube perimeter, the resultant of the axial tension force (N) acts through the midheight of each wall. As a result, half of the axial tension force is resisted by each of the top and bottom chords, as given in Eq. (10). Longitudinal reinforcement with a tensile strength $A_l E_{fl}\varepsilon_{fl}$ is required to resist the sum of the axial tension forces acting in all walls of the tube, as given in Eq. (11)

$$F_{Top} = F_{Bottom} = \frac{\sum N}{2} = \frac{A_l E_{fl}\varepsilon_{fl}}{2} = 1.3\left(\frac{0.45p_o T_f}{2A_o}\right) \quad (10)$$

$$T_f = \frac{A_o A_l E_{fl}\varepsilon_{fl}}{1.3(0.45p_o)} \quad (11)$$

where T_f is the factored torsional resistance; A_o is the gross area enclosed by the shear flow path around the tube perimeter; A_l is the total area of the GFRP longitudinal bars; P_o is the length of the line joining the centers of the bars in the corners of the tube; E_{fl} is the modulus of elasticity of the GFRP longitudinal bars; and ε_{fl} is the tensile strain of the GFRP longitudinal bars.

Based on the test results, the observed tensile strain in the GFRP longitudinal bars at specimen failure was insignificant compared to its ultimate value. This is due to the specimens' failure mode, which was not controlled by the rupture of the GFRP longitudinal bars. Past studies reported the same behavior with the rectangular solid beams reinforced with only GFRP longitudinal bars (Mohamed and Benmokrane 2016; Hadhood et al. 2020). Therefore, in RC box girders

subjected to pure torsion, the tensile strain in the GFRP longitudinal bars should be limited to $\varepsilon_{fl} = 2000$ με.

Comparison of experimental and theoretical results

Considering the preceding discussion, the torsional moment-twist curves were predicted theoretically for the concrete box girders reinforced with only longitudinal GFRP bars. Figure 11 shows the experimental and theoretical torsional moment-twist curves for all GFRP-reinforced box girders. The theoretical value of the cracking torsional strength in Fig. 11 was determined with Bredt's thin-tube theory. Furthermore, the ultimate torsional strength was estimated theoretically with Eq. (11). To assess the uncracked torsional stiffness, a value of 0.6 was used for the reduction factor (R). The points corresponding to cracking and ultimate strength are identified in the graph. In general, Fig. 11 shows that the theoretical curves predicted the experimental curves well, thereby validating the calculation procedure described previously. Figure 11 shows that the torsional strength calculated with Eq. (11) was nearly 4% lower than the ultimate torsional strength of specimen BGW-16 but 9% higher than that of specimen BGW-20. In contrast, Eq. (11) provided ultimate torsional strength for specimens BGW-8 and BGW-12 lower than their cracking torsional strength. This is in good agreement with the experimental test results. Table 4 presents the ratios of the experimental to theoretical torsional stiffness in the first and second zones, the theoretical cracking torsional moment, and the ratios of the experimental to theoretical cracking torsional moment ($T_{cr(exp)}/T_{cr(Theo)}$). Different theories and code equations were used to predict the cracking torsional moment—namely, the skew-bending theory, Bredt's thin-tube theory, the theory of elasticity, CSA A23.3:19, CSA S6:19, and AASHTO 2018. The resistance factor of concrete ϕ for all codes was taken as being equal to unity. The concrete tensile strength f_t' was taken as being equal to $5\sqrt{f_c'}$ in the prediction with the theory of elasticity as reported by Hsu (1984). Table 4 indicates that the skew-bending theory and theory of elasticity overestimated the cracking strength of the specimens, as the average values of $T_{cr(exp)}/T_{cr(Theo)}$ were 0.86 and 0.89, respectively. In contrast, the results given by Bredt's thin-tube theory were in good agreement with the experimental test results, with an average value of 0.96. Table 4 shows that the CSA S6:19 equation underestimated the cracking torsional strength, with an average $T_{cr(exp))}/T_{cr(Theo)}$ value of 1.28. In contrast, the CSA A23.3:19 and AASHTO 2018 equations showed reasonable but rather conservative results, where the average values of $T_{cr(exp)}/T_{cr(Theo)}$ were 1.11 and 1.17, respectively. Saint-Venant's theory overestimated the uncracked torsional stiffness, as the average value of $K_{un(exp)}/K_{un(Theo)}$ was 0.84. Hsu's equation accurately predicted the post-cracking torsional stiffness, with an average $K_{cr(exp)}/K_{cr(Theo)}$ value of 1.01.

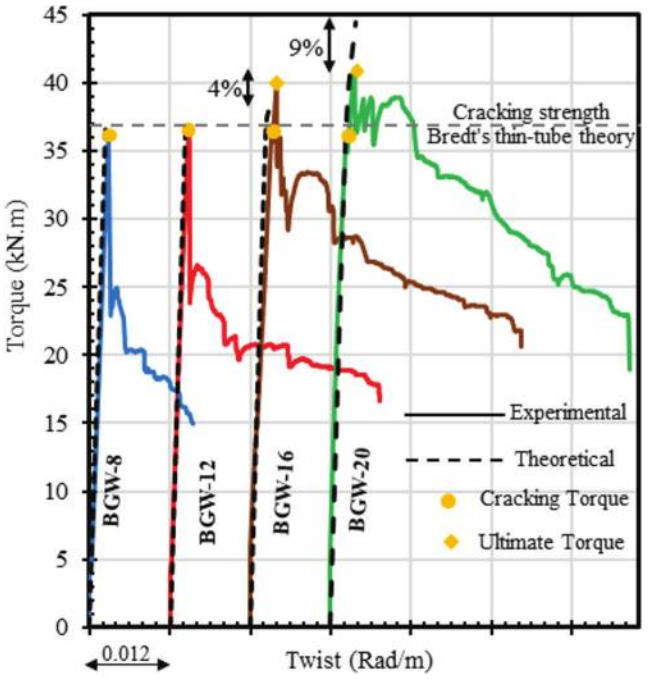

Fig. 11—Experimental versus theoretical torsional moment-twist curve. (Note: 1 kN·m = 0.7376 kip·ft; 1 rad/m = 0.305 rad/ft.)

Table 4—Experimental to theoretical cracking torque strength and stiffness assessment

Specimen ID	$K_{un(exp)}/K_{un(Theo)}$	$K_{cr(exp)}/K_{cr(Theo)}$	Skew-bending theory		Bredt's thin-tube theory		Theory of elasticity		CSA A23.3:19		CSA S6:19		AASHTO 2018	
			$T_{cr(Theo)}$, kN·m	$T_{cr(exp)}/T_{cr(Theo)}$	$T_{cr(Theo)}$, kN·m	$T_{cr(exp)}/T_{cr(Theo)}$	$T_{cr(Theo)}$, kN·m	$T_{cr(exp)}/T_{cr(Theo)}$	$T_{cr(Theo)}$, kN·m	$T_{cr(exp)}/T_{cr(Theo)}$	$T_{cr(Theo)}$, kN·m	$T_{cr(exp)}/T_{cr(Theo)}$	$T_{cr(Theo)}$, kN·m	$T_{cr(exp)}/T_{cr(Theo)}$
BSW-12	0.91	0.99	42.54	0.87	37.88	0.97	41.11	0.90	32.96	1.12	28.63	1.29	31.15	1.18
BGW-8	0.75	—	42.54	0.85	37.88	0.95	41.11	0.88	32.96	1.10	28.63	1.26	31.15	1.16
BGW-12	0.81	—	42.54	0.86	37.88	0.96	41.11	0.89	32.96	1.11	28.63	1.28	31.15	1.17
BGW-16	0.82	0.95	42.54	0.87	37.88	0.97	41.11	0.90	32.96	1.12	28.63	1.29	31.15	1.18
BGW-20	0.93	1.10	42.54	0.85	37.88	0.96	41.11	0.88	32.96	1.10	28.63	1.26	31.15	1.16
Average	0.84	1.013	—	0.86	—	0.96	—	0.89	—	1.11	—	1.28	—	1.17
Standard deviation	0.075	0.078	—	0.009	—	0.010	—	0.009	—	0.011	—	0.013	—	0.012
COV, %	8.85	7.67	—	1.047	—	1.042	—	1.011	—	0.99	—	1.02	—	0.103

Note: 1 kN·m = 0.7376 kip·ft.

CONCLUSIONS

This study investigated the contribution of the longitudinal reinforcement to the torsional strength of reinforced concrete (RC) box girders reinforced with longitudinal glass fiber-reinforced polymer (GFRP) bars but no transverse reinforcement. Five full-scale concrete box girders reinforced with GFRP or steel bars were constructed and tested under pure torsional loading up to failure. The test parameters included the longitudinal reinforcement ratio and the type of longitudinal reinforcement (GFRP or steel). The torsional moment-twist curves were predicted theoretically. In addition, the experimental cracking strength was compared with the three different theories and the current codes. The following are the main conclusions drawn from this investigation:

1. The torsional failure of all specimens was controlled by concrete splitting attributed to the absence of transverse torsional reinforcement, and a major diagonal spiral crack developed with a crushed surface formed at the midheight of the test region's front face.

2. The test results pointed out that the increase in the GFRP longitudinal reinforcement ratio of specimens from 1.10% (BGW-8) to 1.66% (BGW-12) had no significant effect on the post-cracking torsional stiffness and strength. Moreover, the ultimate torsional capacity of these specimens coincided with the corresponding cracking torque.

3. The specimens with relatively higher GFRP longitudinal reinforcement ratios (BGW-16 and BGW-20) exhibited an increase in their torsional strength of approximately 8% and 14%, respectively, after the appearance of the first diagonal crack.

4. The torsional strength and stiffness of the RC box girders without web reinforcement after cracking were highly dependent on the axial stiffness of the longitudinal reinforcing bars.

5. The ultimate torsional strength of RC box girders reinforced with only GFRP longitudinal bars was predicted with the CSA S806-12 (2017) design equation with a modification related to the GFRP tensile strain.

6. The skew-bending theory and theory of elasticity overestimated the predictions of the cracking torsional strength of the tested specimens, whereas Bredt's thin-tube theory was in good agreement with the experimental test results.

7. The torsional cracking strength equation in CSA S6:19 (2019) provided conservative predictions for all specimens tested. In contrast, the CSA A23.3:19 (2019) and AASHTO 2018 (2018) equations yielded reasonable but rather conservative results.

Based on the results found, this study considerably contributes to an understanding of the torsional strength and behavior of RC box girders reinforced with longitudinal GFRP bars under a pure torsional moment. Future work should focus on the structural performance of concrete box girders reinforced internally with longitudinal GFRP bars and with GFRP web reinforcement to study the contribution of the web reinforcement to the torsional behavior and strength.

AUTHOR BIOS

Ibrahim T. Mostafa *is a Doctoral Candidate in the Department of Civil and Building Engineering at the University of Sherbrooke, Sherbrooke, QC, Canada. He received his BSc and MSc in civil engineering from the Faculty of Engineering, Helwan University, Helwan, Cairo, Egypt. His research interests include the use of fiber-reinforced polymers (FRPs) in reinforced concrete structures.*

Salaheldin Mousa *is a Postdoctoral Fellow in the Department of Civil and Building Engineering at the University of Sherbrooke, where he received his PhD. He is also a Lecturer at the Faculty of Engineering at Shoubra, Benha University, Benha, Egypt, where he received his BSc and MSc. His research interests include the use of FRPs in reinforced concrete structures.*

Hamdy M. Mohamed *is a Research Associate and Lecturer in the Department of Civil and Building Engineering at the University of Sherbrooke. He received his BSc and MSc from the Faculty of Engineering, Helwan University, and his PhD from the University of Sherbrooke. His research interests include the use and field applications of FRPs in reinforced concrete structures.*

Brahim Benmokrane, *FACI, is a Professor in the Department of Civil and Building Engineering at the University of Sherbrooke, Tier-1 Canada Research Chair in Advanced Composite Materials Used for Civil Engineering Structures, Senior Industrial Research Chair in Innovative FRP Composite Materials for Concrete Infrastructure, and Director of the University of Sherbrooke Research Center on Structural FRP Composite Materials for Concrete Structures (CRUSMAC). He is a member and past Co-Chair of ACI Subcommittee 440-K, FRP-Material Characteristics, and a member of ACI Committees 435, Deflection of Concrete Building Structures, and 440, Fiber-Reinforced Polymer Reinforcement; and ACI Subcommittees ACI 440-E, FRP-Professional Education; ACI 440-F, FRP-Repair-Strengthening; 440-H, FRP-Reinforced Concrete; ACI 440-I, FRP-Prestressed Concrete; and ACI 440-L, FRP-Durability. He received the ACI Foundation Arthur J. Boase Award in 2022. His research interests include the development of FRP reinforcement for concrete structures and their durability, structural performance, and field applications.*

ACKNOWLEDGMENTS

This research was conducted with funding from the Natural Sciences and Engineering Research Council of Canada (NSERC), the NSERC-Alliance grant program, the Fonds de recherche du Québec – Nature et technologies (FRQNT), and the Tier-1 Canada Research Chair in Advanced Composite Materials Used for Civil Engineering Structures. The authors are grateful to Pultrall Inc. (Thetford Mines, QC, Canada) for the donation of GFRP materials, and the technical staff of the Canada Foundation for Innovation (CFI) structural lab in the Department of Civil and Building Engineering at the University of Sherbrooke.

REFERENCES

AASHTO, 2018, "AASHTO LRFD Bridge Design Guide Specifications for GFRP-Reinforced Concrete," second edition, American Association of State Highway and Transportation Officials, Washington, DC.

ACI Committee 318, 2019, "Building Code Requirements for Structural Concrete (ACI 318-19) and Commentary (ACI 318R-19) (Reapproved 2022)," American Concrete Institute, Farmington Hills, MI, 624 pp.

ACI Committee 440, 2015, "Guide for the Design and Construction of Structural Concrete Reinforced with Fiber-Reinforced Polymer (FRP) Bars (ACI 440.1R-15)," American Concrete Institute, Farmington Hills, MI, 88 pp.

ASTM C39/C39M-21, 2021, "Standard Test Method for Compressive Strength of Cylindrical Concrete Specimens," ASTM International, West Conshohocken, PA, 8 pp.

ASTM C496/C496M-17, 2017, "Standard Test Method for Splitting Tensile Strength of Cylindrical Concrete Specimens," ASTM International, West Conshohocken, PA, 5 pp.

ASTM D7205/D7205M-21, 2021, "Standard Test Method for Tensile Properties of Fiber Reinforced Polymer Matrix Composite Bars," ASTM International, West Conshohocken, PA, 13 pp.

ASTM D7914/D7914M-21, 2021, "Standard Test Method for Strength of Fiber Reinforced Polymer (FRP) Bent Bars in Bend Locations," ASTM International, West Conshohocken, PA, 6 pp.

Bernardo, L. F. A., and Lopes, S. M. R., 2008, "Behaviour of Concrete Beams under Torsion: NSC Plain and Hollow Beams," *Materials and Structures*, V. 41, No. 6, July, pp. 1143-1167. doi: 10.1617/s11527-007-9315-0

CSA A23.3:19, 2019, "Design of Concrete Structures," CSA Group, Toronto, ON, Canada, 301 pp.

CSA S6:19, 2019, "Canadian Highway Bridge Design Code," CSA Group, Toronto, ON, Canada, 1182 pp.

CSA S806-12(R2017), 2017, "Design and Construction of Building Components with Fibre-Reinforced Polymers," CSA Group, Toronto, ON, Canada.

CSA S807:19, 2019, "Specification for Fibre-Reinforced Polymers," CSA Group, Toronto, ON, Canada, 67 pp.

Deifalla, A.; Hamed, M.; Saleh, A.; and Ali, T., 2014, "Exploring GFRP Bars as Reinforcement for Rectangular and L-Shaped Beams Subjected to Significant Torsion: An Experimental Study," *Engineering Structures*, V. 59, Feb., pp. 776-786. doi: 10.1016/j.engstruct.2013.11.027

El-Salakawy, E.; Masmoudi, R.; Benmokrane, B.; Brière, F.; and Desgagné, G., 2004, "Pendulum Impacts into Concrete Bridge Barriers Reinforced with Glass Fibre Reinforced Polymer Composite Bars," *Canadian Journal of Civil Engineering*, V. 31, No. 4, Aug., pp. 539-552. doi: 10.1139/l04-006

Eladawy, M.; Hassan, M.; and Benmokrane, B., 2019, "Experimental Study of Interior Glass Fiber-Reinforced Polymer-Reinforced Concrete Slab-Column Connections under Lateral Cyclic Load," *ACI Structural Journal*, V. 116, No. 6, Nov., pp. 165-180. doi: 10.14359/51716803

Hadhood, A.; Gouda, M. G.; Agamy, M. H.; Mohamed, H. M.; and Sherif, A., 2020, "Torsion in Concrete Beams Reinforced with GFRP Spirals," *Engineering Structures*, V. 206, Mar., Article No. 110174. doi: 10.1016/j.engstruct.2020.110174

Hsu, T. T. C., 1968, "Torsion of Structural Concrete—A Summary on Pure Torsion," *Torsion of Structural Concrete*, SP-18, American Concrete Institute, Farmington Hills, MI, pp. 165-178.

Hsu, T. T. C., 1973, "Post-Cracking Torsional Rigidity of Reinforced Concrete Sections," *ACI Journal Proceedings*, V. 70, No. 5, May, pp. 352-360.

Hsu, T. T. C., 1984, *Torsion of Reinforced Concrete*, Van Nostrand Reinhold, New York, NY.

Hsu, T. T. C., and Mo, Y. L., 1985, "Softening of Concrete in Torsional Members—Theory and Tests," *ACI Journal Proceedings*, V. 82, No. 3, May-June, pp. 290-303. doi: 10.14359/10335

Jeng, C.-H.; Chiu, H.-J.; and Peng, S.-F., 2013, "Design Formulas for Cracking Torque and Twist in Hollow Reinforced Concrete Members," *ACI Structural Journal*, V. 110, No. 3, May-June, pp. 457-467. doi: 10.14359/51685603

JSCE, 1997, "Recommendation for Design and Construction of Concrete Structures Using Continuous Fiber Reinforcing Materials," Concrete Engineering Series 23, A. Machida, ed., Japan Society of Civil Engineers, Tokyo, Japan, 325 pp.

Khagehhosseini, A. H.; Porhosseini, R.; Morshed, R.; and Eslami, A., 2013, "An Experimental and Numerical Investigation on the Effect of Longitudinal Reinforcements in Torsional Resistance of RC Beams," *Structural Engineering and Mechanics*, V. 47, No. 2, July, pp. 247-263. doi: 10.12989/sem.2013.47.2.247

Koutchoukali, N.-E., and Belarbi, A., 2001, "Torsion of High-Strength Reinforced Concrete Beams and Minimum Reinforcement Requirement," *ACI Structural Journal*, V. 98, No. 4, July-Aug., pp. 462-469. doi: 10.14359/10289

Leonhardt, F., and Schelling, G., 1974, *Torsionsversuche an Stahlbetonbalken*, Deutscher Ausschuss für Stahlbeton: Schriftenreih, V. 239, Ernst & Sohn, Berlin, Germany, 122 pp. (in German)

Mitchell, D., and Collins, M. P., 1974, "Diagonal Compression Field Theory — A Rational Model for Structural Concrete in Pure Torsion," *ACI Journal Proceedings*, V. 71, No. 8, Aug., pp. 396-408.

Mohamed, H. M., and Benmokrane, B., 2014, "Design and Performance of Reinforced Concrete Water Chlorination Tank Totally Reinforced with GFRP Bars: Case Study," *Journal of Composites for Construction*, ASCE, V. 18, No. 1, Feb., p. 05013001. doi: 10.1061/(ASCE)CC.1943-5614.0000429

Mohamed, H. M., and Benmokrane, B., 2015, "Torsion Behavior of Concrete Beams Reinforced with Glass Fiber-Reinforced Polymer Bars and Stirrups," *ACI Structural Journal*, V. 112, No. 5, Sept.-Oct., pp. 543-552. doi: 10.14359/51687824

Mohamed, H. M., and Benmokrane, B., 2016, "Reinforced Concrete Beams with and without FRP Web Reinforcement under Pure Torsion," *Journal of Bridge Engineering*, ASCE, V. 21, No. 3, Mar., p. 04015070. doi: 10.1061/(ASCE)BE.1943-5592.0000839

Mohamed, H. M.; Ali, A. H.; Hadhood, A.; Mousa, S.; Abdelazim, W.; and Benmokrane, B., 2020, "Testing, Design, and Field Implementation of GFRP RC Soft-Eyes for Tunnel Construction," *Tunnelling and Underground Space Technology*, V. 106, Article No. 103626. doi: 10.1016/j.tust.2020.103626

Mohamed, H. M.; Chaallal, O.; and Benmokrane, B., 2015, "Torsional Moment Capacity and Failure Mode Mechanisms of Concrete Beams Reinforced with Carbon FRP Bars and Stirrups," *Journal of Composites for Construction*, ASCE, V. 19, No. 2, Apr., p. 04014049. doi: 10.1061/(ASCE)CC.1943-5614.0000515

Mousa, S.; Mohamed, H. M.; and Benmokrane, B., 2018, "Flexural Strength and Design Analysis of Circular Reinforced Concrete Members with Glass Fiber-Reinforced Polymer Bars and Spirals," *ACI Structural Journal*, V. 115, No. 5, Sept., pp. 1353-1364. doi: 10.14359/51702282

Park, S.-K.; Ko, W.-J.; and Kim, H.-Y., 2001, "Estimation of Torsional Crack Width for Concrete Structural Members," *Magazine of Concrete Research*, V. 53, No. 5, Oct., pp. 337-345. doi: 10.1680/macr.2001.53.5.337

Pultrall Inc., 2019, Composite Reinforcing Rods Technical Data Sheet, Thetford Mines, QC, Canada.

Rahal, K. N., and Collins, M. P., 1995, "Analysis of Sections Subjected to Combined Shear and Torsion—A Theoretical Model," *ACI Structural Journal*, V. 92, No. 4, July-Aug., pp. 459-469. doi: 10.14359/995

Rausch, E., 1953, *Drillung, Schub und Scheren im Stahlbetonbau* (*Torsion, Diagonal Tension, and Shear in Reinforced Concrete*), Deutscher Ingenieur-Verlag GmbH, Düsseldorf, Germany, 168 pp. (in German)

Shehab, H. K.; El-Awady, M. E.; and Husain, M., Sayed Mandour, 2009, "Behavior of Concrete Beams Reinforced by FRP Bars under Torsion," *Proceedings of the Thirteenth International Conference on Structural and Geotechnical Engineering (13th ICSGE)*, Cairo, Egypt, pp. 931-942.

Zhou, J.; Shen, W.; and Wang, S., 2017, "Experimental Study on Torsional Behavior of FRC and ECC Beams Reinforced with GFRP Bars," *Construction and Building Materials*, V. 152, Oct., pp. 74-81. doi: 10.1016/j.conbuildmat.2017.06.131

ACI STRUCTURAL JOURNAL TECHNICAL PAPER

Title No. 120-S83

Experimental Study on Drilled Shaft Reinforcing Bar Anchorage in Footings

by Yousun Yi, Hyunsu Kim, Jongkwon Choi, Juan Murcia-Delso, and Oguzhan Bayrak

This paper presents an experimental study on the anchorage behavior of drilled shaft reinforcement subjected to tension in drilled shaft footings loaded under combined axial force and uniaxial bending moment. Four large-scale tests were conducted on drilled shaft footing specimens employing an equivalent loading condition introducing tension in the drilled shaft reinforcement. Three different anchorage details were tested: straight bars, hooked bars, and headed bars. The drilled shaft reinforcement was capable of developing its full yield strength in tension in all the tests, regardless of the anchorage detail. The tensile stresses in drilled shaft bars were primarily developed in the region of the embedment length closest to the interface between the drilled shaft and the footing, while negligible stress and slip were measured in the vicinity of the unloaded end of the bars for all three anchorage details. Finally, a critical section is also proposed in this study to perform the anchorage check for the drilled shaft reinforcement in drilled shaft footings designed with the strut-and-tie method. The definition of the critical section provides a safe estimate of the available development length of the drilled shaft bars according to the findings of the experimental program.

Keywords: bar anchorage; bond; development length; drilled shaft footing; drilled shaft reinforcement; large-scale tests; strut-and-tie method (STM).

INTRODUCTION

A drilled shaft footing is a component of a pier foundation transferring forces from the pier to a group of drilled shafts. Drilled shaft footings are generally considered to behave as D-regions due to their reduced shear span-depth ratios and are therefore recommended to be designed using the strut-and-tie method (STM). Three-dimensional (3-D) strut-and-tie models are required to represent internal forces in drilled shaft footings supported on a grid of drilled shafts. The configuration of the 3-D strut-and-tie model depends on the loading combination applied through the pier. Figure 1 presents two strut-and-tie models for a drilled shaft footing subjected to uniaxial flexure and vertical compression loading. The model in Fig. 1(a) corresponds to a column subjected to combined axial force and a moderate axial bending moment, resulting in tension at one face of the column and nonuniform compression in drilled shafts, while the model in Fig. 1(b) corresponds to a case of combined axial force and a large uniaxial bending moment, resulting in tension not only at one face of the column but also at two of four drilled shafts. Both column and drilled shaft tie elements in the model are connected with smeared nodes, in which the nodal geometry cannot be clearly established due to the absence of well-defined geometrical constraints (for example, bearing area or strut width limitation).

To ensure full tensile yield capacity of the tie elements comprising a strut-and-tie model, sufficient development length (anchorage length) should be provided beyond the point at which the tie meets the strut anchoring it. Current STM provisions[1,2] establish the critical section at which the bar should be developed based on the geometry of the extended nodal zone bounded by the edge of the strut in a singular node (for example, a node with a well-bounded bearing face). Specifically, the critical section is defined at the point where the centroid of the tie element intersects the extended nodal zone, as shown in Fig. 2(a). For smeared nodes, it is not possible to identify the critical section for tension development based on the extended nodal zone owing to the absence of a well-defined nodal geometry. An alternative method was proposed by Yi et al.[3] to determine the critical section of the column ties in Fig. 2(b), corresponding to a drilled shaft footing subjected to combined axial force and a moderate uniaxial bending moment. This method assumes a large compression field bounded by the idealized diagonal struts near the column tie element of the 3-D strut-and-tie model, and the stress field is used to define the critical section for the column tie element at the smeared node. The proposed compression field is considered to perform a similar role to the extended nodal zone in determining the critical section, as shown in Fig. 2(b). The safety of this critical section criterion was verified experimentally.[3] However, the same criterion cannot be used for the case represented by the 3-D strut-and-tie model in Fig. 1(b) due to its different configuration of struts and ties. Therefore, it remained unclear how to perform the anchorage check for the column and drilled shaft tie elements in the 3-D strut-and-tie model for drilled shaft footings under combined axial force and a large uniaxial bending moment.

Most previous experimental studies[4-10] on drilled shaft footings were conducted for the simplest loading condition: a pier subjected to uniaxial compression. To the authors' knowledge, a limited number of experimental studies[3,11] have been conducted on drilled shaft footings subjected to uniaxial compression combined with the moderate flexural moment, inducing tension at the column reinforcement and nonuniform compression in drilled shafts. However, no experimental studies have been reported to investigate

ACI Structural Journal, V. 120, No. 5, September 2023.

MS No. S-2022-257.R1, doi: 10.14359/51738837, received January 21, 2023, and reviewed under Institute publication policies.

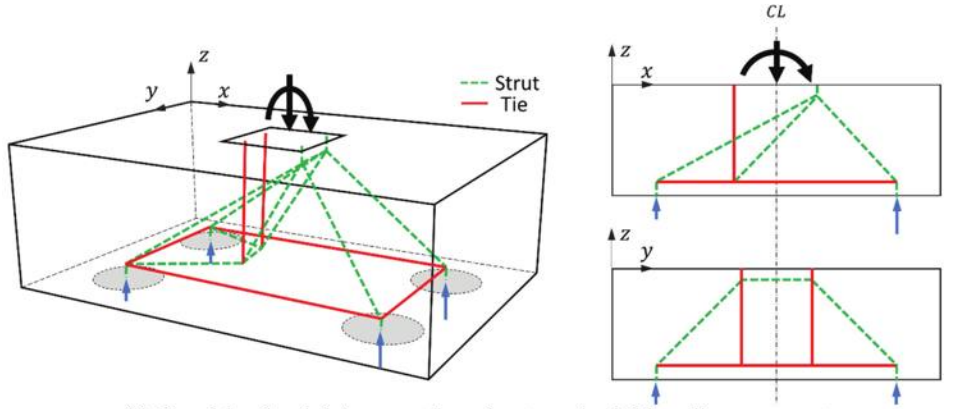

(a) Combined axial force and moderate uniaxial bending moment

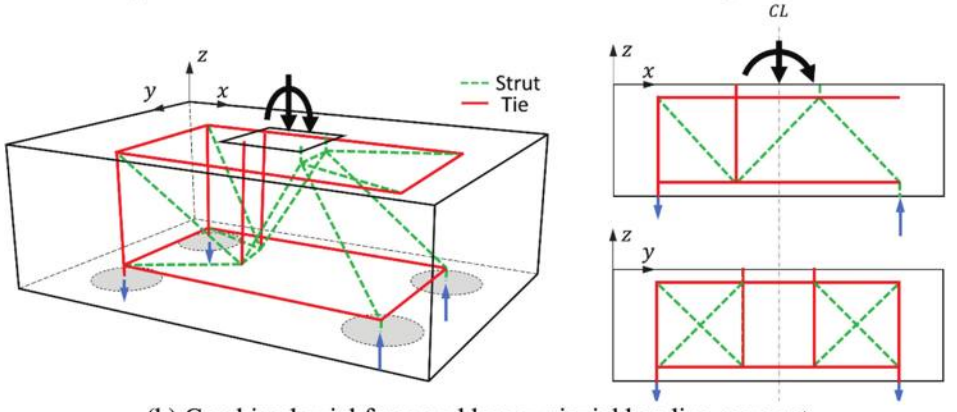

(b) Combined axial force and large uniaxial bending moment

Fig. 1—Three-dimensional strut-and-tie model for drilled shaft footing on four drilled shafts subjected to axial force and uniaxial bending moments.

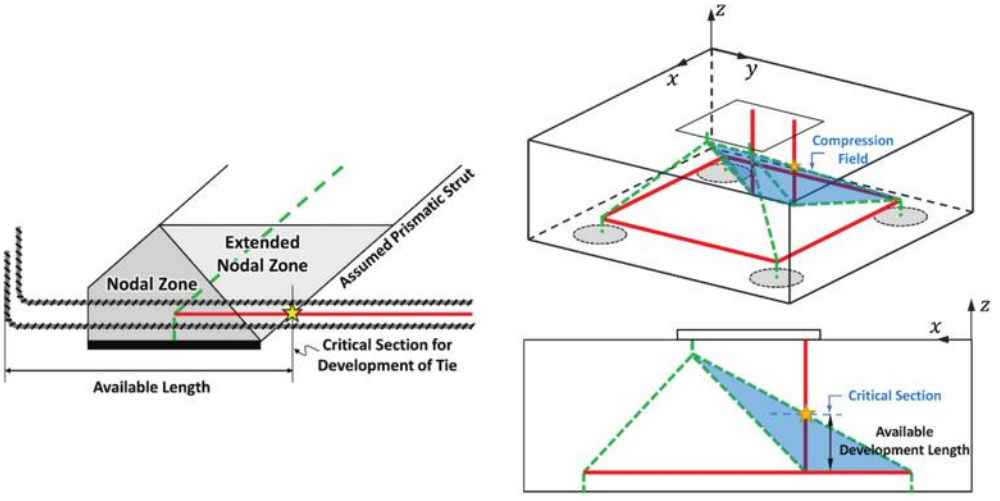

(a) Definition of extended nodal zone (adapted from AASHTO LRFD[1])

(b) Definition of compression field bounded by diagonal struts (adopted from Yi et al.[3])

Fig. 2—Critical section for anchorage verification of column tie elements in drilled shaft footings subjected to combined axial force and moderate uniaxial bending moment.

the response of drilled shaft footings subjected to flexural moments large enough to induce tension in the drilled shafts.

Therefore, due to this limited experimental database, studies[12-20] on STM-based analytical models for drilled shaft footings that correspond only to uniaxial compression have been conducted. A few studies[21,22] proposed STM-based design recommendations and examples for drilled shaft footings subjected to combined axial force and a large uniaxial bending moment, resulting in tension in two of four drilled shafts. They proposed anchorage details for drilled shaft reinforcement under tension based on conservative assumptions and best construction practices given the lack of in-depth experimental or computational studies on this problem. The design example provided by Widianto

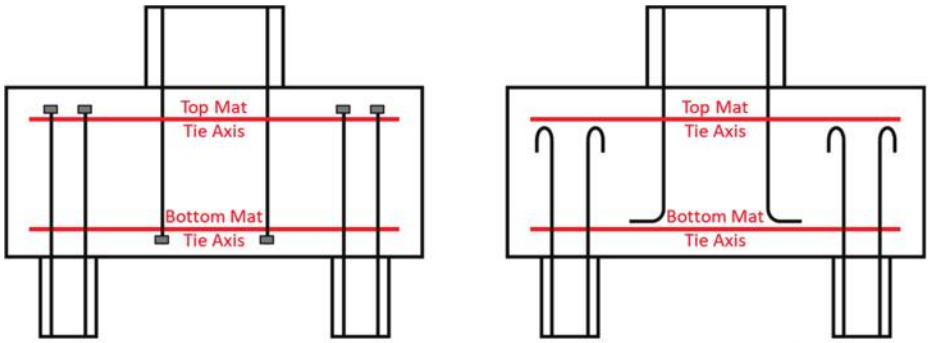

(a) Widianto and Bayrak[21] (b) Williams et al.[22]

Fig. 3—Detailing of column reinforcement anchorage proposed in literature.

and Bayrak[21] proposed using headed ends to develop the tension capacity of both the drilled shaft reinforcing bars and column bars extending beyond the mat reinforcement on the opposite face of the footing, as shown in Fig. 3(a). This was a conservative approach because it assumed that the bars had to be fully developed at the end point of the ties, without consideration of an extended nodal zone. On the other hand, 180-degree hooked drilled shaft reinforcing bars were proposed in a similar design example by Williams et al.,[22] as shown in Fig. 3(b). The hooked bars were recommended to extend up to right before the mat reinforcement in the opposite face of the footing, considering successful long-term construction practice. The development length of the drilled shaft reinforcement was not verified against code requirements in any of these design examples, and the recommended anchorage details were not experimentally verified.

There are currently a number of unknowns and ambiguities related to the development length requirements and detailing of drilled shaft reinforcement subjected to tension in drilled shaft footings. Experimental data are needed to resolve open questions related to the development of this type of reinforcement in the context of the 3-D STM. The present study conducted large-scale structural tests on drilled shaft footing specimens where the drilled shaft reinforcement was loaded under tension. Three different anchorage details were investigated: straight bars, 90-degree hooked bars, and headed bars. This paper provides a comprehensive description and discussion of the experimental program and test results. Design recommendations for the development length calculation of the drilled shaft reinforcement are also provided and discussed using experimental results.

RESEARCH SIGNIFICANCE

The large-scale experimental tests conducted in this study provide valuable data on the behavior of drilled shaft footings governed by yielding of the drilled shaft reinforcement. The test results characterize the anchorage response of drilled shaft reinforcement with three different anchorage details. The development length verification recommendations can contribute to overcoming the lack of guidance and uncertainties related to the use of the 3-D STM in the design of drilled shaft footings subjected to large flexural moments.

EXPERIMENTAL PROGRAM

Equivalent loading condition

The experimental program presented in this paper is part of a comprehensive research project on drilled shaft footings[23] conducted in the Ferguson Structural Engineering Laboratory at The University of Texas at Austin. The experiments presented here are specifically intended to study the effects of a high bending moment applied at the interface of the column, resulting in tensile reactions at two of four drilled shafts. To investigate the response of a footing specimen subjected to such a high moment demand, a large load eccentricity or lateral load would need to be applied to the column. Furthermore, yielding of the column reinforcement would need to be prevented to investigate the anchorage of drilled shaft reinforcement developing their yield strength, which would require a very large amount of column reinforcement. Hence, it is difficult to directly reproduce this boundary condition in large-scale laboratory testing. To overcome the difficulty, this study adopted a simpler, equivalent loading condition for the experimental program by directly applying a tensile load to the vertical reinforcement of two drilled shafts, representing the expected tensile reactions under a high moment demand. To further simplify the test setup, the column tie elements shown in Fig. 1(b) were substituted by post-tensioning forces applied on the top surface of the footing to prevent the failure induced by the column tie elements, as illustrated in Fig. 4.

The strut-and-tie model obtained from the equivalent loading is simpler than that resulting from combined axial force and a large uniaxial bending moment, as depicted in the comparison between Fig. 4 and Fig. 1(b). The discrepancies between the models are caused by the existence or not of a compressive reaction at the other two drilled shafts of the footing. Although the horizontal ties and struts placed on the plane of the bottom mat reinforcement do not exist in the equivalent model, they do not affect the anchorage of the vertical tie element for drilled shaft reinforcement because these elements are self-equilibrated at the node. Similarly, the confinement effect owing to the horizontal struts is also negligible. However, those two models have identical strut-and-tie model configurations near the tip of the drilled shaft ties, which represents the force-transfer mechanism of the drilled shaft ties. Therefore, the equivalent loading condition was employed for the experimental program of this study to

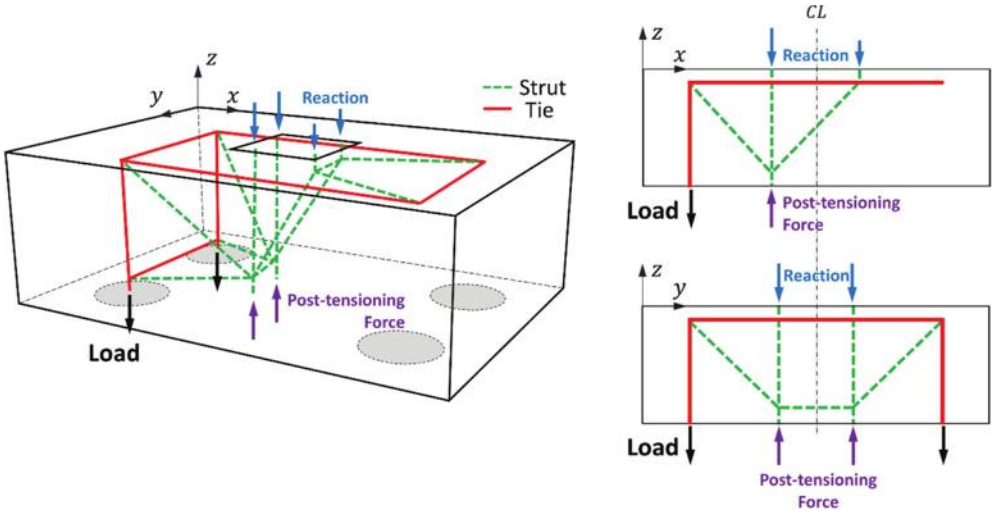

Fig. 4—Three-dimensional strut-and-tie model for drilled shaft footing under equivalent loading condition.

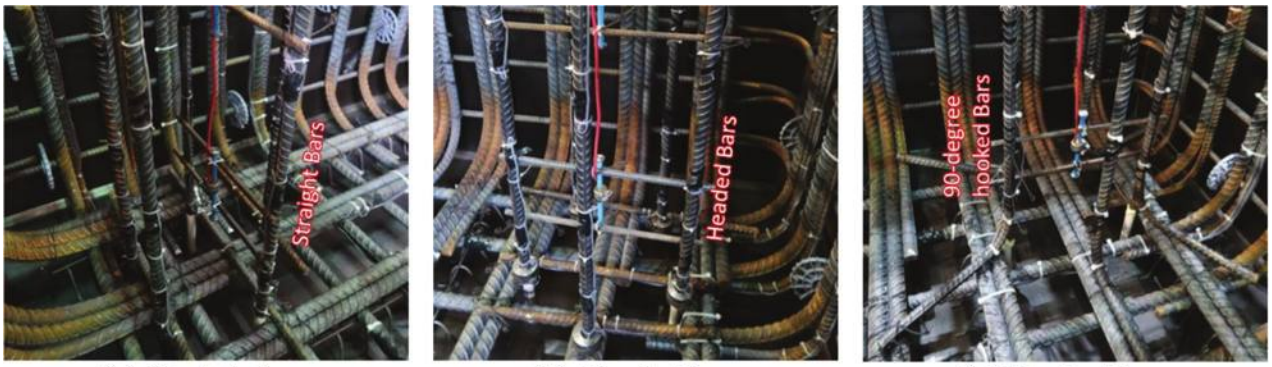

Fig. 5—Drilled shaft reinforcement anchorage details installed in specimens.

investigate the anchorage behavior of the drilled shaft reinforcement subjected to tension in drilled shaft footings.

Test variables

By employing the equivalent loading condition, the drilled shaft reinforcement behavior in each pair of drilled shafts can be investigated without influencing the pair of drilled shafts on the opposite side. Therefore, two tests can be conducted per each footing specimen. Two footing specimens were fabricated, and each specimen contained two different anchorage types of drilled shaft reinforcement. To compare the behavior of different anchorage types, the first specimen had drilled shaft reinforcement with straight bars and headed anchorages, and the second one had reinforcement with straight bars and hooked anchorages, as depicted in Fig. 5. The headed bar has a disk-shaped mechanical anchor at the end of the reinforcing bar, which has an effective bearing area of four times the nominal area of the reinforcing bar used. The hooked bars employed standard 90-degree hooks employing permissible bend radii in accordance with AASHTO LRFD Bridge Design Specifications[1] (AASHTO LRFD) and ACI 318-19.[2] As illustrated in Fig. 5(c), the hooked drilled shaft reinforcing bars were oriented radially toward the outside of the reinforcement cage, which is the typical detail employed for in-practice footings. The test matrix is given in Table 1.

Table 1—Test matrix

	Test ID	Specimen ID	Drilled shaft reinforcement	
			Number and size	Anchorage detail
1	VII–TD-ST	VII-TD	Five No. 6 (reinforcement ratio: 1.09%*)	Straight
2	VII–TD-HD			Headed
3	VII–TK-ST	VII-TK		Straight
4	VII–TK-HK			90-degree hooked

*For 16 in. (406 mm) diameter drilled shaft.

Specimen design

The geometry of the footing specimens was determined from a database comprising 35 drilled shaft footings constructed between 1994 and 2004 for 16 bridge projects in the state of Texas.[23] The test specimens were approximately one-third scale of the average footing within the database. The footing specimens were 132 in. (3353 mm) long, 96 in. (2438 mm) wide, and 40 in. (1016 mm) deep. The drilled shaft reinforcement embedded in the footing corresponded to four 16 in. (406 mm) diameter drilled shafts. To replicate the reinforcement details of the in-service drilled shaft footing, reinforcing bars were placed at all faces of footings (that is, bottom mat, top mat, and side reinforcement). The footing specimens were constructed and tested upside down to allow the direct application of an upward (tension)

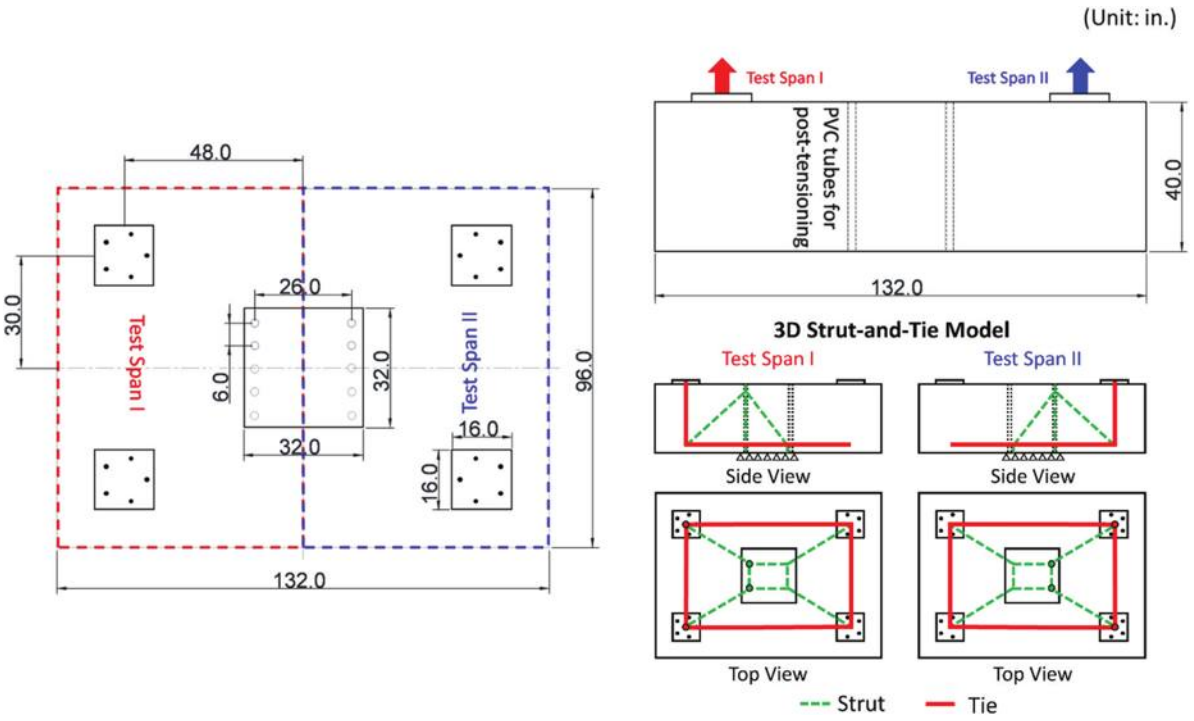

Fig. 6—Geometry of test specimens.

force to the drilled shaft reinforcement and to develop stable support capable of resisting the large overturning moment due to the equivalent loading condition. For clarity, the reinforcing bars comprising the specimen will be conventionally referred to with respect to their locations in an actual drilled shaft footing (for example, top mat for the longitudinal reinforcement on the drilled shafts side and bottom mat for the longitudinal reinforcement on the column side). Figure 6 illustrates the geometry of the test specimens.

The amount of the top mat reinforcement within the footing and the column reinforcement within the footing specimens was determined to prevent its yielding during testing, based on the predicted tie forces in the 3-D strut-and-tie model at ultimate state governed by fracture of the drilled shaft reinforcement. The nodal positions in the strut-and-tie model and the effective width of the ties for the top mat reinforcement were determined based on criteria proposed by Williams et al.[22] Specifically, the CCC nodes (that is, the nodes subjected to triaxial compression) beneath the bearing pad for post-tensioning force are positioned at a depth of 10% of the footing height, and only the top mat reinforcement placed within the drilled shaft diameter is considered to resist the horizontal tie forces. To preclude any premature failures in the footing, side-face reinforcement was provided orthogonally on the side surfaces of the test specimens in an amount exceeding the minimum crack control reinforcement ratio (0.30%) of the STM specifications in AASHTO LRFD.[1] Even though crack control reinforcement would be required in the same plane as the struts to control the width of the splitting cracks induced by these struts, a previous experimental study[10] on drilled shaft footings under uniform compression showed that side-face reinforcement effectively controls the surface crack and ensures the triaxial confinement at the internal struts within the footing. Therefore, the test specimens in this study were designed with side reinforcement ratios larger than 0.30% in both the transverse (0.31%) and longitudinal (0.37%) directions. The minimum reinforcement ratio for shrinkage and temperature reinforcement (>0.18%) was also provided to the bottom mat reinforcement of the footing in accordance with AASHTO LRFD.[1] Additionally, large-diameter threaded rods (1.625 in. [40 mm] diameter) were inserted through polyvinyl chloride (PVC) pipes embedded in the footing to apply the post-tensioning forces that replace the vertical column tie elements for the strut-and-tie model of the equivalent loading. Those rods were post-tensioned and bolted to a supporting frame to prevent a slack between the specimen and the frame during the testing. To avoid any damage related to the bursting and bearing actions introduced by post-tensioning forces, anti-bursting and spiral reinforcement were provided at the midheight of the footing and bearing faces, respectively (refer to Fig. 7).

The size and embedment length of drilled shaft reinforcement was determined based on the compiled database of drilled shaft footings constructed in the state of Texas to design the drilled shaft reinforcement with the size proportioned accordingly to the specimen size. The drilled shaft reinforcement of some footings in the database was extended up to the level of the top mat reinforcement—the same detail as that proposed by Williams et al.[22] Nevertheless, most of the drilled shaft reinforcement in the database usually did not extend to the top mat reinforcement, and the provided embedment lengths are presumed to satisfy the anchorage requirement in accordance with the sectional design approach. The collected footings might not have been designed for load cases inducing tension in the drilled shafts or lacked the STM-based design recommendations regarding drilled shaft reinforcement anchorage at the

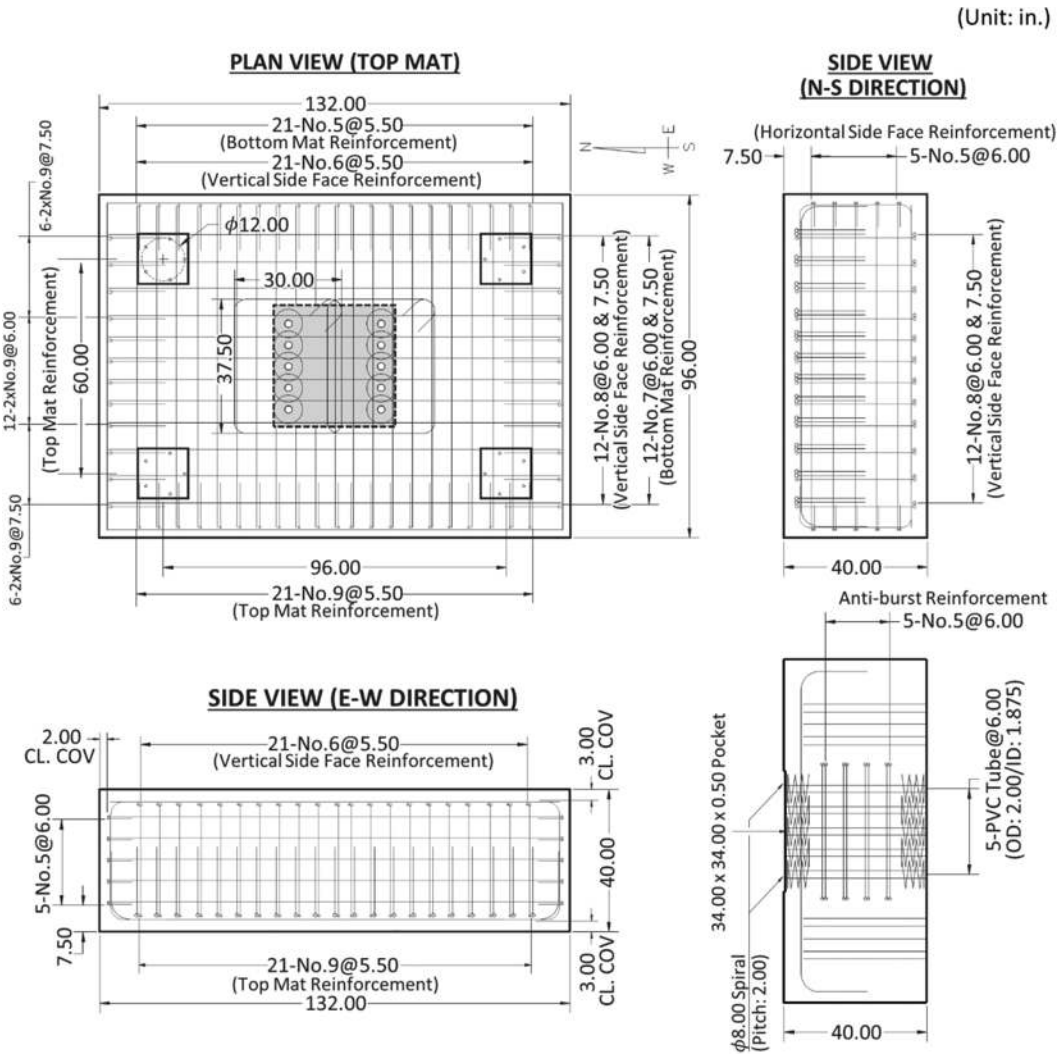

Fig. 7—Reinforcement details of test specimens.

Table 2—Footing reinforcement details

Bottom mat reinforcement		Side-face reinforcement		Top mat reinforcement	
N-S direction	W-E direction	Longitudinal direction	Transverse direction	N-S direction	W-E direction
12-2xNo. 9 @ 6.00 and 7.50 in.	21-No. 9 @ 5.50 in.	No. 5 @ 5.00 in.	No. 6 @ 5.50 in. No. 8 @ 6.00 and 7.50 in.	12-No. 7 @ 6.00 and 7.50 in.	21-No. 5 @ 5.50 in.

Note: N-S is north-south; W-E is west-east; 1 in. = 25.4 mm.

time of design. Therefore, this study defined the available embedment length ($l_{p,a}$), an extended embedment length of drilled shaft reinforcement that extends up to the elevation of the top mat reinforcement, to determine an adequate size for the drilled shaft reinforcement. Given the geometry of the footing specimens, the size of the drilled shaft bars was determined to provide a realistic ratio between the available embedment length ($l_{p,a}$) and bar diameter ($d_{b,s}$) according to the footing database. The number of bars was then determined to have a similar drilled shaft reinforcement ratio (ρ_s) as that observed in the footing database. To reproduce a similar available embedment length ratio ($l_{p,a}/d_{b,s}$ = 43.1) and drilled shaft reinforcement ratio (ρ_s = 1.05%) averaged from the footing database, five No. 6 reinforcing bars (ρ_s = 1.09%) were provided and extended up to the top mat reinforcement ($l_{p,a}/d_{b,s}$ = 46.3) for each 16 in. (406 mm) diameter drilled shaft of the specimens. The reinforcement details are summarized in Table 2 and illustrated in Fig. 7.

Material properties

Two batches of concrete were used to fabricate each footing specimen. The mixture proportions were identical for all batches of concrete with a design compressive strength of 3.6 ksi (24.8 MPa). ASTM A706/A706M-16[24] Grade 60 reinforcing bars were used for the drilled shaft reinforcement. ASTM A706/A706M[24] bars were chosen to be able to weld them to a steel plate needed to apply the tensile load, as will be discussed later. The rest of the reinforcement in the test specimens were ASTM A615/A615M-20[25] Grade 60 reinforcing bars. The mechanical properties of the concrete and reinforcement were determined from the average results of materials testing on a minimum of three samples of each

Table 3—Mechanical properties of materials

Test ID			VII-TK-ST	VII-TK-HK	VII-TD-ST	VII-TD-HD
Anchorage detail of drilled shaft reinforcement			Straight	Hooked	Straight	Headed
Concrete		Compressive strength (f_c'), ksi (day of test)	5.18	5.44	4.44	4.56
Reinforcement	Bottom mat	Yield strength ($f_{y,b}$), ksi	62.9			
		Tensile strength ($f_{u,b}$), ksi	107.9			
	Drilled shaft	Yield strength ($f_{y,s}$), ksi	68.2			
		Tensile strength ($f_{u,s}$), ksi	102.8			

Note: 1 ksi = 6.89 MPa.

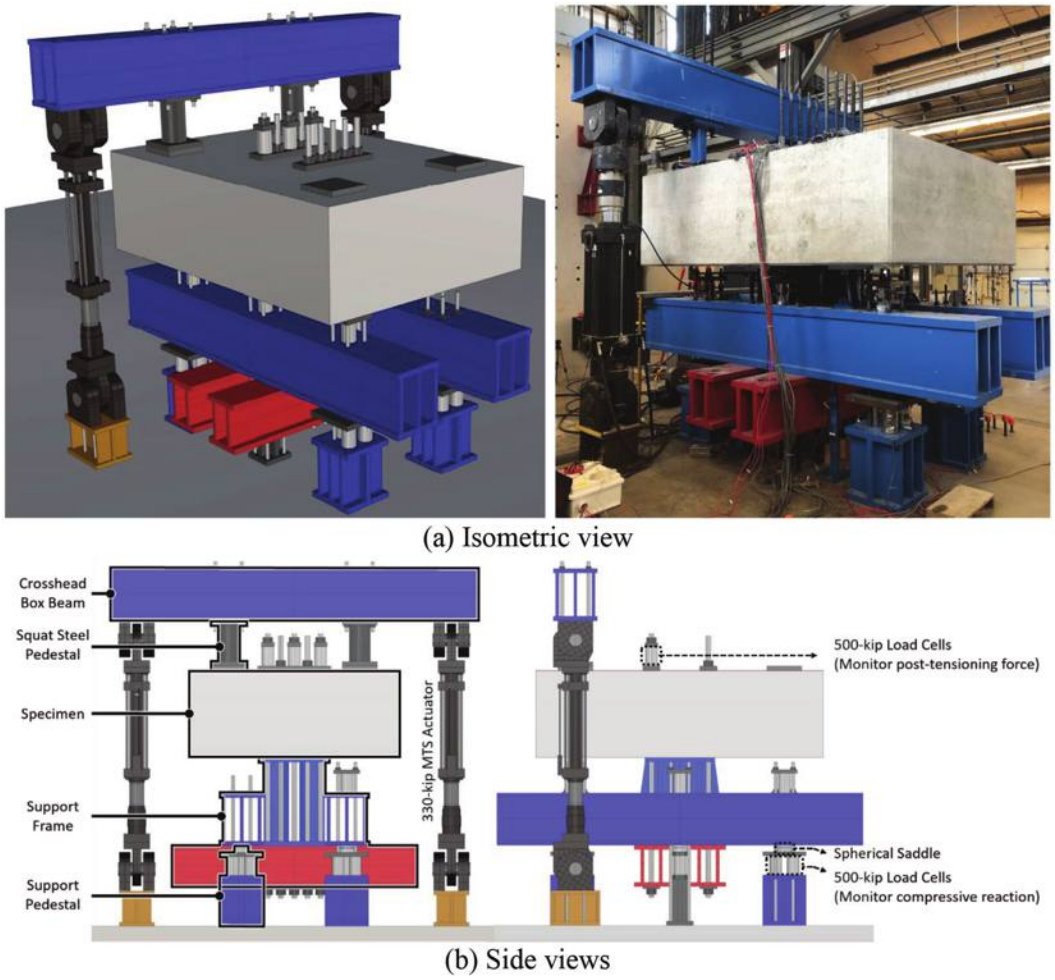

Fig. 8—Test setup for planned equivalent loading conditions.

batch. Furthermore, the compressive concrete strengths of the two batches used in a single test specimen were averaged to represent the compressive concrete strength of the footing. The materials testing for concrete and reinforcement was conducted in accordance with ASTM C39/C39M-21[26] and ASTM A370-21,[27] respectively. The average material properties are summarized in Table 3.

Test setup

The equivalent loading condition consisted of applying an upward (tensile) force to the drilled shaft reinforcement extending from the footing. A test setup was meticulously designed and fabricated to ensure the tensile load was applied in the normal direction with respect to the plane of the footing, and the proper load-transfer mechanisms from the drilled shaft footing to the strong floor. The test setup configuration is illustrated in Fig. 8.

The eccentrically applied upward force (48 in. [1.2 m] eccentricity with respect to the centroid of the specimen) results in a large overturning moment at the center reaction region on the bottom surface of the specimen, which represents the interface between the column and the footing. A support frame was designed to redistribute the moment to the strong floor with tensile and compressive reactions. The supporting frame consists of a large pedestal supporting the specimen, and staggered box beams are placed under it to

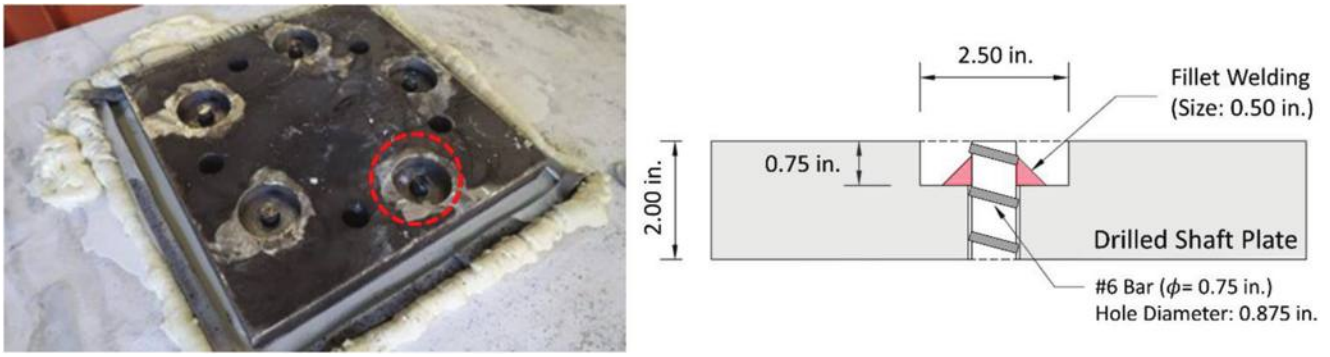

Fig. 9—Connection detail between drilled shaft reinforcement and drilled shaft plate.

transfer the moment to six support pedestals on the strong floor.

Each support pedestal was connected to the box beam with four threaded rods, and the rods were post-tensioned with 50 kip (0.2 MN) to compensate for tensile reactions caused by the overturning moment. The test specimen was anchored to the support frame with two rows of five large-diameter (1.625 in. [40 mm] diameter) post-tensioning threaded rods passing through the PVC pipes embedded in the footing. For each test, the rods in a row located at the axis of the vertical tie elements on the column side were post-tensioned with 150 kip (0.7 MN) per rod to prevent a slack between the specimen and the supporting frame before yielding the drilled shaft reinforcement.

Figure 9 illustrates the detail of the connection between the drilled shaft reinforcement extending out from the footing and the steel plates used to apply the vertical load. The drilled shaft bars were welded to these plates inside pockets 0.75 in. (19 mm) deep and 2.5 in. (64 mm) in diameter. The two drilled shaft plates were connected to a crosshead box beam through squat steel pedestals. Two 330 kip (1.5 MN) capacity servo-controlled actuators were placed at both sides of the specimen under the crosshead box beam to apply a tensile force to the drilled shaft reinforcement. Each actuator had a swivel head at both ends, permitting rotation and translation in the loading point of the specimen.

Instrumentation and loading protocol

The applied load was monitored in two ways: by means of load cells embedded in the actuators, and load cells installed in the support pedestals. The support frame was placed on top of four corner pedestals and two center-located pedestals, as shown in Fig. 8. A total of three 500 kip (2.2 MN) capacity load cells were provided at the base of each corner pedestal, and one 500 kip (2.2 MN) capacity load cell was provided at the base of each center-located pedestal.

To investigate the strain development along the embedment length of the drilled shaft reinforcement during testing, the drilled shaft bars were instrumented with strain gauges. The measured bar strains were used to develop tensile stress profiles to compare the behavior of different anchorage details. The strain gauges were installed on longitudinal ribs of the drilled shaft bars to minimize an adverse effect on the bond properties. In addition, the bottom mat reinforcement was also instrumented with strain gauges to monitor their strains during the tests.

To further examine the anchorage behavior of the drilled shaft reinforcement, bar slip was measured at the top and bottom ends of the drilled shaft reinforcement. On the top surface of the footing, linear potentiometers were installed near the center of the four side surfaces of the drilled shaft plates. While fabricating the specimens, small PVC pipes were installed right under the tips of two out of the five drilled shaft bars for each drilled shaft. The PVC pipes ensured the creation of deep and small voids in the concrete. Linear potentiometers were installed through the holes to measure the reinforcement slip at the bottom end of the drilled shaft reinforcement during testing. Whereas the straight and the headed anchorages have a flat surface at the bottom tip, the hooked anchorage does not due to its bend radius. Therefore, a small steel rod was welded at the bend radius of the hooked anchorage to make a flat surface at its tip to monitor the slip of the hooked reinforcement.

Test specimens were loaded under displacement control using the actuators at a rate of 0.025 in. (0.6 mm) per minute. During testing, loading was stopped at 50 kip (0.2 MN) increments, up to the load when at least one drilled shaft reinforcement yielded, to inspect and document the condition of the specimens. After all drilled shaft reinforcements exceeded their yield strain, the specimens were continuously loaded under displacement control until approximately 90% of the expected ultimate load corresponding to the full tensile strength of the drilled shaft bars (400 kip [1.8 MN]) was attained. The tests were stopped at 400 kip (1.8 MN) to prevent fracture of the drilled shaft reinforcement, which can potentially cause impact damage on the test setup or actuators.

EXPERIMENTAL RESULTS

Overall response

The overall response of the specimens is compared in Table 4 in terms of the loads at yielding of drilled shaft bars and maximum bar stresses. The applied loading could not be evenly distributed among all drilled shaft reinforcement during the tests due to the deflection of the specimen. For example, the maximum stress difference between bars corresponding to the same drilled shaft were between 12 and 15 ksi (83 and 103 MPa) (approximately 15%) at a load of 400 kip (1.8 MN). Furthermore, the load corresponding to the first yielding of the bars in each test presents a wide range of values (209 to 290 kip [0.9 to 1.3 MN]). However, there was no significant difference between the

Table 4—Summary of test results

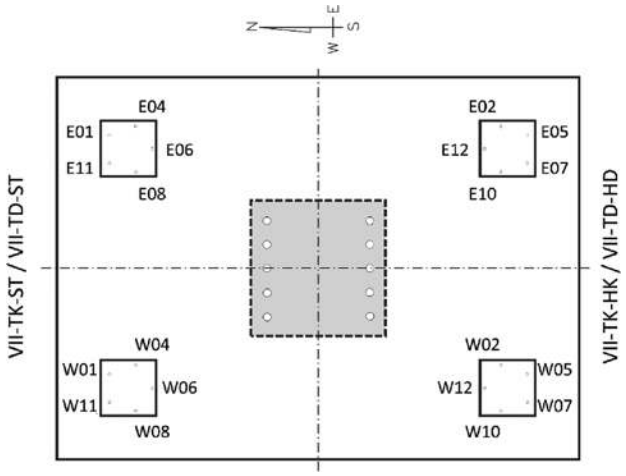

Test ID	VII-TK-ST	VII-TK-HK	VII-TD-HD	VII-TD-ST
Anchorage detail of drilled shaft reinforcement	Straight	Hooked	Headed	Straight
Measured load at the first yielding of a drilled shaft bar* $P_{fy,s}$, kip (reinforcing bar position†)	209 (E04)	249 (W10)	290 (E02)	277 (E06)
Measured load corresponding to yielding of all drilled shaft bars* $P_{y,s}$, kip	344	329	374	342
Maximum bar stress at 400 kip loading* $f_{s,max}$, ksi (reinforcing bar position†)	94.8 (E04)	90.5 (W07)	92.4 (W10)	90.3 (E06)
$P_{y,s}/P_{STM}$	1.15	1.10	1.25	1.14

*Strain data analyzed to find stresses of reinforcement.

†Refer to figure in table.

Note: 1 kip = 4.4 kN; 1 ksi = 6.9 MPa.

loads corresponding to the yielding of all the drilled shaft reinforcing bars. As shown in Table 4, these load values are within 10% of the average value of 347 kip (1.5 MN) of the four tests. The maximum stresses of the drilled shaft reinforcement were computed based on strain gauge data at the maximum applied load of 400 kip (1.8 MN). For all specimens, the maximum stresses were commonly developed at the measurement location closest to the top surface of the footing (2 in. [51 mm] below the top surface), and they exceeded 90% of the tensile strength of the bars in all cases.

The theoretical capacity of the specimens according to the 3-D STM would correspond to the yielding of the drilled shaft reinforcement at a load of 300 kip (1.3 MN). The difference between the theoretical yield load and the experimental values of the load for first yielding and complete yielding of the bars, indicated in Table 4, can be explained by the fact that the distribution of tensile forces among the bars was not perfectly uniform, as will be discussed later based on the analysis of bar stress data.

The overall test response is also analyzed in terms of the load applied to one drilled shaft versus the average elongation of its drilled shaft bars in Fig. 10. To this end, the measurements obtained from the linear potentiometers attached on the drilled shaft plates were averaged to calculate the average displacement of the plate with respect to the footing, which represents the average elongation (or slip) of the drilled shaft reinforcement at the top surface of the footing. Some linear potentiometers installed at one drilled shaft plate on the specimen measured unstable data after drilled shaft reinforcement yielding due to the conical cracks formed around the drilled shaft plate. Therefore, the west-side plate was selected for VII-TK-ST (straight drilled shaft reinforcement), and the east-side plate was selected for the other specimens to represent the behavior of the drilled shaft reinforcement embedded in the footing. The load in Fig. 10 corresponds to the load measured by the load cell in the same side's actuator. Figure 10 also presents the results in terms of the average stress level on the drilled shaft reinforcement by dividing the applied load by the total area of reinforcement connected to one drilled shaft plate. As shown, all four tests presented a consistent bar stress-elongation response. The average drilled shaft reinforcement stress exceeded the yield stress at a load of approximately 300 kip (1.3 MN) and reached a tensile stress of approximately 90 ksi (621 MPa) at a load of 400 kip (1.8 MN).

The reinforcement slip measured at the bottom tip of the drilled shaft reinforcement showed a trend to increase as load increased; however, the values were very small (of the order of 10^{-5} in. [10^{-4} mm]) for all anchorage types. Hence, the slip was negligible.

Visual observations

During each test, all faces of the tested span of the footing were visually inspected. During testing of VII-TK-ST, a series of horizontal cracks formed at midheight of the north face of the specimen as the load increased. Those cracks are

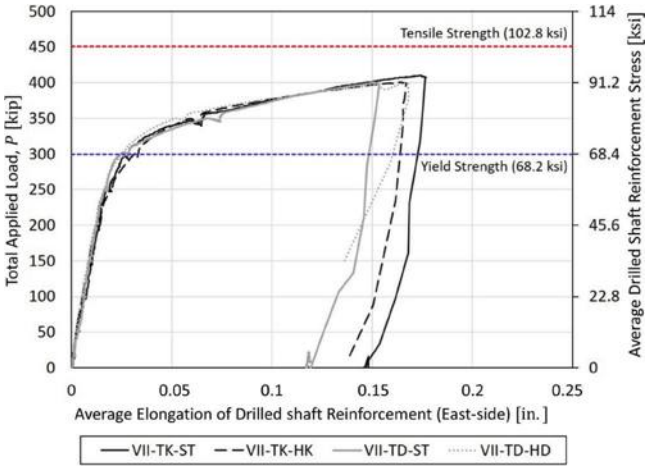

Fig. 10—Load versus bar elongation.

presumed to be microcracks that already existed between two concrete batches comprising the specimen. Most of the cracks were first observed at the load levels of 100 and 150 kip (0.4 and 0.7 MN), and no additional crack propagation was observed afterward. Furthermore, those cracks were not observed in the other three tests. Otherwise, all specimens showed a similar crack pattern. Only a few hairline cracks occurred on the side surfaces of the footing in all specimens during the tests.

The post-tensioning forces applied for anchoring the test specimen to the support frame increased during the testing as the load increased. It indicates that the post-tensioning rods were elongated during the testing; therefore, the desired fixed support condition could not be perfectly provided to the test specimen. Because of the actual boundary condition, the test specimens showed a rocking behavior during the testing, which hindered the formation of flexural cracks in the footings. This observation is in line with the bottom mat reinforcement strains measured during the tests. All the bottom mat reinforcing bars experienced a low strain level (corresponding to a tensile stress less than 1.5 ksi [10 MPa]) at the installed strain gauge locations at any time of the tests.

In spite of this rocking motion, all tested drilled shaft reinforcement were successfully loaded beyond their yield capacity and up to a maximum stress of over 90% of their tensile strength. The test specimens were dissected diagonally after the testing to inspect internal cracks, as shown in Fig. 11. Regardless of the anchorage types, concrete spalling around the drilled shaft plates was observed after the tests due to the formation of shallow conical failure planes near the loaded end of the bar above the bottom footing mat, caused by the bond of the drilled shaft reinforcement, whereas almost no cracking or damage was observed from the middepth to the bottom end of the drilled shaft reinforcement. Figure 12 presents the inspected crack maps after testing the span of each drilled shaft reinforcement anchorage type.

Tensile stress and bond stress profiles of column reinforcement

The anchorage response of drilled shaft reinforcement during the testing was investigated through the data obtained from strain gauges installed at 7 in. (178 mm) spacing. The stress-strain relationships obtained from tension tests on reinforcing bars were used to convert measured strains to stresses. The drilled shaft reinforcing bars in a drilled shaft plate were subjected to different loads because the position of the plate was not perfectly perpendicular to the direction of the applied load during testing owing to the deformation of the specimen. However, the stress profiles of all drilled shaft reinforcing bars showed a similar tendency regardless of their position and anchorage type. The drilled shaft reinforcing bar in the east-side drilled shaft reinforcement group positioned closest to the central axis of the footing (E06 for VII-TK-ST and VII-TK-HK; E12 for VII-TD-ST and VII-TD-HD) was selected to investigate the behavior of the drilled shaft reinforcement and establish a comparison between the specimens, as this was the only bar in all specimens with all strain gauges functional until the end of testing. Figure 13 presents the stress profiles corresponding to the different load levels ranging from 50 to 400 kip (0.4 to 1.8 MN).

All tested drilled shaft reinforcement anchorages were able to develop the yield stress within approximately 16 in. (406 mm) of their embedment length measured from the topmost strain gauge, installed at 2 in. (50 mm) below the top surface of the footing. This is inferred from the stress curves corresponding to the bar yielding (at a load of 300 kip [1.3 MN]), which practically go to zero at a depth of 16 in. (406 mm). Beyond this load level, the stress level near the top of the footing increased to approximately 90 ksi (621 MPa), which is 90% of the tensile strength (99 ksi [683 MPa]) of the reinforcement. In contrast, the stresses near the bottom tip of the drilled shaft reinforcement were negligible in all cases. This indicates that the headed and hooked drilled shaft reinforcement did not activate the bearing action of the head and hook to resist the tensile force in the reinforcing bar, and that tension was developed solely by bond stresses on the surface of the bar.

To examine the bond behavior of the drilled shaft reinforcement, average bond stresses (τ_b) between two consecutive gauges were calculated based on equilibrium using Eq. (1)

$$\tau_b = \frac{A_s}{d_b \pi}\left(\frac{\Delta f_s}{\Delta l}\right) \quad (1)$$

where A_s is the cross-sectional area of reinforcement to be anchored; d_b is the diameter of reinforcement to be anchored; Δf_s is the change in stress between two consecutive gauges; and Δ_l is the center-to-center distance between two consecutive gauges. Figure 14 presents the average bond stress profiles of the drilled shaft reinforcement obtained from each test. For reference, Fig. 14 also includes the theoretical value of the local bond strength ($\tau_{bu,split}$) corresponding to a splitting bond failure calculated in accordance with *fib* Model Code (MC) 2010[28] using Eq. (2)

$$\tau_{bu,split} = \eta_2 6.5\left(\frac{f_c'}{25}\right)^{0.25}\left(\frac{25}{d_b}\right)^{0.2}\left[\left(\frac{c_{min}}{d_b}\right)^{0.33}\left(\frac{c_{max}}{c_{min}}\right)^{0.1}\right] \quad (2)$$

where η_2 is a reinforcing bar position factor (equal to 1 for vertical bars); f_c' is the concrete strength; and c_{min} and c_{max}

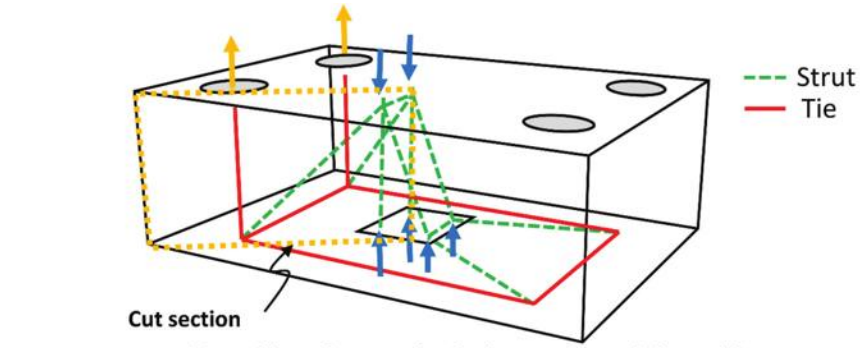

(a) Position of cut section in the 3D strut-and-tie model

(b) Cracks formed at drilled shaft reinforcement (W06*)

Fig. 11—Diagonal cut section of VII-TK-ST.

are parameters that depend on the concrete cover and bar spacing as defined in Eq. (3a) and (3b)

$$c_{min} = \min\{c_s/2,\ c_x,\ c_y\} \quad (3a)$$

$$c_{max} = \max\{c_s/2,\ c_x\} \quad (3b)$$

where c_s is the clear spacing of the reinforcing bars; c_x is the clear side cover to the bar in the direction parallel to the splitting crack; and c_y is the clear cover to the bar in the direction perpendicular to the splitting crack. The confinement term for transverse reinforcement of the original *fib* MC 2010 equation was not included in Eq. (2) by neglecting the confinement effect achieved from the side-face reinforcement.

The magnitude of the bond stresses increases with the level of loading, and relatively large bond stresses concentrate near the top surface of the specimen, as shown in Fig. 14. The maximum bond stress values at and after bar yielding vary between 1.0 and 1.5 ksi (6.9 and 10.3 MPa), and are developed in the upper 7 in. (178 mm) segment in most cases or in the segment right below it. As shown, these maximum values are smaller than the theoretical local bond resistance $\tau_{bu,split}$, but this is reasonable because the local peak of the actual bond stress distribution is expected to be larger than the average value obtained from a 7 in. (178 mm) segment. The bond stress diagrams also confirm that bond stresses are negligible at depths below 16 in. (406 mm) at yielding (load of 300 kip [1.3 MN]) and below 23 in. (584 mm) at the maximum load (400 kip [1.8 MN]). All bond stress distributions were very similar regardless of the anchorage details and concrete strength of the specimens. While the values of f_c' presented a maximum difference of 20% between specimens, the impact of such variation on bond resistance is very limited, as evidenced by the 5% maximum difference in theoretical bond strength, as shown in Fig. 14.

DISCUSSION

Effects of anchorage type

The experimental study by Yi et al.[3] on drilled shaft footings subjected to combined axial force and a moderate uniaxial bending moment, represented by the 3-D strut-and-tie model in Fig. 1(a), showed that an assumed large compression field bounded by the idealized diagonal struts induced bar stresses in the vicinity of the bottom tip of the column reinforcement. Hence, different column reinforcement force-transfer actions were found depending on the anchorage details provided at the ends of the column reinforcing bars.

In contrast, the overall behavior of the drilled shaft reinforcement observed in all four tests of this study was comparable regardless of the anchorage type. The development of tensile capacity of the bars was concentrated in the upper half of the embedment length owing to the bond forces in this region (Fig. 13 and 14), and the bearing action of the heads or hooks was not activated. Almost no tensile reinforcing bar stresses were developed near the end of drilled shaft reinforcement, even though the strut-and-tie model in Fig. 6 considers a diagonal strut flowing to the end of the vertical drilled shaft tie element. A possible explanation is that the compression field stemming from the post-tensioning force was combined with a tensile stress field in the concrete in the upper half of the embedment length. This observation is in line with observations from the inspected cut section (Fig. 11), which does not reveal cracking of concrete along the embedment length of the bar, except for the shallow cone failure at the very top.

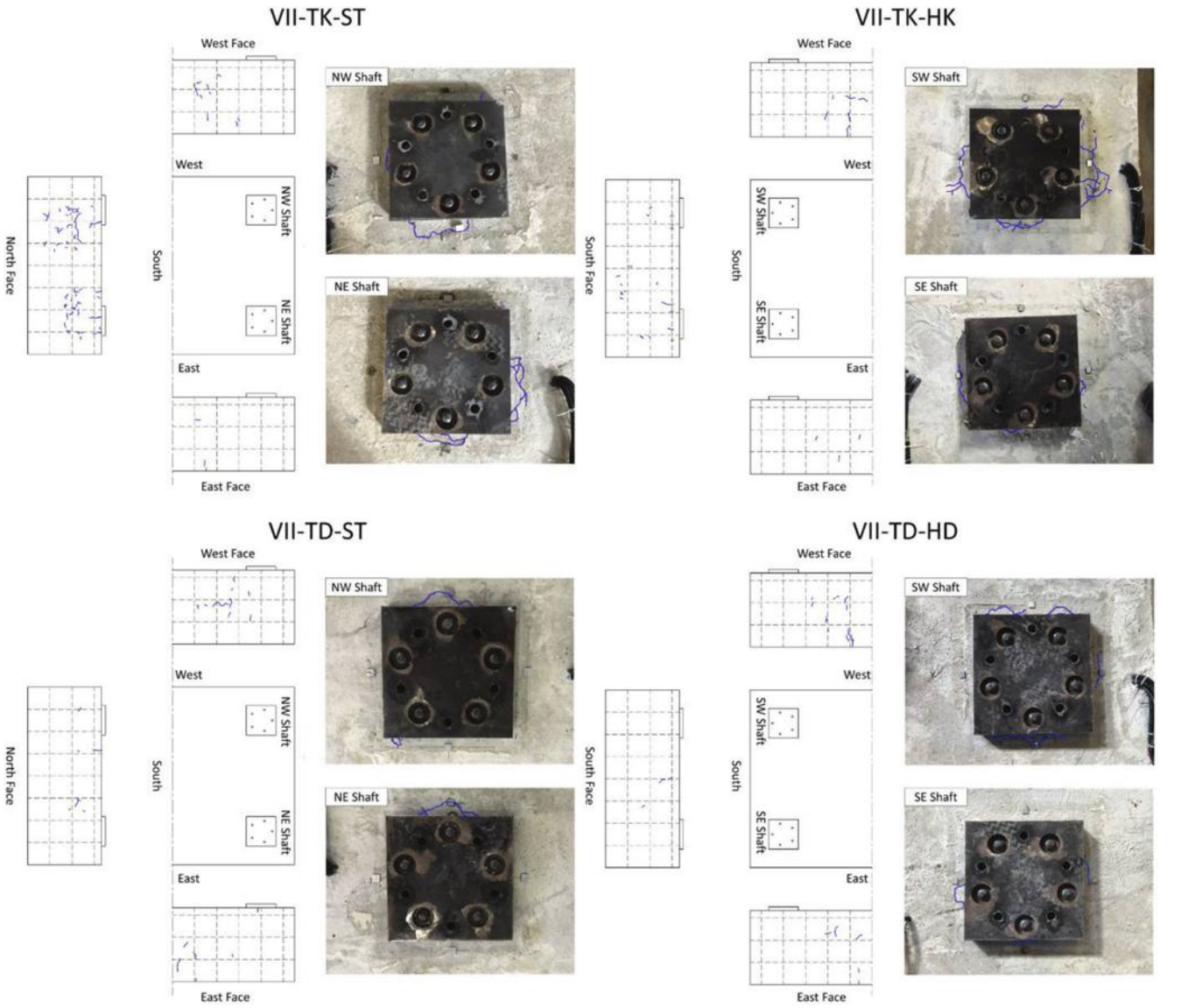

Fig. 12—Crack map of test specimens after testing.

Critical section for anchorage length verification

Although the diagonal strut in Fig. 6 did not seem to influence reinforcing bar stress developments in the vicinity of the drilled shaft reinforcement during the tests, a critical section of the drilled shaft tie element needs to be established to ensure the development of its full yield strength consistent with the existing stress flows in the context of the 3-D STM-based design procedure. Therefore, the internal force flow of the test specimens was reviewed to propose the critical section beyond which the drilled shaft reinforcement needs to be developed.

The diagonal strut acting at the end of the drilled shaft reinforcement embedded is classified as a fan-shaped strut because this end corresponds to a smeared node, as shown in Fig. 15. Therefore, the strut boundary spreads out from the edge of the bearing pad placed on the test specimen for applying the post-tensioning force. The minimum strut angle specified in AASHTO LRFD,[1] 25 degrees, is employed for defining the upper boundary of the fan-shaped strut. The resulting compression field, shaded in blue in Fig. 15, is assumed to perform the same role as an extended nodal zone for the purpose of developing the tensile forces of the tie. The point at which the drilled shaft reinforcing bar intersects the boundary of the fan-shaped strut would correspond to the critical section at which the bar starts to be developed, between 12.1 and 17.2 in. (307 and 437 mm) from the top surface depending on the bar. Figure 15 also indicates the section at which the yield strength of the bar was actually developed at the end of the test, which lies somewhere between 2 and 9 in. (51 and 229 mm) from the top surface. This indicates that the assumed critical section for the development of drilled shaft reinforcement is conservative with respect to the test results. To simplify, the critical section can be assumed to be at the point where the theoretical compression field meets the vertical tie of the drilled shaft regardless of the bar position in the drilled shaft.

The available development lengths measured from the proposed critical section at all drilled shaft reinforcing bar positions in the footing are compared with the minimum development lengths required for the different anchorage types in accordance with both AASHTO LRFD[1] and ACI 318.[2] The available development length is measured from

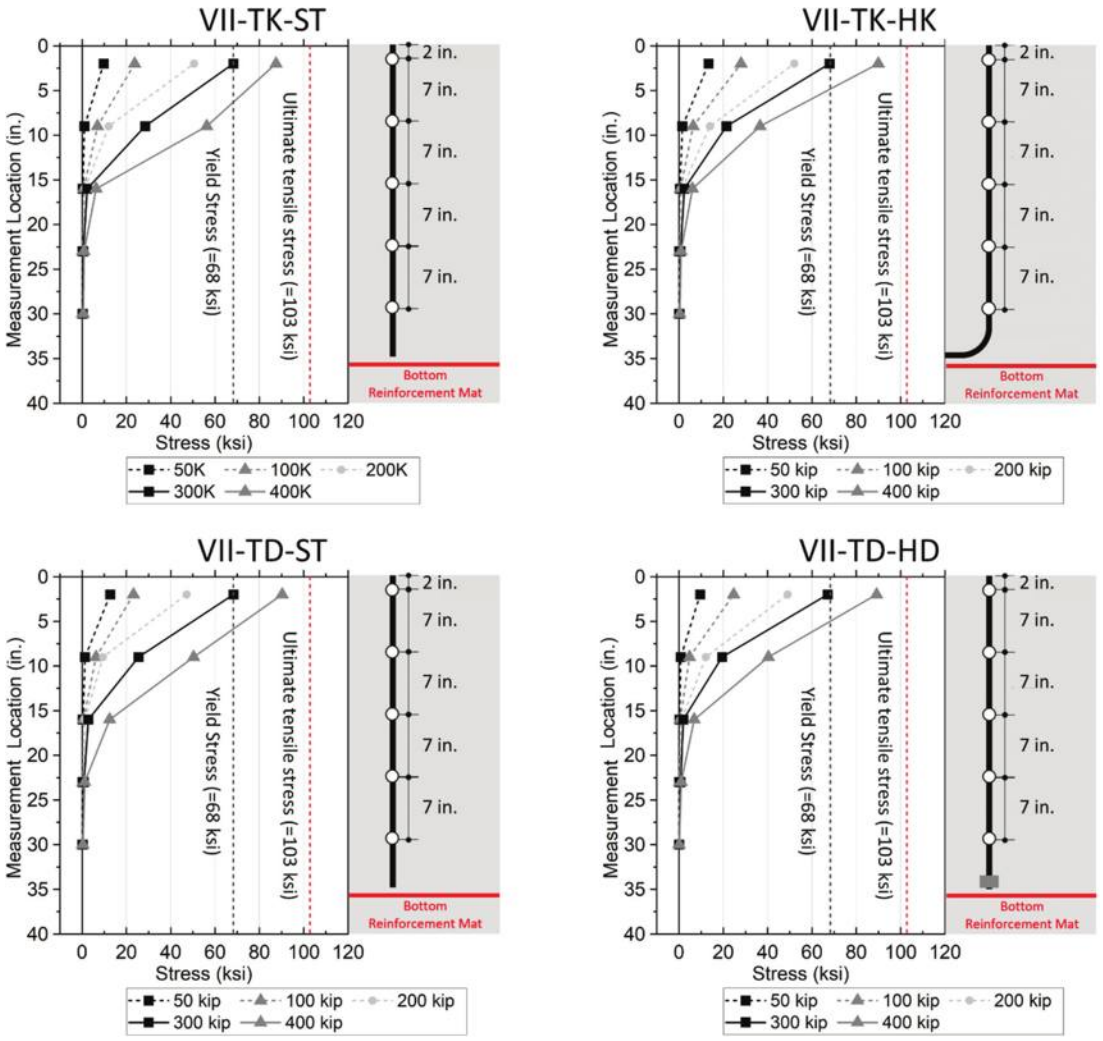

Fig. 13—Stress profiles of drilled shaft reinforcement.

the end of the drilled shaft reinforcement to the proposed critical section. The comparison results are summarized in Table 5. As shown, all drilled shaft reinforcing bars in the specimens satisfy the anchorage requirement, except for the straight bars. Even though the available length measured for the straight bars is shorter than the minimum development lengths computed with the provisions, the straight column reinforcement could develop its yield strength during the testing. This confirms the conservativeness of the proposed critical section.

The significant level of conservatism of the critical section estimation for these tests could be explained in part by the capacity of concrete to carry tensile stresses in the anchorage zone of the bars, as mentioned earlier. This type of behavior is not guaranteed in general as larger amounts of drilled shaft reinforcement could result in cracking of the anchorage zone, leading to more widely distributed bond stresses in agreement with the proposed inclined compression field. Regardless, the proposed definition of the critical section is consistent with the general principles of the STM and current anchorage checks for ties based on extended nodal zones, and as such is intended to provide safe solutions.

The critical section proposed in Fig. 15 is specific to test specimens where an equivalent loading condition was used to represent the effect of column reinforcement using post-tensioning forces. In an actual footing subjected to combined axial force and a large uniaxial bending moment, an analogous critical section can be defined based on the compression field that forms between the drilled shaft reinforcement and the column reinforcement, as shown in Fig. 16. The assumed compression field (shaded in blue in Fig. 16) represents a noncontact lap splice transfer mechanism between the column and drilled shaft reinforcement. Similar to the compression field conservatively defined for the equivalent loading condition, a minimum strut angle of 25 degrees is also employed for the compression stress field enabling the noncontact lap splice, as depicted in Fig. 16. Therefore, the critical section of the drilled shaft reinforcement can be defined at the position where the drilled shaft tie element intersects the boundary of the assumed compression field. Likewise, the critical section of the column reinforcement under this loading condition is defined as the intersection of the column tie and the boundary of the compression field.

CONCLUSIONS

This experimental study investigated the anchorage response of drilled shaft reinforcement subjected to tension in drilled shaft footings subjected to combined axial force

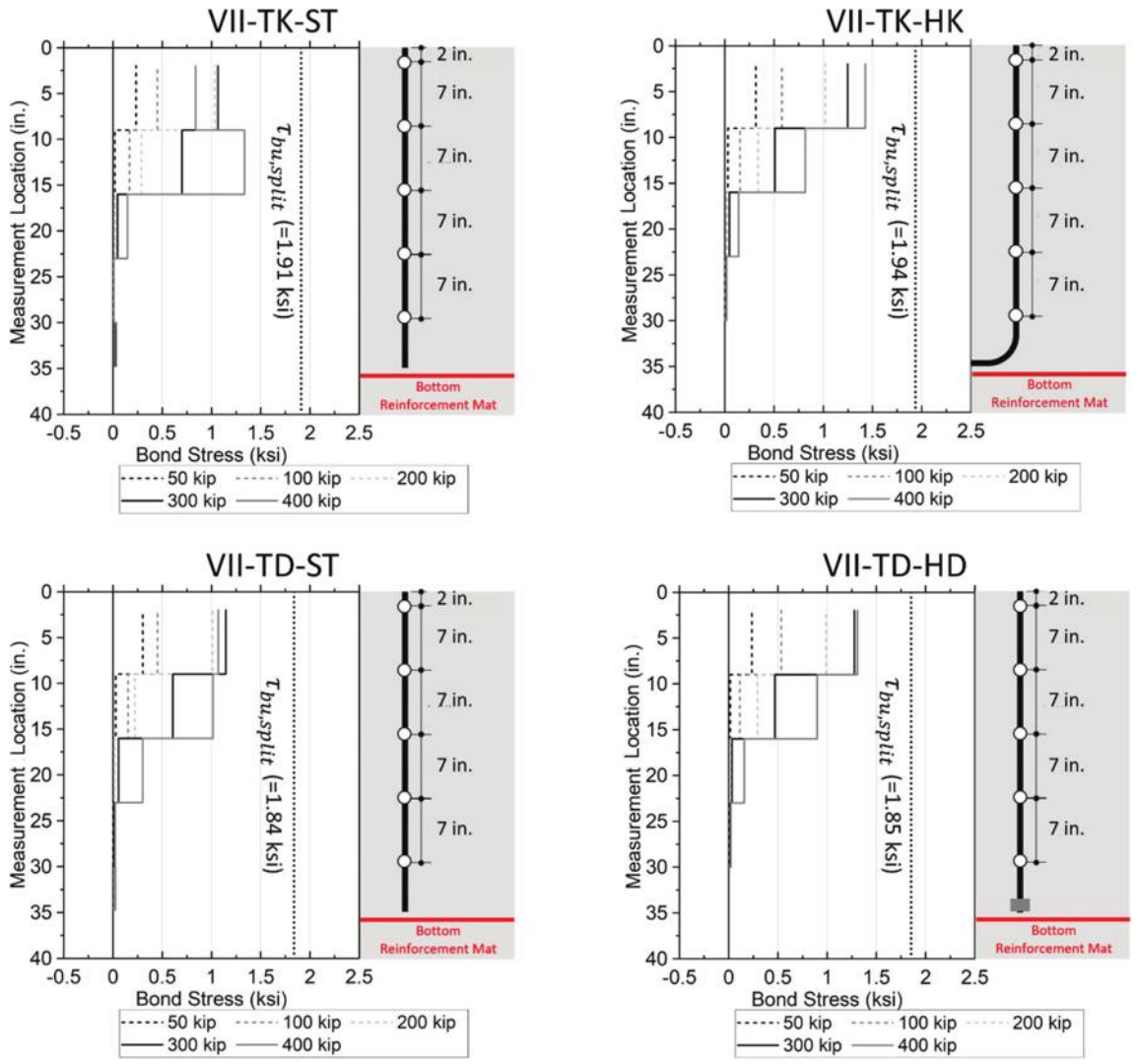

Fig. 14—Bond stress profiles of drilled shaft reinforcement.

and a large uniaxial bending moment by means of an equivalent boundary condition. Two drilled shaft footing specimens containing various types of drilled shaft reinforcement (straight, headed, and 90-degree hooked) were fabricated, and the anchorage behavior of the drilled shaft reinforcement embedded in each half span of the footing was examined in four independent tests. All the bar types were loaded in tension beyond their yield capacity. The main conclusions and findings of the study are the following:

1. All drilled shaft reinforcing bars were able to develop their full yield strength and sustained large inelastic deformations regardless of the anchorage type. In addition, the load-bar elongation responses of the four test specimens were practically identical.

2. The experimentally derived stress profiles of bars with different anchorage types of bars were comparable to each other. The tensile stress increment of the drilled shaft reinforcement was observed in the upper half of their embedment length (near their loaded end). The largest bond stresses typically occurred near the top surface of the specimen, which represented the interface between the footing and drilled shaft.

3. The slip and tensile bar stresses at the unloaded end of the drilled shaft reinforcement were negligible. The bearing action of the hook or head was not able to be activated because no splitting crack was caused by the diagonal fan-shaped strut flowing down to the end of the drilled shaft tie element, as evidenced by post-testing section cuts. Therefore, the development of these bars was solely provided by bond stresses along the top and central portion of the embedment lengths.

4. A compression field formed by the boundary of the fan-shaped strut was used for theoretical anchorage verifications using a three-dimensional (3-D) strut-and-tie model of the test specimens. The proposed compression field is regarded as an extended nodal zone to determine the critical section of the drilled shaft tie element. This simple criterion provides conservative results about the available length to develop the bars in tension. For actual drilled shaft footings subjected to combined axial force and a large uniaxial bending moment, similar critical section definitions for the column and drilled shaft reinforcement are proposed based on a compression field representing the noncontact lap splice behavior between the column and drilled shaft tie elements.

Although the proposed critical section of the drilled shaft reinforcement provided conservative estimations of the available development length in the test specimens, the validation of this approach is limited to four tests studying a

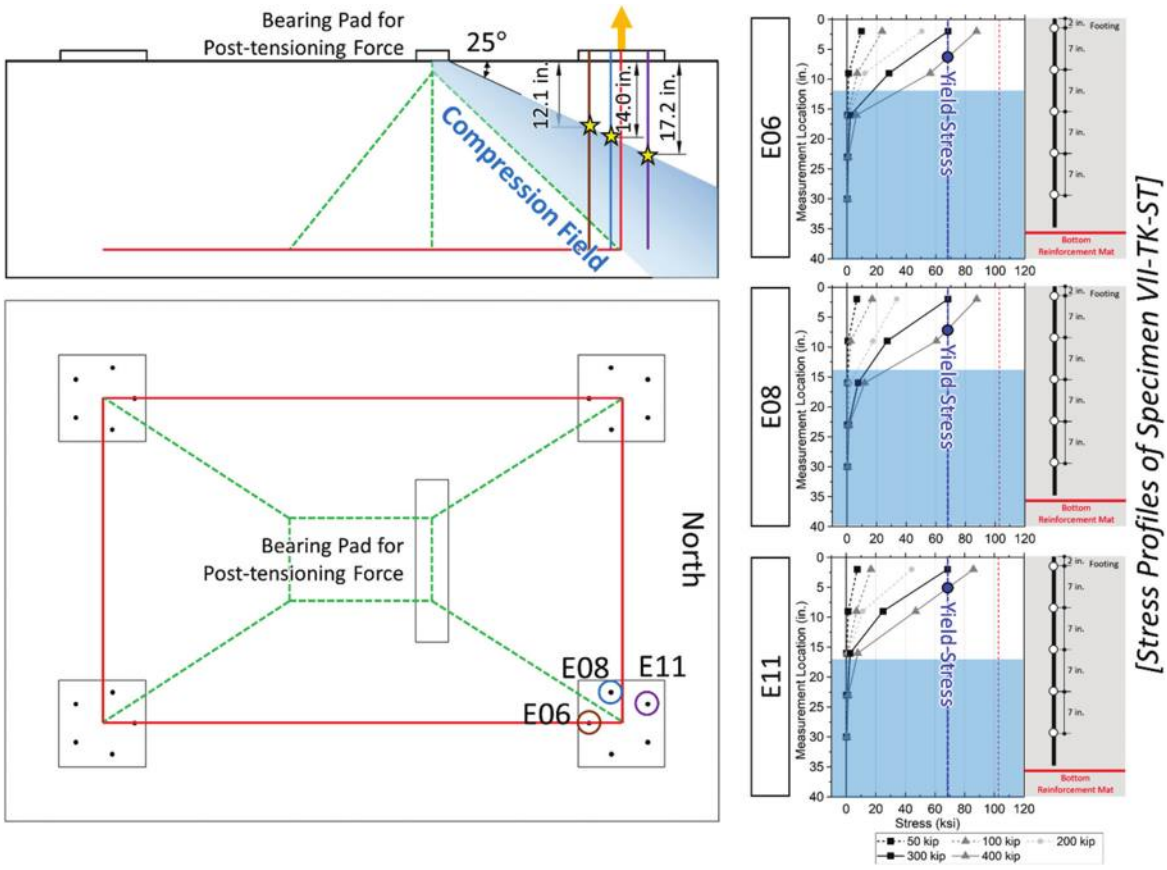

Fig. 15—Assumed compression field and proposed critical section of drilled shaft reinforcement in test specimens.

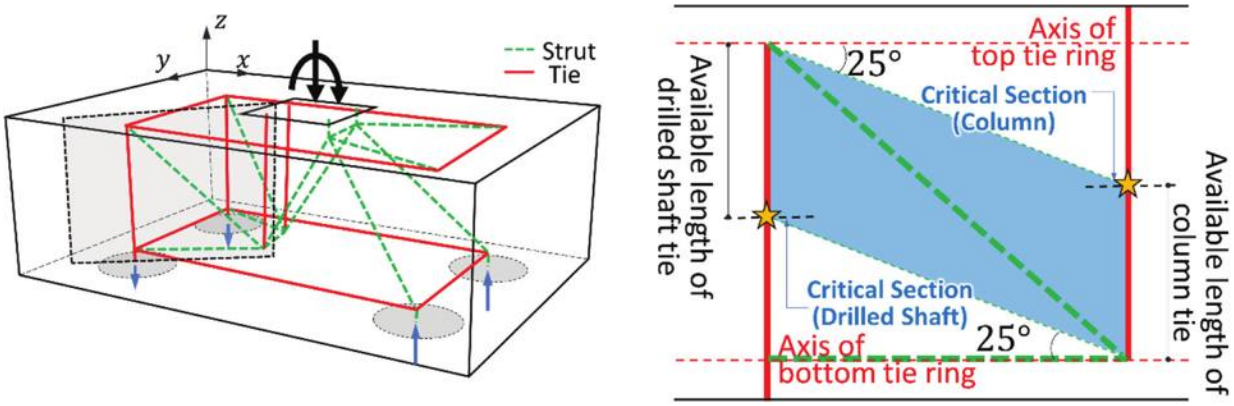

Fig. 16—Proposed critical sections for column and drilled shaft reinforcement in drilled shaft footings under combined axial force and large uniaxial bending moment.

Table 5—Anchorage check based on proposed critical section

		Test ID			
		VII-TK-ST	VII-TK-HK	VII-TD-ST	VII-TD-HD
Anchorage types		Straight	Hooked	Straight	Headed
Available length (l_a), in.		14.9			
AASHTO LRFD (2020)	Minimum development length (l_d), in.	17.1	10.5	18.4	N/A*
	l_a/l_d	0.87	1.42	0.81	
ACI 318-19 (2019)	Minimum development length (l_d), in.	21.6	11.1	23.3	7.9
	l_a/l_d	0.69	1.62	0.64	1.88

*Minimum development length for headed bars is not specified in AASHTO LRFD.[1]

Note: 1 in. = 25.4 mm.

single design parameter (anchorage type) and an idealized loading scheme. Therefore, further studies are recommended to study the response of noncontact lap splices between the column and drilled shaft reinforcement, including the effects of other design parameters (for example, footing geometry or drilled shaft reinforcement size and area).

AUTHOR BIOS

Yousun Yi *is a Postdoctoral Fellow in the Ferguson Structural Engineering Laboratory at The University of Texas at Austin, Austin, TX, where he received his PhD in civil engineering in 2022. His research interests include the strut-and-tie method and nonlinear analysis of reinforced concrete structures.*

Hyunsu Kim *is a Structural Specialist at COWI North America, Inc. He received his BS and MS from Seoul National University, Seoul, South Korea, in 2008 and 2010, respectively, and his PhD from The University of Texas at Austin in 2022. His research interests include the refinement of the strut-and-tie method for drilled shaft footings and numerical analysis of concrete structures.*

ACI member **Jongkwon Choi** *is an Assistant Professor in the Department of Civil and Environmental Engineering at Hongik University, Seoul, South Korea. He received his BS and MS from Seoul National University and his PhD from The University of Texas at Austin. His research interests include the mechanical behavior, experiment, and analysis of reinforced concrete and prestressed concrete structures, and the structural assessment of aging concrete structures.*

ACI member **Juan Murcia-Delso** *is an Assistant Professor at Universitat Politècnica de Catalunya - BarcelonaTech (UPC), Barcelona, Catalonia, Spain. He received his BS and MS from UPC and his PhD from the University of California, San Diego, La Jolla, CA. He is a member of Joint ACI-ASCE Committee 408, Bond and Development of Steel Reinforcement. His research interests include the nonlinear behavior, design, and assessment of concrete structures.*

Oguzhan Bayrak*, FACI, is a University Distinguished Teaching Professor and Phil M. Ferguson Professor in the Department of Civil, Architectural and Environmental Engineering at The University of Texas at Austin. He is a member of ACI Committees S803, Faculty Network Coordinating Committee, and 341, Performance-Based Seismic Design of Concrete Bridges; and Joint ACI-ASCE Committees 441, Reinforced Concrete Columns, and 445, Shear and Torsion.*

ACKNOWLEDGMENTS

The authors wish to express their gratitude and sincere appreciation to the Texas Department of Transportation (TxDOT) for funding this study through Project 0-6953. The findings and suggestions reported in this paper are those of the authors and do not necessarily reflect the perspectives of TxDOT.

REFERENCES

1. AASHTO, "AASHTO LRFD Bridge Design Specifications," ninth edition, American Association of State Highway and Transportation Officials, Washington, DC, 2020, 1912 pp.

2. ACI Committee 318, "Building Code Requirements for Structural Concrete (ACI 318-19) and Commentary (ACI 318R-19) (Reapproved 2022)," American Concrete Institute, Farmington Hills, MI, 2019, 624 pp.

3. Yi, Y.; Kim, H.; Bohem, R. A.; Webb, Z. D.; Choi, J.; Murcia-Delso, J.; Hrynyk, T. D.; and Bayrak, O., "Experimental Study on Column Reinforcing Bar Anchorage in Drilled Shaft Footings," *ACI Structural Journal*, V. 120, No. 4, July 2023, pp. 191-206. doi: 10.14359/51738721

4. Sabnis, G. M., and Gogate, A. B., "Investigation of Thick Slab (Pile Cap) Behavior," *ACI Journal Proceedings*, V. 81, No. 1, Jan.-Feb. 1984, pp. 35-39.

5. Suzuki, K.; Otsuki, K.; and Tsubata, T., "Influence of Bar Arrangement on Ultimate Strength of Four-Pile Caps," *Transactions of the Japan Concrete Institute*, V. 20, 1998, pp. 195-202.

6. Suzuki, K.; Otsuki, K.; and Tsubata, T., "Experimental Study on Four-Pile Caps with Taper," *Transactions of the Japan Concrete Institute*, V. 21, 1999, pp. 327-334.

7. Suzuki, K.; Otsuki, K.; and Tsuchiya, T., "Influence of Edge Distance on Failure Mechanism of Pile Caps," *Transactions of the Japan Concrete Institute*, V. 22, 2000, pp. 361-367.

8. Suzuki, K., and Otsuki, K., "Experimental Study on Corner Shear Failure of Pile Caps," *Transactions of the Japan Concrete Institute*, V. 23, 2002, pp. 303-310.

9. Clarke, J. L., "Behaviour and Design of Pile Caps with Four Piles," Technical Report No. 42.489, Cement and Concrete Association, Wexham Springs, UK, 1973, 19 pp.

10. Kim, H.; Boehm, R. A.; Yi, Y.; Mühlberg, S.; Webb, Z. D.; Choi, J.; Murcia-Delso, J.; Hrynyk, T. D.; and Bayrak, O., "Effects of Reinforcement Details on Behavior of Drilled Shaft Footings," *ACI Structural Journal*, V. 120, No. 1, Jan. 2023, pp. 285-301.

11. Miguel-Tortola, L.; Miguel, P. F.; and Pallarés, L., "Strength of Pile Caps under Eccentric Loads: Experimental Study and Review of Code Provisions," *Engineering Structures*, V. 182, 2019, pp. 251-267. doi: 10.1016/j.engstruct.2018.12.064

12. Dey, S., and Karthik, M. M., "Modelling Four-Pile Cap Behaviour Using Three-Dimensional Compatibility Strut-and-Tie Method," *Engineering Structures*, V. 198, 2019, Article No. 109499. doi: 10.1016/j.engstruct.2019.109499

13. Mogili, S., and Hwang, S.-J., "Softened Strut-and-Tie Model for Shear and Flexural Strengths of Reinforced Concrete Pile Caps," *Journal of Structural Engineering*, ASCE, V. 147, No. 11, 2021, p. 04021169. doi: 10.1061/(ASCE)ST.1943-541X.0003141

14. Meléndez, C.; Sagaseta, J.; Sosa, P. F. M.; and Rubio, L. P., "Refined Three-Dimensional Strut-and-Tie Model for Analysis and Design of Four-Pile Caps," *ACI Structural Journal*, V. 116, No. 4, July 2019, pp. 15-29. doi: 10.14359/51714485

15. Broms, C. E., "Strut-and-Tie Model for Punching Failure of Column Footings and Pile Caps," *ACI Structural Journal*, V. 115, No. 3, May 2018, pp. 689-698. doi: 10.14359/51702042

16. Chetchotisak, P.; Yindeesuk, S.; and Teerawong, J., "Interactive Strut-and-Tie-Model for Shear Strength Prediction of RC Pile Caps," *Computers and Concrete*, V. 20, No. 3, 2017, pp. 329-338.

17. Mathern, A.; Chantelot, G.; Svahn, P.-O.; Kettil, P.; Rempling, R.; and Engström, B., "Enhanced Strut-and-Tie Model for Reinforced Concrete Pile Caps," *International Association for Bridge and Structural Engineering, 39th IABSE Symposium – Engineering the Future*, Sept. 21-23, 2017, Vancouver, BC, Canada, pp. 607-614.

18. de Araújo, J. M., "Design of Rigid Pile Caps through an Iterative Strut-and-Tie Model," *Journal of Advanced Concrete Technology*, V. 14, No. 8, 2016, pp. 397-407. doi: 10.3151/jact.14.397

19. Park, J.; Kuchma, D.; and Souza, R., "Strength Predictions of Pile Caps by a Strut-and-Tie Model Approach," *Canadian Journal of Civil Engineering*, V. 35, No. 12, 2008, pp. 1399-1413. doi: 10.1139/L08-062

20. Yun, Y. M.; Chae, H. S.; Kim, B.; and Ramirez, J. A., "Verification of Three-Dimensional Grid Strut-and-Tie Model Approach in Structural Concrete," *ACI Structural Journal*, V. 115, No. 1, Jan. 2018, pp. 27-40. doi: 10.14359/51700946

21. Widianto, and Bayrak, O., "Example 11: Deep Pile Cap with Tension Piles," *Further Examples for the Design of Structural Concrete with Strut-and-Tie Models*, SP-273, K.-H. Reineck and L. C. Novak, eds., American Concrete Institute, Farmington Hills, MI, 2011, pp. 169-190.

22. Williams, C.; Deschenes, D.; and Bayrak, O., "Strut-and-Tie Model Design Examples for Bridges," Report No. FHWA/TX-12/5-5253-01-1, Center for Transportation Research, The University of Texas at Austin, Austin, TX, 2012, 276 pp.

23. Yi, Y.; Kim, H.; Boehm, R. A.; Webb, Z. D.; Choi, J.; Wang, H.-C.; Murcia-Delso, J.; Hrynyk, T. D.; and Bayrak, O., "3D Strut-and-Tie Modeling for Design of Drilled Shaft Footings," Report No. FHWA/TX-21/0-6953-R1, Center for Transportation Research, The University of Texas at Austin, Austin, TX, 2021, 466 pp.

24. ASTM A706/A706M-16, "Standard Specification for Deformed and Plain Low-Alloy Steel Bars for Concrete Reinforcement," ASTM International, West Conshohocken, PA, 2016, 7 pp.

25. ASTM A615/A615M-20, "Standard Specification for Deformed and Plain Carbon-Steel Bars for Concrete Reinforcement," ASTM International, West Conshohocken, PA, 2020, 8 pp.

26. ASTM C39/C39M-21, "Standard Test Method for Compressive Strength of Cylindrical Concrete Specimens," ASTM International, West Conshohocken, PA, 2021, 8 pp.

27. ASTM A370-21, "Standard Test Methods and Definitions for Mechanical Testing of Steel Products," ASTM International, West Conshohocken, PA, 2021, 50 pp.

28. *fib*, "*fib* Model Code for Concrete Structures 2010," International Federation for Structural Concrete, Lausanne, Switzerland, 2013, 434 pp.

ACI STRUCTURAL JOURNAL TECHNICAL PAPER

Title No. 120-S84

Design of Glass Fiber-Reinforced Polymer-Reinforced Concrete Columns per ACI CODE-440.11-22

by Zahid Hussain and Antonio Nanni

This paper is an attempt at a better understanding of design provisions of ACI CODE-440.11-22, building code for the design of glass fiber-reinforced polymer (GFRP)-reinforced concrete (RC) columns. Sway and a non-sway column examples originally designed with steel reinforcement were redesigned using GFRP longitudinal bars and ties as per provisions of ACI CODE-440.11-22 to analyze the effect of changing reinforcement type. Columns were designed with both low-modulus (E_f = 6500 ksi), and high-modulus (E_f = 8700 ksi) GFRP bars. A parametric study was carried out by varying the concrete compressive strength, the cross-section aspect ratio, and the resultant load eccentricity. GFRP-RC columns require larger cross-section dimensions and more reinforcement area than steel-RC columns irrespective of the GFRP elastic modulus when subjected to the same demand. The concrete strength has a significant effect on the dimensions of GFRP-RC columns, and rectangular sections were found to be more efficient than square sections with the same gross concrete area in the presence of moment. GFRP-RC columns subject to high eccentricity loads take advantage of GFRP tensile properties and, thus, are more efficient.

Keywords: building code; concrete columns; eccentricity; glass fiber-reinforced polymer (GFRP) reinforcement.

INTRODUCTION

Fiber-reinforced polymer (FRP) bars, being a competitive option for reinforced concrete (RC) members in aggressive environments, were not allowed in compression members in the previous editions of the ACI 440 Guide.[1] The primary reason for this exclusion was a lack of information regarding the behavior of FRP-RC members subjected to compressive loads. However, researchers have been actively investigating the behavior of glass FRP (GFRP)-RC columns during the last decade and have found GFRP-RC columns to be permissible structural elements. In fact, several experimental studies investigated the effect of the compressive behavior of longitudinal GFRP bars by testing RC columns[2-5] with an overall positive assessment of their feasibility. Jawaheri Zadeh and Nanni[6] provided information on flexural stiffness in frame analysis for GFRP-RC that resulted in close correspondence to limits proposed by Bischoff.[7] Similarly, Hadhood et al.,[8] among other researchers,[9] proposed a 1% minimum reinforcement necessary to maintain section integrity to achieve a nominal capacity of columns. Khorramian and Sadeghian[10] performed structural tests validating the performance of GFRP-RC columns with reinforcement ratios as high as 5.3%. Given, these significant advances in research over the past decade, the new ACI CODE-440.11-22 Building Code[11] permits the use of GFRP-RC columns with limitations to non-seismic zones and structures not requiring fire resistance. The addition of provisions for compressive members is a critical development for practitioners interested in nonmetallic reinforcement as it allows designing and construction of a building entirely with GFRP-RC.

Though ACI CODE-440.11-22 permits the design of columns using GFRP bars, due to their lower reliability, the minimum compressive strength properties of GFRP bars are not specified in ASTM D7957.[12] As stipulated in ACI CODE-440.11-22, in pure compression, their presence can be treated as having the same stiffness and strength as those of the surrounding concrete. However, in the presence of moment, GFRP reinforcement may effectively contribute to the column capacity. Therefore, this study is carried out to show the implications of current Code provisions on the design of GFRP-RC compressive members.

RESEARCH SIGNIFICANCE

The recently published ACI CODE-440.11-22[11] allows the design of columns with GFRP reinforcement. Due to remaining knowledge gaps in the behavior of GFRP-RC columns, some Code provisions were only analytically developed and verified by incorporating differences in material properties with steel-RC. This study shows the implications of Code provisions and highlights the areas for further research.

METHODOLOGY

In this study, a column part of a sway frame from the ACI Reinforced Concrete Design Handbook,[13] a Companion to ACI 318-19,[14] is selected and redesigned using GFRP reinforcement. This column is part of an interior, continuous, six-bay frame, and built integrally with a 7 in. (178 mm) deep slab, as shown in Fig. 1(a). The constituent materials selected for column design are listed in Table 1. The concrete strength f_c' is 5000 psi (35 MPa), while the GFRP type is compliant with material specification based on ASTM D7957.[12] For the non-sway case, a column from a frame part of an industrial building was taken from the textbook by Wight and Macgregor,[15] as shown in Fig. 1(b). This is a laterally braced column with a beam on one side, as shown in Fig. 1(b). The concrete strength f_c' for this column was 4000 psi (28 MPa) (as given in the textbook), while

ACI Structural Journal, V. 120, No. 5, September 2023.

MS No. S-2022-307.R3, doi: 10.14359/51738838, received April 10, 2023, and reviewed under Institute publication policies.

Table 1—Properties of GFRP reinforcement and concrete

Designation	Nominal diameter, in.	Nominal area, in.^{2}	Elastic modulus, ksi	Guaranteed tensile strength, ksi	Ultimate strain, %	Concrete strength, psi		Clear cover, in.
						Sway column	Non-sway column	
GFRP-4	0.5	0.2	6500	108	0.016	5000	4000	1.5
GFRP-8	1.0	0.79		84.5	0.013			
GFRP-9	1.128	1.0		82	0.013			
GFRP-4*	0.5	0.2	8700	139.5	0.016			
GFRP-8*	1.0	0.79		120	0.013			
GFRP-9*	1.128	1.0		115	0.013			

*New-generation GFRP bars with higher modulus of elasticity and guaranteed strength as proposed in an ASTM material spec under development.

Note: GFRP-4 = M13; GFRP-8 = M25; GFRP-9 = M29; 1 in. = 25.4 mm; 1 in.^{2} = 645 mm^2; 1 ksi = 6.89 MPa.

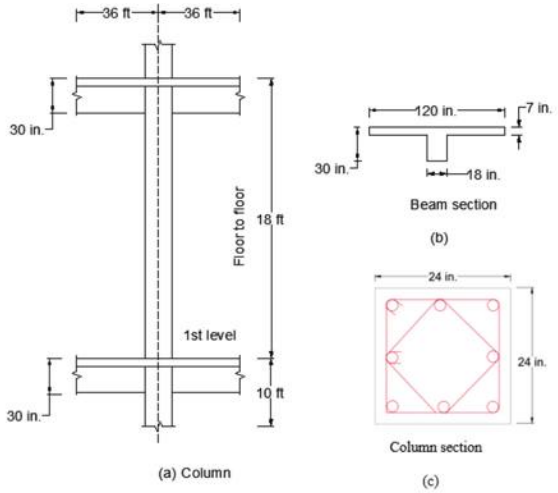

(a) Sway column (ACI Reinforced Concrete Design Handbook)[13]

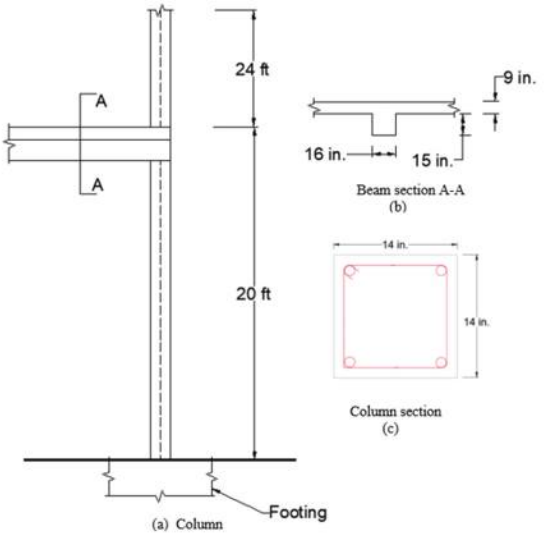

(b) Non-sway column (Textbook by Wight and Macgregor)[15]

Fig. 1—Geometrical dimensions for: (a) sway column; and (b) non-sway column.

the GFRP has the same properties as for the sway column. Given that a new ASTM material specification is under development for a class of GFRP bars with higher modulus of elasticity and strength, this class of GFRP bars was also considered. This study uses No. 8 and 9 (M25 and M29) nominal bar sizes for longitudinal reinforcement and No. 4 (M13) for stirrups/ties in all columns. The mechanical properties of GFRP bars in tension affecting design are listed in Table 1 and include guaranteed ultimate tensile strength f_{fu}, corresponding ultimate strain ε_{fu}, and modulus of elasticity E_f. GFRP compressive properties (that is, strength and stiffness) are not provided because, in design, the area of longitudinal GFRP bars in compression is considered equivalent to concrete.

Table 2—Strength reduction factor Φ for moment, axial force, or combined moment and axial force (ACI CODE-440.11-22, Section 21.2.2)

Net tensile strain at failure in outermost layer of GFRP reinforcement ε_f	Classification	Φ
$\varepsilon_f = \varepsilon_{fu}$	Tension-controlled	0.55
$\varepsilon_{fu} > \varepsilon_f > 0.8\varepsilon_{fu}$	Transition	$1.05 \text{ to } 0.5\varepsilon_f/\varepsilon_{fu}$
$\varepsilon_f \le 0.8\varepsilon_{fu}$	Compression-controlled	0.65

COLUMN PROVISIONS IN ACI CODE-440.11-22

For applicable factored load combinations, design strength at all sections shall satisfy the requirements of ACI CODE-440.11-22, Section 10.5.1.1, given as follows

$$\Phi S_n \ge U \tag{1}$$

where S_n is nominal moment, shear, axial, or torsional strength; U is strength of a member or cross section required to resist factored loads; and Φ is strength reduction factor as per ACI 440.11-22 and given in Table 2.

Because GFRP compression reinforcement will not contribute to the compression capacity of the cross section, the strength of a column subject to pure axial load is calculated using the gross concrete area and f_c', while treating GFRP as if it were concrete, as given in the Code Section 22.4.2.2

$$P_o = 0.85 f_c' A_g \tag{2}$$

where P_o is nominal axial strength at zero eccentricity.

The design tensile strain and strength of GFRP bar, in this study, were used as provided in Code Section 10.3.2.1, given as follows

$$\text{If } P_u > 0.10 f_c' A_g$$

Then, the limit on tensile strain is

$$\varepsilon_f = 0.01$$

Also,

$$\text{Design strength} = \min\begin{pmatrix} f_{fu} \\ 0.01E_f \end{pmatrix}$$

Code Section 10.6.1 specifies a minimum reinforcement of 1% of the gross concrete area (A_g) to provide resistance to bending and possibly concrete creep. Similarly, maximum reinforcement of 8% is specified to avoid congestion of reinforcing bars and to ensure that concrete can be properly consolidated.

The minimum number of bars is indicated by the Code Section 10.7.3, given as

$$\text{Minimum number of longitudinal bars} = \begin{cases} 4 & \text{Rectangular or circular ties} \\ 3 & \text{Triangular ties} \\ 6 & \text{Enclosed by spirals} \end{cases}$$

For longitudinal reinforcement, the minimum clear spacing between bars is specified in the Code Section 25.2.3 as follows

$$\text{Minimum spacing between bars} = \max\begin{pmatrix} 1.5 \text{ in.}(38 \text{ mm}) \\ 1.5d_b \\ 4/3d_{agg} \end{pmatrix}$$

where d_b is diameter of the longitudinal bar; and d_{agg} is diameter of the aggregate.

Code Section 25.7.2.3 states that every corner or alternate bar shall have lateral support by the corner of a tie with an included angle of not more than 135 degrees. Also, every bar shall have less than 6 in. (152 mm) clear on each side along the tie from a laterally supported bar.

The column size may be found from Eq. (2) by introducing a strength reduction factor; however, the values obtained in this study were significantly lower than those required by GFRP-RC columns. The stricter limits on slenderness for GFRP-RC columns will usually require bigger size columns. Authors, by trial and error, found following relations to give good approximation for an initial estimate for the size of a square column

$$\text{Sway columns: } A_g = \frac{P_u}{0.25 f_c'}$$

$$\text{Non-sway columns: } A_g = \frac{P_u}{0.15 f_c'}$$

ACI CODE-440.11-22 provides three conditions to determine if the frame can be considered non-sway—namely, Code Sections 6.2.5, 6.6.4.3(a), and 6.6.4.3(b), listed as follows:

1. 6.2.5 states that, if the stiffness of bracing elements exceeds 12 times the gross lateral stiffness of the columns in the direction considered, a column in that story can be considered as non-sway.
2. 6.6.4.3 implies analyzing the columns as non-sway if condition (a) or (b) is satisfied:

(a) The increase in column end moments due to second-order effects does not exceed 5% of the first-order end moments.

(b) The stability index does not exceed 0.05. The stability index for a given story, Q, shall be calculated as shown

$$Q = \frac{\sum P_u \delta_o}{V_{us} l_c} \tag{3}$$

where $\sum P_u$ is total factored vertical load; V_{us} is horizontal story shear; δ_o is first-order relative lateral displacement between the top and bottom of that story; and l_c is height of the column from the center to center of the joints.

GFRP-RC columns are more susceptible to the slenderness effects than steel-RC due to the lower stiffness of GFRP reinforcement compared to steel bars; therefore, more strict limits are imposed when checking slenderness effects for GFRP-RC columns. Slenderness effects can be neglected in both sway and non-sway frames if the following conditions of Code Sections 6.2.5.1(a) or 6.2.5.1(b) are satisfied, given herein as Eq. (4a), (4b), and (4c)

(a) For columns not braced against sidesway

$$\frac{k l_u}{r} \leq 17 \tag{4a}$$

(b) For columns braced against sidesway

$$\frac{k l_u}{r} \leq 29 + 12\frac{M_1}{M_2} \tag{4b}$$

$$\frac{k l_u}{r} \leq 35 \tag{4c}$$

where M_1/M_2 is negative if the column is bent in single curvature and positive for double curvature; l_u is unsupported length of column; and k is effective length factor for compression members. The effective length factor reflects column-end restraint conditions, which depend on the relative stiffness of the columns to the floor members at the top and bottom of joints given by

$$\omega = \frac{\left(\frac{EI}{l_c}\right)_{col,above} + \left(\frac{EI}{l_c}\right)_{col,below}}{\left(\frac{EI}{l}\right)_{beam,left} + \left(\frac{EI}{l}\right)_{beam,right}} \tag{5}$$

The values obtained by Eq. (5) are used to calculate k, using Fig. R6.2.5.1a and Fig. R6.2.5.1b for non-sway and sway frames, respectively, shown as Fig. 2, which is then

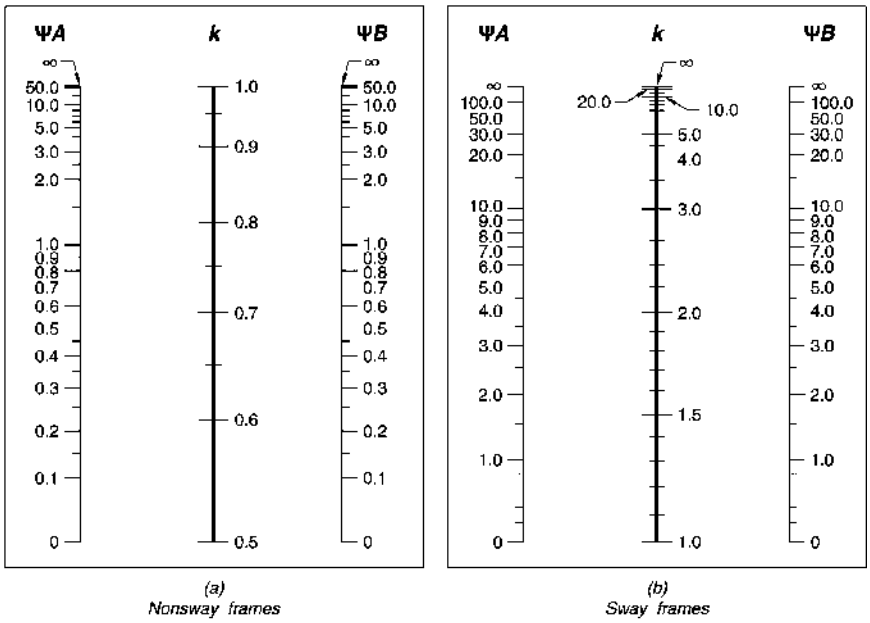

Fig. 2—Jackson and Moreland alignment charts (as given in ACI CODE-440.11-22).

used in Eq. 6.2.5.1a (4a), 6.2.5.1b (4b), and 6.2.5.1c (4c) to determine if the slenderness of columns could be neglected.

r is the radius of gyration. Its value can be calculated as given in Code Section 6.2.5.2

$$\sqrt{I_g/A_g}$$

which is (a) 0.30 times the dimension in the direction stability being considered for rectangular columns; or (b) 0.25 times the diameter of circular columns.

The moment of inertia and cross-sectional areas for elastic analysis at factored load level may be calculated by Code Section 6.6.3.1.1 and is shown in Table 3. It should be noted that moment of inertia values in ACI CODE-440.11-22 are lower than those provided in ACI 318-19 for steel-RC due to lower stiffness of GFRP reinforcement.

Code Section 6.6.4.6.4 requires magnifying the first-order moment to consider the second-order effects produced by slenderness in sway frames, given as Eq. (6a) and (6b)

$$M_1 = M_{1ns} + \delta_s M_{1s} \quad (6a)$$

$$M_2 = M_{2ns} + \delta_s M_{2s} \quad (6b)$$

where M_1 is the lesser factored end moment on a compression member; M_{1ns} is the factored end moment on a compression member at the end at which M_1 acts, due to loads that cause no appreciable sidesway, calculated using a first-order elastic frame analysis; M_{1s} is the factored end moment on a compression member at the end at which M_1 acts, due to loads that cause appreciable sidesway, calculated using a first-order elastic frame analysis; and M_2 is the greater factored end moment (always positive) on a compression member. If transverse loading occurs between supports, M_2 is taken as the largest moment occurring on a member; M_{2ns} is the factored end moment on a compression member at the end at which M_2 acts, due to loads that cause no appreciable sidesway, calculated using a first-order frame analysis; M_{2s} is the factored end moment on a compression member at the end at which M_2 acts, due to loads that cause appreciable sidesway, calculated using a first order elastic frame analysis; and δ_s is the moment magnification factor for sway frames. Code Section 6.6.4.6.2 provides two ways to calculate its value, given as Eq. (7a) and (7b)

Table 3—Moment of inertia and cross-sectional area for elastic analysis

Member end condition		Moment of inertia	Cross-sectional area for axial deformations	Cross-sectional area for shear deformations
Columns		$0.4I_g$	$1.0A_g$	b_w x h
Walls	Uncracked	$0.4I_g$		
	Cracked	$0.15I_g$		
Beams		$0.15I_g$		

$$\delta_s = \frac{1}{1-Q} \geq 1 \quad (7a)$$

$$\delta_s = \frac{1}{1-\dfrac{\sum P_u}{0.75\sum P_c}} \geq 1 \quad (7b)$$

The critical buckling load P_c is calculated by Code Section 6.6.4.4.2, given as

$$P_c = \frac{\pi^2 (EI)_{eff}}{(k l_u)^2} \quad (8)$$

where P_c is critical buckling load; kl_u is effective length (the length of a pin-ended column having same buckling load as original column); and $(EI)_{eff}$ is effective moment of inertia, which can be calculated by Code Section 6.6.4.4.4a and 6.6.4.4.4b, given herein as Eq. (9a) and (9b)

$$(EI)_{eff} = \frac{0.24 E_c I_g}{1 + B_{dns}} \quad (9a)$$

$$(EI)_{eff} = \frac{0.2 E_c I_g}{1 + B_{dns}} + 0.75 E_f I_f \quad (9b)$$

where B_{dns} is the ratio of maximum factored sustained axial load to maximum factored axial load; and I_f is the moment of inertia of the GFRP bars about the centroid of the cross section.

Code Section 6.6.4.5 implies amplifying M_2 for the effects of member curvature in a non-sway frame given as

$$M_c = \delta M_2 \quad (10)$$

where M_c is factored moment amplified for the effects of member curvature; and δ is magnification factor for non-sway frames as given in Code Section 6.6.4.5.2

$$\delta = \frac{C_m}{1 - \frac{P_u}{0.75 P_c}} \geq 1.0 \quad (11)$$

where C_m (factor relating actual moment diagram to an equivalent uniform moment diagram) shall be in accordance with 6.6.4.5.3a and 6.6.4.5.3b, given herein as Eq. (12a) and (12b):

(a) For columns without transverse loads applied between supports

$$C_m = 0.6 - 0.4 \frac{M_1}{M_2} \quad (12a)$$

(b) For columns with transverse loads applied between supports

$$C_m = 1.0 \quad (12b)$$

EXAMPLES OF COLUMN DESIGN AND DISCUSSION

The required strength for the two columns subjected to lateral and gravity loads was checked using the factored load combinations in Chapter 5 and analysis procedures in Chapter 6 of the ACI CODE-440.11. The calculated values of axial load, moment, and shear demands used in this study are given in Table 4 as originally available from the sources of the steel-RC cases.[12,15] It should be noted that for simplicity, a single combination of ultimate axial load and moment (that is, P_u and M_u) for each of the two columns was adopted, whereas in practice, the demand of several combinations of loads and moments must be satisfied. Also, the design was carried out by keeping the reinforcement amount as close as possible to the minimum requirements of the Code (that is, 1%A_g).

Sway column using low- and high-modulus GFRP bars

The column was designed using the Code-referenced low-modulus (E_f = 6500 ksi [44,815 MPa]) GFRP bars, with a concrete strength of 5000 psi (35 MPa). The columns were designed as per procedure provided in ACI CODE-440.11-22, Fig. R6.2.5.3. The column in this design example is laterally unbraced; therefore, slenderness effects were checked as per ACI CODE-440.11-22, Eq. (6.2.5.1a) (that is, $kl_u/r < 17$). The unsupported length of the column, as shown in Fig. 1(a), is 15.5 ft (4.72 m) and its cross-section dimensions were calculated using relations provided in this paper equal to 26 x 26 in. (660 x 660 mm). The effective length factor was calculated using alignment charts given in Fig. R6.2.5.1 in ACI CODE-440.11-22 (that is, Fig. 2), which depend on the relative stiffnesses of columns to the floor members at column top and bottom joints. In this design example, the column frames into beams at the top joint, whereas it frames at bottom in a two-way slab. It was assumed that the columns in the stories above and below had the same cross-section dimensions. The gross moment of inertia of the column was equal to 38,080 in.^{4} (15.8 × 10^9 mm^4), and the effective moment of inertia calculated as per Table 3 was equal to 15,232 in.^{4} (6.3 × 10^9 mm^4).

Table 4—Factored axial, shear, and moment values

Ultimate loads	Sway column	Non-sway column
V_u, kip	22	—
P_u, kip	789	134
$(M_u)_{top}$, kip-ft	145	38
$(M_u)_{bott}$, kip-ft	197	94.4

Note: 1 kip = 4.44 kN; 1 kip-ft = 1.35 kN-m.

As stated in ACI CODE-440.11-22, Section R6.6.3.1.1, it is sufficiently accurate to take the gross moment of inertia of a T-beam equal to twice that of its web. Using this approach, the moment of inertia of T-beams framing into the column at the top joint was calculated equal to 81,000 in.^{4} (33.7 × 10^9 mm^4), and the effective moment of inertia as per Table 3 was equal to 12,150 in.^{4} (5 × 10^9 mm^4). Similarly, the moment of inertia at the lower joint was calculated for the slab framing into the column. The width of the slab in the transverse direction was considered equal to 14 ft (4.3 m) and its thickness equal to 7 in. (178 mm), as given in the ACI 318-19 Design Handbook.[13] Its gross moment of inertia was calculated equal to 4802 in.^{4} (2 × 10^9 mm^4), which reduced to 720 in.^{4} (0.3 × 10^9 mm^4) when calculating effective moment of inertia as per Table 3.

The relative stiffness at the top and bottom joints was calculated as per Eq. (5) of this paper (as given in ACI CODE-440.11-22), which were found equal to 3 for top and 30 for bottom joints, respectively. Using relative stiffness factors in alignment charts given in Fig. 2, the effective length factor was calculated equal to 2.8 and radius of gyration equal to 7.5 from ACI CODE-440.11-22, Section 6.2.5.2. The values of effective length factor, unsupported length of column, and radius of gyration were used in Eq. (6.2.5.1a). It was observed that slenderness effects cannot be neglected; hence the column should be designed by considering the second-order effects.

The second step after slenderness is to investigate if the column should be analyzed as sway or non-sway. ACI CODE-440.11-22, Section 6.6.4.3 states that a column can be analyzed as part of a non-sway frame if: (a) column end moments due to second-order effects do not exceed 5% of the first-order end moments; and (b) the stability index

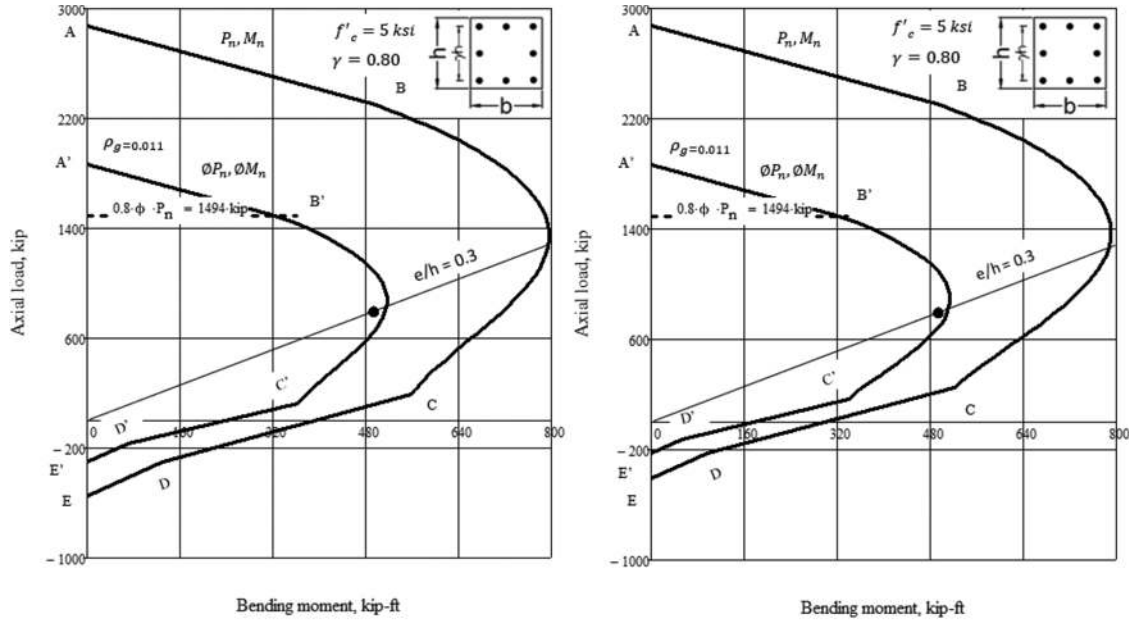

Fig. 3—Interaction diagram for GFRP-RC sway columns.

calculated as per 6.6.4.4.1 does not exceed 0.05. The sum of all factored column and wall gravity loads were considered as given in ACI 318-19 Design Handbook[13] equal to 25,700 kip (114,320 kN) and horizontal story shear equal to 775 kip (3450 kN). Because the first story of a building is often assumed hinged at $0.67l_u$, the following equation was used to calculate deflection at a distance l to the hinge

$$\delta_o = \frac{V_{us} l^3}{3\sum EI} \tag{13}$$

The deflection was found equal to 1.16 in. (29 mm), and the stability index (calculated as per Eq. (3)) was equal to 0.176, which is greater than 0.05; hence, the column was analyzed and designed as part of a sway frame. For a sway frame, the secondary moments at the end of the column due to differential movement of the ends of columns were calculated as per ACI CODE-440.11-22 Section 6.6.4.6.4 as given by Eq. (6a) and (6b) in this paper. The sway magnification factor was calculated as per Section 6.6.4.6.2, given as Eq. (7a) and (7b) in this paper. ACI CODE-440.11-22 allows three approaches for calculating moment magnifier, including: the *Q* method, the sum of *P* method, and second-order elastic analysis. Because the example is based on hand calculations, the sum of *P* method was used to calculate sway magnification factor, as given by Eq. (7b). The critical buckling load can be calculated as per Section 6.6.4.4.2 in ACI CODE-440.11-22, given by Eq. (8) in this paper. The effective stiffness was calculated as per Section 6.6.4.4.4a, given by Eq. (9a), where factor B_{dns} was considered equal to zero for short-term lateral loads as allowed in ACI CODE-440.11-22, Section R6.6.4.6.2. The effective stiffness was calculated equal to 36.8×10^6 kip-in.^{2} (105.6×10^9 kN-mm^2) and critical load equal to 1340 kip (5960 kN). The sway magnification factor calculated as per Eq. (7b) was equal to 2.5. The magnified moments calculated as per Section 6.6.4.6.1 were the lesser moment (M_1) equal to 368 kip-ft (500 kN-m) and the larger end moment (M_2) equal to 493 kip-ft (670 kN-m).

ACI CODE-440.11-22, Section 10.6.1.1 states that area of longitudinal reinforcement shall be at least $0.01A_g$. Once the concrete cross-section dimensions and reinforcement amount are selected, the strength interaction diagram for that case is constructed by means of the spreadsheet specifically developed for GFRP-RC. The spreadsheet allows placing the reinforcement in the first (d_1) and last (d_n) layers as close to the outer column face as permitted by the Code. Bars could also be inserted along the two lateral sides of the cross section. The spreadsheet recomputes capacity resulting from changes in sectional strain to create a smooth plot of a nominal strength interaction diagram (P_n-M_n). The values of nominal axial force and moment are multiplied by strength reduction factors, and limits on axial strength are applied to create the design strength interaction diagram (ϕP_n-ϕM_n). As an example of the output of the spreadsheet, Fig. 3 shows the design interaction diagram developed for the 26 x 26 in. (660 x 660 mm) cross section of the sway column with reinforcement consisting of eight No. 9 (M29) bars for both low- and high-modulus GFRP. The horizontal dotted line in the interaction diagrams shows the limit on the nominal axial compressive strength to account for accidental eccentricities as per ACI CODE-440.11-22, Table 22.4.2.1 (that is, 0.8 for a column with ties).

The interaction diagram shown in Fig. 3 was constructed by locating critical points according to x (that is, the location of neutral axis) based on selected P_n-M_n pairs. The two *P*-*M* curves show nominal strength (that is, points shown with plain letters A, B, C, D, and E) and design strength (that is, points shown with dashed letters A′, B′, C′, D′, and E′). Specifically, point A in Fig. 3 represents the maximum nominal

Table 5—Steel-RC and GFRP-RC sway column analysis and design

Ultimate loads		Column analysis				Column design					
		Effective length factor		Moment magnification factor		Steel-RC column			GFRP-RC column		
Applied load, kip	Moment, kip-ft	Steel	GFRP	Steel	GFRP	Magnified moment, kip-ft	Size, in.	Reinforcement area, in.^{2} (ratio, %)	Magnified moment, kip-ft	Size, in.	Reinforcement area, in.^{2} (ratio, %)
789	197	2.2	2.8	1.12	2.5	221	24 x 24	8 No. 8 (1.0)	493	26 x 26	8 No. 9 (1.1)

Note: 1 kip = 4.44 kN; 1 kip-ft = 1.35 kN-m; 1 in.^{2} = 645 mm^2.

compressive force corresponding to zero eccentricity (M_n = 0 and x = +¥), which is the uppermost point in the interaction diagram. Point B′ on the design domain limit represents the case of maximum compressive force usable in design. The two modes of failure (tension and compression-controlled modes) are separated by the "balanced failure" shown by point C′, representing FRP rupture (note: the guaranteed strength of GFRP bars is replaced by $0.01E_f$, as specified in the Code) and concrete crushing simultaneously ($x = x_b$). If the neutral axis shifts beyond x_b, the failure mode shifts from compression to tension. The lowermost point in the interaction diagram (E′) corresponds to maximum tensile force (M_n = 0 and x = –¥), and maximum strain in the reinforcement. Any combination of ultimate axial load and moment (that is, P_u-M_u, shown by a black dot) laying within the interaction curve represents safe (and outside, an unsafe) column design.

The GFRP-RC column subjected to same ultimate loads required larger cross section compared to steel-RC as the axial strength of GFRP reinforcement is not considered in resistance calculations and is replaced with equal area of concrete. Also, the higher magnification factor resulted in a very large, magnified moment, as given in Table 5, together with the limits on the maximum strength of GFRP bars, the GFRP-RC column required bigger cross-sectional dimensions than a steel-RC column. For example, a column designed with GFRP reinforcement failed with dimensions similar to that of the steel-RC (24 x 24 in. [610 x 610 mm]); therefore, the column size was increased to 26 x 26 in. (660 x 660 mm) to augment its load-carrying capacity to exceed the demand. The minimum reinforcement depends on the gross area of the cross section (A_{fmin} = $0.01A_g$); therefore, a GFRP-RC column required more reinforcement area than steel-RC. For example, a column designed with GFRP-RC required eight No. 9 (M29) bars, whereas that with steel-RC required eight No. 8 (M25) bars. The values of effective length factor, moment magnification factor, cross-sectional area, and longitudinal reinforcement for a column in sway frame are provided in Table 5, which includes values for steel-RC taken from ACI 318-19 Design Handbook.[13]

This study also investigated the effect of high-modulus (E_f = 8700 ksi [60,000 MPa]) GFRP reinforcement on column design. The compressive strength of GFRP reinforcement is not considered in resistance calculations when the GFRP is in compression (that is, the area of GFRP replaced with concrete); hence, the column dimensions remained same as with low-modulus GFRP bars (26 x 26 in. [660 x 660 mm]). Further, due to a limit on maximum GFRP tensile strain (that is, 0.01) by Code Section 10.3.2.1, only a slight increase in the capacity (9%) for the column subjected to same demand (that is, as a low-modulus GFRP-RC column given in Table 5) was noticed. The column cross section, reinforcement details, and interaction diagrams developed for both low- and high-modulus GFRP-RC columns are shown in Fig. 3.

Non-sway column using low- and high-modulus GFRP bars

The column example taken from the textbook by Wight and Macgregor[15] was redesigned with GFRP reinforcement, considering it as part of a non-sway frame as the stability index (Q = 0.04) and magnified moment were within the limits stated in Section 6.6.4.3 for a non-sway frame. The magnification factor calculated by analysis was 0.7; hence, a minimum magnification factor of 1.0 was used to calculate the magnified moment. The *P-M* diagram developed for non-sway columns showing the nominal and design capacity curves is shown in Fig. 4. The (P_n, M_n) curve shows the capacity before and (ΦP_n, ΦM_n) after the application of the strength reduction factors. The column failed with dimensions of the steel-RC section (14 x 14 in. [356 x 356 mm]) and reinforcement consisting of four No. 8 (M25) bars, as shown in Fig. 4(a), where the demand (P_u-M_u) shown by the black dot lies outside the design capacity curve. Therefore, the cross-section dimensions were increased to 18 x 18 in. (460 x 460 mm) and reinforcement consisting of four No. 9 (M29) bars to satisfy the demand. As shown in Fig. 4(b), the demand is within the design capacity curve, representing a safe column. It was observed that GFRP-RC columns require bigger cross sections and reinforcement areas than steel-RC. The effective length factor, moment magnification factor, cross-sectional dimensions, and required reinforcement are shown in Table 6.

Similar to the case of sway frames, an effort was made to investigate the impact of using high-modulus bars on non-sway column design. The high-modulus bars showed a 12% increase in the column capacity compared to low-modulus GFRP-RC column subjected to same demand (that is, the low-modulus GFRP-RC column given in Table 6). The column cross section, reinforcement details, and interaction diagrams developed for non-sway column are shown in Fig. 4.

PARAMETRIC STUDY

A parametric study was carried out by varying concrete compressive strength f_c', aspect ratio, and applied load eccentricity to evaluate implications on the design of GFRP-RC column cross sections. For comparison, steel-RC sections

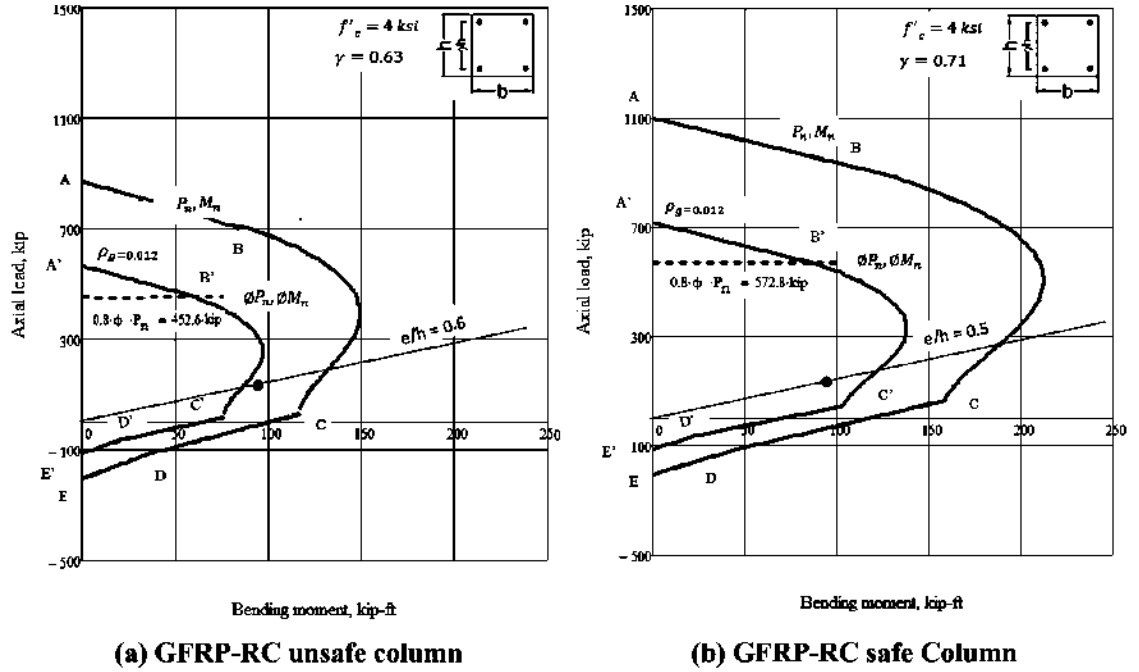

(a) GFRP-RC unsafe column (b) GFRP-RC safe Column

Fig. 4—Interaction diagram of GFRP-RC non-sway columns.

Table 6—Steel-RC and GFRP-RC non-sway column analysis and design

Ultimate loads		Column analysis				Column design					
		Effective length factor		Moment magnification factor		Steel-RC column			GFRP-RC column		
Applied load, kip	Moment, kip-ft	Steel	GFRP	Steel	GFRP	Magnified moment, kip-ft	Size, in.	Reinforcement area, in.^{2} (ratio, %)	Magnified moment, kip-ft	Size, in.	Reinforcement area, in.^{2} (ratio, %)
134	94.4	0.77	0.80	0.53	0.7	94.4	14 x 14	4 No. 7 (1.2)	94.4	18 x 18	4 No. 9 (1.2)

Note: 1 kip = 4.44 kN; 1 kip-ft = 1.35 kN-m; 1 in.^{2} = 645 mm^2.

were also designed by changing the parameters stated previously. The yielding strength of steel used was 60 ksi (414 MPa) and modulus of elasticity 29,000 ksi (200 GPa), whereas the GFRP reinforcement used was compliant with ASTM D7957 as referenced by ACI CODE-440.11-22. To compare results with steel-RC, both sections (steel-RC and GFRP-RC) were subjected to same demand (that is, no magnification factors were applied). Therefore, a cross section of 20 x 20 in. (508 x 508 mm) was used and varied as required. The reinforcement ratio was kept as close to minimum required 1% as possible throughout the parametric study.

Design with different f_c' values

Four different values of concrete strength (f_c' = 2500, 5000, 7500, and 10,000 psi [18, 35, 52, 70 MPa]) were used. The cross sections (steel-RC and GFRP-RC) were subjected to ultimate axial compressive load of 789 kip (3510 kN) and ultimate moment of 2367 kip-in. (267 kN-m) (no magnification factors applied). The reinforcement area was kept as close to 1% of gross concrete area as possible. As expected, RC cross-section dimensions significantly decreased with increasing concrete strength. For example, as shown in Table 7, at concrete strength of 5000 psi (3 MPa), the required GFRP cross section to satisfy the demand (P_u = 789 kip [3510 kN] and M_u = 2367 kip-in. [267 kN-m]) is 22 x 22 in. (560 x 560 mm), which decreased to 18 x 18 in. (460 x 460 mm) and 16 x 16 in. (406 x 406 mm) as concrete compressive strength increased to 7500 and 10,000 psi (52 and 70 MPa) respectively. Similarly, the required reinforcement decreased from six No. 9 (M29) bars at f_c' = 5000 psi (35 MPa) to four No. 9 (M29) and four No. 8 (M25) at f_c' = 7500 and 10,000 psi (52 and 70 MPa), respectively (note: reinforcement used at all three concrete strengths is 1.2%A_g). It was further noticed that, at higher concrete strength, GFRP-RC sections performed similar to steel-RC. For example, as shown in Table 7, at f_c' = 5000 psi (35 MPa) the required dimensions for GFRP-RC section are 22 x 22 in. (560 x 560 mm), whereas those for steel-RC are 20 x 20 in. (508 x 508 mm). However, when concrete strength increased to 7500 psi (52 MPa) and above, the required dimensions for both RC sections are the same.

In contrast, when concrete strength was decreased to 2500 psi (18 MPa), the required cross sections significantly increased to satisfy the demand. Similar effects were observed in the case of steel-RC; however, unlike steel-RC, GFRP-RC dimensions and reinforcement area increased more rapidly. For example, the steel-RC section satisfied the demand with cross-sectional dimensions equal to 26 x 26 in. (660 x 660 mm) with eight No. 9 (M29) bars (ρ = 0.011A_g), whereas GFRP-RC required 28 x 28 in. (710 x 710 mm) with eight No. 9 (M29) bars (ρ = 0.01A_g). It has

Table 7—Cross sections at different f_c' values

Demand		Eccentricity, in.	Concrete strength, psi	Steel-RC			GFRP-RC		
Applied load, kip	Ultimate moment, kip-in.			h/6	Size, in.	Reinforcement area, in.^{2} (ratio, %)	h/6	Size, in.	Reinforcement area, in.^{2} (ratio, %)
789	2367	3.0	f_c' = 2500	4.3	26 x 26	8 No. 9 (1.1)	4.6	28 x 28	8 No. 9 (1.0)
			f_c' = 5000	3.3	20 x 20	4 No. 9 (1.0)	3.6	22 x 22	6 No. 9 (1.2)
			f_c' = 7500	3.0	18 x 18	4 No. 9 (1.2)	3.0	18 x 18	4 No. 9 (1.2)
			f_c' = 10,000	2.7	16 x 16	4 No. 8 (1.2)	2.7	16 x 16	4 No. 8 (1.2)

Note: 1 kip = 4.44 kN; 1 kip-in. = 113 kN-mm; 1 in. = 25.4 mm; 1 in.^{2} = 645 mm^2.

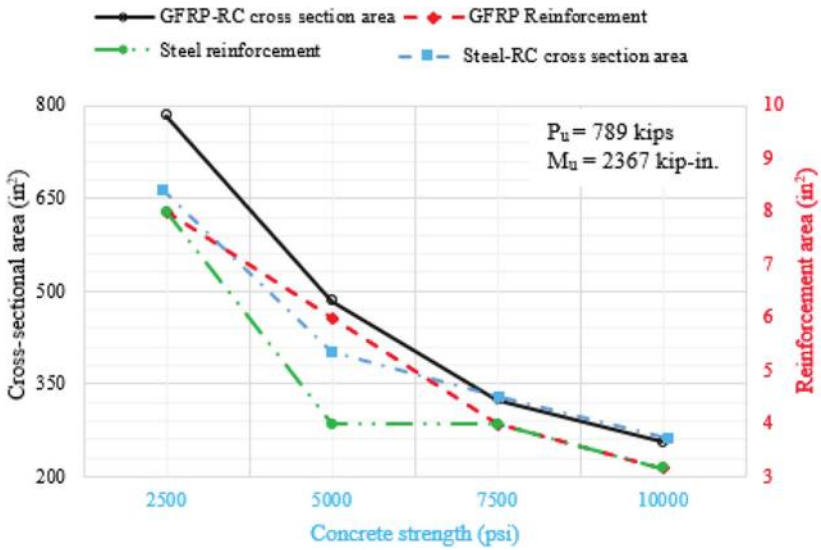

Fig. 5—Cross sections at different f_c' *values.*

been noted that higher concrete strengths have profound effects on cross-sectional dimensions and reinforcement area of GFRP-RC. The effect of changing concrete strength on cross-sectional dimensions and reinforcement area can be visualized in Table 7 and Fig. 5.

Also, it is worth noting here that kern distance significantly decreases with increasing concrete strength. For example, for GFRP-RC, at f_c' = 5000 psi (35 MPa), the applied axial load acts at e = 3.0 in. (76 mm), which is within kern distance (h/6 = 3.6 in. [92 mm]), implying that the axial load does not cause tension in the section. However, at a concrete strength of 7500 psi (52 MPa), the kern distance significantly decreased and ultimately, the eccentricity falls outside the kern (e = 3.0 in. [76 mm] and h/6 = 2.7 in. [69 mm]) when f_c' = 10,000 psi (70 MPa). Therefore, as observed by calculations, higher concrete strength help decreasing cross-sectional dimensions and axial load causes tension in the section. Subsequently, GFRP-RC cross sections take advantage of tensile properties of GFRP reinforcement and require dimensions similar to steel-RC. For example, as shown in Table 7, at f_c' = 7500 and 10,000 (52 and 70 MPa), GFRP-RC required cross-sectional areas of 18 x 18 in. (460 x 460 mm) and 16 x 16 in. (406 x 406 mm) and reinforcement of four No. 9 (M29) and four No. 8 (M25) bars, respectively—the same as steel-RC.

Design with different cross-section aspect ratio

The cross-section aspect ratio was changed from 1.0 to 1.5 and 2.0. The ultimate axial load and moment were kept same for both RC cross sections (steel-RC and GFRP-RC) with no magnification factors applied (P_u = 789 kip [3510 kN], M_u = 2367 kip-in. [267 kN-m]). The reinforcement ratio was kept as close to 1% of the gross concrete area as possible and concrete strength was 5000 psi (35 MPa).

As expected, when changing the cross-section aspect ratio from 1.0 to 1.5 and 2.0, the required dimensions for both RC sections decreased. For example, as shown in Table 8, the GFRP-RC cross-sectional area decreased to 17 x 26 in. (432 x 660 mm) from 22 x 22 in. (560 x 560 mm) and steel-RC to 16 x 24 in. (406 x 610 mm) from 20 x 20 in. (508 x 508 mm) when changing aspect ratio from 1.0 to 1.5. It further decreased to 14 x 28 in. (356 x 710 mm) and 13 x 26 in. (330 x 660 mm) for GFRP-RC and steel-RC, respectively, when increasing the aspect ratio to 2.0. It can be observed in Table 8 that the required dimensions and reinforcement area for GFRP-RC are larger than steel-RC for the three aspect ratios investigated. It should be noted that, in all three cross sections the axial load is applied at e = 3.0 in. (76 mm), which falls within the kern distance (h/6). This implies that the applied load does not cause tension in the cross section. The effect of changing the aspect ratio may be more prominent for GFRP-RC cross sections subjected to highly eccentric loads (that is, eccentricity exceeding kern distance h/6). Therefore, an attempt was made to investigate the cross

Table 8—Cross sections at different aspect ratios

Demand				Steel-RC			GFRP-RC		
Applied load, kip	Ultimate moment, kip-in.	Eccentricity, in.	Aspect ratio	*h*/6	Size, in.	Reinforcement area, in.^{2} (ratio, %)	*h*/6	Size, in.	Reinforcement area, in.^{2} (ratio, %)
789	2367	3.0	1.0	3.3	20 x 20	4 No. 9 (1.0)	3.7	22 x 22	6 No. 9 (1.2)
			1.5	4.0	16 x 24	4 No. 9 (1.0)	4.3	17 x 26	6 No. 8 (1.0)
			2.0	4.3	13 x 26	4 No. 9 (1.1)	4.6	14 x 28	4 No. 9 (1.0)
395	2367	6.0	1.0	3.0	18 x 18	4 No. 9 (1.2)	3.0	20 x 20	4 No. 9 (1.0)
			1.5	3.7	14 x 22	4 No. 8 (1.0)	3.7	14 x 22	4 No. 8 (1.0)
			2.0	4.0	12 x 24	4 No. 8 (1.0)	4.0	12 x 24	4 No. 8 (1.0)

Note: 1 kip = 4.44 kN; 1 kip-in. = 113 kN-mm; 1 in. = 25.4 mm; 1 in.^{2} = 645 mm^2.

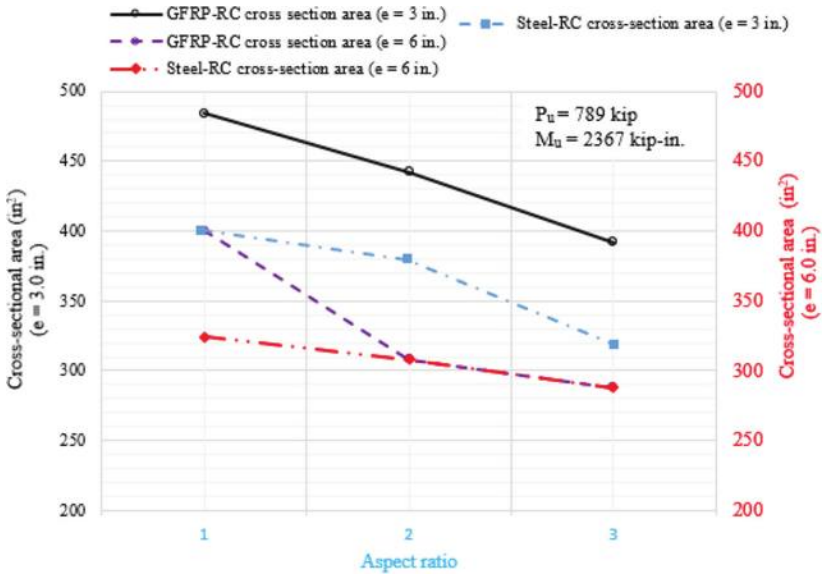

Fig. 6—Cross sections at different aspect ratios.

sections by increasing the eccentricity to 6.0 in. (152 mm). The axial load was decreased to half (395 kip [1760 kN]) while moment was kept the same (2367 kip-in. [267 kip-ft]). For the GFRP-RC, it was observed that at an aspect ratio of 1.0, the required dimensions decreased to satisfy the demand (20 x 20 in. [508 x 508 mm] from 22 x 22 in. [560 x 560 mm]), as the axial load decreased to half of original load). It was further observed that for GFRP-RC the required dimensions and reinforcement area significantly decreased with increasing aspect ratio and were similar to steel-RC at aspect ratios equal to 1.5 and 2.0. For example, as shown in Table 8, at aspect ratios of 1.5 and 2.0, the required dimensions for GFRP-RC are 14 x 22 in. (356 x 560 mm) and 12 x 24 in. (305 x 610 mm), which are 23% and 28% less from a cross section with an aspect ratio of 1.0 (that is, 20 x 20 in. [508 x 508 mm]) and are the same as steel-RC at same aspect ratios. For all three aspect ratios, the eccentricity is outside the kern distance (*h*/6), implying that there is tension in the cross sections. Figure 6 shows the trend of changing the cross-sectional area when increasing the aspect ratio at eccentricities of 3.0 and 6.0 in. (76 and 152 mm).

Design with different load eccentricities

The analysis was carried out with the intent of changing eccentricities by altering the values of axial load while keeping the moment constant (M_u = 2367 kip-in. [267 kN-m]), with no magnification factors applied, to evaluate the effect on cross-sectional dimensions and reinforcement area. The eccentricities were gradually enhanced at increments of 0.5 in. (13 mm), except for the points inside (0.1*h*), exactly on (*h*/6), and outside (0.2*h*) the kern (note: the kern distances are based on GFRP-RC cross-section dimensions). For square cross sections, the eccentricity values used in the calculations are 1.0., 1.5, 2.0, 2.4, 2.5, 3.0, 3.6, and 4.0. The reinforcement ratio was kept as close to a minimum 1% of the gross concrete area as possible and the concrete strength used was 5000 psi (35 MPa). To compare the efficacy of GFRP-RC, steel-RC cross sections were also designed by changing the same parameters as stated previously. It should be noted that both RC sections were subjected to same demand (that is, no magnification factors were applied).

The cross-section design started with minimum cross-sectional area sufficient to satisfy the demand at e = 1.0 in. (25.4 mm), as shown in Table 9. It can be observed in Table 9 that when axial loads are high, the required cross-sectional dimensions for GFRP-RC increase more rapidly compared to steel-RC. For example, at an eccentricity value equal to 1.0 in. (25.4 mm) (P_u = 2367 kip [10,530 kN]), the required dimensions for GFRP-RC are 34 x 34 in. (860 x 860 mm),

Table 9—Cross sections with different eccentricities at constant moment

Eccentricity, in.	Ultimate load, kip	Steel-RC			GFRP-RC		
		e/*h*	Cross-section area, in.	Reinforcement area, in.^{2} (ratio, %)	*e*/*h*	Cross-section area, in.	Reinforcement area, in.^{2} (ratio, %)
1.0	2367	0.03	32 x 32	12 No. 9 (1.1)	0.03	34 x 34	12 No. 9(1.0)
1.5	1578	0.05	26 x 26	8 No. 9 (1.1)	0.05	28 x 28	8 No. 9(1.0)
2.0	1184	0.09	22 x 22	6 No. 9 (1.2)	0.08	24 x 24	6 No. 9(1.0)
2.4 (0.1*h*)	1075	0.10			0.10		
2.5	947	0.11			0.11	22 x 22	6 No. 9(1.2)
3.0	789	0.15	20 x 20	4 No. 9 (1.0)	0.13		
3.6 (*h*/6)	710	0.18			0.18	20 x 20	4 No. 9(1.0)
4.0 (0.2*h*)	592	0.2			0.2		

Note: 1 in. = 25.4 mm; 1 kip = 4.44 kN; 1 in.^{2} = 645 mm^2.

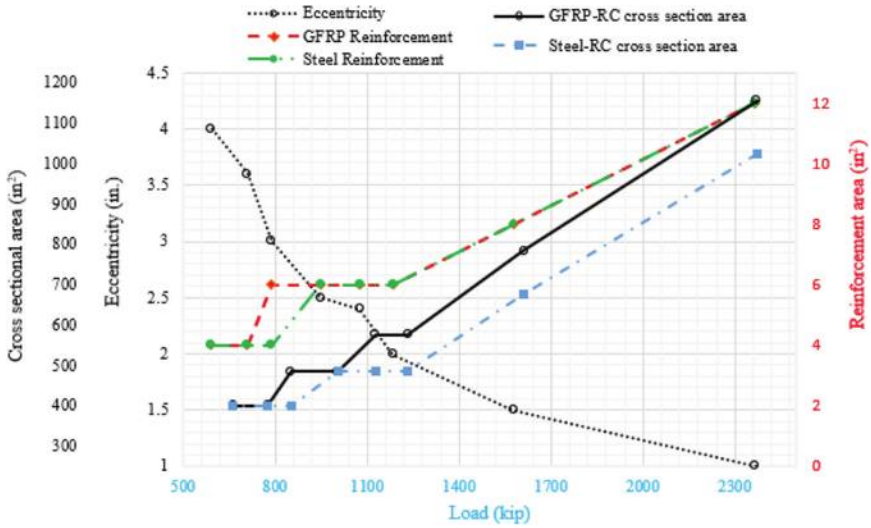

Fig. 7—Cross sections with different eccentricities at constant moment.

and those for steel-RC are 32 x 32 in. (812 x 812 mm). However, when the eccentricity value increases to 4.0 in. (100 mm), the required dimensions for two RC sections are the same. Similarly, the required reinforcement area also decreases and is the same for GFRP-RC and steel-RC (four No. 9 [M29] bars). Despite stricter design limits compared to steel-RC, the GFRP was found effective to resist loads with high eccentricities, especially for values exceeding the kern distance (*h*/6). For example, in Table 9, at eccentricity *e* = 4.0 in. (100 mm), the axial load acts outside the kern distance (*h*/6 = 3.6), causing tension in the cross section and requires that cross-section dimensions for two RC sections are same. The required reinforcement and cross-sectional area with changing eccentricity values can be seen in Table 9 and increase in reinforcement requirements and cross-sectional area with increasing eccentricities are visualized in Fig. 7.

COLUMN PROVISIONS FOR SHEAR IN CODE-440.11-22

ACI CODE-440.11-22 Section 10.5.3.1 references Section 22.5 for the calculation of nominal shear strength of column, which can be calculated as given in Section 22.5.1.1

$$V_n = V_c + V_f \tag{14}$$

where V_n is nominal shear strength; V_c is nominal shear strength provided by the concrete; and V_f is nominal shear strength provided by GFRP shear reinforcement.

The shear strength provided by concrete is calculated as the greater of two expressions, given by Code Sections 22.5.5.1a and 22.5.5.1b as follows

$$\begin{aligned} V_c &= 5\lambda k_{cr}\sqrt{f_c'}bd \quad \text{(US units)} \\ V_c &= 0.42\lambda k_{cr}\sqrt{f_c'}bd \quad \text{(SI units)} \end{aligned} \tag{15a}$$

$$\begin{aligned} V_c &= 0.8\lambda\sqrt{f_c'}bd \quad \text{(US units)} \\ V_c &= 0.066\lambda\sqrt{f_c'}bd \quad \text{(SI units)} \end{aligned} \tag{15b}$$

where k_{cr} is ratio of the depth of elastic cracked section neutral axis to the effective depth given by the Code Commentary Section R22.5.5.1, shown as follows

$$k_{cr,rect} = \sqrt{2\rho_f n_f + (\rho_f n_f)^2} - \rho_f n_f$$

where $\rho_f = (A_f/bd)$ is the reinforcement ratio; A_f is the area of GFRP reinforcement; $n_f = (E_f/E_c)$ is the modular ratio; and E_c is the concrete elastic modulus calculated as given by Code Section 19.2.2.1

$$\begin{aligned} E_c &= 57,000\sqrt{f_c} \quad \text{(US units)} \\ E_c &= 4700\sqrt{f_c} \quad \text{(SI units)} \end{aligned} \tag{17}$$

and $\lambda = \sqrt{2/(1 + [d/10])}$ ($\sqrt{2/(1 + 0.004d)}$ is the size effect factor as given in ACI CODE-440.11-22, Section 22.5.5.1.3.

The size effect factor was considered for these examples because h exceeded 10 in. (254 mm).

The shear strength provided by the GFRP reinforcement is as given in Code Section 22.5.8.5.3

$$V_f = A_{fv} f_{ft} (d/s) \tag{18}$$

where A_{fv} is the area of shear reinforcement as given in Code Commentary Eq. (R22.5.8.5)

$$\frac{A_{fv}}{s} = \frac{V_u - \Phi V_c}{\Phi f_{ft} d} \tag{19}$$

and f_{ft} is the permissible stress in the GFRP shear reinforcement. The design tensile strength of GFRP transverse reinforcement is controlled by the strength of the bent portion of the bar and by a strain limit of 0.005, as given by Code Section 20.2.2.6

$$f_{ft} \le (f_{fb}, 0.005E_f) \tag{20}$$

where f_{fb} is the guaranteed ultimate tensile strength of the bent portion of the bar. Its minimum value be taken as specified in ASTM D7957; and s is center-to-center spacing of transverse reinforcement.

Maximum spacing s_{max} between legs of shear reinforcement is calculated as the least of maximum spacing limitations given by Code in 10.6.2.2 and its Commentary in R22.5.8.5

$$s_{max} = \frac{A_{fv} \Phi f_{ft} d}{V_u - \Phi V_c} \tag{21}$$

$$\begin{aligned} s_{max} &= \frac{A_{fv} f_{ft}}{0.75\sqrt{f_c} b} \quad \text{(US units)} \\ s_{max} &= \frac{A_{fv} f_{ft}}{0.062\sqrt{f_c} b} \quad \text{(SI units)} \end{aligned} \tag{22a}$$

$$\begin{aligned} s_{max} &= \frac{A_{fv} f_{ft}}{50b} \quad \text{(US units)} \\ s_{max} &= \frac{A_{fv} f_{ft}}{0.35b} \quad \text{(SI units)} \end{aligned} \tag{22b}$$

The maximum tie spacing requirement is also provided in the Code Section 22.7.2.1. The maximum tie spacing shall not exceed $12d_b$ of longitudinal bar, $24d_b$ of tie bar, h, or b.

EXAMPLE OF SHEAR DESIGN AND DISCUSSION

The sway GFRP-RC column was designed for gravity load and magnified moment (P_u = 789 kip [3510 kN], M_u = 493 kip-ft [670 kN-m]) that required a cross-sectional area equal to 26 x 26 in. (660 x 660 mm). This section discusses the shear design of the aforementioned cross section subjected shear force (V_u) of magnitude 22 kip (98 kN), as given in Table 4. The shear strength provided by the concrete cross section (ΦV_c) was calculated with Eq. (22.5.5.1a) and (22.5.5.1b), as given in column provisions for shear. The GFRP bars used as transverse reinforcement were compliant with ASTM D7957,[12] which states that the guaranteed ultimate tensile force of the bent portion of a bar shall be greater than or equal to 60% of the values of guaranteed ultimate tensile force provided in ASTM D7957, Table 3.[12] Also, for transverse reinforcement, No. 4 (M13) bars were used, having a minimum inside diameter of the bend equal to 3 in. (76 mm) as given in ASTM D7957, Table 4.[12]

It was observed from the calculations that shear strength provided by the concrete cross section alone is not sufficient to resist the shear force. Hence the shear capacity must increase by means of shear reinforcement to satisfy the shear demand. It should be noted that limits on the shear strength provided by concrete resulted in lower V_c together with a 40% reduction in the strength at the bend of GFRP transverse reinforcement[12] significantly affect shear design. The limits on the maximum strength of GFRP transverse reinforcement given by Code Section 20.2.2.6 only allowed the maximum design tensile strength of reinforcement equal to 32.5 ksi (224 MPa), which is 70% less than actual strength value of No. 4 (M13) bars.

In this column example, to augment the shear strength of the cross section, No. 4 (M13) bars were used at 9 in. (228 mm) center-to-center. Whereas the same column when designed with steel-RC only required minimum shear reinforcement (that is, No. 4 [M29] at 16 in. [406 mm] center-to-center) to hold the longitudinal reinforcement, as the shear strength provided by the concrete cross section for steel-RC (24 x 24 in. [610 x 610 mm]) was sufficient to satisfy the shear demand.

The Code Sections 25.7.2.3a, 25.7.2.3b, and 25.7.2.3c require that lateral support from ties be provided for bars at every corner, and to bars with greater than 6 in. (152 mm) clear on each side. Therefore, in this column example, two C-shaped tie bars forming a diamond shape for middle longitudinal bars, in addition to two overlapping C-shaped tie bars for corner longitudinal reinforcement, were used, as shown in Fig. 8. The tie size, its dimensions, and their distribution along column height are schematically shown in Fig. 8 for a sway column.

The non-sway GFRP-RC column was subjected to an axial compressive load of 134 kip (596 kN), magnified moment of 94.4 kip-ft (128 kN-m), and no shear force value is specified in reference source.[15] To resist the gravity load and applied moment, the column required a cross-sectional area equal to 18 x 18 in. (460 x 460 mm) and four No. 9 (M29) longitudinal bars. Though no shear force is given in the column example, minimum reinforcement was still used to hold the longitudinal bars in position and avoid buckling.

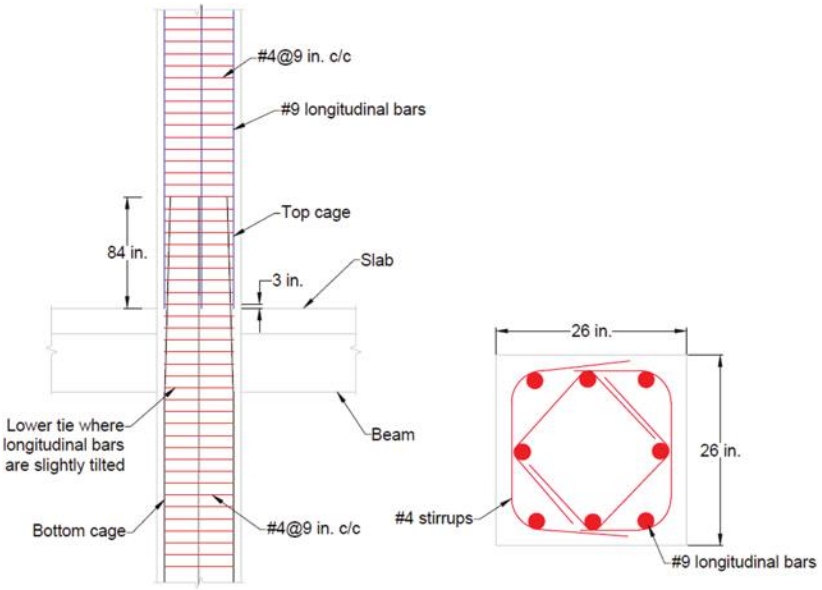

Fig. 8—Schematic of reinforcement details in sway GFRP-RC column.

The transverse reinforcement was used at maximum specified spacings as given in Code Sections 10.6.2.2 and 25.7.2.1 and Code Commentary Section R22.5.8.5.

In this column, for transverse reinforcement, No. 4 (M13) bars having an inside bend diameter equal to 3 in. (76 mm) as stated in ASTM D7957,[12] Table 4 was used. As mentioned in previous sections, the maximum spacing of ties cannot exceed $12d_b$, 24 diameter of tie bar, and the smallest dimensions of the member. Therefore, with the given cross-section dimensions and longitudinal reinforcement information in this column example, No. 4 (M13) ties were used at 12 in. (300 mm) center-to-center.

COLUMN PROVISIONS FOR DETAILING IN CODE-440.11-22

Code Section 25.4.1.1 requires that tension or compression reinforcement at each section of a member shall be developed on each side of that section by embedment length, hook, mechanical device, or a combination thereof. Development length l_d for bars in tension shall be greater of the values calculated by Code Sections 25.4.2.1(a), 25.4.2.1(b), and 25.4.2.1(c)

$$l_d = \frac{d_b\left(\frac{f_{fr}}{\sqrt{f_c}} - 340\right)}{13.6 + \frac{c_b}{d_b}}\omega \quad \text{(US units)}$$

$$l_d = \frac{d_b\left(\frac{f_{fr}}{0.083\sqrt{f_c}} - 340\right)}{13.6 + \frac{c_b}{d_b}}\omega \quad \text{(SI units)} \tag{23a}$$

in which c_b/d_b shall not be taken greater than 3.5, and where c_b is the lesser of: (a) the distance from center of a bar to nearest concrete surface, and (b) one-half the center-center spacing of bars being developed; d_b is the nominal bar diameter; f_{fr} is the GFRP tensile stress required to develop the full nominal section capacity; ω is the bar location modification factor, taken equal to 1.5, if more than 12 in. (300 mm) of fresh concrete is placed below the reinforcement being developed and 1.0 for all other cases.

$$20d_b \tag{23b}$$

$$12 \text{ in. } (300 \text{ mm}) \tag{23c}$$

The lap splice lengths in columns shall be calculated in accordance with 10.7.5 and 25.5. Code Section 10.7.5.2 states that in a column subjected to moment and axial force, tensile stresses may occur on one face of the column for moderate or large eccentricities. If such stresses occur, Code Section 10.7.5.2.2 requires tension splices to be used, which can be classified as Class A or Class B lap splices and calculated in accordance with Code Section 25.5.2.1, as given in Table 10.

Code Section 10.7.5.2.1 states that if the bar is compressive due to factored loads, compression lap splices shall be permitted. Given no experimental data on development length for GFRP bars in compression (l_{dc}), Code Section 25.4.9.1 states that the development length in compression shall be conservatively taken the same as that for tension as in Code Section 25.4.2.1.

The minimum overlap of tie bar ends shall be greater of $20d_b$ or 6 in. (152 mm), as in 25.7.2.3.1.

Code Section 10.7.6.2 states that the bottom tie shall be located not more than one-half the tie spacing above the top of footing or slab; similarly, the top tie shall be located not more than one-half the tie spacing below the lowest horizontal reinforcement in the slab, drop panel, or shear cap. If beams frame into all sides of column, the top tie shall be located not more than 3 in. (76 mm) below the lowest horizontal reinforcement in the shallowest beam.

Table 10—Lap splice length of GFRP bars in tension (ACI CODE-440.11-22, Section 25.5.2.1)

$A_{f,provided}/A_{f,required}$* over length of splice	Maximum percent of A_f spliced within required lap length	Splice type	l_{st}	
≥2.0	50	Class A	Greater of:	$1.0l_d$, $20d_b$, and 12 in.
	100	Class B	Greater of:	$1.3l_d$, $20d_b$, and 12 in.
<2.0	All classes	Class B		

*Ratio of area of reinforcement provided to area of reinforcement required by analysis at splice location.

Note: 1 in. = 25.4 mm.

DETAILING OF REINFORCEMENT FOR COLUMN EXAMPLES

The Code permits the use of the same equation for development lengths of GFRP bars in compression and tension (Eq. (25.4.2)). Therefore, the development length equation for GFRP bars was conservatively adopted as given in Code Section 25.4.2. Also, there is more than 12 in. (300 mm) of fresh concrete to be placed below the longitudinal bar being developed in a sway column; hence, the bar location modification factor (ω = 1.5) was also used. The Code specifies a maximum limit for the term c_b/d_b as 3.5, which in this column resulted as 1.83, well below the permitted limit. The development length was calculated using three equations mentioned in Code Section 25.4.2 and Eq. (25.4.2.1(a)) governed, which resulted in 64 in. (1625 mm).

The tensile bar stress at a point reaches its maximum value (limited by maximum strain 0.01), which is greater than $0.5f_{fu}$; also, the ratio of area of reinforcement provided to the area of reinforcement required in this example is less than 2.0 (that is, 1.18); therefore, Class B lap splices were used. The splice length was calculated as given in Code Section 25.5.2.1 (that is, the greater of $1.3l_d$, $20d_b$, and 12 in. [300 mm]), which resulted 84 in. (3134 mm).

The lap splice calculated for the steel-RC column was 33 in. (840 mm), which shows that GFRP-RC columns require very large splice lengths (2.5 times greater than steel-RC). Unlike steel, GFRP bars cannot be bent on site and together with more GFRP reinforcement required, they increase the complexity in cage preparation. It is the sole responsibility of the contractor to splice column reinforcement cages. As shown in Fig. 7, the bottom cage bars are shown slightly tilted just after the start of the beam to differentiate from top bars.

Code Section 10.7.6.2 explains the distribution of ties in a beam-column joint. It states that the bottom tie shall be located not more than one-half the tie spacing above the top of footing or slab; similarly, the top tie shall be located not more than one-half the tie spacing below the lowest horizontal reinforcement in the slab, drop panel, or shear cap. In this example, the first tie was placed at 3 in. (76 mm) from the floor top, followed by others at the required spacing. Two pieces of C-shaped stirrups with minimum overlap as the greater of $20d_b$ and 6 in. (152 mm) were used as per Code Section 25.7.2.3.1. In current column design, No. 4 (M13) bars are used; hence, an overlap of 10 in. (254 mm) is provided.

The development length for non-sway GFRP-RC column (18 x 18 in. [460 x 460 mm]) was calculated using Code-specified Eq. 25.4.2.1(a), 25.4.2.1(b), and 25.4.2.1(c). The development length equation for GFRP bars in tension (Eq. (25.4.2a)) was conservatively adopted for this case as well. Also, the bar location modification factor (ω = 1.5) was used to calculate the development length. The term c_b/d_b in this column resulted in 1.83, which is well below the permissible limit of 3.5. The development length calculated for non-sway column as per Code Section 25.4.2 resulted in 75 in. (1900 mm). Because the tensile bar stress reaches its full capacity at a point (limited by maximum strain 0.01) which is greater than $0.5f_{fu}$, and the ratio of area of reinforcement provided to area of reinforcement required is less than 2.0, therefore, Class B lap splices were selected. The splice length was calculated as given in Code Section 25.5.2.1, which resulted a value equal to 98 in. (2490 mm).

Code Section 10.7.6.2 explains the distribution of ties in a beam-column joint. The first tie was conservatively placed at 3 in. (76 mm), as required by Code Section 10.7.6.2, followed by the required spacing. C-shaped ties were used in the non-sway column, with an overlap as stated in Code Section 25.7.2.3.1, which resulted in 10 in. (254 mm) when using No. 4 (M13) ties.

CONCLUSIONS AND RECOMMENDATIONS

In this study, a sway column example originally designed with steel reinforcement was taken from the ACI Design Handbook,[13] a companion to ACI 318-19,[14] and a non-sway column example from the textbook by Wight and Macgregor.[15] These two columns were redesigned with glass fiber-reinforced polymer (GFRP) reinforcement to show the implications of ACI CODE-440.11-22[11] with both low- (E_f = 6500 ksi [44,815 MPa]) and high-modulus (E_f = 8700 ksi [60,000 MPa]) GFRP bars. A limited parametric study was carried out to evaluate the effects of changing values of f_c', cross-section aspect ratio, and eccentricity. Based on the outcomes of this study, the following conclusions were drawn:

- The stiffness values for GFRP reinforcement result in higher moment magnification factors for GFRP-reinforced concrete (RC) compared to steel-RC columns.
- The advantage of high modulus/strength of new-generation GFRP bars can be beneficial to resist conditions of large eccentricities. However, due to limits on maximum tensile strain (0.01 in./in. [0.01 mm/mm]) to control column curvature, these benefits are not fully used.
- The compressive strength and stiffness of GFRP reinforcement is replaced with an equal area of concrete; hence, bigger cross sections are typically required for GFRP-RC columns when compared to steel-RC.

- Minimum reinforcement depends on the concrete gross area; hence, because of larger cross-section dimensions, GFRP-RC will require more reinforcement than steel-RC.
- It is obvious that increasing concrete strength helps decrease dimensions of RC sections. However, the concrete strength has an additional effect on the performance GFRP-RC cross sections. For the case considered and at concrete strength of 7500 psi (52 MPa) and above, the required dimensions for steel-RC and GFRP-RC were the same, as opposite at lower concrete strengths.
- As expected, the rectangular sections performed better than square sections, and in most cases, GFRP-RC and steel-RC required the same cross sections when axial load acted outside the kern (that is, large eccentricities).
- The current development length equation in the Code result in very large values compared to steel-RC because there is no distinction in the requirements for compression and tension splices. Research should be undertaken to reassess provision parameters by incorporating improvements in material properties.
- It is observed that replacing the contribution of GFRP reinforcement in compression with an equal area of concrete significantly affected the design. With the recent advancements in material properties and manufacturing techniques, there is need to re-investigate the contribution of GFRP bars in the axial compressive capacity of GFRP-RC columns using high-modulus GFRP reinforcement.

AUTHOR BIOS

Zahid Hussain *is a PhD Student in Civil and Architectural Engineering Department at the University of Miami, Coral Gables, FL. He is a member of ACI Committee 440, Fiber Reinforced Polymer Reinforcement. His research interests include sustainable materials, computational methods, design, and behavior of fiber-reinforced polymer (FRP)-reinforced structures.*

Antonio Nanni, *FACI, is an Inaugural Senior Scholar, Professor, and Chair of the Department of Civil and Architectural Engineering at the University of Miami. He is a member of ACI Committees 440, Fiber Reinforced Polymer Reinforcement, and 549, Thin Reinforced Cementitious Products and Ferrocement.*

ACKNOWLEDGMENTS

The authors would like to thank the National Science Foundation, Grant No. 1916342, and the Higher Education Commission of Pakistan for their financial support of the lead author.

REFERENCES

1. ACI Committee 440, "Guide for the Design and Construction of Structural Concrete Reinforced with Fiber-Reinforced Polymer (FRP) Bars (ACI 440.1R-15)," American Concrete Institute, Farmington Hills, MI, 88 pp.

2. Zhang, P.; Lv, X.; Zhang, H.; Liu, Y.; Chen, B.; Gao, D.; and Shaikh, S. A., "Experimental Investigations of GFRP Reinforced Columns with Composite Spiral Stirrups under Concentric Compression," *Journal of Building Engineering*, V. 46, No. 4, 2022, pp. 1-21. doi: 10.1016/j.jobe.2021.103768

3. Hasan, H. A.; Sheikh, M. N.; and Hadi, M. N. S., "Performance Evaluation of High Strength Concrete and Steel Fiber High Strength Concrete Columns Reinforced with GFRP Bars and Helices," *Construction and Building Materials*, V. 134, No. 2, 2017, pp. 297-310. doi: 10.1016/j.conbuildmat.2016.12.124

4. De Luca, A.; Matta, F.; and Nanni, A., "Behavior of Full Scale GFRP Reinforced Concrete Columns under Axial Load," *ACI Structural Journal*, V. 107, No. 2, Mar.-Apr. 2010, pp. 589-596.

5. De Luca, A.; Matta, F.; and Nanni, A., "Structural Response of Full Scale Reinforced Concrete Columns with Internal FRP Reinforcement under Compressive Load," *9th International Symposium on Fiber Reinforced Polymer Reinforcement for Concrete Structures*, D. Oehlers, M. Griffith, and R. Seracino, eds., Sydney, Australia, July 13-15, 2010.

6. Jawaheri Zadeh, H., and Nanni, A., "Flexural Stiffness and Second Order Effects in FRP-RC Frames," *ACI Structural Journal*, V. 114, No. 2, Mar. 2017, pp. 533-544.

7. Bischoff, P. H., "Member Stiffness for Frame Analysis for GFRP Reinforced Concrete Structures," *IABSE Symposium—Engineering the Future*, Sept. 21-23, 2017.

8. Hadhood, A.; Mohamed, H. M.; Benmokrane, B.; Nanni, A.; and Shield, C. K., "Assessment of Design Guidelines of Concrete Columns Reinforced with Glass Fiber-Reinforced Polymer Bars," *ACI Structural Journal*, V. 116, No. 4, July 2019, pp. 193-207. doi: 10.14359/51715663

9. Guérin, M.; Mohamed, H. M.; Benmokrane, B.; Shield, C. K.; and Nanni, A., "Effect of Glass Fiber-Reinforced Polymer Reinforcement Ratio on Axial-Flexural Strength of Reinforced Concrete Columns," *ACI Structural Journal*, V. 115, No. 4, July 2018, pp. 1049-1061. doi: 10.14359/51701279

10. Khorramian, K., and Sadeghian, P., "Experimental and Analytical Behavior of Short Concrete Columns Reinforced with GFRP Bars under Eccentric Loading," *Engineering Structures*, V. 151, 2017, pp. 761-773. doi: 10.1016/j.engstruct.2017.08.064

11. ACI Committee 440, "Building Code Requirements for Structural Concrete Reinforced with Glass Fiber-Reinforced Polymer (GFRP) Bars (ACI CODE-440.11-22) and Commentary," American Concrete Institute, Farmington Hills, MI, 266 pp.

12. ASTM D7957/D7957M-22, "Standard Specifications for Solid Round Glass Fiber Reinforced Polymer Bars for Concrete Reinforcement," ASTM International, West Conshohocken, PA, 2022, 5 pp.

13. MNL-17(21), *ACI Reinforced Concrete Design Handbook, A Companion to ACI 318-19*, American Concrete Institute, Farmington Hills, MI, 2019, 568 pp.

14. ACI Committee 318, "Building Code Requirements for Structural Concrete (ACI 318-19) and Commentary (ACI 318R-19) (Reapproved 2022)," American Concrete Institute, Farmington Hills MI, 2019, 624 pp.

15. Wight, J. K., and Macgregor, J. G., *Reinforced Concrete Mechanics and Design*, sixth edition, Pearson Education, Inc., Upper Saddle River, NJ, 2019.

ACI in Your Classroom

Integrate ACI into your classroom!

To support future leaders, ACI has launched several initiatives to engage students in the Institute's activities and programs – select programs that may be of interest to Educators are:

- **Free student membership –** encourage students to sign up
- **Special student discounts on *ACI 318 Building Code Requirements for Structural Concrete*, *ACI 530 Building Code Requirements and Specification for Masonry Structure*, & *Formwork for Concrete* manual.**
- **Access to *Concrete International* –** free to all ACI student members
- **Access to *ACI Structural Journal* and *ACI Materials Journal* –** free to all ACI student members
- **Free sustainability resources –** free copies of Sustainable Concrete Guides provided to universities for use in the classroom
- **Student competitions –** participate in ACI's written and/or team-based competitions
- **Scholarships and fellowships –** students who win awards are provided up to $15,000 and may be offered internships and paid travel to attend ACI's conventions
- **ACI Award for University Student Activities –** receive local and international recognition for your University's participation in concrete-related activities
- **Free access to the *ACI Collection of Concrete Codes, Specifications, and Practices* –** in conjunction with ACI's chapters, students are provided free access to the online ACI Collection
- **ACI online recorded web sessions and continuing education programs –** online learning tools ideal for use as quizzes or in-class study material

https://www.concrete.org/educatorsandresearchers/aciinyourclassroom.aspx

ACI STRUCTURAL JOURNAL TECHNICAL PAPER

Title No. 120-S85

Cover Spalling in Reinforced Concrete Beams Subjected to Pure Torsion

by Allan Kuan, Evan C. Bentz, and Michael P. Collins

Cover concrete plays an important role in the torsional behavior of reinforced concrete members because the resulting shear stresses are concentrated in these areas. Modeling its behavior is difficult due to: 1) compression softening; and 2) the possibility of spalling at high loads. Traditional approaches, which only consider one effect or the other, are limited in their ability to model the ultimate strength and torque-twist response of members over a wide range of cover thicknesses. This paper presents a mechanics-based model which can predict when torsional spalling occurs and quantify its effect on a member's strength and stiffness. Its application within a nonlinear analysis framework and a design procedure based on ACI 318-19 is shown. Using the proposed model together with existing compression-softening models results in improved strength predictions of 187 pure torsion tests found in the literature.

Keywords: design; reinforced concrete; softening; space truss; spalling; torsion.

INTRODUCTION

Cover spalling has commonly been observed in experiments of reinforced concrete beams subjected to pure torsion, like those shown in Fig. 1, or torsion in combination with other actions.[1,2] Spalling, which usually affects the corners of the cross section but can propagate into the side cover as well, has important implications for design.[3] For example, design codes such as ACI 318-19,[4] CSA A23.3:19,[5] and AASHTO LRFD[6] have special detailing requirements to avoid premature failures caused by torsional spalling, and neglect the cover concrete when determining a member's torsional strength.

Early analysis tools for torsion, such as the Diagonal Compression Field Theory[7] (DCFT) developed by Mitchell and Collins in 1974, assumed that the entirety of a member's cover would spall to the depth of the hoop reinforcement at failure. This is because the authors found that if the unspalled section geometry and concrete stress-strain response obtained from a cylinder test were used together, the torsional strength would be systematically overestimated. To address this issue, they recommended using the fully spalled dimensions because it improved the quality of the strength predictions and appeared to be consistent with their experimental observations. The DCFT still forms the basis for the torsion provisions in the previously mentioned design codes, which share its assumption that the cover fully spalls at failure.[8,9]

In the 1980s, research investigating the shear behavior of reinforced concrete led to further improvements in understanding how reinforced concrete members resist torsion. Experiments performed on panels subjected to pure shear showed that cracked concrete exhibits a weaker compressive response than what would be observed during a cylinder test, a phenomenon known as compression softening.[10] Its discovery led to the issue of spalling in torsion being revisited by Hsu and Mo[11] in 1985. They suggested that the tendency of the DCFT to overestimate the torsional strength of a member when the unspalled dimensions were used was not due to cover spalling. Instead, they argued that it was because the compression-softening effect—which would weaken the response of the concrete under torsional stresses, but had not yet been discovered in 1974—was not considered in the model. They proposed a new model which was similar to the DCFT but, like analytical tools for shear modeling, neglected spalling and accounted for compression softening. Their model showed good agreement with experiments whose cover thickness were within a narrow range of values.

Despite further improvements in understanding how reinforced concrete resists shear and torsion, there is still a lack of consensus on the role of spalling in torsion behavior and how to address it. Most analytical models for torsion developed since the 1980s have followed Hsu and Mo's "softened approach" by neglecting spalling and considering compression softening,[12-23] while most codified design provisions[4-6] adopt a "spalled approach" that considers spalling but neglects compression softening like the original DCFT. There are weaknesses to both methods. The strength predictions made by "spalled approaches" can be very conservative for members that have thick covers or contain small quantities of reinforcement, and the stiffness is usually underestimated. Spalled approaches are also inconsistent with modeling practices for flexural or shear behavior because: 1) the assumed section geometry neglects the cover; and 2) compression softening is neglected when the concrete is subjected to biaxial or triaxial stress states. On the other hand, softened approaches can seriously overestimate the torsional strength of members with thick covers.[24] A weakness shared by both methods is that spalling is treated as a binary issue, with the cover being entirely considered or entirely neglected, when experimental evidence—such as the beams shown in Fig. 1—suggests that the reality is somewhere in between. The shortcomings of these approaches

ACI Structural Journal, V. 120, No. 5, September 2023.
MS No. S-2022-311.R1, doi: 10.14359/51738839, received April 21, 2023, and reviewed under Institute publication policies.

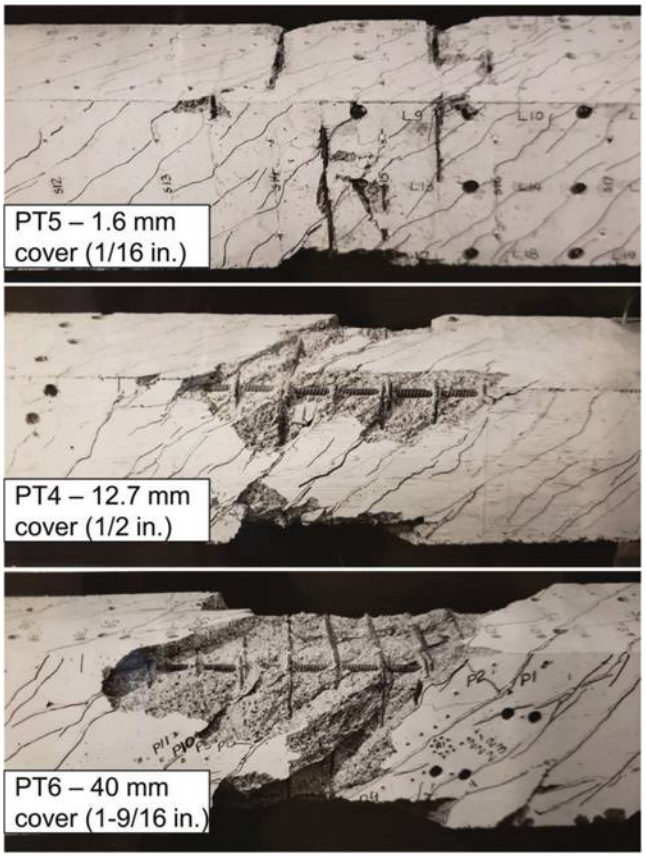

Fig. 1—Pure torsion experiments by Mitchell and Collins showing effect of cover thickness on degree of spalling.[1]

require engineers to use their judgement when addressing issues of torsion because a more general method is not yet available.

Accounting for the effects of both compression softening and spalling on torsion behavior can address the weaknesses of these traditional approaches. However, it is shown later in this paper that simply considering both at the same time is too conservative. The main challenge is that spalling, which can but does not always influence the torsional response, is difficult to account for because the underlying mechanism is not fully understood. One attempt at solving this problem was made by Rahal and Collins,[25] who formulated a model to predict when spalling due to torsion would occur and implemented it into an analytical tool which also considered compression softening. Although their model showed good agreement with a selection of torsion experiments, their spalling check was empirically derived using a small set of torsion tests and is relatively complex to use for design. Furthermore, it is unable to predict how much concrete is lost after spalling took place, which, as seen in Fig. 1, is not always the full cover.

This paper attempts to improve design and analysis practices for torsion by presenting a general methodology which considers both compression softening and spalling. A central part of the methodology is a new model which derives the mechanism of torsional spalling from first principles. In addition to having the ability to predict when spalling occurs, the model also considers and quantifies the resulting loss of concrete, which is something that has not been investigated by others previously. The application of the general methodology is demonstrated in two ways: within a nonlinear analysis framework based on the DCFT, and within a design procedure based on the ACI 318-19 torsion provisions. Both applications are then validated using pure torsion experiments drawn from the literature.

RESEARCH SIGNIFICANCE

Traditional methods of accounting for cover spalling in reinforced concrete members can be inadequate for members with very thick or very shallow covers. This paper presents a simple model which can determine when torsional spalling occurs and quantify its effect on a member's strength and stiffness. Implementing this model into existing analysis tools and design procedures improves their ability to predict the torsional strength and torque-twist response of members over a wide range of cover thicknesses. The improved accuracy can be particularly beneficial for the evaluation of torsion-critical members in existing structures.

PROPOSED MODEL

Consider the cracked concrete member subjected to pure torsion shown in Fig. 2(a). If the torsion is assumed to be primarily resisted by circulating shear stresses and not warping torsion, then the member can be represented by a thin tube which carries a uniform shear flow around its perimeter. If tensile stresses in the cracked concrete are neglected, the shear flow will be the result of diagonal compressive stresses in the concrete, which are equilibrated by tensile stresses in the longitudinal and hoop reinforcement. These compressive stresses, which vary through the thickness of the tube, can be represented using an equivalent rectangular stress block[7,11] with an average stress of $f_{2,av} = \alpha_1 \beta_{cs} f_c'$ that acts over a width a_o, where f_c' is the concrete strength obtained from a cylinder test, β_{cs} is a factor accounting for compression softening, and α_1 is a stress block factor which is a function of the principal compressive strain on the surface, ε_{2s}. If the member is unspalled, the line of action of the shear flow will be at a depth of $0.5a_o$ beneath the outside surface of the cross section. This is shown in Fig. 2(b).

Case 1 in Fig. 2(c) shows a corner detail of a member with a very thin cover as it resists an applied torque. A simple representation of the tensile forces in the hoop reinforcement, T, and the compressive forces which make up the shear flow, C, is also shown. To satisfy equilibrium at the corner where these forces change direction, an additional diagonal force must be present. This force will be compressive because the tensile forces in the hoops will be closer to the surface than the compressive forces from the shear flow. In this situation, the cover is not expected to spall because there are no tensile stresses in the concrete.

Case 2 in Fig. 2(c) again shows the corner detail of a member subjected to torsion. Here, the cover is thicker than in Case 1 and hence, the compressive forces which make up the shear flow will be closer to the outside surface than the tensile forces in the hoops. The diagonal force in the corner will now be tensile, and if the resulting tensile stress exceeds the cracking stress of the concrete, diagonal cracking causing spalling will occur. For a 90-degree corner with a uniform

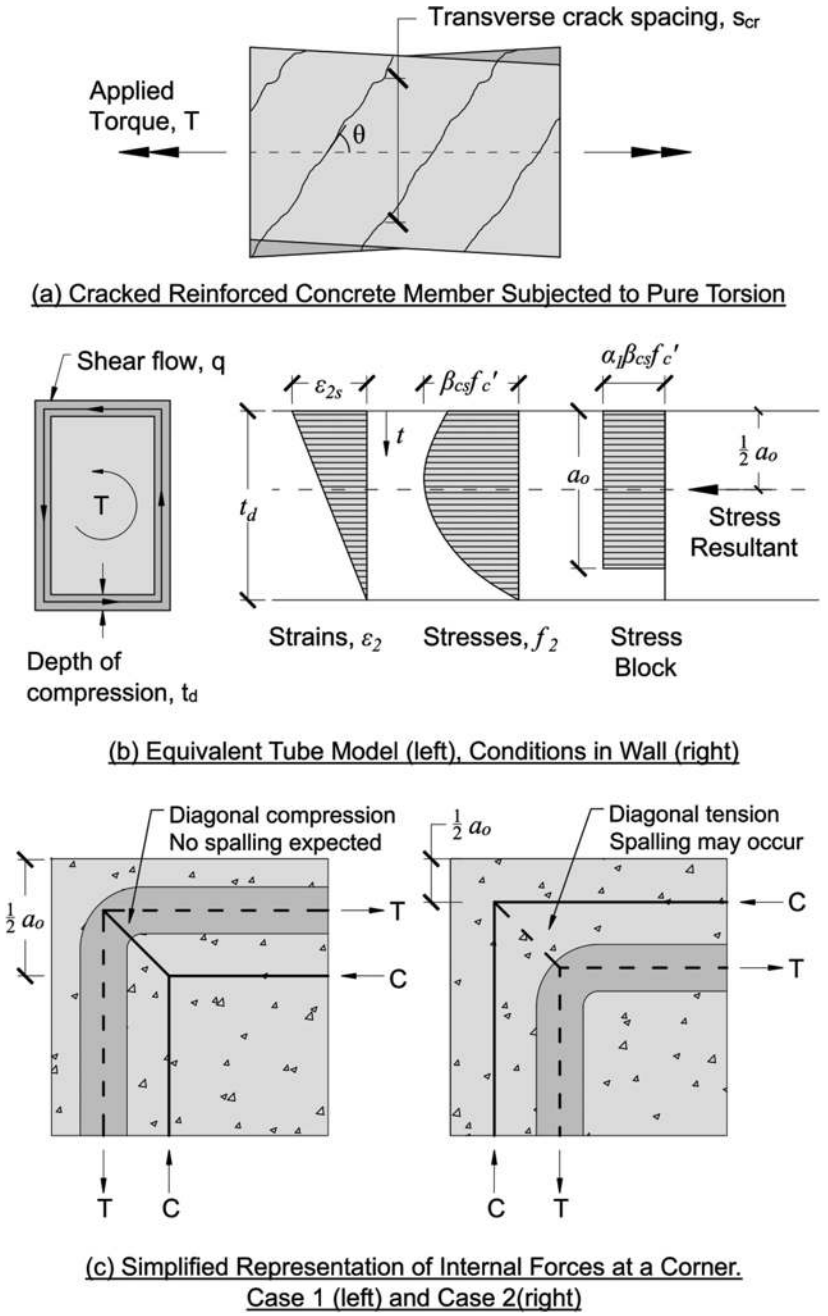

Fig. 2—Model conditions (top and middle) and corner details if shear flow path is within (bottom left) or outside (bottom right) hoop reinforcement.

cover thickness, the diagonal tensile force per unit length along the beam will be

$$F_t = \sqrt{2}\frac{A_h f_h}{s} \tag{1}$$

where f_h is the stress in the hoop; and A_h and s are the area and spacing of the hoop reinforcement, respectively. When spalling occurs, a diagonal failure plane will form at a 45-degree angle that intersects with the horizontal and vertical faces of the member, causing cracks to appear on the surface. If the distance between these cracks, measured along the perimeter around the corner, is equal to the transverse crack spacing, s_{cr}, then the length of the diagonal failure plane will be equal to $s_{cr} \times 0.5\sqrt{2}$. If it is then assumed that the tensile force in Eq. (1) acts uniformly over this plane, the average tensile stress in the concrete at the moment of cracking will be equal to

$$f_t = \sqrt{2}\frac{A_h f_h}{s} \cdot \frac{1}{0.5\sqrt{2} \cdot s_{cr}} = 2\frac{A_h f_h}{s_{cr} s} \tag{2}$$

The average crack spacing can be calculated using the 1978 CEB-FIP equation,[26] though this value should not exceed the smaller of the side lengths which meet at the corner, b_i

$$s_{cr} = 2(c + 0.1s) + k_1 k_2 \frac{d_b}{\rho_h} \leq \min\{b_i\} \tag{3}$$

In Eq. (3), c is the cover, measured from the outside surface to the centerline of the hoops; k_1 and k_2 are factors which account for bond and strain conditions (taken as 0.4 and 0.25, respectively)[27]; d_b is the bar diameter of the hoops; and ρ_h is the quantity of hoop reinforcement. If p_{cp} and A_{cp} are the perimeter and area defined by the unspalled dimensions of the cross section, respectively, then a nominal value of ρ_h can be taken as

$$\rho_h = \frac{A_h p_{cp}}{A_{cp} s} \tag{4}$$

Having defined the tensile stress in the concrete due to the applied loads, the cracking stress must now be determined to predict when spalling takes place. The concrete, which is triaxially stressed, will crack at a lower stress than under uniaxial stress conditions because of the coexisting diagonal compressive stresses which circulate around the member. This phenomenon was noted by Kupfer et al.[28] when performing tests on biaxially loaded specimens and Foster et al.[29] when studying cover spalling in columns subjected to axial compression. A simple equation that accounts for this effect is a modified version of the model proposed by Kupfer and Gerstle,[30] which is shown as follows

$$f_{cr} = f_t'\left(1 - 0.8\frac{f_2}{f_{2,max}}\right) \tag{5}$$

In Eq. (5), f_{cr} is the cracking strength; f_t' is the uniaxial tensile strength; f_2 is the accompanying principal compressive stress; and $f_{2,max}$ is the peak compressive stress after considering compression softening, equal to $\beta_{cs} f_c'$. Note that unlike Kupfer and Gerstle's original model, the softened compressive strength is used instead of the uniaxial compressive strength. This is because the concrete at the corner is in a triaxial state of stress instead of being biaxially loaded as in Kupfer et al.'s experiments.[28]

For a member subjected to torsion, f_2—and hence, f_{cr}—will not be constant though the thickness of the cover. However, the average cracking stress, $f_{cr,av}$, can be obtained by using the average compressive stress in the rectangular stress block, $f_{2,av}$. Substituting the definitions of $f_{2,av}$ and $f_{2,max}$ into Eq. (5) gives

$$f_{cr,av} = f_t'\left(1 - 0.8\frac{\alpha_1 \beta_{cs} f_c'}{\beta_{cs} f_c'}\right) = f_t'(1 - 0.8\alpha_1) \tag{6}$$

The uniaxial tensile strength can be taken as

$$f_t' = 0.33\sqrt{f_c'};\ f_c' \text{ in MPa} \tag{7a}$$

$$f_t' = 4\sqrt{f_c'};\ f_c' \text{ in psi} \tag{7b}$$

Spalling will then occur when the applied stress exceeds the cracking stress, which results in the following condition when Eq. (2), (6), and (7) are combined

$$2\frac{A_h f_h}{s_{cr} s} \geq 0.33\sqrt{f_c'}(1 - 0.8\alpha_1);\ f_c' \text{ in MPa} \tag{8a}$$

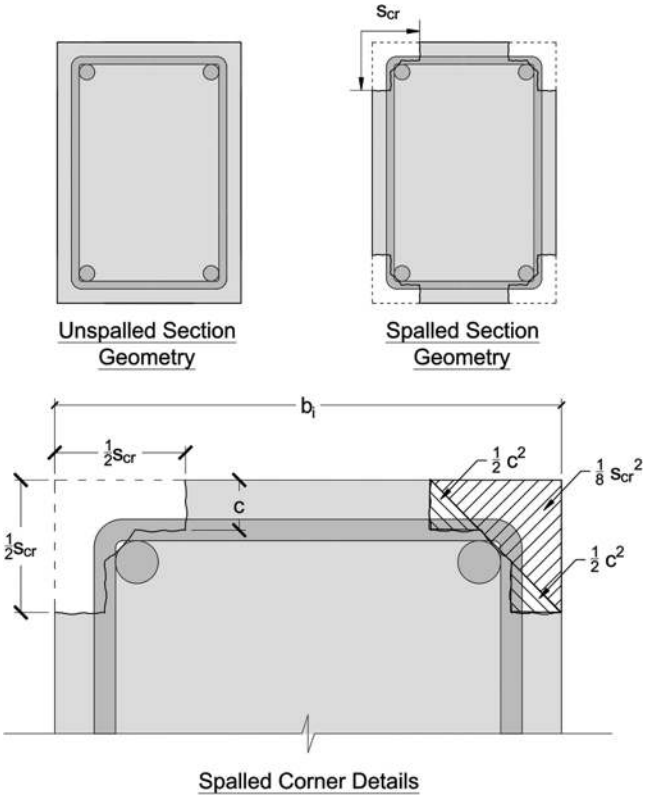

Fig. 3—Simplified model for section loss following cover spalling.

$$2\frac{A_h f_h}{s_{cr} s} \geq 4\sqrt{f_c'}(1 - 0.8\alpha_1);\ f_c' \text{ in psi} \tag{8b}$$

If Eq. (8) is satisfied and the centroid of the shear flow falls outside of the hoop reinforcement, the corner of the cross section will spall off and no longer contribute to the member's torsional resistance. An idealization of the spalled member is shown in Fig. 3. The distance between the failure planes that define the spalled concrete is the crack spacing, which matches the assumption used to derive Eq. (8), and within the cover, the failure plane is assumed to extend along the centerline of the hoop reinforcement due to microcracking. These L-shaped failure patterns at the corners of the section lead to the following reductions to the overall cross-section geometry

$$A_{sp} = A_{cp} - \sum_{i=1}^{n}\left(\frac{1}{8}s_{cr,i}^2 + c_i^2\right) \geq A_{oh} \tag{9}$$

$$p_{sp} = p_{cp} - \sum_{i=1}^{n} s_{cr,i}\left(1 - \frac{1}{2}\sqrt{2}\right) \geq p_h \tag{10}$$

where A_{sp} and p_{sp} are the reduced area and perimeter after spalling, respectively; and n is the number of corners that have spalled off, which can be conservatively taken as four for rectangular sections. A_{sp} is generally larger than the area enclosed by the hoop reinforcement, A_{oh}, but will approach A_{oh} for members that have widely spaced cracks relative to the size of the cross section. Note that Eq. (9) and (10) assume that the failure plane forms at a 45-degree angle, which is a reasonable assumption for members subjected to pure torsion. Instances where the failure plane is unlikely

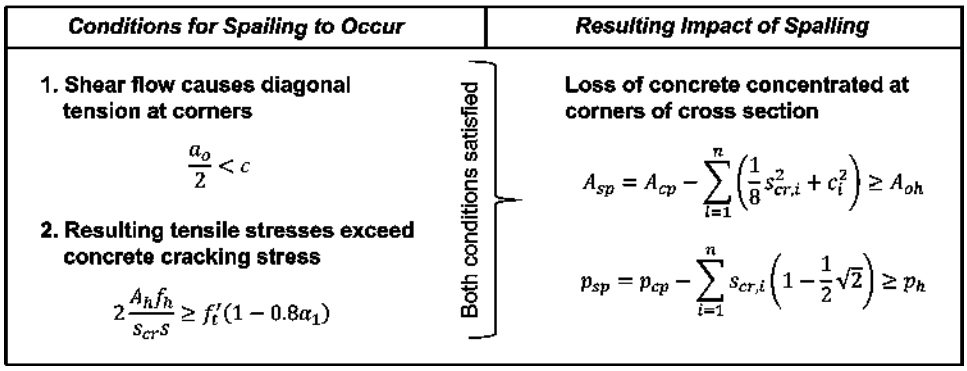

Fig. 4—Model summary.

to assume this shape include cases where the cover thickness varies around the member's perimeter, or if the shear stresses do not remain constant as they turn the corner, such as in the case of combined torsion and shear.

The proposed model, whose key equations are summarized in Fig. 4, suggests that spalling is strongly affected by the crack control provided by the hoop reinforcement. According to Eq. (8), spalling is less likely to occur in lightly reinforced members because the cracks in such members will be widely spaced as a result of their poor crack control. However, if spalling occurs, then the impact on the member's torsional response will be significant because more concrete is expected to be lost, as shown in Eq. (9) and (10). Conversely, heavily reinforced members with good crack control, and hence a small crack spacing, are more likely to spall. The impact of spalling on such members is expected to be relatively minor however, since less concrete will be lost. In the limiting case where the amount of reinforcement provided results in a failure caused by crushing before yielding, good predictions of strength can be obtained by neglecting spalling completely.[31] These predictions are consistent with experimental evidence, like the beams shown in Fig. 1, and previous remarks about spalling.[1,2] It is interesting to note that although the CEB-FIP equation was not originally intended to be used for torsional spalling, it gives reasonable predictions of how much concrete is lost after it occurs. Consider the PT series of beams tested by Mitchell and Collins,[1] which are shown in Fig. 1. The predicted crack spacings for PT4 and PT6, which had unspalled dimensions of 381 × 381 mm and 432 × 432 mm (15 × 15 in. and 17 ×17 in.), are 179 and 258 mm (7.0 and 10.2 in.), respectively. These values represent losses of approximately 47% and 60% of the cover along each face, which has reasonable agreement with the photos shown in Fig. 1.

It should be noted that—based on equilibrium of the forces drawn in Fig. 2—spalling is only expected to occur if the centerline of the shear flow acts within the clear cover. However, the forces drawn in the figure are a simplification of the actual state of stress at the corners of the cross section. In reality, the compressive stresses that make up the shear flow are distributed over the depth of compression instead of only being concentrated at the centerline, so some tensile stresses in the concrete will always be needed to turn the corner, even if the resultant shear flow does not appear to require any. Therefore, all external or salient corners are expected to spall at high torsional stresses, while internal or re-entrant corners are expected to remain unspalled.

IMPLEMENTATION IN NONLINEAR ANALYSIS

To study the application of the proposed model within a nonlinear analysis framework, a modified version of the DCFT, which can predict a member's complete torque-twist behavior, was developed that accounts for both compression softening and corner spalling. Details of the original DCFT, which assumes full spalling and neglects both tensile stresses in the cracked concrete and compression softening, can be found elsewhere.[7]

In addition to employing the proposed spalling model instead of assuming full spalling, the model differed from the DCFT in its choice of constitutive relationships for the concrete stress-strain behavior. To be applicable to both normal-strength and high-strength concrete, a modified version of Popovics model[27,32-34] was used as a base curve for the compressive response of the concrete. The compression softening relationship suggested by the Modified Compression Field Theory[10] (MCFT) was chosen, though alternative relationships by others could also have been used.[35-39] The MCFT equation for β_{cs} is

$$\beta_{cs}(t) = \frac{1}{0.8 + 170\,\varepsilon_1(t)} \leq 1.0 \tag{11}$$

In Eq. (11), β_{cs} is a compression-softening coefficient used to reduce the strength of the concrete, so $f_{2,max} = \beta_{cs} f_c'$; ε_1 is the principal tensile strain; and t is the depth from the outside surface of the cross section. ε_1 can be calculated using the following equation if positive values of the principal compressive strain, ε_2, indicate compression

$$\varepsilon_1(t) = \varepsilon_l(t) + \varepsilon_h(t) + \varepsilon_2(t) \tag{12}$$

The degree of softening through the tube walls is not constant because ε_1 varies through the thickness. Determining the variation of β_{cs} therefore requires ε_1—and by extension, ε_l, ε_h, and ε_2—to be known at each point in the depth of compression, t_d. This can be done by revisiting some of the assumptions employed by the DCFT in its original formulation. First, the longitudinal reinforcement is assumed to be uniformly distributed around the perimeter of the member, so it will remain straight as it twists and hence,

the longitudinal strain ε_l will not be a function of t. ε_2 is assumed to vary linearly from a maximum on the surface to a value of zero at the depth of compression, as shown in Fig. 2(b), and this variation can be determined from the twist of the member.[7] Finally, the transverse strains, ε_h, can be found using the assumption that the angle of the diagonal compression field, θ, remains constant throughout the depth of compression t_d. This is done using the following relationship between θ and the longitudinal, transverse, and principal compressive strains

$$\varepsilon_h(t) = \frac{\varepsilon_l(t) + \varepsilon_2(t)}{\tan^2\theta} - \varepsilon_2(t);\ 0 \le t \le t_d \qquad (13)$$

With the principal tensile and principal compressive strains known at all locations in the tube wall, the principal compressive stresses in the concrete f_2 can be obtained using the Popovics model and Eq. (11). The stress block factors, α_1 and β_1, and the average value of the compression softening coefficient, β_{cs}, can then be determined for any given strain state by integrating the stress distribution so that the equivalent rectangular stress block shares the same net force and line of action of the actual stress distribution.[27]

In determining a member's torque-twist behaviour, the DCFT calculates the stress block factors, the stresses in the hoop reinforcement, f_h, and the depth of the shear flow path, a_o, at each load step. Using this information, spalling was considered using Eq. (8) and checking if the centerline of the shear flow path was inside of the clear cover after each converged load step. If both conditions were satisfied, then the area and perimeter of the member were reduced using Eq. (9) and (10) for the remainder of the analysis.

Experimental validation

The numerical model was validated using 187 tests of nonprestressed beams subjected to pure torsion.[1,40-52] Each of the beams considered in the study had a rectangular cross section which varied in size from 160 × 275 to 600 × 600 mm (6.3 × 10.8 to 23.6 × 23.6 in.). The normalized cover, defined as the ratio of the cover concrete to the total cross-sectional area or $c \times p_{cp}/A_{cp}$, varied from 7 to 83%, and the concrete cylinder compressive strength varied from 2080 to 16,000 psi (14.3 to 110 MPa). The specimens in the dataset covered a range of failure modes, including yielding of the reinforcement, crushing of the concrete before any yielding, or spalling following initial cracking.

Four modeling approaches were taken to study how different assumptions about compression softening and cover spalling would affect the strength predictions of these beams. The first was a "spalled-only approach," which neglected compression softening and assumed that the full cover was spalled during the entire analysis. The second was a "softened-only approach," which employed the MCFT compression-softening relationship but ignored cover spalling. The third approach considered both full cover spalling and compression softening. Finally, the fourth approach used the proposed framework by considering compression softening and the suggested corner spalling model.

Figure 5 shows the strength predictions obtained from each modeling approach plotted against the normalized cover. The spalled-only approach made reasonable strength predictions over the full range of normalized cover values. Most of the predictions were conservative and had test-to-predicted ratios which fell between 1.0 and 2.0. The strength predictions made using the softened-only approach were on average more accurate than those obtained from the spalled-only method. However, the number of specimens whose strength was overestimated increased from 26.2 to 69%, and the predictions were increasingly unconservative as the normalized cover increased. The test-to-predicted ratios of the eight members with thick covers—that is, those exceeding a normalized cover of 50%—were all less than 0.65, which is less than the reduction factor used by ACI 318-19 for torsion, $\phi = 0.75$, and therefore unsafe. Accounting for both compression softening and full cover spalling gave less-accurate but more conservative predictions, with an average test-to-predicted ratio of 1.41 compared to 1.12 and 0.93 made by the first two approaches, respectively. The spread of the predictions was much larger than the first two approaches. The proposed model gave the most accurate predictions of the four methods studied, and unlike the softened-only approach, maintained its accuracy as the normalized cover increased.

The trends observed in Fig. 5 can also be seen in the test-to-predicted summary statistics shown in Table 1. Based on the statistics obtained using the full dataset, the proposed method made the most accurate predictions of strength (average test-to-predicted ratio of 1.07) and had the smallest coefficient of variation (COV) and spread. Table 1 also contains statistical parameters which were generated by fitting a normal distribution to the lower half of the test-to-predicted data, which are the tests of interest from the perspective of safety. For methods one and three, the lower-half analyses yielded better average test-to-predicted values and coefficients of variation than the corresponding values obtained from the full dataset. This indicates that strength predictions made by the fully spalled methods were not symmetrically distributed, but were instead biased towards the conservative side due to several test-to-predicted ratios exceeding 2.0. The opposite was true for the softened-only method, which saw an increase in the COV from 17.4 to 20.3%. The predictions made using the proposed approach had comparable average test-to-predicted values and coefficients of variation for both statistical analyses, indicating that the test-to-predicted values were distributed with low skew. Examining the first percentile values, which approximate the required strength reduction factor to offset the 1% likelihood of failure,[53] shows that the proposed method with corner spalling and compression softening is as safe as the spalled-only approach despite being 5% less conservative on average.

The role of the proposed corner spalling model on the predicted torque-twist response can be seen in Fig. 6, which shows the observed and predicted behavior of two companion beams tested at the University of Toronto. These beams, whose appearances after failure are shown in Fig. 1, contained identical reinforcement cages but had different

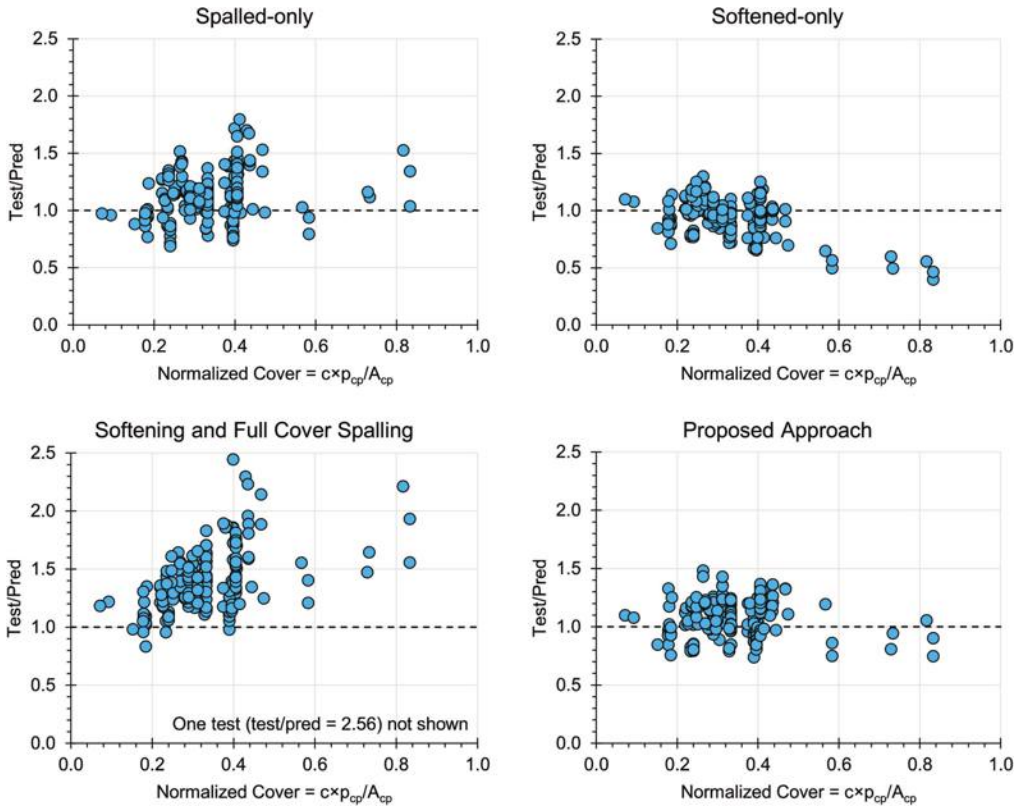

Fig. 5—Summary of strength predictions obtained from nonlinear analyses.

Table 1—Summary of analysis results: nonlinear models

Full dataset				
Test/Pred	Spalled only	Softened only	Softened and spalled	Proposed
Count	187	187	187	187
Mean	1.12	0.93	1.41	1.07
COV	18.3%	17.4%	19.9%	14.6%
Maximum	1.80	1.30	2.56	1.48
Minimum	0.69	0.40	0.83	0.74
% Tests < 1.0	26.2%	69.0%	2.7%	34.8%
Lower half of dataset only				
Mean	1.10	0.96	1.35	1.05
COV	15.6%	20.3%	13.5%	13.7%
First percentile	0.70	0.51	0.92	0.72

cover thicknesses. Despite the thicker cover, PT6 failed at the same torque as PT5 and exhibited severe spalling at failure. The proposed model correctly predicted that PT5 did not experience spalling. This is because the shear flow was contained within the hoop reinforcement for the entire analysis, so diagonal tension did not develop at the corners. The ultimate strength and ductility were somewhat underestimated, though this may be because the confinement provided by the hoop reinforcement was not considered when modeling the concrete's compressive response. The ultimate strength and torque-twist response of PT6 were predicted with excellent accuracy. Like the experiment, the cover was predicted to spall, and the calculated post-spalling response followed the experimentally observed behavior especially well. It should be noted the initial stiffness of both beams was underestimated because tensile stresses in the cracked concrete (that is, tension stiffening) were neglected in the analysis.

The results of a more detailed study comparing the four modeling approaches against a broader variety of variables (such as concrete strength, reinforcement strength, aspect ratio, and so on) can be found in the first author's doctorate thesis.[54]

SIMPLIFICATION FOR DESIGN

Although the proposed spalling model improves the predictive capabilities of the DCFT, its full formulation is too complex to use in design. In this section, a

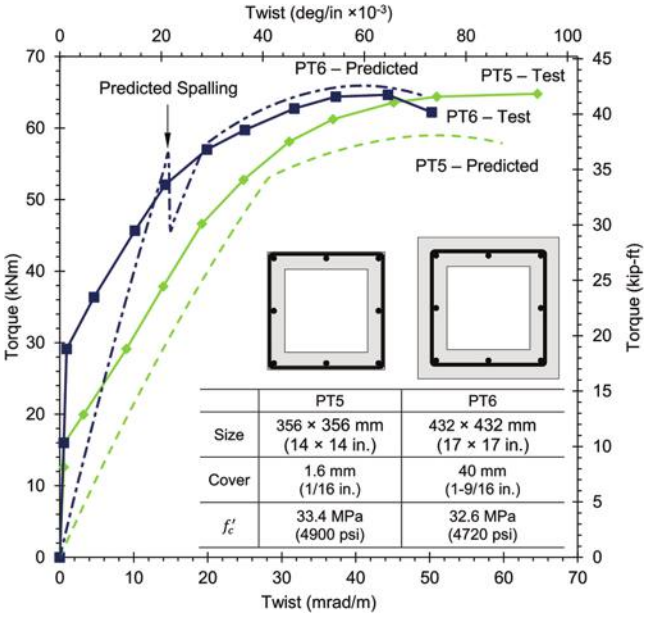

Fig. 6—Modeling PT5 and PT6 beams.

simplified version, which retains the essential characteristics of the general model, is derived, and its application within a modified version of the ACI 318-19 torsion procedures is demonstrated.

The condition for spalling given in Eq. (8) can be rewritten in terms of the applied torsion, T_u, if it is assumed that there are no tensile stresses in the cracked concrete. This allows the torque to be written in terms of the stresses carried by the hoop reinforcement f_h, the area enclosed by the shear flow path A_o, and the angle of inclination of the diagonal compression θ

$$T_u = 2A_o\frac{A_h f_h}{s}\cot\theta \tag{14}$$

Substituting Eq. (14) into Eq. (2) and rearranging terms allows the tensile stress which initiates spalling, f_t, to be expressed in terms of the applied torque

$$f_t = \frac{T_u}{A_o s_{cr}}\tan\theta \tag{15}$$

As before, spalling will occur when this tensile stress is equal to the cracking stress of the concrete, f_{cr}. The cracking stress can be determined using Kupfer et al.'s model and a suitable value of α_1. Kuan et al.[31] derived an expression for α_1 corresponding to a principal compressive strain of 0.003 on the surface of the cross section, which is appropriate for ultimate strength calculations. Their expression is

$$\alpha_1 = 1.0 - 0.005f_c';\ f_c' \text{ in MPa} \tag{16a}$$

$$\alpha_1 = 1.0 - \frac{0.035f_c'}{1000};\ f_c' \text{ in psi} \tag{16b}$$

Substituting Eq. (16) into Eq. (8) allows the cracking stress to be expressed solely in terms of f_c'. f_{cr} can be expressed in an even simpler manner by linearizing the resulting relationship, which is shown in Fig. 7. The proposed expression for f_{cr} then becomes

$$f_{cr} = 0.02f_c' \tag{17}$$

It should be emphasized that Eq. (17) represents the cracking stress under biaxial conditions when the concrete is also subjected to significant coexisting compressive stresses. As shown in Fig. 7, the cracking stress predicted by Eq. (17) is typically smaller than the uniaxial tensile strength predicted by Eq. (7).

At ultimate limit states, spalling must be considered when the applied torque exceeds a threshold value, T_{spall}. T_{spall} can be determined by equating Eq. (15) and (17), approximating A_o as $0.85A_{cp}$, and taking θ as 45 degrees for nonprestressed members

$$T_{spall} = 0.017A_{cp}s_{cr}f_c' \tag{18}$$

Equation (18) can be simplified further by noting that Eq. (7) can underestimate the tensile strength of concrete, especially when the tensile stresses are concentrated in a small volume of concrete,[55] which is the case when dealing with cover concrete in the corner of a cross section. Therefore, the suggested expression for T_{spall} becomes

$$T_{spall} = 0.02A_{cp}s_{cr}f_c' \tag{19}$$

For design purposes, using Eq. (3) to determine s_{cr} is inconvenient because it requires the arrangement of the transverse reinforcement to be known in advance. An approximate value for design can be obtained by considering that the maximum spacing of hoop reinforcement allowed by ACI 318-19 is 305 mm (12 in.), and the maximum spacing of longitudinal torsional reinforcement around the perimeter is also 305 mm (12 in.). The diagonal crack spacing, s_θ, can then be taken as half the maximum reinforcement spacing as done in the CSA A23.3:19 shear provisions,[5] giving a value of s_θ = 152 mm (6 in.). The diagonal crack spacing can be related to the longitudinal crack spacing, s_x, and the transverse crack spacing, s_y, using the following equation suggested by Vecchio and Collins[10]

$$s_\theta = \frac{1}{\frac{\sin\theta}{s_x} + \frac{\cos\theta}{s_y}} \tag{20}$$

If it is assumed that θ = 45 degrees, s_θ = 152 mm (6 in.), and both s_x and s_y are equal to s_{cr}, then s_{cr} will equal to 216 mm (8.5 in.). Modifying this base value to include the influence of the cover thickness on s_{cr} in the same way as the CEB-FIP equation gives the following simple expression for s_{cr}

$$s_{cr} = 200 + 2c \le \min\{b_i\};\ c \text{ in mm} \tag{21a}$$

$$s_{cr} = 8 + 2c \le \min\{b_i\};\ c \text{ in in.} \tag{21b}$$

When the applied torque exceeds T_{spall}, the spalled geometry should be obtained using Eq. (9) and (10). Although

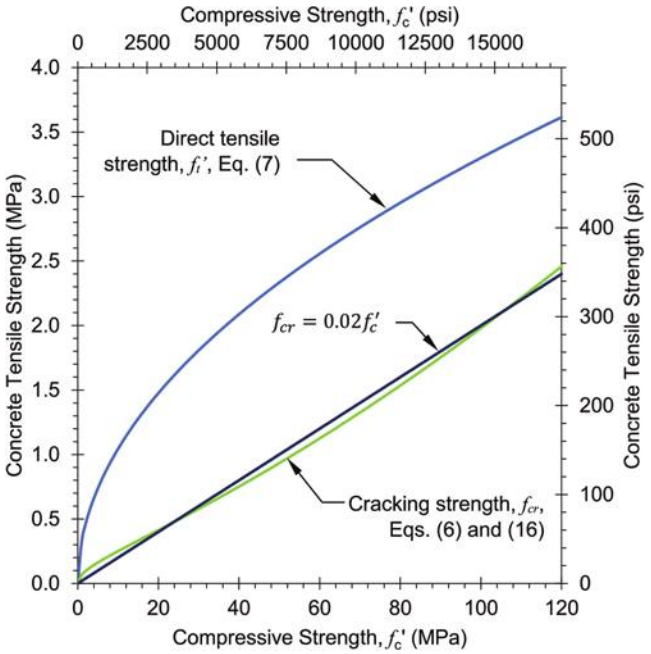

Fig. 7—Derivation of simplified cracking stress equation.

the general model also requires the shear flow to act within the cover to cause spalling, a reasonable simplification for design is to neglect this check and use the partially spalled geometry whenever the applied torsion exceeds T_{spall}.

Implementation in design procedures

The basic equations for torsional strength given by ACI 318-19 which correspond to yielding of the hoop reinforcement and longitudinal reinforcement, respectively, are

$$T_n = \min\begin{cases} 2A_o\dfrac{A_h f_{yh}}{s}\cot\theta \\ 2A_o\dfrac{A_l f_{yl}}{p_o}\tan\theta \end{cases} \quad (22)$$

where p_o is the perimeter of the shear flow path; and f_{yh} and f_{yl} are the yield strengths of the hoop and longitudinal reinforcement, respectively. ACI 318-19 defines $p_o = p_h$, $A_o = 0.85A_{oh}$, and suggests a value of $\theta = 45$ degrees for nonprestressed members.

Using the model presented in this paper, A_o and p_o can be determined by considering corner spalling, equilibrium conditions, and compression softening instead of simply assuming $A_o = 0.85A_{oh}$ and $p_o = p_h$, which is currently done in ACI 318-19. To determine A_o and p_o from A_{sp} and p_{sp}, the width of the equivalent rectangular stress block, a_o, must be known. Its value can be obtained if the equation previously derived by Collins and Mitchell[9,27] is modified to account for corner spalling and compression softening

$$a_o = \frac{A_{sp}}{p_{sp}}\left(1 - \sqrt{1 - \frac{T_u p_{sp}}{\alpha_1 \beta_{cs} f_c' A_{sp}^2}(\tan\theta + \cot\theta)}\right) \quad (23)$$

Equation (23) can be simplified by introducing a series of assumptions about the strain state of the member at failure. Like before, θ can be taken as 45 degrees, and if the member fails by yielding, the longitudinal strain and hoop strain can be taken as 0.002 for 400 MPa (60 ksi) steel. If the principal compressive strain in the concrete on the surface equals to 0.003 at failure, then the principal tensile strain can be conservatively taken as 0.007, which results in a value of $\beta_{cs} = 0.50$ if the MCFT compression softening relationship given in Eq. (11) is used. Substituting these terms into Eq. (23) gives

$$a_o = \frac{A_{sp}}{p_{sp}}\left(1 - \sqrt{1 - 4\frac{T_u p_{sp}}{\alpha_1 f_c' A_{sp}^2}}\right) \quad (24)$$

In Eq. (24), the stress block factor α_1 is calculated using Eq. (16), and if the terms under the square root sign result in a negative number, a_o should be taken as $a_o = A_{sp}/p_{sp}$. Once a_o has been found, then A_o and p_o can be calculated as

$$A_o = A_{sp} - \frac{1}{2}p_{sp}a_o \quad (25)$$

$$p_o = p_{sp} - 4a_o \quad (26)$$

ACI 318-19 also includes a third equation for torsional strength to account for crushing or excessive crack widths. In the absence of an applied shear force, this equation is

$$\frac{T_u p_h}{1.7A_{oh}^2} \le 0.83\sqrt{f_c'};\ f_c' \text{ in MPa} \quad (27a)$$

$$\frac{T_u p_h}{1.7A_{oh}^2} \le 10\sqrt{f_c'};\ f_c' \text{ in psi} \quad (27b)$$

When using this equation within the proposed framework, A_{oh} and p_h can be replaced with A_{sp} and p_{sp} if T_u exceeds T_{spall}. If T_u is less than T_{spall}, then each instance of A_{sp} and p_{sp} in Eq. (23) to (27) can be replaced with the unspalled geometry, A_{cp} and p_{cp}.

To determine the torsional strength of a member using the proposed design procedure, the following steps should be followed:

1. Determine T_{spall} using Eq. (19) and (21). If the applied torque T_u exceeds this value, determine A_{sp} and p_{sp} using Eq. (9) and (10), respectively.
2. Obtain the depth of the stress block, a_o, using Eq. (24) and calculate A_o and p_o using Eq. (25) and (26).
3. The torsional strength, T_n, is the smallest value obtained from Eq. (22) and (27). When using Eq. (27) to check concrete crushing or excessive cracking, the relevant modifications described in the previous paragraph shall be used.

Experimental validation

The predictive ability of the proposed design method was evaluated using the same dataset of beams that was used to validate the spalling model within the nonlinear analysis framework. Figure 8 shows the strength predictions obtained using ACI 318-19, the proposed method where s_{cr} is calculated using Eq. (3), and the proposed method if s_{cr} is calculated using Eq. (21). Again, the predictions are plotted with respect to the normalized cover. The ACI predictions are

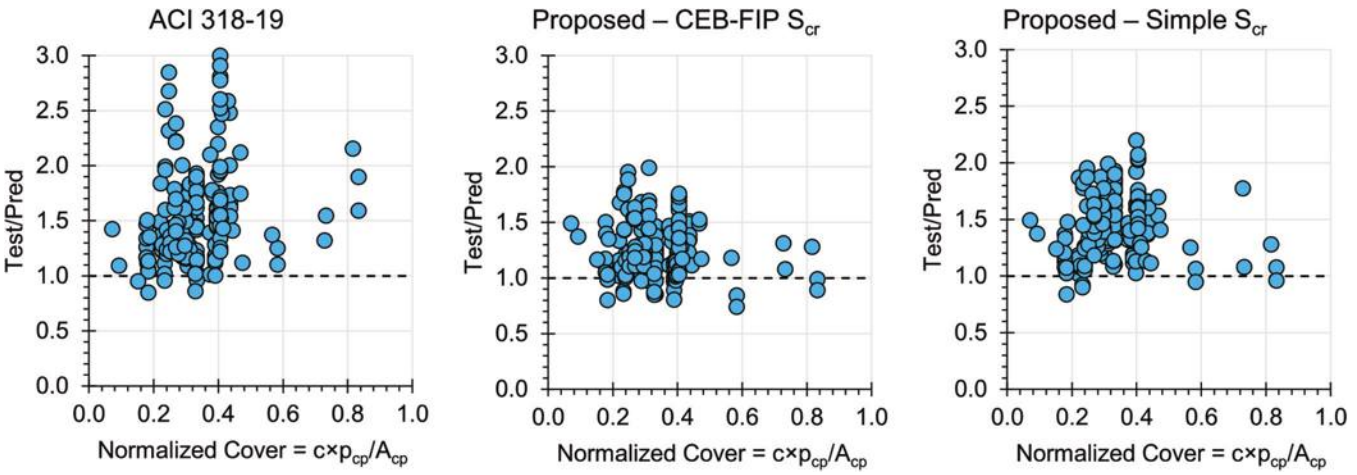

Fig. 8—Summary of strength predictions obtained from design procedures.

generally conservative across the full range of cover thicknesses, and 23 tests have a test-to-predicted ratio of 2.0 or higher. The predictions obtained using the proposed design methods are generally more accurate, but can be unconservative for very thick covers if the CEB-FIP equation is used to calculate s_{cr}. Using the simpler equation for s_{cr} generally gives more conservative predictions than the CEB-FIP equation, with fewer test-to-predict ratios below 1.0, but is still more accurate than using ACI 318-19.

Table 2 shows the summary statistics obtained using the three design methods represented in Fig. 8. Like before, two sets of statistics, one corresponding to the full dataset and another corresponding to a normal distribution fitted to the lower half of the test-to-predicted data, are shown. The proposed method with the CEB-FIP equation to calculate s_{cr} made significantly better predictions than ACI 318-19, with the average test-to-predicted ratio and COV improving from 1.54 to 1.24 and 27.9 to 19.2%, respectively, when considering the full dataset. Using the simpler equation to calculate s_{cr} gave comparable statistics to the more complex equation, with the mean test-to-predicted value being higher at 1.43, but the COV being 0.6% smaller. Despite the proposed methods being less conservative than ACI 318-19 on average, the lower-half analyses resulted in comparable first percentile values for all three methods. This indicates that the proposed methods offer a similar margin of safety against failure than the current code, and because they give first-percentile values exceeding the reduction factor used by ACI 318-19 for torsion, $\phi = 0.75$, are also compatible with the current ACI design framework.

Table 2—Summary of analysis results: design procedures

Full dataset			
Test/Pred	ACI 318-19	Proposed—CEB-FIP s_{cr}	Proposed—Simplified s_{cr}
Count	187	187	187
Mean	1.54	1.24	1.43
COV	27.9%	19.2%	18.6%
Maximum	3.00	1.99	2.20
Minimum	0.85	0.74	0.84
% Tests < 1.0	2.7%	12.3%	2.7%
Lower half of dataset only			
Mean	1.42	1.18	1.40
COV	16.6%	13.7%	16.4%
First percentile	0.87	0.81	0.86

CONCLUSIONS

In this paper, a model was presented that can predict when torsional spalling occurs and quantify its effect on a member's strength and stiffness. The model was implemented into a nonlinear analysis framework and a design procedure and then validated using a large database of pure torsion experiments.

The main findings from this study are:

1. Modeling approaches that consider compression softening but not spalling are generally more accurate those that consider spalling but not softening. However, they become increasingly unconservative as the cover thickness increases, and are unsafe when applied to members whose normalized cover exceeds 50%.

2. Considering both full cover spalling and compression softening is conservative but gives less accurate strength predictions than traditional spalled and softened methods. This suggests that quantifying the loss of the cover concrete at the corner, rather than assuming that the full cover is lost following spalling, is more appropriate when compression softening is also considered.

3. The proposed spalling model predicts that the crack control provided by the transverse reinforcement plays an important role in determining when spalling occurs and how much concrete is lost. Based on equilibrium and experimental evidence, spalling is assumed to be concentrated at the corners of the cross section.

4. Although it was originally derived for other applications, the 1978 CEP-FIP crack spacing equation makes good predictions when used in the proposed spalling model for torsional spalling.

5. Nonlinear analysis tools and design procedures that use the proposed spalling model and the Modified Compression

Field Theory compression-softening relationship make better strength predictions than existing alternatives.

Future work should investigate how spalling propagates into the side cover, a phenomenon which appears to be caused by a different mechanism than the corner spalling discussed in this paper. Experiments examining the influence of member size on spalling should also be investigated, as the proposed model suggests that the impact of spalling becomes smaller as the overall size gets larger. Finally, spalling due to combined moment, shear, and torsion should also be investigated.

AUTHOR BIOS

Allan Kuan *is a Structural Designer at RJC Engineers, Toronto, ON, Canada. He received his BASc in engineering science in 2015 and his PhD in civil engineering in 2022 from the University of Toronto, Toronto, ON, Canada. His research interests include shear and torsion in reinforced and prestressed concrete structures.*

Evan C. Bentz, *FACI, is Professor and Associate Chair (undergrad) of civil engineering at the University of Toronto. He received his BASc from the University of Waterloo, Waterloo, ON, Canada, in 1994, and his PhD from the University of Toronto in 2000. He is a member of Joint ACI-ASCE Committee 445, Shear and Torsion, and is past Chair of ACI Committee 365, Service Life Modeling. He received the ACI Chester Paul Seiss Award in 2018 and the ACI Design Award twice.*

ACI Honorary Member **Michael P. Collins** *is a University Professor Emeritus of structural engineering at the University of Toronto, where he has led a long-term research project aimed at developing rational but simple shear and torsion design procedures for both reinforced and prestressed concrete members. The results of this work have influenced design provisions for buildings, bridges, nuclear containment structures, and offshore concrete platforms. He has six awards from ACI.*

NOTATION

A_{cp} = area enclosed by outside perimeter of concrete cross section
A_h = area of one leg of transverse torsional (hoop) reinforcement
A_l = total area of longitudinal torsional reinforcement
A_o = area enclosed by shear flow path
A_{oh} = area enclosed by centerline of closed transverse reinforcement
A_{sp} = area enclosed by outside perimeter of concrete cross section after considering corner spalling
a_o = depth of equivalent rectangular stress block/equivalent tube thickness
b_i = shorter of two side lengths which meet at i-th corner of cross section
C = compression force in concrete making up shear flow due to tension
c = cover, measured from outside surface to centerline of hoop reinforcement
d_b = bar diameter of hoop reinforcement
f_c' = specified compressive strength of concrete
f_{cr} = cracking strength of concrete
$f_{cr,av}$ = average concrete cracking strength within tube thickness
f_h = stress in transverse (hoop) reinforcement
f_t = tensile stress in concrete
f_t' = uniaxial tensile strength of concrete
f_{yh} = specified yield strength of transverse reinforcement
f_{yl} = specified yield strength of longitudinal reinforcement
f_2 = principal compressive stress in concrete
$f_{2,av}$ = Average concrete principal compressive stress within tube thickness
n = number of spalled corners
p_{cp} = outside perimeter of concrete cross section
p_h = perimeter of centerline of closed transverse torsion reinforcement
p_o = perimeter of shear flow path
p_{sp} = outside perimeter of concrete cross section after considering corner spalling
q = shear flow as result of applied torque
s = spacing of transverse torsional reinforcement
s_{cr} = average crack spacing in transverse direction
s_x = average crack spacing in longitudinal direction
s_y = average crack spacing in transverse direction
T = tension force in hoop reinforcement as result of torsion; torsion
T_n = nominal torsional strength
T_{spall} = threshold torsion above which corner spalling must be considered
T_u = factored torsional demand at section
t = distance through thickness of equivalent tube
t_d = depth of compression within equivalent tube
α_1 = ratio of average unsoftened stress in rectangular compression block to concrete cylinder strength
β_1 = ratio of depth of rectangular compression block to thickness of equivalent tube
β_{cs} = factor accounting for compression-softening effects
ε_c' = concrete strain corresponding to peak compressive stress
ε_h = strain in transverse direction
ε_l = strain in longitudinal direction
ε_1 = principal tensile strain
ε_2 = principal compressive strain
ϕ = ACI 318-19 reduction factor for torsion; $\phi = 0.75$.
θ = angle of inclination of diagonal compressive stresses to longitudinal axis of member
ρ_h = nominal quantity of transverse torsional reinforcement.

REFERENCES

1. Mitchell, D., "The Behaviour of Structural Concrete Beams in Pure Torsion," PhD thesis, Department of Civil Engineering, University of Toronto, Toronto, ON, Canada, 1974, 140 pp.

2. Rahal, K. N., and Collins, M. P., "Effect of Thickness of Concrete Cover on the Shear-Torsion Interaction—An Experimental Investigation," *ACI Structural Journal*, V. 92, No. 3, May-June 1995, pp. 334-342.

3. Mitchell, D., and Collins, M. P., "Detailing for Torsion," *ACI Journal Proceedings*, V. 73, No. 9, Sept. 1976, pp. 506-511.

4. ACI Committee 318, "Building Code Requirements for Structural Concrete (ACI 318-19) and Commentary (ACI 318R-19) (Reapproved 2022)," American Concrete Institute, Farmington Hills, MI, 2019, 623 pp.

5. CSA A23.3:19, "Design of Concrete Structures," Canadian Standards Association, Mississauga, ON, Canada, 2019, 295 pp.

6. AASHTO, "AASHTO LRFD Bridge Design Specifications and Commentary," ninth edition, American Association of State Highway and Transportation Officials, Washington, DC, 2020, 1912 pp.

7. Mitchell, D., and Collins, M. P., "Diagonal Compression Field Theory—A Rational Model for Structural Concrete in Pure Torsion," *ACI Journal Proceedings*, V. 71, No. 8, Aug. 1974, pp. 396-408.

8. MacGregor, J. G., and Ghoneim, M. G., "Design for Torsion," *ACI Structural Journal*, V. 92, No. 2, Mar.-Apr. 1995, pp. 211-218.

9. Collins, M. P., and Mitchell, D., "Shear and Torsion Design of Prestressed and Non-Prestressed Concrete Beams," *PCI Journal*, V. 25, No. 5, 1980, pp. 32-100. doi: 10.15554/pcij.09011980.32.100

10. Vecchio, F. J., and Collins, M. P., "The Modified Compression Field Theory for Reinforced Concrete Elements Subjected to Shear," *ACI Journal Proceedings*, V. 83, No. 2, Mar.-Apr. 1986, pp. 219-231.

11. Hsu, T. T. C., and Mo, Y. L., "Softening of Concrete in Torsional Members – Theory and Tests," *ACI Journal Proceedings*, V. 82, No. 3, May-June 1985, pp. 290-303.

12. *PCI Design Handbook—Precast and Prestressed Concrete*, eighth edition, Precast/Prestressed Concrete Institute, Chicago, IL, 2017.

13. Zia, P., and Hsu, T. C., "Design for Torsion and Shear in Prestressed Concrete Flexural Members," *PCI Journal*, V. 49, No. 3, 2004, pp. 34-42. doi: 10.15554/pcij.05012004.34.42

14. Lucier, G.; Walter, C.; Rizkalla, S.; Zia, P.; and Klein, G., "Development of a Rational Design Methodology for Precast Concrete Slender Spandrel Beams: Part 2, Analysis and Design Guidelines," *PCI Journal*, V. 56, No. 4, 2011, pp. 106-133. doi: 10.15554/pcij.09012011.106.133

15. Rahal, K. N., "Torsional Strength of Normal and High Strength Reinforced Concrete Beams," *Engineering Structures*, V. 56, 2013, pp. 2206-2216. doi: 10.1016/j.engstruct.2013.09.005

16. Rahal, K. N., and Collins, M. P., "Simple Model for Predicting Torsional Strength of Reinforced and Prestressed Concrete Sections," *ACI Structural Journal*, V. 93, No. 6, Nov.-Dec. 1996, pp. 658-666.

17. Rahal, K. N., "A Unified Approach to Shear and Torsion in Reinforced Concrete," *Structural Engineering and Mechanics*, V. 77, No. 5, Mar. 2021, pp. 691-703.

18. Jeng, C. H., and Hsu, T. T. C., "A Softened Membrane Model for Torsion in Reinforced Concrete Members," *Engineering Structures*, V. 31, No. 9, 2009, pp. 1944-1954. doi: 10.1016/j.engstruct.2009.02.038

19. Kuan, A.; Bruun, E. P. G.; Bentz, E. C.; and Collins, M. P., "Nonlinear Sectional Analysis of Reinforced Concrete Beams and Shells Subjected to Pure Torsion," *Computers & Structures*, V. 222, Oct. 2019, pp. 118-132. doi: 10.1016/j.compstruc.2019.07.001

20. Vecchio, F. J., and Selby, R. G., "Towards Compression-Field Analysis of Reinforced Concrete Solids," *Journal of Structural Engineering*, ASCE, V. 117, No. 6, 1991, pp. 1740-1758. doi: 10.1061/(ASCE)0733-9445(1991)117:6(1740)

21. Valipour, H. R., and Foster, S. J., "Nonlinear Reinforced Concrete Frame Element with Torsion," *Engineering Structures*, V. 32, No. 4, 2010, pp. 988-1002. doi: 10.1016/j.engstruct.2009.12.026

22. Nguyen, T.-A.; Nguyen, Q.-H.; and Somja, H., "Nonlinear Analysis of RC Members Subjected to Combined Bending–Shear–Torsion Stresses: A Numerical Multi-Fiber Displacement-Based Finite Element Model with Warping," *Acta Mechanica*, V. 232, No. 7, 2021, pp. 2635-2658. doi: 10.1007/s00707-021-02966-x

23. Bairan Garcia, J. M., and Mari, A. R., "Coupled Model for the Nonlinear Analysis of Anisotropic Sections Subjected to General 3D Loading. Part 2: Implementation and Validation," *Computers & Structures*, V. 84, No. 31-32, 2006, pp. 2264-2276. doi: 10.1016/j.compstruc.2006.08.035

24. Ibrahim, M. S., and Gebreyouhannes, E., "Spalling of Concrete Cover due to Torsion: Examination of Advanced Theoretical Models," *Proceedings of the* fib *Symposium* 2020, Nov. 2020, pp. 694-701.

25. Rahal, K. N., and Collins, M. P., "Analysis of Sections Subjected to Combined Shear and Torsion – A Theoretical Model," *ACI Structural Journal*, V. 92, No. 44, July-Aug. 1995, pp. 459-469.

26. CEB-FIP, 1978, "Model Code for Concrete Structures," CEB-FIP International Recommendations, third edition, Comité Euro-International du Béton, Paris, France, 348 pp.

27. Collins, M. P., and Mitchell, D., *Prestressed Concrete Structures*, Prentice Hall, Englewood Cliffs, NJ, 1991, 766 pp.

28. Kupfer, H. B.; Hilsdorf, H. K.; and Rusch, H., "Behavior of Concrete Under Biaxial Stresses," *ACI Journal Proceedings*, V. 66, No. 8, Aug. 1969, pp. 656-666.

29. Foster, S. J.; Liu, J.; and Sheikh, S. A., "Cover Spalling in HSC Columns Loaded in Concentric Compression," *Journal of Structural Engineering*, ASCE, V. 124, No. 12, 1998, pp. 1431-1437. doi: 10.1061/(ASCE)0733-9445(1998)124:12(1431)

30. Kupfer, H. B., and Gerstle, K. H., "Behaviour of Concrete under Biaxial Stresses," *Journal of Engineering Mechanics*, V. 99, No. 4, 1973, pp. 853-866.

31. Kuan, A.; Bentz, E. C.; and Collins, M. P., "Torsional Strength of Reinforced Concrete Members Failing by Crushing," *ACI Structural Journal*, V. 119, No. 6, Nov. 2022, pp. 233-244. doi: 10.14359/51736115

32. Popovics, S., "A Numerical Approach to the Complete Stress-Strain Curve of Concrete," *Cement and Concrete Research*, V. 3, No. 5, 1973, pp. 583-599. doi: 10.1016/0008-8846(73)90096-3

33. Thorenfeldt, E.; Tomaszewics, A.; and Jensen, J. J., "Mechanical Properties of High-Strength Concrete and Application in Design," *Proceedings of the Symposium Utilization of High Strength Concrete*, Tapir, Trondheim, Norway, 1987, pp. 149-159.

34. Collins, M. P., and Porasz, A., "Shear Design for High Strength Concrete," *CEB Bulletin d'Information*, V. 193, Dec. 1989, pp. 77-83.

35. Belarbi, A., and Tsu, T. T. C., "Constitutive Laws of Reinforced Concrete in Biaxial Tension-Compression," Research Report UHCEE 91-2, University of Houston, Houston, TX, 1991.

36. Vecchio, F. J., and Collins, M. P., "Compression Response of Cracked Reinforced Concrete," *Journal of Structural Engineering*, ASCE, V. 119, No. 12, 1993, pp. 3590-3610. doi: 10.1061/(ASCE)0733-9445(1993)119:12(3590)

37. Mikame, A.; Uchida, K.; and Noguchi, H., "A Study of Compressive Deterioration of Cracked Concrete," *Proceedings from the International Workshop on Finite Element Analysis of Reinforced Concrete*, Columbia University, New York, NY, 1991.

38. Miyahara, T.; Kawakami, T.; and Maekawa, K., "Nonlinear Behavior of Cracked Reinforced Concrete Plate Element Under Uniaxial Compression," *Concrete Library International*, V. 11, 1988, pp. 306-319.

39. Kollegger, J., and Mehlhor, G., "Experimentelle Untersuchungen zur Bestimmung der Druckfestigkeit des gerissenen Stahlbetons bei einer Querzugbeanspruchung," Report 413, Deutscher Ausschuss Für Stahlbeton, Berlin, Germany, 1990.

40. Bernardo, L. F. A., and Lopes, S. M. R., "Torsion in High-Strength Concrete Hollow Beams: Strength and Ductility Analysis," *ACI Structural Journal*, V. 106, No. 1, Jan.-Feb. 2009, pp. 39-48.

41. Fang, I. K., and Shiau, J. K., "Torsional Behavior of Normal- and High-Strength Concrete Beams," *ACI Structural Journal*, V. 101, No. 3, May-June 2004, pp. 304-313.

42. Hsu, T. T. C., "Torsion of Structural Concrete—Behavior of Reinforced Concrete Rectangular Members," *Torsion of Structural Concrete*, SP-18, American Concrete Institute, Farmington Hills, MI, 1968, pp. 261-306.

43. Jeng, C. H.; Peng, S. F.; Chiu, H. J.; and Hsiao, C. K., "New Torsion Experiment on large-Sized Hollow Reinforced Concrete Beams," *ACI Structural Journal*, V. 111, No. 6, Nov.-Dec. 2014, pp. 1469-1480. doi: 10.14359/51687166

44. Koutchoukali, N. E., and Belarbi, A., "Torsion of High-Strength Reinforced Concrete Beams and Minimum Reinforcement Requirement," *ACI Structural Journal*, V. 98, No. 4, July-Aug. 2001, pp. 462-469.

45. Lampert, P., and Thürlimann, B., "Torsionsversuche an Stahlbetonbalken," Institut fur Baustatik, ETH Zurich, Germany, January 1968.

46. McMullen, A. E., and Rangan, B. V., "Pure Torsion in Rectangular Sections—A Re-Examination," *ACI Journal Proceedings*, V. 75, No. 10, Oct. 1978, pp. 511-519.

47. Rasmussen, L. J., and Baker, G., "Torsion in Reinforced Normal and High-Strength Concrete Beams – Part 1: Experimental Test Series," *ACI Structural Journal*, V. 92, No. 1, Jan.-Feb. 1995, pp. 56-62.

48. Chiu, H. J.; Fang, I. K.; Young, W. T.; and Shiau, J. K., "Behavior of Reinforced Concrete Beams with Minimum Torsional Reinforcement," *Engineering Structures*, V. 29, No. 9, 2007, pp. 2193-2205. doi: 10.1016/j.engstruct.2006.11.004

49. Peng, X. N., and Wong, Y. L., "Behavior of Reinforced Concrete Walls Subjected to Monotonic Pure Torsion—An Experimental Study," *Engineering Structures*, V. 33, No. 9, 2011, pp. 2495-2508. doi: 10.1016/j.engstruct.2011.04.022

50. Joh, C.; Kwahk, I.; Lee, J.; Yang, I. H.; and Kim, B. S., "Torsional Behavior of High-Strength Concrete Beams with Minimum Reinforcement Ratio," *Advances in Civil Engineering*, V. 2019, Jan, 2019, p. 1432697. doi: 10.1155/2019/1432697

51. Ibrahim, M. S.; Gebreyouhannes, E.; Muhdin, A.; and Gebre, A., "Effect of Concrete Cover on the Pure Torsional Behavior of Reinforced Concrete Beams," *Engineering Structures*, V. 216, Aug, 2020, p. 110790. doi: 10.1016/j.engstruct.2020.110790

52. Nagataki, S.; Okamoto, T.; and Lee, S. H., "A Study on Mechanism of Torsional Resistance of Reinforced Concrete Members," *JSCE Transactions*, V. 1988, No. 390, 1988, pp. 179-188. doi: 10.2208/jscej.1988.390_179

53. MacGregor, J. G., "Safety and Limit States Design for Reinforced Concrete," *Canadian Journal of Civil Engineering*, V. 3, No. 4, 1976, pp. 484-513. doi: 10.1139/l76-055

54. Kuan, A., "The Behaviour and Design of Reinforced and Prestressed Concrete Members Subjected to Torsion," PhD thesis, Department of Civil & Mineral Engineering, University of Toronto, Toronto, ON, Canada, 2022, 624 pp.

55. Bentz, E. C., "Empirical Modeling of Cracking in Reinforced Concrete," *ACI Structural Journal*, V. 116, No. 3, May 2019, pp. 233-242. doi: 10.14359/51714476

ACI STRUCTURAL JOURNAL TECHNICAL PAPER

Title No. 120-S86

Behavior of Concrete Bridge-Deck Slabs Reinforced with Basalt Fiber-Reinforced Polymer and Steel Bars

by Yahia M. S. Ali, Xin Wang, Shui Liu, and Zhishen Wu

Recently, hybrid reinforcement by combining steel with fiber-reinforced polymer (FRP) bars has emerged as a new system in reinforced concrete (RC) constructions. This reinforcement system can effectively overcome the ductility and serviceability challenges of FRP-RC structures. A total of 11 full-scale bridge-deck slabs were constructed and tested. The test parameters were reinforcement type, ratio, arrangement, and slab thickness. Moreover, a comparison between the experimental and predicted deflections from design provisions was carried out to verify the efficiency of the models for hybrid RC sections. Based on test results, hybrid RC slabs exhibited ductility leading to an ample warning before failure rather than brittle shear failure observed for FRP-RC slabs. In addition, hybrid RC slabs displayed good stiffness, serviceability, and load-carrying capacity. Furthermore, test results give an average bond-dependent coefficient, k_b*, of 1.27, close to the 1.2 recommended by ACI CODE-440.11-22. In addition, some modifications were proposed to shear equations available in different design codes to be valid for hybrid RC members without shear reinforcement.*

Keywords: basalt fiber-reinforced polymer (BFRP) bar; concrete bridge; hybrid reinforcement; shear behavior.

INTRODUCTION

Bridge-deck slabs are the most critical infrastructure exposed to harsh environments (deicing salts, humidity, freezing-and-thawing cycles, and chlorides) that make these structures very susceptible to corrosion of steel reinforcement. The associated deterioration can accelerate such failure or reduce the expected life span of the structure. Within the past two decades, the most effective way to diminish maintenance costs and extend the life span of structures has been to use fiber-reinforced polymer (FRP) composites as an alternative to traditional steel reinforcement in structural components, especially where steel corrosion is a major concern. In addition to corrosion resistance, FRP composites have many characteristics over steel reinforcement, such as a high strength-to-weight ratio, excellent fatigue resistance, and nonmagnetic and nonconductive nature, which can be used in harsh environments for civil structures. Unfortunately, FRP composites have some drawbacks: a low elastic modulus compared to steel (E_f/E_s = approximately 0.25) and linear-elastic behavior up to failure without presenting any yielding plateau, which resulted in the brittle collapse of the member (Goldston et al. 2016). Many investigations have been performed to study the overall performance of concrete members reinforced with FRP bars. FRP-reinforced slabs had larger deflections and wider crack widths and depths compared to steel-reinforced slabs (Michaluk et al. 1998; Ferrier et al. 2015). Therefore, serviceability criteria often govern the design of FRP-reinforced concrete (RC) members in most instances. ACI 440.1R-15 (ACI Committee 440 2015) and CSA S806-12 (2017) permit using glass FRP (GFRP), carbon FRP (CFRP), and aramid FRP (AFRP) bars in concrete constructions.

Basalt fibers have been introduced as a promising addition to the current types of FRPs. Basalt FRP (BFRP) bars have relatively greater strength and modulus, comparable costs, and higher chemical resistance than GFRP bars (Wu et al. 2015). Thus, using BFRP bars with a relatively high elastic modulus, compared to GFRP bars, would significantly decrease the amount of reinforcement required and reduce the crack width (Elgabbas et al. 2016). Moreover, BFRP-RC beams exhibited acceptable deformability when investigated in flexure and shear (Duic et al. 2018).

LITERATURE REVIEW

In FRP-RC members, deeper cracks reduce the contribution of uncracked concrete to the shear stress due to the lower concrete depth in compression. Moreover, in the transverse direction, FRP bars have lower strength and stiffness, which led to wider cracks and lower aggregate interlock and dowel action supplement to the tensile reinforcement compared to that of an equivalent steel area (El-Sayed et al. 2006a). Finally, the total shear strength of FRP-RC members is lower than that of steel-RC members. However, traditional stirrups are not feasible for constructing slab bridges; consequently, the mode of failure may be dominated by shear (Abdul-Salam et al. 2016). Slabs reinforced with GFRP or CFRP bars failed in diagonal tension failure, while the steel-reinforced slabs failed in ductile flexure mode by steel yielding followed by concrete crushing (El-Salakawy and Benmokrane 2004). In addition, increasing the reinforcement ratio significantly improved the shear strength and the post-cracking stiffness (El-Sayed et al. 2005; Matta et al. 2013). Thus, the reinforcement type and its axial stiffness can be confirmed to have a pronounced effect on the shear strength of the RC sections.

Gradual failure can be attained by using both FRP and steel reinforcements. Therefore, steel reinforcement improves the ductility by the yielding of steel reinforcement and enhances serviceability by decreasing the deflection and crack width, while FRP reinforcement maintains the load-carrying

ACI Structural Journal, V. 120, No. 5, September 2023.
MS No. S-2022-357.R1, doi: 10.14359/51738840, received April 27, 2023, and reviewed under Institute publication policies.

capacity even after the yielding of steel bars (Qin et al. 2017). In addition, hybrid reinforcement resulted in lower crack spacing and smaller widths (Aiello and Ombres 2002). From a durability approach, the FRP bars were placed on the outer layer to attack the harsh conditions, and the steel bars were placed on the inner layer with an adequate cover to keep them away from corrosion. However, placing steel and FRP bars in one layer presented better flexural strength than placing FRP bars in the outer layer and steel bars in the inner layer (Yinghao and Yong 2013). It is found that the effective reinforcement ratio has a major impact on the flexural capacity compared with axial stiffness between GFRP and steel bars (R_f) (Qu et al. 2009). GFRP-steel RC beams showed slightly lower flexural capacity than steel-RC beams. However, the deflection and maximum crack width were large in beams reinforced with steel reinforcement at service load (Ruan et al. 2020). Furthermore, the ductility of hybrid reinforced beams can satisfy the specifications of serviceability limits by adequately regulating the reinforcement ratio and the A_f/A_s value (Ge et al. 2015). In addition, the maximum load and moment for serviceability increased with the GFRP-to-steel ratio. At the ultimate stage, the deflection obviously increases and provides a good pre-failure warning (Xingyu et al. 2020). Applying the principle of equal stiffness, the overall performance of the hybrid RC beams was superior when $A_s/A_f \leq 1.0$; however, it declined intensely when $A_s/A_f > 1.0$ (Wang et al. 2022).

An alternative method was proposed by Nanni et al. (1994) to protect the steel bar from corrosion by covering the steel core with a braided and epoxy-coated aramid or vinylon fiber FRP skin. Wu et al. (2012) developed a new kind of hybrid bar, a steel-FRP composite bar (SFCB) that combines a ribbed steel bar inside and a longitudinal FRP outside in a pultrusion process. The SFCB was created by modifying FRP pultrusion technology. The benefits of an SFCB are: 1) the pultrusion process and the ribbed inner steel bar ensure good interface properties and optimal use of each material; 2) excellent durability with the outer FRP; 3) a high elastic modulus of the SFCB due to the contribution of steel at the initial stage; 4) noticeable post-yield modulus in the stress-strain relationship after the inner steel bar yields; and 5) high strength, good ductility, anti-erosion properties, and low cost (Wu et al. 2009).

Many studies investigated the behavior of concrete members reinforced with SFCBs: beams (Sun et al. 2012; Ge et al. 2020; Yang et al. 2020), slabs (Ali et al. 2023), and columns (Sun et al. 2011; Ibrahim et al. 2017). It is found that beams reinforced with SFCBs displayed stable post-yield stiffness after the inner steel bar yielded. Although yielding the same ratio between steel and FRP, the ultimate capacity of the beam reinforced with BFRP and steel bars showed only 72% of that reinforced with SFCBs. This is attributed to the high bond stress in the hybrid beam, which led to the early slip of BFRP bars (Sun et al. 2012). Moreover, SFCB-RC beams showed enhanced stiffness, reduced crack width, and higher moment capacity than their counterparts reinforced with FRP bars (Ge et al. 2020). Using SFCBs and BFRP bars as the main reinforcement exhibited better serviceability and ductility compared to conventional hybrid RC beams (Yang et al. 2020).

To the authors' best knowledge, no research has been carried out studying the performance of concrete bridge-deck slabs reinforced with hybrid bars. Therefore, it is necessary to comprehend how these types of structures behave and later to allow and incorporate this concept into bridge design codes and specifications. Based on the authors' previous studies of this bridge deck (Ali et al. 2023), the structural behavior of the hybrid RC bridge-deck slabs without shear reinforcement was studied considering the most effective parameters that affect the deck slab performance.

RESEARCH SIGNIFICANCE

The novelty of this paper is to shed light on the structural behavior of the BFRP/steel-RC deck slabs without shear reinforcement. The slabs' performance was evaluated in terms of cracks propagation and failure modes, load-deflection response, reinforcement and concrete strains, stiffness, ductility taking into consideration the effects of reinforcement type and ratio, A_f/A_s ratio, and slab thickness. The experimental test results were used to verify the accuracy of existing models to predict the load-deflection response and to evaluate the bond-dependent coefficients, k_b, of the ribbed BFRP bars. In addition, some modifications were proposed to different code equations to predict the shear strength of hybrid RC slabs with reasonable accuracy.

EXPERIMENTAL INVESTIGATION

Design concept

The sum of the FRP reinforcement ratio, ρ_f, and steel reinforcement ratio, ρ_s, cannot be applied to directly express the reinforcement ratio of hybrid sections owing to the variations in mechanical properties between steel and FRP bars. Two types of reinforcement ratios, $\rho_{sf,s}$ and $\rho_{sf,f}$, were defined to account for combinations of the elastic modulus and strength, respectively (Pang et al. 2016). The corresponding balanced reinforcement ratios can be calculated as: $\rho_{s,b}$ is the reinforcement ratio when concrete crushing and steel yielding happen synchronously; and $\rho_{f,b}$ is the reinforcement ratio when concrete crushing and FRP bar rupturing occur simultaneously as follows

$$\rho_{sf,s} = \rho_s + \frac{E_f}{E_s}\rho_f \tag{1}$$

$$\rho_{sf,f} = \frac{f_y}{f_{fu}}\rho_s + \rho_f \tag{2}$$

$$\rho_{s,b} = \alpha_1\beta_1\frac{f_c'}{f_y}\frac{\varepsilon_{cu}}{\varepsilon_{cu}+\varepsilon_y} \tag{3}$$

$$\rho_{f,b} = \alpha_1\beta_1\frac{f_c'}{f_{fu}}\frac{\varepsilon_{cu}}{\varepsilon_{cu}+\varepsilon_f} \tag{4}$$

Hybrid FRP-steel slabs were designed in which $\rho_{sf,s} \leq \rho_{s,b}$ and $\rho_{sf,f} \geq \rho_{f,b}$. Therefore, the designed failure mode can be defined as follows: firstly, the steel bars yield; subsequently, the concrete is crushed in compression; and lastly, the slab fails. This failure would provide sufficient warning before slab failure can be attained.

Material properties

The deck slab specimens are fabricated using normal-weight ready mixed concrete to cast all the slabs on the same day. The concrete mixture design proportions per cubic meter are 169 L of water, 452 kg of cement, 639 kg of sand, 1088 kg of aggregate, and an air content of 5 to 6% to achieve a slump of 150 ± 30 mm. The average compressive strength was evaluated by testing three standard 150 mm concrete cubes after 28 days of curing. The concrete cubes yielded an average compressive strength of 52 ± 1.3 MPa. It is worth mentioning that the cylinder compressive strength of concrete, f_c', was calculated based on ACI codes, whereas $f_c' = 0.8f_{cu}$. The reinforcing bars used in this paper included ribbed steel bars, BFRP bars, and SFCBs, as shown in Fig. 1. BFRP bars are made of basalt fibers and epoxy resin, and basalt fiber content by weight is 70% according to the manufacturer. For SFCB production, 10 mm diameter inner ribbed steel bars were used and wrapped with basalt fibers that consisted of BFRP combined with a vinyl ester resin. Axial tensile tests were conducted to evaluate the mechanical properties of the different reinforcing bars according to ASTM D7205/D7205M (2016), as applicable. The results of the average three specimens of reinforcing bars are reported in Table 1 and shown in Fig. 2.

Fig. 1—Configuration of BFRP and SFCB reinforcing bars: (a) geometry of BFRP bars and SFCBs; and (b) cross sections.

Test specimens

Eleven large-scale RC slabs with a total length (L_t) of 2900 mm and a width (b) of 1000 mm were used. The boundaries of the slabs were delineated considering the contraflexural lines. Moreover, these dimensions are the most popular size of the bridge-deck slabs for girder-type in North America (El-Salakawy et al. 2003; El-Salakawy and Benmokrane 2004). Nine slabs had a depth (h) of 200 mm (according to the requirements of CSA S6 [2019]), one slab had a depth of 250 mm, and the last one had a depth of 120 mm. The investigated parameters were the reinforcement type, effective reinforcement stiffness $\rho_{sf,s}$, the ratio between the area of FRP and steel bars A_f/A_s, reinforcement arrangement, and slab thickness. All slabs have the same steel reinforcement in all directions, 12 mm with a spacing of 225 mm, except the bottom longitudinal reinforcement. The clear concrete covers were 50 mm and 25 mm for the top and bottom reinforcement, respectively. The slab specimens were identified according to the amount and type of longitudinal reinforcement (XB or XBXS), where the letters X, B, and S indicate the number of bars, BFRP reinforcing bar, and steel reinforcing bar, respectively.

The test program was categorized into four groups based on the test parameters studied. Group A (reference group) consists of two slabs (8B and 5B3S) studying the effect of reinforcement type. In Group B, slabs (5B7S, 6B7S, and 10B6S) investigate the influence of increasing the effective reinforcement stiffness, $\rho_{sf,f}$, compared to Group A. It is worth noting that the slabs in this group were designed with similar $\rho_{sf,s}$ to study the impact of the A_f/A_s ratio. Group C includes slabs (5B5S, 5S5B, and 5B5S-S) that vary in reinforcement arrangement, where S (the last letter in Slab 5B5S-S) represents that the reinforcement is arranged in a single layer. Regarding Slab 5S5B, which placed steel bars at the outer layer, it is not efficient from the durability point of view; this system is examined only to evaluate the influence of the reinforcement arrangement on the structural performance

Table 1—Properties of reinforcing bars

Bar type	d, mm	E_I, GPa	f_y, MPa	E_{II}, GPa	f_u, MPa	ε_u, %
Steel	10	200	420	—	632	3.30
	12	200	452	—	667	3.16
	16	200	494	—	688	3.50
BFRP	15.6	55 ± 0.60	—	—	1163 ± 27.3	2.12 ± 0.12
SFCB	15.5	105 ± 2.4	263 ± 4.7	32 ± 3.2	756 ± 16.2	3.71 ± 0.16

Note: 1 mm = 0.0394 in.; 1 MPa = 145 psi; 1 GPa = 0.145 ksi.

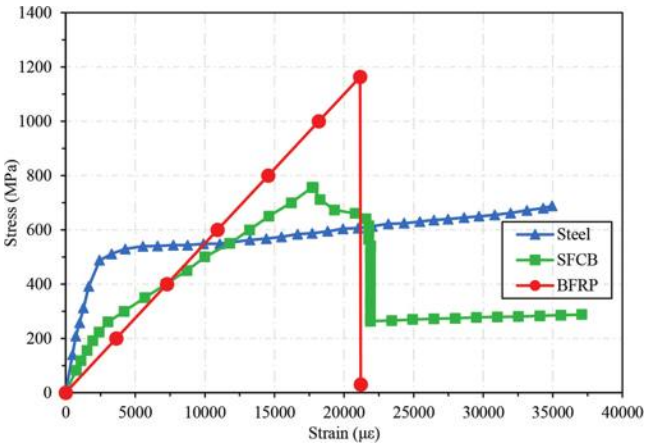

Fig. 2—Stress-strain relationships of reinforcements.

of the hybrid deck slabs. The last group comprised three slabs (9SFCB-200, 9SFCB-250, and 9SFCB-120) with three different thicknesses (200, 250, and 120 mm) to study the effect of different slab thicknesses. Table 2 summarizes the details of the slabs. Figure 3 shows the cross sections of all deck slabs.

Test program and instrumentation

The slabs were tested under four-point bending loading up to failure. Figure 4 provides the test setup and schematic diagram of the slabs. A steel spreader beam was used to transform the two concentrated loads 900 mm apart, yielding a shear span (a) of 900 mm on both sides with a clear span length (L) of 2700 mm. Two half-cylinders with 100 mm diameters were used for loading; however, two full cylinders were used to support the slab specimens, as shown in Fig. 4. The load was applied with displacement control at a constant rate of 0.6 mm/min by the hydraulic jack of 500 kN capacity to measure the applied loads, with a displacement sensor to measure the corresponding deflection. The load gradient was established at 5 kN up to an applied load of 100 kN to detect crack widths. After the applied load reached 100 kN, the load gradient was increased to 10 kN until the failure of the slab. Three linear variable differential transformers (LVDTs) were positioned at the bottom midspan and the two loading points of each slab, and two LVDTs were installed at the supports to offset their settlements. Five electrical strain gauges were attached to the slab surface to measure the concrete strain along the depth of the slab, and four strain gauges were also attached to the surface of the tensile reinforcement. The applied loads, deflections, and strain readings at a frequency of 10 Hz were automatically recorded using a data acquisition system. The crack width was measured using a handheld readout microscope with a magnification factor of 40× with an accuracy of 0.01 mm.

EXPERIMENTAL RESULTS AND DISCUSSION

Crack patterns and propagation

Figure 5 shows the crack distribution of the tested deck slabs upon failure. The first crack was initiated in the pure bending moment zone. Generally, the cracking load was recorded at a similar load level for slabs of the same thickness, while increasing the slab thickness increased the cracking load, as listed in Table 3. As the load increased, more flexural cracks began to develop below or between the point loads. With further loading, flexural-shear and shear cracks appeared and spread in the shear spans, demonstrating the shear stresses in the shear span. Once the steel yielded, the number of cracks increased and propagated, accompanied by the widening of the existing cracks.

Table 2—Details of tested slabs

Group No.	Slab	A_f/A_s	$\rho_{sf,s}$ %	$\rho_{sf,f}$%	$\rho_{sf,s}/\rho_{s,b}$	$\rho_{sf,f}/\rho_{f,b}$
A	8B	—	0.25	0.89	0.09	3.14
	5B3S	1.58	0.59	0.75	0.20	2.65
B	5B7S	0.68	1.18	1.00	0.40	3.53
	6B7S	0.81	1.19	1.12	0.41	3.95
	10B6S	1.58	1.18	1.48	0.40	5.22
C	5B5S	0.95	0.88	0.93	0.30	3.28
	5S5B		0.79	1.00	0.27	3.53
	5B5S-S		0.76	0.88	0.26	3.11
D	9SFCB-200	1.40	0.59	0.82	0.20	2.05
	9SCFB-250		0.46	0.64	0.15	1.60
	9SCFB-120		1.14	1.59	0.38	3.98

Slab 8B showed a larger number of shear cracks, and the crack length propagated quickly due to the low stiffness modulus of the BFRP bar. In addition, Slab 8B yielded higher crack spacing, more severe cracking, and a lower number of cracks than Slab 5B3S, thus tending to suggest substituting BFRP bars with steel bars to improve the axial stiffness of the slab. Increasing the reinforcement ratio increases the number of major and minor cracks, improves the crack distribution length, and reduces the average minor and major crack spacing. This result is clarified by better bond strength as the number of longitudinal bars increases (Nguyen et al. 2020). Moreover, Slab 5B7S displayed low average crack spacing at the same load level compared to Slab 10B6S. The same phenomenon was reported by Ge et al. (2015); the average crack spacing diminishes with the reduction of A_f/A_s.

Modes of failure

The combined effect of high shear force and bending moment leads to a spatially high-stress area; hence, failure occurs in the shear span. Four different failure modes were observed in the experimental tests and are listed in Table 3.

Mode I: Diagonal tension failure (DTF)—This mode was observed only for Slab 8B reinforced with BFRP bars owing to the low stiffness of BFRP bars, as shown in Fig. 5. At a high load level, the shear cracks continued to widen due to the absence of shear reinforcement until failure occurred. The diagonal shear crack occurred at 100 mm far from the support, making it approximately 42 degrees with the horizontal, then extended toward the loading point and widened and propagated, leading to slab collapse. Moreover, the failure was accompanied by local bending of steel bars in the compression zone keeping the slab intact as one part, as shown in Fig. 6. This phenomenon led to improved ductility and integrity of the slab. In contrast, a previous

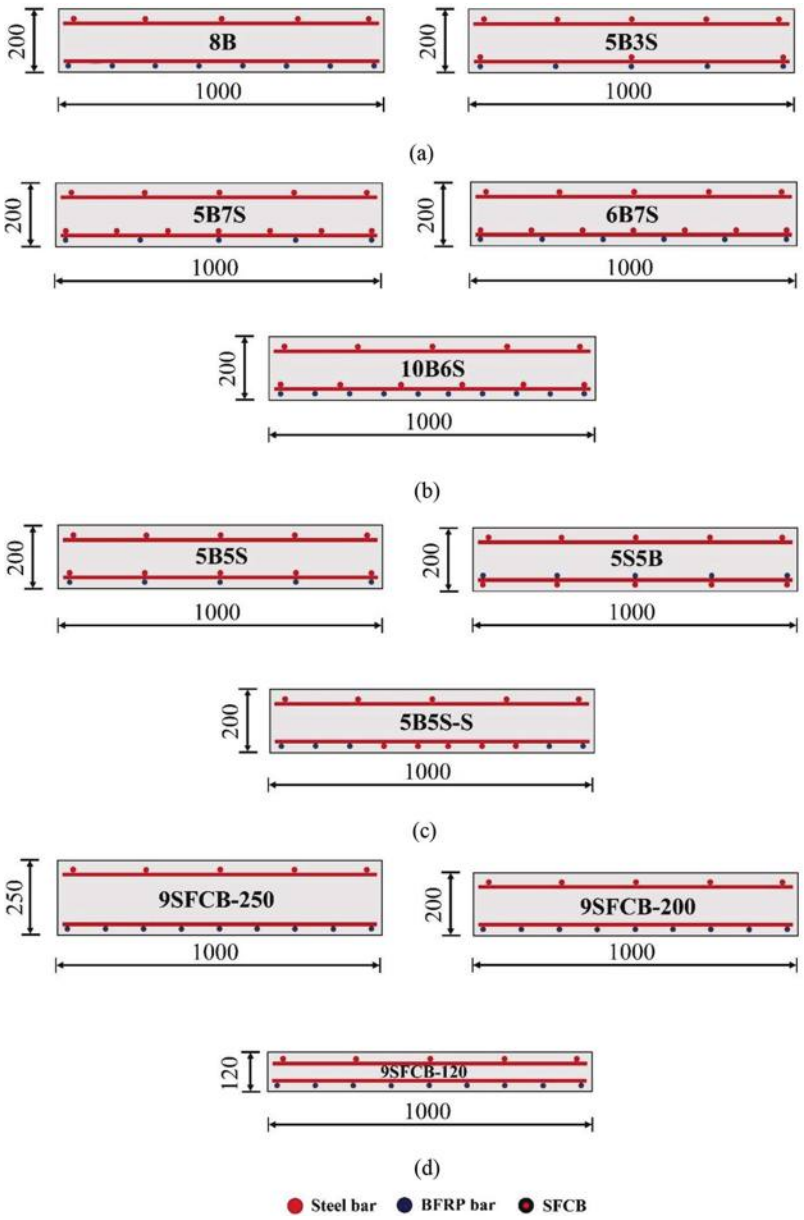

Fig. 3—Reinforcement details of tested deck slabs: (a) Group A; (b) Group B; (c) Group C; and (d) Group D. (Note: Dimensions in mm; 1 mm = 0.0394 in.)

study observed that using FRP bars in the compression zone resulted in the shearing off of FRP bars, and the slabs were divided into two parts (Abdul-Salam et al. 2016).

Mode II: Flexural-shear failure (FSF)—This mode was observed for Slabs 5B3S, 5B5S, 5S5B, and 9SFCB-200, which initiated as a flexural crack closer to the loading point and then propagated inclining upward to the loading point. As shown in Fig. 5, the failure was gradual, and the slabs displayed some ductility before reaching the ultimate load, rather than the brittle shear failure observed in Slab 8B. This may be attributed to the higher load levels reached, which confirms the enhancement of the shear resistance by the improved dowel action of the double-layer reinforcement (Yoo et al. 2016).

Mode III: Shear-compression failure (SCF)—In this mode, the compression zone in the slab was reduced by the inclined flexure-shear cracks; thus, the concrete was crushed in Slabs 6B7S, 10B6S, and 5B5S-S, as shown in Fig. 5. The main crack that makes the failure for these slabs has an inclined degree of 55 to 68 degrees. Additionally, the failure was accompanied by concrete-cover spalling on the tension side without FRP bars shearing off, and the slab maintained its integrity even after failure, which can be attributed to the high reinforcement ratio and A_f/A_s in these slabs. Accordingly, a minimum amount of steel reinforcement with a reasonable value of A_f/A_s is recommended to ensure ductility and prevent the devastating failure of concrete bridge-deck slabs.

Regarding the arrangement of reinforcement, Slab 5B5S-S, with reinforcement arranged in a single layer, exhibited severe failure compared with its counterparts arranged in a double layer owing to deteriorated bond performance caused by the small spacing of the reinforcement (Yang et al. 2020). Minor differences were noted in the distribution and shape of the flexural cracks for all tested slabs. However, the slab failure mechanism changes between the BFRP-RC slab and

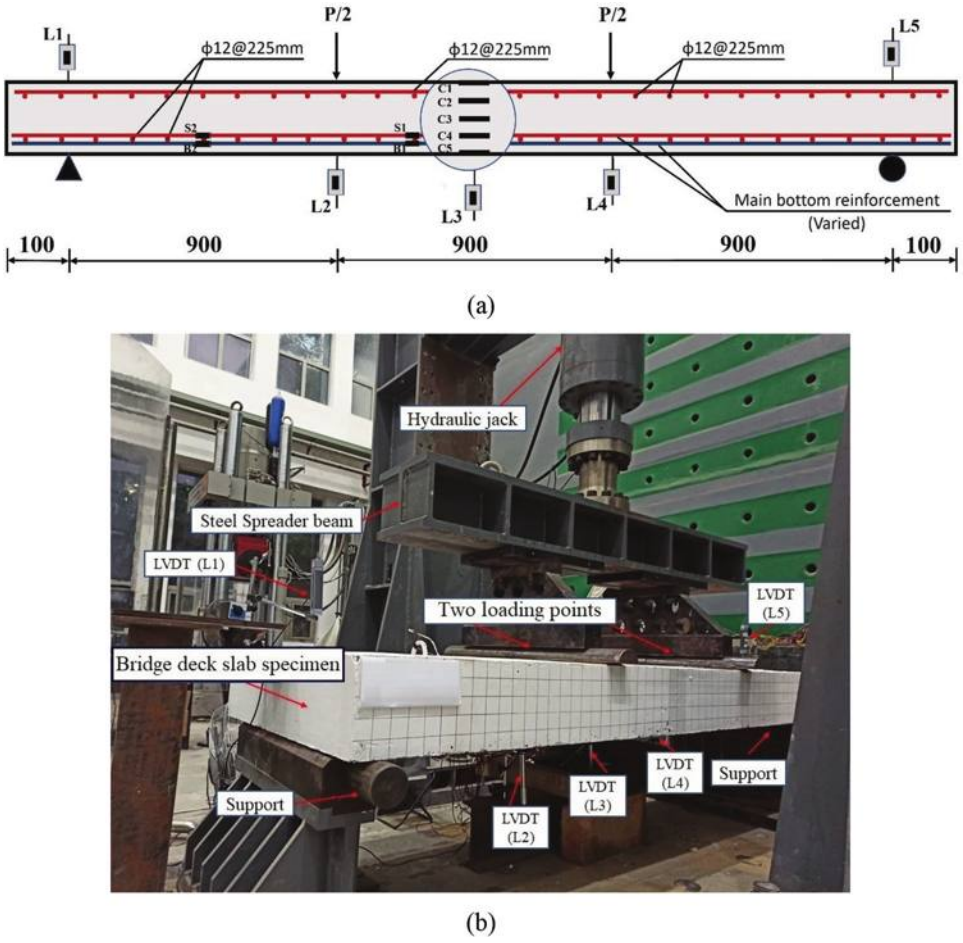

Fig. 4—Test setup: (a) schematic drawing; and (b) slab specimen ready for testing. (Note: Dimensions in mm; 1 mm = 0.0394 in.)

hybrid RC slabs could be due to the difference in the shear-crack location. The shear crack in Slab 8B initiated closer to the support due to the diagonal tension stresses, resulting in a crack closer to the support (100 mm). In contrast, Slab 5B3S experienced no significant shear cracks, which moved the crack location closer to the loading point (300 mm). It can be related to the contribution of arch action, which was dependent on the critical shear-crack location. The crack was far from the support in hybrid slabs, allowing the arch action to contribute more.

A discussion of flexural analysis was presented (refer to the Appendix*), demonstrating that the hybrid RC slabs reached their flexural capacities before failure. Therefore, this failure is considered a combination of flexural and shear failure.

Mode IV: Flexural failure (FF)—This mode was observed for Slabs 5B7S, 9SFCB-250, and 9SFCB-120 by steel yielding where the main crack was approximately under the point load. These slabs did not display any bond-splitting cracks, which shifted the crack location closer to the loading point. Generally, using hybrid reinforcement to reinforce the deck slabs, either separate reinforcing bars or SFCBs, could achieve some plastic deformations of concrete before total failure; thus, this type of section is admissible in the design of hybrid RC members without shear reinforcement.

Strain distribution

Figure 7 shows the strain distribution of concrete along the cross-section height at various loading stages. The average concrete strain along the cross-section height is almost linear and proportional to the distance from the neutral axis, reflecting that the assumption of the plane cross section is valid for hybrid RC slabs, as shown in Fig. 7. The depth of the neutral axis of FRP-reinforced deck slab 8B was smaller than the depth of the neutral axis of hybrid reinforced deck slab 5B3S, indicating the influence of the modulus of the steel bars when added to the slab reinforcement.

Ultimate capacity

The ultimate capacity for all tested slabs is listed in Table 3. The test results revealed that hybrid slab 5B3S showed a slight increase of 6% in the ultimate capacity compared with Slab 8B reinforced with pure BFRP bars. This is attributed to the amount of BFRP bars in Slab 5B3S being less than that of Slab 8B, whereas BFRP bars are responsible for carrying the additional load after the steel yielded. In addition, the ultimate capacity increased, as did the reinforcement ratio (Tureyen and Frosch 2002). For example, Slab 6B7S showed an increase in the ultimate capacity of 39% compared to control slab 5B3S. This is due to the function

*The Appendix is available at **www.concrete.org/publications** in PDF format, appended to the online version of the published paper. It is also available in hard copy from ACI headquarters for a fee equal to the cost of reproduction plus handling at the time of the request.

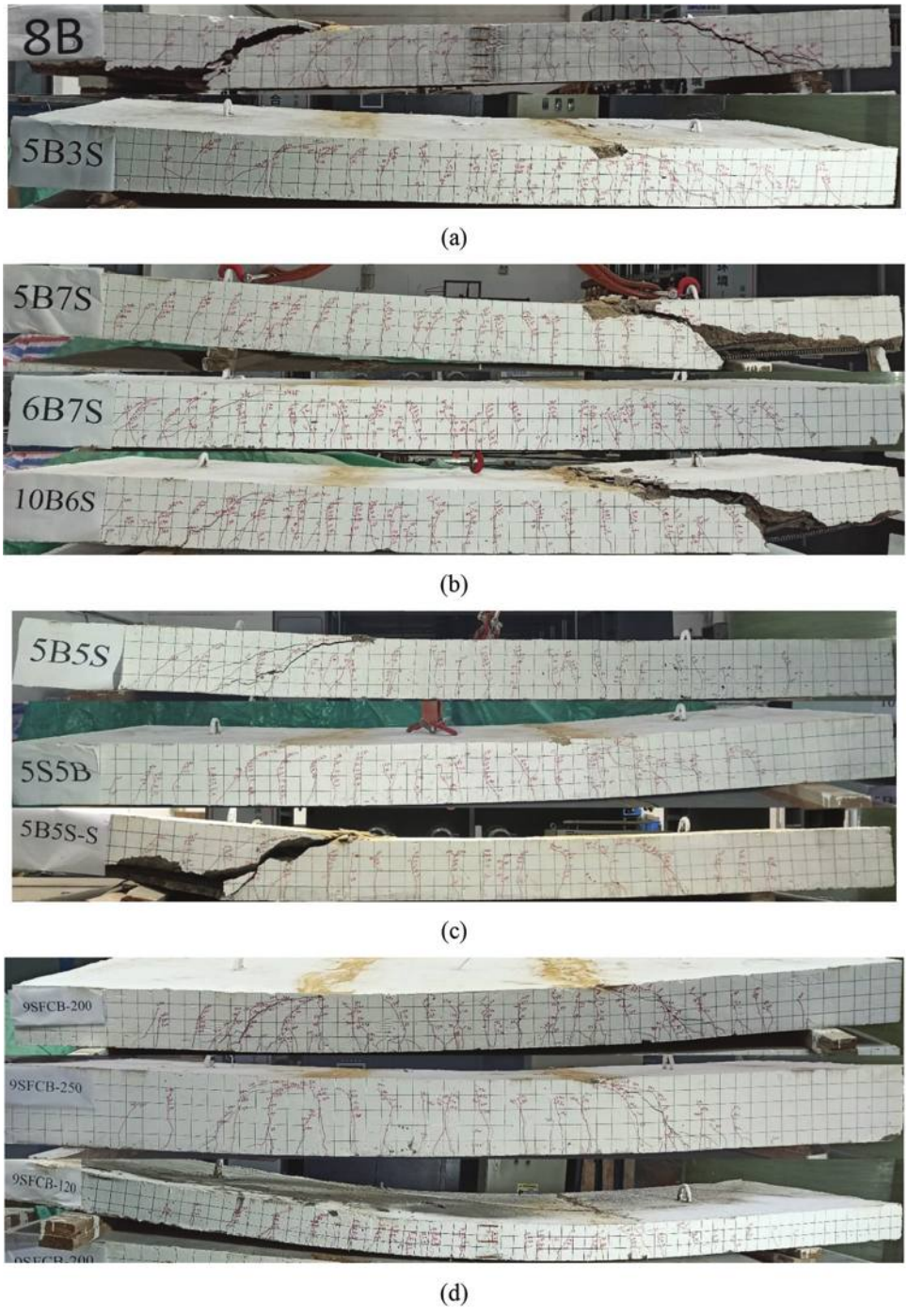

Fig. 5—Crack patterns and failure modes of tested slabs: (a) Group A; (b) Group B; (c) Group C; and (d) Group D.

of the longitudinal reinforcement in decreasing the opening and propagation of cracks resulting in smaller crack width, which increases the uncracked concrete depth and improves the aggregate interlock across the cracks. Moreover, Slab 10B6S contains the highest FRP-to-steel content (A_f/A_s = 1.58) and showed an improvement in ultimate capacity by 13% compared with Slab 5B7S (A_f/A_s = 0.68).

The reinforcement arrangement affects the ultimate capacity because Slab 5B5S-S, reinforced in a single layer, exhibited higher ultimate capacity than slabs arranged in a double layer. The ultimate capacity of Slab 5B5S-S is approximately 1.22 and 1.18 times the ultimate capacity of Slabs 5B5S and 5S5B, respectively. From the mechanical point of view, placing the BFRP and steel bars at the outer layer is more effective than placing the BFRP bars at the outer layer. Experimental results from Slab 9SFCB-250 showed that shear capacity could be enhanced with increasing slab stiffness compared to Slab 9SFCB-200. The ultimate shear capacity of Slab 9SFCB-200 was 292 kN, while Slab 9SFCB-250 failed at 359 kN, that is, a 23% improvement. Increasing the slab thickness increases the surface area that resists the shear stresses, yielding higher shear capacity.

Load-deflection relationship

Figure 8 shows the load-midspan deflection curves for the tested deck slabs. All slabs showed a steep linear behavior at the pre-cracking stage with low deflection values. In the post-cracking stage, slab stiffness was significantly degraded

Table 3—Test results of tested slabs

Group	Slab	Δ_{cr}, mm	Δ_y, mm	Δ_u, mm	P_{cr}, kN	P_y, kN	P_u, kN	M_{exp}/M_{pred}	Failure mode
A	8B	2.3	—	63	36	—	295	0.80	DTF
	5B3S	1.7	19.1	78	41	179	314	1.43	FSF
B	5B7S	1.2	22.3	67	42	260	414	1.56	FF
	6B7S	2.0	20.1	49	46	251	437	1.59	SCF
	10B6S	1.9	20.3	45	47	294	470	1.62	SCF
C	5B5S	2.3	20.6	68	43	190	325	1.42	FSF
	5S5B	2.3	18.4	73	38	190	335	1.34	FSF
	5B5S-S	3.7	16.5	58	49	211	396	1.51	SCF
D	9SFCB-200	1.5	13.3	77	34	146	292	1.23	FSF
	9SFCB-250	3.1	13.2	65	99	212	359	1.22	FF
	9SFCB-120	8.8	21.9	144	26	69	147	2.18	FF
Average*			—	—	—	—	—	1.51	—
Standard deviation*			—	—	—	—	—	0.26	—
Coefficient of variation*, %			—	—	—	—	—	17	—

*These characteristics were calculated only for hybrid RC deck slabs; DTF is diagonal tension failure; FSF is flexural-shear failure; FF is flexural failure; SCF is shear-compression failure.

Note: 1 mm = 0.0394 in.; 1 kN = 0.225 kip.

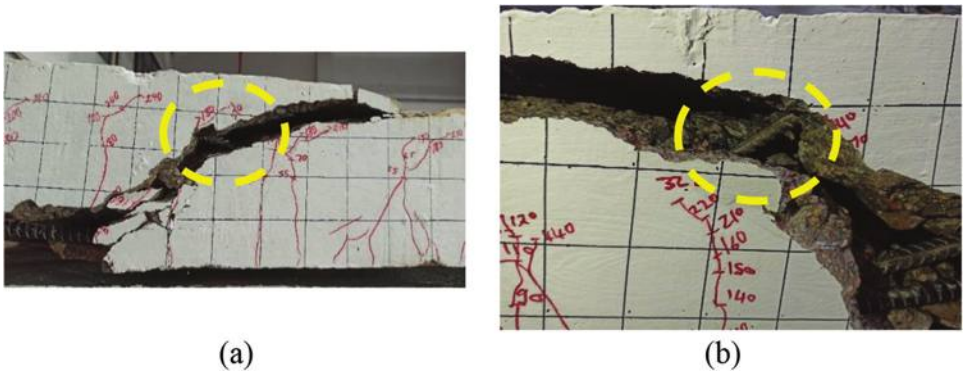

(a) (b)

Fig. 6—Bending of steel bars in compression zone: (a) 8B; and (b) 10B6S.

due to flexural cracks, which reduced the moment of inertia. Slab 8B exhibited a bilinear load-midspan deflection curve and degraded faster than hybrid RC slabs due to the lower elastic modulus of the BFRP bars, as shown in Fig. 8(a). Conversely, hybrid RC slabs exhibited trilinear load-deflection curves owing to the presence of steel bars. As shown in Fig. 8, after steel yielded, a pronounced reduction in the slope of the load-deflection curves as the load increased to high levels means that steel reinforcement cannot resist any additional load, and only the BFRP reinforcement carried the load upon failure. In this stage, the deflection of hybrid deck slabs was lower than the deflection of Slab 8B, attributed to the efficiency of the BFRP bars restricting the excessive deflection even after steel yielding. Hence, using hybrid bars to reinforce the concrete bridge-deck slabs keeps the load growing with a reasonable deflection value.

In Group A, Slab 8B suffered a larger deflection than Slab 5B3S under the same load level, as shown in Fig. 8(a). This is attributed to the high elastic stiffness of steel bars compared to BFRP bars, which increased the rigidity of the hybrid slabs. At the yielding load of Slab 5B3S, the deflection decreased by 43% compared to Slab 8B. After steel yielding, a secondary stiffness was detected only for hybrid deck slabs. This observation proves the concept of the hybrid section that the significant role of FRP bars brightens after steel yielding. For Group B, increasing the reinforcement ratio increased the post-cracking stiffness, and hence decreased the deflection at similar load levels (El-Sayed et al. 2006b).

Regarding the A_f/A_s, there was a slight influence of the ratio of A_f/A_s on the stiffness after cracking. However, a significant enhancement in stiffness was noticed after steel yielding for Slab 5B7S in comparison to Slab 10B6S; thus, as A_f/A_s increases, the deflection decreases (Safan 2013). For example, at the load of 294 kN, the deflection of Slab 10B6S was 30% lower than the deflection of Slab 5B7S because the former had a high A_f/A_s, which enhanced the slab rigidity by restricting the excessive deflection after the steel yielded. The foregoing results proved the significant influence of the A_f/A_s on the post-elastic strength of bridge-deck slabs with sufficient deformability and stiffness.

Considering the reinforcement arrangement in Group C, both slabs reinforced in a double layer developed larger deflection than the slabs arranged in a single layer, as shown

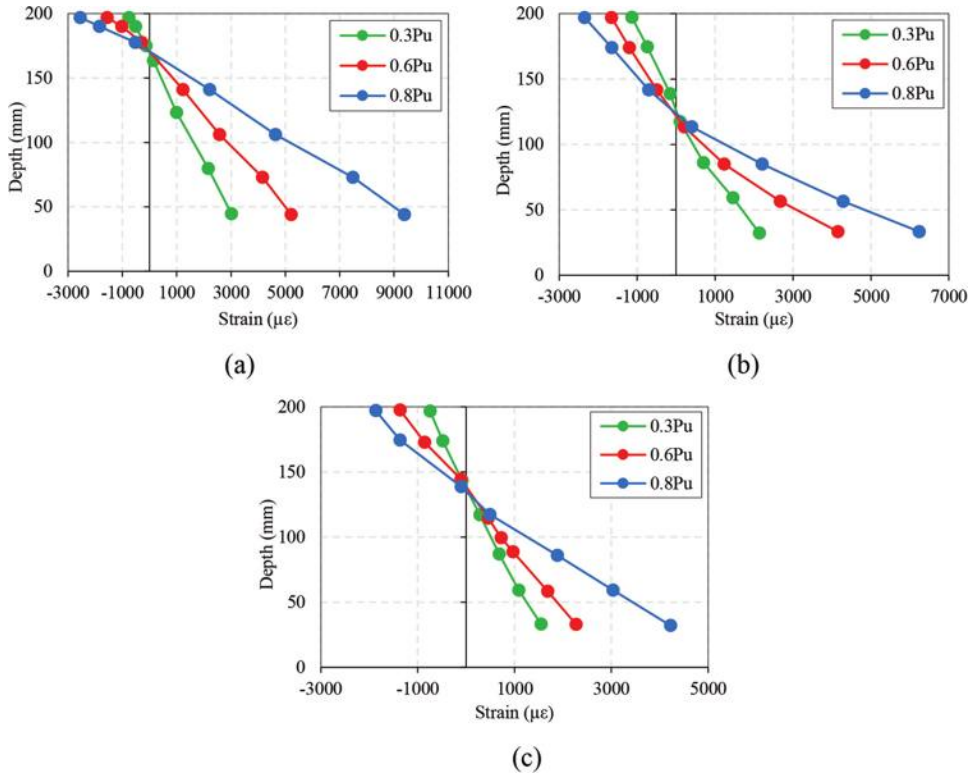

Fig. 7—Strain distribution of tested slabs: (a) 8B; (b) 5B3S; and (c) 10B6S. (Note: 1 mm = 0.039 in.)

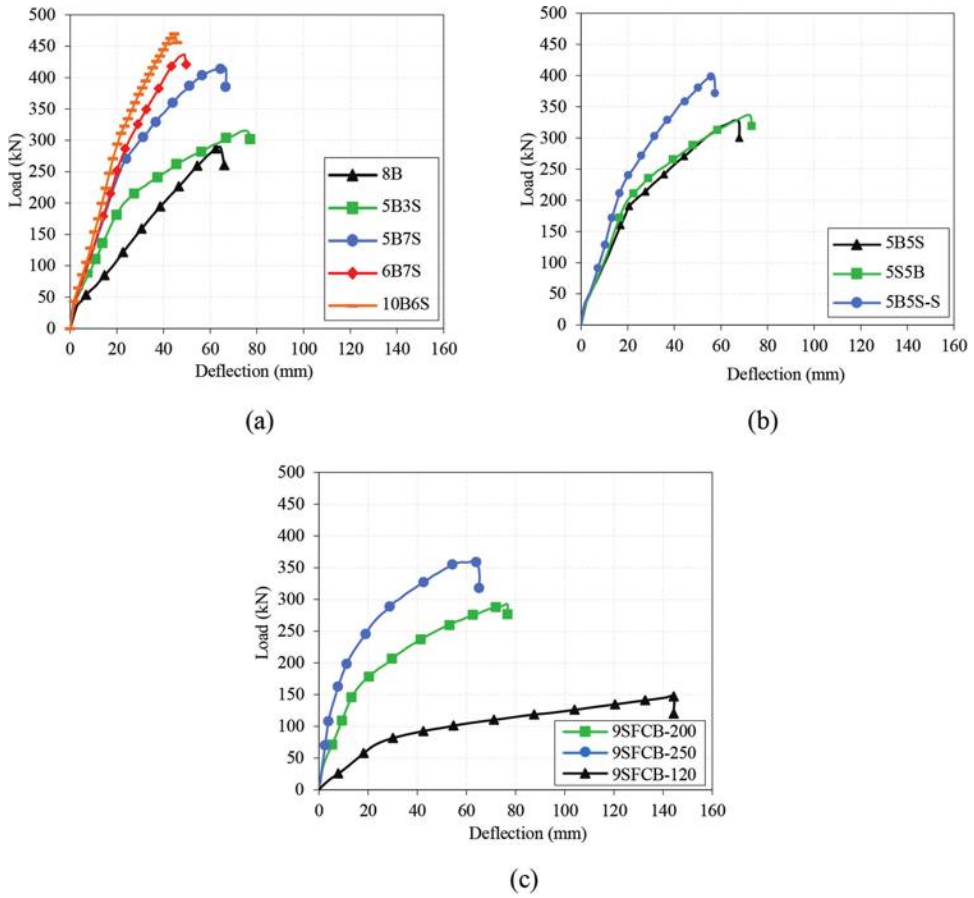

Fig. 8—Load-deflection relationships of tested slabs: (a) Groups A and B; (b) Group C; and (c) Group D. (Note: 1 kN = 0.225 kip; 1 mm = 0.0394 in.)

in Fig. 8(b). At a load of 200 kN (approximately the yielding load of this group), the deflections of Slabs 5B5S, 5S5B, and 5B5S-S were 23.9, 20.2, and 15.7 mm, respectively. This means that by increasing the depth of the steel bars layer, the stiffness degradation of the double-layer hybrid deck slab was faster than that of the single-layer hybrid deck slab (Yinghao and Yong 2013). The slab thickness had a clear effect on the stiffness of SFCB slabs, as shown in Fig. 8(c). An apparent reduction in the deflection was found when increasing the slab thickness from 120 mm to 200 and 250 mm while maintaining a constant reinforcement amount. This is due to increasing the moment of inertia of the slabs.

Stiffness

Based on the experimental test results, two stiffness factors were calculated to measure the stiffness of the tested deck slabs before and after yielding: the initial equivalent stiffness, K_I, and secondary stiffness, K_{II}, respectively (Sun et al. 2019).

$$K_I = \frac{P_y}{\Delta_y} \tag{5}$$

$$K_{II} = \frac{P_u - P_y}{\Delta_u - \Delta_y} \tag{6}$$

The stiffness factors are listed in Table 4. The results showed that the slab stiffness tended to improve with increasing the effective reinforcement ratio, $\rho_{sf,f}$, due to the improvement in the axial stiffness of the deck slab. Thus, Slab 5B3S designed with a low $\rho_{sf,f}$ suffered from stiffness degradation after cracking. Increasing the reinforcement ratio from 0.59 to 1.19% in Slabs 5B3S and 10B6S increased the initial and secondary stiffness K_I and K_{II} by 54% and 218%, respectively. A slight influence of A_f/A_s on the initial stiffness, K_I, and a significant enhancement of 83% in the secondary stiffness, K_{II}, were observed for Slab 6B7S in comparison to Slab 5B7S. This indicated that the initial equivalent stiffness was affected by steel reinforcement rather than BFRP reinforcement due to the significant variation in the elastic modulus (Nguyen et al. 2020). In contrast, the secondary stiffness depended on BFRP reinforcement due to steel yielding, which could not bear any additional load. The post-yielding stiffness of hybrid RC slabs can lead to a smaller residual deformation during unloading.

Consequently, the equal stiffness design principle is recommended to realize a damage-controllable structure under earthquakes (Wu et al. 2009; Wang et al. 2022). For Group C, the secondary stiffness, K_{II}, did not show a big difference between the two slabs arranged in double layers. However, K_{II} for Slab 5B5S-S was higher than both Slabs 5B5S and 5S5B, which means that the stiffness degradation of the double-layer hybrid deck slab was faster than that of the single-layer hybrid deck slab (Yinghao and Yong 2013). Among all the tested slabs, Slab 9SFCB-250 showed the highest initial stiffness, 16.15 kN/mm, due to increasing the moment of inertia, hence improving the slab stiffness; on the other hand, Slab 9SFCB-120 showed the lowest one, 3.13 kN/mm.

Table 4—Stiffness and ductility of tested slabs

Group	Slab	K_I	K_{II}	J_{mod}
A	8B	—	—	4.2
	5B3S	9.44	2.28	7.5
B	5B7S	11.64	3.48	5.3
	6B7S	12.52	6.38	5.1
	10B6S	14.50	7.24	4.8
C	5B5S	9.23	2.86	5.7
	5S5B	10.32	2.63	6.2
	5B5S-S	12.80	4.52	6.5
D	9SFCB-200	10.96	2.31	7.5
	9SFCB-250	16.15	2.80	6.3
	9SFCB-120	3.13	1.13	6.0

Ductility

Ductility refers to the amount of inelastic deformation that can be undergone without losing load-carrying capacity before complete failure. This paper adopted the deformation-based approach to evaluate the ductility of hybrid reinforced deck slabs. The overall performance factor, J, was adopted by CSA S6:19, which combines the strength and deformability provided by Eq. (7).

$$J = \frac{\Psi_u M_u}{\Psi_s M_s} \tag{7}$$

The moment and curvature at the serviceability limit state are taken as the point when the maximum concrete compressive strain reaches a value of 0.001. CSA S6:19 states that the overall performance factor, J, should be at least 4.0 for rectangular sections. Equation (7) uses service moments, M_s, at a concrete strain of 0.001, as recommended by CSA S6:19, neglecting the yielding of steel bars. Therefore, a modified overall performance factor, J_{mod}, was suggested for hybrid reinforced beams taken as the ratio of the product of moment and curvature at the ultimate to the product of moment and curvature at the yielding of steel reinforcement, as given in Eq. (8) (El Refai et al. 2015). It should be mentioned that J_{mod} was used only for slabs reinforced with hybrid reinforcement.

$$J_{mod} = \frac{\Psi_u M_u}{\Psi_y M_y} \tag{8}$$

Table 4 shows the values of the modified overall performance factor, J_{mod}, of all tested deck slabs. The inclusion of steel bars in Slab 5B3S improved the J_{mod} by 79% compared to Slab 8B. Slabs with lower reinforcement ratios showed a higher performance due to the proportional decrease in the stiffness of the slabs with the decrease in the reinforcement ratio (Liu et al. 2022). Increasing the reinforcement ratio from 0.59 to 1.18% (Slabs 5B3S and 10B6S) reduced the J_{mod} from 7.5 to 4.8. This is attributed to the enhanced reinforcement axial stiffness; increasing the reinforcement

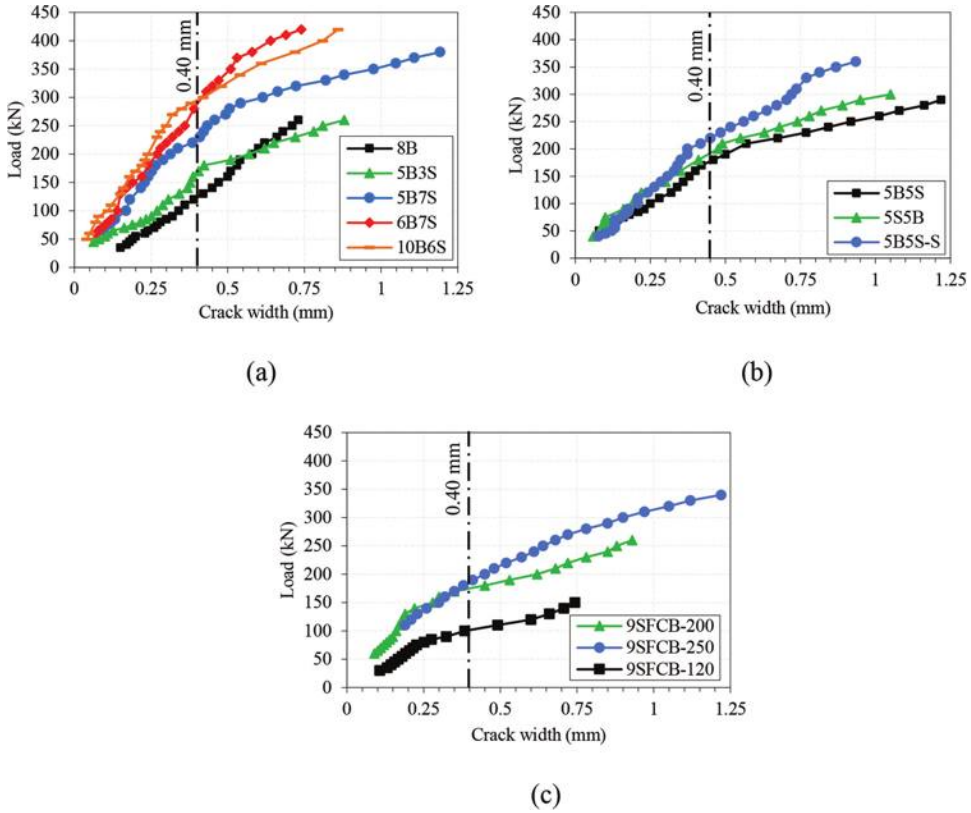

Fig. 9—Load-maximum crack width relationships of tested slabs: (a) Groups A and B; (b) Group C; and (c) Group D. (Note: 1 kN = 0.225 kip; 1 mm = 0.0394 in.)

axial stiffness restricts the propagation of cracks, leading to narrower and shorter cracks. While the overall performance factor retracted slowly with the increase in A_f/A_s, it can record its maximum value at a low value of A_f/A_s. This is because the ultimate deflection and the ultimate load show variations, changing trends with the increase in A_f/A_s. With respect to the reinforcement arrangement, it can be found that the overall performance factor of the single-layer hybrid RC slab 5B5S-S is 6.5, which is larger than that of the double-layer hybrid RC slab (5.7 for 5B5S). The values of the modified overall performance factor satisfied the CSA S6:19 requirements, which ranged from 4.2 to 7.5. The higher values of the overall performance factor imply more ample warning by exhibiting a significant deformation at the ultimate state of the hybrid RC deck slabs before failure. Therefore, the hybrid RC slabs can meet the requirements of deformability by using an adequate value of A_f/A_s.

Crack width

Figure 9 shows the applied load-crack width curves. The load-crack width relationship was almost linear for the pure BFRP-RC slab; however, all hybrid deck slabs exhibited a bilinear curve owing to the yielding of steel bars. In Group A, replacing the BFRP bars with steel bars could restrain crack depth and fast propagation due to the higher elastic modulus of the steel bars. As shown in Fig. 9(a), the crack widths were inversely proportional to the reinforcement ratio. Thus, the measured crack width was lower in the case of Slab 6B7S than in Slab 5B3S. Moreover, a higher ratio of FRP-to-steel amount A_f/A_s led to better secondary stiffness and hence narrower crack widths. Placing BFRP reinforcement in the outer layer recorded a wider crack width for Slab 5B5S, followed by Slabs 5S5B and 5B5S-S. Figure 9(c) shows that higher crack width values were recorded for Slab 9SFCB-120, indicating that decreasing the slab thickness to 120 mm, which is less than the CSA S6:19 minimum allowable thickness of 175 mm, resulted in wider cracks.

Different codes and design guidelines proposed a limit for the crack width of bridge-deck slabs. The American Association of State Highway and Transportation Officials (AASHTO) LRFD Bridge Design Specifications (AASHTO 2018) recommended a limit value of 0.5 mm for maximum crack width when using GFRP reinforcement. Furthermore, CSA S6:19, Clause 16.8.2.3, states that crack width should not exceed 0.5 mm and 0.7 mm for exterior and interior exposure, respectively. As shown in Fig. 9, the maximum crack widths for all test slabs reached 0.4 mm after nearly 54 to 79% of the ultimate load. These loads were much higher than the service loads; thus, the authors recommended that for hybrid RC deck slabs, the maximum crack width limit should be 0.4 mm for exterior exposure.

Reinforcement and concrete strains

The applied load versus measured strains at the midspan of both concretes at the top fiber, and the tensile BFRP bars or SFCBs, are shown in Fig. 10. Before cracking, all the tested deck slabs showed approximately similar concrete and reinforcement strains. After cracking, the BFRP strain of Slab 8B showed a rapid linear increase, increasing the load up to failure. Using steel bars instead of BFRP bars, Slab 5B3S yielded a significant reduction in BFRP strain compared to Slab 8B, as shown in Fig. 10(a). The influence

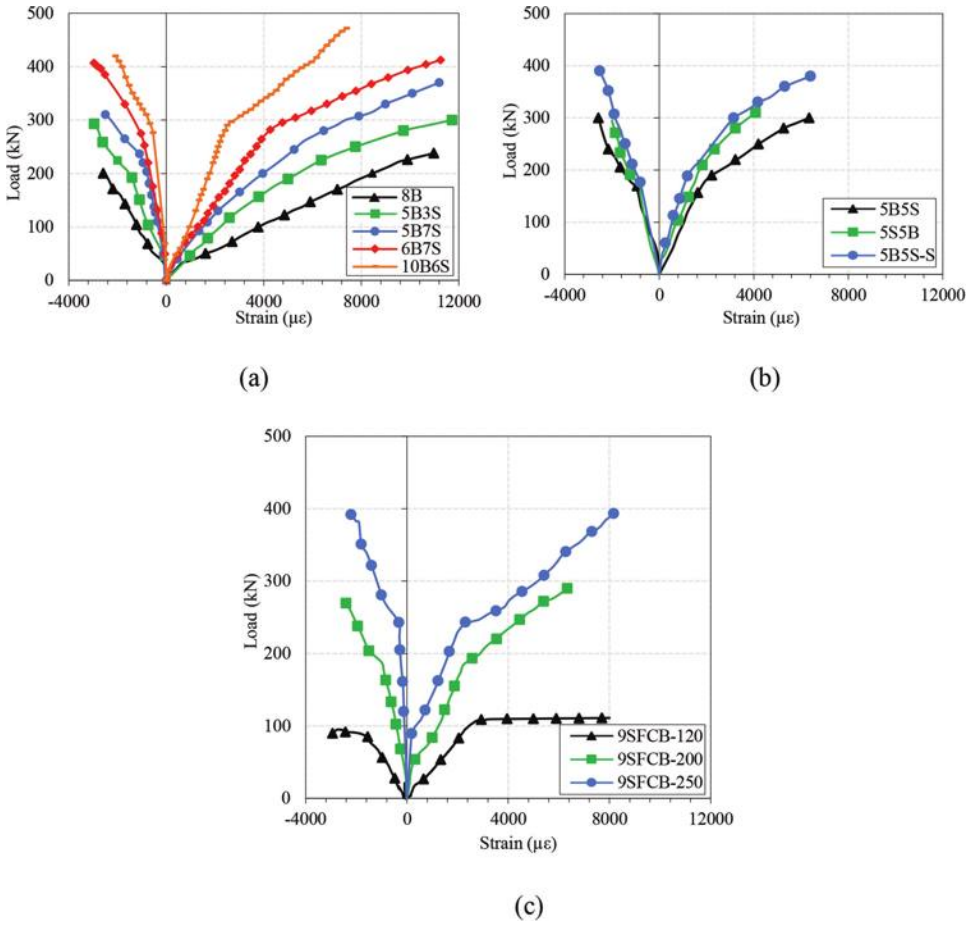

Fig. 10—Load-BFRP reinforcement and concrete-strain relationships: (a) Groups A and B; (b) Group C; and (c) Group D. (Note: 1 kN = 0.225 kip.)

of the reinforcement ratio can be realized in Slabs 5B3S and 10B6S; high reinforcement and lower strains were recorded at the same load levels. Increasing the steel reinforcement controlled the BFRP bar strain development in the hybrid deck slabs, as demonstrated by the lower tensile strain readings in the BFRP bars of Slab 5B3S compared to Slab 5B7S. These results tend to indicate the effect of increasing the effective reinforcement ratio to improve the serviceability performance of the hybrid slabs. Moreover, as the A_f/A_s increased, the BFRP strains decreased, as shown in Fig. 10(a). The BFRP strain in Slab 10B6S (A_f/A_s = 1.58) recorded 2422 με, which was considerably lower than the BFRP strain of Slab 6B7S (A_f/A_s = 0.81) of 4273 με at the yielding load. The secondary stiffness (provided by either BFRP bars or the outer FRP of SFCBs) can restrict the strain development of tensile reinforcements after the steel is yielded (Yang et al. 2020). As shown in Fig. 10(b), there was no clear effect of the reinforcement arrangement on the yielding load, while Slab 5B5S read a high value of BFRP strain of 1932 με, followed by values of 1518 με and 1198 με for Slabs 5S5B and 5B5S-S, respectively. Therefore, the BFRP reinforcement undergoes more tensile stress when placed in the outer layer.

COMPARISON OF TEST RESULTS WITH DIFFERENT DESIGN CODE PREDICTIONS

Prediction of midspan deflection

Equations from different design codes and available models in the literature (refer to the Appendix) were used to predict the midspan deflections of the tested slabs at two load levels, 30 and 60% of the ultimate load capacity, P_u, of each slab. Figure 11 compares the experimental and predicted deflections up to 60% of the ultimate load. Figure 11(a) shows clearly that both the Bischoff model (Bischoff 2007) and ACI 440.1R-15 yielded highly underestimated deflections for Slab 8B; however, CSA S806-12 showed good results with experimental deflections. As shown in Fig. 11(b), the midspan deflections of Slab 5B3S reinforced with a low reinforcement ratio (ρ_{eff} = 0.59%) were underestimated by all the equations; however, the CSA S806-12 equation showed good results with experimental deflections. However, better prediction of deflections was noticed when increasing the reinforcement ratio in Group B. Moreover, a similar trend is also valid for the hybrid slabs of Group C. An excellent agreement between the predicted and the experimental deflections was noticed for Slabs 6B7S and 5B5S, especially for CSA S806-12, illustrated in Fig. 11(e). From a design point of view, CSA S806-12 showed the most accurate method of predicting the deflection of hybrid RC members among all current models at both $0.30P_u$ and $0.60P_u$, with an average of $V_{c,exp}/V_{c,pred}$ of 1.02 ±

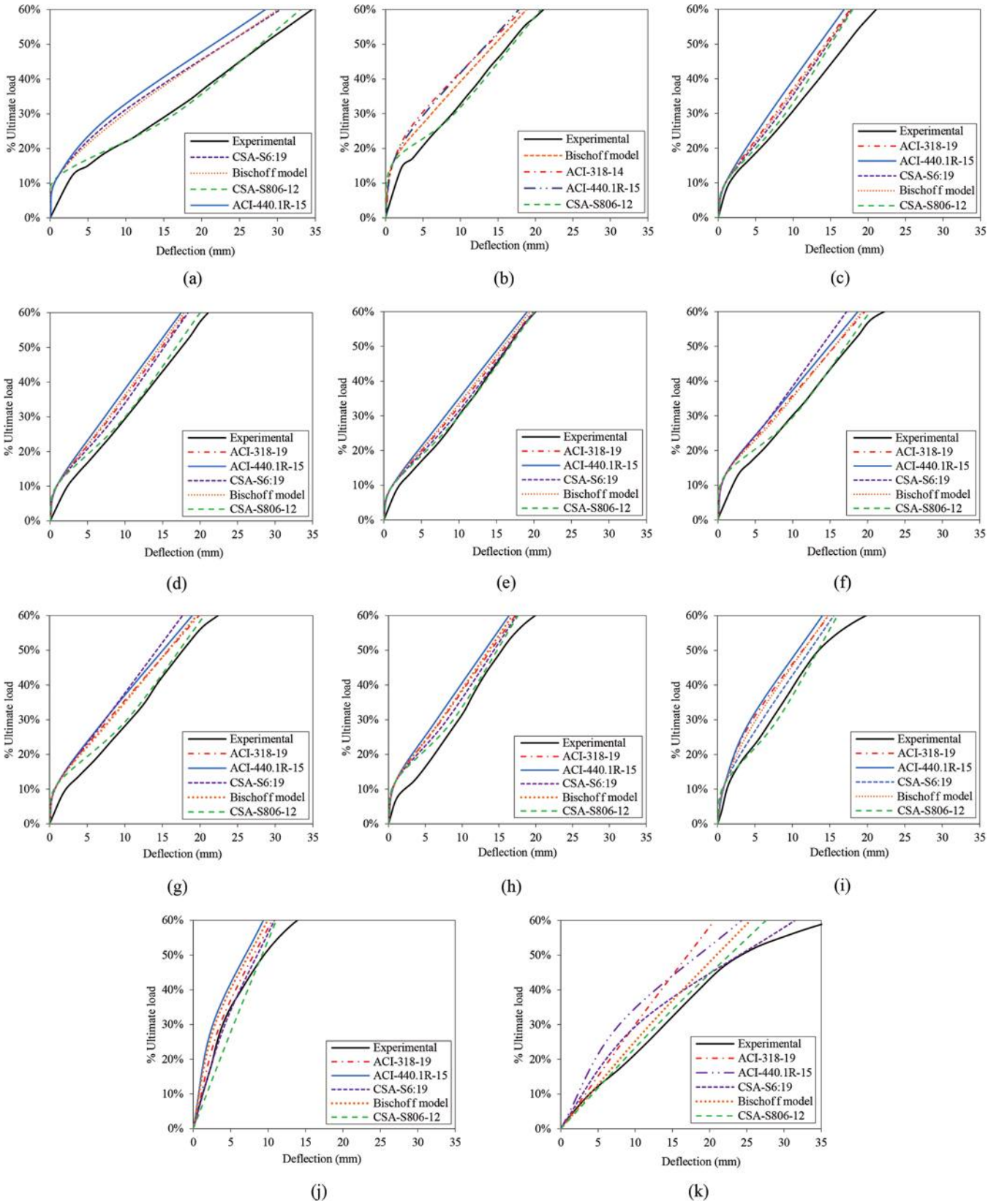

Fig. 11—Comparisons of midspan deflection versus experimental and calculated results of tested deck slabs: (a) 8B; (b) 5B3S; (c) 5B7S; (d) 6B7S; (e) 10B6S; (f) 5B5S; (g) 5S5B; (h) 5B5S-S; (i) 9SFCB-200; (j) 9SFCB-250; and (k) 9SFCB-120. (Note: 1 mm = 0.0394 in.)

0.26 and 1.12 ± 0.10. This might be caused by the cracked moment of inertia in the closed-form equation suggested by CSA S806-12.

Bond-dependent coefficient prediction

Both design codes ACI CODE-440.11-22 (ACI Committee 440 2022) and CSA S6:19 provided the same expression for

predicting the maximum crack width of FRP-RC members, as shown in Eq. (9). The bond-dependent coefficient, k_b, considered the variety of concrete sections and different FRP bars. In addition, the bond degree of FRP bars within the concrete, which is always indicated by the bond coefficient in existing design codes, should be determined before computing the crack width. The determination of the bond coefficient, k_b, is suggested to be realized by substituting the experimentally obtained crack widths and tensile strains of the longitudinal reinforcements into Eq. (9). It should be noted that w in Eq. (9) denotes the maximum crack width at the bottom of the tension face, while the measured crack widths of the present study were at the level of BFRP reinforcement. Therefore, the amplification factor β in Eq. (9), which transfers the crack width at the level of reinforcements to that of the tension face, was not considered.

$$w = 2\varepsilon_f \beta k_b \sqrt{d_c^2 + \left(\frac{s}{2}\right)^2} \tag{9a}$$

$$\varepsilon_f = \frac{M_a}{(E_f A_f + E_s A_s)\left[1 - \left(\frac{k}{3}\right)\right]d} \tag{9b}$$

$$\beta = \frac{h - kd}{d - kd} \tag{9c}$$

Herein, the slab results were used to assess the value of the bond coefficient of BFRP bars, k_b, with Eq. (9). The k_b was calculated at two load levels: at $0.3P_u$, which is considered the service load level (Mota et al. 2006; Bischoff et al. 2009; El-Nemr et al. 2013), and at $0.67P_u$, in which the crack pattern reached a stabilized state and no new cracks appeared. Table 5 reports the average k_b measured for each slab specimen. The results showed some variations between k_b determined at the different load levels. The average k_b value was 1.27 ± 0.14 with a coefficient of variation (COV) of 11% for BFRP bars with ribbed surfaces. It was found that this value is close to that recommended by Shield et al. (2019) and ACI CODE-440.11-22 of 1.2 for GFRP bars. However, CSA S6:19 proposed using a k_b of 1.0 for ribbed FRP bars; thus, CSA S6:19 is nonconservative.

Table 5—Bond-dependent coefficient, k_b

Slab	k_b		Average
	$0.30P_u$	$0.67P_u$	
8B	1.11	1.07	1.09
5B3S	1.38	1.37	1.38
5B7S	1.22	1.42	1.32
6B7S	0.92	1.45	1.19
10B6S	1.32	0.97	1.15
5B5S	1.42	1.44	1.43
5S5B	1.43	1.41	1.42
5B5S-S	0.97	1.25	1.11
9SFCB-200	1.28	1.42	1.35
9SFCB-250	1.03	1.12	1.08
9SFCB-120	1.46	1.38	1.42
Average			1.27
Standard deviation			0.14
Coefficient of variation, %			11

Prediction of shear strength

The shear capacities of hybrid reinforced slabs were predicted with the shear models provided in different design codes. To date, no design code or guidelines have been published for designing concrete structures with hybrid reinforcement. Therefore, the authors suggested a modification for some equations that consider the effect of hybrid reinforcement. For example, for the AASHTO specifications (AASHTO 2018), it is recommended to account for the ratio between the stiffness of longitudinal steel reinforcement, E_s, to that of FRP reinforcement, E_f. For CSA S806-12, which considers the effect of FRP reinforcement, ρ_f, the authors proposed replacing the FRP reinforcement with the mechanical reinforcing index, $\rho_{f,eq}$, as shown in Eq. (10). However, CSA S6:19 considers FRP axial stiffness in the shear equations; thus, the authors suggested accounting for the axial stiffness of both steel and FRP reinforcement rather than only FRP reinforcement, as shown in Eq. (11). Moreover, ACI CODE-440.11-22 indirectly incorporates both steel and FRP reinforcement through the coefficient k. Table 6 (refer to the Appendix) summarizes all shear equations after introducing the modifications.

$$\rho_{f,eq} = \rho_f + \frac{f_y}{f_{fu}}\rho_s \tag{10}$$

$$EA = E_s A_s + E_f A_f \tag{11}$$

The accuracy of the predicted results was evaluated and discussed by comparing their predictions with the values that were experimentally determined from the tested slabs. The experimental-to-predicted shear ratios, $V_{c,exp}/V_{c,pred}$, are presented in Table 7. From the results of the prediction, AASHTO yielded very good agreement with the experimental results, with an average $V_{c,exp}/V_{c,pred}$ of 1.23 ± 0.36. After introducing the modifications, ACI CODE-440.11-22 and CSA S806-12 yielded good yet conservative predictions with average $V_{c,exp}/V_{c,pred}$ of 1.65 ± 0.21 and 1.59 ± 0.33 and a COV of 13 and 21%, respectively. However, CSA S6:19 showed very conservative predictions with an average $V_{c,exp}/V_{c,pred}$ of 2.01 ± 0.30 compared to AASHTO. This might be attributed to CSA S6:19 accounting for the effect of the longitudinal FRP reinforcement ratio and the elastic modulus in one term (axial stiffness, EA) rather than the other codes calculating them separately. Generally, the modifications in the shear equations proposed in this study are suitable for the predictions of the shear capacities of hybrid RC members reinforced with steel and BFRP bars, while extensive investigations are needed in the future to confirm these modifications.

Table 6—Modified shear equations for hybrid RC members

Reference	Equation
ACI CODE-440.11-22	$V_c = 0.4\sqrt{f_c'}b_w kd$
AASHTO (2018)	$V_c = 0.16\sqrt{f_c'}b_w c(E_s/E_f)$; $c = kd$
CSA S806-12	$V_{c,mod} = 0.11\phi_c\sqrt{f_c'}b_w d_v \le 0.05\lambda\phi_c k_m k_{r,mod}(f_c')^{1/3}b_w d_v \le 0.22\phi_c\sqrt{f_c'}b_w d_v$ $k_m = \sqrt{\frac{V_u d}{M_u}} \le 1.0$; $k_{r,mod} = 1 + (E_f\rho_{sf,f})^{1/3}$
CSA S6:19	$V_c = 2.5\beta\phi_c f_{cr} b_w d_v$ $\beta_{mod} = \left[\frac{0.4}{1 + 1500\varepsilon_{x,mod}}\right]\left[\frac{1300}{1000 + s_{ze}}\right]$ $\varepsilon_{x,mod} = \frac{\frac{M_u}{d_v} + V_u}{2(E_f A_f + E_s A_s)} \le 0.003$; $s_{ze} = \frac{35s_z}{15 + a_g} \le 0.85s_z$

Table 7—Experimental-to-predicted shear capacity

Slab	V_u	$V_u/V_{u,pred}$			
		ACI CODE-440.11-22	AASHTO (2018)	CSA S806-12	CSA S6:19
8B	147.5	2.06	2.06	1.24	1.83
5B3S	157	1.49	1.48	1.31	1.77
6B7S	218.5	1.70	1.07	2.01	2.24
10B6S	235	1.86	1.17	2.19	2.46
5B5S	162.5	1.45	0.91	1.51	1.71
5S5B	167.5	1.55	0.98	1.55	1.79
5B5S-S	198	1.71	1.17	1.67	2.44
9SFCB-200	146	1.41	0.97	1.24	1.83
Average		1.65	1.23	1.59	2.01
Standard deviation		0.21	0.36	0.33	0.30
Coefficient of variation, %		13	29	21	15

Note: $V_{c,exp}$ is factored shear (kN); 1 kN = 0.225 kip.

DESIGN RECOMMENDATIONS FOR HYBRID RC MEMBERS WITHOUT SHEAR REINFORCEMENT

Based on the experimental results in this study, under-reinforced hybrid RC slabs exhibit higher stiffness and strength with ductile behavior before failure compared to FRP-RC slabs, which is still adequate to achieve the safety requirement. Hence, it is recommended that designers should follow the under-reinforced section procedures when using hybrid (FRP and steel) bars as tensile reinforcement. Moreover, it is necessary that engineers should be aware of the FRP-to-steel ratio, A_f/A_s, when designing such sections. It is suggested to use a high A_f/A_s, which means a large amount of FRP bars to provide high strength and avoid excessive deflection and rupture of FRP bars after the steel yields. In contrast, using a low A_f/A_s can ensure the ductile performance guaranteed by the yielding of steel bars. In addition, using the proposed shear equations presented in this study can assure the ductile failure of RC flexural elements by making the shear capacity at all sections equal to or greater than the flexural one. Recently, some design recommendations were proposed through an experimental and numerical study made by the authors (Ali et al. 2023). However, further research on the concrete contribution to the shear strength of hybrid RC members is needed.

SUMMARY AND CONCLUSIONS

Eleven deck slabs were constructed and tested up to failure to study the mechanical behavior of hybrid deck slabs. The test parameters are reinforcement type, ratio, and arrangement; the fiber-reinforced polymer (FRP)-to-steel ratio A_f/A_s; and slab thickness. Based on the results and discussion presented herein, the following conclusions are obtained:

1. The observed failure mode of the basalt FRP (BFRP)-reinforced concrete (RC) slab was an undesirable brittle shear failure, while hybrid RC slabs showed gradual shear-compression failure, flexural-shear failure, and flexural failure. The failure of the hybrid RC slabs is significantly affected by the effective reinforcement ratio and A_f/A_s; it becomes more severe when increasing the reinforcement ratio with a high value of A_f/A_s.

2. The effective reinforcement ratio and A_f/A_s had considerable influence on the post-cracking stiffness of the hybrid deck slabs. In addition, increasing the reinforcement ratio by 100% increased the ultimate capacity by 50%. Increasing A_f/A_s from 0.68 to 1.58 significantly reduced the midspan deflections and crack widths and increased the ultimate capacity by 14%.

3. The existing models for predicting the midspan deflections are conservative in predicting the deflections of hybrid RC slabs. However, the models give good predictions for slabs that have high effective reinforcement ratios. CSA

S806-12 provided accurate predictions with the experimental results.

4. The test results were used to assess the bond-dependent coefficient of BFRP bars. The calculations yielded an average bond-dependent coefficient, k_b, of 1.27, close to the 1.2 recommended by ACI CODE-440.11-22 and larger than the 1.0 proposed by CSA S6:19.

5. The proposed modifications to the design code equations were verified to accurately predict the shear capacity of hybrid RC slabs without shear reinforcement. The AASHTO equation provided the most accurate shear capacity prediction for hybrid RC slabs, with an average ratio of $V_{c,exp}/V_{c,pred}$ of 1.23.

AUTHOR BIOS

ACI member **Yahia M. S. Ali** *is a PhD Candidate in the School of Civil Engineering at Southeast University, Nanjing, Jiangsu, China, and a Teaching Assistant in the Department of Civil Engineering at Assiut University, Assiut, Egypt. He received his BS and MSc in structural engineering from Assiut University. His research interests include structural design and the analysis and testing of concrete structures reinforced with fiber-reinforced polymers (FRPs).*

Xin Wang *is a Professor in the Key Laboratory of Concrete and Prestressed Concrete Structures of Ministry of Education at Southeast University, and a Professor in the Department of Civil Engineering at Southeast University. He received his BS and MSc from Southeast University in 2002 and 2006, respectively, and his PhD from Ibaraki University, Mito, Ibaraki, Japan, in 2010. His research interests include FRP composites and concrete structures with FRP composites.*

Shui Liu *is a PhD Candidate in the Key Laboratory of Concrete and Prestressed Concrete Structures of Ministry of Education at Southeast University and in the Department of Civil Engineering at Southeast University. His research interests include the analysis and design of concrete structures reinforced with a combination of FRP and steel bars.*

Zhishen Wu *is a Professor in the School of Civil Engineering at Southeast University. He received his BS and MS from Southeast University, and his PhD from Nagoya University, Nagoya, Aichi, Japan. His research interests include FRP composites and technologies, maintenance and life-cycle engineering, failure mechanics of composite materials, and structural health monitoring infrastructure systems.*

ACKNOWLEDGMENTS

The authors gratefully acknowledge the financial support provided by the National Key Research and Development Program of China (No. 2022YFB3706503) and the National Natural Science Foundation of China (Grant 52278244).

NOTATION

A_f = area of BFRP reinforcement
A_s = area of steel reinforcement
a = distance between support and point load (shear span)
a_g = nominal maximum size of coarse aggregate
b_w = width of cross section
c = distance from extreme fiber in compression to neutral axis
d = distance from extreme fiber in compression to center of tensile reinforcement
d_f = distance from extreme compression fiber to center of FRP bars
d_s = distance from extreme compression fiber to center of steel bars
d_v = effective shear depth
E_c = modulus of elasticity of concrete
E_f = modulus of elasticity of BFRP bars
E_I = elastic modulus
E_{II} = post-elastic modulus
E_s = modulus of elasticity of steel bars
f_c' = concrete compressive strength
f_{cr} = cracking strength
f_{cu} = cube compressive strength
f_{fu} = ultimate tensile stress in BFRP bars
f_y = yield stress in steel reinforcement
h = overall member thickness
I_{cr} = cracked moment of inertia
I_e = effective moment of inertia
I_g = gross moment of inertia
J = overall performance factor
J_{mod} = modified overall performance factor
k_b = bond coefficient
k_m = moment-shear interaction factor
$k_{r,mod}$ = reinforcement stiffness factor
L = slab length
L_g = distance from support to point where $M = M_{cr}$
M_a = applied moment at critical section
M_{cr} = cracking moment
M_{exp} = experimental moment capacity
M_{pred} = predicted moment capacity
M_s = service moment
M_u = ultimate moment
M_y = yielding moment
n_f = ratio of modulus of elasticity of BFRP bars to modulus of elasticity of concrete
n_s = ratio of modulus of elasticity of steel bars to modulus of elasticity of concrete
P_{cr} = cracking load
P_{th} = theoretical flexural capacity
P_u = ultimate load
P_y = yielding load
s = spacing of reinforcing bars
s_{ze} = effective crack spacing for members without stirrups
$V_{c,mod}$ = modified one-way shear strength provided by concrete and flexural reinforcement
V_u = factored shear
w = maximum crack width
α_1 = ratio of average stress of equivalent rectangular stress block to cylinder compressive strength of concrete
β = ratio of distance between neutral axis and tension face to distance between neutral axis and centroid of reinforcement
β_1 = ratio of depth of equivalent rectangular stress block to depth of neutral axis
Δ_{cr} = cracking deflection at midspan of slab
Δ_m = maximum deflection at midspan of slab
Δ_u = ultimate deflection at midspan of slab
Δ_y = yielding deflection at midspan of slab
ε_{cu} = maximum concrete compressive strain (0.003 for ACI 318-19 [ACI Committee 318 2019] provisions)
ε_f = tensile strain in BFRP bars
ε_s = yield strain in steel bars
$\varepsilon_{x,mod}$ = modified longitudinal strain at middepth of cross section
ϕ_c = material reduction factor for concrete (taken as unity in this paper)
η = reduction coefficient
λ = concrete density factor
ρ_f = BFRP reinforcement ratio
$\rho_{f,b}$ = FRP balanced reinforcement ratio
$\rho_{f,eq}$ = mechanical reinforcing index
ρ_s = steel reinforcement ratio
$\rho_{s,b}$ = steel balanced reinforcement ratio
$\rho_{sf,f}$ = effective reinforcement ratio in hybrid sections with respect to FRP
$\rho_{sf,s}$ = effective reinforcement ratio in hybrid sections with respect to steel
Ψ_s = curvature at service moment
Ψ_u = curvature at ultimate moment
Ψ_y = curvature at yield moment

REFERENCES

AASHTO, 2018, "AASHTO LRFD Bridge Design Guide Specifications for GFRP-Reinforced Concrete," second edition, American Association of State Highway and Transportation Officials, Washington, DC.

Abdul-Salam, B.; Farghaly, A. S.; and Benmokrane, B., 2016, "Mechanisms of Shear Resistance of One-Way Concrete Slabs Reinforced with FRP Bars," *Construction and Building Materials*, V. 127, Nov., pp. 959-970. doi: 10.1016/j.conbuildmat.2016.10.015

ACI Committee 318, 2019, "Building Code Requirements for Structural Concrete (ACI 318-19) and Commentary (ACI 318R-19) (Reapproved 2022)," American Concrete Institute, Farmington Hills, MI, 624 pp.

ACI Committee 440, 2015, "Guide for the Design and Construction of Structural Concrete Reinforced with Fiber-Reinforced Polymer (FRP) Bars (ACI 440.1R-15)," American Concrete Institute, Farmington Hills, MI, 88 pp.

ACI Committee 440, 2022, "Building Code Requirements for Structural Concrete Reinforced with Glass Fiber-Reinforced Polymer (GFRP) Bars—Code and Commentary (ACI CODE-440.11-22)," American Concrete Institute, Farmington Hills, MI, 260 pp.

Aiello, M. A., and Ombres, L., 2002, "Structural Performances of Concrete Beams with Hybrid (Fiber-Reinforced Polymer-Steel) Reinforcements," *Journal of Composites for Construction*, ASCE, V. 6, No. 2, May, pp. 133-140. doi: 10.1061/(ASCE)1090-0268(2002)6:2(133)

Ali, Y. M. S.; Wang, X.; Ding, L.; Liu, S.; and Wu, Z., 2023, "Experimental and Numerical Investigations of the Effects of Various Tensile Reinforcement Types on the Structural Behavior of Concrete Bridge Deck Slabs," *Engineering Structures*, V. 285, June, Article No. 116036. doi: 10.1016/j.engstruct.2023.116036

ASTM D7205/D7205M-06(2016), 2016, "Standard Test Method for Tensile Properties of Fiber Reinforced Polymer Matrix Composite Bars," ASTM International, West Conshohocken, PA, 13 pp.

Bischoff, P. H., 2007, "Deflection Calculation of FRP Reinforced Concrete Beams Based on Modifications to the Existing Branson Equation," *Journal of Composites for Construction*, ASCE, V. 11, No. 1, Feb., pp. 4-14. doi: 10.1061/(ASCE)1090-0268(2007)11:1(4)

Bischoff, P. H.; Gross, S.; and Ospina, C. E., 2009, "The Story Behind Proposed Changes to ACI 440 Deflection Requirements for FRP-Reinforced Concrete," *Serviceability of Concrete Members Reinforced with Internal/External FRP Reinforcement*, SP-264, C. Ospina, P. Bischoff, and T. Alkhrdaji, eds., American Concrete Institute, Farmington Hills, MI, pp. 53-76.

CSA S6:19, 2019, "Canadian Highway Bridge Design Code," CSA Group, Toronto, ON, Canada, 1182 pp.

CSA S806-12 (R2017), 2017, "Design and Construction of Building Structures with Fibre-Reinforced Polymers," CSA Group, Toronto, ON, Canada.

Duic, J.; Kenno, S.; and Das, S., 2018, "Performance of Concrete Beams Reinforced with Basalt Fibre Composite Rebar," *Construction and Building Materials*, V. 176, July, pp. 470-481. doi: 10.1016/j.conbuildmat.2018.04.208

El-Nemr, A.; Ahmed, E. A.; and Benmokrane, B., 2013, "Flexural Behavior and Serviceability of Normal- and High-Strength Concrete Beams Reinforced with Glass Fiber-Reinforced Polymer Bars," *ACI Structural Journal*, V. 110, No. 6, Nov.-Dec., pp. 1077-1088.

El-Salakawy, E., and Benmokrane, B., 2004, "Serviceability of Concrete Bridge Deck Slabs Reinforced with Fiber-Reinforced Polymer Composite Bars," *ACI Structural Journal*, V. 101, No. 5, Sept.-Oct., pp. 727-736.

El-Salakawy, E. F.; Kassem, C.; and Benmokrane, B., 2003, "Flexural Behaviour of Bridge Deck Slabs Reinforced with FRP Composite Bars," *Fibre-Reinforced Polymer Reinforcement for Concrete Structures: Proceedings of the Sixth International Symposium on FRP Reinforcement for Concrete Structures (FRPRCS-6)*, K. H. Tan, ed., World Scientific Publishing, Singapore, pp. 1291-1300.

El-Sayed, A.; El-Salakawy, E.; and Benmokrane, B., 2005, "Shear Strength of One-Way Concrete Slabs Reinforced with Fiber-Reinforced Polymer Composite Bars," *Journal of Composites for Construction*, ASCE, V. 9, No. 2, Apr., pp. 147-157. doi: 10.1061/(ASCE)1090-0268(2005)9:2(147)

El-Sayed, A. K.; El-Salakawy, E. F.; and Benmokrane, B., 2006a, "Shear Strength of FRP-Reinforced Concrete Beams without Transverse Reinforcement," *ACI Structural Journal*, V. 103, No. 2, Mar.-Apr., pp. 235-243.

El-Sayed, A. K.; El-Salakawy, E. F.; and Benmokrane, B., 2006b, "Shear Capacity of High-Strength Concrete Beams Reinforced with FRP Bars," *ACI Structural Journal*, V. 103, No. 3, May-June, pp. 383-389.

El Refai, A.; Abed, F.; and Al-Rahmani, A., 2015, "Structural Performance and Serviceability of Concrete Beams Reinforced with Hybrid (GFRP and Steel) Bars," *Construction and Building Materials*, V. 96, Oct., pp. 518-529. doi: 10.1016/j.conbuildmat.2015.08.063

Elgabbas, F.; Ahmed, E. A.; and Benmokrane, B., 2016, "Experimental Testing of Concrete Bridge-Deck Slabs Reinforced with Basalt-FRP Reinforcing Bars under Concentrated Loads," *Journal of Bridge Engineering*, ASCE, V. 21, No. 7, July, p. 04016029. doi: 10.1061/(ASCE)BE.1943-5592.0000892

Ferrier, E.; Michel, L.; Zuber, B.; and Chanvillard, G., 2015, "Mechanical Behaviour of Ultra-High-Performance Short-Fibre-Reinforced Concrete Beams with Internal Fibre Reinforced Polymer Bars," *Composites Part B: Engineering*, V. 68, Jan., pp. 246-258. doi: 10.1016/j.compositesb.2014.08.001

Ge, W.; Wang, Y.; Ashour, A.; Lu, W.; and Cao, D., 2020, "Flexural Performance of Concrete Beams Reinforced with Steel–FRP Composite Bars," *Archives of Civil and Mechanical Engineering*, V. 20, No. 2, June, Article No. 56. doi: 10.1007/s43452-020-00058-6

Ge, W.; Zhang, J.; Cao, D.; and Tu, Y., 2015, "Flexural Behaviors of Hybrid Concrete Beams Reinforced with BFRP Bars and Steel Bars," *Construction and Building Materials*, V. 87, July, pp. 28-37. doi: 10.1016/j.conbuildmat.2015.03.113

Goldston, M.; Remennikov, A.; and Sheikh, M. N., 2016, "Experimental Investigation of the Behaviour of Concrete Beams Reinforced with GFRP Bars under Static and Impact Loading," *Engineering Structures*, V. 113, Apr., pp. 220-232. doi: 10.1016/j.engstruct.2016.01.044

Ibrahim, A. I.; Wu, G.; and Sun, Z.-Y., 2017, "Experimental Study of Cyclic Behavior of Concrete Bridge Columns Reinforced by Steel Basalt-Fiber Composite Bars and Hybrid Stirrups," *Journal of Composites for Construction*, ASCE, V. 21, No. 2, Apr., p. 04016091. doi: 10.1061/(ASCE)CC.1943-5614.0000742

Liu, S.; Wang, X.; Ali, Y. M. S.; Su, C.; and Wu, Z., 2022, "Flexural Behavior and Design of Under-Reinforced Concrete Beams with BFRP and Steel Bars," *Engineering Structures*, V. 263, July, Article No. 114386. doi: 10.1016/j.engstruct.2022.114386

Matta, F.; El-Sayed, A. K.; Nanni, A.; and Benmokrane, B., 2013, "Size Effect on Concrete Shear Strength in Beams Reinforced with Fiber-Reinforced Polymer Bars," *ACI Structural Journal*, V. 110, No. 4, July-Aug., pp. 617-628.

Michaluk, C. R.; Rizkalla, S. H.; Tadros, G.; and Benmokrane, B., 1998, "Flexural Behavior of One-Way Concrete Slabs Reinforced by Fiber Reinforced Plastic Reinforcements," *ACI Structural Journal*, V. 95, No. 3, May-June, pp. 353-364.

Mota, C.; Alminar, S.; and Svecova, D., 2006, "Critical Review of Deflection Formulas for FRP-RC Members," *Journal of Composites for Construction*, ASCE, V. 10, No. 3, June, pp. 183-194. doi: 10.1061/(ASCE)1090-0268(2006)10:3(183)

Nanni, A.; Henneke, M. J.; and Okamoto, T., 1994, "Tensile Properties of Hybrid Rods for Concrete Reinforcement," *Construction and Building Materials*, V. 8, No. 1, pp. 27-34. doi: 10.1016/0950-0618(94)90005-1

Nguyen, P. D.; Dang, V. H.; and Vu, N. A., 2020, "Performance of Concrete Beams Reinforced with Various Ratios of Hybrid GFRP/Steel Bars," *Civil Engineering Journal*, V. 6, No. 9, pp. 1652-1669. doi: 10.28991/cej-2020-03091572

Pang, L.; Qu, W.; Zhu, P.; and Xu, J., 2016, "Design Propositions for Hybrid FRP-Steel Reinforced Concrete Beams," *Journal of Composites for Construction*, ASCE, V. 20, No. 4, Aug., p. 04015086. doi: 10.1061/(ASCE)CC.1943-5614.0000654

Qin, R.; Zhou, A.; and Lau, D., 2017, "Effect of Reinforcement Ratio on the Flexural Performance of Hybrid FRP Reinforced Concrete Beams," *Composites Part B: Engineering*, V. 108, Jan., pp. 200-209. doi: 10.1016/j.compositesb.2016.09.054

Qu, W.; Zhang, X.; and Huang, H., 2009, "Flexural Behavior of Concrete Beams Reinforced with Hybrid (GFRP and Steel) Bars," *Journal of Composites for Construction*, ASCE, V. 13, No. 5, Oct., pp. 350-359. doi: 10.1061/(ASCE)CC.1943-5614.0000035

Ruan, X.; Lu, C.; Xu, K.; Xuan, G.; and Ni, M., 2020, "Flexural Behavior and Serviceability of Concrete Beams Hybrid-Reinforced with GFRP Bars and Steel Bars," *Composite Structures*, V. 235, Mar., Article No. 111772. doi: 10.1016/j.compstruct.2019.111772

Safan, M. A., 2013, "Flexural Behavior and Design of Steel-GFRP Reinforced Concrete Beams," *ACI Materials Journal*, V. 110, No. 6, Nov.-Dec., pp. 677-686.

Shield, C.; Brown, V.; Bakis, C. E.; and Gross, S., 2019, "A Recalibration of the Crack Width Bond-Dependent Coefficient for GFRP-Reinforced Concrete," *Journal of Composites for Construction*, ASCE, V. 23, No. 4, Aug., p. 04019020. doi: 10.1061/(ASCE)CC.1943-5614.0000978

Sun, Z.; Fu, L.; Feng, D.-C.; Vatuloka, A. R.; Wei, Y.; and Wu, G., 2019, "Experimental Study on the Flexural Behavior of Concrete Beams Reinforced with Bundled Hybrid Steel/FRP Bars," *Engineering Structures*, V. 197, Oct., Article No. 109443. doi: 10.1016/j.engstruct.2019.109443

Sun, Z.-Y.; Wu, G.; Wu, Z.-S.; and Zhang, M., 2011, "Seismic Behavior of Concrete Columns Reinforced by Steel-FRP Composite Bars," *Journal of Composites for Construction*, ASCE, V. 15, No. 5, Oct., pp. 696-706. doi: 10.1061/(ASCE)CC.1943-5614.0000199

Sun, Z. Y.; Yang, Y.; Qin, W. H.; Ren, S. T.; and Wu, G., 2012, "Experimental Study on Flexural Behavior of Concrete Beams Reinforced by Steel-Fiber Reinforced Polymer Composite Bars," *Journal of Reinforced Plastics and Composites*, V. 31, No. 24, Dec., pp. 1737-1745. doi: 10.1177/0731684412456446

Tureyen, A. K., and Frosch, R. J., 2002, "Shear Tests of FRP-Reinforced Concrete Beams without Stirrups," *ACI Structural Journal*, V. 99, No. 4, July-Aug., pp. 427-434.

Wang, X.; Liu, S.; Shi, Y.; Wu, Z.; and He, W., 2022, "Integrated High-Performance Concrete Beams Reinforced with Hybrid BFRP and Steel Bars," *Journal of Structural Engineering*, ASCE, V. 148, No. 1, Jan., p. 04021235. doi: 10.1061/(ASCE)ST.1943-541X.0003207

Wu, G.; Dong, Z.-Q.; Wang, X.; Zhu, Y.; and Wu, Z.-S., 2015, "Prediction of Long-Term Performance and Durability of BFRP Bars under the

Combined Effect of Sustained Load and Corrosive Solutions," *Journal of Composites for Construction*, ASCE, V. 19, No. 3, June, pp. 1-9. doi: 10.1061/(ASCE)CC.1943-5614.0000517

Wu, G.; Sun, Z. Y.; Wu, Z. S.; and Luo, Y. B., 2012, "Mechanical Properties of Steel-FRP Composite Bars (SFCBs) and Performance of SFCB Reinforced Concrete Structures," *Advances in Structural Engineering*, V. 15, No. 4, Apr., pp. 625-635. doi: 10.1260/1369-4332.15.4.625

Wu, Z.; Fahmy, M. F. M.; and Wu, G., 2009, "Safety Enhancement of Urban Structures with Structural Recoverability and Controllability," *Journal of Earthquake and Tsunami*, V. 3, No. 3, Sept., pp. 143-174. doi: 10.1142/S1793431109000561

Xingyu, G.; Yiqing, D.; and Jiwang, J., 2020, "Flexural Behavior Investigation of Steel-GFRP Hybrid-Reinforced Concrete Beams Based on Experimental and Numerical Methods," *Engineering Structures*, V. 206, Mar., Article No. 110117. doi: 10.1016/j.engstruct.2019.110117

Yang, Y.; Sun, Z.-Y.; Wu, G.; Cao, D.-F.; and Pan, D., 2020, "Experimental Study of Concrete Beams Reinforced with Hybrid Bars (SFCBs and BFRP Bars)," *Materials and Structures*, V. 53, No. 4, Aug., Article No. 77. doi: 10.1617/s11527-020-01514-8

Yinghao, L., and Yong, Y., 2013, "Arrangement of Hybrid Rebars on Flexural Behavior of HSC Beams," *Composites Part B: Engineering*, V. 45, No. 1, Feb., pp. 22-31. doi: 10.1016/j.compositesb.2012.08.023

Yoo, D.-Y.; Banthia, N.; and Yoon, Y.-S., 2016, "Flexural Behavior of Ultra-High-Performance Fiber-Reinforced Concrete Beams Reinforced with GFRP and Steel Rebars," *Engineering Structures*, V. 111, Mar., pp. 246-262. doi: 10.1016/j.engstruct.2015.12.003

ACI STRUCTURAL JOURNAL TECHNICAL PAPER

Title No. 120-S87

Failure Mode-Dependent Behavior of Carbon Fiber-Reinforced Polymer Prestressed Concrete Girders

by Yail J. Kim, Jun Wang, Woo-Tai Jung, Jae-Yoon Kang, and Jong-Sup Park

This paper presents the characteristics of concrete girders prestressed with carbon fiber-reinforced polymer (CFRP) tendons when subjected to compression- and tension-controlled failure modes. To understand the full-range behavior of these girders beyond the boundary of design specifications, progressive failure is simulated using an advanced computational approach, agent-based modeling. Five bulb-tee girder sections are adopted with a variable amount of CFRP tendons and their flexural responses are examined until the intended failure modes are accomplished. The rate of capacity reductions in the compression-controlled sections is governed by the degree of concrete crushing in the upper flange and the depth of the girder, whereas the rate in the tension-controlled girders is dominated by the sequential rupture of CFRP without demonstrating size dependency. When the girder concrete cracks, locally unstable responses are observed in the compression-controlled sections, which are not noticed in the other sections. As far as deformability is concerned, both girder configurations are satisfactory. Upon initiation of the progressive failure processes, the level of safety varies differently depending upon the girder type and the arrangement of the tendons. The tension-controlled sections require more activation energy, representing a transition rate from the initial to damaged states, than their compression counterparts.

Keywords: carbon fiber-reinforced polymer (CFRP); failure mode; full-range behavior; prestressed concrete; safety.

INTRODUCTION

Civil infrastructure constitutes the backbone of a nation's economy and is instrumental in the operation of modern society. Aligning with the practical needs for controlled quality, low maintenance, and efficient geometry, prestressed concrete bridges are prevalent and account for a significant portion of highway systems. For example, the National Bridge Inventory of the Federal Highway Administration reports that 66.5% and 57.9% of constructed bridges in Florida and New York were built with prestressed concrete, respectively.[1] Despite such favorable advantages and popularity, durability remains one of the most critical problems when managing prestressed concrete members, epitomized by recent statistics stating that an annual budget of $84,500 to $111,800 was spent per bridge for the last 10 years in the United States.[2] Because hot-rolled steel outperforms cold-formed steel from a material standpoint,[3] prestressing strands comprising multiple wires are more susceptible to failure in comparison with reinforcing bars.[4] The collapse of a precast bridge in Lakeview Drive, Washington, PA, was attributed to a combination of excessive spalling and corrosion damage in the bottom flange of a box girder.[5] Attention should thus be paid to the deterioration of prestressed concrete girders in aggressive service environments. Furthermore, owing to restricted budgets and resources, the demand for sustainable materials is commonplace in federal, state, and municipal agencies.

Carbon fiber-reinforced polymer (CFRP) tendons may be employed for prestressed concrete application due to several benefits: corrosion resistance, high strength and light weight, nonconducting and nonmagnetic characteristics, low relaxation, and tailorable formation.[6] Findings from laboratory research were integrated into design specifications[6,7] and numerous highway bridges have been erected with CFRP-prestressed concrete girders around the world.[8-10] The failure mode of CFRP-prestressed concrete girders plays a crucial role in the context of safety. Because both tension- and compression-controlled sections are allowed,[6,7] the selection of a certain failure mode is largely dependent on practitioners' discretion. Technically speaking, if concrete-crushing governs, the girder suffers progressive failure in conjunction with sequential crushing across its section until force equilibrium is not achieved; on the other hand, if CFRP rupture dominates, the girder collapses as soon as tensile strains exceed the ultimate strain of the tendons. The pros and cons of those sections are currently inconclusive, and the research community has been debating the effectiveness of the design approaches over decades.[11] From a cursory point of view, compression-controlled sections appear to be safer than tension-controlled sections; contrarily, contemplating the high tensile strength of CFRP, expected safety in the tension-controlled sections may be compatible with that of the compression-controlled sections. These unapparent aspects are the sources of the foregoing arguments on the implications of the failure modes.

Assessments on the flexural response of CFRP-prestressed concrete members, particularly for compression-controlled sections, are circumscribed by articles that stipulate the maximum usable strains of concrete (ε_{cu} = 0.003 and 0.0035 in ACI 440.4R-04[6] and SIMTReC,[7] respectively), which were empirically assumed for design purposes[12] and do not mean the actual failure of the members. To expand the scope of investigations over the physical collapse of CFRP-prestressed concrete members, an in-depth understanding of full-range behavior is indispensable beyond the prescribed

ACI Structural Journal, V. 120, No. 5, September 2023.

MS No. S-2022-361.R1, doi: 10.14359/51738841, received April 25, 2023, and reviewed under Institute publication policies.

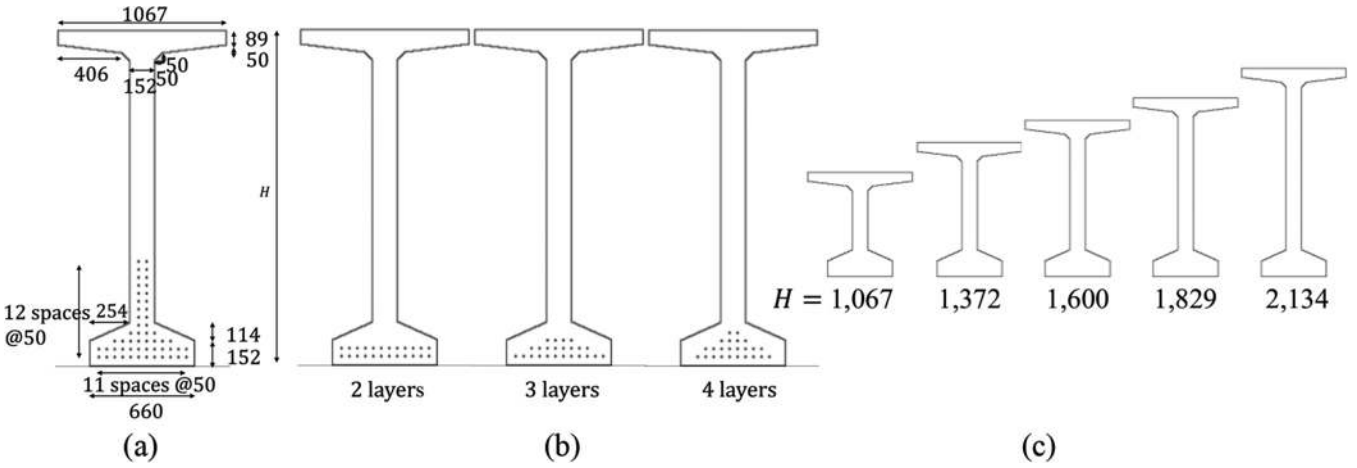

Fig. 1—Design of bulb-tee girders: (a) compression-controlled section; (b) tension-controlled section; and (c) variable girder size. (Note: Units in mm.)

Table 1—Summary of default sections

		Compression-controlled section		Tension-controlled section					
				Two layers of CFRP		Three layers of CFRP		Four layers of CFRP	
ID	H, mm	d_f, mm	M_n, kN·m	d_f, mm	M_n, kN·m	d_f, mm	M_n, kN·m	d_f, mm	M_n, kN·m
BT42	1067	843	7943	991	4720	982	4689	969	4367
BT54	1372	1148	11,535	1295	6427	1287	6389	1274	6231
BT63	1600	1376	14,271	1524	7571	1516	7533	1503	7394
BT72	1829	1605	17,072	1753	8790	1744	8752	1731	8694
BT84	2134	1910	20,786	2057	10,364	2049	10,326	2036	10,267

Note: H is girder depth; d_f is effective depth of tendons; M_n is nominal flexural capacity; compression-controlled section failure mode is crushing of concrete; tension-controlled section failure mode is rupture of CFRP; 1 mm = 0.0394 in.; 1 kN·m = 0.738 kip·ft.

limits. In this paper, an advanced modeling approach is used to elucidate the detailed failure mechanisms of compression- and tension-controlled CFRP-prestressed concrete girders and ensuing outcomes that can quantify the performance and vulnerability associated with each failure mode.

RESEARCH SIGNIFICANCE

Unlike conventional steel-prestressed concrete girders, CFRP-prestressed members are designed with an intended failure mode of either concrete crushing or CFRP rupture. During the course of pursuing a project, bridge engineers choose one of these two possible options; however, there is a concern that their selection is largely based on previous experiences without deliberating adverse impacts when the members encounter catastrophic situations, which are outside the coverage of specifications. Provided that the process of a structural collapse entails a substantial redistribution of stresses from the origination of damage to adjacent regions, the progression of sequential failure and corresponding consequences ought to be documented properly. Nonetheless, knowledge in the subject discipline is incomplete at present and clarifications are essential. By comprehending the repercussions of the complex failure mechanisms, effective design strategies can be established alongside procedural improvements and a paradigm shift in bridge engineering with CFRP-prestressed concrete girders.

MODELING

Outlined in the following are the description of a theoretical framework to predict the behavior of archetypal bridge girders used in the field, the background and implementation of a computational platform, and the numerical representation of failure modes.

Benchmark girders

Pursuant to published guidelines and manuals,[6,13,14] bulb-tee girders were designed (Fig. 1). The height of the girders varied from H = 1067 to 2134 mm (42 to 84 in.), which were designated BT42 to BT84 (Table 1), and each one involved 54 and 24 CFRP tendons for compression- and tension-controlled sections, respectively. The placement of the tendons was constant in the bottom flange when concrete crushing was the primary failure mode (Fig. 1(a)), whereas two to four layers of CFRP were arrayed to generate the progressive rupture of the tendons before the concrete crushed (Fig. 1(b)). In line with ordinary practices in precast plants, the 28-day compressive strength of the girder concrete was set to f_c' = 65 MPa (9427 psi). The diameter of the CFRP tendons was d_b = 12.7 mm (0.5 in.) and the manufacturer-reported tensile strength and modulus were f_{fu} = 1724 MPa (250 ksi) and E_f = 124 GPa (18,000 ksi), respectively, with a rupture strain of ε_{fu} = 0.0139. Tendon stresses at jacking and after transfer were $f_{fj} = 0.65f_{fu}$ and $f_{fi} = 0.6f_{fu}$, respectively, and the effective stress was $f_{fe} = 0.52f_{fu}$.[6] Given that the

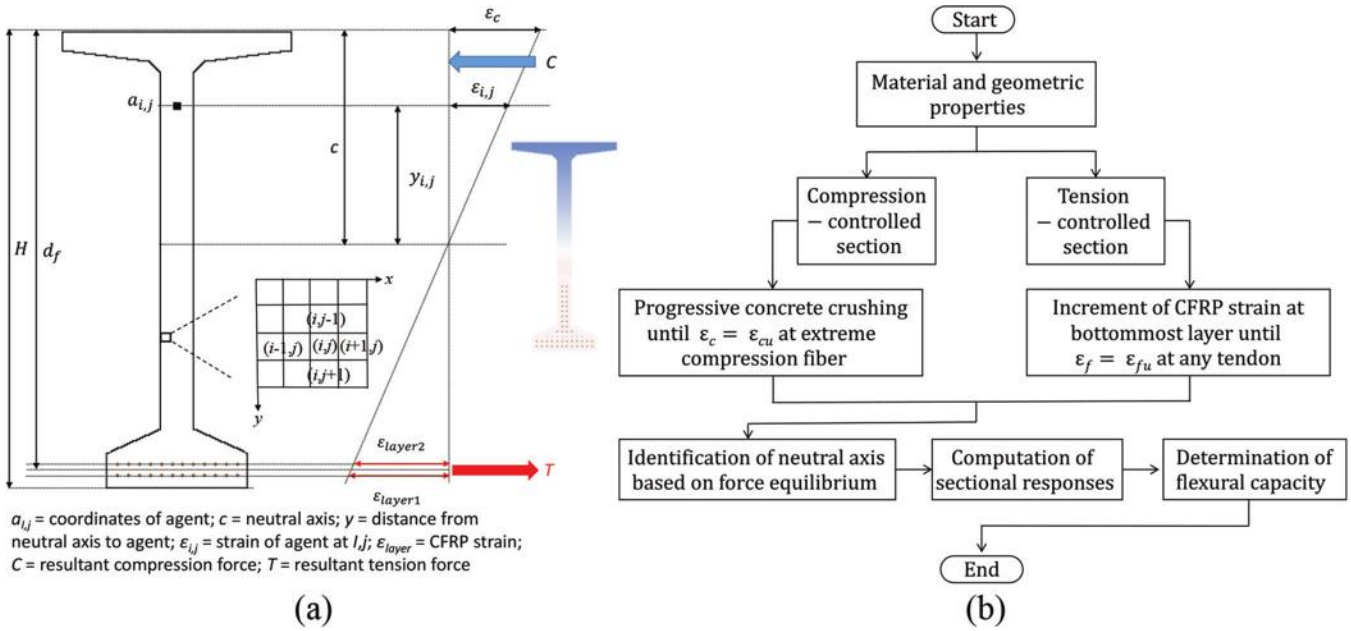

Fig. 2—Agent-based modeling: (a) visualized concept; and (b) overview of modeling.

objective of this study was to examine the failure-dependent behavior of CFRP-prestressed concrete girders, a deck slab was not included. Table 1 enumerates the flexural capacities of the girders (M_n) and, as expected, the compression-controlled sections demonstrated higher resistance by 88.4% in comparison with the tension-controlled sections, on average.

Agent-based modeling

Concept—Agent-based modeling is a contemporary simulation technique, which is prevalent in the discipline of social science, and its general objective is to emulate complex interactions among human beings sharing common backgrounds, interests, physical activities, and spaces.[15,16] Concise descriptions are provided herein, while further details on the principles and implementation methodologies are available elsewhere.[17] The modeling platform is intrinsically a bottom-up approach that comprises a cohort of autonomous entities called agents. The individual components engage one another without a centralized decision-making process[18]—that is, the heterogeneous behavior of each agent is controlled by self-organization in local territory. Accordingly, an agent's response is dominated by the reactions of neighboring agents. The most notable difference between agent-based and traditional analytical models can be found in their focus levels[19]: the former is built upon individual interactions; by contrast, the latter intends to directly attain the solution of a homogeneous system.

Formulation—NetLogo, an open-source programing language,[20] was employed to execute the theory of agent-based modeling. On the two-dimensional graphical user interface linked with command tabs, a grid space was created to computationally reconstruct the benchmark bridge girders (Fig. 2(a)). The size of the agents was 6.35 mm (0.25 in.), and these discrete entities, positioned at the orthogonal lines of the grid, were uniformly distributed in the spatial domain of the girders. The respective agents were mutually adaptive in conformity with a reactive protocol: adjoining agents shared compatible strains and transferred element-level stresses and forces so as to reproduce the development of a girder curvature. The stress propagation of the model continued, and resulting forces in the modularized agents were summed to monitor the status of equilibrium and to characterize the flexural behavior of the girders, contingent upon failure mode, as illustrated in Fig. 2(b). The interdependence of the agents was tied with those simple rules, and all collective patterns at the global level were translated into the macroscopic behavior of the prestressed girders.

Validation

The developed approach was validated using test data and existing equations. Figure 3(a) compares the flexural capacities of experimental beams[21-24] and their modeling counterparts. The tensile strength and modulus of CFRP tendons embedded in the laboratory beams (f_c' = 37 to 63 MPa [5366 to 9137 psi]) were f_{fu} = 1882 to 2275 MPa (273 to 330 ksi) and E_f = 131 to 170 GPa (19,000 to 24,656 ksi), respectively. The prestressing level of CFRP was 0.5 to 0.65f_{fu}. The predicted capacities agreed with the measured ones at an average margin of 9.1%. Shown in Fig. 3(b) are the predicted flexural capacities of the benchmark girders (Table 1) in relation to the capacities calculated by the analytical equations proposed by Peng and Xue,[11] which can cover both compression- and tension-controlled sections. The coefficient of determination of R^2 = 0.9813 corroborates the adequacy of the modeling method.

Sequential failure

After validation, the default sections depicted in Fig. 1 were subjected to sequential failure that was required to simulate the full-range behavior of the girders. For the compression-controlled sections (Fig. 4(a)), the strains of the extreme compression fiber were calculated at every iteration (Fig. 2(b)), and the values were compared with the crushing strain of the concrete (ε_{cu} = 0.003). If the maximum strain

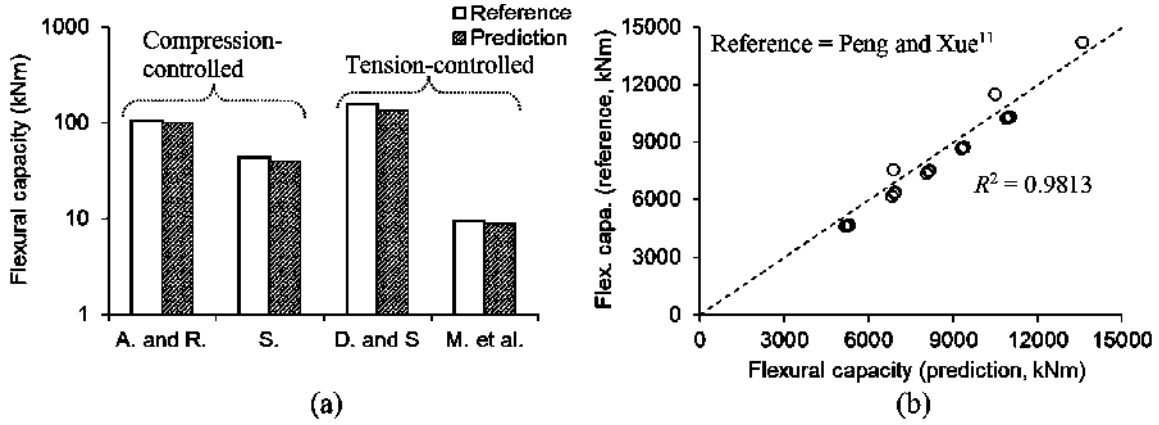

Fig. 3—Validation of modeling approach: (a) experimental (A. and R. is Abdelrahman and Rizkalla[21]; S. is Saeed[22]; D. and S. is Dolan and Swanson[23]; M. et al. is Mertol et al.[24]); and (b) analytical.

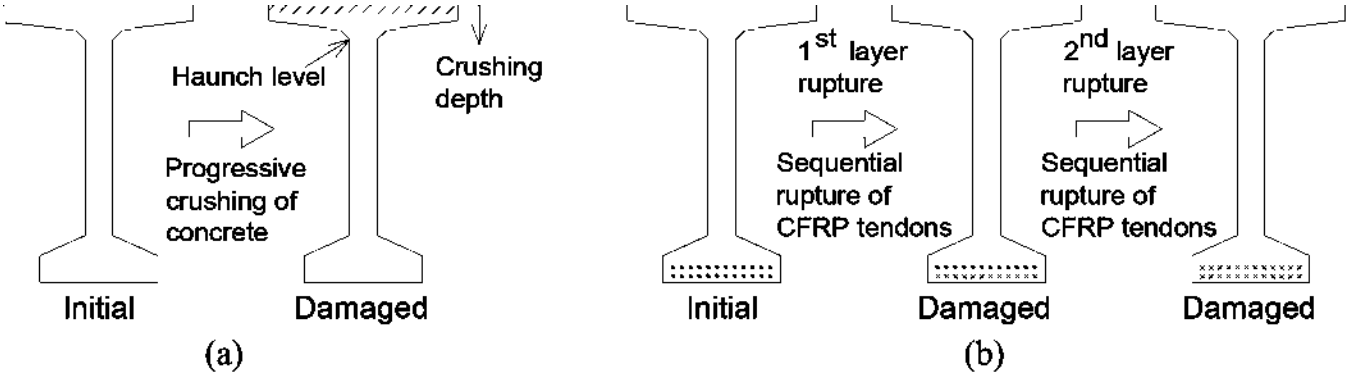

Fig. 4—Schematic of sequential failure modes: (a) crushing of concrete; and (b) rupture of CFRP.

in a layer of the agents was greater than the threshold limit, the layer was deemed to fail and the next layer was reset to be the ultimate compression fiber with a reduced height of the girder. This procedure was repeated until the compression zone reached the haunch depth of the girder. For the tension-controlled sections (Fig. 4(b)), the same procedure was applied, except when a tensile strain of CFRP went over the ultimate strain ($\varepsilon_f \geq \varepsilon_{fu}$): the CFRP layer was regarded to fail without concrete crushing ($\varepsilon_c < \varepsilon_{cu}$, where ε_c is the compressive strain of concrete), which proceeded until all CFRP tendons ruptured.

Characterization of load effects

To evaluate the performance safety of the benchmark girders under the aforementioned failure scenarios, a relationship was characterized between variable load effects and girder resistance. Taken from actual bridge design projects in Colorado, Illinois, Michigan, Pennsylvania, and Texas,[25] the unfactored dead and live load moments (Fig. 5(a)) and the nominal resistance (Fig. 5(b)) of prestressed concrete girders were plotted. The span length of the sampled girders ranged from L = 12 to 42 m (39 to 138 ft). The dead load of the girders (all structural components plus wearing surface: M_{DL} and M_{DW}, respectively) generated a 327% higher moment than the live load (M_{LL}) involving impact factors (IM) and dynamic load allowance (DLA), on average (Fig. 5(a)). The nominal resistance of the girders (M_n) was greater than the unfactored load effects ($M_{DL} + M_{DW} + M_{LL}$) by 53.6%, on average (Fig. 5(b)). For the replication of possible live load intensities during the course of girder failure, four live load factors (α_L) were adopted from published literature,[26,27] which were then coupled with the performance levels elaborated in NCHRP 440[28]: Fully Operational (FO) at α_L = 1.75, Operational (OP) at α_L = 1.00, Life Safety (LS) at α_L = 0.50, and Near Collapse (NC) and α_L = 0.25. The physical interpretation of these performance indicators is as follows: FO is a full design load, OP is the typical service state, LS is an extreme event, and NC is a critical situation. Figure 5(c) provides the distributions of the factored load effects (M_E) versus the factored resistance (M_R) of the girders, where the dead load factors of α_D = 1.25 (structural components) and α_W = 1.50 (wearing surface) and the strength resistance factor[27] of ϕ = 1.0 were associated with the predefined α_L factors. The average ratios of the applied loads and resistance are charted in Fig. 5(d): Case I with the factored dead loads is intended to focus on repair design, whereas Case II with the unfactored dead loads can be used to infer the load effects (fractions of girder resistance) representing specific performance levels for safety assessment.

RESULTS

The ramifications of compression- and tension-controlled sections are delineated for the full-range behavior of CFRP-prestressed concrete girders. Emphasis is placed on failure particulars, flexural responses, safety appraisals, and activation energy with regard to the transition of a girder state.

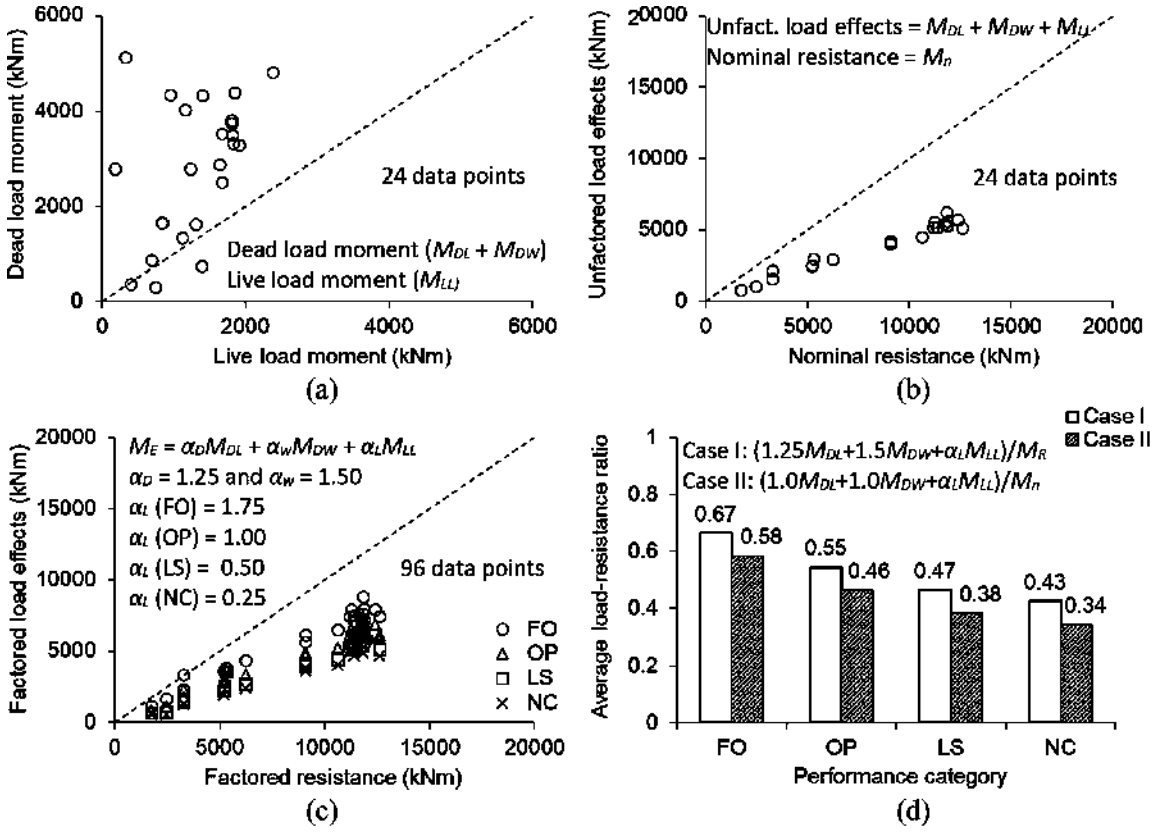

Fig. 5—Characterized relationship between load effects and resistance based on actual bridge design projects in Colorado, Illinois, Michigan, Pennsylvania, and Texas: (a) dead and live moments; (b) load effects versus resistance; (c) variable live load intensities; and (d) ratio of load effects to resistance.

Failure characteristics

Figure 6(a) shows capacity reductions in the compression-controlled girders with progressive failure. As the crushing depth of the concrete increased, the capacity steadily declined in all instances. The descending rate was rapid up to approximately 50 mm (2 in.) when the damage of the upper flange initiated and proceeded, beyond which the response tended to stabilize. The flange played an important role in resisting compressive stress that generated a resultant force counteracting the tensile component for maintaining equilibrium. Although the dimension of the flange was identical across the board (Fig. 1(a)), the evolution of the capacity decrease was size-dependent (Fig. 6(b)): the capacities of BT42 and BT84 at haunch-level crushing with a depth of 189 mm (7.4 in.) were 58.4% and 71.3% of the initial capacities, respectively. This observation is ascribed to the reliance of the lever arm between the compression and tension forces on the girder depth; in other words, the neutral axis location of the stocky girders was altered susceptibly by the concrete crushing, relative to that of the deeper girders (Fig. 6(c)). The amount of the girder concrete was lessened with the elevated crushing depth (Fig. 6(d), inset); however, the loss of the concrete area above the haunch level did not affect the normalized capacity of the girders (Fig. 6(d)) because the repositioned neutral axis necessitated more concrete in the web that brought to a balance with the CFRP tendons.

The moment capacity of the tension-controlled sections also dwindled due to the rupture of CFRP (Fig. 7(a)). Unlike the compression-controlled case, the capacity variation was independent of the girder size (Fig. 7(a), inset). The reason is explained by the fact that the entire upper flange, primarily resisting the compressive stress, was not impaired until the complete failure of the tendons took place and that the progressive rupture of the closely spaced CFRP tendons in the vertical direction was an insignificant determinant for changing the lever arm. Shown in Fig. 7(b) is the impact of the sequential failure of CFRP. While the normalized girder capacity with two CFRP layers plummeted in a linear manner, the downtrend lines of the girders with three and four layers were mitigated because the remaining tendons carried stresses transferred from the previously ruptured tendons. It is thus stated that the vertical distribution of CFRP is desirable for tension-controlled sections and should have as many layers as possible to avoid a catastrophic collapse of the prestressed girders. The neutral axis depth of the BT42 to BT84 girders gradually descended as the rupture depth went up (Fig. 7(c)); mechanically saying, less concrete was needed for responding to the lowered tensile components. Owing to the equilibrium requirements discussed earlier, the tendency of the neutral axis depth normalized by the girder depth appreciably differed between the compression- and tension-controlled sections (Fig. 7(c), inset). Figure 7(d) illustrates the significance of CFRP-area reductions, which reaffirms the betterment of the vertically distributed tendon layers in terms of preserving the load-bearing ability of the girders.

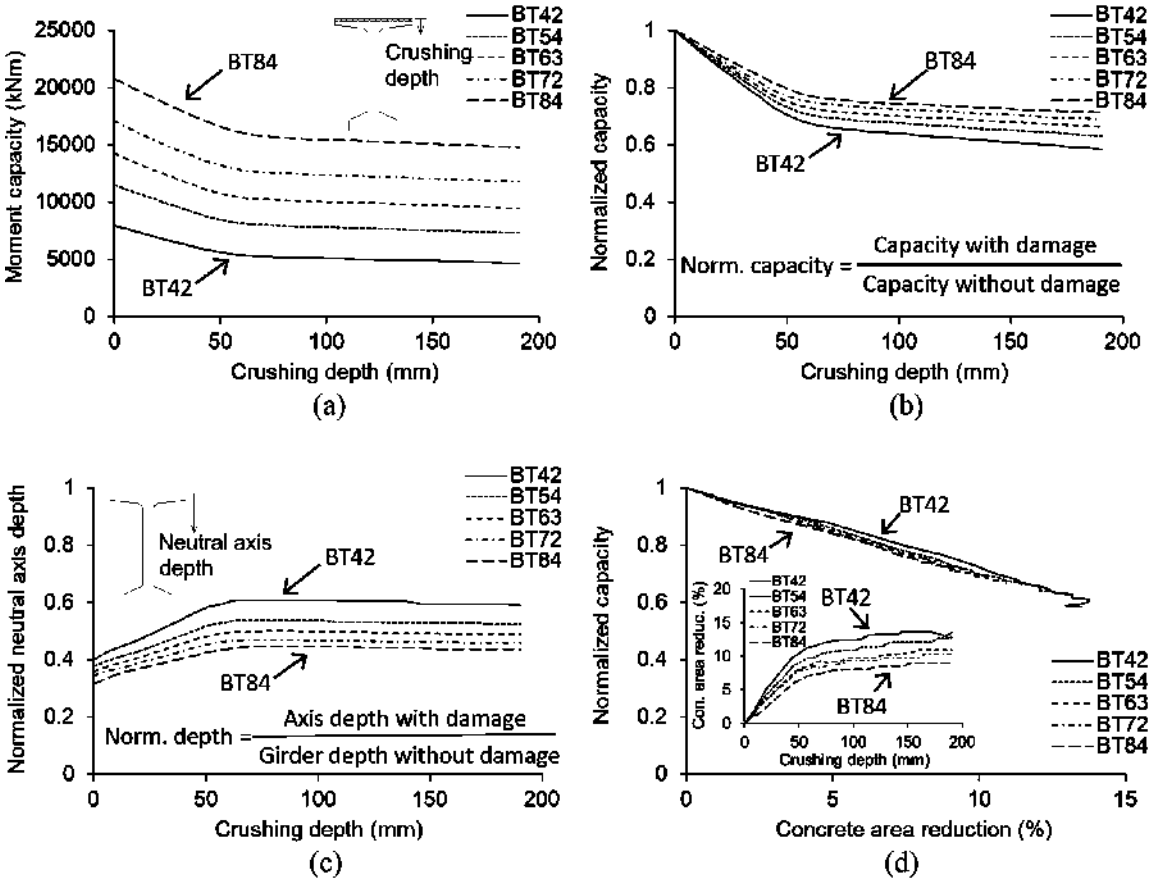

Fig. 6—Failure of compression-controlled sections: (a) flexural capacity; (b) normalized capacity; (c) normalized neutral axis depth; and (d) concrete-area reduction.

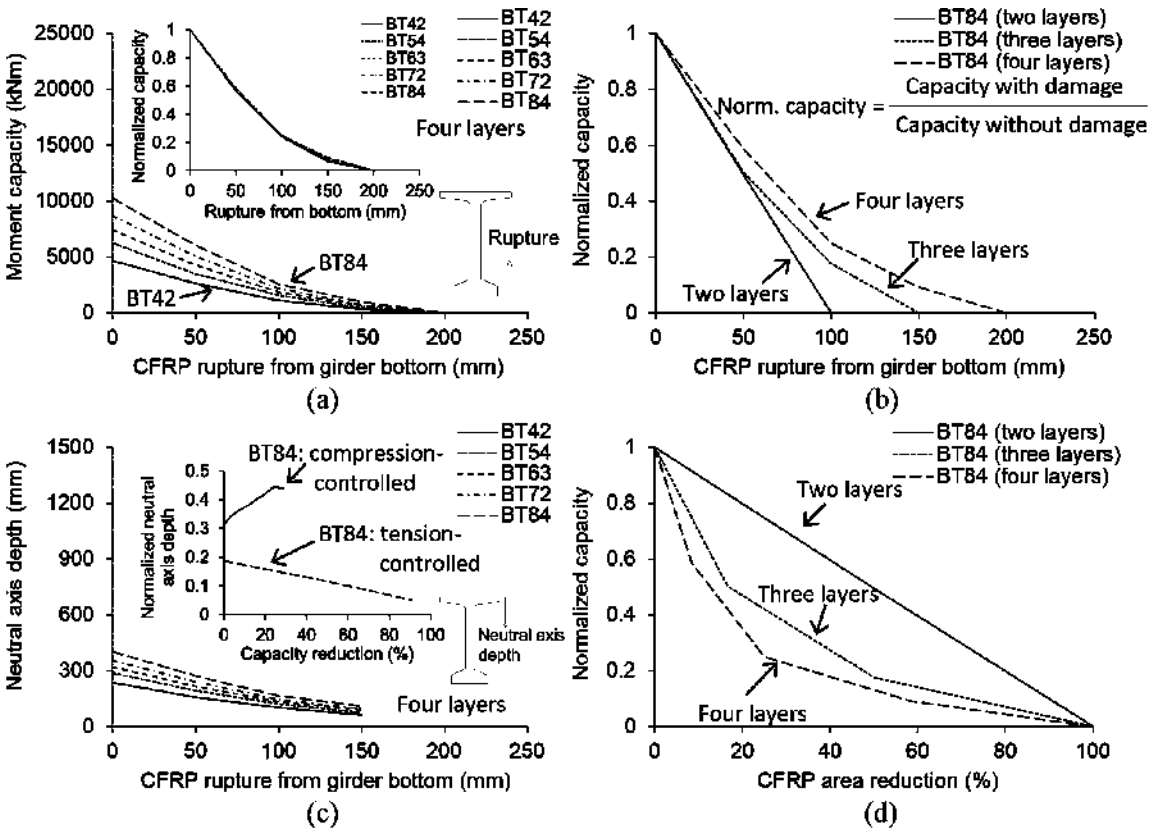

Fig. 7—Failure of tension-controlled sections: (a) flexural capacity with four CFRP layers; (b) normalized capacity for BT84; (c) neutral axis depth with four CFRP layers; and (d) CFRP-area reduction.

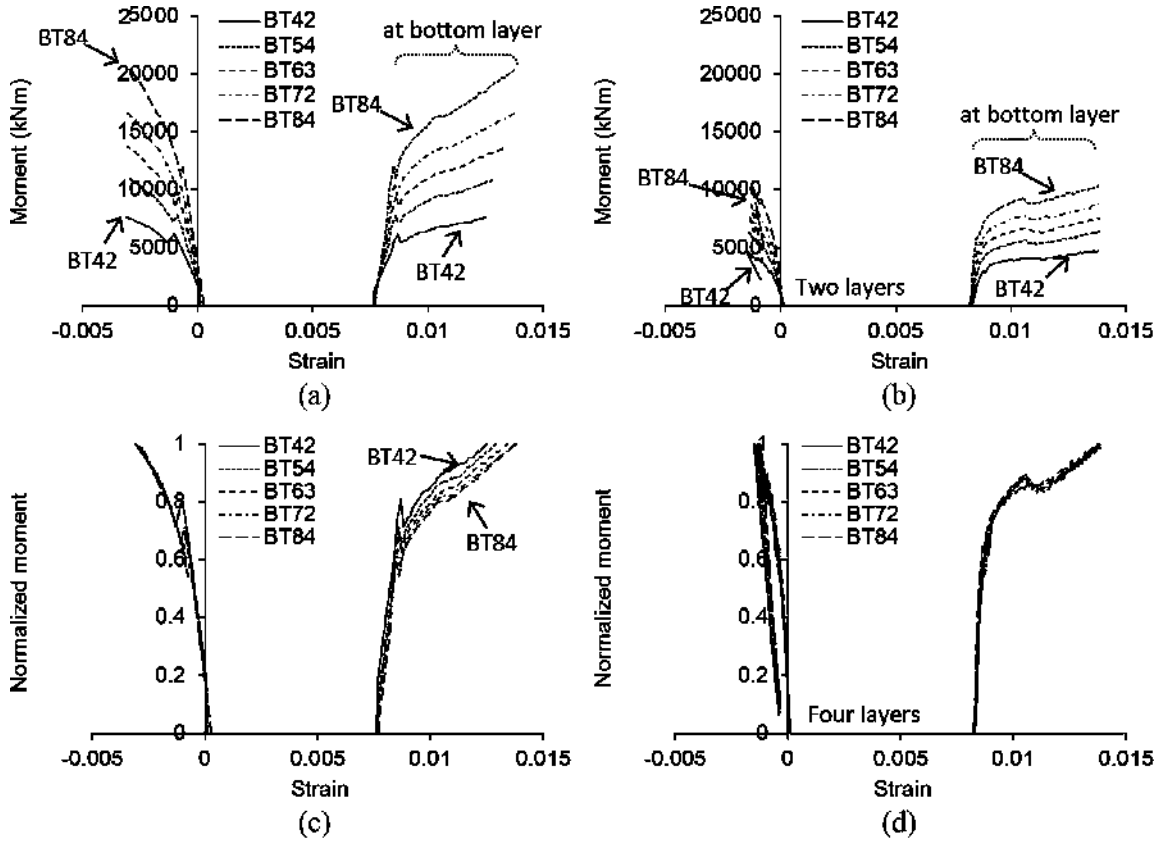

Fig. 8—Moment-strain relationship: (a) compression-controlled sections; (b) tension-controlled sections with two CFRP layers; (c) normalized moment development of compression-controlled sections; and (d) normalized moment development of tension-controlled sections with four CFRP layers.

Strain variation

The moment-strain relationship of the girders is graphed in Fig. 8. For the compression- and tension-controlled sections, the girder size influenced concrete and CFRP strains (Fig. 8(a) and (b)). That is, as the depth of the girders decreased, more sectional rotations were allowed on account of the low moment of inertia; consequently, the strain development became pronounced. The sensitive computational model captured the instantaneous drop of the moment in the compression-controlled girders (ρ = 2.4 to 5.4%, where ρ is the reinforcement ratio based on the web thickness) when the concrete cracked (Fig. 8(a)), which is not available in conventional sectional analysis. These locally unstable responses were attributed to a sudden decrease in the stiffness of the girders incorporating the low-modulus CFRP material.[29] Regarding the tension-controlled girders (Fig. 8(b)), the abrupt local indentation was not obvious because the transition of the moment of inertia before and after cracking was marginal in the lightly reinforced sections (for example, ρ = 0.98% for BT84). Analogous to the normalized capacities given in Fig. 6(b) and 7(a), the propensity for the strain growth was reliant upon the amount of the CFRP tendons. Under the same moment level normalized by the maximum moment (M_{nor}), BT84 exhibited more strains than BT42 for the compression-controlled sections (Fig. 8(c)); conversely, there was no distinguishable facet for the tension-controlled sections (Fig. 8(d)).

Moment-curvature

Figure 9(a) demonstrates the moment-curvature relationship of the compression-controlled sections. The aforementioned momentary diminution was conspicuous in the ordinate, at which a bifurcation occurred when the concrete cracked, and the slope of the curves escalated with the increased girder depth. As far as the tension-controlled sections are concerned (Fig. 9(b)), the pre-cracking stiffness was akin to that of the preceding sections; on the contrary, the post-cracking stiffness was much lower because of the relatively short neutral axis depth (Fig. 7(c)) concomitant with the noticeable cracking of the sections. The three-stage behavior of the tension-controlled girder is epitomized in Fig. 9(c), where BT42 is used as a representative sample: 1) the first stage with the uncracked concrete subjected to service loading ($0 \le M_{nor} \le 0.67$); 2) the second stage with the cracked concrete up to the ultimate moment ($0.67 < M_{nor} \le 1.0$); and 3) the third stage with the successive rupture of the tendons in the post-peak region. It is worth noting that the increment of the normalized curvature was minimal until the normalized moment plunged to M_{nor} = 0.06; namely, the contribution of the multilayered CFRP tendons to the modification of the girder's curvature was negligible (supplementary discussions to follow). The area under the moment-curvature curves of all girders was numerically integrated, which was designated as the "characteristic area" in Fig. 9(d). Irrespective of girder size, the compression-controlled sections revealed higher characteristic areas

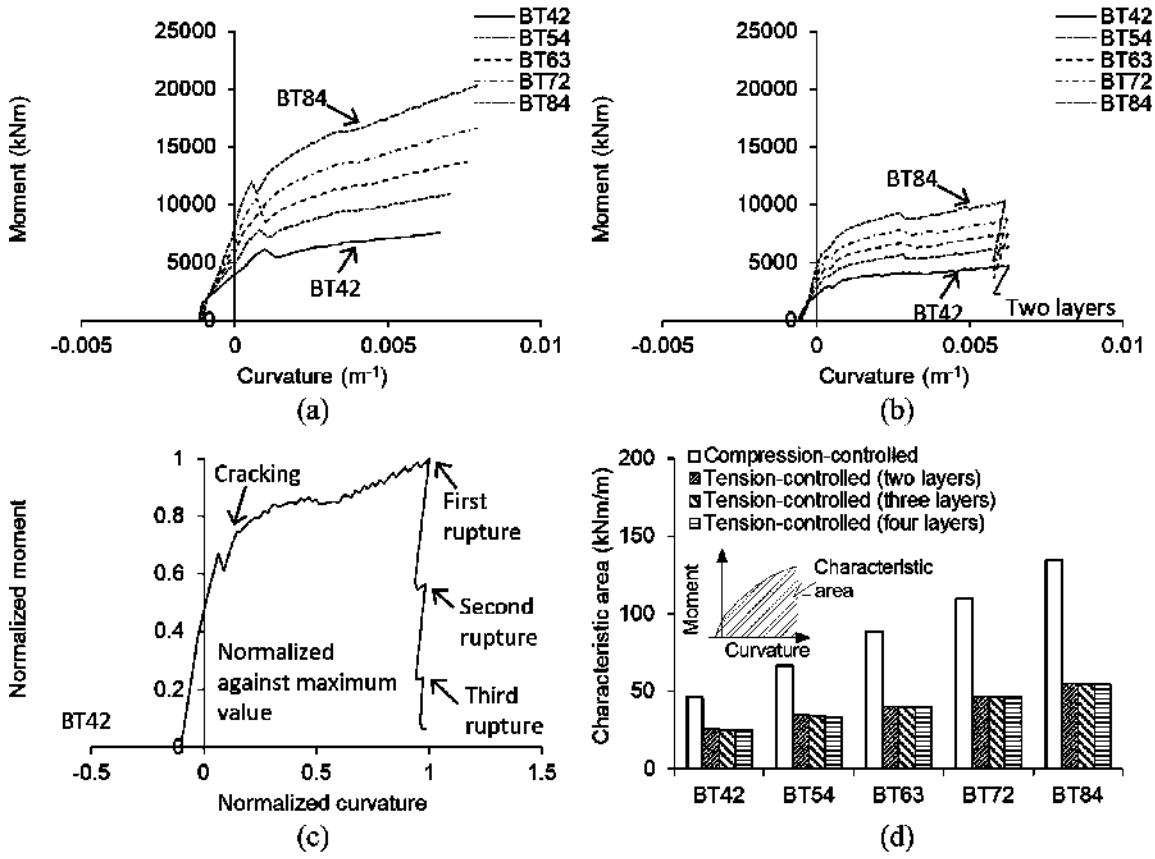

Fig. 9—Moment-curvature relationship: (a) compression-controlled sections; (b) tension-controlled sections with two CFRP layers; (c) stepwise failure of tension-controlled BT42 section with four CFRP layers; and (d) characteristic area.

than the tension-controlled ones, leading to a physical interpretation that the amount of the former's internal energy was greater and conveyed better to the constituent materials until a dissipation process was completed at the time of the girder failure. The almost constant characteristic areas of the tension-controlled sections with two to four CFRP layers verify the ignorable impact of the progressive rupture of the tendons on the sectional deformation of the girders.

Deformability

Because the CFRP tendons and concrete are brittle in nature, the traditional concept of ductility is not applicable.[6] As an alternative to quantify the flexural performance of CFRP-prestressed members, a deformability index (*DI*) may be calculated[6,30]

$$DI = \frac{(1-k)}{1-\alpha/(d_f\beta_1)}\frac{\varepsilon_{fu}}{\varepsilon_{fs}} \quad (1)$$

$$DI = \begin{cases} 1+\dfrac{k\varepsilon_{cu}}{\varepsilon_{fe}} & \text{for compression-controlled section} \\ \dfrac{\varepsilon_{cu}}{\varepsilon_{fe}} & \text{for tension-controlled section} \end{cases} \quad (2)$$

where k is the ratio of the neutral axis depth to the effectiveness depth ($k = c/d_f$); α is the constant ($\alpha = \rho d_f f_{fu}/(0.85f_c')$; ρ is based on the flange width[6]; β_1 is the concrete stress block factor specified in ACI 318-19[12]; ε_{fs} is the service strain of CFRP, which can be approximated to be a prestressing strain[6]; and ε_{fe} is the effective CFRP strain ($\varepsilon_{fe} = f_{fe}/E_f$). Figure 10 charts the deformability indexes of the prestressed girders. A general trend is that the indexes of the compression-controlled sections were less than those of the tension-controlled sections; however, both of them in Fig. 10(b) exceeded the suggested limits (DI = 1.5 and 1.8 for the compression- and tension-controlled sections, respectively[30]). This points out that all sections were technically adequate from a design perspective (it is noted that there is no limit for Eq. (1); thus, it cannot be used for practice, as criticized in Kim and Nickle[30]).

Sectional response

Figure 11 displays the sectional response of the compression- and tension-controlled girders. For comparison, selected attributes were normalized by their maximum values, except for neutral axis depths, which were normalized by the girder depths (Table 1). With an increase in the moment, the neutral axis depth of the entire girder series steadily declined until a normalized moment of approximately M_{nor} = 0.85 was reached (Fig. 11(a)), outside of which distinctions were prominent due to the abrupt failure of the tendons (Fig. 11(a), inset). The curvature response of the two girder types was similar up to M_{nor} = 0.81 (Fig. 11(b)); then, the cracked section of the compression-controlled girder showed transient instability. The steeply rising curvature of the girders again diverged immediately after the normalized moment reached M_{nor} = 1.0 by virtue of the CFRP rupture. As a result of restrictive concrete deformations at the top of the girders within the maximum usable boundary of ε_{cu} = 0.003, the path

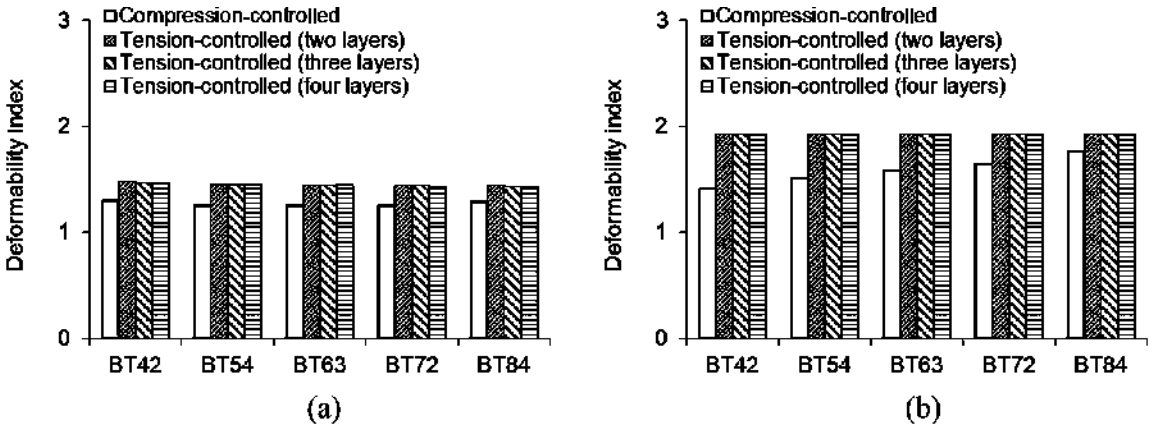

Fig. 10—Deformability index: (a) ACI 440.4R-04[6]; and (b) Kim and Nickle.[30]

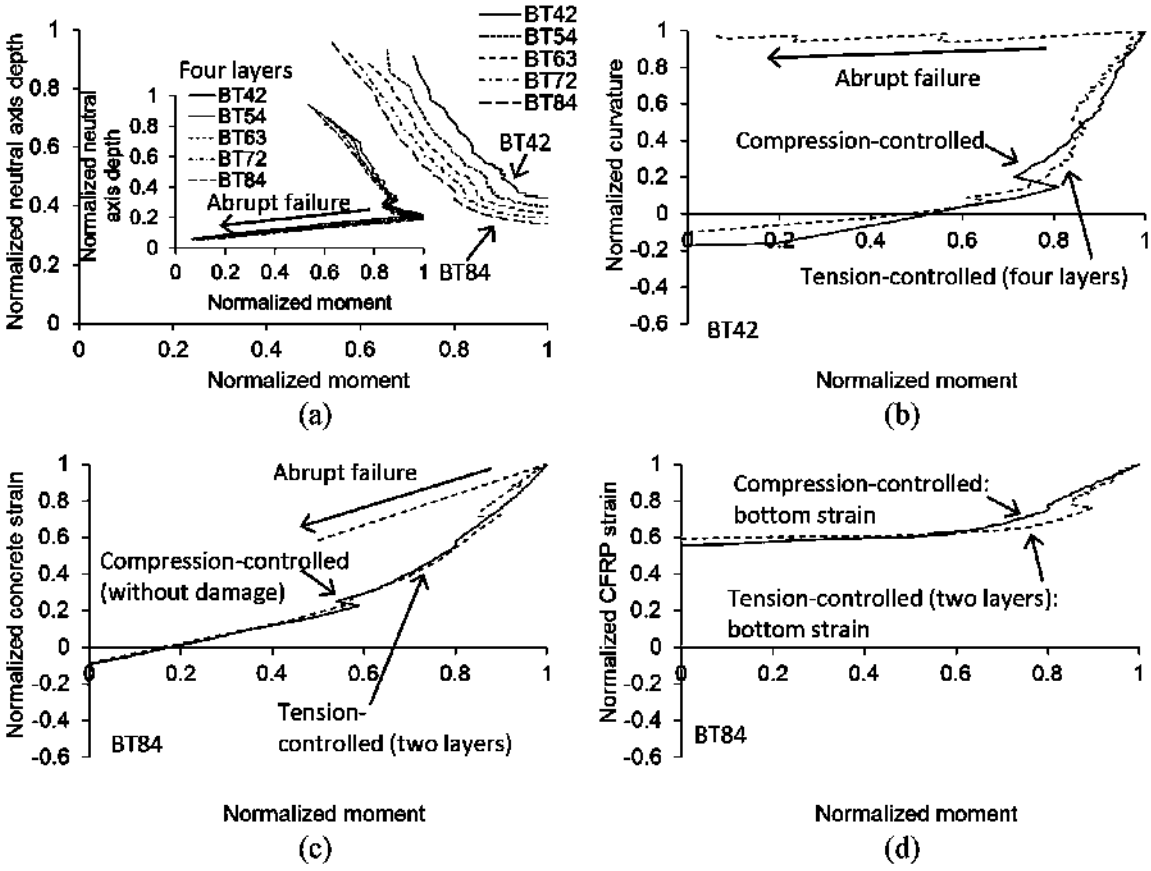

Fig. 11—Normalized sectional response of compression- and tension-controlled girders with moment development: (a) neutral axis; (b) curvature; (c) concrete strain; and (d) CFRP strain.

of the normalized concrete strains was virtually unrelated to the failure modes (Fig. 11(c)). Likewise, the strains of the most-tensioned CFRP near the bottom of the girders were alike from M_{nor} = 0 to 0.6 (Fig. 11(d)), implying that there should be no concerns about the premature failure of these girder configurations under service loading. In excess of M_{nor} = 0.6, the CFRP strain of the compression-controlled girder forged ahead ($\varepsilon_f < \varepsilon_{fu}$) relative to that of the tension-controlled girder suffering the rupture of the tendons ($\varepsilon_f = \varepsilon_{fu}$).

Safety assessment

Mensuration—The safety of the girders was estimated using Eq. (3), indirectly expressing the probability of failure,[31] together with the extent of damage (Eq. (4))

$$\beta = \frac{LN(M_N/M_E)}{\sqrt{(COV_R)^2 + (COV_E)^2}} \quad (3)$$

$$\Omega = \frac{M_{n0} - M_{nD}}{M_{n0}} \quad (4)$$

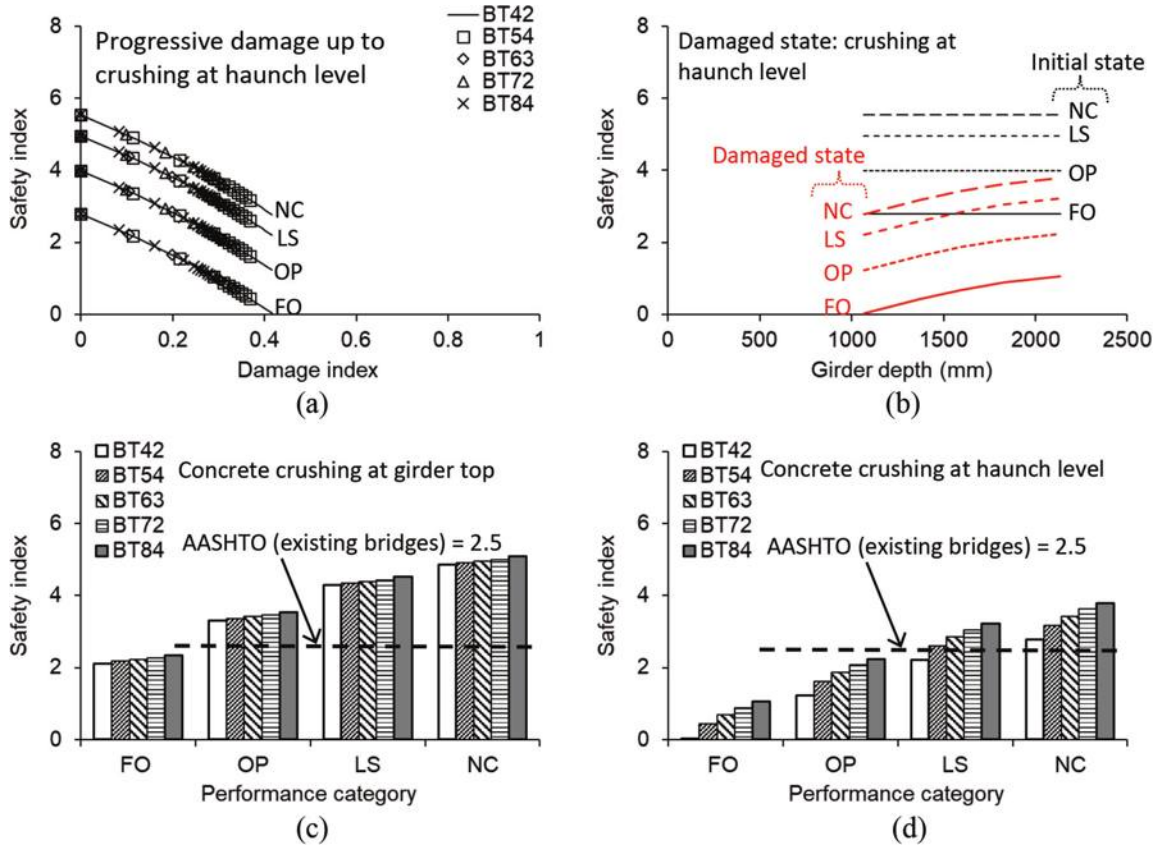

Fig. 12—Safety index with progressive damage in compression-controlled sections: (a) damage level; (b) size effect; (c) performance category at girder-top crushing; and (d) performance category at haunch crushing.

where β is the safety index appertaining to the actual distribution of bridge loads and responses[31]; M_N is the flexural resistance of the girder with and without damage (Fig. 6(a) and 7(a)); M_E is the load effect representing the characterized four performance categories (Case II in Fig. 5(d)); COV_R and COV_E are the coefficients of variation for the M_N and M_E terms, respectively (referring to the literature[31,32]; COV_R = 0.075 and COV_E = 0.18 were assumed); Ω is the damage index; and M_{n0} and M_{nD} are the initial moment capacity and the damaged moment resistance, respectively.

Crushing of concrete—The safety indexes of the compression-controlled sections consistently diminished with the accumulated damage (Fig. 12(a)). The intervals between the performance levels from NC to FO were retained without being affected by the damage index and, in addition, the safety responses were not engaged with the depth of the girders. Figure 12(b) explicates the reliance of the girder safety on its depth. Before the occurrence of damage (the initial state), the indexes were constant; per contra, the indexes with concrete crushing (the damaged state) ascended as the depth increased. The use of a deeper section was thus beneficial in the sense of safety when subjected to compression failure. The influence of the progressive crushing is visible in Fig. 12(c) and (d). With the exception of the FO category (full design load), the safety indexes of the girders undergoing concrete crushing at the top were higher than the AASHTO limit of 2.5 for constructed bridges (Fig. 12(c)),[33] denoting that the girders were still functional in spite of the design-level failure. As the crushing continued to the haunch location, the margin of safety remarkably decreased from the limit (Fig. 12(d)). Therefore, strict traffic control will be imperative under the NC category (α_L = 0.25) if concrete crushing penetrates through the upper flange of such CFRP-prestressed girders.

Rupture of CFRP—Even if the safety indexes of the tension-controlled sections were the same as those of the compression-controlled sections at Ω = 0 (no damage), the brittle rupture of CFRP resulted in swift reductions (Fig. 13(a)). As before, the indexes of the tension-controlled sections at the initial stage were unrelated to the girder depth (Fig. 13(b)), and this trend was maintained when the bottommost layer of the tendons failed (the damaged state indicated in Fig. 13(b)), which was different from the rising pattern of the compression-controlled sections (Fig. 12(b)). The indexes linked with the succeeding tendon ruptures were negative and had no practical significance (not shown in Fig. 13(b)). The number of the vertically distributed CFRP layers was a factor that adjusted the level of safety (Fig. 13(a) and (b)). Specifically, at the moment of the first tendon rupture, the safety indexes of all performance categories in the two-tendon girders were below the AASHTO limit of 2.5 (Fig. 13(c)); however, the average index of the NC category was 2.7 in the four-tendon girders (Fig. 13(d)). Considering these safety features, CFRP tendons should be arranged carefully if the intended failure mode of a prestressed girder is tension-controlled, which is vulnerable in comparison with the compression-controlled case.

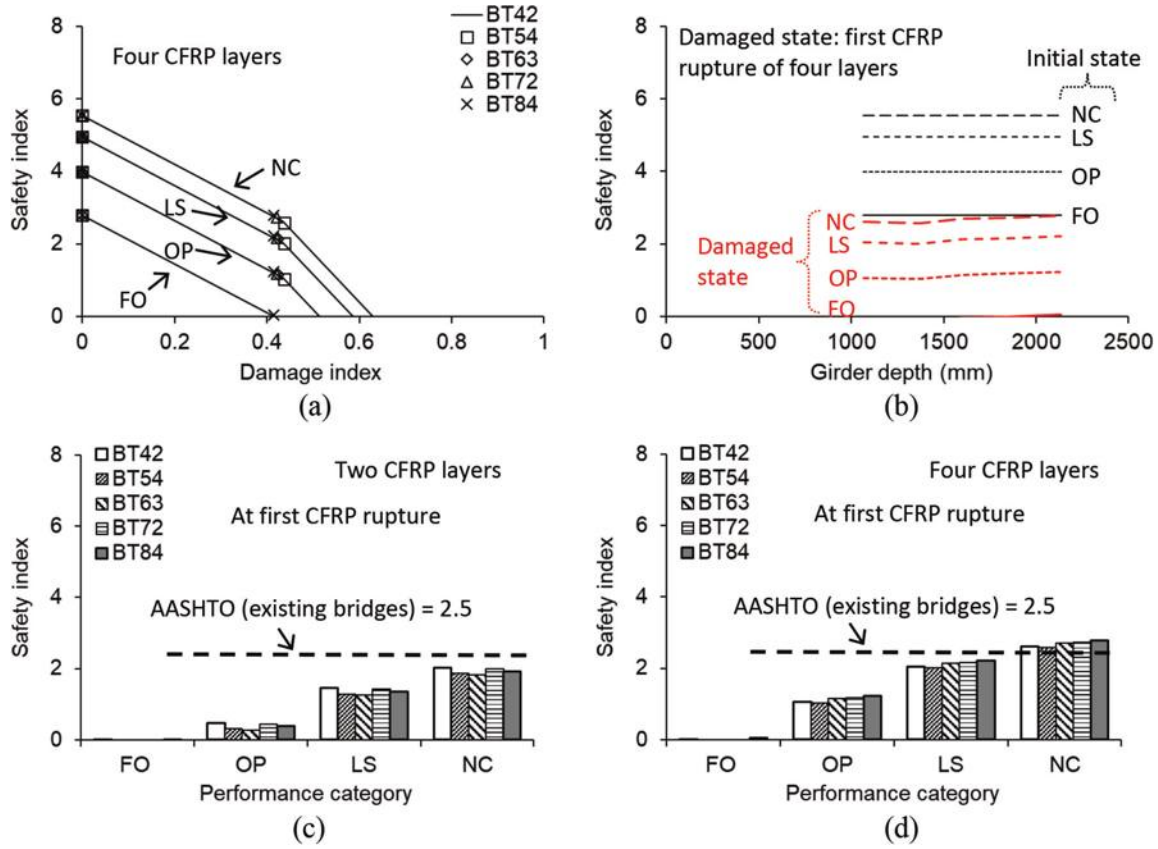

Fig. 13—Safety index with progressive damage in tension-controlled sections: (a) damage level with four CFRP layers; (b) size effect with four CFRP layers; (c) performance category with two CFRP layers; and (d) performance category with four CFRP layers.

Activation energy

To definitize the dependency of the flexural resistance on the girder types, the concept of Arrhenius theory, which is prevalent in physical chemistry, may be taken[34]

$$R_r = e^{-Q/(k_B T)} \tag{5}$$

where R_r is the response rate; Q is the activation energy; k_B is the Boltzmann constant ($k_B = 1.381 \times 10^{-23}$ J/K); and T is the temperature in Kelvin ($T = 298$ K was used, equivalent to 25°C [77°F]). Equation (5) was rearranged to solve for the activation energy in tandem with replacing the R_r term by the moment ratio of M_{nD}/M_{n0}

$$Q = -\ln(M_{nD}/M_{n0})(k_B T) \tag{6}$$

The physical meaning of the activation energy is that it measures the transition rate of reactions between consecutive states at a specific temperature[35]; scilicet, Eq. (6) can figure out a minimum amount of energy that is needed from the initial state to certain damage levels of the girders. As described in Fig. 14(a) and (b), the downward flexural resistance related to the increased damage raised the activation energy. The progression of the activation energy was restrictive for the compression-controlled girders up to the haunch-level crushing (Fig. 14(a)), whereas more activation energy was necessary while the sequential ruptures were in progress for the tension-controlled girders (Fig. 14(b)). Figure 14(c) contrasts the activation energy belonging to all girder series. The shift of the intended failure modes from compression to tension brought about the soaring of the activation energy, signifying the susceptible reactivity of the tension-controlled girders when the state of damage evolved. The degree of changes in the activation energy of the girders was determined by the secant slope of the resistance-energy curves, connecting the initial state with the failure state, and is rendered in Fig. 14(d). The slopes clearly demonstrate the size-dependency of the activation energy: the reaction of the smallest girder, BT42, was conspicuous, during which a transition was made from the undamaged to damaged states, regardless of the failure modes.

SUMMARY AND CONCLUSIONS

This paper has investigated the full-range behavior of carbon fiber-reinforced polymer (CFRP)-prestressed concrete girders that failed in compression and tension. Simulations were conducted using an advanced computational platform, agent-based modeling, which handled decentralized interactions between multiple entities. Employing five bulb-tee sections (BT42 to 84) with a variable amount of CFRP tendons, the consequences of progressive failure were expounded with the aim of quantifying the fundamental hazard of those girders beyond design-level flexural responses. Technical interests lied in load-resisting abilities, performance levels, strain development, deformability,

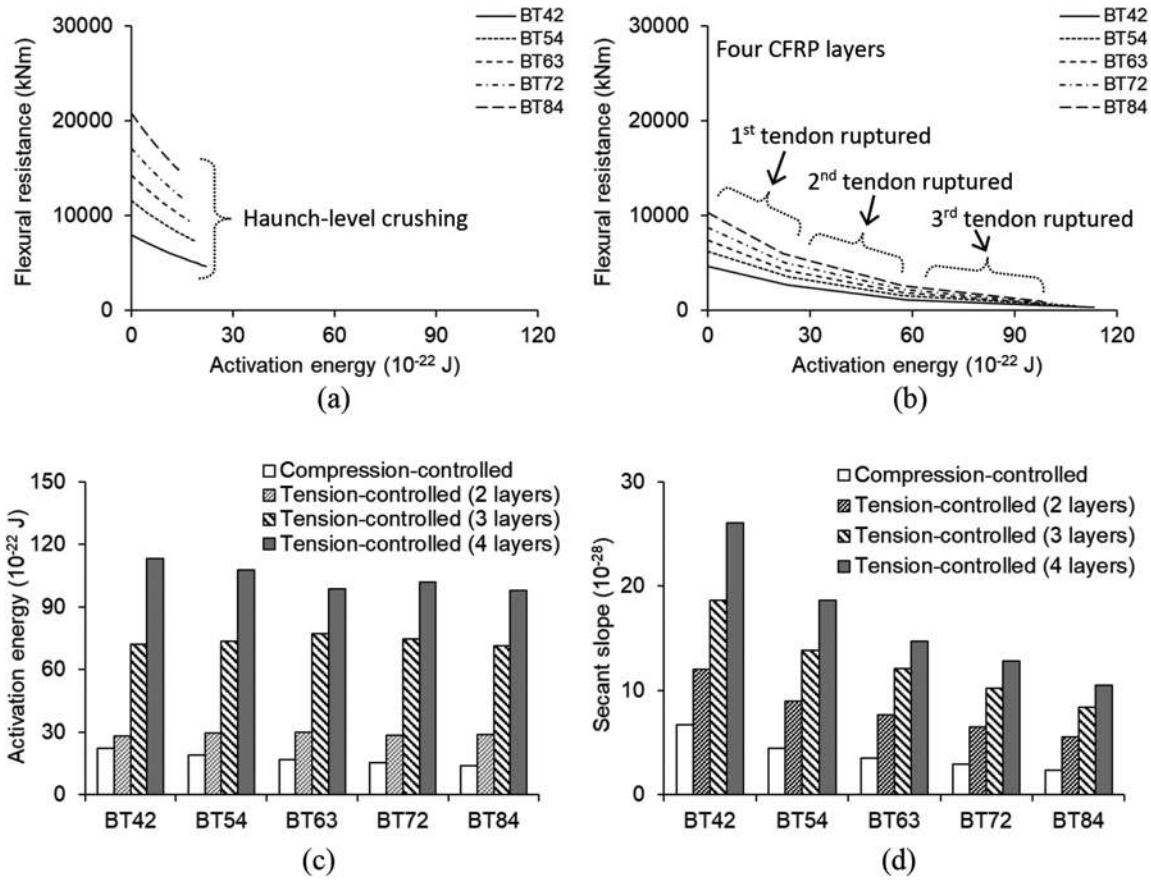

Fig. 14—Activation energy: (a) compression-controlled sections; (b) tension-controlled sections with four CFRP layers; (c) comparison of activation energy at impending failure; and (d) comparison of secant slope at impending failure.

structural safety, and state transitions, depending upon the failure modes. The following conclusions are drawn:

- The capacity-reduction rate of the compression-controlled girders was prompt when half of the upper-flange concrete crushed, whereas the rate became stable as the crushing further progressed. Owing to the relocation of neutral axis depth, the capacities of the damaged girder normalized by the initial capacity were not impinged by the loss of concrete above the haunch level. Different from the compression-controlled girders, the capacity decrease of the tension-controlled girders was scale-invariant. The sequential rupture of CFRP transferred tensile stresses from one layer to another.
- The degree of sectional rotations was a function of the girder depth and controlled the magnitude of CFRP strains. A change in the section stiffness with the low-modulus tendons induced local instability in the compression-controlled girders at the time of cracking, while this trend was not apparent in the tension-controlled girders by virtue of the dissimilar reinforcement ratios. Both girder configurations satisfied deformability requirements, and the premature failure of CFRP was not expected under service loading.
- After the initiation of the sequential failure process, the safety indexes of the compression-controlled sections rose with the increased girder depth; in contrast, the indexes of the tension-controlled sections were not concerned with the depth. The number of vertically distributed CFRP tendons was a crucial factor that governed the level of safety. Under the evolution of damage, the tension-controlled girders demanded more activation energy than the compression-controlled ones. Without reference to the failure modes, the development of the activation energy was size-dependent.

AUTHOR BIOS

Yail J. Kim, *FACI, is President of the Bridge Engineering Institute, An International Technical Society, and a Professor in the Department of Civil Engineering at the University of Colorado Denver, Denver, CO. He is Chair of ACI Subcommittee 440-I, FRP-Prestressed Concrete; past Chair of ACI Committee 345, Bridge Construction and Preservation; and a member of ACI Committees 342, Evaluation of Concrete Bridges and Bridge Elements; 377, Performance-Based Structural Integrity & Resilience of Concrete Structures; 440, Fiber-Reinforced Polymer Reinforcement; and Joint ACI-ASCE Committee 343, Concrete Bridge Design. He received the ACI Chester Paul Siess Award for Excellence in Structural Research in 2019. His research interests include advanced composite materials for rehabilitation; structural informatics; complex systems; and science-based structural engineering including statistical, interfacial, and quantum physics.*

ACI member **Jun Wang** *is a Postdoctoral Fellow in the Department of Civil Engineering at the University of Colorado Denver. She received her BS and MS from Northeast Forestry University, Harbin, China, and the University of Colorado Denver, respectively. She is a member of ACI Committee 345, Bridge Construction and Preservation. Her research interests include multi-object interaction, advanced modeling, and concrete structures.*

Woo-Tai Jung *is a Senior Researcher in the Structural Engineering Research Division of the SOC Research Institute at the Korea Institute of Civil Engineering and Building Technology. He received his PhD from Myongji University, Seoul, South, Korea. His research interests include strengthening deteriorated concrete structures with fiber-reinforced polymer (FRP) composites.*

Jae-Yoon Kang *is a Research Fellow in the Structural Engineering Research Division of the SOC Research Institute at the Korea Institute of Civil Engineering and Building Technology. He received his MS and PhD from Dongguk University, Seoul, South, Korea.*

Jong-Sup Park *is a Research Fellow in the Structural Engineering Research Division of the SOC Research Institute at the Korea Institute of Civil Engineering and Building Technology. He received his MS and PhD from Myongji University.*

ACKNOWLEDGMENTS

The research was conducted as part of the Strategic Research Project of the Korea Institute of Civil Engineering and Building Technology (KICT). The authors thank the members of ACI Subcommittee 440-I, FRP-Prestressed Concrete, for their discussions and valuable suggestions. To avoid commercialism, all proprietary information, such as product names and manufacturers, was not included. The technical contents presented in this paper are based on the opinion of the authors and do not necessarily represent that of others.

REFERENCES

1. FHWA, "National Bridge Inventory (NBI)," Federal Highway Administration, Washington, DC, 2022, https://www.fhwa.dot.gov/bridge/nbi/ascii.cfm. (last accessed Aug. 16, 2023)

2. Fiorillo, G., and Ghosn, M., "Risk-Based Life-Cycle Analysis of Highway Bridge Networks under Budget Constraints," *Structure and Infrastructure Engineering*, V. 18, No. 10-11, 2022, pp. 1457-1471. doi: 10.1080/15732479.2022.2059525

3. Bamonte, P.; Kalaba, N.; and Felicetti, R., "Computational Study on Prestressed Concrete Members Exposed to Natural Fires," *Fire Safety Journal*, V. 97, 2018, pp. 54-65. doi: 10.1016/j.firesaf.2018.02.006

4. Kotsovinos, P.; Judge, R.; Walker, G.; and Woodburn, P., "Fire Performance of Structural Cables: Current Understanding, Knowledge Gaps, and Proposed Research Agenda," *Journal of Structural Engineering*, ASCE, V. 146, No. 8, 2020, p. 03120002. doi: 10.1061/(ASCE)ST.1943-541X.0002703

5. Naito, C.; Sause, R.; Hodgson, I.; Pessiki, S.; and Desai, C., "Forensic Evaluation of Prestressed Box Beams from the Lake View Drive over I-70 Bridge," Report No. FHWA-PA-2006-017-EMG002, Center for Advanced Technology for Large Structural Systems, Lehigh University, Bethlehem, PA, 2006.

6. ACI Committee 440, "Prestressing Concrete Structures with FRP Tendons (ACI 440.4R-04) (Reapproved 2011)," American Concrete Institute, Farmington Hills, MI, 2004, 35 pp.

7. Campbell, I., "Prestressing Concrete Structures with Fibre-Reinforced Polymers (Design Manual No. 5)," Structural Innovation and Monitoring Technologies Resource Centre (SIMTReC), Winnipeg, MB, Canada, 2008.

8. Frankhauser, W.; Elkaissi, J.; Khal, S.; McMilan, S.; Potter, W.; Rister, D.; Wilson, D.; and O'Connor, J., "Advances in Fiber-Reinforced Polymer (FRP) Composites in Transportation Infrastructure," NCHRP 20-68A, Transportation Research Board, Washington, DC, 2013.

9. Rizkalla, S., "Innovative Use of FRP for Sustainable Precast Concrete Bridges and Structures," Proceedings of the Transport Research Arena, Paris, France, 2014.

10. Ozyildirim, H. C., and Sharp, S. R., "Concrete Beams Prestressed Using Carbon Fiber Reinforced Polymer," Report No. VTRC 19-R29, Virginia Transportation Research Council, Charlottesville, VA, 2019.

11. Peng, F., and Xue, W., "Analytical Approach for Flexural Capacity of FRP Prestressed Concrete T-Beams with Non-Prestressed Steel Bars," *Journal of Composites for Construction*, ASCE, V. 22, No. 6, 2018, p. 04018063. doi: 10.1061/(ASCE)CC.1943-5614.0000903

12. ACI Committee 318, "Building Code Requirements for Structural Concrete (ACI 318-19) and Commentary (ACI 318R-19) (Reapproved 2022)," American Concrete Institute, Farmington Hills, MI, 2019, 624 pp.

13. CDOT, "Bridge Design Manual," Colorado Department of Transportation, Denver, CO, 2012.

14. PCI, *PCI Bridge Design Manual*, third edition, Precast/Prestressed Concrete Institute, Chicago, IL, 2014.

15. Duffy, V. G., *Digital Human Modeling and Applications in Health, Safety, Ergonomics and Risk Management*, Springer Nature, Cham, Switzerland, 2021.

16. Engel, U.; Quan-Haase, A.; Liu, S. X.; and Lyberg, L., *Handbook of Computational Social Science*, Routledge, Oxfordshire, UK, 2021.

17. Railsback, S. F., and Grimm, V., *Agent-Based and Individual-Based Modeling: A Practical Introduction*, second edition, Princeton University Press, Princeton, NJ, 2019.

18. DeAngelis, D. L., and Diaz, S. G., "Decision-Making in Agent-Based Modeling: A Current Review and Future Prospectus," *Frontiers in Ecology and Evolution*, V. 6, 2019, p. 237. doi: 10.3389/fevo.2018.00237

19. Gilbert, N., *Agent-Based Models*, second edition, SAGE Publications, Inc., Thousand Oaks, CA, 2020.

20. Wilensky, U., and Rand, W., *An Introduction to Agent-Based Modeling: Modeling Natural, Social, and Engineered Complex Systems with NetLogo*, MIT Press, Cambridge, MA, 2015.

21. Abdelrahman, A. A., and Rizkalla, S. H., "Serviceability of Concrete Beams Prestressed by Carbon-Fiber-Reinforced-Plastic Bars," *ACI Structural Journal*, V. 94, No. 4, July-Aug. 1997, pp. 447-457.

22. Saeed, Y. M., "Behavior of Prestressed Concrete Beams with CFRP Strands," MS thesis, Portland State University, Portland, OR, 2016.

23. Dolan, C. W., and Swanson, D., "Development of Flexural Capacity of a FRP Prestressed Beam with Vertically Distributed Tendons," *Composites Part B: Engineering*, V. 33, No. 1, 2002, pp. 1-6. doi: 10.1016/S1359-8368(01)00053-1

24. Mertol, H. C.; Rizkalla, S.; Scott, P.; Lees, J. M.; and El-Hacha, R., "Durability of Concrete Beams Prestressed with CFRP Bars," *Case Histories and Use of FRP for Prestressing Applications*, SP-245, R. El-Hacha and S. H. Rizkalla, eds., American Concrete Institute, Farmington Hills, MI, 2007, pp. 1-20.

25. Nowak, A. S., "Calibration of LRFD Bridge Design Code," NCHRP Report 368, National Academy of Sciences, Washington, DC, 1993.

26. Ghosn, M.; Moses, F.; and Wang, J., "Design of Highway Bridges for Extreme Events," NCHRP Report 489, National Academy of Sciences, Washington, DC, 2003.

27. AASHTO, "LRFD Bridge Design Specifications," ninth edition, American Association of State Highway and Transportation Officials, Washington, DC, 2020.

28. Marsh, M. L., and Stringer, S. J., "Performance-Based Seismic Bridge Design (NCHRP Synthesis 440)," Transportation Research Board, Washington, DC, 2013.

29. Karayannis, C. G.; Kosmidou, P.-M. K.; and Chalioris, C. E., "Reinforced Concrete Beams with Carbon-Fiber-Reinforced Polymer Bars—Experimental Study," *Fibers*, V. 6, No. 4, 2018, p. 99. doi: 10.3390/fib6040099

30. Kim, Y. J., and Nickle, R. W., "Long-Term Multipliers and Deformability of Fiber-Reinforced Polymer-Prestressed Concrete," *ACI Structural Journal*, V. 115, No. 1, Jan. 2018, pp. 223-234. doi: 10.14359/51700988

31. Barker, R. M., and Puckett, J. A., *Design of Highway Bridges: An LRFD Approach*, fourth edition, John Wiley & Sons, Inc., Hoboken, NJ, 2021.

32. Nowak, A. S., and El-Hor, H. H., "Serviceability Criteria for Prestressed Concrete Bridge Girders," 4th International Bridge Engineering Conference, Transportation Research Board, National Research Council, Washington, DC, 1995, pp. 181-187.

33. AASHTO, *The Manual for Bridge Evaluation*, third edition, American Association of State Highway and Transportation Officials, Washington, DC, 2018.

34. Atkins, P.; de Paula, J.; and Keeler, J., *Physical Chemistry: Molecular Thermodynamics and Kinetics*, Oxford University Press, Oxford, UK, 2019.

35. McMurry, J. E., *Organic Chemistry*, eighth edition, Cengage Learning, Boston, MA, 2012.

CALL FOR ACTION

ACI Invites You To...

Share your expertise

Do you have EXPERTISE in any of these areas?

- BIM
- Chimneys
- Circular Concrete Structures Prestressed by Wrapping with Wire and Strand
- Circular Concrete Structures Prestressed with Circumferential Tendons
- Concrete Properties
- Demolition
- Deterioration of Concrete in Hydraulic Structures
- Electronic Data Exchange
- Insulating Concrete Forms, Design, and Construction
- Nuclear Reactors, Concrete Components
- Pedestal Water Towers
- Pipe, Cast-in-Place
- Strengthening of Concrete Members
- Sustainability

Then become a REVIEWER for the *ACI Structural Journal* or the *ACI Materials Journal*.

Become a Reviewer for the ACI Journals

How to become a Reviewer:

1. Go to: **http://mc.manuscriptcentral.com/aci**;
2. Click on "Create Account" in the upper right-hand corner; and
3. Enter your E-mail/Name, Address, User ID and Password, and Area(s) of Expertise.

Update your Manuscript Central user account information

Did you know that the database for MANUSCRIPT CENTRAL, our manuscript submission program, is separate from the ACI membership database?

How to update your user account:

1. Go to **http://mc.manuscriptcentral.com/aci**;
2. Log in with your current User ID & Password; and
3. Update your E-mail/Name, Address, User ID and Password, and Area(s) of Expertise.

QUESTIONS?

E-mail any questions to Journals.Manuscripts@concrete.org.

American Concrete Institute

Always advancing

ACI STRUCTURAL JOURNAL TECHNICAL PAPER

Title No. 120-S88

Deflection Control Methodologies for Curvilinear Concrete Members Reinforced with Glass Fiber-Reinforced Polymer Bars

by Seyed Mohammad Hosseini, Salaheldin Mousa, Hamdy M. Mohamed, and Brahim Benmokrane

This paper reports the results of a comprehensive analytical study implemented to develop deflection prediction methodologies for curvilinear reinforced concrete (RC) members with glass fiber-reinforced polymer (GFRP) reinforcement, focusing on precast concrete tunnel lining (PCTL) segments. The first step involved modifying the procedures for estimating elastic deflection, cracking moment, and cracked moment of inertia, which were then introduced for use with curvilinear members. In the next step, three methodologies of effective moment of inertia, integration of curvature, and integration of curvature considering tension stiffening were developed for curvilinear members. Then, the analytical results were compared to the experimental database, and a novel method was developed for predicting deflection in curvilinear GFRP-RC members. In the third and final step, a procedure was developed to adapt the presented methodologies for use with a tunnel segment under real load and boundary conditions. The results indicate that the proposed method could predict the deflection of curvilinear GFRP-RC members with high accuracy.

Keywords: curvilinear reinforced concrete (RC) members; deflection; effective moment of inertia; glass fiber-reinforced polymer (GFRP); precast concrete tunnel lining (PCTL) segments; reinforced concrete (RC).

INTRODUCTION

Curvilinear reinforced concrete (RC) elements are widely used in many types of structures, such as tunnels, bridges, water tanks, and culverts.[1] Precast concrete tunnel lining (PCTL) segments number among the most frequently used curvilinear RC elements. When a tunnel is bored with a tunnel boring machine (TBM), such segments are placed sequentially as the boring advances.[2] Corrosion is one of the major problems associated with RC structures reinforced with conventional steel reinforcement. Such issues are exacerbated in the corrosive environment of tunnels.[3,4] Replacing steel reinforcement with glass fiber-reinforced polymer (GFRP) reinforcement is recognized as a viable solution for dealing with corrosion issues.[5] Serviceability often governs the design of flexural members reinforced with GFRP bars either through cracking, deflection, or stress verification.[6] In general, curvature, loading distribution, span length, and boundary conditions do not play a considerable role in cracking control and stress verification procedures as they are mainly related to sectional properties. These issues must be considered in predicting deflection. Due to commercial GFRP bars having lower moduli of elasticity than steel reinforcing bars, deflection in GFRP-RC flexural members at service load is generally greater than in steel-RC members.[7] Therefore, employing effective methodologies to predict the deflection of GFRP-RC members with high accuracy is of great importance.

Two common approaches can be employed to calculate the immediate deflection of flexural RC elements: 1) using the general assumptions of elastic deflection calculation along with the effective moment of inertia (I_e); and 2) integration of curvature along the length of the member. I_e considers the effective transition between the gross moment of inertia (I_g) in uncracked regions of a member to the cracked moment of inertia (I_{cr}) in the cracked part considering the effect of tension stiffening. Branson[8] originally assumed the rigidities of the cracked and uncracked parts of a RC element as springs in parallel. His assumption can be written in the form of Eq. (1) as a general model to predict I_e in RC members

$$I_e = k_1 I_g + k_2 I_{cr} \leq I_g \tag{1}$$

where k_1 and k_2 are functions of the ratio of cracking to applied moment (M_{cr}/M_a), which has been empirically proposed. Equation (1), based on Branson's recommendations, can predict the deflection of simply supported straight rectangular concrete beams reinforced with typical amounts of steel reinforcement with reasonable accuracy. Such models, however, underestimate the deflection of FRP-RC elements, as it was correlated for beams with I_g/I_{cr} smaller than approximately 4.0, while I_g/I_{cr} in FRP-RC members generally ranges between 5 and 25.[9] Besides, supposing parallel springs for the rigidities of uncracked and cracked sections in Eq. (1) is an incorrect assumption because they are series springs.[10,11] By neglecting such wrong assumptions, various researchers tried to modify the values of k_1 and k_2 based on the experimental results of FRP-RC beams.[12-21] Bischoff[9] developed a new form of equation (Eq. (2)) for I_e based on the true assumption of series springs for the cracked and uncracked rigidities in a flexural member

ACI Structural Journal, V. 120, No. 5, September 2023.

MS No. S-2022-397.R1, doi: 10.14359/51738842, received May 1, 2023, and reviewed under Institute publication policies.

$$I_e = \frac{I_{cr}}{1 - \eta\beta(M_{cr}/M_a)} \leq I_g \quad (2)$$

where $\eta = 1 - I_{cr}/I_g$; and β is the tension-stiffening factor, varying between 0 and 1 for the case of no tension stiffening and full tension stiffening, respectively, suggested to be taken as M_{cr}/M_a. Employing Eq. (2) yielded reasonably conservative estimations for deflection of simply supported FRP-RC members.

Integration of curvature along the member is another approach to general deflection calculation proposed in the literature by various researchers and in standards.[22-25] The general concept of this method is to obtain curvature in each section and integrate it along the length of the member. Curvature in uncracked and cracked parts is calculated using the gross and cracked moment of inertia, respectively, neglecting the effect of tension stiffening. The effect of tension stiffening can be considered by obtaining the curvature of the cracked part with the effective moment of inertia in each section[22] or by linear interpolation of the section curvature.[24] Bischoff and Gross[22] employed an approach integrating curvature, assuming the gross moment of inertia in the uncracked regions and the effective moment of inertia derived from Eq. (2) for the cracked regions. They proposed the following equation as the equivalent moment of inertia by simplifying the integrals based on different load and boundary conditions

$$I_e = \frac{I_{cr}}{1 - \gamma\eta(M_{cr}/M_a)^2} \leq I_g \quad (3)$$

where γ is a factor considering the effect of load and boundary conditions. Equation (3) seems to be the most theoretically correct method in the literature; it has also been adopted by ACI 440.1R-15.[6] In general, neglecting tension stiffening led to deflection being overestimated, while considering it equal to what was proposed by Bischoff and Gross[22] underestimated deflection. The accuracy, however, depends on the reinforcement's axial stiffness, estimated cracking moment, estimated concrete modulus of elasticity, moment level on which deflecting is calculated, load and boundary conditions, and so on.[9,10,22,26]

The deflection prediction methodologies in the literature for FRP-RC members generally deal with straight members without axial load. In addition, there are no recommendations for adapting the available methodologies for complex load and boundary conditions in real applications. This paper presents an analytical study performed to propose deflection prediction methodologies to estimate the deflection of curvilinear GFRP-RC members under service load conditions. The focus of this study was to adapt the methodologies for PCTL segments. The methodologies, however, are general and can be used for any type of curvilinear member.

RESEARCH SIGNIFICANCE

Predicting the deflection of GFRP-RC curvilinear members at the service load stage is crucial for their design. However, the current deflection prediction methodologies, as proposed by ACI 440.1R-15[6] and CSA S806-12,[23] only account for serviceability control in straight GFRP-RC members. Moreover, there is a lack of methodologies available in the literature for predicting the deflection of curvilinear GFRP-RC elements. This study fills this gap and presents novel deflection prediction methodologies specifically developed for curvilinear GFRP-RC elements, with a particular focus on PCTL segments. The proposed methodologies were validated through testing 11 full-scale GFRP-reinforced PCTL segments. The findings of this study will significantly benefit design engineers and contribute to improving design standards. Notably, this study introduces novel equations and procedures that cannot be found elsewhere in the literature.

SUMMARY OF EXPERIMENTAL PROGRAM

Eleven full-scale curvilinear GFRP-reinforced PCTL segments were constructed and tested under bending load. An overview of the specimens' details, reinforcement characteristics, test setup, and instrumentation is reported in the following. Detailed information can be found in papers previously published by the authors.[27,28] The specimens had internal and external radii of 3250 and 3500 mm, respectively, and measured 3100 mm in length, 1500 mm in width, and 250 mm in thickness (Fig. 1). The test parameters include reinforcement ratio (0.48, 0.69, 0.90, and 1.28%), concrete type (normal-strength concrete [NSC] and fiber-reinforced concrete [FRC]), concrete strength (NSC and high-strength concrete [HSC]), and tie configuration (closed ties and U-shaped ties). The reinforcement ratio of 0.48% was chosen to ensure that the specimen exhibits a favorable compression-controlled failure, as per the requirements outlined in the provisions of ACI 440.1R-15[6] and CSA S806-12.[23] Subsequently, higher reinforcement ratios (0.69, 0.90, and 1.28%) were employed to accommodate larger bar sizes and closer bar spacing while still considering construction feasibility. Sand-coated No. 5 and No. 6 GFRP bars were used as longitudinal reinforcement and end-anchorage U-shaped bars. The transverse ties were sand-coated No. 4 GFRP bars, either U-shaped or closed ties. It should be noted that the tie configuration is a critical parameter that significantly impacts the construction process of GFRP cages in GFRP-RC curvilinear members such as tunnel segments. Therefore, it is imperative to compare the serviceability behavior of specimens reinforced with two common types of transverse ties—namely, closed ties and U-shaped ties. Tables 1 and 2 report the properties of reinforcement and concrete, respectively. The specimens were tested under three-point bending load until failure (Fig. 1). The selected test setup provides a determined system for establishing the relationship between internal forces, external loads, and deflection required for analytical procedures. This allows for reliable evaluation of deflection-calculation procedures and the development of general prediction models for any load or boundary condition. Three linear potentiometers (LPOTs) recorded midspan deflection; the quarterspan deflection was recorded with two LPOTs installed at the quarterspan. Table 2 presents the test matrix and the key experimental results for the tested specimens. To investigate the deflection behavior at the service stage and compare the experimental results

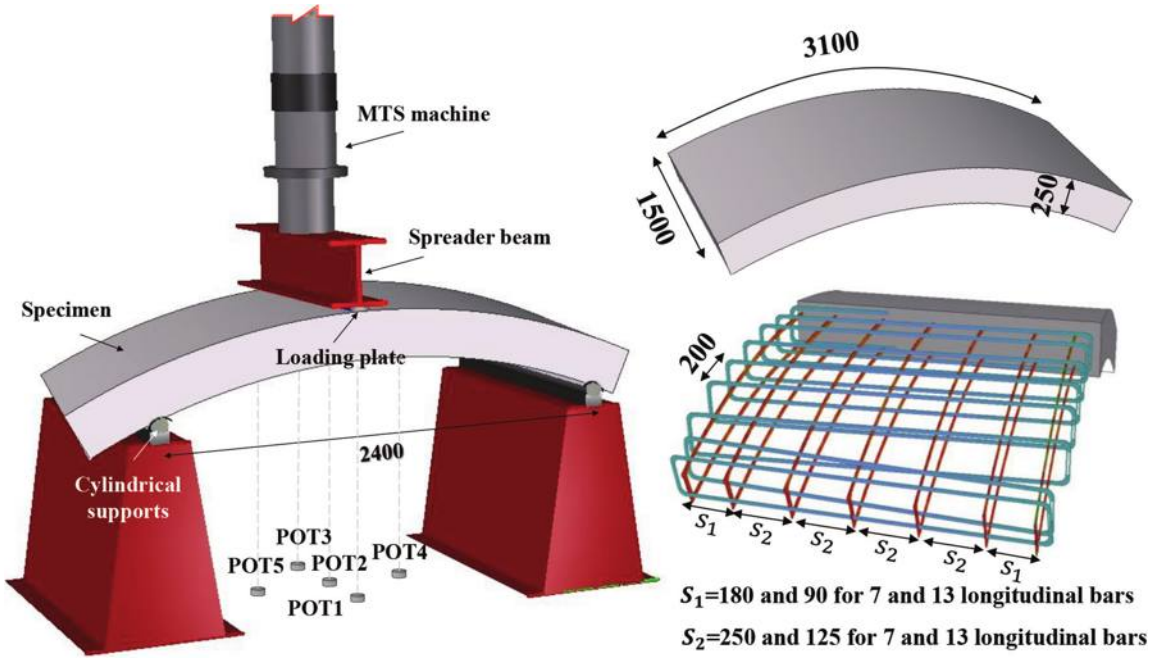

Fig. 1—Specimen geometry, reinforcement details, test setup, and instrumentations. (Note: Dimensions in mm; 1 mm = 0.0394 in.)

Table 1—Mechanical properties of GFRP reinforcement

Reinforcement type	Bar size	Bar diameter, mm	Nominal cross-sectional area, mm^2	Tensile modulus of elasticity, GPa	Ultimate strength, MPa	Ultimate strain, %
Curvilinear longitudinal GFRP bars	No. 5	15.0	199	55.1 ± 1.25	1115 ± 60	2.0 ± 0.1
	No. 6	20.0	284	52.9 ± 0.6	1068 ± 49	2.0 ± 0.1
U-shaped GFRP bars*	No. 5	15.0	199	53.5 ± 1.1	1283 ± 42	2.4 ± 0.1
	No. 6	20.0	284	53.2 ± 2.9	1131 ± 35	2.1 ± 0.0
U-shaped and closed GFRP ties*	No. 4	3.0	129	55.6 ± 1.6	1248 ± 74	2.2 ± 0.1

*Reported values are based on applying tension to straight bars manufactured with same process as bent bars.

Note: 1 mm = 0.0394 in.; 1 mm^2 = 0.00155 in.^{2}; 1 GPa = 145 ksi; 1 MPa = 145 psi.

Table 2—Test matrix and test results

Specimen ID	Concrete type	Longitudinal reinforcement	Tie configuration	f_c', MPa	f_p, MPa	f_{150}^D, MPa	M_{cr}, kN·m	M_n, kN·m	Deflection at service moment, mm		
									$0.3M_p$	2000 με	$1.1M_{cr}$
7G No. 5	NC	7 No. 5 bars	Closed ties	48	—	—	38	213	11.7	2.5	3.0
7G No. 6	NC	7 No. 6 bars	Closed ties	54	—	—	42	243	9.2	3.5	2.6
13G No. 5	NC	13 No. 5 bars	Closed ties	51	—	—	42	243	6.2	5.2	1.8
13G No. 6	NC	13 No. 6 bars	Closed ties	47	—	—	42	273	6.9	6.0	1.5
7G No. 5U	NC	7 No. 5 bars	U-shaped ties	44	—	—	37	177	9.5	2.6	3.3
7G No. 5H	HSC	7 No. 5 bars	Closed ties	86	—	—	49	247	10.4	2.7	3.4
13G No. 5H	HSC	13 No. 5 bars	Closed ties	90	—	—	44	257	6.5	3.7	1.9
7G No. 5HU	HSC	7 No. 5 bars	U-shaped ties	87	—	—	41	227	9.8	2.1	2.9
7G No. 5F	FRC*	7 No. 5 bars	Closed ties	50	4.5	0.8	33	210	9.8	2.5	2.5
13G No. 5F	FRC	13 No. 5 bars	Closed ties	44	4.0	1.3	30	273	8.2	3.8	1.9
7G No. 5FU	FRC	7 No. 5 bars	U-shaped ties	46	4.3	1.0	31	230	9.6	3.1	1.9

*Polypropylene fibers, 12 mm in length, were used to fabricate FRC.

Note: 1 mm = 0.0394 in.; 1 kN·m = 0.7376 kip·ft; 1 MPa = 145 psi.

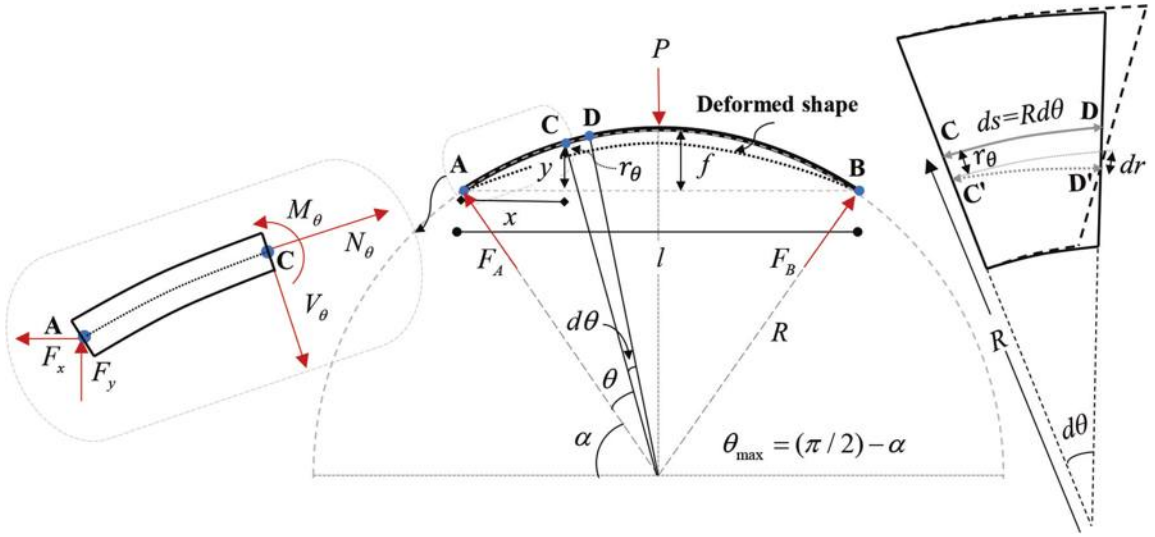

Fig. 2—Geometrical parameters, deformation parameters, external loads, and internal forces in curvilinear member with load and boundary conditions similar to test specimens (deformations and curvatures are exaggerated).

with the analytical procedure, some reference points must be specified. As the design of GFRP-RC flexural elements is generally governed based on serviceability requirements, the bending moment under service load conditions is typically much lower than their nominal bending moment capacity. In the following, two reference points for service load conditions of GFRP-reinforced flexural elements were defined according to the literature[26,29]: 1) moment corresponding to 30% of the peak moment; and 2) moment corresponding to a strain of 2000 με in the tensile reinforcement. The latter sometimes leads to defining a service moment that is lower than the cracking moment. This might lead to unrealistic predictions for deflection at the service load. Therefore, a moment corresponding to 1.1 times the cracking moment was introduced as an alternative to the moment corresponding to a strain of 2000 με when the obtained service moment is smaller than the cracking moment. Mota et al.[7] applied the same approach.

ANALYTICAL INVESTIGATIONS

This section presents the deflection prediction methodologies developed for use with GFRP-reinforced curvilinear members. Initially, two methods were proposed to calculate elastic deflection in curvilinear structural elements. The cracking moment to be used in calculating deflection is discussed and proposed. After that, the procedures and models developed to obtain the cracked moment of inertia in GFRP-reinforced NSC, HSC, and FRC PCTL segments are described. Subsequently, three procedures for calculating deflection are presented and adapted for use in curvilinear RC members. Thereafter, the results obtained from the presented procedures are compared with the experimental results. Subsequently, a model capable of predicting deflection in curvilinear GFRP-RC members with high accuracy is proposed. Lastly, a procedure was developed to employ the deflection prediction methodologies presented for tunnel segments under actual loading and boundary conditions. While the methodologies presented focus mainly on tunnel segments, they can also be used effectively to estimate the service load deflection of different types of curvilinear GFRP-RC members.

Calculating elastic deflection in curvilinear members

When the ratio of radius to the sectional height in a curved member is greater than 2, the fundamental concepts related to the relationship between curvature and deflection, as well as the strain energy due to the bending, can be approximated by that of straight members.[30] As follows, the two methods commonly used to calculate elastic deflection in straight members were modified for use with curvilinear members.

Figure 2 shows the centerline of a curvilinear member before and after deformation induced by an external force. The radial deflection at each point is r_θ. Consider a small element of CD with arc length *ds*. The exaggerated shape shows that the centerline of the segment is specified as CD and C′D′ after deformation. Radial deformation at the point C is r_θ, while such deformation is $r_\theta + dr$ at point D. Therefore, the relationship between the radial deflection and curvature in the element is

$$\frac{d^2 r}{ds^2} = -\phi_\theta = \frac{M_\theta}{E_\theta I_\theta} \tag{4}$$

Obtaining the previous equation assumed small deformations. Moreover, the influence of curvilinearity on the fundamental assumptions of the distribution of internal stresses and the curvature of the cross section was not considered. This is attributed to the high ratio of curvature to thickness within the considered curvilinear members. In such scenarios, the impact of curvilinearity on stress distribution and the moment-curvature correlation in the cross section is considered insignificant, as supported by Boresi et al.[30] Considering $ds = Rd\theta$, rotation can be obtained with the following equation

$$\Theta_\theta = \int -\phi_\theta R d\theta + C_1 \tag{5}$$

where C_1 can be obtained according to the boundary conditions. Using a similar approach, radial deflection in each section can be obtained as follows

$$r_\theta = \int\left(\int -\phi_\theta ds + C_1\right)Rd\theta + C_2 \quad (6)$$

To obtain the vertical deflection, *dr*, each point should be multiplied by sin(θ) in the integral. Therefore, the following equation is obtained to calculate the vertical deflection in a polar coordinate system in a curvilinear member

$$\Delta_\theta = \int\left(\int -\phi_\theta Rd\theta + C_1\right)R\sin(\theta)d\theta + C_2 \quad (7)$$

where C_2 can be obtained using boundary conditions. When it is aimed to calculate the deflection at a certain location, deflection can be obtained using a virtual work method with this equation

$$\Delta = \sum\int\frac{m_\theta M_\theta}{E_\theta I_\theta}Rd\theta \quad (8)$$

where m_θ is the moment induced because of a unit dummy load applied at the point where deflection is being calculated. It should be noted that the deflections resulting from shear and axial forces are neglected as they are generally insignificant when the span length-to-depth ratio is large.[30] According to the presented methods, an equation for calculating the elastic deflection of the test specimens was developed, as reported in Appendix A.*

Cracking moment

Cracking moment (M_{cr}) is one of the most influential parameters in estimating the deflection in an RC member. Therefore, predicting the exact cracking moment is of great importance in accurately estimating deflection. Equalizing the maximum tensile stress in the uncracked section to the maximum tensile capacity of concrete ($0.62\sqrt{f_c'}$ according to ACI 318-19[31]) yields the theoretical cracking moment ($M_{cr,theo}$). Shrink restraint in an RC member might lead to pre-existing tensile stresses in the member, which reduce the cracking moment.[32] Bischoff and Gross[22] reported a range of 0.48 to 1.44 with a median of 0.85 for the ratio of theoretical to experimental cracking moment based on the extensive data from the literature for FRP-RC flexural members. ACI 318-19[31] recommends multiplying the theoretical cracking moment by 0.67 in the deflection-calculation procedure. The ratio of theoretical to experimental cracking moment in the tested specimens was 0.7 ± 0.02, 0.58 ± 0.04, and 0.61 ± 0.02 for NSC, HSC, and FRC specimens, respectively. There is a need for an extensive study to determine the value of cracking moment in different concrete types for FRP-RC members. Given the lack of such study, the author's study recommends taking M_{cr} equal to $0.7M_{cr,theo}$ for NSC GFRP-reinforced tunnel segments and $0.6M_{cr,theo}$ for HSC and FRC GFRP-reinforced tunnel segments according to the experimental results. However, considering the various factors that can influence the cracking moment value in different conditions, it is reasonable to use more conservative values for the cracking moment in practical design applications.

Cracked moment of inertia

Calculating the cracked moment of inertia is essential in all the deflection-calculation methods presented. In the following, the procedures to calculate the cracked moment of inertia for GFRP-reinforced NSC, HSC, and FRC tunnel segments were presented. The contribution of reinforcing top bars is neglected in the presented procedures as a simplifying and conservative assumption.

GFRP-reinforced NSC and HSC curvilinear members—When there is no axial load, the cracked moment of inertia does not depend on the applied bending moment on a section in which a linear stress-strain relationship is considered for concrete in compression. When axial load is present, both the axial load and bending moment in the section affect the cracked moment of inertia. The cracked moment of inertia in such conditions can be calculated with the following equation when the contribution of the top reinforcement is neglected.

$$I_{cr} = (bd^3/3)k_a^3 + n_f A_f d^2(1 - k_a)^2 \quad (9)$$

where Eq. (10) can be used to calculate k_a

$$k_a = \frac{\sqrt{N^2 - 2N\omega n\rho_f + \omega^2 n\rho_f(n\rho_f + 2)} - n\rho_f\omega + N}{\omega} \quad (10)$$

where $\omega = E_c\varepsilon_c bd$. As can be inferred from Eq. (10), the uncracked depth depends on the level of axial load and the maximum concrete compressive strain. Equation (11) presents the relationship between the bending moment, axial load, k_a, and ε_c in a section.

$$M_a = n\rho_f\omega d(1 - k_a)\left(\frac{3 - k_a}{9}\right) + N\left(\frac{h}{2} - \frac{k_a d}{3}\right) \quad (11)$$

Inserting k_a from Eq. (10) into (11) yields an equation with ε_c as its unknown variable. Due to complexity, however, there is no closed-form solution for that equation. In such situations, the value of ε_c can be found by trial and adjustment. Subsequently, the values of k_a and I_{cr} can be calculated. The presented equations are based on the linear concrete stress-strain assumption in compression, which is valid until approximately $0.7f_c'$.[33] According to a preliminary comparison conducted by the authors for the tested specimens, neglecting the effect of axial load led to an error of approximately 10% in the value of k_a for a given value of M_a when the axial load was below $\pm 0.0045f_c'A_g$. When the axial load was increased, neglecting such contributions led to considerable errors.

Curvilinear GFRP-reinforced FRC members—Finding the cracked moment of inertia in an FRC section considering the contribution of fibers requires assuming a stress-strain model for FRC in compression and tension. The authentic

*The Appendix is available at **www.concrete.org/publications** in PDF format, appended to the online version of the published paper. It is also available in hard copy from ACI headquarters for a fee equal to the cost of reproduction plus handling at the time of the request.

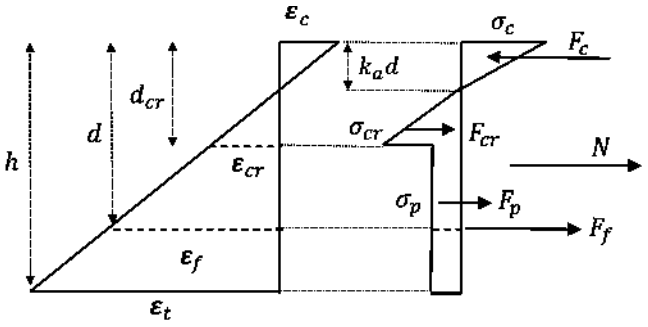

Fig. 3—Assumed model for distribution of stress and strain in cross section of FRC specimens.

stress-strain properties of FRC under compression and tension can be accurately determined through the corresponding tests and used in the analysis. Nevertheless, in the design of FRC components, simple models are commonly used.[34] Figure 3 presents the assumed stress and strain distribution in the section based on the stress-strain model for FRC. This model was adopted and simplified for the service stage based on the provisions in ACI 544.4R-18.[34] The parameters used in the stress-strain response of FRC can be obtained with beam testing as well as stress and strain compatibility. σ_{cr} and σ_p can be taken equal to f_p and $0.37f^D_{150}$, respectively.[2,34,35] Equations (12) and (13) form a system of equations with two unknown variables—ε_c and k_a—which can be obtained through trial and adjustment.

$$F_f + F_{cr} + F_p + N - F_c = 0 \tag{12}$$

$$M_a = F_f d + F_{cr}\left(\frac{k_a d + 2d_{cr}}{3}\right) + F_p\left(\frac{d_{cr} + h}{2}\right) + N\left(\frac{h}{2}\right) - F_c\left(\frac{k_a d}{3}\right) \tag{13}$$

After obtaining ε_c and k_a, the cracked moment of inertia considering the contribution of fibers can be calculated with the following equation

$$I_{cr} = \frac{M_a k_a d}{E_c \varepsilon_c} \tag{14}$$

Deflection prediction using effective moment of inertia

The effective moment of inertia proposed by Bischoff[9] (Eq. (2)) can be replaced with the value of I_θ in the methods presented to calculate deflection when the relationship between the applied loads and internal forces can be specified. This method is referred to herein as I_e. This procedure does not consider the effect of load and boundary conditions or variations in the axial load in the member. It does consider the effect of tension stiffening by using the tension-stiffening factor β. This factor theoretically varies between 0 and 1 depending on the level of bending moment. Bischoff[9] recommended using M_{cr}/M_a as the tension-stiffening factor. As this method supposes a constant effective moment of inertia along the member, it is simple to use, but its accuracy depends on the types of loading, boundary conditions, reinforcement ratio, and level of bending moment. The best accuracy is expected for simply supported beams with point load or distributed load.[22] In addition, the axial-load level and its variation along the member might greatly affect accuracy. In the case of FRC, the contribution of the fibers can be considered using the effect of fibers on the cracked moment of inertia as well as their effect on the tension-stiffening behavior of the concrete. Bischoff[36] proposed modifications to Eq. (2) to consider the contribution of fibers for both cracking moment of inertia and tension stiffening. This study relies only on the effect of fibers on the cracked moment of inertia to consider the contribution of fibers in the calculation of GFRP-reinforced FRC PCTL segments because considering the effect of FRC on the tension stiffening leads to impractical and complex procedures.

Deflection prediction using integration of curvature

For predicting deflection using integration of curvature, the cracked and uncracked parts of the member should be specified based on the bending-moment diagram. Thereafter, the deflection-calculation equations can be used by substituting I_θ with gross and cracked moment of inertia in the uncracked and cracked sections, respectively. This method is referred to as the Integ. method herein. Equation (15) can be used to calculate the deflection through integration of curvature in the virtual work method.

$$\Delta = \sum_{Uncracked} \int \frac{m_\theta M_\theta}{E_c I_g} R d\theta + \sum_{Cracked} \int \frac{m_\theta M_\theta}{E_c I_{cr,\theta}} R d\theta \tag{15}$$

Equation (15) could be simplified with this approach

$$\Delta = \Delta_g + \delta\Delta_{cr} \tag{16}$$

where Δ_g and $\delta\Delta_{cr}$ can be calculated with these equations (refer to Appendix B)

$$\Delta_g = \frac{1}{E_c I_g} \int m_\theta M_\theta R d\theta \tag{17}$$

$$\delta\Delta_{cr} = \sum_{i=1}^{n} \frac{\eta_i}{E_c} \int \frac{m_\theta M_\theta}{I_{cr,i}} R d\theta \tag{18}$$

These equations are valid for all types of loading and boundary conditions, provided that no settlement or movement has occurred in the supports and that the relationship between the applied load and internal forces can be determined. Because variations in the axial-load level changes the value of I_{cr}, using a constant value for I_{cr} might be a source of errors in the calculation procedure. To account for the effect of axial load on deflection calculation, the cracked sections along the member can be divided into a reasonable number of parts. The values of η_i and $I_{cr,i}$ for each part can be calculated by obtaining $\delta\Delta_{cr}$ and summing $\delta\Delta_{cr,i}$ along the cracked section. When the level of axial load and its variation along the member are not significant, however, the minimum value of I_{cr} along the member expected in a section with the greatest bending moment and the lowest axial load

can be used for all the cracked sections as a conservative simplification.

Simplifying the presented equations for load and boundary conditions similar to the tested specimens leads to the following equation to calculate the deflection at midspan (refer to Appendix B)

$$\Delta = \lambda / E_c I_{cr} \tag{19}$$

where λ is calculated using Eq. (20)

$$\lambda = 2(1-\eta)\left[\int_0^{\frac{\pi}{2}-\alpha} C_\theta R d\theta + \left(\frac{\eta}{1-\eta}\right)\int_{\theta_g}^{\frac{\pi}{2}-\alpha} C_\theta R d\theta\right] \tag{20}$$

where $C_\theta = m_{(\pi/2)-\alpha} M_\theta$. Equation (20) is valid for those types of load and boundary conditions where the distribution of bending moment is symmetrical, and the uncracked section starts at the supports of an angle θ_g, followed by a cracked section from θ_g to midspan. In addition, I_{cr} of the critical section (often located at midspan) was used as the cracked moment of inertia for all the cracked sections in Eq. (15), because the level of axial load was not significant. The angle θ_g corresponds to the angle from the support to the point at which $M_\theta = M_{cr}$. For the load and boundary conditions of the tested specimens, θ_g can be obtained with this equation

$$\theta_g = \sin^{-1}\left(\frac{\cot(\alpha)(2C_b - C_a) - \sqrt{(2PR)^2 + 4C_aC_b - (C_a)^2}}{2PR(\cot^2(\alpha)+1)}\right) - \alpha \tag{21}$$

where $C_a = 2Pf\cot(\alpha) + Pl - 4M_{cr}$; and $C_b = PR\cot(\alpha)$. It should be noted that M_{cr} is dependent on the level of axial load. When the variation in axial load is not significant, however, M_{cr} obtained from the minimum axial load along the member can be used as a conservative assumption for simplicity. For the tested specimens, the integrals in Eq. (20) were obtained and are reported in Appendix B.

Deflection prediction using integration of curvature considering tension stiffening

Due to the effect of tension stiffening, the stiffness in the cracked parts of an element is greater than the cracked moment of inertia.[22] By supposing $I_\theta = I_{cr,\theta}/[1 - \eta_\theta\beta_\theta(M_{cr,\theta}/M_\theta)]$ in the calculations related to the cracked parts of the section, the effect of tension stiffening can be considered. In such situations, deflection can be obtained with

$$\Delta = \sum_{Uncracked}\int \frac{m_\theta M_\theta}{E_c I_g} R d\theta + \sum_{Cracked}\int \frac{m_\theta M_\theta (1-\eta_\theta\beta_\theta(M_{cr,\theta}/M_\theta))}{E_c I_{cr,\theta}} R d\theta \tag{22}$$

This method is referred as Integ. TS herein when β is considered as M_{cr}/M_θ according to the recommendation of Bischoff and Gross.[22] To simplify Eq. (22), Eq. (16) can be used, employing the same equation as Eq. (17) for Δ_g. In this case, $\delta\Delta_{cr}$ should be calculated as

$$\delta\Delta_{cr} = \sum_{i=1}^{n}\frac{\eta_i}{I_{cr,i}E_c}\int m_\theta M_\theta(1-\eta_i\beta_i(M_{cr,i}/M_\theta))Rd\theta \tag{23}$$

Note that Eq. (23) requires greater computational effort than Eq. (18), especially when the effect of axial load is to be considered. For load and boundary conditions similar to those of the test specimens when the axial load and its variation are not significant, it yields

$$\Delta = \frac{2}{E_c I_{cr}}\left[(1-\eta)\int_0^{\frac{\pi}{2}-\alpha} m_\theta M_\theta R d\theta + \eta\int_{\theta_g}^{\frac{\pi}{2}-\alpha} m_\theta M_\theta(1-\beta(M_{cr}/M_\theta))Rd\theta\right] \tag{24}$$

Equation (19) can be used to calculate the midspan deflection once the value of λ has been determined with this equation (refer to Appendix B)

$$\lambda = 2(1-\eta)\left[\int_0^{\frac{\pi}{2}-\alpha} C_\theta R d\theta + \eta\int_{\theta_g}^{\frac{\pi}{2}-\alpha}(C_\theta - C_{\theta_g})Rd\theta\right] \tag{25}$$

where $C_{\theta_g} = (M_{cr})^2/P$.

Evaluation of presented methods with experimental data

Table 3 presents the ratio of the theoretical to the experimental midspan deflection of the tested specimens. In addition, Fig. 4 and 5 compare the experimental and analytical moment-deflection curves of the specimens. The moment-deflection curves were drawn up to 50% of the experimental bending-moment capacity of the specimens. Table 3 provides a comparison of the midspan deflection at the loads corresponding to the three reference points of 2000 με, $1.1M_{cr}$, and $0.3M_n$, when applicable. The deflection in FRC specimens was obtained according to two scenarios of considering or neglecting the contribution of the fibers. The average and standard deviation are presented separately for each concrete type. In this study, $3320\sqrt{f_c'} + 6900$ was used as the concrete modulus of elasticity according to ACI 363R-10.[37]

According to Table 3, applying the I_e and Integ. methods overestimated the deflection of NSC tunnel segment specimens by 20% and 50%, respectively, on average, for different reference points. In contrast, considering tension stiffening based on the Integ. TS method underestimated deflection by 33%, on average. In the HSC specimens, the overestimation yielded by the I_e and Integ. methods was 3% and 33%, respectively. In contrast, considering the tension stiffening with the Integ. TS method underestimated the deflection by 54%. Neglecting the contribution of the fibers in FRC tunnel segment specimens resulted in a significant overestimation of the deflection (42% for I_e and 81% for Integ. methods). Considering the contribution of the fibers by considering their effect on the cracked moment of inertia reduced the

Table 3—Comparison of experimental and analytical results

ID	Deflection-calculation method											
	I_e			Integ.			Integ. TS			Mod. model		
	$\Delta_{theo.}/\Delta_{exp.}$											
	2000 με	$1.1M_{cr}$	$0.3M_n$	2000 με	$1.1M_{cr}$	$0.3M_n$	2000 με	$1.1M_{cr}$	$0.3M_n$	2000 με	$1.1M_{cr}$	$0.3M_n$
NSC specimens												
7G No. 5	—	0.93	0.96	—	1.05	1.13	—	0.29	0.51	—	1.14	1.00
7G No. 6	1.02	0.91	1.13	1.38	1.23	1.37	0.35	0.32	0.66	0.98	0.91	1.07
13G No. 5	1.44	1.68	1.35	1.74	2.24	1.61	0.85	0.64	0.85	1.14	1.15	1.09
13G No. 6	1.17	1.53	1.13	1.39	2.00	1.33	0.81	0.63	0.82	0.91	0.80	0.91
7G No. 5U	—	0.84	0.80	—	1.15	1.04	—	0.27	0.35	—	1.10	0.90
Average	1.21	1.18	1.07	1.50	1.53	1.30	0.67	0.43	0.64	1.01	1.02	0.99
STD	0.21	0.39	0.21	0.21	0.55	0.22	0.28	0.19	0.21	0.12	0.16	0.09
HSC specimens												
7G No. 5H	—	0.63	1.10	—	0.86	1.40	—	0.20	0.53	—	1.01	0.98
13G No. 5H	1.15	1.00	1.23	1.51	1.34	1.50	0.48	0.36	0.73	0.94	1.05	1.01
7G No. 5HU	—	0.92	1.17	—	1.28	1.45	—	0.26	0.63	—	1.15	1.04
Average	1.15	0.85	1.17	1.51	1.16	1.45	0.48	0.27	0.63	0.94	1.07	1.01
STD	—	0.19	0.07	—	0.26	0.05	—	0.08	0.10	—	0.07	0.03
FRC specimens neglecting contribution of fibers												
7G No. 5F	1.09	1.09	1.25	1.50	1.50	1.51	0.33	0.33	0.76	1.34*	1.34	1.32
13G No. 5F	1.83	2.53	1.35	2.23	3.27	1.52	1.07	1.14	1.01	1.68	2.29	1.28
7G No. 5FU	1.32	1.04	1.32	1.78	1.43	1.55	0.47	0.34	0.89	1.57	1.41	1.40
Average	1.41	1.55	1.31	1.84	2.07	1.53	0.62	0.60	0.89	1.63	1.68	1.33
STD	0.38	0.85	0.05	0.37	1.04	0.02	0.39	0.46	0.13	0.08	0.53	0.06
FRC specimens considering contribution of fibers												
7G No. 5F	0.97	0.97	1.18	1.33	1.33	1.43	0.31	0.31	0.72	0.98	0.98	1.11
13G No. 5F	1.39	1.83	1.13	1.69	2.33	1.28	0.83	0.90	0.85	1.06	1.22	0.98
7G No. 5FU	0.90	0.66	1.06	1.27	0.97	1.27	0.37	0.30	0.72	1.00	0.92	1.06
Average	1.09	1.15	1.12	1.43	1.54	1.33	0.50	0.50	0.76	1.01	1.04	1.05
STD	0.27	0.61	0.06	0.23	0.70	0.09	0.28	0.34	0.08	0.04	0.16	0.07

*Values were obtained with same modification parameters as NSC.

Note: Integ. refers to integration-of-curvature method; Integ. TS refers to integration-of curvature method considering tension stiffening; STD refers to standard deviation.

overestimation of the I_e and Integ. methods by 12% and 43%, respectively. The Integ. TS method underestimated the deflection by 30% and 41%, respectively, on average, when neglecting or considering the contribution of the fibers.

Table 3 and Fig. 4 and 5 reveal that the accuracy of these deflection prediction methods depends on the reinforcement ratio and concrete type. For instance, I_e underestimated the deflection of 7G No. 5 by 5%, while it overestimated the deflection of 7G No. 6 and 13G No. 5 by 2% and 49%, respectively. Generally, Integ. TS significantly underestimated the midspan deflection, which was more pronounced at the lower reinforcement ratio. The approach to calculating deflection yielded relatively more reasonable results for FRC specimens (Fig. 5). In general, according to the average for all the specimens and reference points, the ratio of theoretical to experimental deflection was 1.11, 1.41, and 0.55 for the I_e, Integ., and Integ. TS methods, respectively, according to Table 3. Therefore, although using effective moment of inertia is simpler than the other methods, it yielded the most accurate results with acceptable conservativeness. As mentioned previously, however, the method's accuracy depends on the load and boundary conditions.[22]

Proposed model

The method based on integration of curvature considering the tension-stiffening factor equal to M_{cr}/M_θ seems to be theoretically correct. As reported in the preceding section, it considerably underestimated the midspan deflection. Underestimation with such methods is consistent with some studies in the literature.[22,38] The underestimation was greater at the reference points 2000 με and $1.1M_{cr}$, especially in the NSC specimens with lower reinforcement ratios. To help demonstrate the reason for such underestimation, Fig. 6 presents the theoretical midspan moment-curvature diagrams of 7G

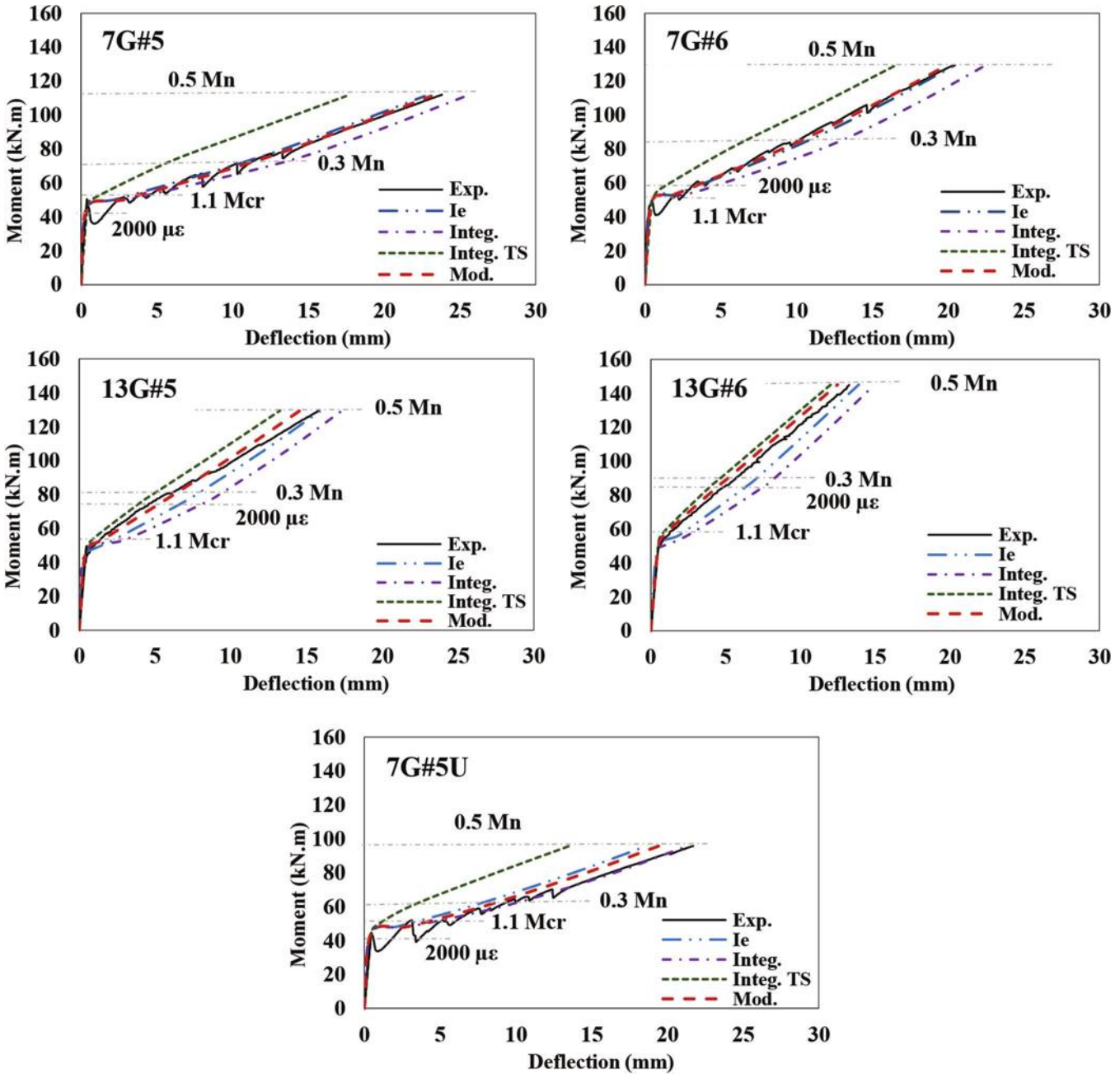

Fig. 4—Comparison of experimental and analytical moment-deflection diagrams of NSC specimens. (Note: 1 mm = 0.0394 in.; 1 kN·m = 0.7376 kip·ft.)

No. 5 and 13G No. 6 specimens obtained based on the I_e, Integ., and Integ. TS methods. In addition, the experimental moment-curvature diagram was drawn for comparison using the strain values recorded during the test. The I_e and Integ. TS methods yielded similar curvatures in a section because they use the same equation for the moment of inertia in a section. Figure 6 shows that the curvature of specimen 7G No. 5 increased rapidly after initiation of the first crack and thereafter approached the curvature obtained from the cracked moment of inertia by increasing the applied bending moment. In contrast, considering tension stiffening by setting the tension-stiffening factor equal to M_{cr}/M_θ did not follow the experimental trend. In that case, the initial increase of curvature upon cracking was not considered and the tension-stiffening factor was overestimated. Increasing the reinforcement ratio in 13G No. 6 eliminated the initial curvature increase, and the tension-stiffening factor was predicted with good accuracy. Comparing the moment-curvature diagrams of all tested specimens revealed that the rapid increase in the curvature at cracking and the accuracy of M_{cr}/M_θ as the tension-stiffening factor depended primarily on the reinforcement ratio, concrete strength, and concrete type. This study developed the following equations to modify the values of η and β for use in the presented method based on Integ. TS

$$\beta_m = m\left(\frac{f_c'\rho_f}{f_{c,n}'\rho_{fb}}\right)^p\left(\frac{M_{cr}}{M_\theta}\right) \text{ where } m\left(\frac{f_c'\rho_f}{f_{c,n}'\rho_{fb}}\right)^p \leq 1.0 \qquad (26)$$

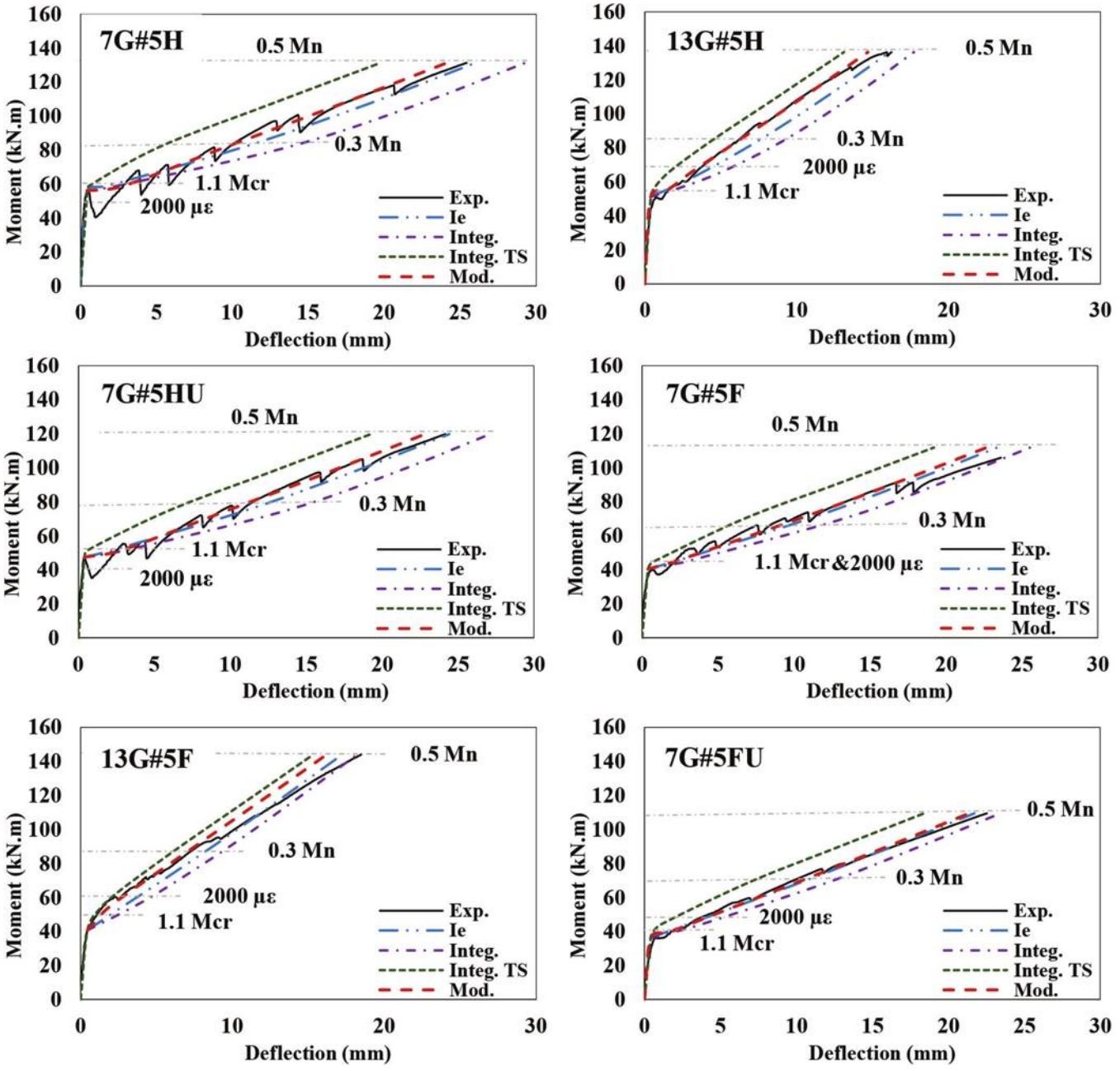

Fig. 5—Comparison of experimental and analytical moment-deflection diagrams of HSC and FRC specimens. (Note: 1 mm = 0.0394 in.; 1 kN·m = 0.7376 kip·ft.)

$$\eta_n = 1 - n\left(\frac{f_{c,n}'\rho_{fb}}{f_c'\rho_f}\right)^q\left(\frac{I_{cr}}{I_g}\right) \text{ where } n\left(\frac{f_{c,n}'\rho_{fb}}{f_c'\rho_f}\right)^q \geq 1.0 \quad (27)$$

where $f_{c,n}'$ is 80 MPa (11.6 ksi) for HSC and 40 MPa (5.8 ksi) for NSC and FRC. The modification constants m, n, p, and q were obtained using regression analysis according to the results for different types of concrete and are reported in Table 4. The effect of the reinforcement ratio on the tension-stiffening characteristic was considered using the ratio of ρ_f to ρ_{fb}. Yost et al.[20] and Mousavi and Esfahani[17] used a similar approach to consider the effect of the reinforcement ratio on the deflection of GFRP-RC beams. In addition, the ratio of $f_{c,n}'/f_c'$ was added to the proposed model to consider the effect of variations in concrete strength in the specimens. Furthermore, as the difference was minimal between the stiffness behavior of the specimens reinforced with closed ties and U-shaped ties, identical constants were proposed for both tie configurations. The modified deflection values can be obtained by replacing the values of η and β in the equations presented to calculate the deflection considering the tension-stiffening factor. Equation (28) presents the modified value of curvature in each section in the proposed modified model.

Table 4—Proposed coefficients to be used in proposed model

Concrete type	m	n	p	q
NSC	0.14	4.0	1.12	1.0
HSC	0.65	5.0	0.26	0.8
FRC	0.30	7.7	0.70	2.3

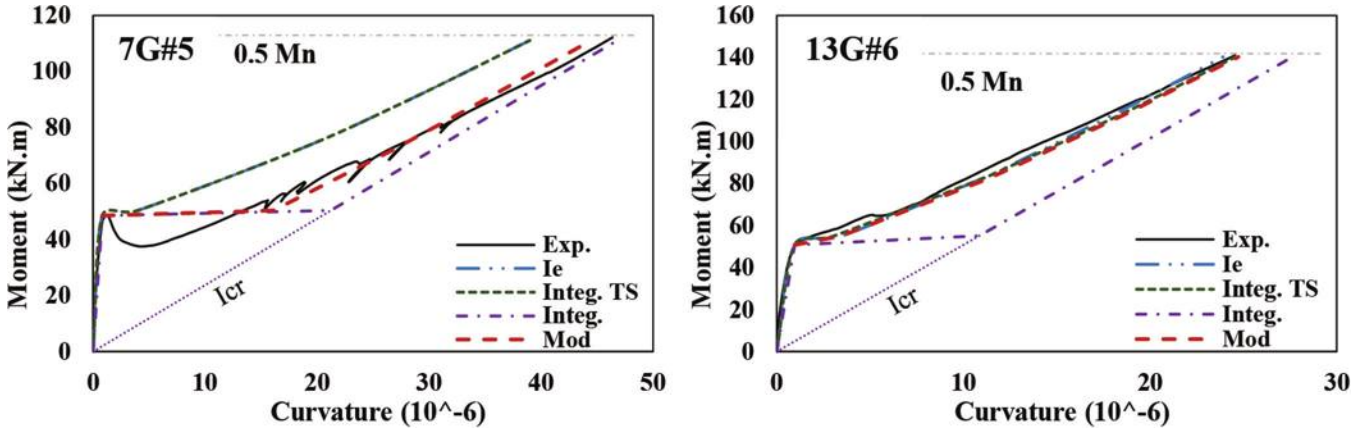

Fig. 6—Comparison of experimental and analytical moment-curvature diagrams for specimens 7G No. 5 and 13G No. 6. (Note: 1 mm = 0.0394 in.; 1 kN·m = 0.7376 kip·ft.)

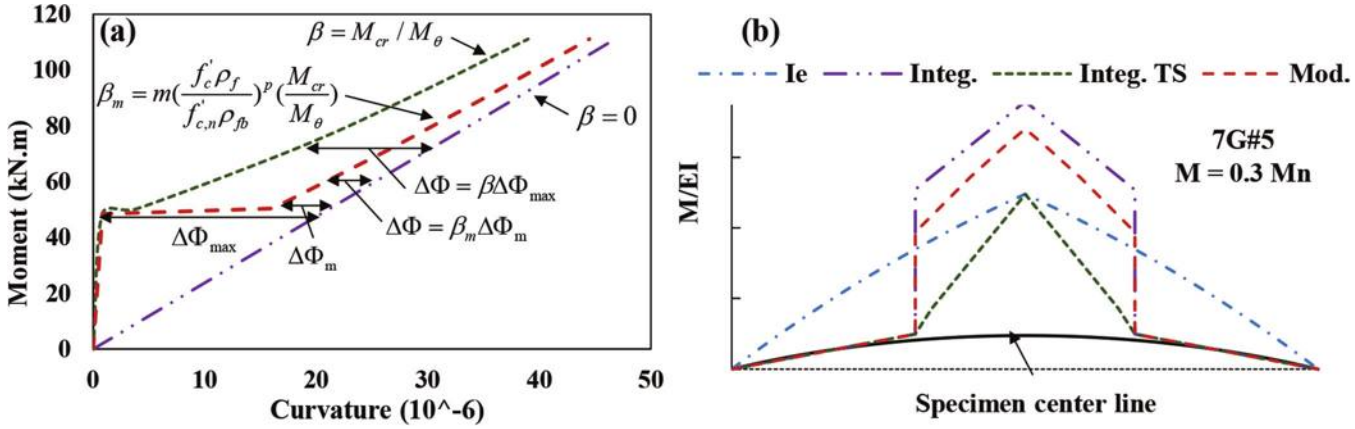

Fig. 7—Comparison of curvature response of different deflection-calculation methods: (a) moment-curvature response; and (b) curvature along specimen. (Note: 1 mm = 0.0394 in.; 1 kN·m = 0.7376 kip·ft.)

$$\phi_\theta = \frac{M_\theta}{E_c I_{cr}}\left(1 - \eta_n \beta_m \frac{M_{cr}}{M_\theta}\right) \quad (28)$$

Appendix C describes the procedure used to obtain the modified equations. Figure 7(a) shows the main concepts of the assumed moment-curvature response in the modified (referred to as Mod. herein) and Integ. TS methods (the graphs are for specimen 7G No. 5). Tension stiffening at a certain bending moment refers to a change in curvature ($\Delta\Phi$) relative to the curvature of the cracked member obtained using I_{cr}. $\Delta\Phi_{max}$ is the maximum possible tension stiffening at cracking. This is the tension-stiffening value considered in Integ. TS right after the formation of the first crack. This can be the main reason for the significant underestimation of the integration-of-curvature method considering tension stiffening in calculating deflection for the bending moments near the cracking load. An indirect method was used to consider the curvature increase when the first crack appeared by modifying the value of η by η_n (refer to Appendix C). By using η_n, the maximum change in curvature will be limited to $\Delta\Phi_m$. Increasing the bending moment decreases the tension-stiffening effect. The ratio of change in curvature at a certain bending moment ($\Delta\Phi$) to the maximum change in curvature at cracking is known as the tension-stiffening factor. Because using M_{cr}/M_θ overestimated the tension-stiffening effect, the modified tension-stiffening factor β_m is proposed, which reduces the value of M_{cr}/M_θ according to the reinforcement ratio, concrete strength, and the modification factors. Figure 7(b) presents the curvature value along the tunnel segment specimen obtained using the I_e, Integ., Integ. TS, and Mod. methods (note that the specimens' centerline was selected as the x-axis for a better view). As can be seen, the methods based on the integration of curvature yielded minimal curvature in the uncracked sections. In the cracked sections, using I_{cr} in the Integ. method eventually increased the curvature right after passing θ_g; the curvature increased linearly up to the midspan. In contrast, using the effective moment of inertia according to Eq. (2) led to a gradual increase in curvature. In the Mod. method, an increase in curvature after passing from the uncracked region is considered, and the curvature is modeled to gradually increase up to midspan.

Figure 6 presents a comparison of the moment-curvature obtained using the proposed equations and the experimental results for 7G No. 5 and 13G No. 6. As can be seen, the modified model fitted well with the experimental moment-curvature of the sections. The moment-deflection relationships obtained with the modified model for different specimens appear in Fig. 4 and 5. As shown, the modified model was quite consistent with the experimental results for all the specimens. In addition, Table 3 gives the

ratio of theoretical to experimental midspan deflection for the modified model. Considering an average for different reference points, the developed modified model predicted the midspan deflection with conservativeness of 1%, 2%, and 3% in the NSC, HSC, and FRC tunnel segment specimens, respectively. Therefore, the modified model accurately predicted the midspan deflection for the tested specimen with acceptable conservativeness of 2% on average.

DISCUSSION

As mentioned, the coefficients presented for the modified model were obtained based on the experimental data. As the number of specimens was limited, the accuracy of the coefficients needs to be further verified with an extensive database. In particular, the coefficients for the FRC specimens are valid when the properties of the FRC are similar or superior to that in the current study. Should the mechanical properties of the FRC be lower than the FRC in this study, the coefficients for NSC herein should be used. In addition, the average compressive strengths of NSC and HSC in this study were 40 and 88 MPa (5.8 and 12.8 ksi), respectively. Therefore, caution should be exercised when using the proposed coefficients in Table 4 for NSC or HSC with compressive strengths that differ significantly from those used in this study. The validity of the coefficients in the presence of axial load also needs to be validated. In fact, the diagrams in Fig. 6 are valid when then the axial load is not significant. It is expected, however, that compressive axial load would improve the tension-stiffening behavior.[39] Furthermore, variations in the surface configuration of the reinforcement can affect the tension-stiffening characteristics and, consequently, influence the accuracy of deflection prediction models[9,11,26] Furthermore, further verification is required to confirm the accuracy of the proposed model for different span-depth ratios.

In general, the Integ. TS method should not be used to calculate deflection in curvilinear GFRP-RC members with low reinforcement ratios as it significantly underestimates deflection. A designer may, however, opt for the I_e, Integ., or Mod. method based on design considerations. In fact, each of these methods has advantages and disadvantages. Using I_e simplifies the deflection-calculation procedure but does not guarantee that the effect of loading and boundary conditions is considered. The Mod. method could provide more accurate results than the other methods, but it requires more computational effort. Lastly, the Integ. method could be a suitable conservative option when the designer is unsure about the member's tension-stiffening characteristics. In addition, this method requires less computational effort than the Mod. method. The following section provides the procedure developed for adopting the I_e, Integ., or Mod. method for GFRP-reinforced PCTL segments under real loading and boundary conditions. The procedure is general and can be used for other types of curvilinear members.

Development of methods for use under real loading and boundary conditions

The integration-based methods presented previously include several assumptions that might not be met in tunnel segments or other curvilinear members under real load and boundary conditions. The equations presented require the relationship between the applied loads and the internal forces in the member. This is because the complexity of the load and boundary conditions in tunnel segments and some curvilinear members make it generally impossible to determine such relationships. In addition, the axial load on the member relates the cracked moment of inertia in each section to the combination of axial load and bending moment. Therefore, some main parameters in the equations vary from section to section. The following procedure adapts the deflection-calculation procedures presented for designing GFRP-reinforced PCTLs under real loading and boundary conditions.

Step I: Finding forces and initial deflection at joints using first-order analysis—Generally, there is interaction between the applied loads and deflection in tunnel segments and other RC structures. In such situations, the internal forces and estimated approximate deformation must be found with a first-order analysis, which requires an estimate of the moment of inertia to be used in the analysis procedure. This must be accomplished despite the moment of inertia varying section by section in RC structures. The common design practice in such cases is to use an initial estimation of the moment of inertia in the members. Zadeh and Nanni[40] proposed the following equations for the first-order estimation of the moment of inertia of GFRP-RC slab members and columns.

$$I_{slab} = [0.10 + 0.15(E_f/E_s)]I_g \le 0.25I_g \quad (29)$$

$$I_{column} = [0.40 + 0.15(E_f/E_s)]I_g \le 0.55I_g \quad (30)$$

When a designer expects the axial load of a member to be greater than $0.1f_c'A_g$, it can be assumed to be a column. Otherwise, the initial moment of inertia proposed for slabs can be used in the analysis. The reduced flexural rigidity (I_r) for use in the related calculations can be obtained with the following equation (where relevant)[3]

$$I_r = I_j + (4/n_s)^2 \times I \quad (31)$$

where I_j is the moment of inertia at the joint, which is taken as zero in the design; n_s is the number of segments in a ring, excluding the key segment, which should be considered greater than four; and I denotes the lining moment of inertia, which can be calculated with Eq. (29) or (30), according to the axial-load level. The internal forces and joint deformations can be estimated with the first-order analysis using one of the analysis methods such as elastic equation method, beam-spring method, finite element modeling (FEM), and discrete element method (DEM).[3]

Step II: Calculating rotation and deflection in selected segments—The critical segments for the deflection control can be determined based on the results from Step I. Figure 8 provides a schematic view of a segment considered for the deflection control procedure. The effect of the other segments and the joints on the boundary conditions of the segment is modeled by vertical, horizontal, and rotational springs.

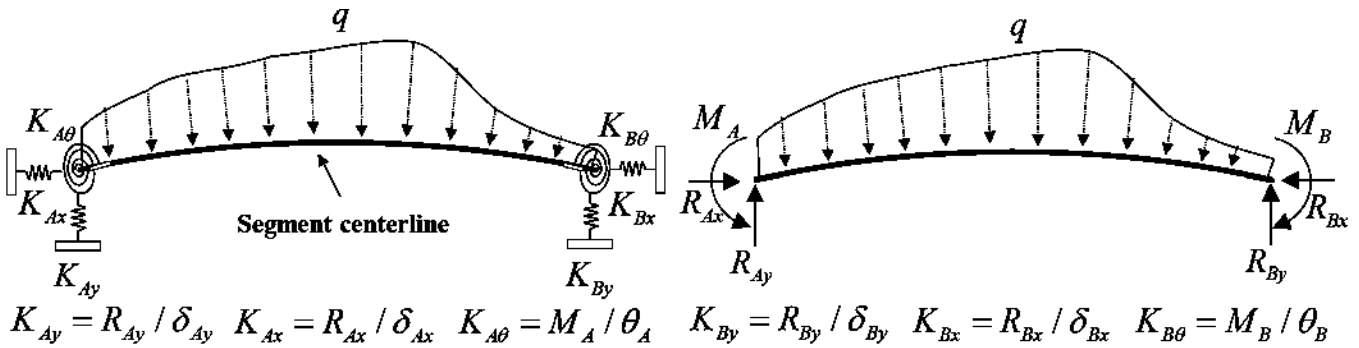

Fig. 8—Schematic view of tunnel segment considered for deflection calculation.

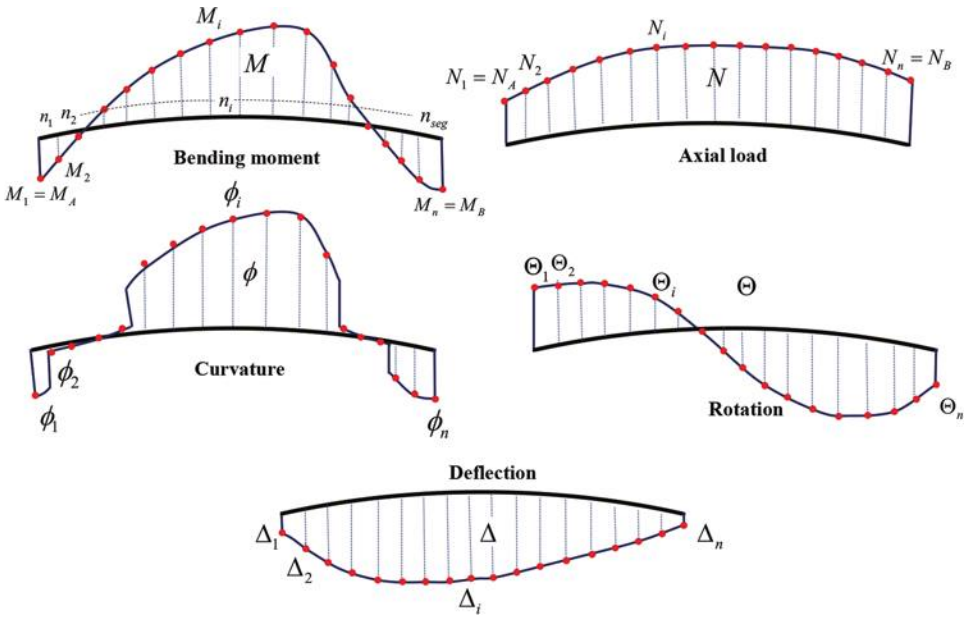

Fig. 9—Schematic view of proposed deflection-calculation procedure for GFRP-reinforced PCTL segments under real load and boundary conditions.

A schematic arbitrary external load is shown, which varies according to the loading conditions. Note that the displayed springs and external load do not play a role in the calculation procedure, which will be described in the following and presented solely to show a semi-real condition of a segment. The analysis in Step 1 is supposed to yield the forces and moments as well as the deformations and rotation of the joints. The following procedure is proposed to obtain the rotation and deflection diagrams of GFRP-reinforced PCTL segments. In addition, Fig. 9 shows a hypothetical schematic view of the proposed procedure.

1. Divide the tunnel segment into certain number of elements (even number) referred to as n_{seg}. In such situations, $\Delta\theta = 2\theta_{max}/n_{seg}$.

2. Designate each element as n_i, $i = 1, 2, 3,\ldots, n_{seg}$. The angle between starting point of the element n_i and the starting point of the segment is $i\Delta\theta$.

3. Specify the axial load (N_i) and bending moment (M_i) at the points corresponding to $\alpha + i\Delta\theta$, where $i = 1, 2, 3,\ldots, n_{seg}$ based on the results in Step I (refer to Fig. 5 for the definitions of α and θ_{max}).

4. Calculate the cracking moment ($M_{cr,i}$) for each point according to the axial-load level.

5. For the points where $M \geq M_{cr,i}$, calculate the cracked moment of inertia ($I_{cr,i}$).

6. For deflection calculation based on the effective moment of inertia, consider the moment of inertia for each point (I_i) according to Eq. (32). For the other methods, where $M \geq M_{cr,i}$, calculate the moment of inertia based on the deflection-calculation method to be used. Equations (33) and (34) represent the moment of inertia based on the Integ. and Mod. methods, respectively. When $M \leq M_{cr,i}$, consider I_i equal to I_g.

$$I_i = \frac{I_{cr,i}}{1 - \eta_i \beta_i \left(\frac{M_{cr,i}}{M_{\theta,i}}\right)} \tag{32}$$

$$I_i = I_{cr} \tag{33}$$

$$I_i = \frac{I_{cr,i}}{1 - \eta_{n,i} \beta_{m,i} \left(\frac{M_{cr,i}}{M_{\theta,i}}\right)} \tag{34}$$

7. Calculate the curvature value at each point using the following equation

$$\phi_i = M_i/E_cI_i \quad (35)$$

8. Use Eq. (5) to find the rotation at each point (Θ_i) using numerical methods to calculate the integral. C_1 is equal to the rotation at the starting point of the segment (Θ_A), determined in Step I. The trapezoidal rule or Simpson's rule might be used to find the rotation based on the curvature at each point (refer to Appendix D for the detailed equations).

9. Use Eq. (36) to find the deflection (Δ) at each point using numerical methods (Δ_A is determined in Step I). Again, the trapezoidal rule or Simpson's rule might be used to find deflection (refer to Appendix D).

$$\Delta_\theta = \int \Theta_\theta R \sin(\theta) d\theta + \Delta_A \quad (36)$$

Appendix D presents a design example according to the presented procedure for one of the specimens tested. In the example, the procedure overestimated the deflection by 8% when following the Mod. method. The procedure entails two main sources of error: 1) using a numerical model to solve the integral; and 2) using an initial moment of inertia to obtain the initial internal forces, rotations, and deformations at the supports in Step I. The former can be minimized by increasing the number of elements in the analysis. In addition, the latter might be improved by performing further rounds of analysis with the data obtained from the preceding rounds. In addition to these sources of error, estimating the exact cracking moment is of great importance in minimizing errors in calculating deflection.

CONCLUSIONS

The following conclusions can be drawn from the results of this study:

1. Applying the effective moment of inertia developed for curvilinear members based on Bischoff's model[9] overestimated deflection by 20%, 3%, and 12% in the normal-strength concrete (NSC), high-strength concrete (HSC), and fiber-reinforced concrete (FRC) specimens, respectively, on average, for different reference points.

2. Neglecting tension stiffening in the integration-of-curvature method overestimated deflection by 50%, 33%, and 43% in the NSC, HSC, and FRC curvilinear specimens, respectively. Considering the contribution of tension stiffening in curvilinear glass fiber-reinforced polymer-reinforced concrete (GFRP-RC) members, however, underestimated deflection by 33%, 54%, and 41% in the NSC, HSC, and FRC specimens, respectively.

3. A comparison of the experimental and analytical results revealed that the accuracy of the methodologies presented depends on the reinforcement ratio, concrete strength, and concrete type. A new model was proposed and validated based on the experimental data to consider the effect of these parameters on a deflection prediction method. The proposed model could predict deflection at the service load with 2% conservativeness.

4. Employing the effective moment of inertia is a simple method with acceptable conservativeness (11% on average in the tested specimens). Its accuracy, however, depends on the load and boundary conditions. The proposed method can provide more accurate results than the other methods, although it requires more computational effort. Lastly, the integration of curvature while neglecting tension stiffening is a conservative option (41% on average) when a designer is not sure about the tension-stiffening characteristics of the member.

AUTHOR BIOS

Seyed Mohammad Hosseini *is a Doctoral Candidate in the Department of Civil and Building Engineering at the University of Sherbrooke, Sherbrooke, QC, Canada. He received his BSc and MSc from Isfahan University of Technology (IUT), Isfahan, Iran. His research interests include the internal and external use of fiber-reinforced polymers (FRPs) in reinforced concrete structures.*

Salaheldin Mousa *is an FRQNT Postdoctoral Fellow in the Department of Civil and Building Engineering at the University of Sherbrooke, where he also received his PhD. He is also a Lecturer at the Faculty of Engineering at Shoubra, Benha University, Cairo, Egypt, where he received his BSc and MSc. His research interests include the use of FRPs in reinforced concrete structures.*

Hamdy M. Mohamed *is a Lecturer and Research Associate in the Department of Civil and Building Engineering at the University of Sherbrooke, where he received his PhD. He received his BSc and MSc from Helwan University, Cairo, Egypt. His research interests include the use and field applications of FRPs in reinforced concrete structures.*

Brahim Benmokrane, *FACI, is a Professor in the Department of Civil and Building Engineering at the University of Sherbrooke, Tier-1 Canada Research Chair in Advanced Composite Materials Used for Civil Engineering Structures, Senior Industrial Research Chair in Innovative FRP Composite Materials for Concrete Infrastructure, and Director of the University of Sherbrooke Research Center on Structural FRP Composite Materials for Concrete Structures (CRUSMAC). He is a member and past Co-Chair of ACI Subcommittee 440-K, FRP-Material Characteristics, and a member of ACI Committees 435, Deflection of Concrete Building Structures, and 440, Fiber-Reinforced Polymer Reinforcement; and ACI Subcommittees ACI 440-E, FRP-Professional Education; ACI 440-F, FRP-Repair-Strengthening; 440-H, FRP-Reinforced Concrete; ACI 440-I, FRP-Prestressed Concrete; and ACI 440-L, FRP-Durability. He received the ACI Foundation Arthur J. Boase Award in 2022. His research interests include the development of FRP reinforcement for concrete structures and their durability, structural performance, and field applications.*

ACKNOWLEDGMENTS

This research was conducted with funding from the Natural Sciences and Engineering Research Council of Canada (NSERC), the Pole de recherche et d'innovation en materiaux avancés au Quebec (PRIMA Quebec), Mathematics of Information Technology and Complex Systems (MITACS), the Fonds de recherche du Québec en nature et technologies (FRQNT), and the Tier-1 Canada Research Chair in Advanced Composite Materials for Civil Structures. The authors are grateful to the precast company (Sym-Tech Béton Préfabriqué, Sainte-Hyacinthe, QC, Canada) and to the GFRP bar manufacturer (Pultrall Inc., Thetford Mines, QC, Canada) for their effective involvement in this project. The authors also acknowledge the contribution of the technical staff of the structural lab in the Department of Civil Engineering at the University of Sherbrooke.

REFERENCES

1. Khaloo, A.; Moradi, H.; Kazemian, A.; and Shekarchi, M., "Experimental Investigation on the Behavior of RC Arches Strengthened by GFRP Composites," *Construction and Building Materials*, V. 235, 2020, p. 117519. doi: 10.1016/j.conbuildmat.2019.117519

2. ACI Committee 544, "Report on Design and Construction of Fiber-Reinforced Precast Concrete Tunnel Segments (ACI 544.7R-16)," American Concrete Institute, Farmington Hills, MI, 2016, 41 pp.

3. ACI Committee 533, "Guide for Precast Concrete Tunnel Segments (ACI 533.5R-20)," American Concrete Institute, Farmington Hills, MI, 2020, 85 pp.

4. Caratelli, A.; Meda, A.; Rinaldi, Z.; and Spagnuolo, S., "Precast Tunnel Segments with GFRP Reinforcement," *Tunnelling and Underground Space Technology*, V. 60, 2016, pp. 10-20. doi: 10.1016/j.tust.2016.07.011

5. Robert, M., and Benmokrane, B., "Combined Effects of Saline Solution and Moist Concrete on Long-Term Durability of GFRP Reinforcing Bars," *Construction and Building Materials*, V. 38, 2013, pp. 274-284. doi: 10.1016/j.conbuildmat.2012.08.021

6. ACI Committee 440, "Guide for the Design and Construction of Structural Concrete Reinforced with Fiber-Reinforced Polymer Bars (ACI 440.1R-15)," American Concrete Institute, Farmington Hills, MI, 2015, 88 pp.

7. Mota, C.; Alminar, S.; and Svecova, D., "Critical Review of Deflection Formulas for FRP-RC Members," *Journal of Composites for Construction*, ASCE, V. 10, No. 3, 2006, pp. 183-194. doi: 10.1061/(ASCE)1090-0268(2006)10:3(183)

8. Branson, D. E., "Instantaneous and Time-Dependent Deflections of Simple and Continuous Reinforced Concrete Beams," HPR Report No. 7, Part I, Alabama Highway Department, Bureau of Public Roads, Montgomery, AL, 1963, pp. 1-78.

9. Bischoff, P. H., "Reevaluation of Deflection Prediction for Concrete Beams Reinforced with Steel and Fiber Reinforced Polymer Bars," *Journal of Structural Engineering*, ASCE, V. 131, No. 5, 2005, pp. 752-767. doi: 10.1061/(ASCE)0733-9445(2005)131:5(752)

10. Bischoff, P. H., "Comparison of Existing Approaches for Computing Deflection of Reinforced Concrete," *ACI Structural Journal*, V. 117, No. 1, Jan. 2020, pp. 231-240. doi: 10.14359/51718072

11. Bischoff, P. H., and Scanlon, A., "Effective Moment of Inertia for Calculating Deflections of Concrete Members Containing Steel Reinforcement and Fiber-Reinforced Polymer Reinforcement," *ACI Structural Journal*, V. 104, No. 1, Jan.-Feb. 2007, pp. 68-75.

12. Adam, M. A.; Said, M.; Mahmoud, A. A.; and Shanour, A. S., "Analytical and Experimental Flexural Behavior of Concrete Beams Reinforced with Glass Fiber Reinforced Polymers Bars," *Construction and Building Materials*, V. 84, 2015, pp. 354-366. doi: 10.1016/j.conbuildmat.2015.03.057

13. Alsayed, S.; Al-Salloum, Y.; and Almusallam, T., "Performance of Glass Fiber Reinforced Plastic Bars as a Reinforcing Material for Concrete Structures," *Composites Part B: Engineering*, V. 31, No. 6-7, 2000, pp. 555-567. doi: 10.1016/S1359-8368(99)00049-9

14. Arabshahi, A.; Tavakol, M.; Sabzi, J.; and Gharaei-Moghaddam, N., "Prediction of the Effective Moment of Inertia for Concrete Beams Reinforced with FRP Bars Using an Evolutionary Algorithm," *Structures*, V. 35, 2022, pp. 684-705.

15. Benmokrane, B.; Chaallal, O.; and Masmoudi, R., "Flexural Response of Concrete Beams Reinforced with FRP Reinforcing Bars," *ACI Structural Journal*, V. 93, No. 1, Jan.-Feb. 1996, pp. 46-55.

16. Gao, D.; Benmokrane, B.; and Masmoudi, R., "A Calculating Method of Flexural Properties of FRP-Reinforced Concrete Beam: Part 1: Crack Width and Deflection," technical report, Department of Civil Engineering, University of Sherbrooke, Sherbrooke, QC, Canada, 1998.

17. Mousavi, S. R., and Esfahani, M. R., "Effective Moment of Inertia Prediction of FRP-Reinforced Concrete Beams Based on Experimental Results," *Journal of Composites for Construction*, ASCE, V. 16, No. 5, 2012, pp. 490-498. doi: 10.1061/(ASCE)CC.1943-5614.0000284

18. Thériault, M., and Benmokrane, B., "Effects of FRP Reinforcement Ratio and Concrete Strength on Flexural Behavior of Concrete Beams," *Journal of Composites for Construction*, ASCE, V. 2, No. 1, 1998, pp. 7-16. doi: 10.1061/(ASCE)1090-0268(1998)2:1(7)

19. Toutanji, H. A., and Saafi, M., "Flexural Behavior of Concrete Beams Reinforced with Glass Fiber-Reinforced Polymer (GFRP) Bars," *ACI Structural Journal*, V. 97, No. 5, Sept.-Oct. 2000, pp. 712-719.

20. Yost, J. R.; Gross, S. P.; and Dinehart, D. W., "Effective Moment of Inertia for Glass Fiber-Reinforced Polymer-Reinforced Concrete Beams," *ACI Structural Journal*, V. 100, No. 6, Nov.-Dec. 2003, pp. 732-739.

21. Zhang, L.; Sun, Y.; and Xiong, W., "Experimental Study on the Flexural Deflections of Concrete Beam Reinforced with Basalt FRP Bars," *Materials and Structures*, V. 48, No. 10, 2015, pp. 3279-3293. doi: 10.1617/s11527-014-0398-0

22. Bischoff, P. H., and Gross, S. P., "Equivalent Moment of Inertia Based on Integration of Curvature," *Journal of Composites for Construction*, ASCE, V. 15, No. 3, 2011, pp. 263-273. doi: 10.1061/(ASCE)CC.1943-5614.0000164

23. CSA S806-12, "Design and Construction of Building Components with Fibre Reinforced Polymers," CSA Group, Toronto, ON, Canada, 2012, 187 pp.

24. Rasheed, H. A.; Nayal, R.; and Melhem, H., "Response Prediction of Concrete Beams Reinforced with FRP Bars," *Composite Structures*, V. 65, No. 2, 2004, pp. 193-204. doi: 10.1016/j.compstruct.2003.10.016

25. Razaqpur, A.; Svecova, D.; and Cheung, M. S., "Rational Method for Calculating Deflection of Fiber-Reinforced Polymer Reinforced Beams," *ACI Structural Journal*, V. 97, No. 1, Jan.-Feb. 2000, pp. 175-184.

26. Bischoff, P. H., and Gross, S. P., "Design Approach for Calculating Deflection of FRP-Reinforced Concrete," *Journal of Composites for Construction*, ASCE, V. 15, No. 4, 2011, pp. 490-499. doi: 10.1061/(ASCE)CC.1943-5614.0000195

27. Hosseini, S. M.; Mousa, S.; Mohamed, H. M.; and Benmokrane, B., "Structural Behavior of Precast Reinforced Concrete Tunnel Segments with Glass Fiber-Reinforced Polymer Bars and Ties under Bending Load," *ACI Structural Journal*, V. 119, No. 1, Jan. 2022, pp. 307-319.

28. Hosseini, S. M.; Mousa, S.; Mohamed, H. M.; Eslami, A.; and Benmokrane, B., "Experimental and Analytical Study on Precast High-Strength Concrete Tunnel Lining Segments Reinforced with GFRP Bars," *Journal of Composites for Construction*, ASCE, V. 26, No. 5, 2022, p. 04022062. doi: 10.1061/(ASCE)CC.1943-5614.0001257

29. ISIS Canada Research Network, "Reinforcing Concrete Structures with Fibre Reinforced Polymers," Design Manual No. 3, University of Manitoba, Winnipeg, MB, Canada, 2007.

30. Boresi, A. P.; Sidebottom, O. M.; and Saunders, H., *Advanced Mechanics of Materials*, fourth edition, John Wiley & Sons Inc., New York, 1985, 763 pp.

31. ACI Committee 318, "Building Code Requirements for Structural Concrete (ACI 318-19) and Commentary (ACI 318R-19) (Reapproved 2022)," American Concrete Institute, Farmington Hills, MI, 2019, 624 pp.

32. Scanlon, A., and Bischoff, P. H., "Shrinkage Restraint and Loading History Effects on Deflections of Flexural Members," *ACI Structural Journal*, V. 105, No. 4, July-Aug. 2008, pp. 498-506.

33. Park, R., and Paulay, T., *Reinforced Concrete Structures*, John Wiley & Sons, Inc., New York, 1991.

34. ACI Committee 544, "Guide to Design with Fiber-Reinforced Concrete (ACI 544.4R-18)," American Concrete Institute, Farmington Hills, MI, 2018, 44 pp.

35. ASTM C1609-19, "Standard Test Method for Flexural Performance of Fiber-Reinforced Concrete (Using Beam with Third-Point Loading), " ASTM International, West Conshohocken, PA, 2019, 9 pp.

36. Bischoff, P., "Deflection Calculation Using an Effective Moment Inertia for FRC," *Deflection and Stiffness Issues in FRC and Thin Structural Elements*, SP-248, P. H. Bischoff and F. Malhas, eds., American Concrete Institute, Farmington Hills, MI, 2007, pp. 17-30.

37. ACI Committee 363, "Report on High-Strength Concrete (ACI 363R-10)," American Concrete Institute, Farmington Hills, MI, 2010, 65 pp.

38. Mousa, S.; Mohamed, H. M.; and Benmokrane, B., "Deflection Prediction Methodology for Circular Concrete Members Reinforced with Fiber-Reinforced Polymer Bars," *ACI Structural Journal*, V. 116, No. 2, Mar. 2019, pp. 279-293. doi: 10.14359/51713293

39. Ng, P. L.; Gribniak, V.; Jakubovskis, R.; and Rimkus, A., "Tension Stiffening Approach for Deformation Assessment of Flexural Reinforced Concrete Members under Compressive Axial Load," *Structural Concrete*, V. 20, No. 6, 2019, pp. 2056-2068. doi: 10.1002/suco.201800286

40. Zadeh, H. J., and Nanni, A., "Flexural Stiffness and Second-Order Effects in Fiber-Reinforced Polymer-Reinforced Concrete Frames," *ACI Structural Journal*, V. 114, No. 2, Mar.-Apr. 2017, pp. 533-543. doi: 10.14359/51689257

ARE YOU A RESEARCHER?

SIGN UP FOR ORCID TODAY!

ORCID provides a persistent digital identifier that distinguishes you from every other researcher and, through integration in key research workflows such as manuscript and grant submission, supports automated linkages between you and your professional activities, ensuring that your work is recognized.

Individuals may use ORCID services freely and it's as easy as **1-2-3**:

1. REGISTER
2. ADD YOUR INFO
3. USE YOUR ORCID ID

For more information and to register, visit:

WWW.ORCID.ORG

ACI STRUCTURAL JOURNAL TECHNICAL PAPER

Title No. 120-S89

Seismic-Fire-Combined Loadings Applied to Carbon Fiber-Reinforced Polymer-Confined Reinforced Concrete Columns

by Ju-Hyung Kim, Yail J. Kim, and Jun Wang

This paper presents analytical investigations into the behavior of a reinforced concrete column with and without carbon fiber-reinforced polymer (CFRP) confinement when subjected to earthquake and fire loadings. A data set of 100 ground motions covering short and long durations is collected and integrated with 0 to 3 hours of fire exposure. Two strengthening categories are implemented: 1) one to six CFRP layers; and 2) six layers of CFRP with a 40 mm (1.6 in.) thick insulation. A computational platform incorporating autonomous discrete entities is used for the simulation of heat transfer, while static pushover and nonlinear dynamic analyses predict the seismic response of the unconfined and confined columns. Thermal gradients are generated across the column section to identify the physical and mechanical properties of constituents at elevated temperatures, which are linked with the static and dynamic models. The CFRP-confined column with insulation outperforms its unconfined counterpart from a behavioral standpoint, specifically for axial capacities, flexural failure, energy dissipation, and deformability. The implications of the seismic-fire-combined loadings are remarkable in terms of degrading the load-resisting ability of the columns compared with those of the uncoupled actions. The duration of the ground motions dominates the development of a relationship between the spectral acceleration and drift ratio of the columns. Design recommendations are rendered to address the limitations of current practice.

Keywords: carbon fiber-reinforced polymer (CFRP); column; earthquake duration; fire endurance; modeling; seismic performance.

INTRODUCTION

The seismic failure of structural elements is contingent upon the degree of resistance to earthquake intensities and wave directions. Sequential earthquakes (also known as aftershocks) aggravate the deterioration of load-bearing components, thereby reducing the overall performance of building structures. Previous studies enunciated that the amplitude, frequency, and duration of oscillating ground motions are crucial factors controlling the detrimental impact of seismic waves.[1,2] Technical regulations allow a certain extent of seismic damage within the boundary of preventing the collapse of buildings by developing plastic hinges that alleviate externally generated excitations.[3] As far as the stability of a structural system is concerned, columns play an important role in maintaining force equilibrium. When seismic loading is applied to a column, the adequacy of axial capacity needs to be combined with appropriate ductility so that the physical failure of the member is retarded until substantial energy is dissipated. The behavior of columns near the base where connections are made with floors or footings is of interest and, that being so, cantilevered configurations are frequently adopted for experimental and theoretical investigations.[4,5]

Numerous buildings built prior to the enforcement of seismic codes, particularly before the 1970s, are considered deficient and may not safely accommodate lateral sway precipitated by earthquakes. Non-seismically designed members thus encounter increased vulnerability to failure and, in lieu of costly reconstruction, rehabilitation is preferred to address assorted issues induced by the inadequate capacity of those nonconforming ones.[3] Because the primary objective of seismic retrofitting is to ameliorate the strength and ductility of structural elements against excessive drift ratios,[6] relevant rehabilitation strategies would mitigate the risk of physical impairment. Among prevalent strengthening techniques that enhance the capacity of reinforced concrete columns, such as enlarging cross sections and adding steel plates,[7] confinement with carbon fiber-reinforced polymer (CFRP) sheets is regarded as a convenient and efficient method[8] and is widely implemented around the world.[9] Specifically speaking, the efficacy of CFRP strengthening is remarkable for seismic upgrading associated with the ductile failure, inelastic rotations, and energy dissipation of substandard columns.[10] Another notable benefit of the CFRP application is that it raises the strength of existing columns without changing stiffness, which is desirable for preserving the magnitude of seismic forces.[11]

Seismic events may ravage energy lines and electricity networks in built environments and can prompt fires. A classical instance is found in the 1906 San Francisco earthquake, which was accompanied by multiple fires: the disaster devastated the city, and 498 people died and more than 225,000 people became homeless.[12] Accordingly, extensive research has been conducted for the last several decades to figure out the implications of earthquakes, fires, and a combination thereof.[13,14] Most cases, however, focused on their own individual consequences,[8,15] and insufficient efforts were expended to understand interactions between these hazards, which can bring about a significantly high level of damage in constructed facilities.[16] It is worth noting that the seismic resistance of fire-damaged members is not comparable to that of intact members, and the likelihood of collapse increases

ACI Structural Journal, V. 120, No. 5, September 2023.

MS No. S-2023-014.R1, doi: 10.14359/51738843, received April 26, 2023, and reviewed under Institute publication policies.

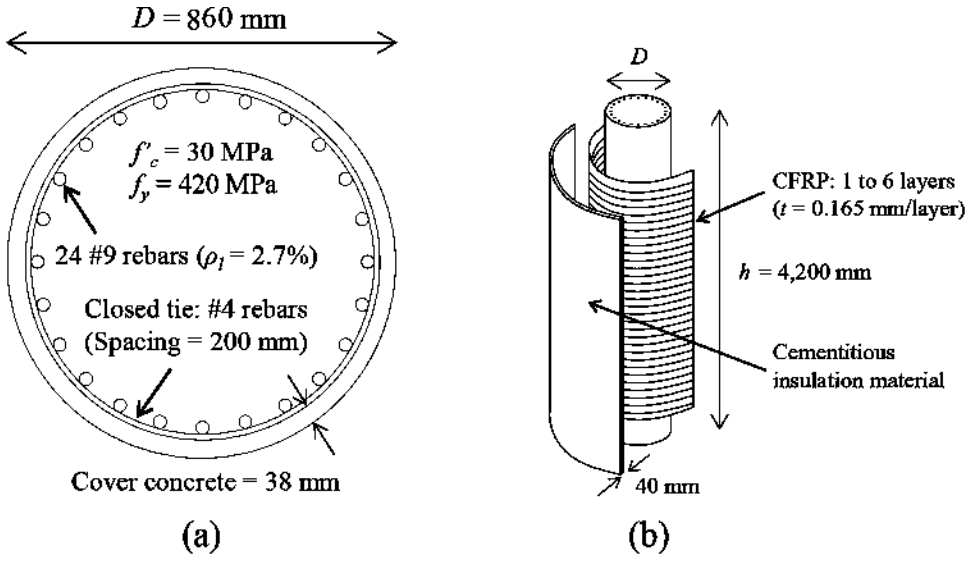

Fig. 1—Benchmark column: (a) dimensions; and (b) strengthening.

under the multi-hazard environment.[17] Contemplating a dearth of provisions in published specifications related to the effects of thermomechanical loadings,[3,18] practitioners may not properly prepare for such an extreme event at the design stage of new and rehabilitated structures.

This paper explores the repercussions of seismic-fire-combined loadings on the behavior of a non-slender reinforced concrete column confined with CFRP sheets. A two-fold analytical program, comprising static pushover and dynamic analyses, is carried out to deal with short- and long-duration earthquakes alongside the ASTM E119-20 standard fire,[19] including a heat transfer model. After validating the predictive approaches, an extensive parametric study is executed with the aim of proposing performance-based design guidelines.

RESEARCH SIGNIFICANCE

The current state of knowledge is incomplete to address concerns arising from synergistic distress consisting of fire and seismic loadings, especially under variable earthquake durations. In addition, there is a lack of information on the behavior of CFRP-strengthened reinforced concrete columns exposed to those adverse circumstances that are presumable in nonconforming buildings. To accomplish resilient structural systems, a scientific understanding of the interrelations between the seismic and fire loadings is a prerequisite, whereas prescriptive specifications do not offer provisions to effectively handle this important aspect.[18] The outcomes from the present study are intended to clarify ambiguous design schemes with and without CFRP for columns subjected to seismic-fire-combined loadings.

BENCHMARK COLUMN

A typical reinforced concrete column was taken from the first floor of a 20-year-old building,[20] and minor adjustments were made for a diameter of D = 860 mm (34 in.) and a height of h = 4200 mm (13.8 ft). The circular column was reinforced with 24 No. 9 bars (A_s = 645 mm^2 [1.0 in.^{2}] each, where A_s is the cross-sectional area of the reinforcing bar), and No. 4 closed ties (A_s = 129 mm^2 [0.2 in.^{2}] each) were placed at spacings of 200 mm (8 in.), as depicted in Fig. 1(a). The compressive strength of the concrete was f_c' = 30 MPa (4350 psi) and the yield strength of the reinforcing steel was f_y = 420 MPa (60 ksi). Given that the column was built on a mat foundation,[20] its geometric configuration was treated as a cantilever: conforming to previous studies,[4,5] this simplified boundary condition was deemed suitable for evaluating hysteretic responses at the connection level under seismic loadings. To upgrade the capacity and ductility of the column, one to six layers of CFRP sheets were applied (Fig. 1(b)). The tensile strength, elastic modulus, and ultimate strain of CFRP were f_{fu} = 3800 MPa (550 ksi), E_f = 227 GPa (33,000 ksi), and ε_{fu} = 0.167, respectively, based on an equivalent fiber thickness of t_f = 0.165 mm (0.0065 in.). The column was assumed to carry an axial load of $P = 0.2f_c'A_g$, where A_g is the gross-sectional area of the column, representing a combination of service design loads.[21] The influence of insulation was also examined using the six-layer CFRP case (designated C6). The insulation type was a sprayable cementitious material,[22] which is commonplace for fireproofing,[23] and possessed a thickness of 40 mm (1.6 in.), an average density of 256 kg/m^3 (15.9 lb/ft^3), a thermal conductivity of 0.0815 W/(m·°C) (0.047 BTU/(h·ft·°F)), and a specific heat of 1047 J/(kg·°C) (0.25 BTU/(lb·°F)). Because a fire rating of 3 hours is the well-accepted norm in the building community,[24] the thermomechanical behavior of the column was studied from 0 (a prefire state for reference) to 3 hours.

DURATION OF EARTHQUAKES

Earthquake ground motions incorporating a variety of durations were collected to simulate the seismic behavior of the benchmark column. A characteristic duration was defined as a time interval between 5 and 75% of cumulative Arias intensity measures ($D_{S5\text{-}75}$), which is useful to appraise the seismic response of a structure[25,26]

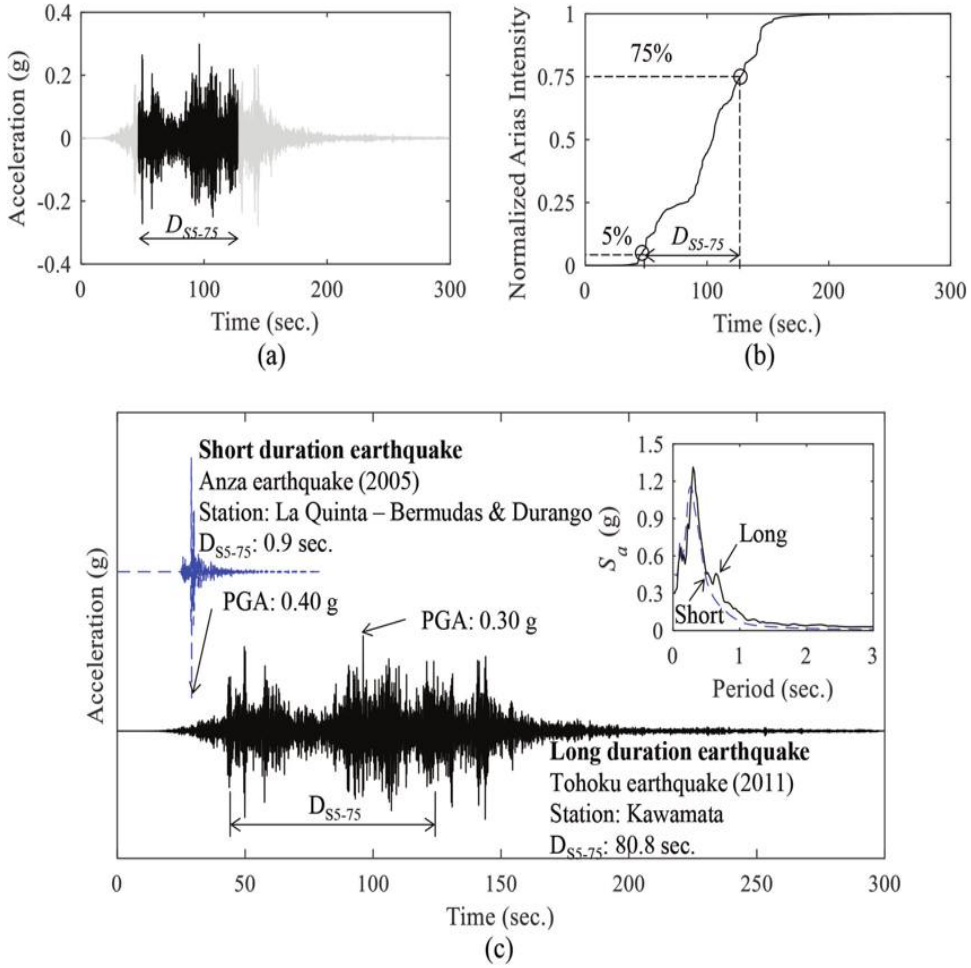

Fig. 2—Description of characteristic earthquake duration ($D_{S5\text{-}75}$): (a) time history; (b) Arias intensity; and (c) spectrally equivalent short- and long-duration motions.

Table 1—Fifty sets of spectrally equivalent earthquake ground motions

	Short duration ($D_{S5\text{-}75}$ < 25 seconds)			Long duration ($D_{S5\text{-}75}$ ≥ 25 seconds)					Short duration ($D_{S5\text{-}75}$ < 25 seconds)			Long duration ($D_{S5\text{-}75}$ ≥ 25 seconds)			
No.	Title (station)	PGA, *g*	$D_{S5\text{-}75}$, seconds	Title (station)	PGA (*g*)	$D_{S5\text{-}75}$ (seconds)	Scale factor	No.	Title (station)	PGA, *g*	$D_{S5\text{-}75}$, seconds	Title (station)	PGA, *g*	$D_{S5\text{-}75}$, seconds	Scale factor
1	Chalfant Valley (CZR)	0.444	2.20	Valparaiso (Llol.)	0.437	27.6	1.31	26	Petrolia (Petrolia)	0.498	2.30	Tohoku (Koho.)	1.044	67.5	1.50
2	Big Bear (SB)	0.111	11.8	Landers (ICC)	0.102	25.1	1.04	27	Loma Prieta (G#1)	0.442	1.40	Tohoku (Niho.)	0.414	75.8	0.71
3	Mt. Lewis (HVGP)	0.147	1.00	Landers (IJR)	0.271	25.8	0.92	28	Whittier (TCHN)	0.537	2.60	Tohoku (Niho.)	0.414	73.5	0.81
4	Landers (BVH)	0.135	12.8	Landers (TPPC)	0.099	25.5	0.97	29	Coalinga (CCS)	0.288	3.10	Tohoku (Aidu.)	0.418	56.7	1.63
5	Alum Rock area (CL)	0.160	1.40	Kocaeli (Fatih)	0.192	27.8	1.31	30	Loma Prieta (G#2)	0.351	1.90	Tohoku (Aidu.)	0.418	69.4	1.67

$$I_A = (\pi/2g)\int_0^{t_d} a(t)^2 dt \quad (1)$$

where I_A is the Arias intensity; g is the gravitational acceleration ($1g = 9.81$ m/s^2 = 32.2 ft/s^2); and t_d and $a(t)$ are the time span and history of the recorded acceleration, respectively. As exemplified in Fig. 2(a) and (b), accelerations recorded at a seismograph station (Fig. 2(a)) were normalized to identify a range of the cumulative intensities from 5 to 75% (Fig. 2(b)); then, the characteristic duration ($D_{S5\text{-}75}$) was determined. In accordance with the methodology proposed by Chandramohan et al.,[27] ground motions were classified into two categories (short [$D_{S5\text{-}75}$ < 25 seconds] and long [$D_{S5\text{-}75}$ ≥ 25 seconds] durations), and these were paired to isolate the effects of earthquake durations with a focus on magnitude and frequency. For implementation, 300 accelerograms of short-duration earthquakes with a magnitude greater than 6.0 were gleaned from various sources (Table 1, footnote) and compared against 100 long-duration

Table 1 (cont.)—Fifty sets of spectrally equivalent earthquake ground motions

6	Chalfant Valley (BSS)	0.125	7.70	Hokkaido (Oiwa.)	0.099	26.3	1.10	31	Northridge (LA-B)	0.239	8.30	Tohoku (Fukush.)	0.318	77.3	1.05
7	Chino Hills (GGCG)	0.177	0.50	Hokkaido (Haya.)	0.132	28.0	1.07	32	Anza (LQBD)	0.397	0.90	Tohoku (Kawa.)	0.299	80.8	0.96
8	Coyote Lake (CLD)	0.249	1.40	Hokkaido (Haya.)	0.132	25.3	1.05	33	La Habra (Walnut)	0.361	0.60	Tohoku (Kawa.)	0.299	85.4	1.01
9	Chi-Chi (HWA003)	0.138	6.70	Hokkaido (Kuri.)	0.109	40.8	1.47	34	Northridge (LA-C)	0.316	5.90	Tohoku (Miharu)	0.503	78.7	1.97
10	Loma Prieta (GSF)	0.542	1.70	Maule (Angol)	0.684	30.2	1.29	35	Whittier (LA116)	0.392	1.50	Tohoku (Miyak.)	0.900	71.3	1.68
11	Calexico (El Centro)	0.383	14.9	Maule (Const.)	0.527	31.9	1.62	36	Northridge (SPD)	0.434	2.00	Tohoku (Sakun.)	0.407	75.5	1.39
12	Northridge (LA-H)	0.389	5.90	Maule (Curico)	0.465	38.2	1.16	37	Big Bear (BBL)	0.545	5.50	Tohoku (Sakun.)	0.407	66.7	0.85
13	Superstition Hills	0.341	7.10	Maule (Hualane)	0.375	33.7	1.53	38	Landers (JTFS)	0.284	21.7	Tohoku (Kakuda)	0.352	69.3	1.31
14	Chi-Chi (CHY047)	0.139	6.30	Maule (Santiago)	0.182	27.6	1.21	39	Tottori (TTR008)	0.391	4.60	Tohoku (Kakuda)	0.352	70.8	0.78
15	Loma Prieta (GGCS)	0.356	1.60	Maule (Talca)	0.462	51.4	1.34	40	Landers (DHS)	0.171	21.4	Tohoku (Iwanu.)	0.254	70.4	1.25
16	Coyote Lake (GH)	0.254	0.90	Maule (Talca)	0.462	51.7	1.61	41	Petrolia (Fortuna)	0.193	4.20	Tohoku (Higash.)	0.199	73.3	1.23
17	Kocaeli (Ambarli)	0.253	9.70	El Mayor (Chih.)	0.244	23.6	0.82	42	San Fernando (SP)	1.171	5.40	Tohoku (Higash.)	0.199	69.1	0.20
18	El Mayor-Cucapah (3)	0.183	15.4	El Mayor (Chih.)	0.244	26.8	1.29	43	Coalinga (2W)	0.109	6.10	Tohoku (Kamin.)	0.120	81.0	1.42
19	Kocaeli (İzmit)	0.230	6.40	El Mayor (Tama.)	0.201	28.3	0.83	44	Coalinga (2E)	0.176	5.60	Tohoku (Yonez.)	0.207	78.1	1.39
20	Tottori (SMN002)	0.179	5.70	Tohoku (Yana.)	0.283	77.1	1.25	45	Niigata (NIG013)	0.132	16.2	Tohoku (Tendou)	0.174	71.2	1.21
21	Parkfield (Zone 15b)	0.229	3.20	Tohoku (Yana.)	0.283	75.8	1.15	46	Landers (Mecca)	0.118	22.4	Tohoku (Tendou)	0.174	64.0	1.84
22	Parkfield (Zone 8)	0.546	1.60	Tohoku (Fukush.)	0.577	74.0	1.15	47	Northridge (PM)	0.178	7.70	Tohoku (Takaha.)	0.204	81.7	1.14
23	La Habra (Fullerton)	0.356	1.30	Tohoku (Fukush.)	0.577	71.2	1.14	48	Big Bear (DHS)	0.225	5.70	Tohoku (Takaha.)	0.204	79.7	0.84
24	La Habra (La Habra)	0.330	1.60	Tohoku (Iitate)	0.506	76.3	1.32	49	Yountville (Napa)	0.340	1.60	Tohoku (Yonez.)	0.208	65.3	0.67
25	La Habra (Brea)	0.703	0.60	Tohoku (Iitate)	0.506	77.9	1.73	50	Landers (FI)	0.122	7.90	Tohoku (Yonez.)	0.208	70.0	1.50

Note: Web sources: Center for Engineering Strong Motion Data (https://www.strongmotioncenter.org/), NGA-West2 database (https://peer.berkeley.edu/ngawest2/databases/), and National Research Institute for Earth Science and Disaster Prevention (https://www.kyoshin.bosa.go.jp/); PGA is peak ground acceleration; $D_{S5\text{-}75}$ is earthquake duration corresponding to 5 to 75% of cumulative Arias intensity; 1 g = 9.81 m/s^2 = 32.2 ft/s^2.

earthquakes excerpted from Chandramohan et al.[27]; afterward, their spectrally equivalent motions were identified in tandem with 5%-damped pseudo-acceleration spectra.[3] Each of the 50 pairs between the 100 short- and long-duration earthquakes revealed minimum squared errors and optimized scale factors for the individual sets listed in Table 1. By using these spectrally equivalent ground motions, unnecessary distractors arising from the morphological dissimilarity of the paired durations are eliminated (Fig. 2(c)). A complete set of the manipulated ground motions is visible in Fig. 3.

HEAT TRANSFER

Conduction and thermal properties

The governing equation of heat transfer in the benchmark column may be expressed by Fourier's law

$$\frac{\partial T(x,t)}{\partial t} = \alpha \frac{\partial T^2(x,t)}{\partial x^2} \quad (2)$$

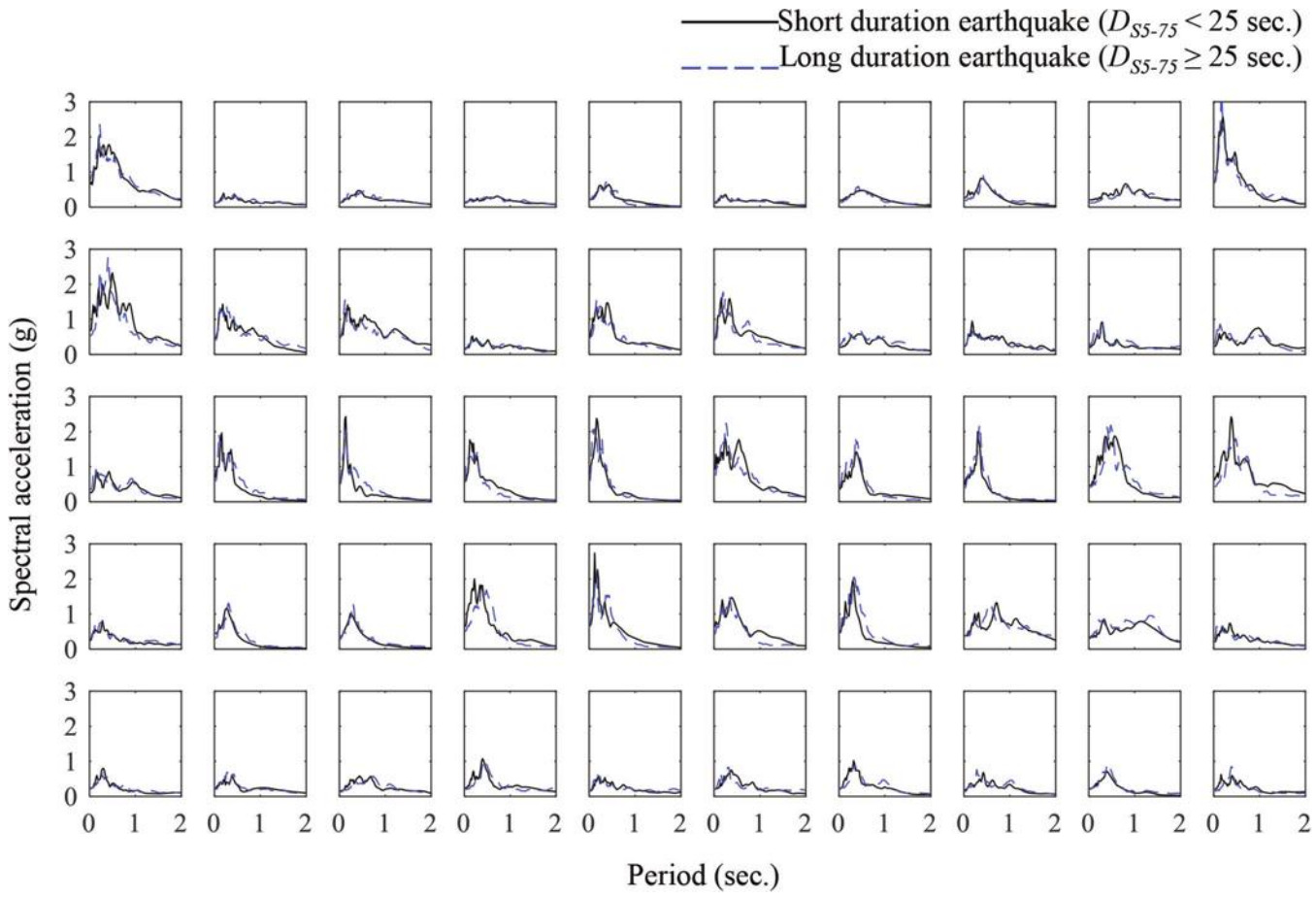

Fig. 3—Fifty spectrally equivalent earthquake motion sets.

where $T(x,t)$ is the temperature at location x and time t; and α is the thermal diffusivity ($\alpha = \lambda/(C_p\rho)$, in which λ is the thermal conductivity; C_p is the specific heat; and ρ is the density). In compliance with the recommendations of preceding research,[28,29] the thermal contribution of reinforcement in the concrete column was ignored. Figure 4 plots the thermal properties of the constituent materials predicted by previously reported equations.[30-32] While the conductivity of the concrete and CFRP descended with temperature (Fig. 4(a) and (b)), that of the insulation was constant (Fig. 4(c)). The abrupt drop in the CFRP's conductivity at 400°C (752°F) was attributed to the breaking of chemical bonds in the resin, accompanied by a chain scission process that lowered the residual mass of effective molecules in the polymeric composition and precipitated interfacial failure between the fibers and the matrix.[33,34] For modeling convenience,[35] the mechanical resistance of CFRP was disregarded beyond the thermal decomposition temperature of 400°C (752°F) that caused the malfunctioning of the composite. Unlike the stable case of the concrete (Fig. 4(d)), the specific heat of the CFRP and insulation was temperature-dependent (Fig. 4(e) and (f), respectively). The endothermic reactions of these materials involving the conversion of molecular kinetic energy to chemical energy were responsible for such erratic behavior.[36-38] The variation in the concrete's density was marginal up to 1063°C (1945°F) on account of changes in its mineralogical composition and free water contents at elevated temperatures (Fig. 4(g)[39]); however, the density of others was invariant (Fig. 4(h) and (i)), except for the thermal decomposition of CFRP at 400°C (752°C). Figures 4(j) to (l) summarize the thermal diffusivity of the concrete, CFRP, and insulation. Equation (3) reproduces the ASTM E119 standard fire,[36] as graphed in Fig. 5(a)

$$T = 750\left(1 - \exp\left(-3.79553\sqrt{t_h}\right)\right) + 170.41\sqrt{t_h} + T_0 \quad (3)$$

where T is the applied temperature in Celsius; t_h is the heating time in hours; and T_0 is the reference temperature ($T_0 = 20$°C [68°F]).

Formulation and validation

A heat transfer model was developed using a computational platform built with discrete entities, which is called agent-based modeling. This nontraditional approach is often employed in social science to study a reciprocal relationship between autonomous individuals,[40] and the concept was useful to predict the interactive behavior of the column components during a fire. An open-source code, NetLogo, formed the basis of heat transfer in conjunction with the aforementioned material properties. Further explanations on the background and implementation of the code are available elsewhere.[41] Figures 5(b) and (c) compare the theoretical temperature of concrete members with and without CFRP strengthening against experimental data obtained from the literature.[22,41] The compressive strength of the concrete spanned between 28 and 39 MPa (4061

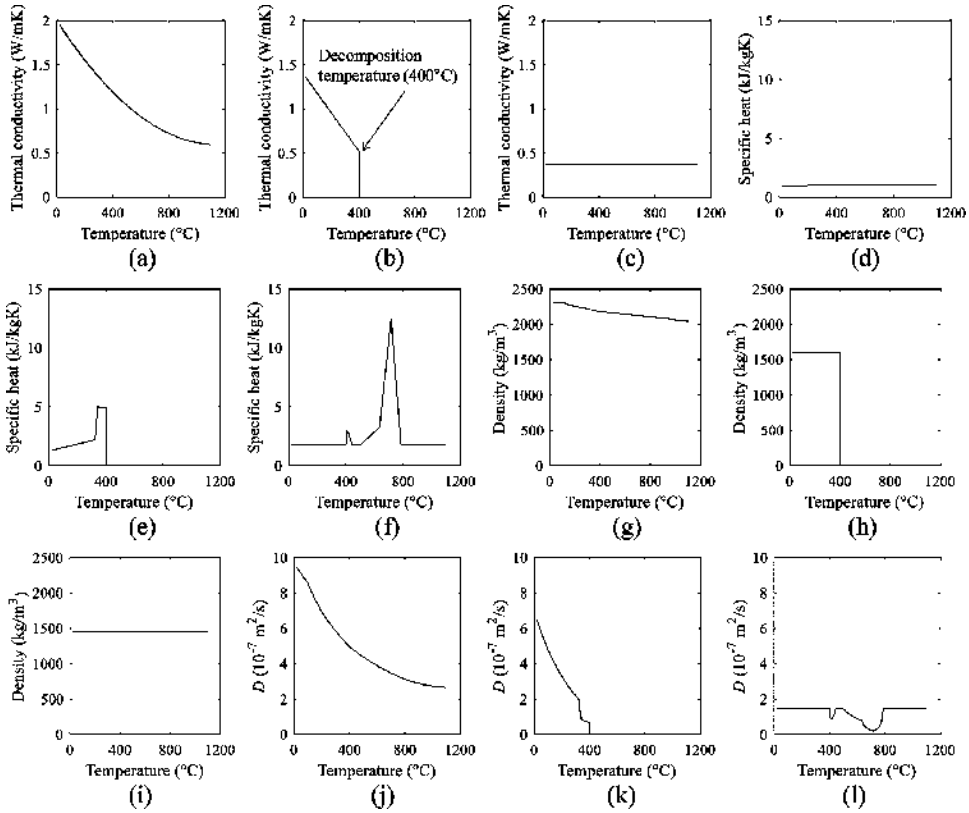

Fig. 4—Temperature-dependent properties of constituent materials: (a) thermal conductivity of concrete; (b) thermal conductivity of CFRP; (c) thermal conductivity of insulation; (d) specific heat of concrete; (e) specific heat of CFRP; (f) specific heat of insulation; (g) density of concrete; (h) density of CFRP; (i) density of insulation; (j) thermal diffusivity of concrete; (k) thermal diffusivity of CFRP; and (l) thermal diffusivity of insulation.

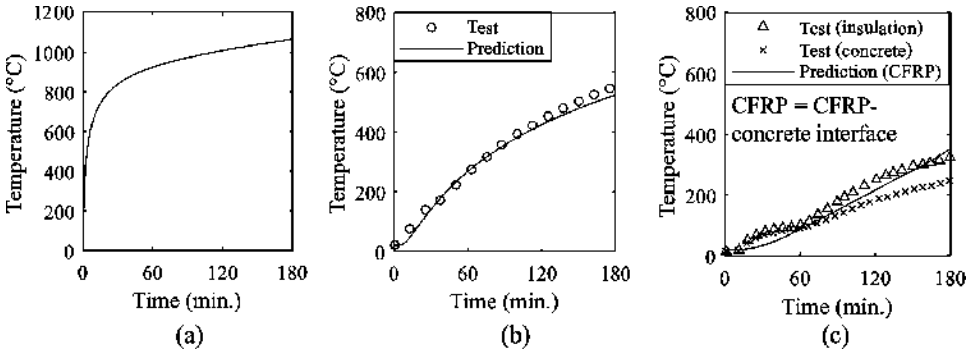

Fig. 5—Validation of heat transfer model: (a) ASTM E119-20[19]; (b) plain concrete (test: Weerasinghe et al.[42]); and (c) confined concrete with insulation (test: Williams et al.[22]).

and 5656 psi). The thickness of the CFRP and insulation layers was 1 mm (0.0394 in.) and 38 mm (1.5 in.), respectively, and their thermal properties were the same as those in the present study (Fig. 4). Temperatures were recorded at 45 mm (1.8 in.) from the concrete surface[42] and in the vicinity of concrete and insulation levels.[22] The computed and measured values agreed across the board.

PREDICTION OF CAPACITY DEGRADATION

Material modeling

Unconfined concrete and reinforcing bar—The full constitutive relationships of plain concrete and reinforcing bars at elevated temperatures were attained from Eurocode 2[31]; Appendix A* contains detailed information. As shown in Fig. 6(a), both the strength and stiffness of the concrete declined with the increased thermal load. The yield strength of the reinforcing bars was sustained up to 400°C (752°F), after which noticeable degradation was rendered (Fig. 6(b)).

CFRP sheet—For the temperature-dependent mechanical properties of CFRP, Eq. (4) and (5) may be used[43]

$$E_f(T)/E_f = 0.475\tanh\{-8.68 \times 10^{-3}(T - 367.41)\} + 0.525 \quad (4)$$

*The Appendix is available at **www.concrete.org/publications** in PDF format, appended to the online version of the published paper. It is also available in hard copy from ACI headquarters for a fee equal to the cost of reproduction plus handling at the time of the request.

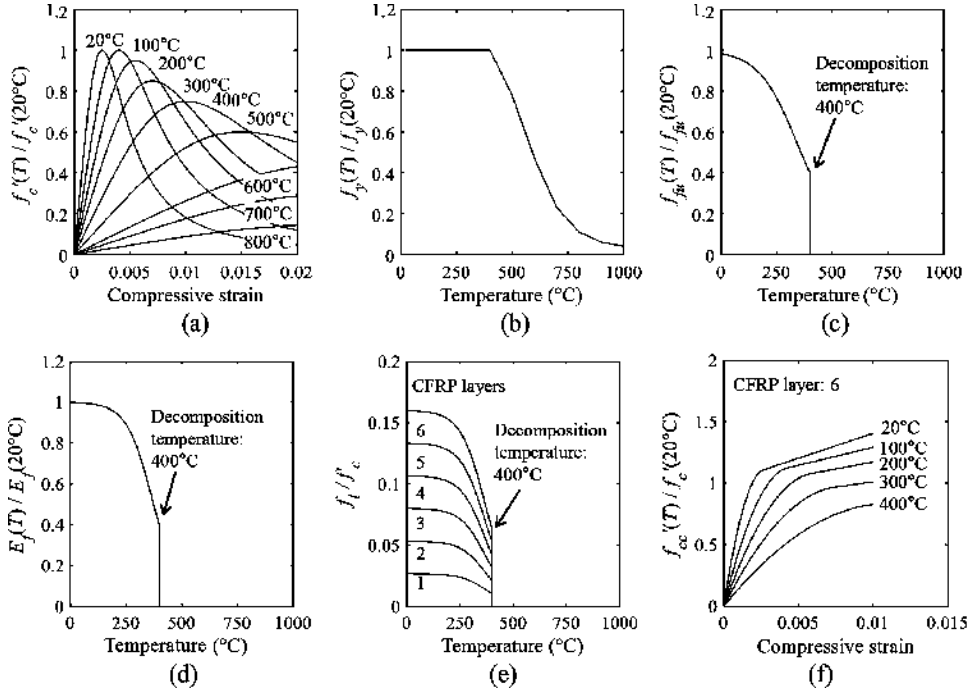

Fig. 6—Material properties at elevated temperatures: (a) compressive stress-strain of unconfined concrete; (b) yield strength of reinforcing bar; (c) elastic modulus of CFRP sheet; (d) tensile strength of CFRP sheet; (e) confining stress; and (f) compressive stress-strain of confined concrete.

$$f_{fu}(T)/f_{fu} = 0.45\tanh\{-5.83 \times 10^{-3}(T - 339.54)\} + 0.55 \quad (5)$$

where $E_f(T)$ and $f_{fu}(T)$ are the elastic modulus and tensile strength of CFRP at temperature T in Celsius. The hyperbolic responses of CFRP dwindled until thermal decomposition occurred (Fig. 6(c) and (d)). According to experimental observations,[44] the linearity of stress-strain in CFRP can be preserved in fire

$$f_f(T) = E_f(T)\varepsilon_f \quad (6)$$

where $f_f(T)$ is the stress of CFRP at temperature T; and ε_f is the CFRP strain.

Confined concrete—Pursuant to ACI 440.2R-17,[10] the confining pressure of core concrete ($f_l(T)$) in the column is calculated by

$$f_l(T) = 2E_f(T)nt_f\varepsilon_{fe}/D \quad (7)$$

where n is the number of the confining layers; and ε_{fe} is the effective strain of CFRP ($\varepsilon_{fe} = 0.55\varepsilon_{fu}$). When more layers were applied, the degree of confinement was raised and its sensitivity to elevated temperatures increased (Fig. 6(e)). This fact points out that the ramifications of fire are significant, justifying the demand for insulation to retain the effectiveness of CFRP strengthening until an intended fire rating is achieved. The stress-strain curve of the confined concrete is written as[10]

$$f_c = \begin{cases} E_c\varepsilon_c - (E_c - E_2)^2/(4f_c') & \text{for } 0 \le \varepsilon_c \le \varepsilon_t' \\ f_c' + E_2\varepsilon_c & \text{for } \varepsilon_t' \le \varepsilon_c \le \varepsilon_{c,max} \end{cases} \quad (8)$$

$$E_2 = \frac{f_{cc}' - f_c'}{\varepsilon_{ccu}} \quad (9)$$

$$\varepsilon_t' = \frac{2f_c'}{E_c - E_2} \quad (10)$$

where f_c and ε_c are the stress and strain of the confined concrete, respectively; and E_c is the elastic modulus of the core concrete. The compressive strength of the confined concrete (f_{cc}') and its maximum strain ($\varepsilon_{c,max}$) are shown in Eq. (11) and (12), respectively[10]

$$f_{cc}' = f_c' + \psi_f 3.3\kappa_a f_l \quad (11)$$

$$\varepsilon_{c,max} \le \varepsilon_{ccu} \le 0.01 \quad (12)$$

$$\varepsilon_{ccu} = \varepsilon_c'(1.50 + 12\kappa_b(f_l/f_c')(\varepsilon_{fe}/\varepsilon_c')^{0.45}) \quad (13)$$

where ψ_f is a reduction factor ($\psi_f = 0.95$); κ_a and κ_b are the geometry and efficiency factors ($\kappa_a = \kappa_b = 1.0$ for circular columns); and ε_c' is the compressive strain of the core concrete ($\varepsilon_c' = 0.002$). Substituting Eq. (7) and (11) into Eq. (8) with the Eurocode model for the unconfined concrete yields the temperature-dependent constitutive relationship of the confined concrete (Fig. 6(f)).

Static pushover analysis

A plastic hinge model was formulated with the following assumptions[3,21,45] to establish a moment-curvature relationship (Fig. 7(a)):

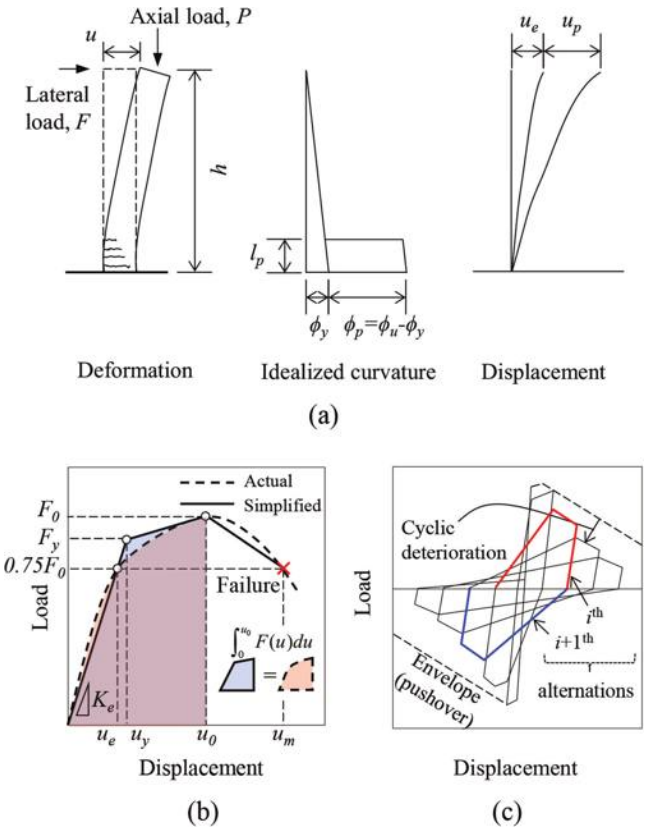

Fig. 7—Hysteretic model: (a) idealized behavior of cantilevered column; (b) trilinear envelope curve; and (c) cyclic deterioration.

- The shear deformation of the benchmark column is negligible.
- Plane sections remain plane before and after bending.
- Strain compatibility is valid between the constituents of the column.
- The interfacial slip of CFRP is negligible at the concrete-surface level.

At fire-exposure time t_h, the lateral capacity and displacement of the column ($F(t_h)$ and $u(t_h)$, respectively) are determined by

$$F(t_h) = M_n(t_h)/h \tag{14}$$

$$u(t_h) = u_e(t_h) + u_p(t_h) = 1/3\phi_y(t_h)h^2 + (\phi_u(t_h) - \phi_y(t_h))l_p(h - 0.5l_p) \tag{15}$$

where $M_n(t_h)$ is the ultimate moment; $u_e(t_h)$ and $u_p(t_h)$ are the elastic and plastic deformations, respectively; $\phi_y(t_h)$ and $\phi_u(t_h)$ are the yield and maximum curvatures, respectively; and l_p is the plastic hinge length, which can be estimated by[46,47]

$$l_{p,unconf}(T) = 0.08h + 0.022d_b f_y(T) \tag{16}$$

$$l_{p,conf}(T) = 0.8(f_l(T)/f_c'(T))h + 0.022d_b f_y(T) \tag{17}$$

where $l_{p,unconf}(T)$ and $l_{p,conf}(T)$ are the hinge length of the unconfined (UC) and CFRP-confined columns, respectively; and d_b is the diameter of the longitudinal reinforcing bar. Compared with the plastic hinge equation of ACI 440.2R-17 that merely considers a gap between adjacent CFRP wraps,[10] Eq. (17) contains the confining term ($f_l(T)$) to interconnect thermally degraded material properties with the hinge length.

Hysteretic simulation

Conceptual development—The benchmark column was modeled as a single-degree-of-freedom (SDOF) system. This archetypal approximation for dynamic analysis is justified by the fact that the plastic hinge region (Fig. 7(a)) dominates the lateral displacement of the column mass.[48] A simplified trilinear load-displacement curve was then constructed (Fig. 7(b)). In line with ACI 374.2R-13,[49] the initial stiffness of the curve (K_e) was characterized using the point at which a lateral load equaled 75% of the maximum load ($0.75F_0$), and the fundamental period of the column was expressed to be $T_1 = 2\pi(P/(gK_e))^{0.5}$, in which P is the axial load. The load and displacement of the column at yielding (F_y and u_y, respectively, and $F_y = K_e u_y$) were calculated as instructed in ASCE/SEI 41-17.[3] When the maximum displacement (u_m) coincided with the value at a post-peak load of $0.75F_0$, tantamount to a capacity loss of 25%, the column failed.[49]

Framework—Because the hysteretic approach proposed by Ibarra et al.[50] adequately models in-cycle deterioration along with seismic energy dissipation that is essential for elucidating structural damage,[7] it was adopted to simulate the behavior of the benchmark column. The extent of cyclic degradation can be quantified through a change in the amount of energy dissipation[50]

$$\beta_i = \left(E_i/\left(E_t - \sum_{j=1}^{i} E_j\right)\right)^c \tag{18}$$

where β_i is the in-cycle degradation parameter at the i-th alternation (one full load reversal comprises the i-th and i+1-th alternations [$i \geq 1$], as retraced in Fig. 7(c)); E_i and E_j are the dissipated hysteretic energy values ($\int F(u)du$, $1 \leq j \leq i$) at the current and previous alternations (that is, ΣE_j is the cumulative hysteretic energy from the first to the i-th alternations); E_t is the reference energy ($E_t = \gamma F_y u_y$, in which γ is an empirical constant: $\gamma = 120$ for UC columns[51] and a value should be found for confined ones); and c is the rate of deterioration ($c = 1.0$ is used for most reinforced concrete columns[51]). With the progression of cyclic loadings, the degradation parameter (β_i) is updated every load reversal so that the in-cycle deterioration of the column is computed from an envelope generated from the pushover analysis (Fig. 7(c))

$$F_i = (1 - \beta_i)F_{i-1} \tag{19}$$

where F_i is the load of the post-peak envelope at the i-th alternation commencing from the initial load of the envelope without cyclic degradation (F_0).

Validation

The validation of the predictive methods is provided in Fig. 8. The dimensions of the test columns[52] were D =

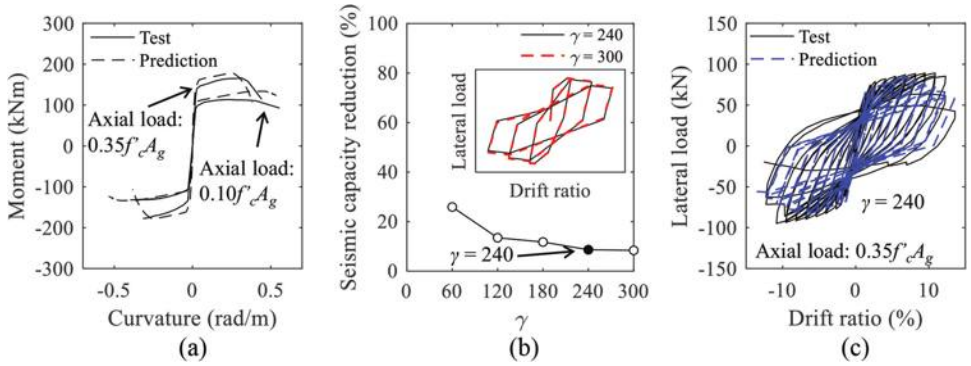

Fig. 8—Validation of predictive methods: (a) pushover; (b) calibration of energy constant γ; and (c) hysteretic behavior.

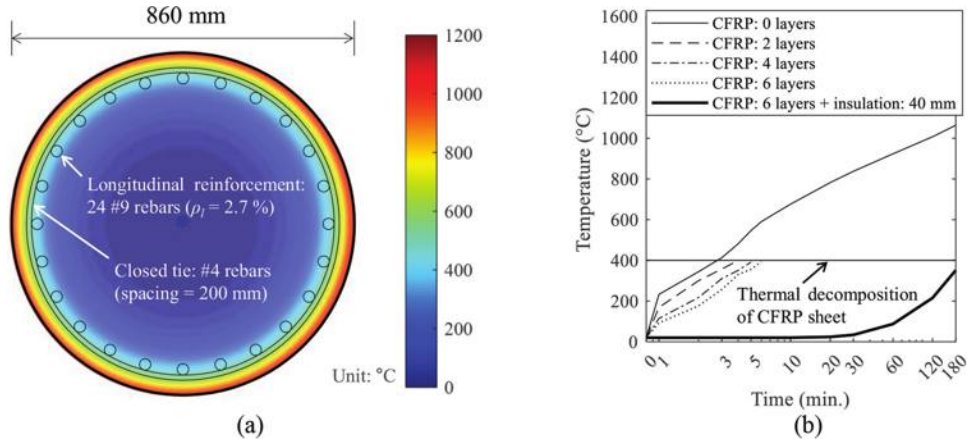

Fig. 9—Thermal conduction across benchmark column: (a) temperature field of unconfined column exposed to fire for 3 hours; and (b) development of temperature at level of concrete surface.

305 mm (12 in.) and h = 2000 mm (6.5 ft), which were confined with CFRP sheets (t_f = 1 mm [0.0394 in.], E_f = 70.6 GPa [10,240 ksi], and f_{fu} = 849 MPa [123 ksi]). Irrespective of axial load, the static moment envelopes created by the pushover model were in agreement with experimental responses (Fig. 8(a)). For the hysteretic simulation of the confined column, the energy constant γ was calibrated against the measured data (Fig. 8(b)). The converged value of γ = 240 was then employed to generate full cyclic curves (Fig. 8(c)). Because others reported that the γ constant was an invariable property with respect to elevated temperatures,[17] γ = 240 was taken for all thermally loaded columns.

NONLINEAR DYNAMIC ANALYSIS

Time-history analysis

The SDOF hysteretic model was expanded to conduct a time-history analysis with the elastic stiffness, fundamental period, damping ratio, and cyclic degradation detailed previously. Nonlinear solutions were sought using the constant average acceleration method, also known as the Newmark method,[53] and the modified Newton-Raphson iteration.[54] A convergence criterion was chosen at a tolerance limit of 10^{-5} mm (3.9×10^{-7} in.). Although complete methodological procedures are omitted due to the page limit, one can refer to dynamics texts.[48] Predictions included time histories for the displacement, velocity, and acceleration of the unconfined and confined columns.

Incremental dynamic analysis

For the evaluation of seismic performance through the foregoing time-history model, incremental dynamic analysis (IDA) was carried out.[55] The intensity of ground motions was increased in a piecewise manner until the columns collapsed. A spectral acceleration at the fundamental frequency of the columns was labeled as $S_a(T_1)$, which was equivalent to the magnitude of an input motion. This numerical technique repeatedly updated input motions using the recorded data (all short- and long-duration motions in Table 1), and ensuing drift ratios were figured out (the execution algorithm is delineated in Vamvatsikos and Cornell[55]). When the maximum drift ratios of the columns reached the preset limits from the pushover analysis (Fig. 7(b)), incremental iterations were terminated and IDA curves ($S_a(T_1)$ versus drift ratio) were drawn.

RESULTS

Thermal gradient

Figure 9(a) exhibits a temperature field in the UC column exposed to the ASTM E119 standard fire for 3 hours. The distribution of temperature was uneven across the section: the cover concrete outside the closed tie was thermally loaded over 1000°C (1832°F), the longitudinal reinforcing bars were subjected to a range of 400 to 550°C (752 to 1022°F), and the inner side of the column underwent below 400°C (752°F). The rise in temperature at the level of the concrete surface is demonstrated in Fig. 9(b). The incipient stage of the UC

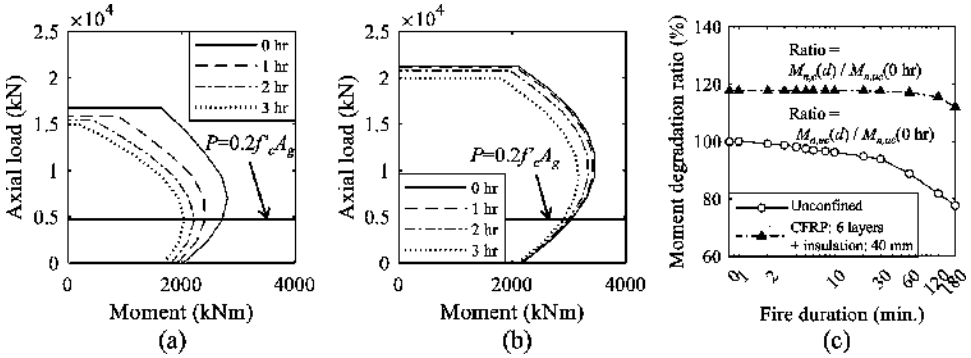

Fig. 10—Capacity of columns exposed to fire: (a) interaction diagram of UC column; (b) interaction diagram of C6 column; and (c) capacity degradation.

Table 2—Lateral resistance of unconfined (UC) and confined (C6) columns

Identification		UC	C6
CFRP confinement		No	Yes
Number of CFRP layers		0	6
Insulation thickness		0 mm	40 mm
Peak strength (M_n/h)	Prefire: 0 hours	647 kN	766 kN
	Fire duration: 1 hour	574 kN	756 kN
	Fire duration: 2 hours	532 kN	743 kN
	Fire duration: 3 hours	503 kN	720 kN
Drift ratio at failure (u_m/h)	Prefire: 0 hours	2.3%	9.0%
	Fire duration: 1 hour	3.5%	8.6%
	Fire duration: 2 hours	4.2%	7.9%
	Fire duration: 3 hours	4.4%	7.0%
Fundamental period ($T_1 = 2\pi(P/(gK_e))^{0.5}$)	Prefire: 0 hours	0.88 seconds	0.79 seconds
	Fire duration: 1 hour	1.07 seconds	0.84 seconds
	Fire duration: 2 hours	1.29 seconds	0.90 seconds
	Fire duration: 3 hours	1.48 seconds	1.01 seconds

Note: T_1 is fundamental period; P is applied axial load; g is gravitational acceleration; K_e is initial stiffness; M_n is ultimate moment; h is column height; u_m is maximum displacement; 1 kN = 0.225 kip; 1 mm = 0.0394 in.; 1 MPa = 145 psi.

column was rapid (233°C [451°F] at 1 minute), followed by a gradual development to 1063°C (1945°F) at 180 minutes. With the presence of CFRP, the evolutionary trend of the surface temperature was retarded until the decomposition temperature of 400°C (752°F) was reached. The increased CFRP layers delayed the transfer of the heat, whereas the extended time to the decomposition was minimal, scilicet, 4 and 6 minutes with two and six layers, respectively. When the confined column was insulated, the surface temperature was maintained below 34°C (93°F) for up to 30 minutes and the highest temperature was 351°C (664°F) at 180 minutes. This observation substantiates the practical significance of proper insulation for CFRP-strengthened columns in the event of a fire.

Capacity degradation in fire

Interactions between the axial load and moment of the UC and confined (C6) columns at failure are given in Fig. 10(a) and (b), respectively, depending upon fire-exposure time. Because the contribution of CFRP to the strength of the uninsulated column was nullified within 6 minutes in a fire (Fig. 9(b)), interaction diagrams without insulation that do not furnish meaningful acquaintance are not shown. The load and moment capacities of the UC column lessened owing to the fire loadings (Fig. 10(a)). The conspicuous diminution of the load plateaus, denoting nominal maximum compression, was ascribed to the decreased pure axial capacity of the column caused by the thermally degraded constituent properties (Fig. 6). With an increase in the exposure time, cracked-section responses below the plateaus deviated from the control response at 0 hours; as a consequence, the flexural failure of the column was accelerated when subjected to the same magnitude of the axial load. Regarding the interaction diagrams of the C6 column (Fig. 10(b)), a modest divergence was noticed in all graphs; for example, the 3-hour moment at a transition point from the plateau to the bulged portion of the curve was 14.3% lower than its 0-hour counterpart. The moments of the C6 column were consistent under the service design load of $0.2f_c'A_g$, regardless of the exposure time; nonetheless, the circumferentially wrapped CFRP sheets were not beneficial in terms of altering the pure moment capacity of the column (2172 kN·m [1602 kip·ft]) relative to the capacity of the UC column (2027 kN·m [1495 kip·ft]) without thermal distress. Figure 10(c) displays the deteriorated moment capacity of the columns: $M_{n,uc}(t_h)$ and $M_{n,c}(t_h)$ are the capacities of the unconfined and confined columns at the service design load level, respectively. Contrary to the sustained capacity of the C6 column showing a loss of 6.0% from 0 to 180 minutes, the capacity of the UC column diminished by over 22.3%.

Lateral resistance

Table 2 enumerates the lateral resistance of the confined and unconfined columns as a function of the fire-exposure time. Despite the fact that the progression of high temperatures exacerbated structural deterioration, the C6 column outperformed the UC column from the perspective of static and dynamic properties. The drops in the peak strength were 22.3% and 6.0% for the UC and C6 columns, respectively, from 0 to 3 hours of thermal loadings. On their drift ratios at failure, a marked improvement was recorded as high as 391.3% (9.0% versus 2.3% at the prefire condition). The fundamental periods of the UC and C6 columns increased by 68.2% and 27.8%, respectively, from 0 to 3 hours, which is indicative of the superior resistance of the C6 column to lateral loading; in other words, the stiffness reduction (ΔK_e) of C6 was lower than that of UC.

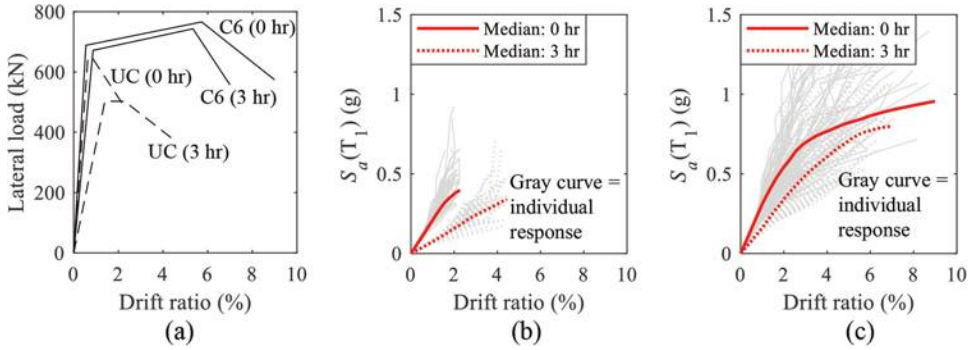

Fig. 11—Seismic-fire-combined load effects: (a) column responses with and without thermal loading; (b) IDA curves of UC column; and (c) IDA curves of C6 column.

Performance under seismic-fire-combined loadings

The thermomechanical behavior of the columns, predicted by the pushover model, is shown in Fig. 11(a). For clarity, the least favorable situation at 3 hours of fire exposure was instantiated with prefire responses at 0 hours. The ultimate strength and stiffness of the UC column dropped by 22.3% and 64.6%, respectively, before and after the exposure; in contrast, those of the C6 column decreased by 6.0% and 38.6%, respectively. Likewise, the maximum tolerable drift ratios of the confined column were improved considerably. The outcomes of the IDA model for the unconfined and confined columns are compiled in Fig. 11(b) and (c), respectively. The exposure-dependent median graphs of these columns were acquired from the individual responses pertaining to the 50 pairs of the ground motions (Table 1). As the exposure time elapsed, the acceleration response of the UC column abated (Fig. 11(b)): the softened slope of the IDA curve at 3 hours signifies the enlarged vulnerability to lateral loadings, which would elevate the risk of structural collapse by allowing inordinate sway. The performance of the C6 column surpassed that of the UC column (Fig. 11(c)): the initial stiffness (K_e) of the unconfined and confined columns decreased by 64.2% and 47.4% from 0 to 3 hours, respectively. The spectral acceleration and drift relationship of the C6 column tended to be bilinear: the deviation of the secondary slope from the initial slope was attributed to the accumulated hysteretic damage in the column together with enhanced deformability that extended the breadth of usable drifts. The secondary slope of the IDA curves was an indication of structural impairment, insinuating that accumulated thermal damage progressively weakened the confinement system.

Dependency of seismic capacity on earthquake duration

Dynamic behavior—Figure 12 reveals the response of the confined column subjected to short- and long-duration earthquakes at 3 hours of fire exposure (only the C6 column is covered under the selected acceleration samples given in Fig. 2(c) for brevity, and comparative assessments in relation to the UC column will follow). The maximum drifts of the column loaded with the short and long durations were 3.1% and 6.1%, as shown in Fig. 12(a) and (b), respectively. It should be noted that these drifts are part of the 7.0% median of the integrated values discussed in Fig. 11(c). The short-duration hysteretic curves (Fig. 12(a)) were inclined to move along the path of the pushover envelope until the seismic excitation attenuated (Fig. 2(c)); by contrast, the long-duration curves suffered a sudden escalation of the drift at 2.7% (the third quadrant, Fig. 12(b)) because of an upsurge in the ground acceleration near 100 seconds in Fig. 2(c) that was linked with the aforementioned hysteretic damage. Upon initiation of the inelastic behavior, the energy dissipation of the column steadily increased (Fig. 12(c)). Even if there was a gap between the short- and long-duration scenarios, their growth rates were almost identical up to 255 kN·m (188 kip·ft) when the short-duration earthquake was active; contrarily, the amount of energy dissipation appertaining to the long-duration earthquake continuously rose up to 154 seconds and stabilized owing to the decay of the ground acceleration (Fig. 2(c)). The strength reduction of the column stemming from the cyclic loading is plotted in Fig. 12(d), where a ratio of the peak of each hysteretic curve ($F_{0,deg}$) to the ultimate strength of the pushover envelop (F_0) is defined (Fig. 12(d), inset). The short-duration earthquake led to a degradation ratio of 0.90 at 60 seconds. On the other hand, the long-duration earthquake resulted in a plunge and entailed a stable ratio beyond 154 seconds when the input acceleration ebbed (Fig. 2(c)). It is thus argued that current design practices, without explicitly taking into account earthquake durations,[56] cannot fully embrace the implications of seismic hazards, and that an alternative approach should be adduced for both confined and unconfined columns.

Assessment of combined load effect—Described in Fig. 13 are the median IDA curves of the columns under the variable earthquake durations coupled with the thermal distress. While the development of spectral acceleration in the UC column was controlled by the fire exposure, its susceptibility to the duration of the seismic excitation was virtually none (Fig. 13(a)). The reason is explained by the low maximum drifts of the UC column that failed before the occurrence of excessive yield deformations tied with the cyclic deterioration (Fig. 12(d)). As for the confined column (Fig. 13(b)), the influence of the 3-hour fire loading was also prominent and the duration effect was inappreciable until the bifurcation of the IDA curves emerged due to the increased fundamental period associated with the dissipation of hysteretic energy in the C6 column (Table 2). The maximum difference between the short- and long-duration-induced spectral accelerations at 0 hours of exposure was 18%, whereas the degree

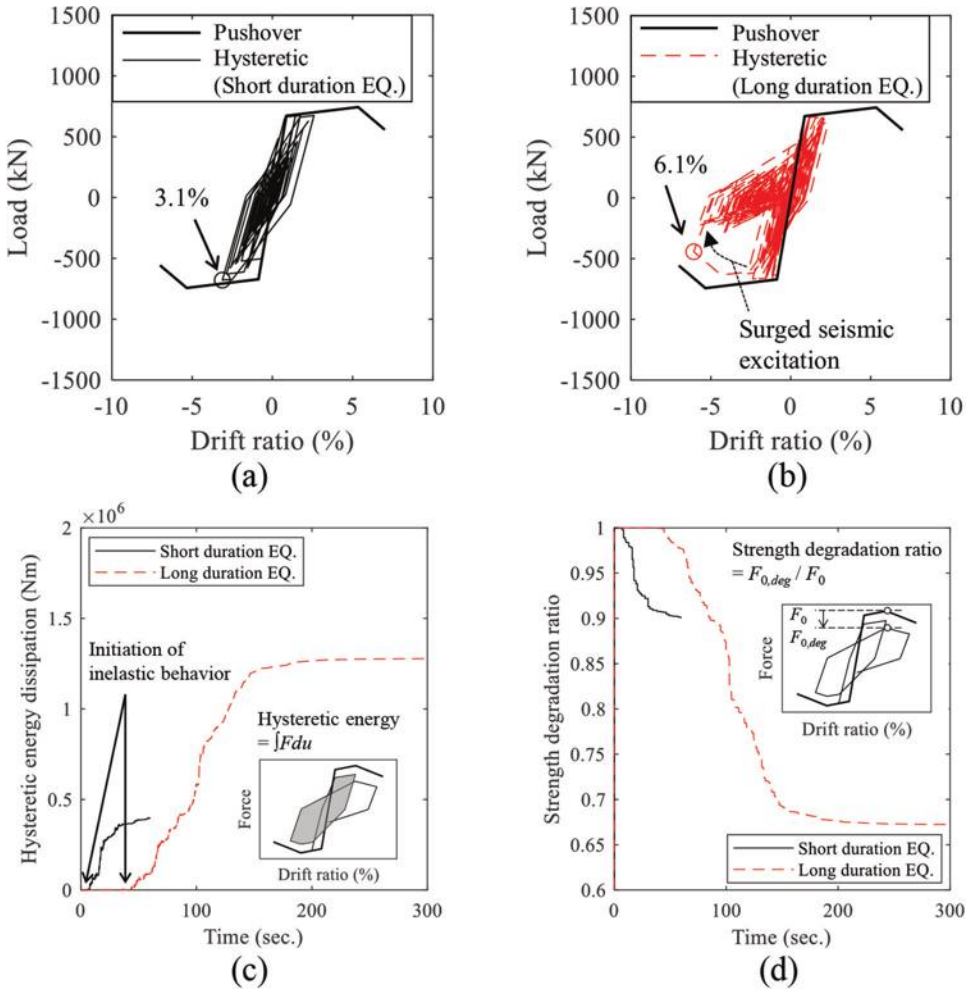

Fig. 12—Dynamic response of C6 subjected to spectrally equivalent earthquake ground motions at 3-hour fire exposure (EQ. is earthquake): (a) short duration; (b) long duration; (c) hysteretic energy dissipation; and (d) cyclic strength degradation.

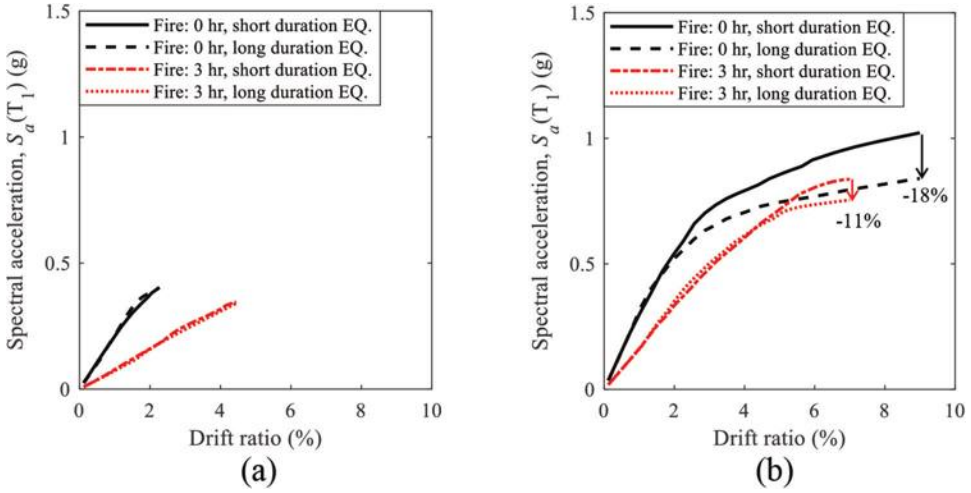

Fig. 13—Median IDA curves as to variable earthquake durations combined with thermal loading (EQ. is earthquake): (a) UC column; and (b) C6 column.

of disparity was reduced to 11% at 3 hours. This fact corroborates that the elevated temperatures mitigated the discrepancy between the short- and long-duration earthquakes.

Reliance on characteristic duration—Figures 14(a) to (d) demonstrate the distribution of cyclically degraded strengths with $D_{S5\text{-}75}$ for the unconfined and confined columns at failure when subjected to the 50 pairs of the spectrally equivalent short and long ground motions under the exposure periods of 0 and 3 hours. The strength of the columns waned as the characteristic durations lengthened, which implies that persistent earthquake loadings need to be a consideration for seismic design. The capacities of the UC and C6 columns,

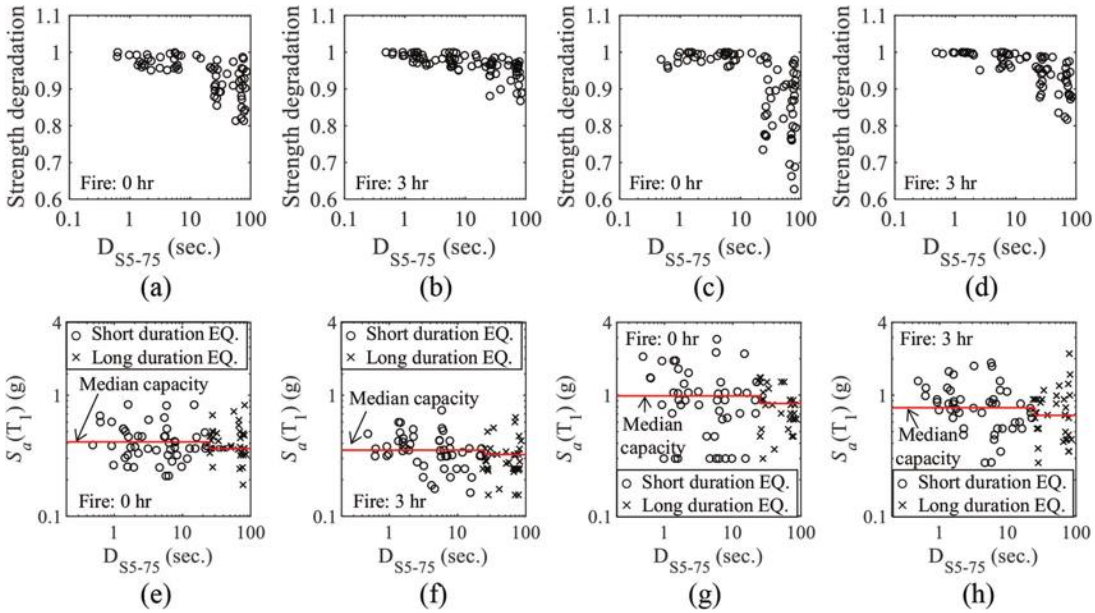

Fig. 14—Influence of earthquake duration on strength degradation (log-scale plots): (a) cyclic strength degradation of UC column at 0 hours; (b) cyclic strength degradation of UC column at 3 hours; (c) cyclic strength degradation of C6 column at 0 hours; (d) cyclic strength degradation of C6 column at 3 hours; (e) seismic capacity of UC column at 0 hours; (f) seismic capacity of UC column at 3 hours; (g) seismic capacity of C6 column at 0 hours; and (h) seismic capacity of C6 column at 0 hours.

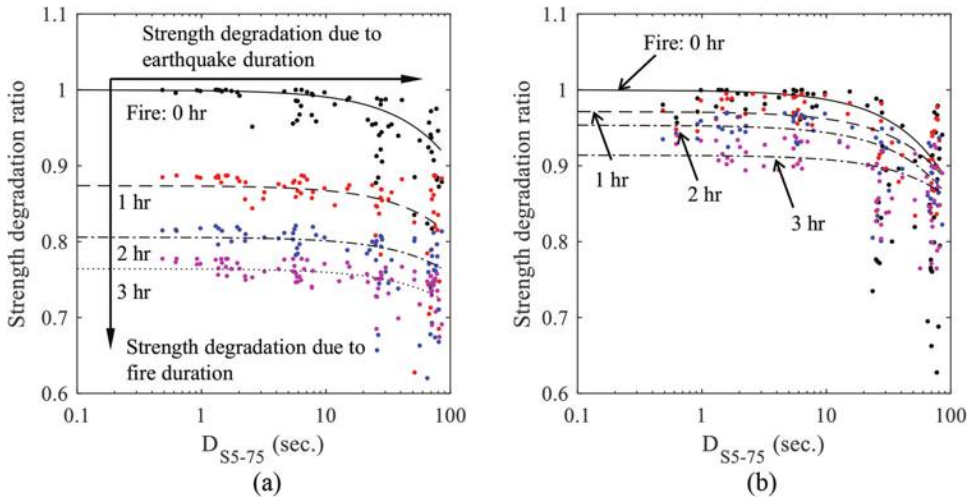

Fig. 15—Seismic capacity degradation with earthquake duration in fire (log-scale plots): (a) UC column; and (b) C6 column.

represented by the peak spectral accelerations, are appraised in Fig. 14(e) to (h). At the threshold duration of 25 seconds, there was a stepwise decrement in the median capacities of the columns (Fig. 14(e) to (h)) and the importance of the durations was once again emphasized.

DESIGN RECOMMENDATIONS

Shown in Fig. 15 are the sets of strength degradation data belonging to the short- and long-duration earthquakes consolidated with the fire-exposure time (100 ground motions collated in Table 1 were used for each temporal category). Regression lines were added to definitize a relationship between the degraded strength and external attributes (dependent and independent variables, respectively). Aligning with Fig. 13(a), the exposure time was more influential in degenerating the strength of the UC column than the earthquake duration (Fig. 15(a)). An opposite trend was, however, noticed for the confined column by virtue of the insulation layer (Fig. 15(b)): the less susceptible variations of the 1- to 3-hour lines in comparison with that of the 0-hour line are ascribed to the hysteretic energy dissipation explained earlier. For a practical appraisal under seismic-fire-combined loadings at the preliminary design phase, the quantity of the strength degradation was equated with a capacity reduction factor (namely, the nominal capacity of a column is multiplied by the factor to estimate its deteriorated capacity without going through rigorous dynamic investigations). Table 3 arranges those factors in the context of column types, earthquake durations, and fire ratings, which were rounded for the simplification of the exact degradation amounts. The applicable boundary of the proposal is an

Table 3—Proposed capacity reduction factors for seismic-fire-combined loading

Column type	Earthquake duration*	Fire rating			
		0 hours	1 hour	2 hours	3 hours
Unconfined without insulation (before strengthening)	$D_{S5\text{-}75} < 25$ seconds	0.95	0.85	0.80	0.75
	$D_{S5\text{-}75} \geq 25$ seconds	0.90	0.80	0.75	0.70
CFRP-confined with insulation (after strengthening)	$D_{S5\text{-}75} < 25$ seconds	0.95	0.95	0.90	0.90
	$D_{S5\text{-}75} \geq 25$ seconds	0.90	0.90	0.85	0.85

*Applicable range: 0 seconds ≤ duration ≤ 85 seconds.

earthquake duration of 0 to 85 seconds in agreement with the range of the sampled seismic events (Table 1).

SUMMARY AND CONCLUSIONS

This paper has discussed analytical procedures to comprehend the behavior of reinforced concrete columns with and without carbon fiber-reinforced polymer (CFRP) confinement in a multi-hazard scenario, comprising earthquake and fire loadings. A data set of 100 short- and long-duration earthquakes was gleaned and partitioned at 25 seconds, which was amalgamated with a fire-exposure period of 0 to 3 hours. The strengthening scheme involved two categories: 1) one to six layers of CFRP sheets; and 2) six CFRP layers with a 40 mm (1.6 in.) thick insulation. Heat transfer was modeled on a discrete entity platform, and the mechanical response of the columns was predicted by static pushover and nonlinear dynamic methods (time-history analysis and incremental dynamic analysis [IDA]). After linking the seismic approaches with the distribution of temperature from the conduction model, the performance of the unconfined (UC) and confined columns was studied. Technical interests lay in capacity degradation, load-moment interactions, lateral resistance, a relationship between spectral acceleration and drift ratio, and hysteretic energy dissipation. Findings were integrated to suggest performance-based design guidelines. The following conclusions are drawn:

- The initial development of temperature was rapid at the surface of the column concrete (233°C [451°F] at 1 minute) and, as uneven thermal distributions progressed across the section, the growth rate became stable up to 1063°C (1945°F) at 180 minutes. Whereas the degree of heat transfer was delayed in part by wrapping the column with CFRP, insulation was required to reach a 3-hour fire rating (351°C [664°F] at 180 minutes).
- The thermally degraded properties of the constituent materials were responsible for lowering the pure axial capacity of the UC column and accelerating its flexural failure. The influence of the fire exposure was marginal on the behavior of the confined column with the insulation layer (C6), leading to reasonable retention of the capacity with a 6.0% loss at the design service load of $0.2f_c'A_g$.
- Through the pushover model, it was construed that the seismic-fire-combined distress was more detrimental than the uncoupled actions. The hysteretic analysis confirmed the increased vulnerability of the UC column to stability failure when the exposure period was enlarged. The bilinear IDA curves of the C6 column, established on cyclically accumulated damage plus the widened usable drifts that enabled high-level deformability, were a metric to gauge the functionality of the CFRP system.
- The intensity of ground motions and earthquake durations dominated the pattern of conformational loops in the hysteretic curves. Besides, the seismic-fire-combined loading was a critical factor for dissipating the energy of the UC and C6 columns. Upon examining the features of the characteristic duration ($D_{S5\text{-}75}$), the prominence of the persistent earthquake loadings was recognized.
- The proposed reduction factors addressed the limitations of current practice,[56] which is reliant on risk-targeted maximum considered earthquake responses (MCER) without allowing for the duration of ground motions. The factors can facilitate the design of UC and CFRP-confined columns under the combined loadings with an earthquake duration of 0 to 85 seconds and a fire rating of up to 3 hours.

AUTHOR BIOS

Ju-Hyung Kim *is a Postdoctoral Fellow in the Department of Civil Engineering at the University of Colorado Denver, Denver, CO. He received his BE, MS, and PhD from the Department of Architecture and Architectural Engineering at Seoul National University, Seoul, South Korea. His research interests include seismic design, performance evaluation, and statistical analysis of reinforced concrete structures.*

Yail J. Kim, *FACI, is President of the Bridge Engineering Institute, An International Technical Society, and a Professor in the Department of Civil Engineering at the University of Colorado Denver. He is Chair of ACI Subcommittee 440-I, FRP-Prestressed Concrete, past Chair of ACI Committee 345, Bridge Construction and Preservation, and a member of ACI Committees 342, Evaluation of Concrete Bridges and Bridge Elements; 377, Performance-Based Structural Integrity & Resilience of Concrete Structures; and 440, Fiber-Reinforced Polymer Reinforcement; and Joint ACI-ASCE Committee 343, Concrete Bridge Design. He received the Chester Paul Siess Award for Excellence in Structural Research in 2019. His research interests include advanced composite materials for rehabilitation; structural informatics; complex systems; and science-based structural engineering, including statistical, interfacial, and quantum physics.*

ACI member **Jun Wang** *is a Postdoctoral Fellow in the Department of Civil Engineering at the University of Colorado Denver. She received her BS and MS from Northeast Forestry University, Harbin, Heilongjiang, China, and her PhD from the University of Colorado Denver. She is a member of ACI Committee 345, Bridge Construction and Preservation. Her research interests include multi-object interaction, concrete structures, and advanced modeling.*

ACKNOWLEDGMENTS

This research is in part supported by the U.S. Department of Transportation through the Mountain-Plains Consortium, for which the authors are grateful. Proprietary information is not included to avoid commercialism. Technical contents presented herein are based on the opinion of the writers and do not necessarily represent that of others.

REFERENCES

1. Li, Q., and Ellingwood, B. R., "Performance Evaluation and Damage Assessment of Steel Frame Buildings under Main Shock–Aftershock Earthquake Sequences," *Earthquake Engineering & Structural Dynamics*, V. 36, No. 3, Mar. 2007, pp. 405-427. doi: 10.1002/eqe.667

2. Bessason, B.; Rupakhety, R.; and Bjarnason, J. Ö., "Comparison and Modelling of Building Losses in South Iceland Caused by Different Size Earthquakes," *Journal of Building Engineering*, V. 46, Apr. 2022, Article No. 103806. doi: 10.1016/j.jobe.2021.103806

3. ASCE/SEI 41-17, "Seismic Evaluation and Retrofit of Existing Buildings," American Society of Civil Engineers, Reston, VA, 2017.

4. Lavorato, D., and Nuti, C., "Pseudo-Dynamic Tests on Reinforced Concrete Bridges Repaired and Retrofitted after Seismic Damage," *Engineering Structures*, V. 94, July 2015, pp. 96-112. doi: 10.1016/j.engstruct.2015.01.012

5. Xu, J. J.; Demartino, C.; Shan, B.; Heo, Y. A.; and Xiao, Y., "Experimental Investigation on Performance of Cantilever CFRP-Wrapped Circular RC Columns under Lateral Low-Velocity Impact," *Composite Structures*, V. 242, June 2020, Article No. 112143. doi: 10.1016/j.compstruct.2020.112143

6. Lignos, D. G.; Moreno, D. M.; and Billington, S. L., "Seismic Retrofit of Steel Moment-Resisting Frames with High-Performance Fiber-Reinforced Concrete Infill Panels: Large-Scale Hybrid Simulation Experiments," *Journal of Structural Engineering*, ASCE, V. 140, No. 3, Mar. 2014, p. 04013072. doi: 10.1061/(ASCE)ST.1943-541X.0000877

7. FEMA 547, "Techniques for the Seismic Rehabilitation of Existing Buildings," Federal Emergency Management Agency, Washington, DC, 2006, 571 pp.

8. Gkournelos, P. D.; Triantafillou, T. C.; and Bournas, D. A., "Seismic Upgrading of Existing Reinforced Concrete Buildings: A State-of-the-Art Review," *Engineering Structures*, V. 240, Aug. 2021, Article No. 112273. doi: 10.1016/j.engstruct.2021.112273

9. Naser, M. Z.; Hawileh, R. A.; and Abdalla, J. A., "Fiber-Reinforced Polymer Composites in Strengthening Reinforced Concrete Structures: A Critical Review," *Engineering Structures*, V. 198, Nov. 2019, Article No. 109542. doi: 10.1016/j.engstruct.2019.109542

10. ACI Committee 440, "Guide for the Design and Construction of Externally Bonded FRP Systems for Strengthening Concrete Structures (ACI 440.2R-17)," American Concrete Institute, Farmington Hills, MI, 2017, 112 pp.

11. Zou, X. K.; Teng, J. G.; De Lorenzis, L.; and Xia, S. H., "Optimal Performance-Based Design of FRP Jackets for Seismic Retrofit of Reinforced Concrete Frames," *Composites Part B: Engineering*, V. 38, No. 5-6, July-Sept. 2007, pp. 584-597. doi: 10.1016/j.compositesb.2006.07.016

12. Ager, P.; Eriksson, K.; Hansen, C. W.; and Lønstrup, L., "How the 1906 San Francisco Earthquake Shaped Economic Activity in the American West," *Explorations in Economic History*, V. 77, July 2020, Article No. 101342. doi: 10.1016/j.eeh.2020.101342

13. Wang, Y.; Kodur, V. K. R.; Fu, C.; Liu, C.; Zhou, H.; and Naser, M. Z., "Seismic Performance of Reinforced Concrete Frame Joints after Exposure to Fire," *ACI Structural Journal*, V. 118, No. 3, May 2021, pp. 3-14.

14. Chian, S. C., and Kolathayar, S., "Recent Advances in Earthquake Engineering—An Introduction," *Recent Advances in Earthquake Engineering: Select Proceedings of VCDRR 2021*, S. Kolathayar and S. C. Chian, eds., *Lecture Notes in Civil Engineering*, V. 175, Springer Nature, Singapore, 2022, pp. 1-8.

15. Mohan, A. T.; Van Coile, R.; Hopkin, D.; Jomaas, G.; and Caspeele, R., "Risk Tolerability Limits for Fire Engineering Design: Methodology and Reference Case Study," *Fire Technology*, V. 57, No. 5, Sept. 2021, pp. 2235-2267. doi: 10.1007/s10694-021-01118-w

16. Uchiyama, T.; Kawaguchi, K.; and Wakabayashi, T., "Effect of Simultaneous Consideration for Seismically Induced Events on Core Damage Frequency," *Journal of Power and Energy Systems*, V. 5, No. 3, 2011, pp. 360-375. doi: 10.1299/jpes.5.360

17. Wang, J. H.; Zhang, X.; Kunnath, S.; He, J.; and Xiao, Y., "Post-Earthquake Fire Resistance and Residual Seismic Capacity of Reinforced Concrete Columns," *ACI Structural Journal*, V. 118, No. 4, July 2021, pp. 123-136.

18. ACI Committee 318, "Building Code Requirements for Structural Concrete (ACI 318-19) and Commentary (ACI 318R-19) (Reapproved 2022)," American Concrete Institute, Farmington Hills, MI, 2019, 624 pp.

19. ASTM E119-20, "Standard Test Methods for Fire Tests of Building Construction and Materials," ASTM International, West Conshohocken, PA, 2020, 36 pp.

20. Haselton, C. B.; Goulet, C. A.; Mitrani-Reiser, J.; Beck, J. L.; Deierlein, G. G.; Porter, K. A.; Stewart, J. P.; and Taciroglu, E., "An Assessment to Benchmark the Seismic Performance of a Code-Conforming Reinforced Concrete Moment-Frame Building," PEER Report 2007/12, Pacific Earthquake Engineering Research Center, Berkeley, CA, 2008, 382 pp.

21. Moehle, J., *Seismic Design of Reinforced Concrete Buildings*, McGraw-Hill Professional, New York, 2014, 760 pp.

22. Williams, B.; Bisby, L.; Kodur, V.; Green, M.; and Chowdhury, E., "Fire Insulation Schemes for FRP-Strengthened Concrete Slabs," *Composites Part A: Applied Science and Manufacturing*, V. 37, No. 8, Aug. 2006, pp. 1151-1160. doi: 10.1016/j.compositesa.2005.05.028

23. Lahoti, M.; Tan, K. H.; and Yang, E.-H., "A Critical Review of Geopolymer Properties for Structural Fire-Resistance Applications," *Construction and Building Materials*, V. 221, Oct. 2019, pp. 514-526. doi: 10.1016/j.conbuildmat.2019.06.076

24. SDI, "Basic Fire Door, Fire Door Frame, Transom/Sidelight Frame, and Window Frame Requirements (SDI 118-19)," Steel Door Institute, Cleveland, OH, 2019, 12 pp.

25. Somerville, P. G.; Smith, N. F.; Graves, R. W.; and Abrahamson, N. A., "Modification of Empirical Strong Ground Motion Attenuation Relations to Include the Amplitude and Duration Effects of Rupture Directivity," *Seismological Research Letters*, V. 68, No. 1, Jan.-Feb. 1997, pp. 199-222. doi: 10.1785/gssrl.68.1.199

26. Foschaar, J. C.; Baker, J. W.; and Deierlein, G. G., "Preliminary Assessment of Ground Motion Duration Effects on Structural Collapse," 15th World Conference on Earthquake Engineering (15WCEE), Lisbon, Portugal, 2012, 10 pp.

27. Chandramohan, R.; Baker, J. W.; and Deierlein, G. G., "Quantifying the Influence of Ground Motion Duration on Structural Collapse Capacity Using Spectrally Equivalent Records," *Earthquake Spectra*, V. 32, No. 2, May 2016, pp. 927-950. doi: 10.1193/122813eqs298mr2

28. O'Meagher, A. J., and Bennetts, I. D., "Modelling of Concrete Walls in Fire," *Fire Safety Journal*, V. 17, No. 4, 1991, pp. 315-335. doi: 10.1016/0379-7112(91)90026-U

29. Hajiloo, H.; Green, M. F.; Noël, M.; Bénichou, N.; and Sultan, M., "Fire Tests on Full-Scale FRP Reinforced Concrete Slabs," *Composite Structures*, V. 179, Nov. 2017, pp. 705-719. doi: 10.1016/j.compstruct.2017.07.060

30. Griffis, C. A.; Masumura, R. A.; and Chang, C. I., "Thermal Response of Graphite Epoxy Composite Subjected to Rapid Heating," *Journal of Composite Materials*, V. 15, No. 5, Sept. 1981, pp. 427-442. doi: 10.1177/002199838101500503

31. EN 1992-1-2:2004, "Eurocode 2: Design of Concrete Structures - Part 1-2: General Rules - Structural Fire Design," European Committee for Standardization, Brussels, Belgium, 2004, 99 pp.

32. Chowdhury, E. U.; Bisby, L. A.; Green, M. F.; and Kodur, V. K. R., "Investigation of Insulated FRP-Wrapped Reinforced Concrete Columns in Fire," *Fire Safety Journal*, V. 42, No. 6-7, Sept.-Oct. 2007, pp. 452-460. doi: 10.1016/j.firesaf.2006.10.007

33. Chapiro, A., "Radiation Effects in Polymers," *Encyclopedia of Materials: Science and Technology*, second edition, K. H. Jürgen Buschow, M. C. Flemings, E. J. Kramer, P. Veyssière, R. W. Cahn, B. Ilschner, and S. Mahajan, eds., Elsevier, Amsterdam, the Netherlands, 2004, pp. 1-8.

34. Zhou, G.; Mikinka, E.; Golding, J.; Bao, X.; Sun, W.; and Ashby, A., "Investigation of Thermal Degradation and Decomposition of Both Pristine and Damaged Carbon/Epoxy Samples with Thermal History," *Composites Part B: Engineering*, V. 201, Nov. 2020, Article No. 108382. doi: 10.1016/j.compositesb.2020.108382

35. Zhou, F.; Zhang, J.; Song, S.; Yang, D.; and Wang, C., "Effect of Temperature on Material Properties of Carbon Fiber Reinforced Polymer (CFRP) Tendons: Experiments and Model Assessment," *Materials (Basel)*, V. 12, No. 7, Apr. 2019, Article No. 1025. doi: 10.3390/ma12071025

36. Lie, T. T., *Structural Fire Protection*, Manuals and Reports on Engineering Practice No. 78, American Society of Civil Engineers, Reston, VA, 1992.

37. Bai, Y., and Keller, T., "Time Dependence of Material Properties of FRP Composites in Fire," *Journal of Composite Materials*, V. 43, No. 21, Oct. 2009, pp. 2469-2485. doi: 10.1177/0021998309344641

38. Luo, Y.; Klima, K. M.; Brouwers, H. J. H.; and Yu, Q., "Effects of Ladle Slag on Class F Fly Ash Geopolymer: Reaction Mechanism and High Temperature Behavior," *Cement and Concrete Composites*, V. 129, May 2022, Article No. 104468. doi: 10.1016/j.cemconcomp.2022.104468

39. Xing, Z.; Beaucour, A.-L.; Hebert, R.; Noumowe, A.; and Ledesert, B., "Aggregate's Influence on Thermophysical Concrete Properties at Elevated Temperature," *Construction and Building Materials*, V. 95, Oct. 2015, pp. 18-28. doi: 10.1016/j.conbuildmat.2015.07.060

40. Rand, W., and Stummer, C., "Agent-Based Modeling of New Product Market Diffusion: An Overview of Strengths and Criticisms," *Annals of Operations Research*, V. 305, No. 1-2, Oct. 2021, pp. 425-447. doi: 10.1007/s10479-021-03944-1

41. Wilensky, U., and Rand, W., *An Introduction to Agent-Based Modeling: Modeling Natural, Social, and Engineered Complex Systems with NetLogo*, MIT Press, Cambridge, MA, 2015, 504 pp.

42. Weerasinghe, P.; Nguyen, K.; Mendis, P.; and Guerrieri, M., "Large-Scale Experiment on the Behaviour of Concrete Flat Slabs Subjected to Standard Fire," *Journal of Building Engineering*, V. 30, July 2020, Article No. 101255. doi: 10.1016/j.jobe.2020.101255

43. Bisby, L. A., "Fire Behaviour of Fibre-Reinforced Polymer (FRP) Reinforced or Confined Concrete," PhD thesis, Queen's University, Kingston, ON, Canada, 2003, 397 pp.

44. Zhou, F.; Pang, R.; Zhang, P.; and Cui, J., "Experimental Investigation of the Mechanical Properties of Carbon Fiber-Reinforced Polymer (CFRP) Tendons during and after Exposure to Elevated Temperatures," *Materials and Structures*, V. 55, No. 2, Mar. 2022, Article No. 82. doi: 10.1617/s11527-022-01923-x

45. Nawy, E. G., *Reinforced Concrete: A Fundamental Approach*, sixth edition, Pearson, Hoboken, NJ, 2009.

46. Paulay, T., and Priestley, M. J. N., *Seismic Design of Reinforced Concrete and Masonry Buildings*, John Wiley & Sons, Inc., New York, 1992, 768 pp.

47. Youssf, O.; ElGawady, M. A.; and Mills, J. E., "Displacement and Plastic Hinge Length of FRP-Confined Circular Reinforced Concrete Columns," *Engineering Structures*, V. 101, Oct. 2015, pp. 465-476. doi: 10.1016/j.engstruct.2015.07.026

48. Chopra, A. K., *Dynamics of Structures: Theory and Applications to Earthquake Engineering*, sixth edition, Pearson, London, UK, 2016.

49. ACI Committee 374, "Guide for Testing Reinforced Concrete Structural Elements under Slowly Applied Simulated Seismic Loads (ACI 374.2R-13)," American Concrete Institute, Farmington Hills, MI, 2013, 18 pp.

50. Ibarra, L. F.; Medina, R. A.; and Krawinkler, H., "Hysteretic Models That Incorporate Strength and Stiffness Deterioration," *Earthquake Engineering & Structural Dynamics*, V. 34, No. 12, Oct. 2005, pp. 1489-1511. doi: 10.1002/eqe.495

51. Haselton, C. B.; Liel, A. B.; Lange, S. T.; and Deierlein, G. G., "Beam-Column Element Model Calibrated for Predicting Flexural Response Leading to Global Collapse of RC Frame Buildings," PEER Report 2007/03, Pacific Earthquake Engineering Research Center, Berkeley, CA, 2008, 152 pp.

52. Paultre, P.; Boucher-Trudeau, M.; Eid, R.; and Roy, N., "Behavior of Circular Reinforced-Concrete Columns Confined with Carbon Fiber–Reinforced Polymers under Cyclic Flexure and Constant Axial Load," *Journal of Composites for Construction*, ASCE, V. 20, No. 3, June 2016, p. 04015065. doi: 10.1061/(ASCE)CC.1943-5614.0000624

53. Werkle, H., *Finite Elements in Structural Analysis: Theoretical Concepts and Modeling Procedures in Statics and Dynamics of Structures*, Springer Nature, Cham, Switzerland, 2021.

54. Leondes, C. T., *Structural Dynamic Systems Computational Techniques and Optimization: Finite Element Analysis (FEA) Techniques*, CRC Press, Boca Raton, FL, 2021.

55. Vamvatsikos, D., and Cornell, C. A., "Incremental Dynamic Analysis," *Earthquake Engineering & Structural Dynamics*, V. 31, No. 3, Mar. 2002, pp. 491-514. doi: 10.1002/eqe.141

56. ASCE/SEI 7-22, "Minimum Design Loads and Associated Criteria for Buildings and Other Structures," American Society of Civil Engineers, Reston, VA, 2022.

ACI STRUCTURAL JOURNAL

The American Concrete Institute (ACI) is a leading authority and resource worldwide for the development and distribution of consensus-based standards and technical resources, educational programs, and certifications for individuals and organizations involved in concrete design, construction, and materials, who share a commitment to pursuing the best use of concrete.

Individuals interested in the activities of ACI are encouraged to explore the ACI website for membership opportunities, committee activities, and a wide variety of concrete resources. As a volunteer member-driven organization, ACI invites partnerships and welcomes all concrete professionals who wish to be part of a respected, connected, social group that provides an opportunity for professional growth, networking, and enjoyment.

American Concrete Institute